



UNIVERSITAT DE
BARCELONA

Compositional Engineering of Colloidal Nanoparticles for Energy Conversion

Zhishan Luo

ADVERTIMENT. La consulta d'aquesta tesi queda condicionada a l'acceptació de les següents condicions d'ús: La difusió d'aquesta tesi per mitjà del servei TDX (www.tdx.cat) i a través del Dipòsit Digital de la UB (diposit.ub.edu) ha estat autoritzada pels titulars dels drets de propietat intel·lectual únicament per a usos privats emmarcats en activitats d'investigació i docència. No s'autoritza la seva reproducció amb finalitats de lucre ni la seva difusió i posada a disposició des d'un lloc aliè al servei TDX ni al Dipòsit Digital de la UB. No s'autoritza la presentació del seu contingut en una finestra o marc aliè a TDX o al Dipòsit Digital de la UB (framing). Aquesta reserva de drets afecta tant al resum de presentació de la tesi com als seus continguts. En la utilització o cita de parts de la tesi és obligat indicar el nom de la persona autora.

ADVERTENCIA. La consulta de esta tesis queda condicionada a la aceptación de las siguientes condiciones de uso: La difusión de esta tesis por medio del servicio TDR (www.tdx.cat) y a través del Repositorio Digital de la UB (diposit.ub.edu) ha sido autorizada por los titulares de los derechos de propiedad intelectual únicamente para usos privados enmarcados en actividades de investigación y docencia. No se autoriza su reproducción con finalidades de lucro ni su difusión y puesta a disposición desde un sitio ajeno al servicio TDR o al Repositorio Digital de la UB. No se autoriza la presentación de su contenido en una ventana o marco ajeno a TDR o al Repositorio Digital de la UB (framing). Esta reserva de derechos afecta tanto al resumen de presentación de la tesis como a sus contenidos. En la utilización o cita de partes de la tesis es obligado indicar el nombre de la persona autora.

WARNING. On having consulted this thesis you're accepting the following use conditions: Spreading this thesis by the TDX (www.tdx.cat) service and by the UB Digital Repository (diposit.ub.edu) has been authorized by the titular of the intellectual property rights only for private uses placed in investigation and teaching activities. Reproduction with lucrative aims is not authorized nor its spreading and availability from a site foreign to the TDX service or to the UB Digital Repository. Introducing its content in a window or frame foreign to the TDX service or to the UB Digital Repository is not authorized (framing). Those rights affect to the presentation summary of the thesis as well as to its contents. In the using or citation of parts of the thesis it's obliged to indicate the name of the author.

Programa de Doctorat en Nanociències

Compositional Engineering of Colloidal Nanoparticles for Energy Conversion

Tesi que presenta **Zhishan Luo**

per obtenir el títol de Doctor per la Universitat de Barcelona

Directors de la tesi:

Prof. Andreu Cabot Codina i Dra. Maria Ibáñez Sabaté

Tutor de la tesi:

Dra. Anna M. Vilà Arbonés

Departament d'Electrònica

Institut de Recerca en Energia de Catalunya (IREC)



UNIVERSITAT DE
BARCELONA

Contents

List of acronyms used in this work	1
Acknowledgements	2
Preface: Publications and summary of the thesis	4
Prefacio: Publicaciones y resumen de la tesis.....	11
Chapter: General Introduction	18
1.1 The energy challenge.....	19
1.2 Colloidal NPs for energy conversion and storage	20
1.3 Colloidal synthesis of NPs	20
1.3.1 General Solution-based Strategy to Colloidal synthesis of NPs.....	21
1.3.2 Strategies for NP engineering.....	25
1.4 Objectives of the thesis	29
Chapter 2: Semiconductor NPs and HNPs.....	30
2.1 CZTS NCs	31
2.1.1 Synthesis of copper-based chalcogenides NPs.....	31
2.1.2 Scalable Heating-Up Synthesis of Monodisperse $\text{Cu}_2\text{ZnSnS}_4$ NCs.....	37
2.1.2 $\text{Cu}_2\text{ZnSnS}_4$ Nanocrystals as Highly Active and Stable Electrocatalysts for the Oxygen Reduction Reaction.....	48
2.2 Synthesis of CZTS-based HNPs and their potential photocatalytic application	62
2.2.1 $\text{Cu}_2\text{ZnSnS}_4$ -Pt and $\text{Cu}_2\text{ZnSnS}_4$ -Au Heterostructured NPs for Photocatalytic Water Splitting and Pollutant Degradation	65
2.2.2 $\text{Cu}_2\text{ZnSnS}_4$ - Ag_2S Nanoscale p-n Heterostructures as Sensitizers for Photoelectrochemical Water Splitting.....	78
Chapter 3: Multimetallic NPs and Their Catalytic Property	93
3.1 Multimetallic NPs and their catalytic property	94
3.1.1 Synthesis of multimetallic NPs.....	94
3.1.2 Size and Aspect Ratio Control of Pd_2Sn Nanorods and Their Water Denitration Properties.....	100
3.1.3 Pd_2Sn nanorods as Highly Active and Stable Catalyst for Ethanol Oxidation Reaction	120
3.1.4 Au- Pd_2Sn heterostructures nanoalloy: tuning alloy composition and catalytic property	129
Chapter 4: Heterostructured Metal Oxide NPs and Their Electrocatalytic Properties... 157	
4.1 Heterostructured metal oxide NPs and their electrocatalytic properties	158

4.1.1 HNPs based on colloidal NCs	158
4.1.2 $\text{Mn}_3\text{O}_4@\text{CoMn}_2\text{O}_4\text{-Co}_x\text{O}_y$ Nanoparticles: Partial Cation Exchange Synthesis and Electrocatalytic Properties Toward the Oxygen Reduction and Evolution Reactions	165
4.1.3 4.1.3 $\text{Fe}_3\text{O}_4@\text{NiFe}_x\text{O}_y$ Nanoparticles with Enhanced Electrocatalytic Properties for Oxygen Evolution in Carbonate Electrolyte	197
Chapter 5: Conclusions	236
References	239
Curriculum Vitae	250

List of acronyms used in this work

NP – Nanoparticle

NC – Nanocrystal

NR – Nanorod

HNP – Heterostructured nanoparticles

CZTS – $\text{Cu}_2\text{ZnSnS}_4$

ORR – Oxygen reduction reaction

OER – Oxygen evolution reaction

EOR – Ethanol oxidation reaction

CIS – CuInS_2

CZTSe – $\text{Cu}_2\text{ZnSnSe}_4$

CIGS – $\text{Cu}_2\text{InGaS}_4$

CISE – Cu_2InSe_2

OLA – Oleylamine

ODE – Octadecene

OA – Oleic acid

TOP – Tri-n-cetylphosphine

DDT – Dodecanethiol

TEM – Transmission electron microscopy

HRTEM – High-resolution transmission electron microscopy

XRD – X-ray diffraction

XPS – X-ray photoelectron spectroscopy

SEM – Scanning electron microscopy

EDS – Energy dispersive X-ray spectroscopy

SERS – Surface-Enhanced Raman Scattering

Acknowledgements

When I first time came to Barcelona four years ago to start my PhD research work, I knew it would be a wonderful and memorable journey in my life. Actually it has been. I have met many people in this amazing city and worked with them at IREC and University of Barcelona. So, it is time to say my gratitude to them.

Firstly, I would like to give sincere thanks to my supervisors, Prof. Andreu Cabot and Dr. Maria Ibáñez. Thank you for both guiding my research work during four years. You let me know “hard work does pay off”. Thanks Andreu, offering me the opportunity to join the Functional Nanomaterials group at IREC, open a new door in science for me, under your guidance, I learn how do a right scientific work and to be a researcher. You deeply impress me not only scientifically but also in life experience with your wisdom and learnedness, it will be a huge influence on my futrue career. Thanks Maria, you showed me my first colloidal synthesis in the laboratory, and introduced me into the world of material chemistry. You always opened to new ideas and provided helpful guidance which I benefited greatly by improving my creativity and indenpedence on my research. Conducting research sometimes can be very diffcult, but Andreu and Maria, you both never let me get bored with science.

I joyfully express my deepest gratitude to all the members of the Functional Nanomaterials group at IREC: Alexey, Raquel, Doris, Alex, Silvia, Alejandro, Gihan, Pablo, Marcos Batista, Michaela, Taisiia, Oleksandr, Evgenii and, Marcos Sanles. I will not forget thevery useful discussions and help provided on my experiments and in the laboratory. I won't neither forget when we drove to France for the EMRS meeting; our *calçotadas* every year. I won't forget wheb we play basketball and other funny sports. There are a lot of unforgettable and happy moments together, they will be fantastic memories in my life.

Also, I would like to thank people from other groups at IREC. Thank toErdem and Cristian for their extraordinary experimental work in our collaborative project. I am very thankful to Jordi, Aziz and Sara for checking HRTEM of my samples, their nice work play an important role on my papers and reasearch work.

I would like to give a special thank to the Chinese community in IREC: Fan, Shaofeng, Wenhua, Haibing, Xianyun, Xuelian, Liu, Yu, Junfeng, Xiaoting, Kai pan, Pengyi, Yue, Junshan and Yong. I am really lucky to know them and work with them. The each “eating time” with talking something interesting in chinese always made me very pleasant and relaxed. Because of them, my life in Barcelona would not be duller and they have a special meaning in my abroad study experience.

I also need to thank the China Scholarship Council for providing me the financial support for my PhD research work.

I am appreciative to my beloved family. Thank to them for their constant love and unconditional support to do anything I wanted to do. Last but not the least, I would like to express my gratitude to Tiantian, who has light up my life and inspired me to move on. Thank you for your love and I love you!

Preface

Publications and summary of the thesis

This PhD thesis is based on research work performed by the PhD candidate Zhishan Luo at the Catalonia Institute for Energy Research (IREC) in Sant Adrià de Besòs (Barcelona-Spain), from 2012 to 2016, and supported by Chinese Scholarship Council (No. 201206740024). The thesis is particularly focused on the design, synthesis, manipulation and application of multi-component NPs, which have unique electronic and optical properties suitable for energy applications.

The thesis is built around 9 articles in preparation for or published in peer-reviewed journals presented below these lines. These collection of articles are in agreement with the requirements for the Doctor of Philosophy in Nanoscience at the Physics Faculty at the University of Barcelona.

1. Yu, X.; Shavel, A.; An, X.; **Luo, Z.**; Ibáñez, M.; Cabot, A. Cu₂ZnSnS₄-Pt and Cu₂ZnSnS₄-Au Heterostructured Nanoparticles for Photocatalytic Water Splitting and Pollutant Degradation. *J. Am. Chem. Soc.* **2014**, *136* (26), 9236-9239.
2. **Luo, Z.**; Ibáñez, M.; Antolin, A. M.; Genç, A.; Shavel, A.; Contreras, S.; Medina, F.; Arbiol, J.; Cabot, A. Size and Aspect Ratio Control of Pd₂Sn Nanorods and Their Water Denitration Properties. *Langmuir* **2015**, *31* (13), 3952-3957.
3. Yu, X.; Liu, J.; Genç, A.; Ibáñez, M.; **Luo, Z.**; Shavel, A.; Arbiol, J.; Zhang, G.; Zhang, Y.; Cabot, A. Cu₂ZnSnS₄-Ag₂S Nanoscale p-n Heterostructures as Sensitizers for Photoelectrochemical Water Splitting. *Langmuir* **2015**, *31* (38), 10555-10561.
4. Shavel, A.; Ibáñez, M.; **Luo, Z.**; De Roo, J.; Carrete, A.; Dimitrievska, M.; Genç, A.; Meyns, M.; Pérez-Rodríguez, A.; Kovalenko, M. V.; Arbiol, J.; Cabot, A. Scalable Heating-Up Synthesis of Monodisperse Cu₂ZnSnS₄ Nanocrystals. *Chem. Mater.* **2016**, *28*(3), 720-726.
5. **Luo, Z.**; Irtem, E.; Ibáñez, M.; Nafria, R.; Martí, S.; Genç, A.; Mata, M.; Liu, Y.; Cadavid, D.; Llorca, J.; Arbiol, J.; Andreu, T.; Morante, J. R.; Cabot, A. Mn₃O₄@CoMn₂O₄-Co_xO_y Nanoparticles: Partial Cation Exchange Synthesis and Electrocatalytic Properties Toward the Oxygen Reduction and Evolution Reactions. *ACS Appl. Mater. Interfaces.* **2016**, *8*(27), 17435-17444.
6. **Luo, Z.**; Martí, S.; Nafria, R.; Joshua, G.; Mata, M.; Guardia, P.; Boubeta, C.; Simeonidis, K.; Llorca, J.; Arbiol, J.; Ibáñez, M.; Cabot, A. Fe₃O₄@NiFe_xO_y Nanoparticles with Enhanced Electrocatalytic Properties for Oxygen Evolution in Carbonate Electrolyte. *ACS Appl. Mater. Interfaces.* Just Accepted.
7. **Luo, Z.**; Lu, J.; Flox, C.; Nafria, R.; Genç, A.; Arbiol, J.; Llorca, J.; Ibáñez, M.; Morante, J. R.; Cabot, A. Pd₂Sn [010] Nanorods as a Highly Active and Stable Ethanol Oxidation Catalyst. *J. Mater. Chem. A.* Major corrections required (under second round review)

8. Nafria, R.; **Luo, Z.**; Ibáñez, M.; Marti, S.; Mata, M.; Llorca, J.; Arbiol, J.; Kovalenko, M. V.; Grabulosa, A.; Muller, G.; Cabot, A. Pd₂Sn and Au-Pd₂Sn Nanorods in Catalytic Hydrogenation and Sonogashira Coupling Reactions. Submitted.
9. Yu, X.; Wang, D.; Liu, J.; **Luo, Z.**; Du, R.; Liu, L-M.; Zhang, G.; Zhang, Y.; Cabot, A. Cu₂ZnSnS₄ Nanocrystals as Highly Active and Stable Electrocatalysts for the Oxygen Reduction Reaction. Submitted.

The thesis is structured into five chapters. The first chapter is an introduction to the synthesis of colloidal NPs. The second chapter is divided into two parts, one focus on the synthesis and characterization of CZTS NPs and the other of CZTS-based HNPs. In the first part, a high-yield and easily scalable synthesis protocol to produce CZTS NPs, with high compositional and morphological uniformities is presented. This work was published earlier this year on the journal Chemistry of Materials with the title “Scalable heating-up synthesis of monodisperse Cu₂ZnSnS₄ nanocrystals”. Additionally, CZTS NPs with different crystal structures (kesterite vs wurtzite) were tested as electrocatalysts for the ORR measurements. First-principles calculations and experiments both indicated that kesterite CZTS NPs exhibit improved electrocatalytic activities toward ORR. This work, entitled “Cu₂ZnSnS₄ Nanocrystals as Highly Active and Stable Electrocatalysts for the Oxygen Reduction Reaction” has been submitted and is currently under review. In the second part of chapter 2, an epitaxial method to prepare CZTS-based HNPs and their use as photocatalysis is presented, particularly, semiconductor-metal heterostructures such as CZTS-Au and CZTS-Pt or p-n semiconductor junction such as CZTS-Ag₂S. In all cases the HNPs were tested as sensitizers for photoelectrochemical applications. The results of these works were published in Journal of the American Chemical Society in 2014 and Langmuir in 2015 with the titles “Cu₂ZnSnS₄-Pt and Cu₂ZnSnS₄-Au Heterostructured Nanoparticles for Photocatalytic Water Splitting and Pollutant Degradation” and “Cu₂ZnSnS₄-Ag₂S Nanoscale p-n Heterostructures as Sensitizers for Photoelectrochemical Water Splitting” respectively.

The third chapter includes the development of highly active, low cost and stable multi-metallic NPs and their use as catalyst for different reactions. In the first part of the chapter, a solution phase synthesis to produce Pd₂Sn NPs with control of morphology and size was developed by co-reducing metal salts in the presence of TOP, amine, and chloride ions. Depending on reaction conditions a preferential organic ligand desorption from Pd₂Sn NPs tip facets could be promoted enabling the growth of asymmetric Pd₂Sn NPs. Additionally, the influence of NP size and geometry on the catalytic properties was studied. In particular, we evaluated them for the reduction of nitrophenol, water denitration and EOR. This part of the chapter is based on the following publications: “Size and Aspect Ratio Control of Pd₂Sn Nanorods and Their Water Denitration Properties” published on Langmuir in 2015 and “Pd₂Sn [010] Nanorods as a Highly Active and Stable Ethanol Oxidation Catalyst” under review. In the second part of this chapter, we report a procedure based on a galvanic replacement reaction to grow Au NPs onto Pd₂Sn NRs, hence producing Au-Pd₂Sn HNPs. Finally, in both cases, either Pd₂Sn or Au-Pd₂Sn NPs, we studied and compared their performance in alkene and alkyne hydrogenation and in Sonogashira coupling reactions. An

article entitled “Pd₂Sn and Au-Pd₂Sn Nanorods in Catalytic Hydrogenation and Sonogashira Coupling Reactions” is under revision.

The fourth chapter is focused on heterostructured metal oxide colloidal NPs and their electrocatalytic properties. The first part of the chapter presents a simple and effective method to produce core-shell Mn₃O₄@CoMn₂O₄ and Mn₃O₄@CoMn₂O₄-CoO NPs by selecting different cobalt precursors. Both types of NPs exhibited superior activity and stability versus commercial electrocatalysts for ORR/OER reaction in alkaline solution. This part of the chapter is based on the paper published earlier this year entitled “Mn₃O₄@CoMn₂O₄-Co_xO_y Nanoparticles: Partial Cation Exchange Synthesis and Electrocatalytic Properties Toward the Oxygen Reduction and Evolution Reactions”. The second part of this chapter is a case study on ultrathin transition metal oxide shell coating iron oxide NPs system for water oxidation in carbonate electrolyte. An article with the title “Fe₃O₄@NiFe_xO_y Nanoparticles with Enhanced Electrocatalytic Properties for Oxygen Evolution in Carbonate Electrolyte” has been recently accepted in ACS Applied Material and Interfaces.

The final chapter of the thesis includes a summary and conclusions of the work.

Finally, during the development of this PhD, Zhishan Luo has participated on different side projects that end up on the following publications which are not included in this thesis:

1. Ibáñez, M.; **Luo, Z.**; Genç, A.; Piveteau, L.; Ortega, S.; Cadavid, D.; Dobrozhan, O.; Liu, Y.; Nachttegaal, M.; Zebarjadi, M.; Arbiol, J.; Kovalenko, M. V.; Cabot, A. High-Performance Thermoelectric Nanocomposites from Nanocrystal Building Blocks. *Nat. Commun.* **2016**, 7, 10766.10.1038/ncomms10766.
2. Ibáñez, M.; Korkosz, R. J.; **Luo, Z.**; Riba, P.; Cadavid, D.; Ortega, S.; Cabot, A.; Kanatzidis, M. G. Electron Doping in Bottom-up Engineered Thermoelectric Nanomaterials through HCl-Mediated Ligand Displacement. *J. Am. Chem. Soc.* **2015**, 137, 4046–4049.

Authors' contributions to publications in the thesis

The work presented in this thesis has been carried out at the Electronics Department of the Physics Faculty at the University of Barcelona and at the Advanced Material Research Department of the Catalonia Institute for Energy Research. Zhishan Luo has contributed to the design and coordination of the experiments work, data analysis, and manuscript writing of all the publications presented. The impact factor of the corresponding journal is provided for each publication. None of these publications has been previously presented in any other PhD dissertation. In all the publications, Andreu Cabot and Maria Ibáñez coordinated and strongly participated in the designing and writing of all the papers.

Chapter 2:

1. Yu, X.; Shavel, A.; An, X.; **Luo, Z.**; Ibáñez, M.; Cabot, A. Cu₂ZnSnS₄-Pt and Cu₂ZnSnS₄-Au Heterostructured Nanoparticles for Photocatalytic Water Splitting and Pollutant Degradation. *J. Am. Chem. Soc.* **2014**, *136* (26), 9236-9239.

Impact factor 2015: 13.038

In this work, Z. Luo participated in the materials synthesis, characterization and discussion. X. Yu designed the experiments and wrote the paper. A. Shavel and X. An participated in the materials characterization and discussion.

2. Shavel, A.; Ibáñez, M.; **Luo, Z.**; De Roo, J.; Carrete, A.; Dimitrievska, M.; Genç, A.; Meyns, M.; Pérez-Rodríguez, A.; Kovalenko, M. V.; Arbiol, J.; Cabot, A. Scalable Heating-Up Synthesis of Monodisperse Cu₂ZnSnS₄ Nanocrystals. *Chem. Mater.* **2016**, *28*(3), 720-726.

Impact factor 2015: 9.407

In this work, Z. Luo participated in the materials synthesis, characterization and discussion. A. Shavel designed the experiments and wrote the paper. J. De Roo, A. Carrete, M. Dimitrievska, M. Meyns, A. Pérez-Rodríguez and M. V. Kovalenko participated in the materials characterization, measurements and discussion. Genç, A. and Arbiol, J. performed the HRTEM analysis and atomic models.

3. Yu, X.; Liu, J.; Genç, A.; Ibáñez, M.; **Luo, Z.**; Shavel, A.; Arbiol, J.; Zhang, G.; Zhang, Y.; Cabot, A. Cu₂ZnSnS₄-Ag₂S Nanoscale p-n Heterostructures as Sensitizers for Photoelectrochemical Water Splitting. *Langmuir* **2015**, *31* (38), 10555-10561.

Impact factor 2015: 3.993

In this work, Z. Luo participated in the materials synthesis, characterization and discussion. X. Yu designed the experiments and wrote the paper. J. Liu, A. Shavel, G. Zhang and Y. Zhang participated in the materials characterization, measurements and discussion. Genç, A. and Arbiol, J. performed the HRTEM analysis and atomic models.

4. Yu, X.; Wang, D.; Liu, J.; **Luo, Z.**; Du, R.; Liu, L-M.; Zhang, G.; Zhang, Y.; Cabot, A. Cu₂ZnSnS₄ Nanocrystals as Highly Active and Stable Electrocatalysts for the Oxygen Reduction Reaction. (Submitted)

In this work, Z. Luo participated in the materials synthesis, characterization and discussion. X. Yu designed the experiments and wrote the paper. D. Wand, R. Du, L-M. Liu, G. Zhang and Y. Zhang participated in the characterization, measurements, discussion and DFT calculation.

Chapter 3:

5. **Luo, Z.**; Ibáñez, M.; Antolin, A. M.; Genç, A.; Shavel, A.; Contreras, S.; Medina, F.; Arbiol, J.; Cabot, A. Size and Aspect Ratio Control of Pd₂Sn Nanorods and Their Water Denitration Properties. *Langmuir* **2015**, *31* (13), 3952-3957.

Impact factor 2015: 3.993

In this work, Z. Luo designed the experiments and wrote the paper. A. Genç and J. Arbiol performed the HRTEM analysis and atomic models. A. M. Antolin, A. Shavel, S. Contreras and F. Medina participated in the materials synthesis, characterization, measurements and discussion.

6. **Luo, Z.**; Lu, J.; Flox, C.; Nafria, R.; Genç, A.; Arbiol, J.; Llorca, J.; Ibáñez, M.; Morante, J. R.; Cabot, A. Pd₂Sn [010] Nanorods as a Highly Active and Stable Ethanol Oxidation Catalyst. *J. Mater. Chem. A*. Major corrections required (under second round review).

Impact factor 2015: 8.262

In this work, Z. Luo designed the experiments and wrote the paper. A. Genç, and J. Arbiol performed the HRTEM analysis and atomic models. J. Lu, C. Flox, R. Nafria and J. R. Morante participated in the materials synthesis, characterization, measurements and discussion.

7. Nafria, R.; **Luo, Z.**; Ibáñez, M.; Marti, S.; Mata, M.; Llorca, J.; Arbiol, J.; Kovalenko, M. V.; Grabulosa, A.; Muller, G.; Cabot, A. Pd₂Sn and Au-Pd₂Sn Nanorods in Catalytic Hydrogenation and Sonogashira Coupling Reactions (Submitted)

In this work, R. Nafria and Z. Luo designed the experiments and wrote the paper. S. Marti, M. Mata and J. Arbiol performed the HRTEM analysis and atomic models. J. Llorca, M. V. Kovalenko, A. Grabulosa, and G.

Muller participated in the materials synthesis, characterization, measurements and discussion.

Chapter 4:

8. **Luo, Z.**; Irtem, E.; Ibáñez, M.; Nafria, R.; Marti, S.; Genç, A.; Mata, M.; Liu, Y.; Cadavid, D.; Llorca, J.; Arbiol, J.; Andreu, T.; Morante, J. R.; Cabot, A. $\text{Mn}_3\text{O}_4@\text{CoMn}_2\text{O}_4\text{-Co}_x\text{O}_y$ Nanoparticles: Partial Cation Exchange Synthesis and Electrocatalytic Properties Toward the Oxygen Reduction and Evolution Reactions. *ACS Appl. Mater. Interfaces*. **2016**, 8(27), 17435-17444.

Impact factor 2015: 7.145

In this work, Z. Luo and E. Irtem designed the experiments and wrote the paper together. S. Marti, M. Mata and J. Arbiol performed the HRTEM analysis and atomic models. R. Nafria, Y. Liu, D. Cadavid, J. Llorca, T. Andreu and J. R. Morante participated in the materials synthesis, characterization, measurements and discussion.

9. **Luo, Z.**; Marti, S.; Nafria, R.; Joshua, G.; Mata, M.; Guardia, P.; Flox, C.; Boubeta, C.; Simeonidis, K.; Llorca, J.; Morante, J. R.; Arbiol, J.; Ibáñez, M.; Cabot, A. $\text{Fe}_3\text{O}_4@\text{NiFe}_x\text{O}_y$ Nanoparticles with Enhanced Electrocatalytic Properties for Oxygen Evolution in Carbonate Electrolyte. *ACS Appl. Mater. Interfaces*. Accepted.

Impact factor 2015: 7.145

In this work, Z. Luo designed the experiments and wrote the paper. S. Marti, M. Mata and J. Arbiol performed the HRTEM analysis and atomic models. R. Nafria, G. Joshua, P. Guardia, C. Flox, C. Boubeta, K. Simeonidis, J. Llorca and J. R. Morante participated in the materials synthesis, characterization, measurements and discussion.

Prof. Andreu Cabot

and Dr. Maria Ibáñez



certify the information provided above is true.

Barcelona, 09/30/2016

Prefacio

Publicaciones y resumen de la tesis

Esta tesis doctoral se basa en el trabajo de investigación realizado por el doctorando Zhishan Luo en el Instituto de Investigación en Energía de Cataluña (IREC) en Sant Adrià de Besòs (Barcelona) entre 2012 y 2016. La tesis fue parcialmente financiada por el Consejo de Becas de China (Nº 201206740024).

La tesis está basada en 9 artículos en proceso de publicación o bien ya publicados en revistas especializadas. Dichos artículos están enumerados debajo de estas líneas y cumplen los requisitos para obtener el título de Doctor en Filosofía en Nanociencia en la Facultad de Física de la Universidad de Barcelona:

1. Yu, X.; Shavel, A.; An, X.; **Luo, Z.**; Ibáñez, M.; Cabot, A. Cu₂ZnSnS₄-Pt and Cu₂ZnSnS₄-Au Heterostructured Nanoparticles for Photocatalytic Water Splitting and Pollutant Degradation. *J. Am. Chem. Soc.* **2014**, *136* (26), 9236-9239.
2. **Luo, Z.**; Ibáñez, M.; Antolin, A. M.; Genç, A.; Shavel, A.; Contreras, S.; Medina, F.; Arbiol, J.; Cabot, A. Size and Aspect Ratio Control of Pd₂Sn Nanorods and Their Water Denitration Properties. *Langmuir* **2015**, *31* (13), 3952-3957.
3. Yu, X.; Liu, J.; Genç, A.; Ibáñez, M.; **Luo, Z.**; Shavel, A.; Arbiol, J.; Zhang, G.; Zhang, Y.; Cabot, A. Cu₂ZnSnS₄-Ag₂S Nanoscale p-n Heterostructures as Sensitizers for Photoelectrochemical Water Splitting. *Langmuir* **2015**, *31* (38), 10555-10561.
4. Shavel, A.; Ibáñez, M.; **Luo, Z.**; De Roo, J.; Carrete, A.; Dimitrievska, M.; Genç, A.; Meyns, M.; Pérez-Rodríguez, A.; Kovalenko, M. V.; Arbiol, J.; Cabot, A. Scalable Heating-Up Synthesis of Monodisperse Cu₂ZnSnS₄ Nanocrystals. *Chem. Mater.* **2016**, *28*(3), 720-726.
5. **Luo, Z.**; Irtem, E.; Ibáñez, M.; Nafria, R.; Marti, S.; Genç, A.; Mata, M.; Liu, Y.; Cadavid, D.; Llorca, J.; Arbiol, J.; Andreu, T.; Morante, J. R.; Cabot, A. Mn₃O₄@CoMn₂O₄-Co_xO_y Nanoparticles: Partial Cation Exchange Synthesis and Electrocatalytic Properties Toward the Oxygen Reduction and Evolution Reactions. *ACS Appl. Mater. Interfaces.* **2016**, *8*(27), 17435-17444.
6. **Luo, Z.**; Marti, S.; Nafria, R.; Joshua, G.; Mata, M.; Guardia, P.; Boubeta, C.; Simeonidis, K.; Llorca, J.; Arbiol, J.; Ibáñez, M.; Cabot, A. Fe₃O₄@NiFe_xO_y Nanoparticles with Enhanced Electrocatalytic Properties for Oxygen Evolution in Carbonate Electrolyte. *ACS Appl. Mater. Interfaces.* Aceptado.
7. **Luo, Z.**; Lu, J.; Flox, C.; Nafria, R.; Genç, A.; Arbiol, J.; Llorca, J.; Ibáñez, M.; Morante, J. R.; Cabot, A. Pd₂Sn [010] Nanorods as a Highly Active and Stable Ethanol Oxidation Catalyst. *J. Mater. Chem. A.* Bajo revisión.
8. Nafria, R.; **Luo, Z.**; Ibáñez, M.; Marti, S.; Mata, M.; Llorca, J.; Arbiol, J.; Kovalenko, M. V.; Grabulosa, A.; Muller, G.; Cabot, A. Pd₂Sn and Au-Pd₂Sn Nanorods in Catalytic Hydrogenation and Sonogashira Coupling Reactions. Enviado.

9. Yu, X.; Wang, D.; Liu, J.; **Luo, Z.**; Du, R.; Liu, L-M.; Zhang, G.; Zhang, Y.; Cabot, A. Cu₂ZnSnS₄ Nanocrystals as Highly Active and Stable Electrocatalysts for the Oxygen Reduction Reaction. Enviado.

El objetivo principal de esta tesis se centra en el diseño e ingeniería de nanopartículas (NPs) coloidales y su aplicación en la conversión y almacenamiento de energía. Esto incluye principalmente la síntesis y caracterización de NP coloidales semiconductoras, metálicas y basadas en óxidos, y la exploración a fondo de sus propiedades (electro/foto) catalíticas. Se prestó especial atención es la síntesis y caracterización de NPs de calcogenuros de cobre, óxido de metales de transición y NPs multimetálicas.

El capítulo dos de la tesis trata sobre NPs de calcogenuros de cobre. El trabajo está centrado en el desarrollo de rutas sintéticas para producir NPS de Cu₂ZnSnS₄ (CZTS) y heteroestructuras a partir de CZTS: CZTS-Au, CZTS-Pt y CZTS-Ag₂S. La composición, el tamaño y la forma de las NPS se controlaron mediante la regulación de la concentración de precursor, el uso de tensioactivos, el burbujeo de gas y el ajuste de la rampa de calentamiento. Utilizamos estas NPS como fotocatalizadores para la degradación de tintes y para la producción de hidrogeno a partir del agua y también como electrocatalizadores para la reacción de reducción de oxígeno. En la tesis se presentan los cuatro artículos resultantes de estos trabajos después de un breve resumen para cada artículo.

El tercer capítulo trata sobre NPs multimetálicas. Se desarrollaron métodos de síntesis para producir nanorods (NRs) de Pd₂Sn y para el crecimiento de dominios cristalográficos de Au encima de estos: Au-Pd₂Sn. Se determinó así mismo el mecanismo de control de la morfología de las NPs de estos materiales. Estas NPs se utilizaron con éxito en diversas aplicaciones catalíticas. Las NPs de Pd₂Sn se utilizaron para la reducción de nitrofenol y la desnitrificación del agua. También se usaron para la reacción electrocatalítica de oxidación del etanol. Se compararon los resultados obtenidos con los NRs con partículas de igual composición pero con morfología esférica y también con NPs de Pd esféricas. Se observó que los NRs resultaban en mejores actividades. Las NPs de Au-Pd₂Sn fueron investigadas para reacciones de hidrogenación y de acoplamiento. En la tesis se presentan los tres artículos resultantes de estos trabajos después de un breve resumen para cada artículo.

El cuarto capítulo de la tesis trata de NPs de óxidos metálicos. NPs heteroestructuradas de Mn₃O₄@CoMn₂O₄-CoO se prepararon mediante la reacción de intercambio catiónico parcial a partir de semillas de Mn₃O₄. Tales heteroestructuras mostraron una excepcional actividad electrocatalítica y estabilidad para las reacciones de reducción y evolución de oxígeno en solución alcalina. En base a esta vía de síntesis coloidal, NPs de Fe₃O₄@Ni_xFe_{3-x}O₄ fueron obtenidas mediante la reacción de precursores de perclorato de níquel con semillas de Fe₃O₄. Estas NPs se usaron como electrocatalizadores de oxidación de agua, demostrando una excepcional actividad catalítica. En la tesis se presentan los tres artículos resultantes de estos trabajos después de un breve resumen para cada artículo.

El último capítulo de la tesis incluye un resumen de la tesis y las conclusiones del trabajo.

Finalmente, durante el desarrollo de esta tesis Zhishan Luo participó diferentes proyectos paralelos que terminaron en los siguientes artículos pero no se incluyen en esta tesis:

1. Ibáñez, M.; **Luo, Z.**; Genç, A.; Piveteau, L.; Ortega, S.; Cadavid, D.; Dobrozhan, O.; Liu, Y.; Nachtegaal, M.; Zebarjadi, M.; Arbiol, J.; Kovalenko, M. V.; Cabot, A. High-Performance Thermoelectric Nanocomposites from Nanocrystal Building Blocks. *Nat. Commun.* **2016**, *7*, 10766.10.1038/ncomms10766.

2. Ibáñez, M.; Korkosz, R. J.; **Luo, Z.**; Riba, P.; Cadavid, D.; Ortega, S.; Cabot, A.; Kanatzidis, M. G. Electron Doping in Bottom-up Engineered Thermoelectric Nanomaterials through HCl-Mediated Ligand Displacement. *J. Am. Chem. Soc.* **2015**, *137*, 4046–4049.

Contribuciones de los autores a las publicaciones que aparecen en la tesis

El trabajo presentado en esta tesis ha sido llevado a cabo en el Departamento de Electrónica de la Facultad de Física en la Universitat de Barcelona y en el Área de Materiales Avanzados para la Energía del Institut de Recerca en Energia de Catalunya. Zhishan Luo ha contribuido al diseño y coordinación del trabajo experimental, el análisis de los resultados y a la escritura del manuscrito de todas las publicaciones aquí presentadas. El factor de impacto de 2015 de la revista se muestra para cada publicación. Ninguna de estas publicaciones ha sido previamente incluida en ninguna otra defensa de tesis doctoral. Andreu Cabot y Maria Ibáñez coordinaron y participaron activamente en el diseño y redacción de cada publicación.

Capítulo 2:

1. Yu, X.; Shavel, A.; An, X.; **Luo, Z.**; Ibáñez, M.; Cabot, A. Cu₂ZnSnS₄-Pt and Cu₂ZnSnS₄-Au Heterostructured Nanoparticles for Photocatalytic Water Splitting and Pollutant Degradation. *J. Am. Chem. Soc.* **2014**, *136* (26), 9236-9239.

Factor de impacto 2015: 13.038

En este trabajo, Z. Luo participó en la síntesis de los materiales, su caracterización y discusión de los resultados. X. Yu diseñó el experimento y escribió el manuscrito. A. Shavel y X. An participaron en la caracterización y discusión de los resultados.

2. Shavel, A.; Ibáñez, M.; **Luo, Z.**; De Roo, J.; Carrete, A.; Dimitrievska, M.; Genç, A.; Meyns, M.; Pérez-Rodríguez, A.; Kovalenko, M. V.; Arbiol, J.; Cabot, A. Scalable Heating-Up Synthesis of Monodisperse Cu₂ZnSnS₄ Nanocrystals. *Chem. Mater.* **2016**, *28*(3), 720-726.

Factor de impacto 2015: 9.407

En este trabajo, Z. Luo participó en la síntesis de los materiales, su caracterización y discusión de los resultados. A. Shavel diseñó el experimento y escribió el documento. J. De Roo, A. Carrete, M. Dimitrievska, M. Meyns, A. Pérez-Rodríguez y M. V. Kovalenko participaron en la caracterización de los materiales, medidas y análisis de los resultados. Genç, A. y Arbiol, J. realizaron el análisis HRTEM y el análisis de modelos atómicos.

3. Yu, X.; Liu, J.; Genç, A.; Ibáñez, M.; **Luo, Z.**; Shavel, A.; Arbiol, J.; Zhang, G.; Zhang, Y.; Cabot, A. Cu₂ZnSnS₄-Ag₂S Nanoscale p-n Heterostructures as Sensitizers for Photoelectrochemical Water Splitting. *Langmuir* **2015**, *31* (38), 10555-10561.

Factor de impacto 2015: 3.993

En este trabajo, Z. Luo realizó la síntesis de los materiales, su caracterización y discusión de los resultados. X. Yu diseñó el experimento y escribió el manuscrito. J. Liu, A. Shavel, G. Zhang y Y. Zhang participaron en la caracterización de los materiales, las mediciones realizadas y el análisis de datos. Genç, A. y Arbiol, J. realizaron el análisis HRTEM y el análisis de modelos atómicos.

4. Yu, X.; Wang, D.; Liu, J.; **Luo, Z.**; Du, R.; Liu, L-M.; Zhang, G.; Zhang, Y.; Cabot, A. Cu₂ZnSnS₄ Nanocrystals as Highly Active and Stable Electrocatalysts for the Oxygen Reduction Reaction. Enviado

En este trabajo, Z. Luo realizó la síntesis de los materiales, su caracterización y discusión de los resultados. X. Yu diseñó el experimento y escribió el manuscrito para su publicación. D. Wand, R. Du, L-M. Liu, G. Zhang y Y. Zhang participaron en la caracterización de los materiales, las medidas experimentales, el análisis de los datos y los cálculos DFT.

Capítulo 3:

5. **Luo, Z.**; Ibáñez, M.; Antolin, A. M.; Genç, A.; Shavel, A.; Contreras, S.; Medina, F.; Arbiol, J.; Cabot, A. Size and Aspect Ratio Control of Pd₂Sn Nanorods and Their Water Denitration Properties. *Langmuir* **2015**, *31* (13), 3952-3957.

Factor de impacto 2015: 3.993

En este trabajo, Z. Luo diseñó el experimento y escribió el manuscrito. A. Genç y J. Arbiol realizaron el análisis HRTEM y el análisis de modelos atómicos. A. M. Antolin, A. Shavel, S. Contreras y F. Medina participaron en la síntesis de los materiales, su caracterización, medidas y discusión de los resultados experimentales.

6. **Luo, Z.**; Lu, J.; Flox, C.; Nafria, R.; Genç, A.; Arbiol, J.; Llorca, J.; Ibáñez, M.; Morante, J. R.; Cabot, A. Pd₂Sn [010] Nanorods as a Highly Active and Stable Ethanol Oxidation Catalyst. *Journal of Materials Chemistry A*. Bajo revisión.

Factor de impacto 2015: 8.262

En este trabajo, Z. Luo diseñó el experimento y escribió el documento. A. Genç y J. Arbiol realizaron el análisis HRTEM y el análisis de modelos atómicos. J. Lu, C. Flox, R. Nafria y J. R. Morante participaron en la síntesis de los materiales, su caracterización, medidas y discusión de los resultados experimentales.

7. Nafria, R.; **Luo, Z.**; Ibáñez, M.; Marti, S.; Mata, M.; Llorca, J.; Arbiol, J.; Kovalenko, M. V.; Grabulosa, A.; Muller, G.; Cabot, A. Pd₂Sn and Au-Pd₂Sn Nanorods in Catalytic Hydrogenation and Sonogashira Coupling Reactions. Enviado.

En este trabajo, R. Nafria y Z. Luo diseñaron el experimento y escribieron el manuscrito. S. Marti, M. Mata y J. Arbiol realizaron el análisis HRTEM y el análisis de modelos atómicos. J. Llorca, M. V. Kovalenko, A. Grabulosa y G. Muller participaron en la síntesis de los materiales, su caracterización, medidas y discusión de los resultados experimentales.

Capítulo 4:

8. **Luo, Z.**; Irtem, E.; Ibáñez, M.; Nafria, R.; Marti, S.; Genç, A.; Mata, M.; Liu, Y.; Cadavid, D.; Llorca, J.; Arbiol, J.; Andreu, T.; Morante, J. R.; Andreu, C. $Mn_3O_4@CoMn_2O_4-Co_xO_y$ Nanoparticles: Partial Cation Exchange Synthesis and Electrocatalytic Properties Toward the Oxygen Reduction and Evolution Reactions. *ACS Appl. Mater. Interfaces.* . **2016**, 8(27), 17435-17444.

Factor de impacto 2015: 7.145

En este trabajo, Z. Luo y E. Irtem diseñaron el experimento y escribieron el documento juntos. S. Marti, M. Mata y J. Arbiol realizaron el análisis HRTEM y el análisis de modelos atómicos. R. Nafria, Y. Liu, D. Cadavid, J. Llorca, T. Andreu y J. R. Morante participaron en la síntesis de los materiales, su caracterización, medidas y discusión de los resultados experimentales.

9. **Luo, Z.**; Marti, S.; Nafria, R.; Joshua, G.; Mata, M.; Guardia, P.; Flox, C.; Boubeta, C.; Simeonidis, K.; Llorca, J.; Morante, J. R.; Arbiol, J.; Ibáñez, M.; Cabot, A. $Fe_3O_4@NiFe_xO_y$ Nanoparticles with Enhanced Electrocatalytic Properties for Oxygen Evolution in Carbonate Electrolyte. *ACS Appl. Mater. Interfaces.*

Aceptado

Factor de impacto 2015: 7.145

En este trabajo, Z. Luo diseñó el experimento y escribió el documento. S. Marti, M. Mata y J. Arbiol realizaron el análisis HRTEM y el análisis de modelos atómicos. R. Nafria, G. Joshua, P. Guardia, C. Flox, C. Boubeta, K. Simeonidis, J. Llorca y J. R. Morante participaron en la síntesis de los materiales, su caracterización, medidas y discusión de los resultados experimentales.

Prof. Andreu Cabot

Y Dr. Maria Ibáñez



Dan fe de que la información que aquí aparece es verdadera.

Barcelona, 09/30/2016

Chapter 1

General Introduction

1.1 The energy challenge

One of the major challenges of the 21st century is the foundation of a sustainable future in terms of environmental integrity and economic viability for the present and future generations. Energy has become one of the strategic factors driving the development of global environment and economy. Currently, most of the energy consumption is derived from the burning of fossil fuels in the form of petroleum, coal and natural gas. Renewable resources such as wind, biomass, photovoltaics and geothermal conversion account for about 9% (Figure 1.1).¹ Therefore, the optimization of current energy sources and the development of cheap, efficient renewable power are becoming critical.

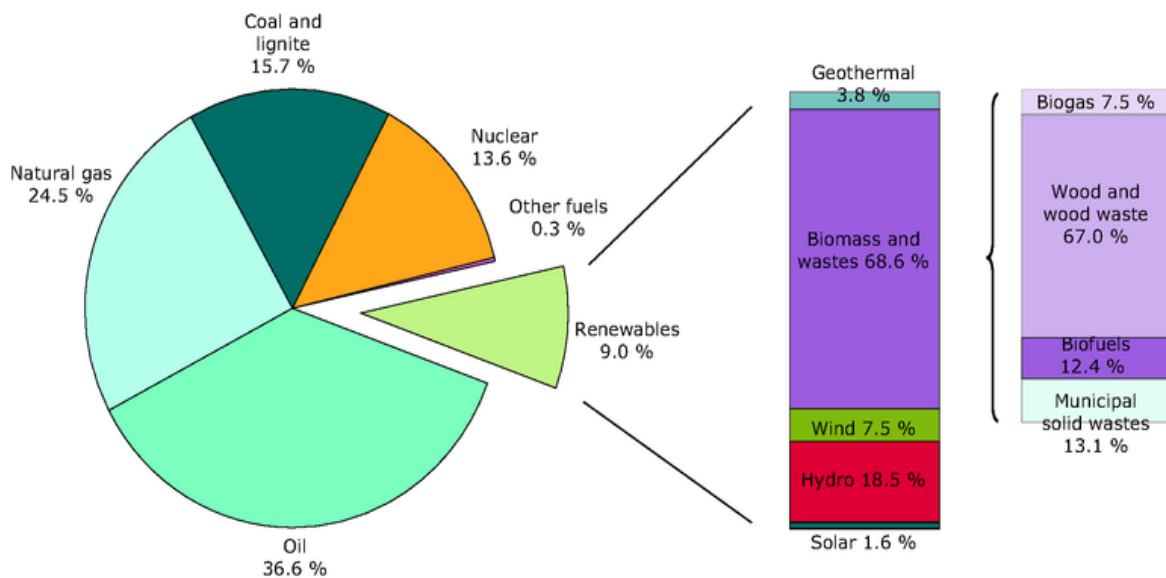


Figure 1.1 European Union Energy Consumption by type¹ (Source: <http://www.eea.europa.eu/data-and-maps/indicators/renewable-primary-energy-consumption/renewable-primary-energy-consumption-assessment-7>)

In the future of energy conversion and storage, catalysis will play a key role. Therefore, important efforts are devoted to the understanding of catalytic mechanisms and to the development of novel catalysts. Over the past decade, impressive progress has been made towards controlling the shape and size of metal nanostructures.²⁻⁴ For catalytic NPs, it is not only important to control the novel shape-dependent properties of these nanostructures but also the size-dependency. Currently, the interest migrates to the synthesis and application of more complex structures, such as multi-shell and heterogeneous NPs due to their superior and synergetic properties.⁵⁻⁷ The goal is to develop and optimize preparative strategies to produce efficient and environmentally benign systems for cleaner technologies throughout both industry and academia.

1.2 Colloidal NPs for energy conversion and storage

Solution based colloidal NPs have special size- or shape-dependent mechanical, optical, and electronic properties compared to their bulk materials.⁸⁻¹² The large surface-to-volume ratio enhances surface properties of nanomaterials, enabling application of nanomaterials in catalysis. The control of the size and shape of colloidal NPs, and especially of its composition and the distribution of elements within each NC is of essential importance to comprehensively understand and be able to optimize the performance of a catalytic system (see Figure 1.2).¹³

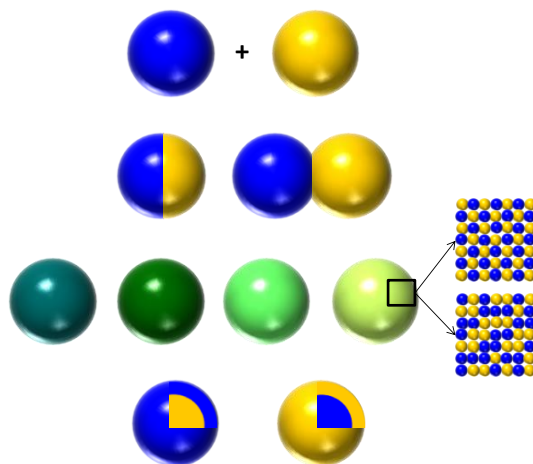


Figure 1.2 Scheme of the different NPs that will be produced and used to determine the effect of the catalyst composition and the distribution of its constituents on its catalytic activity.

1.3 Colloidal synthesis of NPs

Colloidal synthesis routes and bottom-up assembly procedures allow an extremely precise control over material properties at the nanometer scale. Moreover, such control of material at its lowest organization level does not require high capital cost equipment or extremely complex procedures, but it is compatible with the production of materials with high-throughput and high yield with ambient pressure and low temperature synthetic routes. The huge potential of such solution-based strategies to tune material properties at the nanoscale resides in the ability to chemically manipulate material formation from the very initial combination of atoms into clusters, to the growth of nanometer scale entities.^{14,15} Chemical manipulation is accomplished through the use of surface active agents or surfactants, which regulate the incorporation of atom/ions at each surface site by locally controlling surface energy and charge. This strategy allows huge amounts of colloidal NPs to simultaneously nucleate and grow, all self-evolving at the same rate and in the same conditions. Thus, massive amounts of particles with precisely tuned properties can be produced in a simple, fast and cost-effective manner.

1.3.1 General Solution-based Strategy to Colloidal synthesis of NPs

Colloidal synthesis methods have been demonstrated to provide the highest degree of control over the NPs properties. This synthetic methods allow to tune not only the particle size, morphology and composition, but also the distribution of the constituent elements at the nanoscale.¹⁶ Typically, a general solution-based colloidal synthetic route consists of three parts: monomer formation, nucleation and growth. Considering a thermodynamic system, nucleation is the formation of a new phase (nuclei) in a metastable primary phase and it related to the Gibbs free energy for the formation of nuclei.¹⁷ The classical nucleation theory was developed by LaMer in the 1950s.¹⁸⁻²⁰ After the burst of nucleation, NC enters the growth regime. The growth rate of NC will depend on the monomer flux supply (a diffusion process that can be express by the Fick's law) and the size of the NC via the Gibbs-Thomson equation.²¹ Figure 1.3 displays the 3 principal phases during NC synthesis: (I) monomer formation, (II) nucleation; and (III) growth. Below these lines the phenomena occurring in each phase is briefly described.

I) Monomer concentration increases gradually and reaches a critical supersaturation level (S_c), at this time, the nucleation occurs.

II) Monomer concentration further increases to overcome the energy barrier (determined by minimizing the Gibbs free energy) leading to a rapid self-nucleation. The burst of nucleation abruptly deplete the monomer concentration bellow the supersaturation level required to produce nuclei entering thereby in the growth phase.

III) As the NCs growth, monomer concentration is further reduced. The growth rate of the NC will depend on their size and the diffusion of monomers in solution towards the already formed NCs.

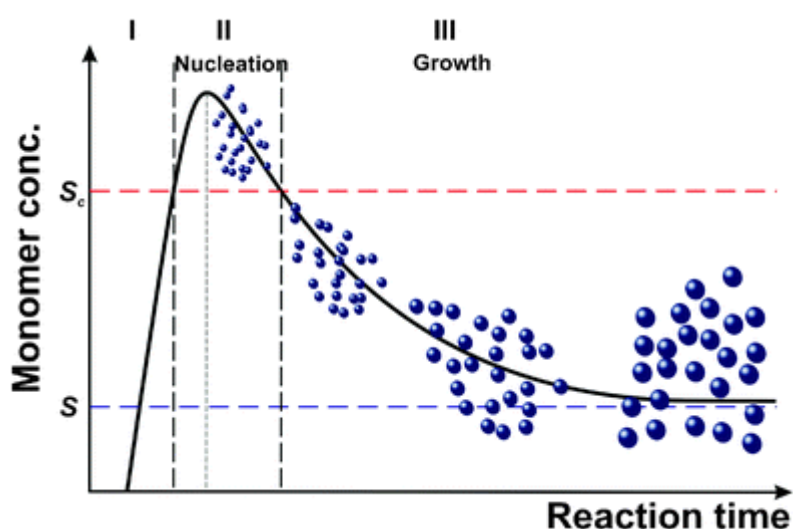


Figure 1.3 LaMer plot illustrating the separation of nucleation and growth during the synthesis of monodisperse NPs. S and S_c are supersaturation and critical supersaturation, respectively.¹⁸

Nucleation:

Nucleation can occur either heterogeneously (nucleation at preferential sites of surfaces) or homogeneously (uniformly throughout the solution phase); and both kinds of nucleation can occur consecutively or parallel. The heterogeneous nucleation can be seen as the driving force for a successful seed-mediated growth. For homogeneous nucleation, considering spherical particles, the Gibbs free energy of a nuclei (ΔG) is given as:

$$\Delta G = \frac{4}{3}\pi r^3 |\Delta G_V| + 4\pi r^2 \gamma \quad (1)$$

where r is radius of a spherical particle, γ is the surface energy per unit area and ΔG_V is the free energy change between monomers in the solution and a unit volume of bulk crystal, defined as:

$$\Delta G_V = -\frac{RT \ln S}{V_m} \quad (2)$$

where R is the gas constant, T is the absolute temperature in Kelvin, S is the degree of supersaturation (defined as $S=[M]/[M]_o$, where $[M]$ is the monomer concentration and $[M]_o$ is the equilibrium monomer concentration of the bulk solid) and V_m is the molar volume of the bulk crystal. In addition, the critical nucleus r_c , which determine the energy barrier or activation energy ΔG_c for self-nucleation to occur can be determined by solving equation (1) for $d\Delta G/dr=0$ leading to:

$$r_c = \frac{2\gamma}{|\Delta G_V|} = \frac{2\gamma V_m}{k_B T \ln S} \quad (3)$$

The critical radius determines if the NCs once formed will dissolve or will grow. NCs with critical size below the critical radius will dissolve.

The corresponding energy barrier ΔG_c , can be determined by substituting r in equation (1) with r_c from equation (3) yields the express for ΔG_c :

$$\Delta G_c = \frac{16\pi\gamma^3}{|\Delta G_V|^2} \quad (4)$$

Then the nucleation rate $J(t, \Delta G_c)$ can be expressed using the Arrhenius equation as following:

$$J(T, \Delta G_c) = A \exp\left(\frac{-\Delta G_c}{k_B T}\right) \quad (5)$$

Colloidal stability:

To get monodisperse colloidal NP, it is important to overcome NP aggregation in the solvent due to van der Waals interaction-NPs attraction force. Such inter particles force can be described with the following equation:

$$W_{total}(D) = W_a(D) + W_r(D) + W_{steric} \quad (6)$$

where $W_a(D)$ correspond to van der Waals interaction energy, $W_r(D)$ to interparticle energy and W_{steric} represent the repulsive forces of steric stabilization. W_{steric} is mainly determined by the molecules adsorbed at the NC surface to prevent aggregation and hence depend on the concentration, temperature, chain length and solubility of those molecules. The other interaction between NPs will depend on their size and on the distance between NP, which will be defined as the surface to surface distance between two spherical nanoparticles (D). Among them, $W_a(D)$ is expressed by the following equation:

$$W_a(D) = -\frac{\pi^2 \rho_1 \rho_2}{6} B \frac{2r_1 r_2}{c^2 - (r_1 + r_2)^2} + \frac{2r_1 r_2}{c^2 - (r_1 - r_2)^2} + \ln\left(\frac{c^2 - (r_1 + r_2)^2}{c^2 - (r_1 - r_2)^2}\right) \quad (7)$$

where ρ_1 and ρ_2 are electron density of two particles, B is constants of attractive van der Waals, r_1 and r_2 are radius of two particles and c is center to center distance between the two particles. In which considering identical particles ($r_1=r_2=r$) in close proximity ($D \ll r$) and $D = c - (r_1 + r_2)$; $W_a(D)$ can be expressed as:

$$W_a(D) = -\frac{Ar}{12D} \quad (8)$$

where A is the Hamaker constant.

$W_r(D)$ can be described as:

$$W_r(D) = 2\pi\epsilon\epsilon_0 r \psi^2 \delta \exp(-\kappa D) \quad (9)$$

Where ϵ is the permittivity of vacuum ($8.854 \times 10^{-12} \text{ C J}^{-1} \text{ m}^{-1}$), ϵ_0 is the dielectric constant, ψ is the electrical potential, κ is the Debye constant; and again r is the radius of two spherical particles and D is a distance of surface to surface between two spherical particles.

Growth:

Considering that the distance between particles is sufficiently large, the growth of each NP can be treated independently. The diffusion process can be expressed by Fick's first law:^{20, 22}

$$J = 4\pi x^2 d \frac{dC}{dx} \quad (10)$$

where J is the flux of monomers, diffusing through the surface of the particle, d is the diffusion coefficient, x is the distance to the center of the particle, C is concentration at distance x . In the NC surface vicinity at a distance from the NC center of $r + \delta$, the gradient concentration is determined by:

$$J = 4\pi d \frac{r(r+\delta)}{\delta} (C_b - C_s) \quad \xrightarrow[r \ll \delta]{} \quad J = 4\pi r d (C_b - C_s) \quad (11)$$

where C_b is the bulk concentration of monomers at the distance of $r + \delta$ and C_s is the concentration of monomers at the solid/liquid interface (NC surface).

Similarly, on a reaction controlled growth with κ being the reaction rate constant and C_r the solubility of the particles with radius r :

$$J = 4\pi r^2 k(C_s - C_r) \quad (12)$$

In this two scenarios the NC growth rate is:

$$\frac{dr}{dt} = (C_b - C_r) \frac{V_m d}{r} \quad (13)$$

for a diffusion-controlled model

$$\frac{dr}{dt} = (C_b - C_r) k V_m \quad (14)$$

for a reaction-controlled growth

$$\frac{dr}{dt} = (C_b - C_r) \frac{V_m d}{r + D/k} \quad (15)$$

for a neither diffusion- nor surface-reaction controlled growth.

On the other hand, considering the Gibbs-Thomson effect, the solubility of the NP depends on the particle size. A spherical particle with radius r has an extra chemical potential ($\Delta\mu = \frac{2\gamma V_m}{r}$). The solubility of the particle of radius r (C_r) can express as:

$$C_r = C_b e^{\frac{2\gamma V_m}{rkT}} \quad (16)$$

Combining Fick's law and the Gibbs-Thomson effect, a general expression for NC growth is given by:

$$\frac{dr^*}{dt} = \frac{S - e^{\frac{1}{r^*}}}{r^* + K e^{\frac{1}{r^*}}} \quad (17)$$

with

$$r^* = \frac{RT}{2\gamma V_m} r \quad (18)$$

and

$$K = \frac{RT}{2\gamma V_m} \frac{d}{k} \quad (19)$$

as the Damköhler number (K), an indicator of diffusion- or reaction-controlled system.

At small values of K (< 0.01), the overall growth rate is dominated by the rate of mass transfer (diffusion-controlled growth). When K is larger than 10,²³ the growth rate is mainly determined by the surface reaction rate (reaction-controlled growth).

1.3.2 Strategies for NP engineering

Colloidal synthesis routes are also extremely versatile, allowing production of elemental or multinary NPs with metallic, semiconductor, magnetic, plasmonic, etc. character with unmatched composition, size, shapes and phases control.²⁴⁻²⁶ Colloidal synthesis routes also allow producing multi-material nanostructures with organized phase distribution by parallel or sequential growth of one material at the surface of the other or by replacing part of the ions of a preformed nanostructure.^{27, 28} In the following sub-chapter, the different strategies used to prepare engineered NPs will be presented.

1.3.2.1 Co-Precipitation

The co-precipitation method is one of the most classical techniques to prepare NPs.^{29, 30} As shown in Figure 1.5, this method consists of mixing anions and cations solution. The advantages are large-scale production and simplicity, but the biggest problem is the broad particles size distribution and poor control of morphology.

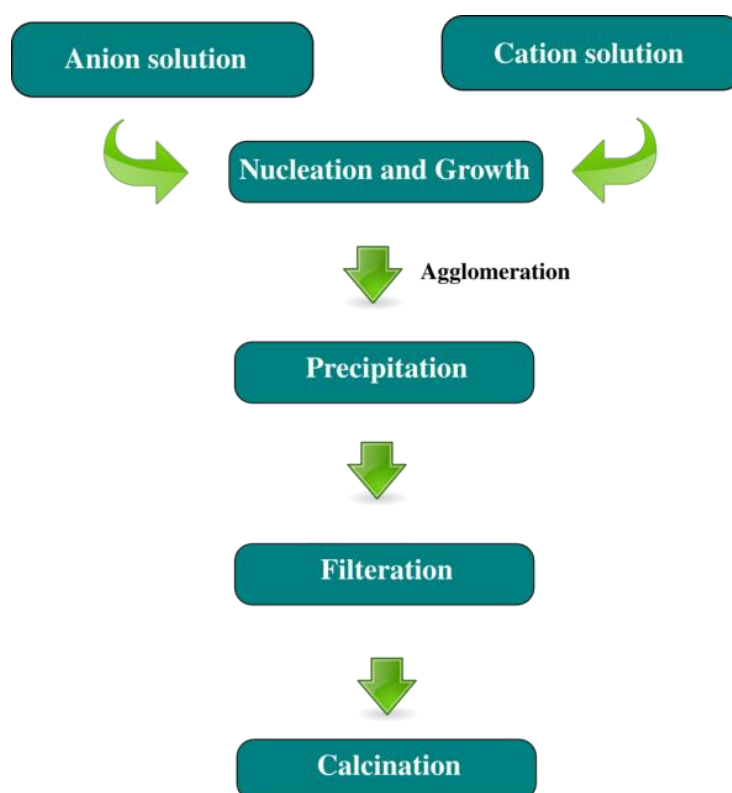


Figure 1.5 Typical co-precipitation methods for micro and NPs synthesis.²⁶

1.3.2.2 Solvothermal and Hydrothermal Synthesis

Solvothermal/hydrothermal strategies have been used to prepare various NPs.³¹⁻³⁴ The key disadvantage of this synthesis route is the requirement of both high temperature and high pressure. If the solvent is an aqueous solution, this method is called hydrothermal, otherwise is known as solvothermal. The main advantage of this method is the possibility to grow good-quality crystalline NPs with controlled size, shape and phase when compared to co-precipitation method. In particular, the ability of create crystalline phase which are not stable at the melting point. Wang et al. had reported a general strategy for NP synthesis by hydrothermal method (Figure 1.6).³⁵ However, the high cost and the inability to observe the growth of crystal limited the development of this method.

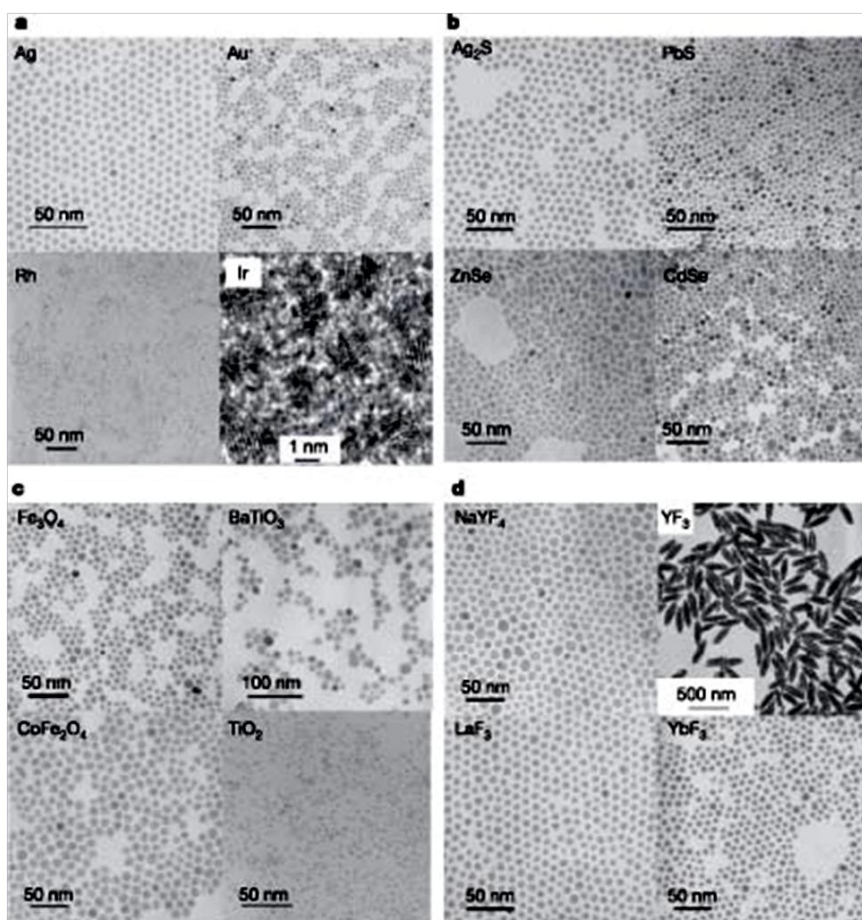


Figure 1.6 TEM images of a variety of NPs.³⁵ (a) shows noble metal NPs including Ag, Au, Rh and Ir. (b) a shows chalcogenides NPs including Ag₂S, PbS, ZnSe and CdSe. (c) shows metal oxide NPs including Fe₃O₄, BaTiO₃, CoFe₂O₄ and TiO₂. (d) shows upconversion NPs including NaYF₄, YF₃, LaF₃ and YbF₃.

1.3.2.3 Thermal Decomposition

So far, the best strategy for precisely controlling of the production of highly monodisperse NPs with a narrow size distribution, morphology and composition is the mid-to-high-temperature thermal decomposition/reaction method, which is based on the decomposition/reaction of metal-organic or metal salt precursors in high-boiling non-polar solvent and in presence of surfactant agents.³⁶⁻³⁹ Figure 1.7 shows a typical set-up in our laboratory for this thermal decomposition method. This technique is beneficial for controlling concentrations of precursors and surfactants, reaction temperature, heating rate, reaction time, etc. For instance, Hyeon and co-workers demonstrated a synthesis of highly crystalline and monodispersed iron oxide NPs without any size-selection process by the thermal decomposition of iron-oleate complex in presence of oleic acid in high-temperature boiling point solvent.⁴⁰ It should be noted that the NPs obtained are generally stable in solution in nonpolar solvents due to the hydrophobicity of the common surfactant used.

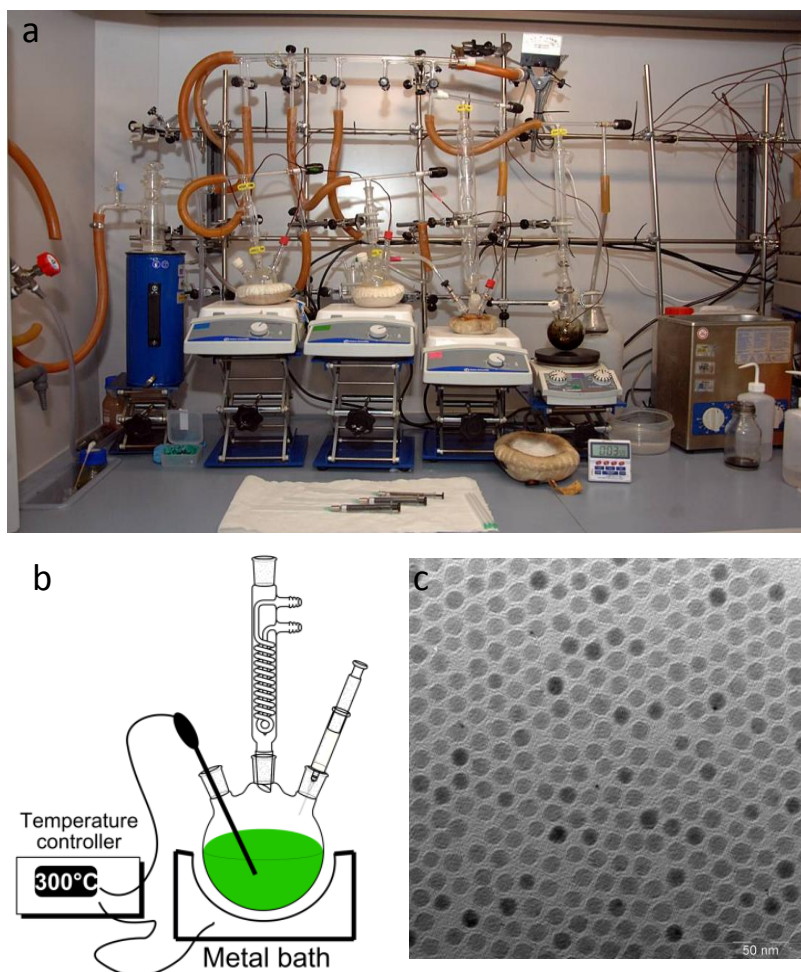


Figure 1.7 (a) Photograph of laboratory setup. (b) Scheme of set-up in laboratory for the synthesis of monodisperse NPs by decomposition of suitable metal precursors using a metal bath with temperature controller.³⁷ (c) TEM-image of as-prepared Fe₃O₄ NPs.

Besides the above-mentioned methods, numerous physical or chemical methods can be used to synthesize NPs, such as biosynthesis route,⁴¹⁻⁴³ sol-gel reaction,⁴⁴⁻⁴⁶ microwave-assisted method,⁴⁷⁻⁵¹ electrochemical method⁵²⁻⁵⁵ and so on. Table 1 shows a brief summary about the principal characteristics of the most common NP synthetic methods. Currently, the major difficulties in the synthesis of colloidal NPs are still to control size, morphology, composition, and size distribution at the nanoscale to the desired level. Therefore, the demand of a facile and flexible method to produce colloidal NPs with the perfect design is of extreme importance to realize the full potential of these materials for many different applications among which is catalysis.

Table 1. Summary comparison of the synthetic methods for producing NPs.

Method	Reaction and conditions	Reaction temp. °C	Reaction period	Size distribution	Shape control	Yield
Co-precipitation	Simple, ambient	20-150	minutes	Broad	Not good	High/scalable
Solvo- or hydrothermal	Simple, high pressure	150-220	Hours-days	Narrow	Good	High/scalable
Thermal decomposition	Complicated, insert atmosphere	100-350	Minutes Hours-days	Very narrow	Very good	High/scalable
biosynthesis	Complicated, ambient	Room temp.	Hours-days	Broad	Bad	Low
Electrochemical methods	Complicated, ambient	Room temp.	Hours-days	Medium	Medium	Medium
Microwave-assisted synthesis	Complicated, ambient	20-80	Minutes	Medium	Good	Medium
sol-gel reaction	Complicated, ambient	25-200	Hours	Narrow	Good	medium

1.4 Objectives of the thesis

The main objective of this thesis focuses on the design and engineering of colloidal NPs and its application in energy conversion and storage. This mainly includes the synthesis and characterization of colloidal semiconductor, metallic and metal oxides NP and the depth exploration of their properties; in particular electro/photo-catalytic. Special attention was paid is the synthesis and characterization of copper chalcogenide, transition metal oxide and multi-metallic NP.

These works can be summarized as follows:

(1) Copper chalcogenides NPs: I focused on the development of synthetic routes to produce CZTS NP and HNP with CZTS: CZTS-Au, Pt and CZTS-Ag₂S. The composition, size and shape of the NPs are controlled by regulating the concentration of precursor, the use of surfactants, the gas flow and adjusting the heating ramp. The NPs produced were used as photocatalysts for dye degradation, water splitting and as electrocatalysts for ORR.

(2) Multi-metallic NPs: I developed synthetic methods for producing NRs of Pd₂Sn and for growing Au crystallographic domains above them, i.e. Au-Pd₂Sn. The mechanism to control NP morphology NPs of these materials was determined. These NPs were successfully used in various catalytic applications. The Pd₂Sn NPs were used for nitrophenol reduction and water denitration. They were also used for the electrocatalytic oxidation reaction of ethanol. The results obtained with NRs were compared with particles of the same composition but with spherical morphology and with spherical Pd NPs. NRs resulted in better catalytic activities. Au-Pd₂Sn were investigated for hydrogenation reactions and coupling.

(3) Metal oxide NPs: HNPs of Mn₃O₄@CoMn₂O₄-CoO were prepared by partial cation exchange from seeds of Mn₃O₄. Such heterostructures showed exceptional electrocatalytic activity and stability for reduction reactions and oxygen evolution in an alkaline solution. Based on this synthesis pathway, Fe₃O₄@Ni_xFe_{3-x}O₄ NP were obtained by reaction of nickel perchlorate precursors with Fe₃O₄ seeds. These NPs were used as electrocatalysts for water oxidation, demonstrating exceptional catalytic activity.

Chapter 2

Semiconductor NPs and HNPs

2.1 CZTS NCs

This first chapter focus on the synthesis of high quality monodisperse CZTS NCs using a facile heating-up method, reaching a 90% yield, which provide 6 to 10 fold higher amounts of material than common NCs synthesis procedures. The results obtained were published in *Chemistry of Materials* in 2016. Secondly, we discuss the application of CZTS NCs for ORR. Results in this direction have been sent for publication. Then CZTS-Pt and CZTS-Au HNPs with strongly electrically coupled interfaces were prepared based on the CZTS host. These heterostructures were tested for photodegradation of pollutants and for photocatalytic hydrogen generation. We describe their enhanced photocatalytic activity toward photodegradation of RhB and H₂ production by water splitting when compared to pure CZTS. The results were published in the *Journal of the American Chemical Society* in 2014. In addition, CZTS-Ag₂S p-n HNPs with tuned composition were produced involving the cation exchange route, such CZTS-Ag₂S p-n nanoheterostructures outperformed pure CZTS NCs as photoelectrocatalyst for water splitting because of a higher separation efficiency of the photogenerated electron-hole pairs. The results obtained were published in *Langmuir* in 2015. The four papers mentioned above these lines are presented after a brief summary in the corresponding subchapter.

2.1.1 Synthesis of copper-based chalcogenides NPs

Recently, the development of colloidal synthetic approaches to produce copper-based chalcogenides NP, such as Cu_{2-x}S, CIS, CZTS, CZTSe, etc. have attracted extensive attention. The main reasons are: their low toxicity, environmental friendliness, low cost and the very wide range of compositions and crystal phase structures which enable them to be used in very diverse applications.⁵⁶⁻⁵⁹ In particular, the large plethora of copper-based chalcogenides NP not only can offer similar properties but also offer unique features (e.g. plasmonic properties) compared to conventional chalcogenide NPs contain toxic heavy metal such as Cd, Pb or Hg.⁶⁰ For example, by modifying their composition, copper-based chalcogenides offer a high flexibility for tuning the band gap without toxic elements (Table 2.1)⁶¹ Figure 2.1 shows a scheme of general copper-based chalcogenide NPs with different size, morphology and compositions, such as binary Cu₂X (X= S, Se and Te), ternary CuInX₂ (X= S and Se), CuSnS₃ and quaternary CZTS, CIGS NPs, and their application in plasmonic devices, photovoltaic cells and light-emitting diodes among others.⁶²⁻⁷¹ In order to better understand the properties of copper-based chalcogenide NPs and to improve their performance in the different application possible, is important to produce high-quality copper-based chalcogenide NPs with control of the size, shape, and composition. However, the synthesis of colloidal copper chalcogenide NPs, and especially of those with three or four elements such as CZTS NCs is extremely challenging.

CZTS is a I₂-II-IV-VI₄ quaternary semiconducting compound which has received a great deal of interest for applications such as photocatalysis, thermoelectric and solar cells.⁷² One of the main difficulties during the

synthesis of CZTS NPs is the tendency to form secondary phases like binary (i.e., CuS, ZnS and SnS) and ternary sulfides (CTS).⁷³ It is therefore important to understand the nucleation and growth mechanism of CZTS NP formation to be able to develop reproducible synthetic route for pure-phase CZTS NPs. Tan Rui et al. reported the growth mechanism of wurtzite CZTS NPs using Surface-Enhanced Raman Scattering (SERS) as a sensitive tool.⁷⁴ They found the formation of CZTS proceeds via three steps: (I) Cu_{2-x}S NP nucleation, (II) Sn^{4+} diffusion into Cu_{2-x}S to form kinetically driven CTS NPs and; (III) Zn^{2+} diffusion into CTS NPs to form CZTS NPs (Figure 2.2).

Table 2.1 Band gaps, crystal structures and lattice parameters of the some bulk copper-based chalcogenides semiconductors

Material	Band gap at 300 K (eV)	Crystal structure	Lattice parameters
CuInS_2	1.53	Chalcopyrite	a = 5.52 c = 11.12
CuInSe_2	1.05	Chalcopyrite	a = 5.61 c = 11.02
$\text{Cu}(\text{In}_{0.5}\text{Ga}_{0.5})\text{S}_2$	1.6	Chalcopyrite	a = 5.67 c = 11.32
$\text{Cu}(\text{In}_{0.5}\text{Ga}_{0.5})\text{Se}_2$	1.3	Chalcopyrite	a = 5.45 c = 10.88
CuGaS_2	1.68	Chalcopyrite	a = 5.61 c = 11.02
CuFeS_2	0.6	Chalcopyrite	a = 5.28 c = 10.41
$\text{Cu}_2\text{ZnSnS}_4$	1.50	Kesterite	a = 5.45 c = 10.86
$\text{Cu}_2\text{ZnSnS}_4$	1.02	Kesterite	a = 5.61 c = 11.20

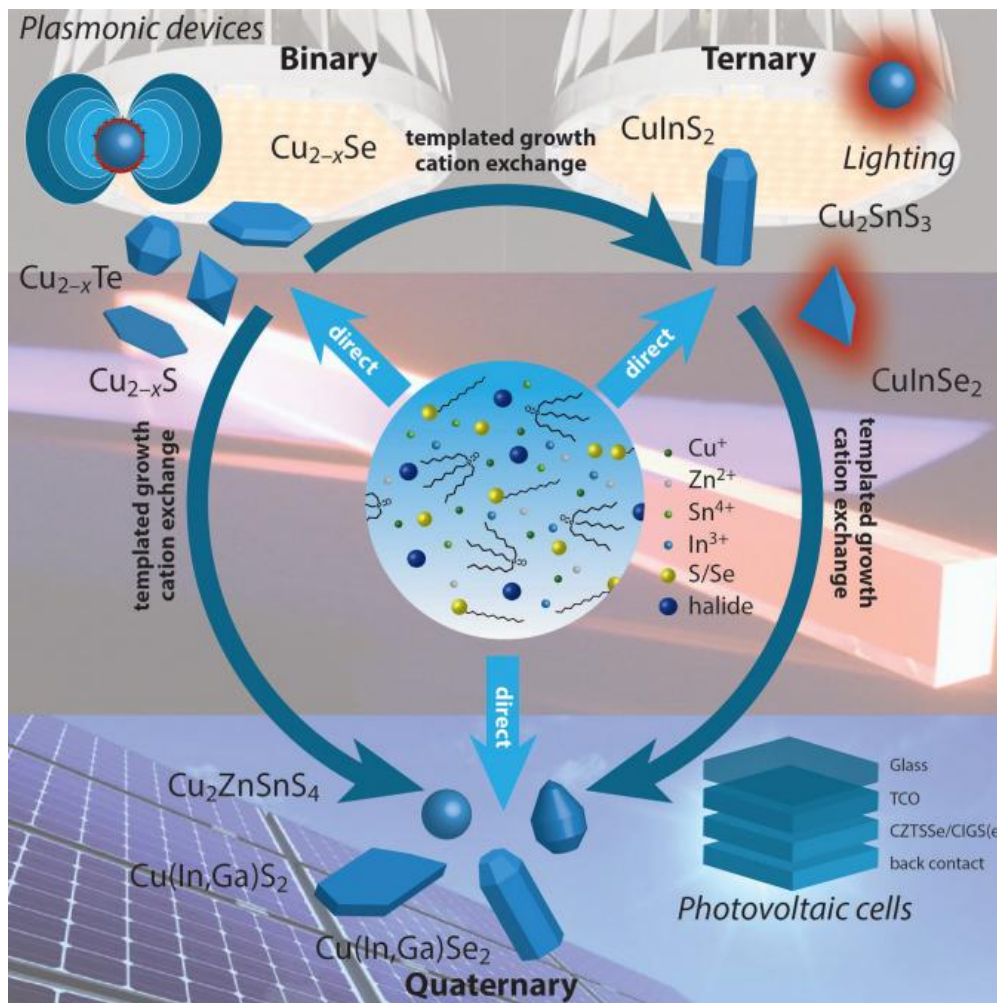


Figure 2.1 Scheme of colloidal copper-based chalcogenide NPs and various applications, e.g. plasmonic devices, photovoltaic cells and light-emitting diodes.⁵⁹

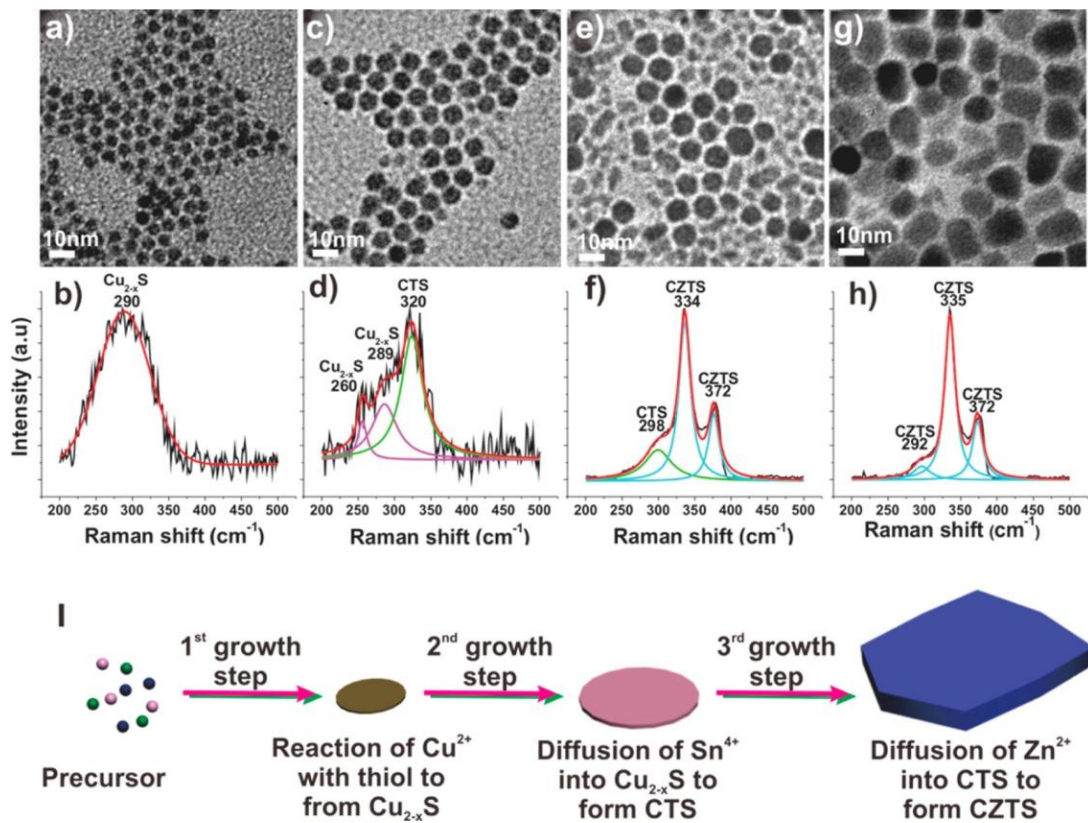


Figure 2.2 CZTS NPs extracted at different reaction times at 240 °C. (a) TEM images and (b) SERS spectra at 2 min, (c) TEM images and (d) SERS spectra at 8 min, (e) TEM images and (f) SERS spectra at 12 min, and (g) TEM images and (h) SERS spectra at 90 min. (i) Pictorial representation of the three step growth process for the formation of CZTS NPs.⁷⁴

Coughlan et al. performed a detailed study on the composition and shape evolution of CZTS NPs during the synthesis and they found out a similar growth mechanism (Figure 2.3).⁷⁵

CZTS NPs with different morphologies including NRs, ellipsoids, tadpole and P-shaped NCs were obtained by tuning the amine concentration. In addition, polytypic NCs with mixed wurtzite and zinc blende phase were synthesized by proper selection of the metal precursors.

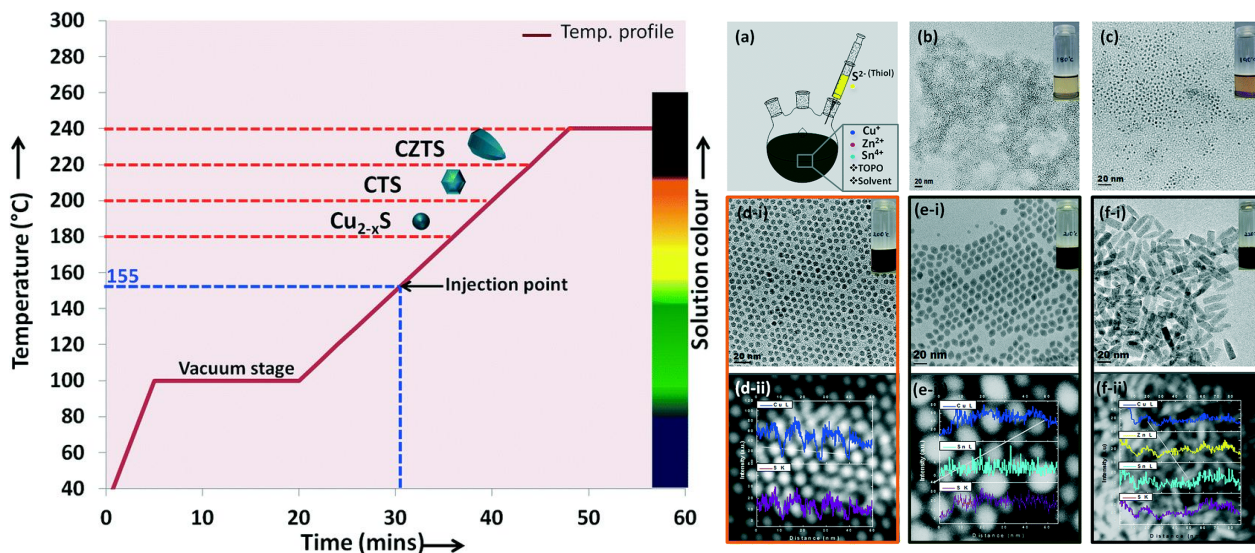


Figure 2.3 Schematic illustration of the growth mechanism for CZTS NCs during the temperature ramp (left figure); Schematic of the hot injection approach to form CZTS NRs and TEM images, DF-STEM and EDX line of as-obtained CZTS NPs at different temperature (right figure).⁷⁵

In addition, for practical applications, the scalability of NC production needs to be considered. Actually, the ability to produce large scale quantities of NCs is rather important for research but even more for implement the use of this material in real applications. Our group reported a continuous production method to obtain relatively large amounts of chalcogenide NPs, in particular CZTS with controlled chemical composition through the reaction of the metals' amino complexes with elemental sulfur in a continuous-flow reactor at moderate temperatures (Figure 2.4).⁷⁶ There is another similar work presented by Grover et al., where a supercritical carbon dioxide continuous-flow reactor is used to deposit CZTS microparticles and NPs onto a silicon wafer from metal dithiocarbamate precursors.⁷⁷

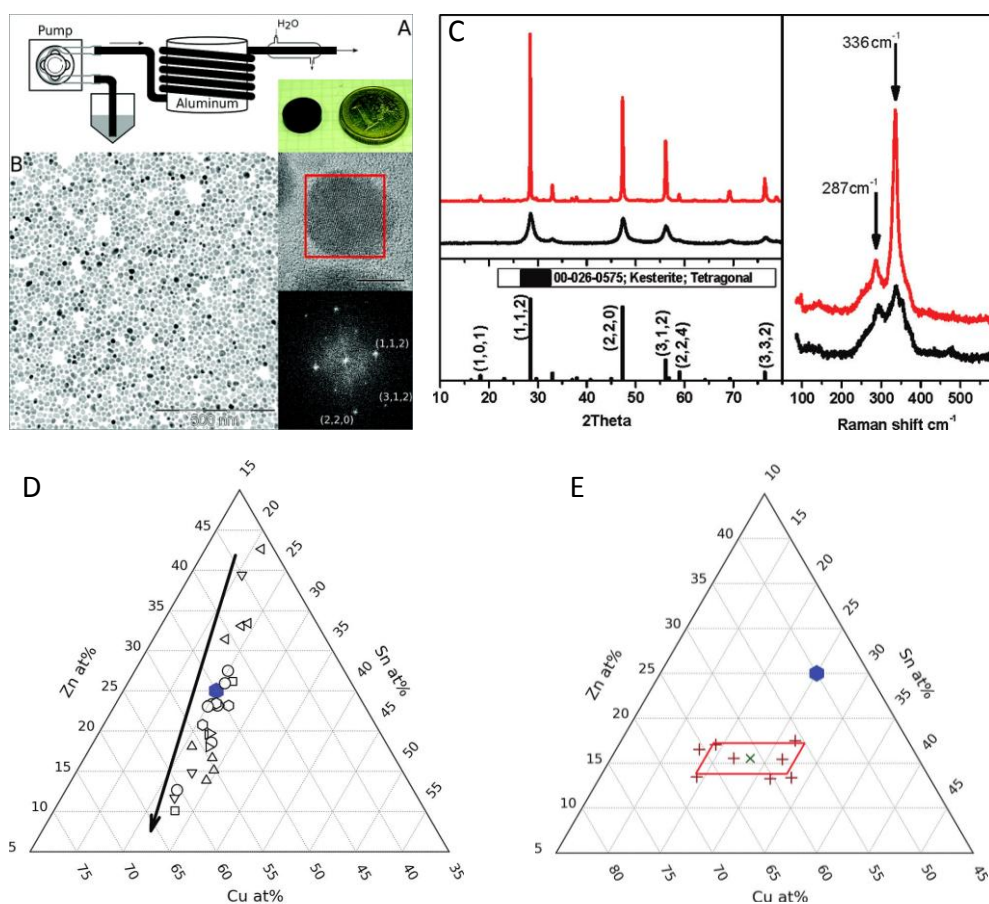


Figure 2.4 (A) Scheme of the flow reactor setup and image of a 1 g pellet made of CZTS NPs. (B) TEM micrograph of cleaned CZTS NPs prepared inside the flow reactor at 300 °C at a flow rate of 2.0 mL/min. The inset shows an HRTEM image of a CZTS NC and the corresponding SAED pattern. (C) XRD patterns (left) and Raman spectra (right) of the prepared NPs before (black) and after (red) annealing at 500 °C for 1 h. As a reference, the diffraction pattern of CZTS (JCPDS no. 00-026-0575) is shown. The lattice parameters for the heated sample were $a = b = 5.40$ Å and $c = 10.40$ Å. (D) CZTS cationic ratios obtained from SEM-EDX. The arrow points the direction of increasing flow rate. Different symbols denote different reaction conditions. (E) Single-particle composition (red +) obtained by HRTEM-EDX analysis of a number of CZTS NPs synthesized at 315 °C. The green X shows the mean composition obtained by averaging the values obtained from several NPs. The blue hexagon in each graph shows the nominal composition of the precursor solution.⁷⁶

2.1.2 Scalable Heating-Up Synthesis of Monodisperse $\text{Cu}_2\text{ZnSnS}_4$ NCs

This year, our group developed with my contribution a new method to produce large scale amounts of CZTS NPs with unprecedented control over NP size distribution and composition. The article entitled as the heading of this section was published in *Chemistry of Material* **2016**, 2, 720-726. The article as well as the corresponding supporting information can be found at the end of this section. The article describes a facile phosphine-free synthesis protocol to produce monodisperse CZTS NCs with tuned composition and morphology. In this work, we reported a heat-up synthesis strategy and high initial concentration of precursors to yield 90% of CZTS NPs using OLA and ODE as organic ligand and solvent. A minucious characterization by means of TEM, HRTEM, XRD and SERS demonstrated that the CZTS NC produced were purely wurtzite CZTS NCs (Figure 2.5). The growth mechanism was discussed in this paper, we found out that the inert gas bubbling rate and the heating ramp stability influences the quality of the final CZTS NPs produced. Besides the concentration of precursors, the different Cu: Zn: Sn ratio, and the presence of 1-DDT and tDDT were key parameters to control CZTS NCs morphology. In the final part of the paper, we studied different ligand exchange reaction to replace the bulky OLA with shorter ligands. The goal behind this study was to reduce the final carbon content of the NC ensemble to promote the charge transfer between/from/to NCs necessary for most potential applications. Elemental analysis experiments showed carbon contents within the limit of detection.

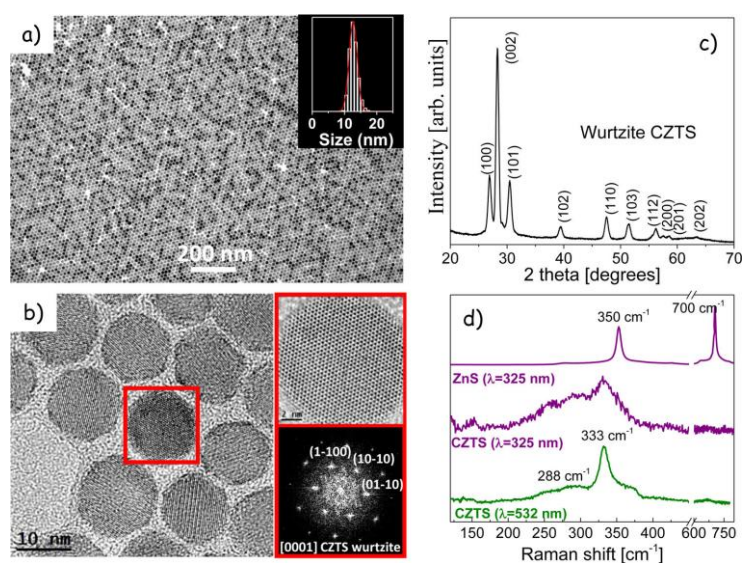


Figure 2.5 (a) TEM micrograph and a typical size histogram of CZTS NCs (NCs); (b) HRTEM micrograph and corresponding indexed power spectrum on the selected CZTS NC in the red square; (c) XRD pattern and (d) Raman spectra with 532 and 325 nm excitation of CZTS NCs. The resonant Raman spectrum of ZnS obtained under 325 nm excitation is also shown as a reference.

Scalable Heating-Up Synthesis of Monodisperse Cu₂ZnSnS₄ Nanocrystals

Alexey Shavel,^{*,†,‡,§} Maria Ibáñez,[†] Zhishan Luo,[†] Jonathan De Roo,[∇] Alex Carrete,[†] Mirjana Dimitrievska,[†] Aziz Genç,[‡] Michaela Meyns,[†] Alejandro Pérez-Rodríguez,^{‡,§} Maksym V. Kovalenko,^{‡,§,||} Jordi Arbiol,^{‡,¶} and Andreu Cabot^{†,¶}

[†]Catalonia Institute for Energy Research (IREC), Sant Adrià del Besòs, 08930 Barcelona, Spain

[‡]Catalan Institute of Nanoscience and Nanotechnology (ICN2), CSIC and The Barcelona Institute of Science and Technology, Campus UAB, Bellaterra, 08193 Barcelona, Catalonia, Spain

[§]Departament d'Electrònica, Universitat de Barcelona, 08028 Barcelona, Spain

[¶]Institució Catalana de Recerca i Estudis Avançats—ICREA, 08010 Barcelona, Spain

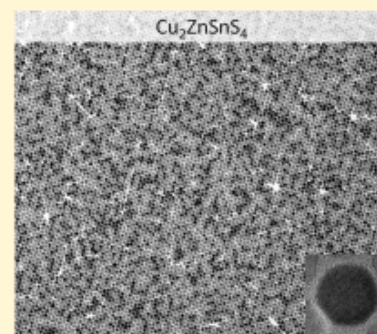
[∇]Department of Inorganic and Physical Chemistry, Ghent University, Krijgslaan 281 S3, 9000 Gent, Belgium

[‡]Institute of Inorganic Chemistry, Department of Chemistry and Applied Biosciences, ETH Zürich, CH-8093 Zürich, Switzerland

^{||}Empa-Swiss Federal Laboratories for Materials Science and Technology, Dübendorf, CH-8600, Switzerland

Supporting Information

ABSTRACT: Monodisperse Cu₂ZnSnS₄ (CZTS) nanocrystals (NCs), with quasi-spherical shape, were prepared by a facile, high-yield, scalable, and high-concentration heat-up procedure. The key parameters to minimize the NC size distribution were efficient mixing and heat transfer in the reaction mixture through intensive argon bubbling and improved control of the heating ramp stability. Optimized synthetic conditions allowed the production of several grams of highly monodisperse CZTS NCs per batch, with up to 5 wt % concentration in a crude solution and a yield above 90%.



1. INTRODUCTION

Ternary and quaternary semiconductors have recently attracted immense interest in photovoltaics, photocatalysis, and thermoelectrics.^{1–11} Among numerous chalcogenides, Cu₂ZnSnS₄ (CZTS), which is composed of abundant and nontoxic elements, has particularly appealing characteristics, such as high absorption coefficient in the visible region (>10⁴ cm⁻¹) and a suitable band gap (1.45–1.50 eV) for solar energy conversion. These properties make it an excellent absorber material, not only for the next generation of solar cells,¹ but also for photocatalysts.^{6–9}

The availability of these quaternary semiconductors in the form of nanocrystal (NC)-based inks allows low-cost solution processing by common techniques such as spray coating or inkjet printing. Inexpensive and scalable bottom-up approaches are increasingly needed for transferring the compositional versatility and homogeneity of individual NCs to the device-level macroscale (large-area thin films or bulklike nanogranular materials).^{12–14}

The preparation of multinary nanocrystals has proven to be much more difficult than the synthesis of elemental and binary nanocrystals. In particular, formation of quaternary chalcoge-

nides requires narrow parametric spaces, because it competes with simultaneous formation of binary and ternary phases, all having similar energies of formation and similar crystal structures. Of course, diversity of phases and compositions in multicomponent systems offers also important and useful advantages. For instance, Cu-poor and Zn-rich CZTS materials have demonstrated better performances as absorbers in solar cells than nearly stoichiometric materials.² In contrast, Cu-rich CZTS have shown improved photocatalytic properties.⁶ Furthermore, the compositional control allows tuning of the semiconductor charge carrier concentration, which is key to optimize performance in applications such as thermoelectrics.¹⁵

Control and analysis of compositional and phase homogeneities are experimentally challenging and require, for instance, scanning transmission electron microscopy (STEM) combined with high-spatial-resolution chemical analysis with energy-dispersive X-ray spectroscopy (EDX) or electron energy loss spectroscopy (EELS) to unravel the complexity within the

Received: September 2, 2015

Revised: January 16, 2016

Published: January 17, 2016

individual NC. To obtain NC-to-NC variation in atomistic uniformity, one would need to map thousands of NCs, which is difficult experimentally, while other characterization techniques provide only average information. In this regard, very useful is the observation that shape and size uniformity of multinary NCs are indicative of their intrinsic chemical homogeneity.^{16–19} In other words, monodisperse NCs are more likely to be also chemically identical/similar. Since photovoltaic, catalytic, and almost all other applications require large quantities of NCs with a minimal particle-to-particle variation in composition, the objective of this work was to develop a high-yield and easily scalable synthesis protocol to produce CZTS NCs, with high compositional and morphological uniformities.

The “heating-up” synthesis—when all reagents and solvents are premixed and then simply heated—is generally easier to scale up than the injection-based procedures, primarily because of highly homogeneous concentrations and temperatures throughout the process.²⁰ When the injection of a reagent is involved, the scaleup is limited by difficulties in achieving fast mixing of large volumes of reagents. Few gram-scale synthesis protocols to produce CZTS NCs have been already proposed. Among them, the solvent-free, mechanochemical synthesis approach is a remarkably simple pathway,^{21–23} albeit with limited control over the composition and morphology of CZTS NCs.

Here, we report a 90%-yield synthesis of monodisperse CZTS NCs, using a heating-up procedure and high initial concentration of precursors, up to 0.6 mmol per gram of a reaction mixture, which is a factor of 8–10 higher than that commonly used in NC synthesis. We also present a detailed nuclear magnetic resonance (NMR) study of the surface capping ligands and an efficient organic ligand displacement procedure, with a final carbon content of just 0.1–0.2 wt %.

2. EXPERIMENTAL SECTION

Chemicals and Solvents. *tert*-Dodecanethiol (tDDT, 98.5%), 1-dodecanethiol (DDT, ≥98%), tin(IV) chloride pentahydrate (SnCl₄·5H₂O, 98%), zinc oxide (ZnO, ≥99%), copper(II) chloride dihydrate (CuCl₂·2H₂O, ≥99%), 1-octadecene (ODE, 90%), and oleylamine (OLA, 70%) were purchased from Aldrich. Chloroform, isopropanol, dimethyl formamide (DMF), and tetrahydrofuran (THF) were analytical grade and obtained from various sources. OLA was vacuum-distilled before its use. The use of “as received” OLA results in poor NC size distributions and irregular NC shapes. Others precursors and solvents were used without further purification. Cole-Parmer “Digi-Sense R/S” temperature controllers with enabled “autotuning” mode were used for the accurate control of the heating rate during the synthesis.

CZTS Nanocrystals. Quasi-spherical CZTS NCs were prepared by the reaction of copper and tin chlorides and zinc oxide with a mixture of tDDT and DDT in the presence of OLA. In a typical synthesis, 5.4 mmol (920 mg) of CuCl₂·2H₂O, 4.8 mmol (391 mg) of ZnO, and 1.8 mmol (630 mg) of SnCl₄·5H₂O were dissolved in a minimal amount of THF. Afterward, 24 mmol (6.43 g) of distilled OLA and 20 g of ODE were added to the reaction mixture. The solution was heated under argon flow (ca. 30 mL/min) to 175 °C and maintained at this temperature for ~1 h to ensure the removal of traces of low-boiling-point impurities and water. Three issues to be noted at this point:

- (i) the purification time may be significantly optimized in a large-scale production scenario;
- (ii) the main reason to use THF as a co-solvent is to facilitate the metal salts dissolution, but it also helped to remove water from the reaction mixture; and
- (iii) ZnO is soluble only with the presence of SnCl₄·5H₂O in solution.

After purging, the mixture was cooled to 100 °C and 50 mmol (10.12 g) of tDDT and 5 mmol (1.012 g) of DDT were added through a syringe. The solution then was heated to 250 °C during 10 min and maintained at this temperature for 1 h. A constant heating rate and a high argon flow during the heating were key to obtaining monodisperse NCs. The formation of NCs was noted by a gradual darkening of the reaction mixture at ~135–145 °C. Final CZTS NCs were thoroughly purified by multiple precipitation and redispersion steps, using 2-propanol and chloroform. Finally, CZTS NCs were dissolved in THF and the solution was centrifuged at 9000 rpm for 5–15 min to precipitate poorly soluble unreacted metal complexes and large (>100 nm) Zn-rich particles (note the initial nonstoichiometric precursor ratio). The supernatant was recovered and stored for its posterior use. No additional size-selective precipitation was performed. The proposed synthetic route allowed to prepare ~670 mg of CZTS NCs in 30 g of reaction mixture, and with a precursor metal concentration of 0.3 mmol/g. It is worth mentioning that the total precursor concentration might be doubled simply by reducing the amount of solvent. However, by doing so, the viscosity of the reaction mixture increased significantly, reducing the product quality and rendering the synthetic procedure less convenient. Instead, we propose to proportionally scale up the synthesis by a factor of 10 by conducting the synthesis in a 1 L flask. In fact, we regularly performed this synthesis protocol at 5–7-fold scale, producing 5–6 g of CZTS NCs per batch with essentially the same results. The typical yield of the synthesis was ~90%.

Characterization Techniques. The morphological, chemical, and structural characterizations of the NCs were carried out by transmission electron microscopy (TEM) and high-resolution transmission electron microscopy (HRTEM). Carbon-coated TEM grids from Ted-Pella were used as substrates. A solution of the CZTS NCs in THF was deposited dropwise directly onto the grids and dried under ambient conditions. HRTEM images were obtained using a FEI Tecnai F20 field-emission gun microscope operated at 200 keV with an embedded Gatan image filter for EELS analyses. Images were analyzed by means of Gatan Digital Micrograph software. Powder X-ray diffraction (XRD) patterns were obtained with Cu K α (λ = 1.5406 Å) radiation in a reflection geometry on a Bruker D8 system operating at 40 kV and 40 mA. Raman scattering measurements were performed in backscattering configuration with a LabRam Model HR800-UV Horiba–Jobin Yvon spectrometer, using the 532 nm line from a Nd:YAG solid-state laser and the 325.0 nm line from a HeNe laser as excitation lights. Elemental analyses were performed using an elemental organic analyzer (Thermo, Model EA 1108), working under a helium flow of 120 mL/min; the combustion furnace temperature was 1000 °C, the chromatographic column oven temperature was 60 °C, and the pressure of the 10 mL oxygen loop was 100 kPa.

Nuclear magnetic resonance (NMR) measurements were recorded on a Bruker Model Avance III HD Spectrometer operating at a ¹H frequency of 500.26 MHz and equipped with a BBFO-Z probe. The sample temperature was set to 298.2 K. One-dimensional (1D) ¹H and 2D NOESY (nuclear Overhauser effect spectroscopy) spectra were acquired using standard pulse sequences from the Bruker library. For the quantitative 1D ¹H measurements, 64k data points were sampled with the spectral width set to 20 ppm and a relaxation delay of 30 s. The NOESY mixing time was set to 300 ms and 4096 data points in the direct dimension for 512 data points in the indirect dimension were sampled, with the spectral width set to 12 ppm. Diffusion measurements (2D DOSY) were performed using a double-stimulated echo sequence for convection compensation and with monopolar gradient pulses.²⁴ Smoothed rectangle gradient pulse shapes were used throughout. The gradient strength was varied quadratically from 2% to 95% of the probe's maximum value in 64 increments, with the gradient pulse duration and diffusion delay optimized to ensure a final attenuation of the signal in the final increment of <10%, relative to the first increment. For 2D processing, the spectra were zero-filled until a 4096–2048 real data matrix. Before Fourier transformation, the 2D spectra were multiplied with a squared cosine bell function in both dimensions, the 1D spectra were multiplied with an exponential

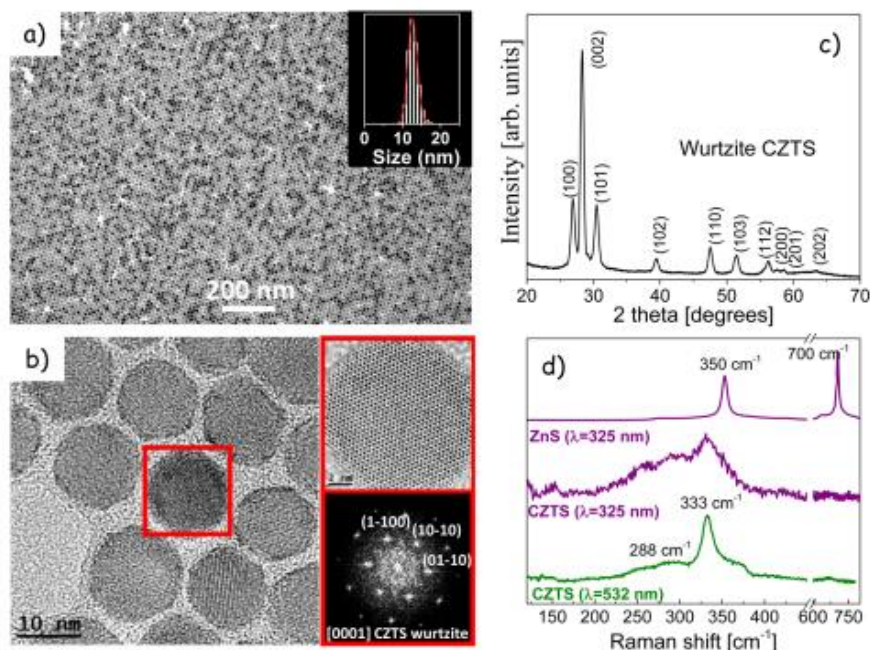


Figure 1. (a) Representative TEM micrograph and a typical size histogram of CZTS nanocrystals (NCs); (b) HRTEM micrograph and corresponding indexed power spectrum on the selected CZTS NC in the red square; (c) XRD pattern and (d) Raman spectra with 532 and 325 nm excitation of CZTS NCs. The resonant Raman spectrum of ZnS obtained under 325 nm excitation is also shown as a reference.

window function. Concentrations were obtained using the Digital ERETIC method, as provided in the standard software of Bruker. The diffusion coefficients were obtained by fitting the appropriate Stejskal–Tanner equation to the signal intensity decay.²⁵

3. RESULTS AND DISCUSSION

Representative TEM and HRTEM micrographs of the CZTS NCs prepared following the above detailed heating-up procedure are shown in Figures 1a and 1b, respectively. CZTS NCs have slightly faceted, almost isotropic spherical shapes. Importantly, the size dispersion was below 10% (estimated as full-width at half-maximum (fwhm) of the size histogram collected from several hundred NCs). The power spectrum, shown in Figure 1b, unambiguously revealed CZTS NCs with a wurtzite phase and lattice parameters; $a = b = 0.3839$ nm and $c = 0.6339$ nm ($P6_3mc$ space group). XRD analysis confirmed the wurtzite crystal phase of the CZTS NCs (Figure 1c). The presence of alkylthiols in the reaction mixture was found to be crucial to obtain CZTS NCs of this crystal structure. In contrast, sulfur as a precursor causes the formation of nanoparticles with a kesterite structure.³⁰ Raman spectra of the produced materials are shown in Figure 1d. Various excitation wavelengths were used to enhance the signal of the possible secondary and ternary impurity phases. The Raman spectrum obtained with a 532 nm excitation shows two broad bands, at 333 and 288 cm^{-1} , which agree well with the reported spectra of wurtzite CZTS. The presence of CuS, SnS, SnS₂, SnS₃, or Cu₂SnS₃ would have associated bands at 475 cm^{-1} , 190–220 cm^{-1} , 315 cm^{-1} , 310, or 350 cm^{-1} ,¹⁹ respectively, which were not observed. Raman spectra with 325 nm excitation were also obtained to verify the possible presence of ZnS, which is characterized by the presence of two peaks at 350 and 700 cm^{-1} . None of these peaks was observed, ruling out the presence of this phase in the final material.

Figure 2 shows the programmed temperature profiles and actual readouts from the thermocouples during the synthesis.

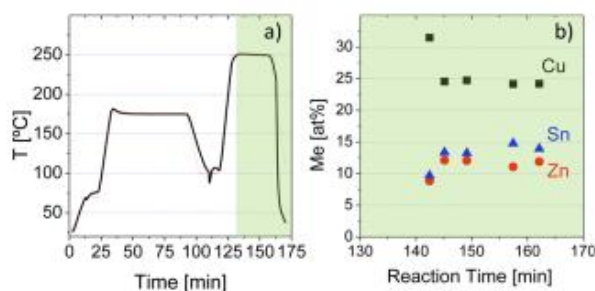


Figure 2. (a) Programmed (red) and real (black) temperature profiles. (b) Evolution of the composition of the CZTS NCs during the synthesis: (■) Cu, (●) Zn, and (▲) Sn.

The initial formation of NCs was observed as a clear change of color of the reaction mixture from yellow to dark-brown at 135–145 °C. At this point, copper sulfide NCs nucleated first due to high chalcophilicity of this metal. These NCs then grew via the incorporation of all other metals from the reaction medium (Cu, Zn, and Sn ions) as the temperature increased. A similar mechanism of the formation of quaternary phases, based on the progressive incorporation of the different cations in an initially formed copper chalcogenide lattice, was observed for several Cu-based quaternary chalcogenide semiconductors, such as Cu₂CdSnSe₄ (see ref 26) and CZTS.^{27–29} The formation of the CZTS NCs was completed close to reaching the peak temperature of the temperature ramp (250 °C). The final composition and size remained unchanged after further annealing at 250 °C for 30 min.

Surprisingly, the heating rate played an insignificant role on the size and composition of the formed CZTS NCs. For example, constant-rate 10 or 30 min ramps from 100 °C to 250 °C resulted in essentially the same final material. However, the stability of the heating rate had a much more profound effect on the size distribution of the obtained CZTS NCs, as consistently observed in over 20 syntheses shown in Figure 3.

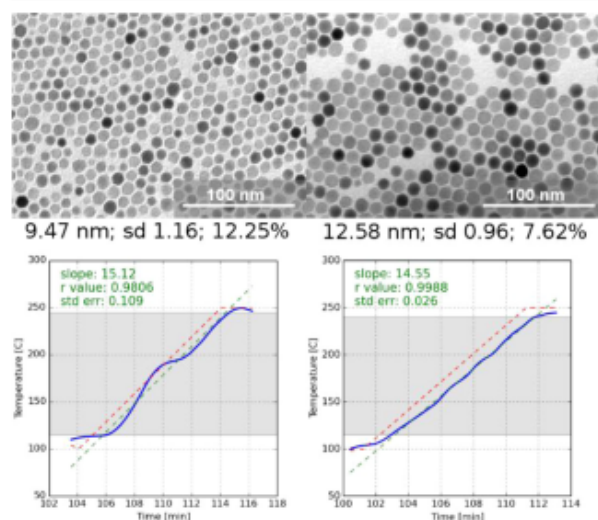


Figure 3. Representative TEM images of CZTS NCs obtained from a floating (left) and a steady (right) heating rate. CZTS NCs with 12% standard size dispersion were obtained using a relatively irregular heating rate. NCs produced with a more stable heating rate were characterized with size distributions of 7.6%.

We associate this result with a better separation of the nucleation and growth stages and a higher temperature homogeneity of the solution with a steady heating rate. Practically, this result points to the need for accurate control

and knowledge of the temperature profile of the NC synthesis. The second main factor determining the size distribution was mixing of the reagents. Intense argon bubbling (few bubbles per second, ca. 30 mL/min) was found to be a key to obtaining high-quality CZTS NCs. Argon bubbling facilitates both mixing and heat transfer during the heat-up process, as previously indicated by Lynch et al. for the heat-up synthesis of iron oxide NCs.³¹

Besides the scalability of the heat-up based syntheses, the ability to synthesize at high concentrations and with high reaction yields is also highly important. Hence, these considerations had also received a great amount of attention in this study. Figure 4a shows a ternary diagram with data points corresponding to the actual composition of CZTS NCs produced at gradually higher precursor concentrations, obtained by reducing the amount of solvent (ODE) and keeping the same quantities of all reagents. Higher precursor concentrations resulted in a decrease in the zinc content and a slight increase in tin content in the final CZTS NCs. These changes were then eliminated by readjusting the ratios of reagents: increasing the amount of ZnO and decreasing the amount of $\text{SnCl}_4 \cdot 5\text{H}_2\text{O}$. As a side effect of additional ZnO, an impurity of large polydisperse ZnS-rich NCs had formed, but could be easily removed by centrifugation. On the other hand, the batch-to-batch compositional dispersion was relatively low, as shown in Figure 4b, showing the composition of 16 CZTS NC batches obtained using the same total metal concentration.

The size, shape, and monodispersity of CZTS NCs did not change significantly with the total precursor concentration when maintaining the metal ratios constant. On the other hand, the Cu:Zn:Sn ratio was a main factor governing the shape of the CZTS nanoparticles. It is well-known that the presence of tDDT in the reaction mixture is a key factor for the production of rod-shaped CZTS and CTS nanoparticles.³² It is considered that, while DDT binds equally to all facets, tDDT preferentially binds to specific facets, leaving the [001] direction for crystal growth. This difference allows the preparation of CZTS or CTS NCs with different aspect ratios.³² It is assumed that DDT

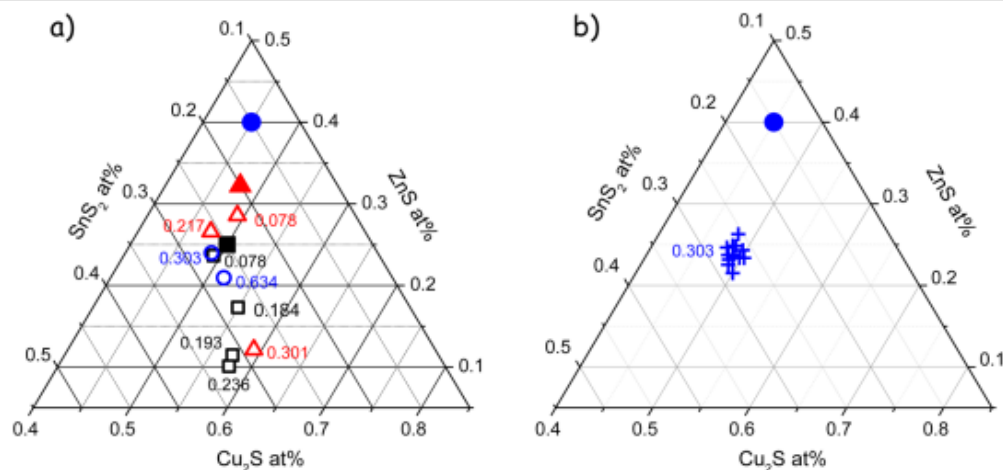


Figure 4. Ternary diagrams of the composition of CZTS NCs: (a) composition for samples obtained using different total metal concentrations in the initial solution, as detailed within the graph (in mmol) of the metals ($\Sigma_{(\text{Cu}+\text{Zn}+\text{Sn})}$) per gram of a reaction mixture. The symbol color and shape display the initial ratio of metals. The [Cu, Zn, Sn] initial concentration ratios were (\square) [2, 1, 1], (\triangle) [2, 1.35, 0.84], and (\circ) [2, 1.78, 0.67]. The solid black square, red triangle, and blue circle mark the initial precursor concentrations used for the materials represented with empty black squares, red triangles and blue circles, respectively. (b) Composition of 16 CZTS samples produced with a metal concentration of 0.303 mmol/g and an initial metal ratio of [Cu, Zn, Sn] = [2, 1.78, 0.67].

binds to the surface of CZTS NCs stronger, allowing for the preparation of smaller but more homogeneous CZTS nanorods. (See Figure S3 in the Supporting Information for representative TEM micrographs of CZTS NCs synthesized with and without DDT.) Surprisingly, we found that, at high precursor concentrations, the presence of tDDT did not significantly influence the shape of the CZTS NCs. Only highly Cu-rich precursor solutions in combination with high initial precursor concentration resulted in the formation of quasi-spherical CZTS nanocrystals, as shown in Figure 5.

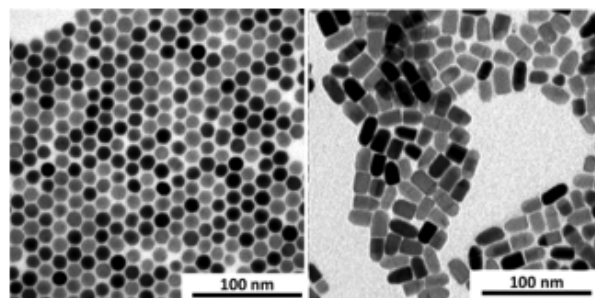


Figure 5. TEM image of CZTS NCs prepared using different Cu:Zn:Sn ratios and concentrations: 3.50:2.67:1.00 and 0.303 mmol/g (left) and 2.40:1.60:1.00 and 0.219 mmol/g (right). A TEM image of the rodlike CZTS NCs prepared with stoichiometric precursor concentrations is presented in Figure S2 in the Supporting Information. The presence of tDDT in the reaction mixture did not influence the shape of CZTS NCs at high precursor concentrations.

To study the surface chemistry of the synthesized CZTS NCs, NMR measurements were performed on a purified dispersion of CZTS NCs (see Figure 6). In the ^1H NMR spectrum, overlapping sharp and broad resonances were detected in the chemical shift range of 0–3 ppm (Figure 6a), rendering it difficult to directly interpret them. However, the isolated alkene resonance at 5.5 ppm was clearly broadened, an effect of slower molecular tumbling, which is attributed to the binding of ligands to NC surfaces.³³ As OLA is the only molecule in the reaction mixture with an internal alkene, and we thus identify OLA as a ligand. Confirmation of the bound nature of OLA is provided by the negative (black) cross peaks between its resonances in the 2D NOESY spectrum (Figure 6b). In addition, we find that the sharp resonances feature

positive (red) cross peaks, which means that the corresponding molecule does not interact with the surface and is a desorbed or unbound ligand.

The overlapping resonances at 0–3 ppm can be separated along the diffusion dimension (Figure 6c) as the broad resonances correspond to bound OLA, diffusing slowly while the sharp resonances belong to a free, yet unidentified molecule, diffusing quickly. The diffusion coefficient of OLA is $41 \mu\text{m}^2/\text{s}$ and can be converted to a solvo-dynamic diameter of 20 nm, using the Stokes–Einstein equation. Since this value is of the same order of magnitude as the NC diameter, we conclude that OLA is tightly bound to the NC.³⁴ Amines typically bind in a NC(L) binding motif (a stoichiometric nanocrystal with an L-type ligand coordinating to surface metal ions) and, although they are generally considered as weakly binding ligands, they were found to bind tightly to copper indium sulfide NCs.³⁵ Here, we find the same tight binding to CZTS NCs, and we infer that this is due to the strong affinity of amines for copper.

Interestingly, neither the reference spectrum of DDT, nor the reference spectrum of tDDT, match the sharp resonances of the unbound compound. However, when DDT is added to the sample, its resonances disappear after 2 weeks and the signals of the unidentified species have increased in intensity, suggesting that this compound is a degradation product of DDT.

Finally, the OLA concentration was quantified to 5.34 mM and with an NC diameter (13 nm) and an NC concentration (13 mM), we calculated a ligand density of 0.8 nm^{-2} . This is a rather low value, since full coverage typically corresponds to 4–5 ligands per square nanometer and it can be explained by assuming that the original ligand shell comprised both thiol and amine and that the thiol degraded over time, possibly even catalyzed by the CZTS NCs. However, to confirm these speculations, a thorough surface chemistry study during all the synthetic steps would be needed, which is outside the scope of this contribution. The solvo-dynamic diameter from the DOSY experiment (20 nm) was also higher than the sum of the NC core diameter (13 nm) and the organic ligand shell (3 nm). This leads us to believe that the NCs agglomerate during the drying step, prior to dissolution in CDCl_3 —because of the low ligand coverage.

Potential applications of CZTS NCs requires displacement of the bulky ligands from the surface of the NCs. Several potentially useful short surfactants were tested as stabilizers of the CZTS nanoparticles in polar media (see Table S1 in the

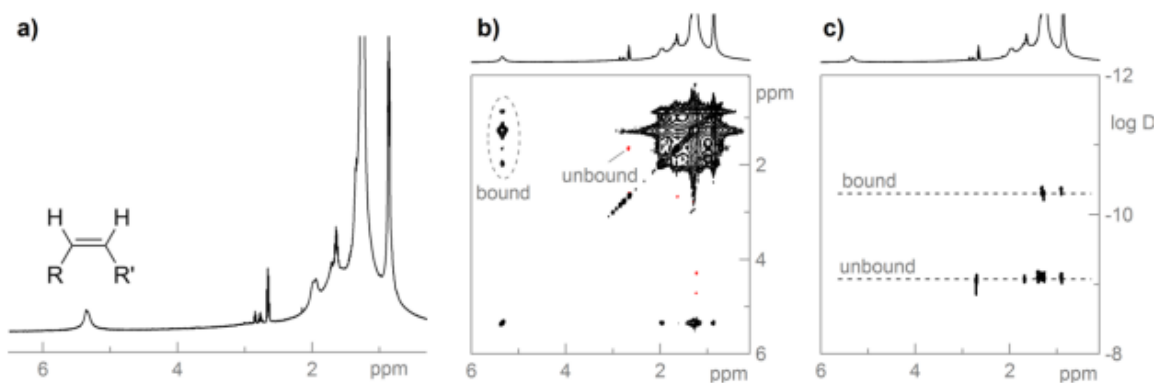


Figure 6. (a) ^1H NMR spectrum of 14 nm CZTS NCs in CDCl_3 ; concentration is $8.4 \mu\text{M}$ particles. (b) NOESY spectrum of the same sample. (c) DOSY spectrum of the same sample.

Supporting Information). Thermogravimetric analysis showed that weight loss upon heat treatment was only a few percent and was mainly dependent on the drying conditions. (See the Supporting Information for details.) Note that DMF and water are tightly bound to the surface of CZTS NCs and an intensive drying procedure needs to be applied in order to remove them completely. CZTS NCs typically lose solubility after such excessive drying. Exchanged samples showed exceptionally low carbon content (<1 wt % with a record value of 0.1–0.2 wt %, which is the practical limit of the used analytical instrument) after heat treatment in a nitrogen atmosphere. We believe that the residual carbon content is dependent more on the practical accuracy during the cleaning procedure after ligand exchange than on the nature of the stabilizer/solvent couple used.

4. CONCLUSION

In summary, we detailed a >90% yield synthesis to prepare highly monodisperse wurtzite CZTS nanocrystals (NCs) with the size distributions below 10%. The synthesis protocol is easy to scale up in order to prepare at least several grams of CZTS NCs per batch. To produce stoichiometric NCs with highly concentrated precursor solutions, initial metal ratios had to be adjusted. Finally, effective mixing and heat exchange using intense argon bubbling and a careful control of the heating ramp stability were found to be key parameters to produce highly monodisperse CZTS NCs.

■ ASSOCIATED CONTENT

Supporting Information

The Supporting Information is available free of charge on the ACS Publications website at DOI: 10.1021/acs.chemmater.5b03417.

Ligand exchange procedure, TEM images of CZTS nanoparticles prepared with and without *tert*-dodecanethiol; TG, zeta potentials and IR spectra of the CZTS nanoparticles; additional HRTEM images of CZTS nanoparticles (PDF)

■ AUTHOR INFORMATION

Corresponding Author

*E-mail: ashavel@medcomadvance.com.

Present Address

#Medcom Advance SA, Edifici N5, Campus de Sescelades, Carrer de Marcel·lí Domingo s/n, 43007 Tarragona, Spain.

Author Contributions

The manuscript was written through contributions of all authors. All authors have given approval to the final version of the manuscript.

Notes

The authors declare no competing financial interest.

■ ACKNOWLEDGMENTS

This work was supported by the European Regional Development Funds and the Framework 7 program under the projects UNION (FP7-NMP-2012-310250), SCALENANO (FP7-NMP-ENERGY-2011-284486) and KESTCELLS (FP7/2007-2013/316488) and the Spanish MINECO Project BOOSTER (ENE2013-46624-C4-3-R). M.L. thanks AGAUR for their Beatriu de Pinós postdoctoral grant (2013 BP-A00344). J.D.R. thanks the FWO (Research Foundation Flanders) for financial support. M.V.K. acknowledges partial financial support

by the European Union (EU) via FP7 ERC Starting Grant 2012 (Project NANOSOLID, GA No. 306733). Authors also acknowledge the funding from Generalitat de Catalunya 2014 SGR 1638.

■ ABBREVIATIONS

CZTS, (Cu₂ZnSnS₄); ODE, 1-octadene; OLA, oleylamine; THF, tetrahydrofuran; tDDT, *tert*-dodecanethiol; DDT, dodecanethiol; NC, nanocrystals

■ REFERENCES

- (1) Todorov, T. K.; Tang, J.; Bag, S.; Gunawan, O.; Gokmen, T.; Zhu, Y.; Mitzi, D. Beyond 11% Efficiency: Characteristics of State-of-the-Art Cu₂ZnSn(S,Se)₄ Solar Cells. *Adv. Energy Mater.* **2013**, *3*, 34–38.
- (2) Chen, S.; Walsh, A.; Gong, X.-G.; Wei, S.-H. Classification of Lattice Defects in the Kesterite Cu₂ZnSnS₄ and Cu₂ZnSnSe₄ Earth-Abundant Solar Cell Absorbers. *Adv. Mater.* **2013**, *25*, 1522–1539.
- (3) Carrete, A.; Shavel, A.; Fontané, X.; Montserrat, J.; Fan, J.; Ibáñez, M.; Saucedo, E.; Pérez-Rodríguez, A.; Cabot, A. Antimony-Based Ligand Exchange To Promote Crystallization in Spray-Deposited Cu₂ZnSnS₄ Solar Cells. *J. Am. Chem. Soc.* **2013**, *135*, 15982–15985.
- (4) Wang, P.; Minegishi, T.; Ma, G.; Takane, K.; Satou, Y.; Maekawa, S.; Kabori, Y.; Kubota, J.; Domen, K. Photoelectrochemical Conversion of Toluene to Methylcyclohexane as an Organic Hydride by Cu₂ZnSnS₄-Based Photoelectrode Assemblies. *J. Am. Chem. Soc.* **2012**, *134*, 2469–2472.
- (5) Patra, B. K.; Shit, A.; Guria, A. K.; Sarkar, S.; Prusty, G.; Pradhan, N. Coincident Site Epitaxy at the Junction of Au–Cu₂ZnSnS₄ Heteronanostructures. *Chem. Mater.* **2015**, *27*, 650–657.
- (6) Yu, X.; Shavel, A.; An, X.; Luo, Z.; Ibáñez, M.; Cabot, A. Cu₂ZnSnS₄-Pt and Cu₂ZnSnS₄-Au Heterostructured Nanoparticles for Photocatalytic Water Splitting and Pollutant Degradation. *J. Am. Chem. Soc.* **2014**, *136*, 9236–9239.
- (7) Yu, X.; An, X.; Shavel, A.; Ibáñez, M.; Cabot, A. The Effect of the Ga Content on the Photocatalytic Hydrogen Evolution of CuIn_{1-x}Ga_xS₂ nanocrystals. *J. Mater. Chem. A* **2014**, *2*, 12317–12322.
- (8) Yu, X.; Liu, J.; Genç, A.; Ibáñez, M.; Luo, Z.; Shavel, A.; Arbiol, J.; Zhang, G.; Zhang, Y.; Cabot, A. Cu₂ZnSnS₄-Ag₂S Nanoscale *p-n* Heterostructures as Sensitizers for Photoelectrochemical Water Splitting. *Langmuir* **2015**, *31*, 10555–10561.
- (9) Yu, X.; An, X.; Genç, A.; Ibáñez, M.; Arbiol, J.; Zhang, Y.; Cabot, A. Cu₂ZnSnS₄-PtM (M = Co, Ni) Nanoheterostructures for Photocatalytic Hydrogen Evolution. *J. Phys. Chem. C* **2015**, *119*, 21882–21888.
- (10) Liu, M.-L.; Chen, L.-W.; Huang, F.-Q.; Chen, L.-D. Improved Thermoelectric Properties of Cu-Doped Quaternary Chalcogenides of Cu₂CdSnSe₄. *Adv. Mater.* **2009**, *21*, 3808–3812.
- (11) Xiao, C.; Li, K.; Zhang, J.; Tong, W.; Liu, Y.; Li, Z.; Huang, P.; Pan, B.; Su, H.; Xie, Y. Magnetic Ions in Wide Band Gap Semiconductor Nanocrystals for Optimized Thermoelectric Properties. *Mater. Horiz.* **2014**, *1*, 81–86.
- (12) Guo, Q.; Hillhouse, H. W.; Agrawal, R. Synthesis of Cu₂ZnSnS₄ Nanocrystal Ink and Its Use for Solar Cells. *J. Am. Chem. Soc.* **2009**, *131*, 11672–11673.
- (13) Ibáñez, M.; Zamani, R.; Gorse, S.; Fan, J.; Ortega, S.; Cadavid, D.; Morante, J. R.; Arbiol, J.; Cabot, A. Core-Shell Nanoparticles As Building Blocks for the Bottom-Up Production of Functional Nanocomposites: PbTe–PbS Thermoelectric Properties. *ACS Nano* **2013**, *7*, 2573–2586.
- (14) Ibáñez, M.; Korkosz, R. J.; Luo, Z.; Riba, P.; Cadavid, D.; Ortega, S.; Cabot, A.; Kanatzidis, M. G. Electron Doping in Bottom-Up Engineered Thermoelectric Nanomaterials through HCl-Mediated Ligand Displacement. *J. Am. Chem. Soc.* **2015**, *137*, 4046–4049.
- (15) Ibáñez, M.; Zamani, R.; Lalonde, A.; Cadavid, D.; Li, W.; Shavel, A.; Arbiol, J.; Morante, J. R.; Gorse, S.; Snyder, G. J.; Cabot, A.

Cu₂ZnGeSe₄ Nanocrystals: Synthesis and Thermoelectric Properties. *J. Am. Chem. Soc.* **2012**, *134*, 4060–4063.

(16) Yang, W.-C.; Miskin, C. K.; Carter, N. J.; Agrawal, R.; Stach, E. A. Compositional Inhomogeneity of Multinary Semiconductor Nanoparticles: A Case Study of Cu₂ZnSnS₄. *Chem. Mater.* **2014**, *26*, 6955–6962.

(17) Haas, W.; Rath, T.; Pein, A.; Rattenberger, J.; Trimmel, G.; Hofer, F. The Stoichiometry of Single Nanoparticles of Copper Zinc Tin Selenide. *Chem. Commun.* **2011**, *47*, 2050–2052.

(18) Shavel, A.; Cadavid, D.; Ibáñez, M.; Carrete, A.; Cabot, A. Continuous Production of Cu₂ZnSnS₄ Nanocrystals in a Flow Reactor. *J. Am. Chem. Soc.* **2012**, *134*, 1438–1441.

(19) Singh, A.; Geaney, H.; Laffir, F.; Ryan, K. M. Colloidal Synthesis of Wurtzite Cu₂ZnSnS₄ Nanorods and Their Perpendicular Assembly. *J. Am. Chem. Soc.* **2012**, *134*, 2910–2913.

(20) van Embden, J.; Chesman, A. S. R.; Jasieniak, J. J. The Heat-Up Synthesis of Colloidal Nanocrystals. *Chem. Mater.* **2015**, *27*, 2246–2285.

(21) Park, B.-I.; Hwang, Y.; Lee, S. Y.; Lee, J.-S.; Park, J.-K.; Jeong, J.; Kim, J. Y.; Kim, B.; Cho, S.-H.; Lee, D.-K. Solvent-Free Synthesis of Cu₂ZnSnS₄ Nanocrystals: A Facile, Green, Up-Scalable Route for Low Cost Photovoltaic Cells. *Nanoscale* **2014**, *6*, 11703–11711.

(22) Chesman, A. S. R.; van Embden, J.; Duffy, N. W.; Webster, N. A. S.; Jasieniak, J. J. *In Situ* Formation of Reactive Sulfide Precursors in the One-Pot, Multigram Synthesis of Cu₂ZnSnS₄ Nanocrystals. *Cryst. Growth Des.* **2013**, *13*, 1712–1720.

(23) Chesman, A. S. R.; Duffy, N. W.; Peacock, S.; Waddington, L.; Webster, N. A. S.; Jasieniak, J. J. Non-injection synthesis of Cu₂ZnSnS₄ nanocrystals using a binary precursor and ligand approach. *RSC Adv.* **2013**, *3*, 1017–1020.

(24) Connell, M. A.; Bowyer, P. J.; Bone, P. A.; Davis, A. L.; Swanson, A. G.; Nilsson, M.; Morris, G. A. Improving the Accuracy of Pulsed Field Gradient NMR Diffusion Experiments: Correction for Gradient Non-Uniformity. *J. Magn. Reson.* **2009**, *198*, 121–131.

(25) Sinnaeve, D. The Stejskal–Tanner Equation Generalized for Any Gradient Shape—An Overview of Most Pulse Sequences Measuring Free Diffusion. *Concepts Magn. Reson., Part A* **2012**, *40A*, 39–65.

(26) Ibáñez, M.; Zamani, R.; Li, W.; Shavel, A.; Arbiol, J.; Morante, J. R.; Cabot, A. Extending the Nanocrystal Synthesis Control to Quaternary Composition. *Cryst. Growth Des.* **2012**, *12*, 1085–109.

(27) Coughlan, C.; Ryan, K. M. Complete Study of the Composition and Shape Evolution in the Synthesis of Cu₂ZnSnS₄ (CZTS) Semiconductor Nanocrystals. *CrystEngComm* **2015**, *17*, 6914–6922.

(28) Liao, H.-C.; Jao, M.-H.; Shyue, J.-J.; Chen, Y.-F.; Su, W.-F. Facile Synthesis of Wurtzite Copper–Zinc–Tin Sulfide Nanocrystals from Plasmonic Djurleite Nuclei. *J. Mater. Chem. A* **2013**, *1*, 337–341.

(29) Collord, A. D.; Hillhouse, H. W. Composition Control and Formation Pathway of CZTS and CZTGS Nanocrystal Inks for Kesterite Solar Cells. *Chem. Mater.* **2015**, *27*, 1855–1862.

(30) Gabka, G.; Bujak, P.; Gryszel, M.; Ostrowski, A.; Malinowska, K.; Zukowska, G. Z.; Agnese, F.; Pron, A.; Reiss, P. Synthesis and Surface Chemistry of High Quality Wurtzite and Kesterite Cu₂ZnSnS₄ Nanocrystals Using Tin(II) 2-Ethylhexanoate as a New Tin Source. *Chem. Commun.* **2015**, *51*, 12985–12988.

(31) Lynch, J.; Zhuang, J.; Wang, T.; LaMontagne, D.; Wu, H.; Cao, Y. C. Gas-Bubble Effects on the Formation of Colloidal Iron Oxide Nanocrystals. *J. Am. Chem. Soc.* **2011**, *133*, 12664–12674.

(32) Wang, J.-J.; Liu, P.; Ryan, K. M. A Facile Phosphine-Free Colloidal Synthesis of Cu₂SnS₃ and Cu₂ZnSnS₄ Nanorods with a Controllable Aspect Ratio. *Chem. Commun.* **2015**, *51*, 13810–13813.

(33) Hens, Z.; Martins, J. C. A Solution NMR Toolbox for Characterizing the Surface Chemistry of Colloidal Nanocrystals. *Chem. Mater.* **2013**, *25*, 1211–1221.

(34) De Roo, J.; Van den Broeck, F.; De Keukeleere, K.; Martins, J. C.; Van Driessche, I.; Hens, Z. Unravelling the Surface Chemistry of Metal Oxide Nanocrystals, the Role of Acids and Bases. *J. Am. Chem. Soc.* **2014**, *136*, 9650–9657.

(35) Dierick, R.; Van den Broeck, F.; De Nolf, K.; Zhao, Q.; Vantomme, A.; Martins, J. C.; Hens, Z. Surface Chemistry of CuInS₂ Colloidal Nanocrystals, Tight Binding of L-Type Ligands. *Chem. Mater.* **2014**, *26*, 5950–5957.

Scalable heating-up procedure to synthesize monodisperse $\text{Cu}_2\text{ZnSnS}_4$ nanocrystals

Supporting Information

Alexey Shavel,^{†,*} Maria Ibáñez,[†] Zhishan Luo,[†] Jonathan De Roo,[‡] Alex Carrete,[†] Mirjana Dimitrievska,[†] Aziz Genç,[§] Michaela Meyns,[†] Alejandro Perez-Rodriguez,^{†,¶} Maksym V. Kovalenko,^{⊥,||} Jordi Arbiol,^{§,§} and Andreu Cabot,^{†,§}

[†] Catalonia Energy Research Institute - IREC, Sant Adrià del Besòs, Barcelona, 08930, Spain.

[§] Catalan Institute of Nanoscience and Nanotechnology (ICN2), CSIC and The Barcelona Institute of Science and Technology, Campus UAB, Bellaterra, 08193 Barcelona, Catalonia, Spain.

[‡] Departament d'Electrònica, Universitat de Barcelona, 08028 Barcelona, Spain.

[§] Institució Catalana de Recerca i Estudis Avançats - ICREA, 08010 Barcelona, Spain.

[‡] Ghent University, Department of Inorganic and Physical Chemistry, Krijgslaan 281 S3, 9000 Gent, Belgium

[⊥] Institute of Inorganic Chemistry, Department of Chemistry and Applied Biosciences, ETH Zürich, CH-8093, Switzerland

^{||} Empa-Swiss Federal Laboratories for Materials Science and Technology, Dübendorf, CH-8600, Switzerland

Ligand exchange strategy: Organic ligands were displaced from the surface of CZTS nanocrystals using various short molecules or ions. Ligand exchange was carried out by mixing 5-10 ml of a 0.05-0.1 M solution of the new ligand (sodium diethyldithiocarbamate Na(dedtc); tetrabutylammonium 1-phenyltetrazol-5-thiolate ThioTz[NBu₄], Na₂S or NaN₃) in formamide with 10 ml of a solution of nanoparticles in chloroform (with concentration approximately equal to the crude solution). The (NH₄)₂S ligand exchange was performed by adding a few drops of (NH₄)₂S (20 wt % in water) and 10 ml of formamide (or water) into a 10 ml solution of CZTS nanoparticles stabilized in chloroform. Both mixtures were vigorously stirred and let stand until phase separation was observed. Nanoparticles moved from the chloroform to the formamide (or water) phase. The final formamide or water solution containing the nanoparticles was washed several times with chloroform to drag all the remaining organic ligands surrounding the nanoparticles. Nanoparticles were finally precipitated using acetonitrile and re-dispersed in N,N-dimethylformamide. Finally, solution was cleaned by precipitation with acetone and re-dispersion in DMF. Few drops of the fresh solution of stabilizer were added every time to DMF in order facilitate dissolution and ensure displacement of the original bulky organic ligand. The resulting nanoparticles could be deposited in the form of thin film and when heated to 500°C in nitrogen atmosphere the final carbon content was analyzed using chemical analysis. Table S1 displays the carbon contents measured for each ligand exchange procedure.

Table S1. Carbon content of the CZTS samples after heat treatment in N₂.

S	Inorganic Stabilizer	N w%	C w%	TG weight loss %
1	[NH ₄] ₂ S in FA	0	0.61-0.67	9
2	ThioTz[NBu ₄] in FA; 0.05M	0	0.15-0.19	3
3	[NH ₄] ₂ S in H ₂ O	0	1.78-1.87	5
4	ThioTz[NBu ₄] in FA; 0.05M	0	0.44	3
5	Na ₂ S in FA	0.10-0.11	0.50-0.51	-
6	Na(dedtc) in FA	0.06	0.98-0.50	14
7	NaN ₃ in FA	0	0.46-0.50	-

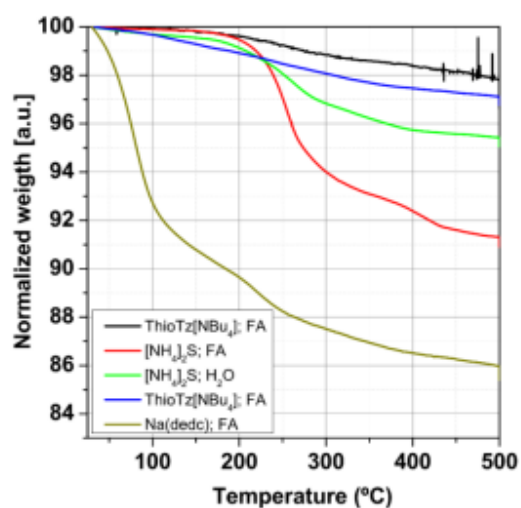


Figure S1. TG of the CZTS nanoparticles after ligand exchange.

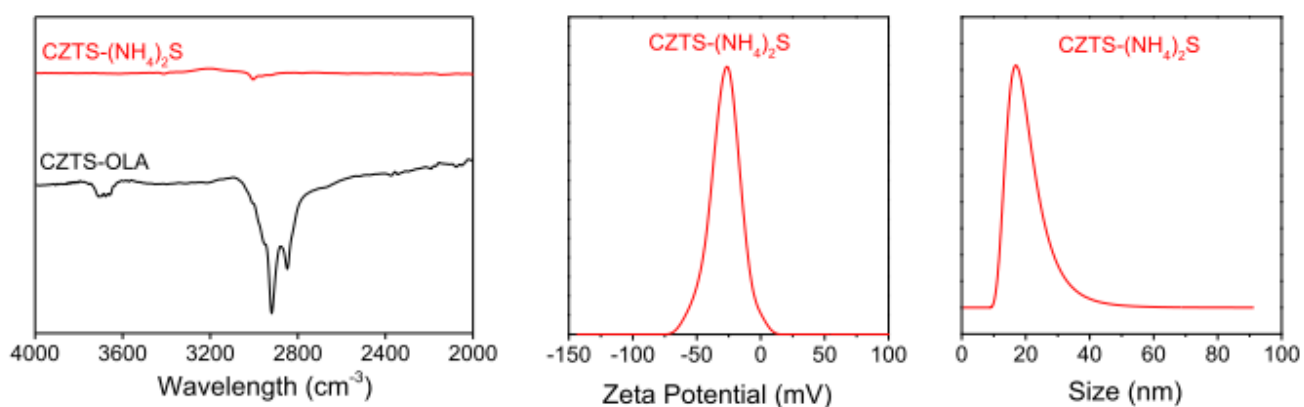


Figure S2. FTIR spectra of CZTS nanocrystals before and after ligand exchange with $(\text{NH}_4)_2\text{S}$ and zeta potential and DLS size distribution of the ligand exchanged CZTS nanocrystals.

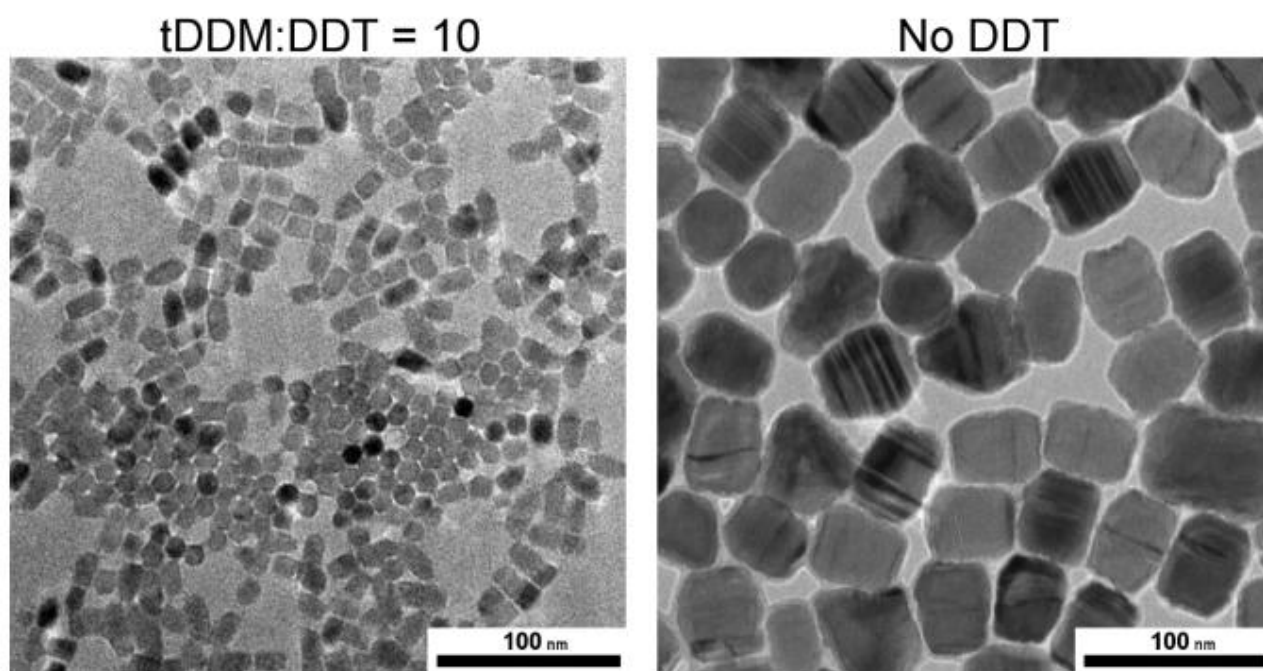


Figure S3. TEM micrographs of the CZTS nanocrystals obtained with (left) and without (right) using of the dodecylmercaptan (DDT) as a co-precursor in the synthesis. Both sample prepared with same Cu:Zn:Sn ratio (2.0:1.0:1.0) and concentration:0.078mmol/g (left) and 0.081mmol/g (right).

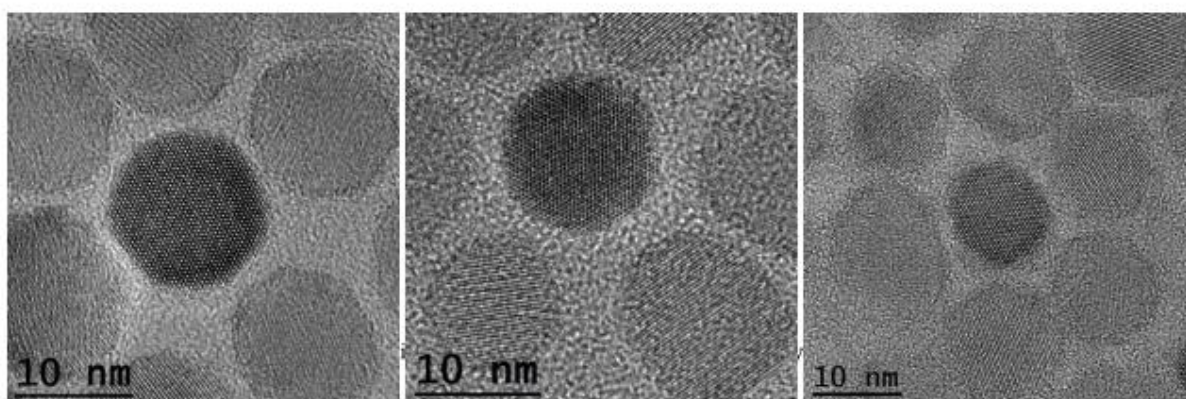


Figure S4: HRTEM micrographs of CZTS nanoparticles.

2.1.2 $\text{Cu}_2\text{ZnSnS}_4$ Nanocrystals as Highly Active and Stable Electrocatalysts for the Oxygen Reduction Reaction

The article with the title “ *$\text{Cu}_2\text{ZnSnS}_4$ Nanocrystals as Highly Active and Stable Electrocatalysts for the Oxygen Reduction Reaction*” has been submitted as is currently under review, also attached in the end of this subchapter. First-principles simulations predicted that CZTS NCs could be high performance electrocatalyst for ORR due to a relatively low energy barrier for O_2 adsorption and subsequent dissociation to OH. We compared the catalytic properties of wurzite and kesterite CZTS NCS toward ORR in alkaline medium, including stability and resistance to methanol. The kesterite CZTS NCs showed exceptional electrocatalytic performance for ORR with high current densities and low onset reduction potential over commercial Pt/C electrocatalysts (Figure 2.6). This electrocatalyst provide a reasonable alternative electrocatalysts based on non-noble metal multinary chalcogenides.

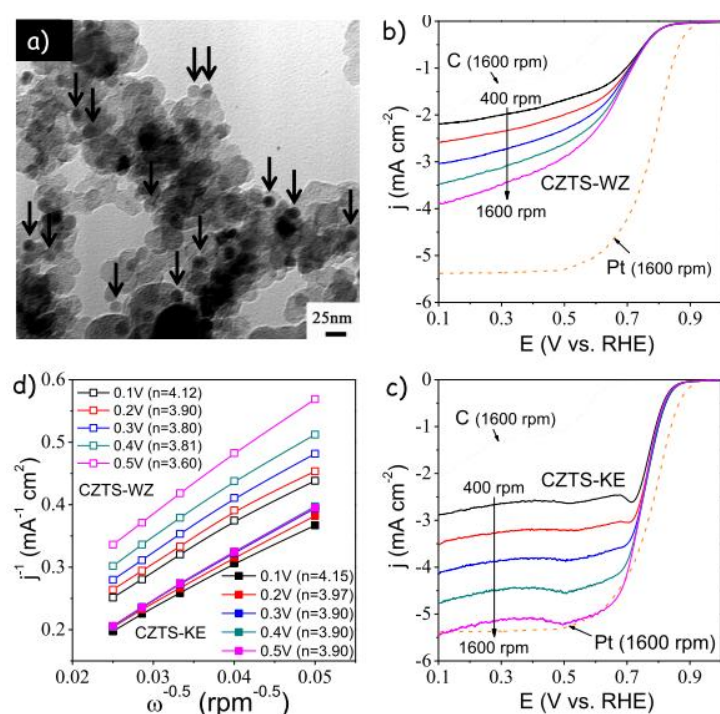


Figure 2.6 (a) TEM micrograph of the CZTS NCs supported on Ketjen carbon. Arrows point at some of the CZTS NCs. (b-c) LSV curves of the ORR at various rotation rates (400, 635, 900, 1225, 1600 rpm) from wurtzite CZTS/C (b) and kesterite CZTS/C (c) electrocatalysts in O_2 -saturated 0.1 M KOH solutions at a scan rate of 10 mV s^{-1} . The RDE voltammograms of the Ketjen carbon and of commercial Pt/C, both obtained at 1600 rpm, are also plotted for reference. (d) Koutecky–Levich plots for wurtzite and kesterite CZTS at various potentials.

Cu₂ZnSnS₄ Nanocrystals as Highly Active and Stable Electrocatalysts for the Oxygen Reduction Reaction

Received 00th January 20xx,
Accepted 00th January 20xx

DOI: 10.1039/x0xx00000x

www.rsc.org/

Xuelian Yu,^{a,*} Da Wang,^{b,†} Jingjing Liu,^c Zhishan Luo,^d Ruifeng Du,^a Li-Min Liu,^{a,b} Guangjin Zhang,^{*,c} Yihe Zhang^a and Andreu Cabot^{d,e}

The implementation of cost-effective fuel cells and metal-air batteries requires developing environmental friendly and cost-effective electrocatalyst with high activity in the oxygen reduction reaction (ORR). While several oxides has been proposed as electrocatalysts for the ORR in basic conditions, some sulfides, particularly copper sulfide, have been shown to provide some of the highest electrical conductivities and overall improved electrocatalytic properties. We use here first-principle calculations to study the oxygen adsorption and ORR kinetics on alternative copper-based sulfides and find out that the inclusion of cations with a higher oxidation state, such as Zn²⁺ and Sn⁴⁺, provides more energetically favorable sites for oxygen adsorption and subsequent formation of hydroxyls. Supported by these calculations, we synthesized Cu₂ZnSnS₄ (CZTS) nanocrystals (NCs) with controlled crystallographic phase by high-yield colloidal synthesis routes, and investigated their electrocatalytic properties toward ORR in alkaline solution. Kesterite CZTS NCs show exceptional electrocatalytic performance for ORR with high current densities (5.45 mA cm⁻² at 0.1 V vs. RHE) and low onset reduction potential (0.89 V vs. RHE), comparable to commercial Pt/C electrocatalysts. Equally important, CZTS NCs exhibit superior stability and resistance to methanol, thus avoiding the poisoning limitation of commercial Pt/C catalyst in the particular case of direct methanol fuel cells.

Introduction

The oxygen reduction reaction (ORR) is a limiting step in several energy conversion and storage technologies, such as fuel cells, metal-air batteries and certain electrolyzers.^[1,2] To accelerate this reaction, platinum-based catalysts are generally required. However, the low abundance and high cost of platinum strongly limits the cost-effective commercialization of these technologies. In addition, platinum-based electrocatalysts suffer from limited durability associated to surface poisoning by certain substances. This is the case, for instance, in direct methanol fuel cells where Pt stability becomes an issue due to methanol crossover.^[3] Alloying Pt with low-cost transition metals which maintain proper ORR activities with a lower usage of Pt represents an insufficient step in the correct direction.^[4-6] Another approach to overcome the

extraordinary challenge that the cost-effective inactivation of the ORR represents is the use of alkaline electrolytes. While the implementation of alkaline solutions still requires further electrolyte or membrane optimization in terms of performance and especially tolerance to CO₂, it has a main advantage in enabling the use of much more cost-effective catalysts. In this regard, a wide range of noble metal-free electrocatalysts have been explored for ORR in alkaline media, such as transition metal oxides, chalcogenides, nitrides, oxynitrides and modified graphene.^[7-10] Among them, copper chalcogenides have been demonstrated to provide outstanding performance and stability, especially when supported on different forms of carbon.^[11-13]

In view of the exceptional electrocatalytic properties of copper sulfides and selenides, it is surprising that other copper-based chalcogenides have not been explored for such a technologically relevant reaction, especially when taking into account that some multinary copper chalcogenides have been demonstrated to overcome binary copper chalcogenide performances in other electrocatalytic applications. This is the case on the reduction reaction of the oxidized electrolyte at the counter electrode of quantum dot sensitized solar cells, for instance.^[14-19]

The ample chemical and structural freedom of multinary chalcogenide enable optimizing this class of materials in multiple applications, including photovoltaics, thermoelectrics and catalysis.^[20,21] The small size and electronegativity differences between transition metals and chalcogens makes them strongly covalent compounds. This covalency, the chalcogen ability to catenate, the variable valences of transition metals, and the higher

^a Beijing Key Laboratory of Materials Utilization of Nonmetallic Minerals and Solid Wastes, National Laboratory of Mineral Materials, School of Materials Science and Technology, China University of Geosciences, 100083 Beijing, P. R. China.

^b Beijing Computational Science Research Center, Beijing 100193 P. R. China.

^c Key Laboratory of Green Process and Engineering, Chinese Academy of Sciences, 100190 Beijing, P. R. China.

^d Catalonia Energy Research Institute - IREC, 08930 Sant Adrià de Besòs, Barcelona, Spain.

^e ICREA, Pg. Lluís Companys 23, 08010 Barcelona, Spain

[†]These authors contributed equally to this work.

Electronic Supplementary Information (ESI) available: Top and side views of the initial state (IS), transition state (TS) and final state (FS) structures for the ORR reactions, Detailed ORR experiments, TEM images and XRD patterns after supported on carbon, CV curve in Ar- and O₂-saturated KOH solution, LSV and K-L plots of carbon black, Comparison of the performances between kesterite CZTS (this work) and other low cost catalysts reported in the literatures. See DOI: 10.1039/x0xx00000x

ability of metal atoms to form metal-metal bonds within chalcogenides result in a very large diversity of multinary chalcogenide stoichiometries and structures, including abundant non-stoichiometric phases and a wide range of solid solutions. This structural and valence variability yields materials with large densities of defects, large charge carrier concentrations and potentially excellent and tunable photocatalytic and electrocatalytic properties.^[22,23]

In this work, we investigate multinary copper-based chalcogenides as low-cost, non-toxic, potentially highly reactive and robust electrocatalysts for ORR. We first use first-principles calculations to determine the potential of $\text{Cu}_2\text{ZnSnS}_4$ (CZTS) for ORR. Then, we produce CZTS nanocrystals (NCs) with two different phases and test their catalytic properties toward ORR, including stability and tolerance to methanol crossover. We show kesterite CZTS NCs to display excellent catalytic properties toward ORR, and therefore to provide a reasonable alternative electrocatalysts based on non-noble metal multinary chalcogenides.

Experimental section

Computational methods: Our calculations were performed based on DFT calculations, as implemented in the Vienna ab initio package (VASP).^[24,25] The general gradient approximation of Perdew-Burke-Ernzerhof (GGA-PBE) was adopted for the exchange-correlation functional.^[26] Moreover, the electron wave functions were expanded by a plane wave cutoff of 400 eV. The (4×4×2) and (4×3×3) supercell kesterite and wurtzite CZTS with the stoichiometry of $\text{Cu}_{64}\text{Zn}_{32}\text{Sn}_{32}\text{S}_{128}$ and $\text{Cu}_{72}\text{Zn}_{36}\text{Sn}_{36}\text{S}_{144}$, respectively, were constructed by periodic boundary condition (PBC), and the vacuum layers were set to be larger than 20 Å to avoid periodic interaction. Reciprocal space was performed by the Monkhorst-Pack special k-point scheme with 2×2×2 grid meshes for structure relaxation for both kesterite and wurtzite CZTS. Atomic relaxation until the total energy variation was smaller than 10^{-6} eV and all forces on each atom were less than 0.01 eV/Å. We determined the free energy barrier for ORR on the CZTS using the climb image nudged elastic band (CL-NEB) method.^[27] A set of images (N=9) was uniformly distributed along the reaction path connecting the initial and final states optimized in our simulation. To ensure the continuity of the reaction path, the images were coupled with elastic forces, and each intermediate state was fully relaxed in the hyperspace perpendicular to the reaction coordinate.

Synthesis of kesterite CZTS NCs: In a typical synthesis, 1.8 mmol of $\text{CuCl}_2\cdot 2\text{H}_2\text{O}$, 1.6 mmol of ZnO and 0.6 mmol of $\text{SnCl}_4\cdot 5\text{H}_2\text{O}$, and 0.5 mmol of octadecylphosphonic acid (ODPA) were mixed with 30 mL of oleylamine (OLA) under argon flow in constant stirring. The mixture was heated to 200 °C and maintained at this temperature for 1 hour. Then the mixture was heated to 300 °C and 1 mL of a 2 M solution of tetraethylthiuram disulfide in dichlorobenzene was injected. The solution was maintained at this temperature for 30 min. NCs were thoroughly purified by multiple precipitation and redispersion steps using 2-propanol and chloroform.

Synthesis of wurtzite CZTS NCs: In a typical synthesis, 1.8 mmol of $\text{CuCl}_2\cdot 2\text{H}_2\text{O}$, 1.6 mmol of ZnO and 0.6 mmol of $\text{SnCl}_4\cdot 5\text{H}_2\text{O}$ were dissolved in a minimum amount of the tetrahydrofuran (THF). Afterward, 8 mmol of OLA and 6.5 g 1-octadecene were added to

the reaction mixture. The solution was heated under flow of argon to 175 °C and maintained at this temperature for 1 hour. Then the mixture was cooled to 100 °C and 16 mmol of tert-dodecylmercaptan and 1.6 mmol of dodecanethiol were injected. Then the solution was heated to 250 °C and maintained at this temperature for 1 hour. The purified process was the same as the kesterite ones.

Characterization: Transmission electron microscopy (TEM) analysis was carried out using a JEOL 2010F field emission gun microscope with a 0.19 nm point-to-point resolution at 200 keV. Powder XRD patterns were obtained with $\text{Cu K}\alpha 1$ ($\lambda = 1.5406$ Å) radiation in a reflection geometry on a Bruker D8 operating at 40 kV and 40 mA. Raman scattering measurements were carried out in backscattering configuration with a LabRam Model HR800-UV Horiba-Jobin Yvon spectrometer, using the 532 nm line of a Nd:YAG solid-state laser.

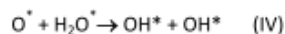
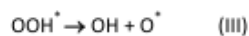
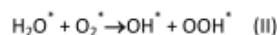
Electrochemistry Experiments: To study the material electrocatalytic performance, NCs were supported on carbon black (Ketjen carbon, C) with a weight ratio of 3:7 (NCs/C) through sonication of the NCs dispersion and C in chloroform. The C-NCs catalysts were activated via thermal annealing under Ar atmosphere at 400 °C for 1 h and then dispersed in a mixture of 0.5 mL deionized water, 0.5 mL isopropanol and 8.75 μL Nafion (10 wt%). Finally, 10 μL of this solution (5 mg/mL) was deposited on the glassy carbon (GC, 4 mm in diameter) rotating disk electrode (RDE) for electrochemical characterization. The prepared electrodes were dried at room temperature overnight before electrochemical tests. Following a similar procedure, a GC electrode coated with Pt/C (20 wt% Pt, purchased from Alfa Aesar) was also fabricated for comparison. Cyclic voltammetry (CV), linear sweep voltammetry (LSV) and chronoamperometric experiments were performed on a CHI760e electrochemical workstation (CHI Instrument Inc.). A standard three-electrode cell was used and controlled at 25 °C during the experiment using a water bath. The prepared thin-film GC electrodes were used as the working electrodes. Platinum foil and Ag/AgCl were used as the counter and reference electrodes, respectively. The Ag/AgCl electrode was calibrated with respect to the reversible hydrogen electrode (RHE) in all measurements (+0.949 V vs. RHE). The electrolyte, consisting of a solution of 0.1 M KOH, was saturated with ultrahigh-purity Ar for 30 min before the measurements. The oxygen reduction experiments were performed by saturating with ultrahigh-purity O_2 for 30 min before the measurements.

Results and discussion

First-principles calculations were carried out to determine the potential of multinary copper-based sulfides toward the ORR. After preliminary analysis of several potentially suitable ternary compounds, e.g. Cu_2SnS_3 , Cu_3SbS_4 , we focused our attention on quaternary $\text{Cu}_2\text{-II-IV-S}_4$ compounds and particularly on CZTS. CZTS is composed of four relatively earth-abundant, low-cost and non-toxic elements. In CZTS, the electronic hybridization is very strong due to the atomic levels of Cu-3d states are just slightly above the S-3p orbitals. This strong p-d hybridization results in a very significant contribution of the Cu-3d states to the near-edge valence band, while Sn mainly contributes to the near-edge conduction band. The presence of multiple elements and with

different valences at their surface also provides CZTS with a wide range of adsorption sites.

Catalytic and electrocatalytic properties not only depend on material composition, but also on its crystal phase and particularly on their surface facets. CZTS crystallizes in three possible phases: kesterite, wurtzite and stannite, being the two former the most commonly encountered. These phases have sensibly different physical and chemical characteristics, which have an impact on the material functionality. As an example, kesterite phase is generally considered the best candidate for photovoltaic application,^[28] but better results were obtained with wurtzite CZTS in the photocatalysis field.^[22] To obtain an initial estimation of the potential of CZTS for the ORR, we undertook the modelling of the two main phases, kesterite and wurtzite. We modelled the (112) surface of kesterite and the (100) surface of wurtzite CZTS following previous literature reports^[29-31] considering these two as the most probably surface facets (as shown in Figure S1). Various possible adsorption configurations and the associated energies of various ORR species on the CZTS surfaces were examined. The corresponding most stable adsorption configurations of various ORR species on the kesterite (112) surface are shown in Figure S2. Due to their higher oxidation state, all ORR species preferentially adsorb on either Sn⁴⁺ or Zn²⁺ instead of Cu⁺ ions. The kinetically most favorable reaction pathway for the ORR process catalyzed by non-precious-metal catalysts in an alkaline solution is considered to be the OOH^{*} dissociation pathway,^[32] which can be divided into four steps: I) the adsorption of an O₂ molecule onto the Cu₂ZnSnS₄ surface site (O₂^{*}); II) the reduction of O₂^{*} with H₂O^{*} to an OOH group adsorbed on the Cu₂ZnSnS₄ site; III) the transition from the OOH^{*} to an adsorbed O^{*} atom; IV) the transition from the O^{*} to an adsorbed OH^{*}. The latter three steps in our DFT calculations were considered as follows:



The relative energy profile of the ORR process on each CZTS surface was calculated, as shown in **Figure 1**. To exhibit the reaction process more clearly, the molecular level of the ORR pathway is also provided in Figures S3 and S4. As illustrated, once the O₂^{*} and H₂O^{*} were adsorbed, O₂^{*} is reduced to OOH^{*} while the H₂O^{*} is simultaneously oxidized to OH^{*}. In this case, the calculated energy barrier is 0.36 eV for the kesterite (112) surface and 0.56 eV for the wurtzite (100) surface. The rate-determining step corresponds to the transition from the OOH^{*} to an adsorbed O^{*} atom (Equation III), which has a relatively low energy barrier of 0.65 eV for kesterite CZTS. This barrier is close to the overall barrier calculated for Pd and PdCu alloys^[33] and similar to the considered as limiting reaction in FeN₄-graphene(O₂→OOH)^[34]. The calculated energy for (100) wurtzite CZTS was still moderate, 0.87 eV, but sensibly higher than that of (211) kesterite CZTS. The final step in the ORR is the O^{*} reduction to OH^{*} aided by a H₂O molecule, for which we calculated energy barriers of 0.38 eV and 0.59 eV for kesterite (112) surface and wurtzite (100) surface, respectively. Overall, DFT results clearly show that CZTS, particularly kesterite CZTS, has an excellent potential for ORR.

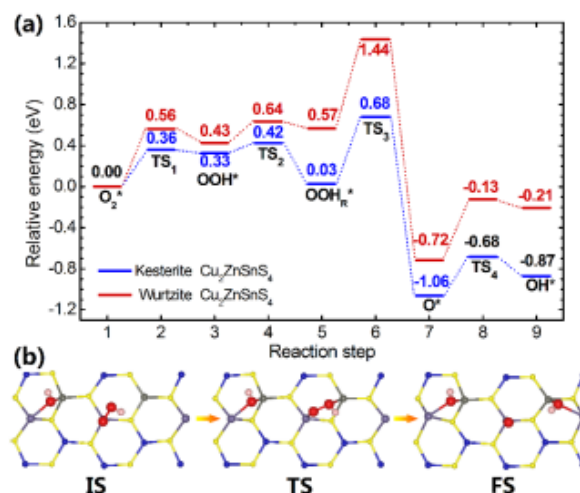


Figure 1. The chemical reactivity of kesterite and wurtzite CZTS. (a) Energy profiles of ORR on kesterite (blue) and wurtzite CZTS (red). (b) The initial state (IS), transition state (TS) and final state (FS) of the rate-determining step on kesterite (112) surface. The blue, yellow, grey, lavender, red, and pink balls represent Cu, S, Sn, Zn, O, and H atoms, respectively.

Motivated by the excellent expectations given by DFT calculations, we produced CZTS nanocrystals using a facile and high yield colloidal synthesis protocol. By modifying the synthesis conditions (see experimental part) we synthesized CZTS NCs with kesterite and wurtzite crystal structures. **Figure 2** shows representative TEM micrographs of as-synthesized kesterite (Figure 2a) and wurtzite CZTS (Figure 2b) NCs. Both CZTS kesterite and wurtzite NCs were highly monodisperse, with average sizes of 15 ± 2 nm. The NC composition, obtained using energy-dispersive X-ray spectroscopy (EDS), was found to be consistent, within the technique error (~10%), with that of stoichiometric CZTS, [Cu]: [Zn]: [Sn]: [S]=2.0: 1.0: 1.0: 4.0. Figure 2c shows the x-ray diffraction (XRD) patterns of the two different NC phases. In the kesterite sample, the main diffraction peaks correspond to the (112), (200), (220), and (312) lattice planes of the tetragonal CZTS phase (JCPDS 00-026-0575). For the wurtzite sample, the diffraction peaks match well with the (100), (002), (101), (102) and (110) planes of the hexagonal CZTS phase.^[35] The Raman spectra in Figure 2d obtained with a 532 nm excitation shows a band at 327 cm⁻¹ and 331 cm⁻¹ for wurtzite and kesterite CZTS, respectively, which agrees well with the reported spectra of CZTS.^[36] The presence of CuS, SnS, SnS₂, SnS₃ or Cu₂SnS₃, which would have associated bands at 475 cm⁻¹, 190-220 cm⁻¹, 315 cm⁻¹, 310 cm⁻¹, or 350 cm⁻¹, was not identified.

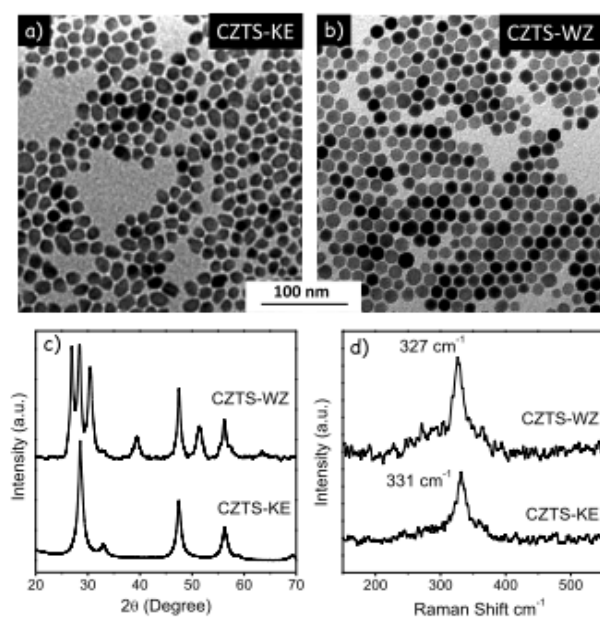


Figure 2. TEM micrographs (a,b), powder XRD patterns (c) and Raman spectra (d) of kesterite and wurtzite CZTS NCs.

To study the electrocatalytic performance of CZTS toward ORR, CZTS NCs were supported on Ketjen carbon (C) up to a weight ratio of 3:7 (NCs/C) through sonication and subsequent annealing. Following this procedure, homogeneous nanocomposites with a high NC dispersion were systematically obtained, as shown in the TEM micrograph of the CZTS-WZ/C electrocatalyst displayed in Figure 3a. XRD analysis of the supported materials revealed that the NCs preserved their crystallographic phase after the annealing process (Figure S6). These nanocomposites were deposited over GC electrodes for electrocatalytic measurements.

Figure S7 displays CVs curves of the GC electrodes modified with kesterite and wurtzite CZTS NCs/C hybrids in a 0.1 M KOH solution saturated with Ar or O₂ during the experiments. Both materials exhibited considerable electrocatalytic activities toward ORR in the O₂-saturated solution. The wurtzite CZTS/C electrocatalyst showed a faradaic current onset potential of $E_{\text{onset}} = +0.86$ V vs. RHE, a potential of the cathodic peak current of $E_{\text{pc}} = +0.66$ V vs. RHE, and a cathodic peak current density of $i_{\text{pc}} = 1.12$ mA cm⁻². Slightly improved values were obtained for kesterite CZTS/C electrocatalyst, with a $E_{\text{onset}} = +0.89$ V vs. RHE, a $E_{\text{pc}} = +0.70$ V vs. RHE and a $i_{\text{pc}} = 1.44$ mA cm⁻².

RDE experiments and Koutecky–Levich analysis were used to study the ORR kinetics. Figure 3b and 3c show the linear sweep voltammetry (LSV) curves of the wurtzite and kesterite CZTS/C catalysts at a rotation speed from 400 rpm to 1600 rpm, with a scan rate of 10 mV s⁻¹ and in an O₂-saturated 0.1 M KOH solution. The increase in the rotation speed contributes to the increase in the diffusion of oxygen at the surface of electrodes, resulting in larger current densities. The limiting current density of kesterite CZTS/C modified electrode at 0.1 V vs. RHE reached 5.45 mA cm⁻², well above that of pure carbon (2.0 mA/cm²) and a very similar value to the one obtained with a commercial Pt/C electrocatalyst. On the

other hand, the wurtzite CZTS/C showed significantly lower current densities, with a saturation value at 1600 rpm of 4.0 mA cm⁻².

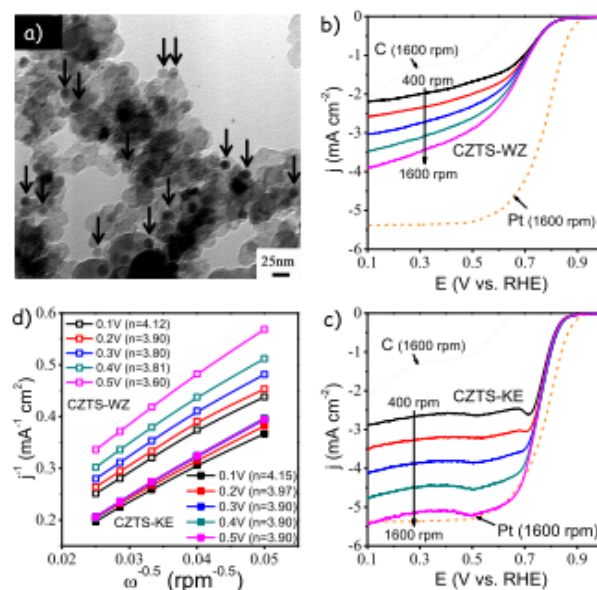


Figure 3. (a) TEM micrograph of the CZTS NCs supported on Ketjen carbon. Arrows point at some of the CZTS NCs. (b–c) LSV curves of the ORR at various rotation rates (400, 635, 900, 1225, 1600 rpm) from wurtzite CZTS/C (b) and kesterite CZTS/C (c) electrocatalysts in O₂-saturated 0.1 M KOH solutions at a scan rate of 10 mV s⁻¹. The RDE voltammograms of the Ketjen carbon and of commercial Pt/C, both obtained at 1600 rpm, are also plotted for reference. (d) Koutecky–Levich plots for wurtzite and kesterite CZTS at various potentials.

While displaying slightly higher onset potentials than Pt/C, kesterite CZTS/C displayed very steep slopes in the kinetic region, pointing toward a highly favorable kinetic behavior. Figure 4d displays the corresponding Koutecky–Levich plots, i.e. the inverse current density (j^{-1}) as a function of the inverse of the square root of the rotation speed ($\omega^{-1/2}$) at different potentials. The good linearity and parallelism of the obtained curves indicate first-order reaction kinetics with respect to the concentration of dissolved oxygen and similar electron transfer numbers for ORR at different potentials.^[37] From the slopes of the Koutecky–Levich plots at potentials ranging from 0.1 to 0.5 V vs. RHE, the number of electrons transferred for the ORR was estimated to be in the range 3.7–4.0 for both electrodes. This high electron transfer numbers indicated that both electrocatalyst have high selectivity toward total oxygen reduction, and that the ORR is mainly dominated by the one-step, four electron pathway. In contrast, the electron-transfer number for C was close to 2, in agreement with the reported data for Vulcan XC-72 carbon support (Figure S8).^[13]

The rotating ring-disk electrode (RRDE) technique was used to confirm the ORR pathway by monitoring the formation of the intermediate peroxide species during the ORR process (see SI for details). As shown in Figure 4, the measured HO₂⁻ yields were about 13–16% for wurtzite CZTS/C electrodes over the potential range 0.1–0.6 V vs. RHE. These yields correspond to an electron transfer

number of about 3.65–3.75 and are in agreement with the RDE measurements. A significant drop of HO_2^- yield (4.3–10 %) was observed on kesterite CZTS/C electrodes, which confirmed the high electron transfer numbers and related excellent catalytic selectivity of this material.

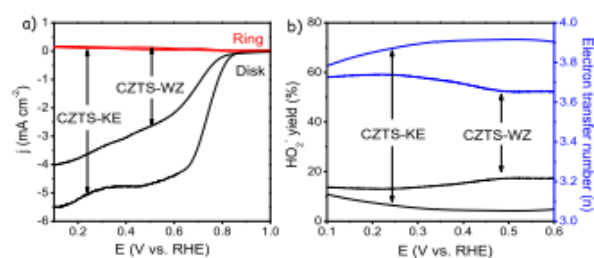


Figure 4. (a) RRDE curves of kesterite CZTS/C and wurtzite CZTS/C in an O_2 -saturated 0.1 M KOH solution at a rotation rate of 1600 rpm with the ring potential kept constant at 1.45 V vs. RHE. (b) Yield of the peroxide species and calculated electron transfer number at different potentials on the kesterite CZTS/C electrode and wurtzite CZTS/C electrode.

Table S1 shows a comparison of the ORR activities of several potentially low cost electrocatalysts reported in the literature. Kesterite CZTS/C catalysts have one of the highest limiting current densities reported at 1600 rpm and comparable onset potentials. It is noteworthy that in the present work CZTS NCs were supported on low cost commercial carbon. Thus, the performances displayed here for CZTS NCs did not rely on the electrocatalytic activity enhancement from expensive carbon support with specific architectures. Conversely, in several previous works, other forms of carbon, with potentially higher performance but also higher costs, were used. This included doped graphene, carbon nanotubes, or highly ordered porous carbon matrices. All these results indicate that kesterite CZTS is indeed a strong and promising candidate as low cost electrocatalyst for ORR in alkaline electrolyte.

The stability and poison tolerance of the catalysts are also extremely important parameters for practical applications. The stability of the kesterite CZTS/C catalyst was assessed by chronoamperometric analysis (Figure 5). These measurements revealed no apparent attenuation of the catalytic activity during a 40,000 s test. Additionally, the catalyst was exposed to methanol to test its tolerance. When 1.2 mL of 3 M methanol solution was added, almost no response was observed for kesterite CZTS NCs/C, while the catalytic activity of Pt/C severely dropped in the same condition due to the methanol oxidation reaction (Figure 5).

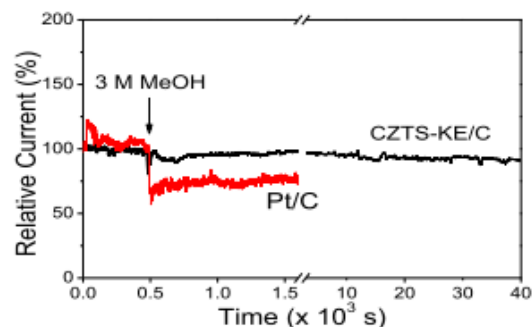


Figure 5. Stability and methanol-tolerance evaluation of kesterite CZTS/C tested by current-time chronoamperometric responses in O_2 -saturated 0.1 M KOH solution. Notice that after 490 s from the start of the test, 1.2 mL of a 3 M methanol solution was added. The commercial 20% Pt/C electrode was used for comparison.

Conclusions

In summary, first-principles calculations pointed toward CZTS NCs as a potentially high performance electrocatalyst for ORR, showing a relatively low energy barrier for O_2 adsorption and subsequent dissociation to OH^* . Accordingly, CZTS NCs with controlled crystal phases, kesterite or wurtzite, were prepared by a high yield and easily up-scalable colloidal synthesis routes. Such CZTS NCs, supported on conventional carbon, were demonstrated to be highly active for ORR and their activity to strongly depend on the crystal phase. We found kesterite CZTS NCs exhibited high current densities (5.45 mA cm^{-2} at 0.1 V vs. RHE) and relatively low onset reduction potential (0.89 V vs. RHE), comparable to commercial Pt/C electrocatalysts. Importantly, kesterite CZTS NCs showed not only excellent electrocatalytic activities, but also much better tolerances to methanol crossover than Pt/C.

Acknowledgements

This work was supported by the National Natural Science Foundation of China (Grant 51222212 and 51572016), Fundamental Research Funds for the Central Universities (2652015086). The computational resources from Tianhe2-JK support are greatly acknowledged. A.C. thanks financial support from the Spanish MINECO project BOOSTER (ENE2013-46624-C4-3-R).

Notes and references

1. G. Wu, K. L. More, C. M. Johnston and P. Zelenay, *Science*, 2011, **332**, 443.
2. M. K. Debe, *Nature*, 2012, **486**, 43.
3. Y. Nie, L. Li and Z. Wei, *Chem. Soc. Rev.*, 2015, **44**, 2168.
4. S. Guo and S. Sun, *J. Am. Chem. Soc.*, 2012, **134**, 2492.
5. H. J. Qiu, X. Shen, J. Wang, A. Hirata, T. Fujita, Y. Wang and M. Chen, *ACS Catal.*, 2015, **5**, 3779.
6. R. Kodiyath, G. V. Ramesh, E. Koudelkova, T. Tanabe, M. Ito,

- M. Manikandan, S. Ueda, T. Fujita, N. Umezawa and H. Noguchi, *Energ. Environ. Sci.*, 2015, **8**, 1685.
7. Y. Liang, Y. Li, H. Wang, J. Zhou, J. Wang, T. Regier and H. Dai, *Nat. Mater.*, 2011, **10**, 780.
8. P. Chen, T. Y. Xiao, H. H. Li, J. J. Yang, Z. Wang, H. B. Yao and S. H. Yu, *ACS Nano*, 2011, **6**, 712.
9. L. Hao, S. Zhang, R. Liu, J. Ning, G. Zhang and L. Zhi, *Adv. Mater.*, 2015, **27**, 3190.
10. P. Chen, L. K. Wang, G. Wang, M. R. Gao, J. Ge, W. J. Yuan, Y. H. Shen, A. J. Xie and S. H. Yu, *Energ. Environ. Sci.*, 2014, **7**, 4095.
11. S. Liu, Z. Zhang, J. Bao, Y. Lan, W. Tu, M. Han, Z. Dai, *J. Phys. Chem. C*, 2013, **117**, 15164.
12. M. Seredych, E. R. Castellon, T. J. Bandoz, *J. Mater. Chem. A*, 2014, **2**, 20164.
13. X. Wang, Y. Ke, H. Pan, K. Ma, Q. Xiao, D. Yin, G. Wu, M. T. Swihart, *ACS Catal.*, 2015, **5**, 2534.
14. Y. Cao, Y. Xiao, J. Y. Jung, H. D. Um, S. W. Jee, H. M. Choi, J. H. Bang, J. H. Lee, *ACS Appl. Mater. Interfaces*, 2013, **5**, 479.
15. X. Zeng, W. Zhang, Y. Xie, D. Xiong, W. Chen, X. Xu, M. Wang, Y. B. Cheng, *J. Power Sources*, 2013, **226**, 359.
16. Y. Zhang, C. Shi, X. Dai, F. Liu, X. Fang, J. Zhu, *Electrochim. Acta*, 2014, **118**, 41.
17. D. Barpuzary, A. Banik, G. Gogoi, M. Qureshi, *J. Mater. Chem. A*, 2015, **3**, 14378.
18. J. Xu,; X. Yang,; Q. D. Yang,; T. L. Wong, C. S. Lee, *J. Phys. Chem. C*, 2012, **116**, 19718.
19. J. Xu, X. Yang, T. L. Wong, C. S. Lee, *Nanoscale*, 2012, **4**, 6537.
20. M. Ibáñez, D. Cadavid, R. Zamani, N. García-Castelló, V. Izquierdo-Roca, W. Li, A. Fairbrother, J. D. Prades, A. Shavel and J. Arbiol, *Chem. Mater.*, 2012, **24**, 562.
21. A. Carrete, A. Shavel, X. Fontané, J. Montserrat, J. Fan, M. Ibáñez, E. Saucedo, A. Pérez-Rodríguez and A. Cabot, *J. Am. Chem. Soc.*, 2013, **135**, 15982.
22. X. Yu, A. Shavel, X. An, Z. Luo, M. Ibáñez and A. Cabot, *J. Am. Chem. Soc.*, 2014, **136**, 9236.
23. E. Ha, L. Y. S. Lee, J. Wang, F. Li, K. Y. Wong and S. C. E. Tsang, *Adv. Mater.*, 2014, **26**, 3496.
24. G. Kresse and J. Furthmüller, *Comput. Mater. Sci.*, 1996, **6**, 15.
25. G. Kresse and J. Furthmüller, *Phys. Rev. B*, 1996, **54**, 11169.
26. J. P. Perdew, J. Chevary, S. Vosko, K. A. Jackson, M. R. Pederson, D. Singh and C. Fiolhais, *Phys. Rev. B*, 1992, **46**, 6671.
27. G. Henkelman, B. P. Uberuaga and H. Jónsson, *J. Chem. Phys.*, 2000, **113**, 9901.
28. K. Yu and E. A. Carter, *Chem. Mater.*, 2015, **27**, 2920.
29. A. Moholkar, S. Shinde, A. Babar, K. U. Sim, Y. B. Kwon, K. Rajpure, P. Patil, C. Bhosale and J. Kim, *Sol. Energy*, 2011, **85**, 1354.
30. P. Xu, S. Chen, B. Huang, H.J. Xiang, X.G. Gong and S.H. Wei, *Phys. Rev. B*, 2013, **88**, 045427.
31. H. Yoo and J. Kim, *Thin Solid Films*, 2010, **518**, 6567.
32. L. Yu, X. Pan, X. Cao, P. Hu and X. Bao, *J. Catal.*, 2011, **282**, 183.
33. Y. Sha, T. H. Yu, B. V. Merinov, and W. A. Goddard, *ACS Catal.*, 2014, **4**, 1189.
34. J. Zhang, Z. J. Wang, Z. P. Zhu, *J. Power Sources*, 2014, **255**, 65.
35. A. Singh, H. Geaney, F. Laffir and K. M. Ryan, *J. Am. Chem. Soc.*, 2012, **134**, 2910.
36. A. Shavel, M. Ibáñez, Z. Luo, J. De Roo, À. Carreté, M. Dimitrievska, A. Genç, M. Meyns, A. Pérez-Rodríguez and M. V. Kovalenko, *Chem. Mater.* 2016, DOI: 10.1021/acs.chemmater.5b03417.
37. B. Chen, R. Li, G. Ma, X. Gou, Y. Zhu and Y. Xia, *Nanoscale*, 2015, **7**, 20674.

Supporting Information

Cu₂ZnSnS₄ Nanocrystals as Highly Active and Stable Electrocatalysts for the Oxygen Reduction Reaction

Xuelian Yu,^{*,a,†} Da Wang,^{b,†} Jingjing Liu,^c Zhishan Luo,^d Ruifeng Du,^a Li-Min Liu,^{*,b} Guangjin Zhang,^{*,c} Yihe Zhang^a and Andreu Cabot^{d,e}

- a. Beijing Key Laboratory of Materials Utilization of Nonmetallic Minerals and Solid Wastes, National Laboratory of Mineral Materials, School of Materials Science and Technology, China University of Geosciences, 100083 Beijing, P. R. China.
- b. Beijing Computational Science Research Center, Beijing 100193, P. R. China.
- c. Key Laboratory of Green Process and Engineering, Chinese Academy of Sciences, 100190 Beijing, P. R. China.
- d. Catalonia Energy Research Institute - IREC, 08930 Sant Adria del Besos, Barcelona, Spain.
- e. ICREA, Pg. Lluís Companys 23, 08010 Barcelona, Spain

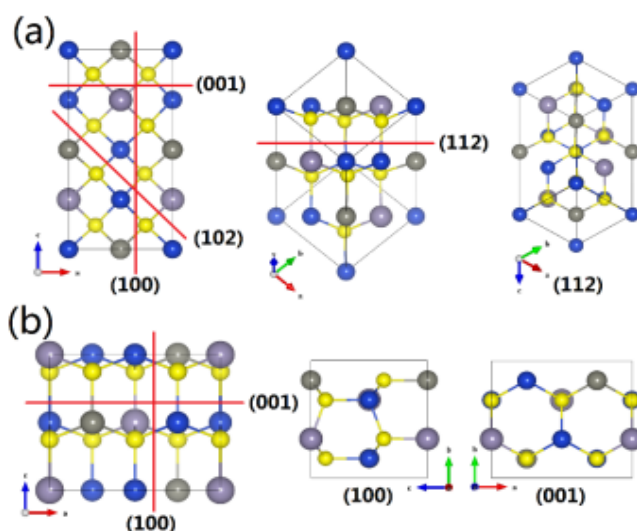


Figure S1. Crystal surfaces of $\text{Cu}_2\text{ZnSnS}_4$. (a) kesterite and (b) wurtzite.

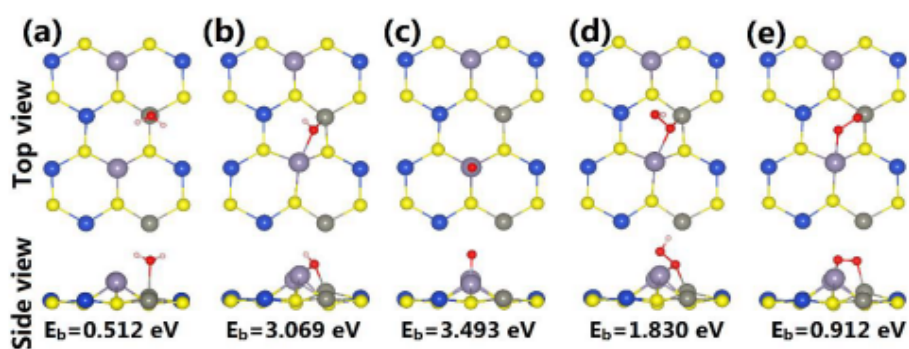


Figure S2. Top and side views of the structures of relaxed geometries for various ORR chemical species adsorbed on the (112) surface of kesterite $\text{Cu}_2\text{ZnSnS}_4$. (a-e) Stable H_2O , OH , O , OOH and O_2 adsorption configurations, respectively. The blue, yellow, grey, lavender, red, and pink balls represent Cu, S, Sn, Zn, O, and H atoms, respectively. E_b indicates the binding energy.

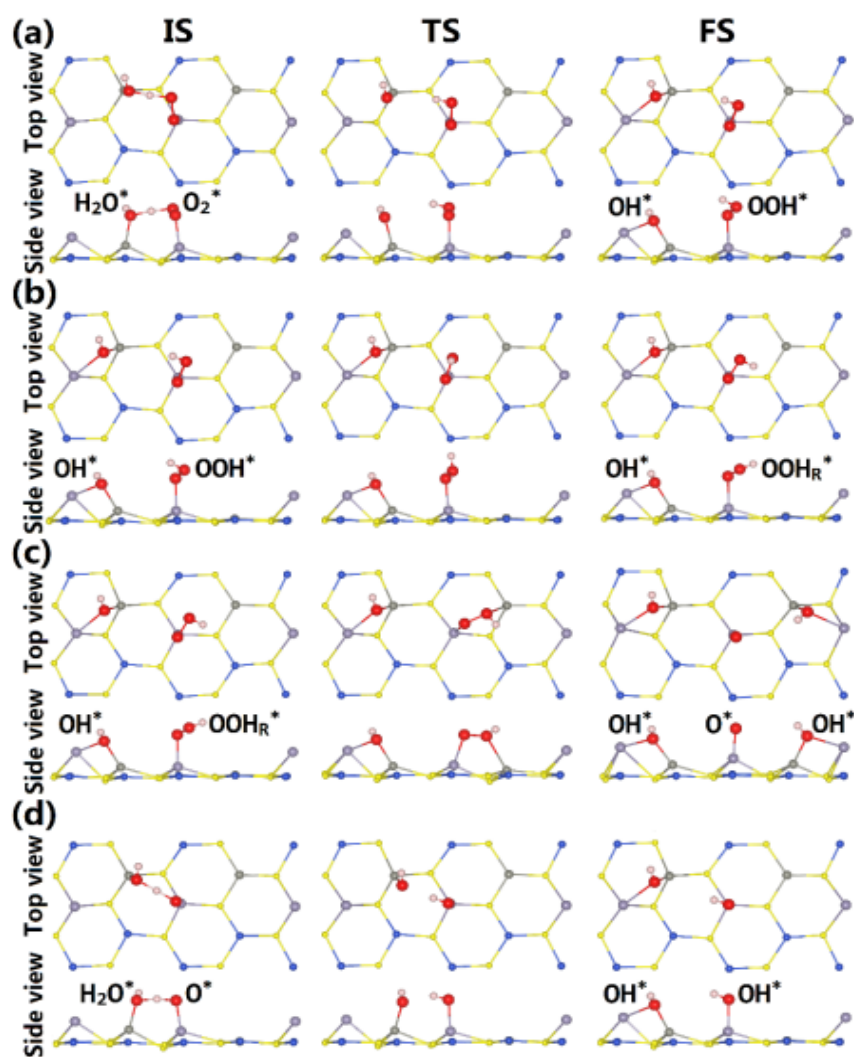


Figure S3. Top and side views of the initial state (IS), transition state (TS) and final state (FS) structures for the ORR reactions of Equations (II-V) on the (112) surface of kesterite $\text{Cu}_2\text{ZnSnS}_4$. (a-d) correspond to Equations (II-V), respectively. The blue, yellow, grey, lavender, red, and pink balls represent Cu, S, Sn, Zn, O, and H atoms, respectively.

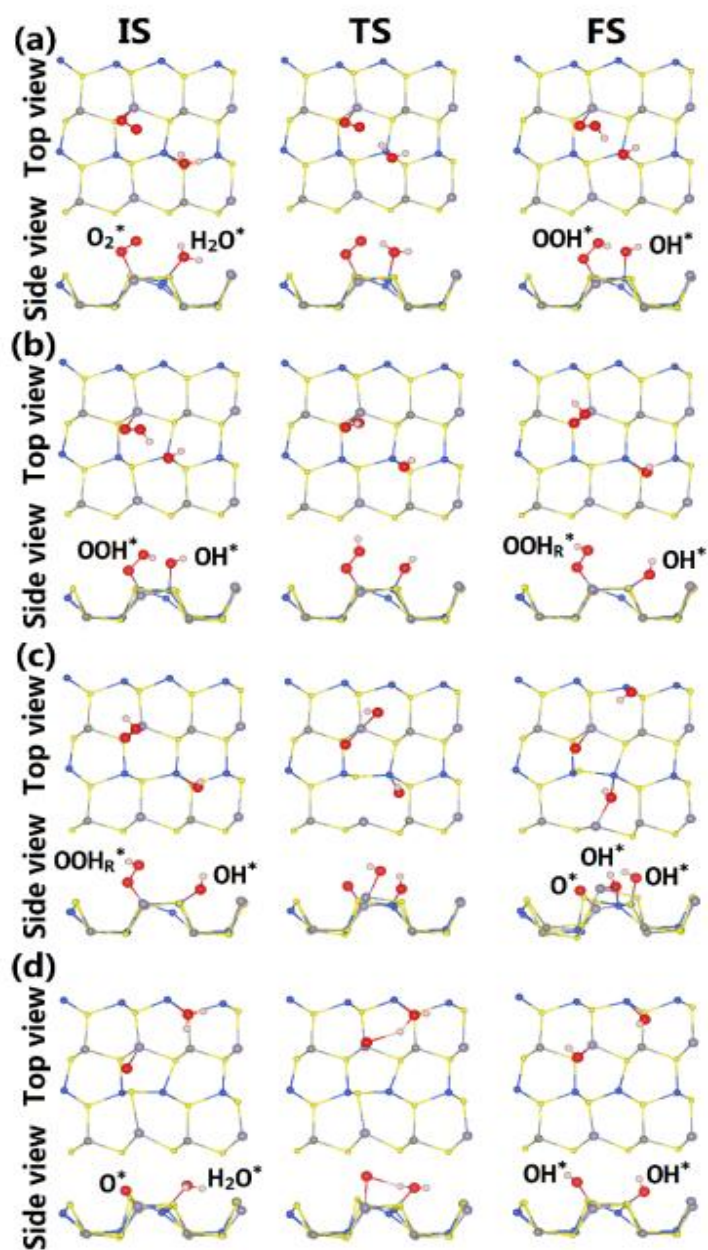


Figure S4. Top and side views of the IS, TS and FS structures for the ORR reactions of Equations (II-V) on the (100) surface of wurtzite $\text{Cu}_2\text{ZnSnS}_4$. (a-d) correspond to Equations (II-V), respectively.

Oxygen Reduction Reaction (ORR) Measurements:

Cyclic voltammetry (CV) testing: CV was conducted in a home-made electrochemical cell. The electrolyte (0.1 M KOH) was saturated with oxygen by bubbling O₂ for at least 30 minutes before the measurements. During the recording of CVs, a flow of O₂ was maintained over the electrolyte to ensure its continued O₂ saturation. The working electrode was cycled for 5 times before the data were recorded. In the control experiments, CVs were performed in an Ar-saturated 0.1 M KOH.

Rotating disk electrode (RDE) measurements: The working electrode was scanned at a rate of 10 mV s⁻¹ with rotating speeds from 400 rpm to 1600 rpm. Koutecky–Levich (K-L) plots (J^{-1} vs. $\omega^{-1/2}$) were analysed at various electrode potentials. The slopes of the linear lines were used to calculate the electron transfer numbers (n) on the base of the K-L equations.

Rotating ring-disk electrode (RRDE) measurements: The disk electrode was scanned cathodically at a rate of 10 mV s⁻¹ and the ring potential was constant at 1.45 V vs. RHE. The % HO₂⁻ and the electron transfer number (n) were calculated from the ratio of the ring current (I_r) and the disk current (I_d) following the equations given in Reference S1.

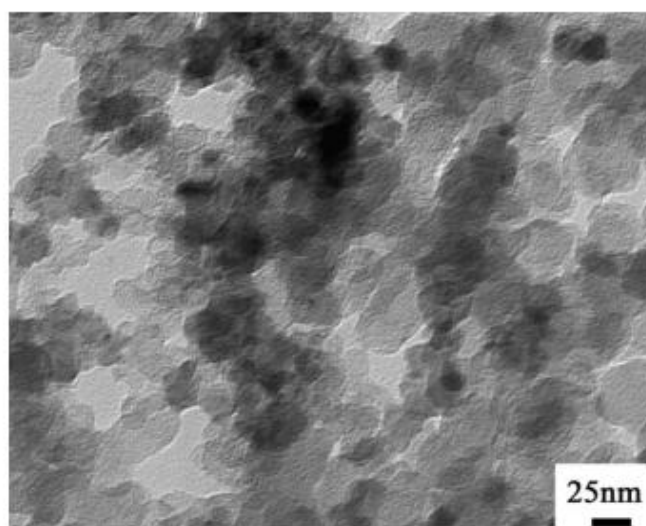


Figure S5. TEM image of the kesterite CZTS nanocrystals supported on carbon.

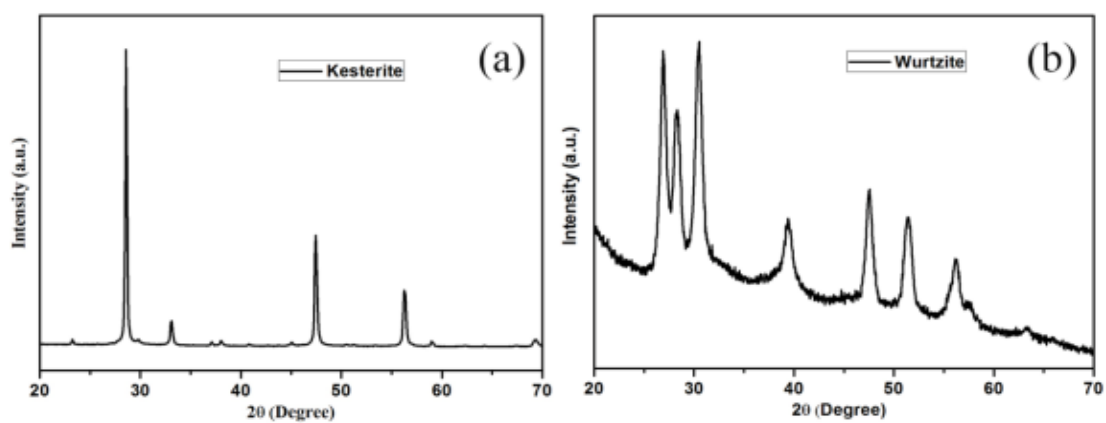


Figure S6. XRD patterns of the kesterite (a) and wurtzite (b) CZTS nanocrystals after annealing process.

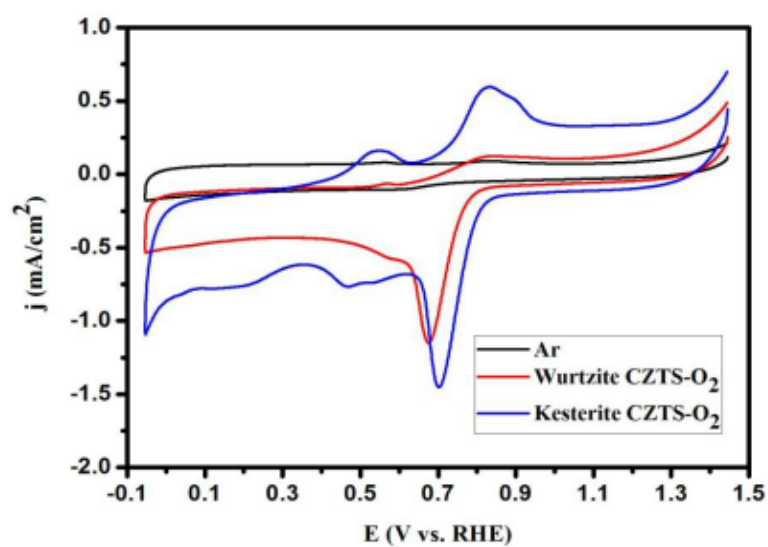


Figure S7. CV curves of kesterite CZTS/C and wurtzite CZTS/C in Ar- and O₂-saturated 0.1 M KOH solution (scanning rate: 10 mV s⁻¹). The argon one is for wurtzite CZTS.

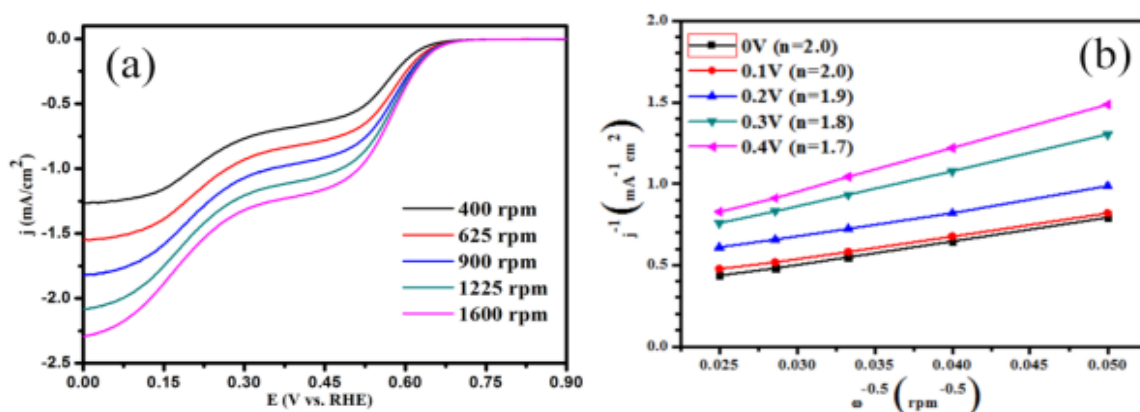


Figure S8. Linear sweep voltammograms (a) and Koutecky-Levich plots (b) recorded at different potentials of C modified GC electrode at different rotating rates in O₂-saturated 0.1 M KOH solution.

Table S1. Comparison of the performances of kesterite CZTS (this work) and other potentially low-cost catalysts reported in the literatures.

Catalysts	E _{onset} (V vs. RHE)	i _d (mA/cm ² , at 0.2V)	References
Kesterite CZTS/C	0.89	5.4	This work
Co ₂ P nanorods/C	0.85	3.9	<i>ACS Nano</i> 2015, 9, 8108-8115
Cu _{2-x} S/graphene	0.9	4.5	<i>ACS Catal.</i> 2015, 5, 2534-2540
Co _{0.85} Se/graphene	0.65	3.5	<i>Nanoscale</i> 2014, 6, 1782-1789
Fe-N-doped carbon nanofibers	0.8	5.3	<i>Angew. Chem. Int. Ed.</i> 2015, 54, 8179-8183
N,F codoped triazine-based framework	0.86	5.4	<i>Adv. Mater.</i> 2015, 27, 3190-3195
N-doped nanoporous carbon nanosheets	0.88	4.7	<i>Energy Environ. Sci.</i> 2014, 7, 4095-4103

Reference

(S1). H. Tang, H. Yin, J. Wang, N. Yang, D. Wang and Z. Tang, *Angew. Chem. Int. Ed.*, 2013, **52**, 5585 -5589.

2.2 Synthesis of CZTS-based HNPs and their potential photocatalytic application

Semiconductor-metal HNPs are emerging as new functional materials for the study of solar-to-chemical energy conversion and a highly control over the size, position, composition, and shape of the different components have been achieved (Figure 2.7).⁷⁸⁻⁸³ In particular, p-n junction HNPs provides new ways to manipulate electron and hole wave functions. In this direction, CZTS-based HNPs are increasing much attention in the past decade, because CZTS uniquely combines both optoelectronic properties and a composition based on elements that are abundant in the Earth's crust and non-toxic. Its direct band gap of 1.5 eV, matches well with the energy requirement for solar water splitting, which makes CZTS a good candidate for water splitting. On the other hand, the fabrication of CZTS heterostructures formed with constituent having different physical and chemical properties together in a single building block allows for fundamental chemistry studies and provides new physical insights into the interfacial junction.

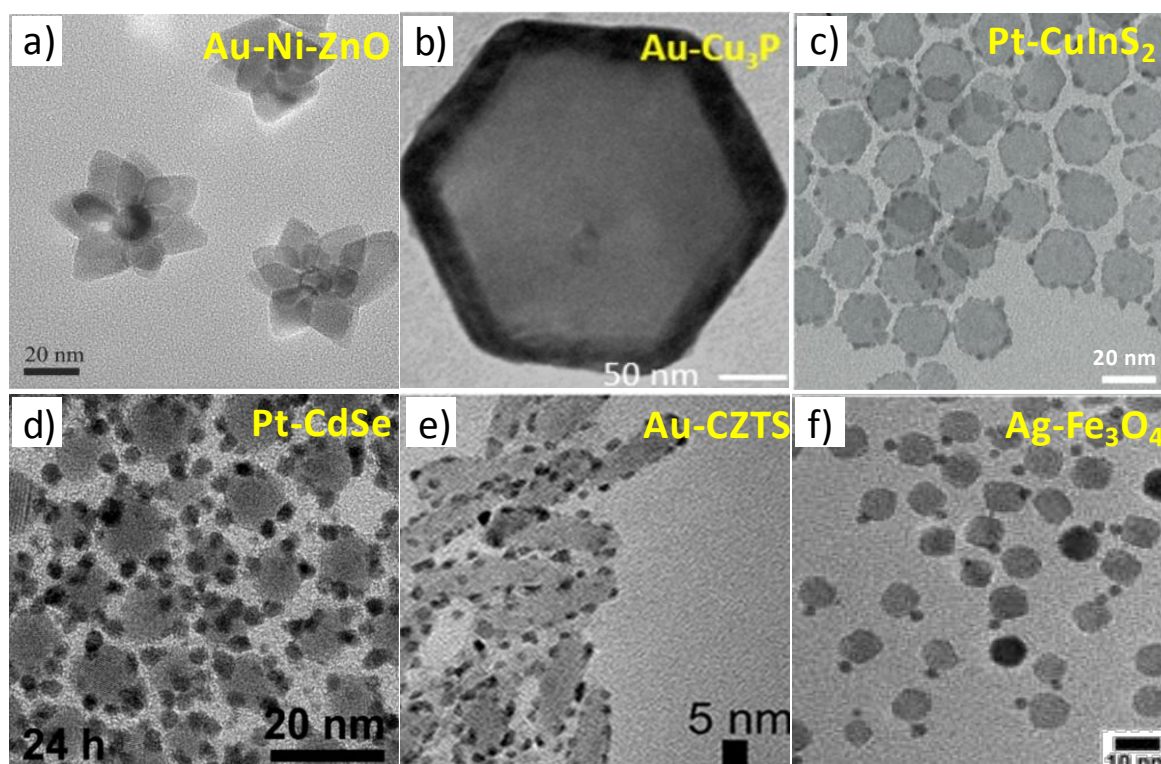


Figure 2.7 Various hybrid NPs showing TEM images. (a) Au-Ni-ZnO flower-like HNPs.⁸⁴ (b) Au-Cu₃P heterostructured nanodisks.⁸⁵ (c) Pt-CuInS₂ HNPs.⁸⁶ (d) Pt-CdSe HNPs, the Pt-domain size is 2.8 nm after 24h reaction time on CdSe NPs.⁸⁷ (e) Au-CZTS heterostructured NRs.⁸⁸ (f) Ag-Fe₃O₄ HNPs.⁸⁹

There have been a few reports for CZTS-based heterostructured NPs. Among these, CZTS-Au core-shell or HNPs have attracted extensive attention due to strongly synergic effect of plasmon-exciton coupling and rapidly charge carrier movement. These HNPs were proven to be an efficient photocatalyst for water splitting under full-arc light

irradiation.^{88, 90-92} Ha Enna et al. reported a Au@CZTS core-shell nanostructure via a simple wet chemistry method. Au@CZTS core-shell NPs showed a superior photoelectrochemical and photocatalytic activities because of enhancing the absorption in the UV-vis-NIR region and generating more photoelectrons in such metal-semiconductor hybrid core-shell structure (Figure 2.8).⁹⁰ Patra B. K. et al. reported the formation of heteroepitaxy at the junction of Au-CZTS heterostructure. CZTS with two different crystal phases wurtzite and tetragonal was prepared, and the epitaxial formation of both phases with Au(0) was analyzed as a new material to study the photocurrent and photoresponse behavior.⁹¹ The results were promising, and the coupled Au-CZTS heterostructures not only increase the photostability of the materials but also showed better photodetector device performances. In addition, one similar work was presented by Dilsaver et al. in which fabrication of CZTS-Au heterostructures by a variety of pathways utilizing both a molecular gold precursor (AuCl_3) and preformed Au NPs under thermal and photochemical deposition conditions.⁸⁸

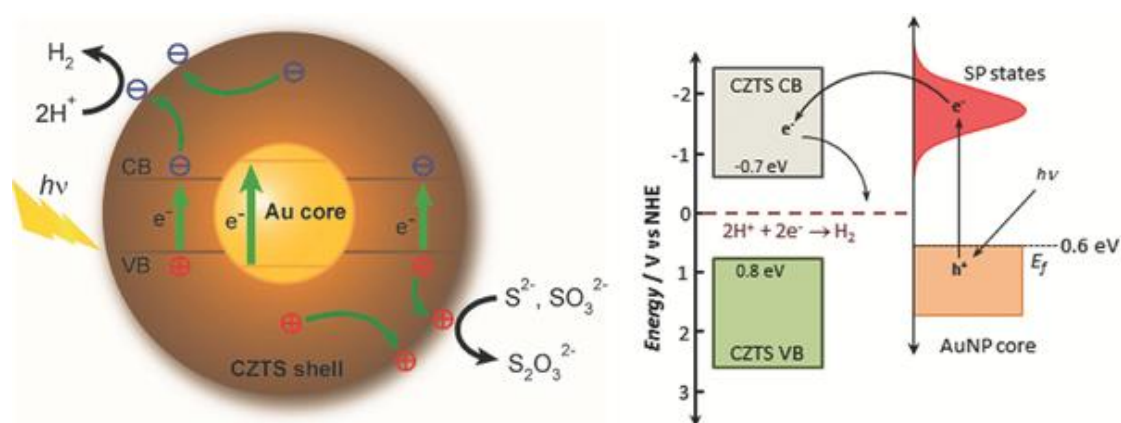


Figure 2.8 Illustration and energy diagram of interfacial charge transfer and photocatalytic redox reaction in Au@CZTS core-shell NPs.⁹⁰

On the other hand, CZTS-based hybrid NPs, such as CZTS-Pt,⁹² CZTS-PtM (M = Co, Ni)⁹³ and CZTS-Ag₂S⁹⁴ HNPs were presented by our group (Figure 2.9). In particular, CZTS-PtCo and CZTS-PtNi nanoheterostructures with combining of a Pt-based magnetic metal alloy with CZTS showed some advantages. One is to minimize the amount of Pt by forming an alloy with lower cost transition metals decreasing the overall cost. The other is alloying Pt with a second element like Co and Ni is effective for increasing the photocatalytic activity due to surface strongly influences its chemical and electronic properties, ultimately determining its functionality. CZTS-PtCo HNPs were characterized up to a 15 folder high photocatalytic activities toward hydrogen generation from water when compared with not only the bare CZTS semiconductor but also two times higher hydrogen evolution rates with CZTS-Pt. The high activity of CZTS-PtCo was ascribed to the enhanced charge carrier separation and transport

efficiency. The presence of Co enhanced the accumulation of photoexcited electrons in the alloy and facilitated the charge transfer to the surface-adsorbed species (Figure 2.9).

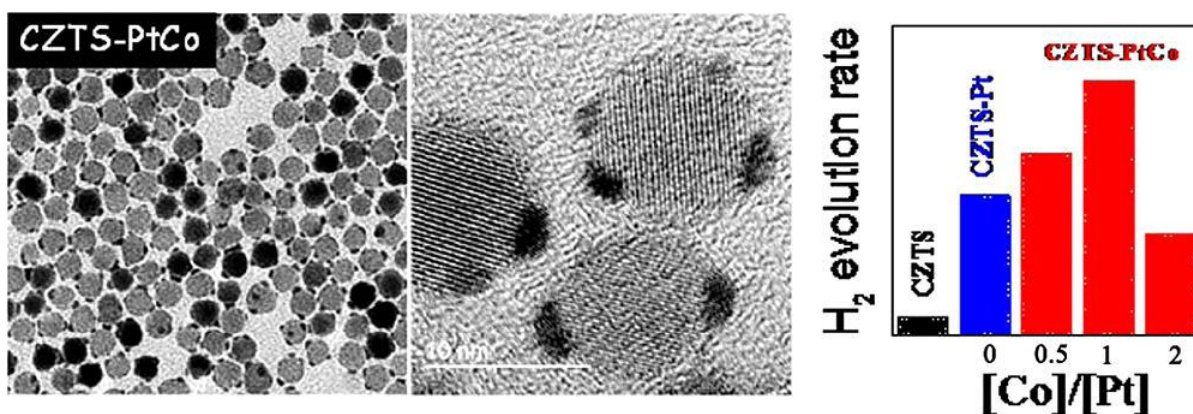


Figure 2.9 TEM and HRTEM micrograph of CZTS-PtCo nanoheterostructures and Comparison of photocatalytic H₂ evolution activity of CZTS, CZTS-Pt, CZTS-PtCo metal alloy heterostructures with different nominal Co/Pt ratios (CZTS-Pt₂Co, CZTS-PtCo, and CZTS-PtCo₂) under full-arc light irradiation.⁹³

2.2.1 $\text{Cu}_2\text{ZnSnS}_4\text{-Pt}$ and $\text{Cu}_2\text{ZnSnS}_4\text{-Au}$ Heterostructured NPs for Photocatalytic Water Splitting and Pollutant Degradation

The paper entitled " *$\text{Cu}_2\text{ZnSnS}_4\text{-Pt}$ and $\text{Cu}_2\text{ZnSnS}_4\text{-Au}$ Heterostructured Nanoaprticles for Photocatalytic Water Splitting and Pollutant Degradation*" is the third article that constitutes this thesis and was published in *Journal of the American Chemical Society* **2014**, 136 (26), 9236-9239. In this paper a procedure to produce colloidal monodisperse CZTS, CZTS-Au and CZTS-Pt HNPs with strongly electrically coupled interface between Au or Pt and CZTS is detailed. Au was chosen due to the possible plasmonic enhancement and Pt because a proper overpotential for hydrogen generation was chosen (Figure 2.10). The produced HNP were characterized by TEM, HRTEM, XRD, XPS and UV-vis. The multiple nucleation sites present at the faceted CZTS NCs resulted in multiple Au or Pt NCs with an average size of 2 nm homogeneously distributed at the surface of each CZTS NC. Such HNPs, which were transferred to aqueous media via a ligand exchange with an inorganic salt, are shown to have excellent photocatalytic properties toward degradation of RhB and hydrogen generation by water splitting when compared to pure CZTS NPs. This highlights the importance of nanoscale interface controlling also in complex quaternary materials for both fundamental understanding and technology applications. The article is presented in the corresponding subchapter.

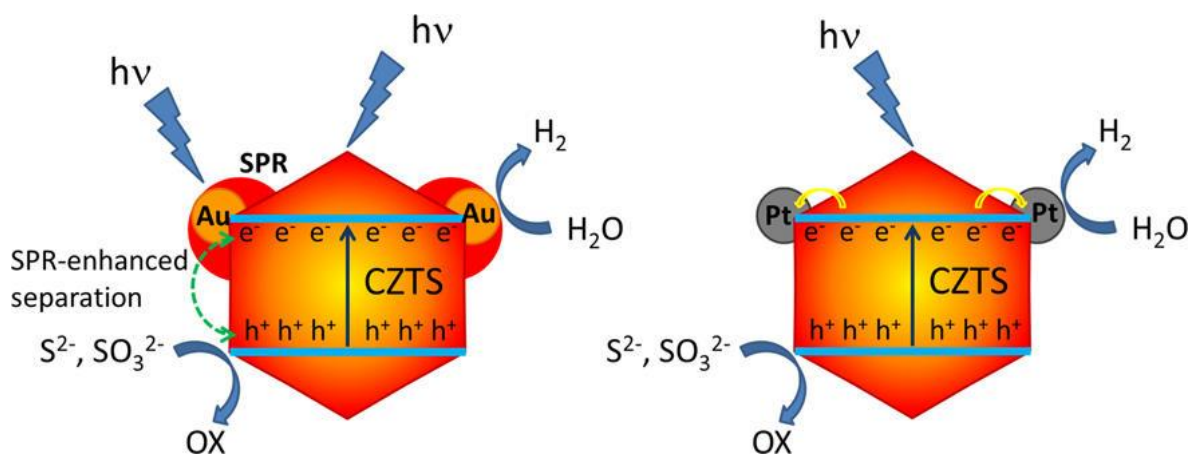


Figure 2.10 Illustration of the possible mechanism of enhancement of the H₂ evolution Rate in CZTS-Au and CZTS-Pt HNPs in the presence of S²⁻ and SO₃²⁻ hole scavengers.

Cu₂ZnSnS₄-Pt and Cu₂ZnSnS₄-Au Heterostructured Nanoparticles for Photocatalytic Water Splitting and Pollutant Degradation

Xuelian Yu,^{†,‡} Alexey Shavel,[†] Xiaoqiang An,^{§,⊥} Zhishan Luo,[†] Maria Ibáñez,[†] and Andreu Cabot^{*,†,||}

[†]Catalonia Energy Research Institute (IREC), 08930 Barcelona, Spain

[‡]Institute of Process Engineering, Chinese Academy of Sciences, 100190 Beijing, China

[§]Department of Chemical Engineering, University College London, London WC1E 7JE, U.K.

[⊥]Research Center for Eco-Environmental Sciences, Chinese Academy of Sciences, 100085 Beijing, China

^{||}Institució Catalana de Recerca i Estudis Avançats (ICREA), 08010 Barcelona, Spain

S Supporting Information

ABSTRACT: Cu₂ZnSnS₄, based on abundant and environmental friendly elements and with a direct band gap of 1.5 eV, is a main candidate material for solar energy conversion through both photovoltaics and photocatalysis. We detail here the synthesis of quasi-spherical Cu₂ZnSnS₄ nanoparticles with unprecedented narrow size distributions. We further detail their use as seeds to produce CZTS-Au and CZTS-Pt heterostructured nanoparticles. Such heterostructured nanoparticles are shown to have excellent photocatalytic properties toward degradation of Rhodamine B and hydrogen generation by water splitting.

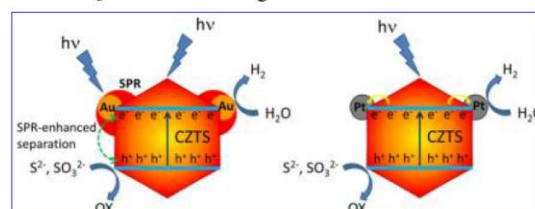
Current functional nanomaterials must meet numerous very demanding properties that cannot be realized with a unique compound. Thus, the use heterostructured nanomaterials or nanocomposites is generally required in a wide range of applications. In such multiphase materials, not only the properties of the compounds but also those of their interface have a determinant influence over their performance. In particular, an efficient photocatalytic system requires an intimate interface between two phases, a light-absorbing semiconductor and a co-catalyst. Such hybrid materials can be produced with composition control at the nanometer scale through the direct growth in solution of one of the compounds from the surface of the other, which acts as a seed.¹ Such direct growth of the heterostructured nanomaterial ensures a fast and efficient charge transfer between the two phases.

Solar energy conversion to electricity or its storage in renewable fuels is a particularly interesting application requiring the development of high-performance, environmental friendly, and cost-effective heterostructured materials. While several semiconductors have been proposed to harvest sunlight,² Cu₂ZnSnS₄ (CZTS) uniquely combines both outstanding optoelectronic properties, with a direct band gap energy of 1.5 eV, and a composition based on elements that abound in the Earth's crust. Such an environmental friendly and low-cost material has been demonstrated to be an excellent light absorber in photovoltaic devices and to have a large potential for photodegradation of pollutants and for photocatalytic generation of hydrogen and other value-added chemicals.³

CZTS and related quaternary nanocrystals can currently be produced by different procedures.⁴ However, due to the difficulties in tuning the composition, phase, size, and shape of such complex materials, the preparation of CZTS-based heterostructures and particularly CZTS-metal hybrid nanoparticles has not yet been achieved.

In the present work, we detail a procedure to produce colloidal CZTS-metal heterostructured nanoparticles with strongly electrically coupled interfaces. Au and Pt were the metals chosen due to their potential for plasmonic enhancement (Au) and a proper over-potential for hydrogen generation (Pt) (Scheme 1). Heterostructures were tested for photo-

Scheme 1. Illustration of the Possible Mechanism of Enhancement of the H₂ Evolution Rate in CZTS-Au and CZTS-Pt Heterostructured Nanoparticles in the Presence of S²⁻ and SO₃²⁻ Hole Scavengers



degradation of pollutants in solution using Rhodamine B as the model system, and for photocatalytic hydrogen generation from water under full-arc light irradiation.

Highly monodispersed CZTS nanocrystals were prepared by the reaction of copper, tin, and zinc salts with *tert*-dodecylmercaptan and dodecanethiol in the presence of oleylamine (OLA). In a typical 1 g scale synthesis, 5.4 mmol (920 mg) of CuCl₂·2H₂O, 4.8 mmol (391 mg) of ZnO, and 1.8 mmol (630 mg) of SnCl₄·5H₂O were dissolved in a minimum amount of tetrahydrofuran (THF). Then, 24 mmol (6.43 g) of distilled OLA and 20 g of distilled 1-octadecene were added to the reaction mixture. The solution was heated to 175 °C under argon flow and maintained at this temperature for 1 h to remove low boiling point impurities and water. After purging,

Received: February 28, 2014

Published: June 11, 2014

the mixture was cooled to 100 °C, and 50 mmol (10.12 g) of *tert*-dodecylmercaptan and 5 mmol (1.012 g) of dodecanethiol were added. The solution was then heated to 250 °C and kept at this temperature for 1 h. The obtained CZTS nanocrystals were thoroughly purified by multiple precipitation and re-dispersion steps using 2-propanol and chloroform. Finally, CZTS nanoparticles were dissolved in THF, and poorly soluble unreacted metal complexes and large Zn-rich particles were precipitated by centrifugation. The supernatant was collected and stored for later use.

CZTS nanocrystals were characterized by a quasi-spherical geometry but having faceted surfaces, as shown in the representative transmission electron microscopy (TEM) micrograph in Figure 1a. They were highly monodisperse, with an

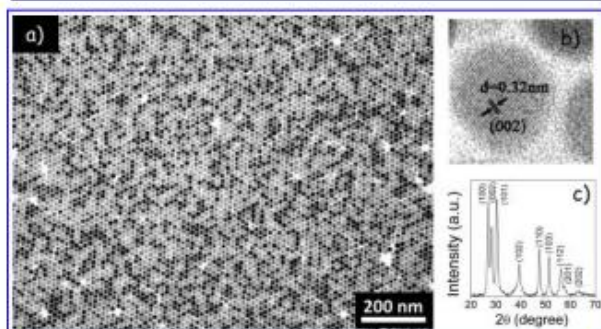


Figure 1. (a) TEM and (b) HRTEM micrographs and (c) XRD pattern of quasi-spherical CZTS nanocrystals produced by the procedure detailed in the text.

average size of 12 nm. High-resolution TEM (HRTEM) micrographs and X-ray diffraction (XRD) analysis showed the crystal structure of the CZTS nanocrystals to be wurtzite (Figure 1b,c).^{4b,5} The nanocrystal composition, obtained by using a scanning electron microscope (SEM) equipped with an energy-dispersive X-ray spectroscopy (EDS) detector, was found to be very close to that of stoichiometric CZTS (Cu:Zn:Sn:S = 2:1:1:4). Further confirmation of the element oxidation states was obtained by X-ray photoelectron spectroscopy (XPS) (Supporting Information, Figure S1). No secondary phases were detected by HRTEM, XRD, EDS, or XPS analysis.

CZTS nanocrystals were used as seeds for the preparation of heterostructured CZTS-Au and CZTS-Pt nanoparticles. To produce CZTS-Au nanoparticles, AuCl₃ (40 mg), didcyl-dimethylammonium bromide (40 mg), and dodecylamine (140 mg) were dissolved in toluene (4.0 mL) using ultrasonic sonication for 30 min. This reaction mixture was added dropwise (80 mL/h) to a toluene dispersion (20 mL) of the CZTS nanocrystals (100 mg) at room temperature.^{1f} Afterward, the product was immediately purified by methanol precipitation and toluene re-dispersion.

To prepare CZTS-Pt heterostructured nanoparticles, oleic acid (0.20 mL), OLA (0.20 mL), 1,2-hexadecanediol (43 mg), and phenyl ether (10 mL) were loaded into the reaction flask and kept at 120 °C for 30 min under a nitrogen flow. In parallel, platinum(II) acetylacetonate (40 mg) was mixed with a dispersion of the CZTS nanocrystals (100 mg) and heated at 65 °C for 10 min. This CZTS suspension containing the Pt precursor was injected into the phenyl ether solution kept at 200 °C.^{1e} After 10 min, the reaction was quenched in a water

bath. The product was purified by ethanol precipitation and toluene re-dispersion.

Figures 2 and 3 display representative TEM and HRTEM micrographs of the CZTS-Au and CZTS-Pt heterostructured

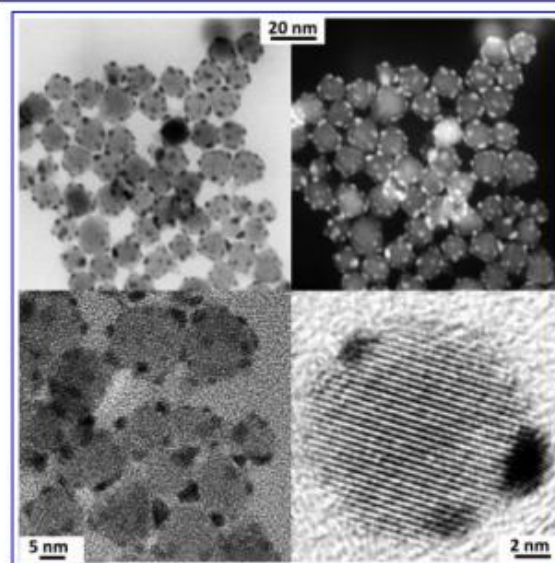


Figure 2. Bright-field and dark-field TEM micrographs and HRTEM image of CZTS-Au heterostructured nanoparticles.

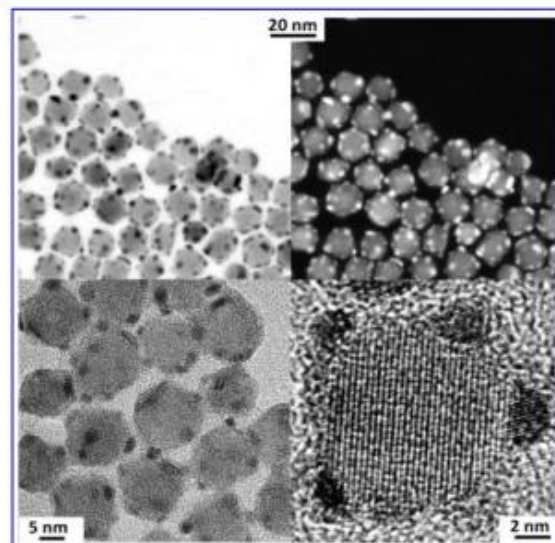


Figure 3. Bright-field and dark-field TEM micrographs and HRTEM image of CZTS-Pt heterostructured nanoparticles.

nanoparticles obtained, respectively. After the noble metal loading, no change of the size and shape of the CZTS nanocrystals was observed. Under the detailed reaction conditions, metals nucleated preferentially at the CZTS nanocrystal surface, and no independent metal particles were observed. In both cases, multiple nucleation sites present at the faceted CZTS nanocrystals resulted in multiple noble metal nanocrystals with an average size of 2 nm homogeneously distributed at the surface of each CZTS nanocrystal. XPS analysis confirmed Au and Pt to be in a metallic oxidation state

(Figure S2). By adjusting the metal salt concentration in the initial solution, the Au and Pt loads could be controlled.

The UV-vis absorption spectra of CZTS-Au and CZTS-Pt heterostructures were analogous to those of pure CZTS nanocrystals (Figure S3). Due to the relatively low concentration of very small Au nanoparticles at the CZTS surface, no evidence of a Au-related plasmon resonance peak was observed.

Prior to the reaction studies, heterostructured nanoparticles were transferred from toluene to aqueous media via a ligand exchange with $(\text{NH}_4)_2\text{S}$. Briefly, a highly concentrated solution of purified CZTS-metal nanoparticles was mixed with 1 vol% of $[\text{NH}_4]_2\text{S}$ (20% aqueous) in formamide. The bi-phase system was vigorously shaken to promote the phase transfer. Almost immediately, the CZTS-metal nanoparticles moved into the upper formamide phase. We discarded the clear, colorless chloroform solution and purified the formamide phase with fresh chloroform several times. CZTS-metal nanoparticles were finally precipitated with acetone and dried under vacuum overnight.

To evaluate the photocatalytic potential of CZTS-metal heterostructures, the degradation under full-arc irradiation of aqueous Rhodamine B (RhB) was tested as a model system. In a typical measurement, 10 mg of nanoparticles was suspended in 50 mL of 10 ppm aqueous solution of RhB. The solution was stirred in the dark overnight to achieve the equilibrium adsorption. The suspension was then illuminated with a 300 W Xe lamp. The RhB concentration change was monitored by measuring the 552 nm optical absorption of the suspensions at regular intervals.

The photodegradation of RhB in the presence of pure CZTS was relatively slow, with 60% of RhB degraded after an illumination time of 4 h (Figure 4). In the presence of CZTS-

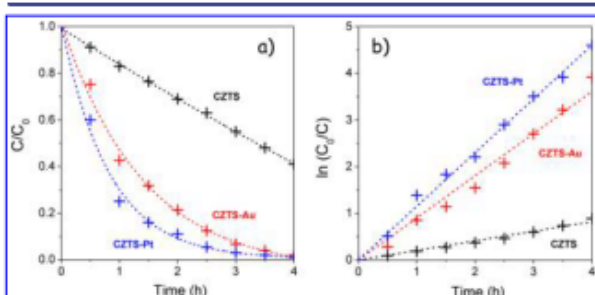


Figure 4. Full arc-light-driven photodegradation of RhB over CZTS, CZTS-Au, and CZTS-Pt nanoparticles.

Au and especially CZTS-Pt, the photodegradation of RhB was much faster, with conversions up to 88% and 95% after 2.5 h, respectively. The photodegradation kinetics were fitted to a pseudo-first-order reaction, $\ln(C_0/C) = kt$, where k is the apparent rate constant (Figure 4b).⁶ CZTS-Pt heterostructures showed the highest average apparent rate constant of 1.17 min^{-1} , about 6-fold higher than that of pure CZTS nanocrystals (0.19 min^{-1}). The average apparent rate constant for CZTS-Au was 0.90 min^{-1} .

We also examined the activity of CZTS, CZTS-Au, and CZTS-Pt toward photocatalytic hydrogen evolution from water splitting. For these experiments, 10 mg of nanoparticles was dispersed in 50 mL of deionized water contained in a glass reactor, and 0.1 M Na_2S and Na_2SO_3 were added as hole scavengers. Just before irradiation using a 300 W Xe lamp, the reactor was thoroughly purged with argon to remove both the

oxygen from the headspace of the reactor and that dissolved in the water. H_2 evolution was monitored by periodically sampling the gas phase inside the glass chamber with a gastight syringe and analyzing it by a gas chromatograph fitted with a thermal conductivity detector.

As shown in Figure 5a, the presence of the noble metals at the surface of CZTS clearly promoted the H_2 production rate.

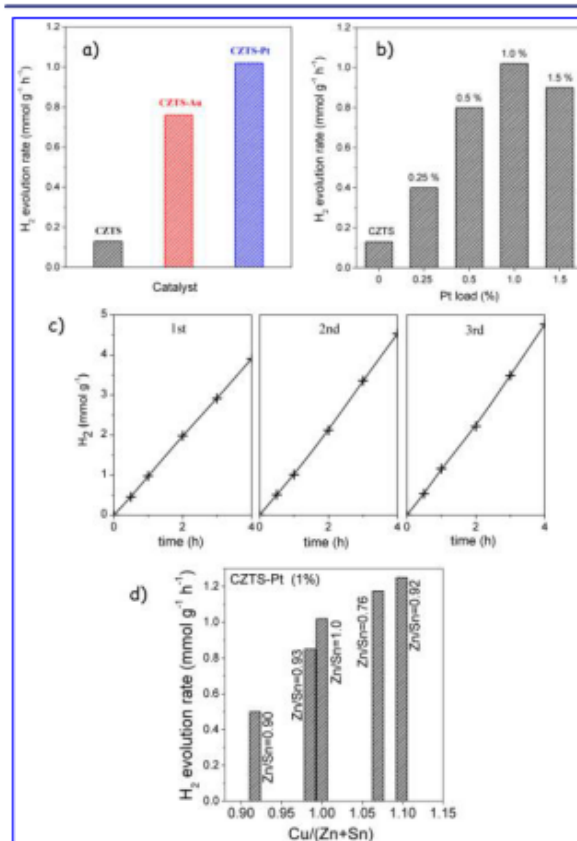


Figure 5. (a) Hydrogen evolution rate of CZTS, CZTS-Au, and CZTS-Pt nanomaterials during a 4 h test. (b) Dependence of the hydrogen evolution rate on the Pt load on CZTS-Pt heterostructures. (c) Recycle hydrogen generation property of 1 wt% CZTS-Pt nanoparticles. (d) Hydrogen evolution rate of CZTS-Pt (1%) as a function of the CZTS composition.

CZTS-Pt provided the highest H_2 evolution rate ($1.02 \text{ mmol/g}\cdot\text{h}$), which was 8-fold higher than that of bare CZTS ($0.13 \text{ mmol/g}\cdot\text{h}$). We further investigated the influence of the noble metal load on the H_2 evolution with CZTS-Pt nanoparticles. As shown in Figure 5b, the H_2 production rate increased with the Pt load until a maximum at around 1% and decreased with further noble metal loading. Such an activity decrease was associated with the nucleation, at too-high Pt loads, of independent Pt nanocrystals outside the CZTS surface (Figure S7). Such independent nanocrystals were much less effective in promoting the water-splitting reaction but still scattered photons, thus decreasing the light absorption on CZTS. The observation of such an optical shielding effect⁷ confirms that an intimate interface between CZTS and the noble metal is key to promote the photocatalytic hydrogen generation.

The photostability of the CZTS-Pt catalyst was tested by measuring the H_2 evolution during consecutive runs (Figure

5c). After each run, the photocatalyst was recovered by centrifugation and re-dispersed in a new deionized water solution containing fresh hole scavengers. No catalyst deactivation was observed after three cycles. Actually, the activity of the CZTS-Pt catalyst increased slightly with time, which may be explained by the decomposition of residual organic molecules at the nanoparticle surface, noticeably increasing the catalyst active area.⁸

We further analyzed the photocatalytic activity of CZTS-Pt nanoparticles with different CZTS compositions (Figure 5d). We observed an increase of the hydrogen evolution rate with increasing Cu/(Zn+Sn) ratio. This is the opposite of the trend observed in the photovoltaics field, where Cu-poor and Zn-rich materials generally result in higher efficiencies. On the other hand, no dependence of the photocatalytic activity on the Zn/Sn ratio was observed.

The above results confirmed that CZTS absorbed the visible light and efficiently transferred the photogenerated charge carriers to the noble metal, enriching its electron concentration and promoting the chemical reaction.⁹ The presence of the co-catalyst reduced the reaction overpotential, decreasing the interface barrier for the charge carrier transfer. In this way, the metal accelerated the surface redox reactions such as water splitting and dye degradation, as confirmed by electrochemical impedance spectroscopy measurements (Figure S14).^{9,10}

In summary, we detail a synthesis route to produce CZTS-noble metal heterostructured nanoparticles. Both CZTS-Au and CZTS-Pt heterostructures showed enhanced photocatalytic activity toward photodegradation of RhB and H₂ production by water splitting when compared to pure CZTS. The intimate contact between the two materials was key to obtain a real semiconductor–noble metal synergistic effect to promote solar energy conversion through an efficient charge transfer of the photogenerated carriers from the semiconductor to the metal co-catalyst and from this to the species in solution. This highlights the importance of nanoscale interface control also in complex quaternary materials for both fundamental understanding and technology applications.

■ ASSOCIATED CONTENT

Supporting Information

Synthesis and characterization details and additional characterization results. This material is available free of charge via the Internet at <http://pubs.acs.org>.

■ AUTHOR INFORMATION

Corresponding Author

acabot@irec.cat

Notes

The authors declare no competing financial interest.

■ ACKNOWLEDGMENTS

This work was supported by the European Regional Development Funds and the Framework 7 program under project SCALENANO (FP7-NMP-ENERGY-2011-284486).

■ REFERENCES

(1) (a) Linic, S.; Christopher, P.; Ingram, D. B. *Nat. Mater.* **2011**, *10*, 911–921. (b) Buck, M. R.; Bondi, J. F.; Schaak, R. E. *Nat. Chem.* **2012**, *4*, 37–44. (c) Costi, R.; Saunders, A. E.; Banin, U. *Angew. Chem., Int. Ed.* **2010**, *49*, 4878–4897. (d) Zhao, Q.; Ji, M.; Qian, H.; Dai, B.; Weng, L.; Gui, J.; Zhang, J.; Ouyang, M.; Zhu, H. *Adv. Mater.* **2014**, *26*, 1387–1392. (e) Habas, S. E.; Yang, P.; Mokari, T. *J. Am. Chem. Soc.*

2008, *130*, 3294–3295. (f) Mokari, T.; Rothenberg, E.; Popov, I.; Costi, R.; Banin, U. *Science* **2004**, *304*, 1787–1790. (g) Buck, M. R.; Schaak, R. E. *Angew. Chem., Int. Ed.* **2013**, *52*, 6154–6178. (h) Costi, R.; Saunders, A. E.; Elmalem, E.; Salant, A.; Banin, U. *Nano Lett.* **2008**, *8*, 637–641. (i) Ibáñez, M.; Zamani, R.; Gorsse, S.; Fan, J.; Ortega, S.; Cadavid, D.; Morante, J. R.; Arbiol, J.; Cabot, A. *ACS Nano* **2013**, *7*, 2573–2586.

(2) (a) Chen, X.; Shen, S.; Guo, L.; Mao, S. S. *Chem. Rev.* **2010**, *110*, 6503–6570. (b) Chen, X.; Liu, L.; Yu, P. Y.; Mao, S. S. *Science* **2011**, *331*, 746–750. (c) Tong, H.; Ouyang, S.; Bi, Y.; Umezawa, N.; Oshikiri, M.; Ye, J. *Adv. Mater.* **2012**, *24*, 229–251. (d) Jiang, Z.; Tang, Y.; Tay, Q.; Zhang, Y.; Malyi, O. I.; Wang, D.; Deng, J.; Lai, Y.; Zhou, H.; Chen, X.; Dong, Z.; Chen, Z. *Adv. Energy Mater.* **2013**, *3*, 1368–1380. (e) Han, Z.; Qiu, F.; Eisenberg, R.; Holland, P. L.; Krauss, T. D. *Science* **2012**, *338*, 1321–1324.

(3) (a) Carrete, A.; Shavel, A.; Fontané, X.; Montserrat, J.; Fan, J.; Ibáñez, M.; Saucedo, E.; Pérez-Rodríguez, A.; Cabot, A. *J. Am. Chem. Soc.* **2013**, *135*, 15982–15985. (b) Zhou, H.; Hsu, W.-C.; Duan, H.-S.; Bob, B.; Yang, W.; Song, T.-B.; Hsu, C.-J.; Yang, Y. *Energy Environ. Sci.* **2013**, *6*, 2822–2838. (c) Miyauchi, M.; Hanayama, T.; Atarashi, D.; Sakai, E. *J. Phys. Chem. C* **2012**, *116*, 23945–23950. (d) Moriya, M.; Minegishi, T.; Kumagai, H.; Katayama, M.; Kubota, J.; Domen, K. *J. Am. Chem. Soc.* **2013**, *135*, 3733–3735.

(4) (a) Shavel, A.; Cadavid, D.; Ibáñez, M.; Carrete, A.; Cabot, A. *J. Am. Chem. Soc.* **2012**, *134*, 1438–1441. (b) Singh, A.; Geaney, N.; Laffir, F.; Ryan, K. M. *J. Am. Chem. Soc.* **2012**, *134*, 2910–2913. (c) Singh, A.; Singh, S.; Levchenko, S.; Unold, T.; Laffir, F.; Ryan, K. M. *Angew. Chem., Int. Ed.* **2013**, *52*, 9120–9124. (d) Ibáñez, M.; Zamani, R.; Li, W.; Shavel, A.; Arbiol, J.; Morante, J. R.; Cabot, A. *Cryst. Growth Des.* **2012**, *12*, 1085–1090. (e) Ibáñez, M.; Zamani, R.; Li, W.; Cadavid, D.; Gorsse, S.; Katcho, N. A.; Shavel, A.; López, A. M.; Morante, J. R.; Arbiol, J.; Cabot, A. *Chem. Mater.* **2012**, *24*, 4615–4622. (f) Ibáñez, M.; Cadavid, D.; Zamani, R.; García-Castelló, N.; Izquierdo-Roca, V.; Li, W.; Fairbrother, A.; Prades, J. D.; Shavel, A.; Arbiol, J.; Pérez-Rodríguez, A.; Morante, J. R.; Cabot, A. *Chem. Mater.* **2012**, *24*, 562–570.

(5) Lu, X.; Zhuang, Z.; Peng, Q.; Li, Y. *Chem. Commun.* **2011**, *47*, 3141–3143.

(6) Yan, S. C.; Li, Z. S.; Zou, Z. G. *Langmuir* **2010**, *26*, 3894–3901.

(7) Bao, N.; Shen, L.; Takata, T.; Domen, K. *Chem. Mater.* **2007**, *20*, 110–117.

(8) (a) Lei, Z.; You, W.; Liu, M.; Zhou, G.; Takata, T.; Hara, M.; Domen, K.; Li, C. *Chem. Commun.* **2003**, 2142–2143. (b) Bang, J. U.; Lee, S. J.; Jang, J. S.; Choi, W.; Song, H. *J. Phys. Chem. Lett.* **2012**, *3*, 3781–3785.

(9) (a) Ikeda, S.; Nakamura, T.; Harada, T.; Matsumura, M. *Phys. Chem. Chem. Phys.* **2010**, *12*, 13943–13949. (b) Huang, S.; Luo, W.; Zou, Z. *J. Phys. D: Appl. Phys.* **2013**, *46*, 235108. (c) Tsuji, I.; Shimodaira, Y.; Kato, H.; Kobayashi, H.; Kudo, A. *Chem. Mater.* **2010**, *22*, 1402–1409. (d) Rawalekar, S.; Mokari, T. *Adv. Energy Mater.* **2013**, *3*, 12–27.

(10) Bu, Y.; Chen, Z.; Li, W. *Appl. Catal., B: Environ.* **2014**, *144*, 622–630.

Cu₂ZnSnS₄-Pt and Cu₂ZnSnS₄-Au heterostructured nanoparticles for photocatalytic water splitting and pollutant degradation

Supporting Information

Xuelian Yu,^{†,‡} Alexey Shavel,[†] Xiaoqiang An,^{‡,&} Zhishan Luo,[†] Maria Ibáñez,[†] and Andreu Cabot^{*,†,‡,‡}

[†] Catalonia Energy Research Institute - IREC, Jardí de les Dones de Negre 1, Sant Adria del Besos, 08930 Barcelona, Spain

[‡] Institute of Process Engineering, Chinese Academy of Sciences, 100190, Beijing, China

[‡] Department of Chemical Engineering, University College London, Torrington Place, London, WC1E 7JE, UK

[&] Research Center for Eco-Environmental Sciences, Chinese Academy of Sciences, 100085, Beijing, China

[‡] Institució Catalana de Recerca i Estudis Avançats (ICREA), 08010 Barcelona, Spain

1. Materials and Methods

1.1. Materials

1.1.1. Chemicals and solvents

Gold(III) chloride hydrate (AuCl₃, >49%Au), Dodecylamine (DDA, 98%), Didecylidimethylammonium bromide (DDAB, 98%), 1,2-hexadecanediol (90%), Platinum(II) acetylacetonate (97%), oleylamine (OLA), diphenyl ether (99%), oleic acid (OA, tech. 90%), copper (II) chloride dihydrate (>99%, CuCl₂·2H₂O), zinc oxide (ZnO), tin (IV) chloride pentahydrate (SnCl₄·5H₂O), tert-dodecylmercaptan (tech. >97%), dodecanethiol (DDT, >98%), octadecene (tech. 90%) were purchased from Aldrich. The purity of the chemicals and especially of the OLA played a very important role in determining the quality (shape and size distribution) of the prepared CZTS nanoparticles. Therefore, OLA, 1-octadecene and also tert-dodecylmercaptan were distilled before using them for the synthesis of CZTS nanoparticles. Chloroform, isopropanol, toluene and methanol were of analytical grade and obtained from various sources.

1.1.2. CZTS Nanoparticles

Quasi-spherical CZTS nanoparticles with wurtzite structure were prepared by the reaction of copper, tin and zinc salts with a mixture of the tert-dodecylmercaptan and dodecanethiol in the presence of OLA. In a typical synthesis, 5.4 mmol (920 mg) of CuCl₂·2H₂O, 4.8 mmol (391 mg) of ZnO and 1.8 mmol (630 mg) of SnCl₄·5H₂O were dissolved in a minimum amount of the tetrahydrofuran (THF). Afterward, 24 mmol (6.43 g) of distilled OLA and 20 g distilled 1-octadecene were added to the reaction mixture. The solution was heated under flow of argon to 175 °C and maintained at this temperature for 1 hour to remove low boiling point impurities and water. The main reason to use THF as co-solvent is to facilitate the metal salts dissolution, but it also helps to remove water from the reaction mixture.

After purging, the mixture was cooled to 100 °C and 50 mmol (10.12 g) of tert-dodecylmercaptan and 5 mmol (1.012 g) of dodecanethiol were added using a syringe. Then the solution was heated to 250 °C and maintained at this temperature for one hour. Finally, the CZTS nanoparticles were thoroughly purified by multiple precipitation and re-dispersion steps using 2-propanol and chloroform. Finally, CZTS nanoparticles were dissolved in THF and the solution was centrifuged at 9000 rpm during 5-15 minutes to precipitate poorly soluble unreacted metal complexes and large Zn-rich particles (note the initial non-stoichiometric precursor ratio). The supernatant was recovered and stored for its posterior use.

1.1.1. CZTS-Au nanoparticles

AuCl₃, DDAB (40 mg), and DDA (140 mg) were dissolved in toluene (4.0 mL) and sonicated for 30 min, until the color of the gold precursor solution turned from dark orange to light yellow. This reaction mixture was added drop-wise to the CZTS nanocrystals dispersion in toluene (20 mL) at a rate of 80 mL/h for 5 min at room temperature. The product was immediately precipitated by adding methanol with centrifugation and finally dispersed in toluene.

1.1.2. CZTS-Pt nanoparticles

OA (0.20 mL), OLA (0.20 mL), 1,2-hexadecanediol (43 mg), and phenyl ether (10 mL) were loaded into the reaction flask and kept at 120 °C for 30 min. Platinum(II) acetylacetonate was mixed with the CZTS nanocrystals dispersion and heated to 65 °C for 10 min. The former mixture of the surfactants and phenyl ether was purged with nitrogen and heated to 200 °C. The latter mixture of the Pt precursor and the CZTS dispersion was injected into the reaction mixture at 200 °C. After 10 min, the reaction was quenched in a water bath. The product was washed with ethanol by precipitation-dispersion cycles, and finally dispersed in toluene.

1.2. Characterization techniques

Transmission electron microscopy (TEM) and high-resolution TEM (HRTEM): The morphological, chemical and structural characterizations of the nanoparticles were carried out by TEM and HRTEM. Carbon-coated TEM grids from Ted-Pella were used as substrates. HRTEM images were obtained using a Jeol 2010F field-emission gun microscope with a 0.19 nm point-to-point resolution at 200 keV with an embedded Gatan image filter for EELS analyses. Images were analyzed by means of Gatan Digital micrograph software.

Scanning electron microscopy (SEM): SEM analysis was done in a ZEISS Auriga SEM with an energy dispersive X-ray spectroscopy (EDX) detector at 20 kV to study the composition of nanoparticles. For SEM characterization, the particles were dissolved in chloroform and were drop casted on silicon substrates.

Powder X-ray diffraction (XRD): Powder XRD patterns were obtained with Cu K α 1 ($\lambda = 1.5406 \text{ \AA}$) radiation in a reflection geometry on a Bruker D8 operating at 40 kV and 40 mA.

Ultraviolet-visible spectroscopy (UV-Vis): Optical absorption spectra were recorded on a LAMBDA 950 UV-Vis spectrophotometer from PerkinElmer.

X-ray photoelectron spectroscopic (XPS): XPS measurements were performed on a Thermo Scientific XPS spectrometer.

1.3 Photocatalytic hydrogen generation experiments

Nanocrystals were rendered water soluble by replacing the initial hydrophobic surfactants with $[\text{NH}_4]_2\text{S}$. In a typical procedure, a highly concentrated and well cleaned solution of CZTS nanoparticles was mixed with 1 v% of $[\text{NH}_4]_2\text{S}$ (20 % aqueous) in formamide. The bi-phase system was vigorously shaken to promote the phase transfer. Almost immediately, CZTS nanoparticles moved into the upper formamide phase. The clear chloroform solution was discarded and the formamide phase was cleaned few times with fresh chloroform. CZTS NPs were precipitated with acetone and dried under vacuum overnight.

For the photocatalytic H_2 generation experiments, 10 mg of powder was dispersed in 50 ml of deionised water, with 0.1 M Na_2S and NaSO_3 as hole scavengers. The whole reaction was carried out in a glass reactor. Before the solution was irradiated, the reactor was thoroughly purged with argon to remove all oxygen in the headspace of the reactor and dissolved oxygen in water. A baseline was taken to ensure that there was little or no detectable oxygen in the system. A 300 W Xe lamp (Newport) was used to irradiate the sample after a suitable baseline was obtained. The reaction product was monitored by periodical sampling the gas phase from the glass chamber using a gas tight syringe and analyzing it by a gas chromatograph (Varian GC-450) fitted with a thermal conductivity detector (TCD, connected to molecular sieve column) to detect H_2 , O_2 and N_2 and a flame ionization detector (FID, connected to CP-SIL 5CB capillary column) to detect hydrocarbons. Argon was used as the gas chromatograph (GC) carrier gas. Photostability was tested by analyzing the photocatalytic activity of the samples on three consecutive runs. In this experiment, the photocatalyst was washed after each run and reused in the H_2 generation experiments.

1.4 Photodegradation of Rhodamine B measurements

To evaluate the photodegradation of Rhodamine B (RhB) under full arc light, 10 mg of photocatalysts were suspended in 50 mL of 10 ppm aqueous solution of RhB. The solution was stirred in the dark overnight to achieve the equilibrium adsorption. Then the suspension was illuminated with a 300 W Xe lamp. The concentration change of RhB was monitored by measuring the UV-vis absorption of the suspensions at regular intervals. The suspension was centrifuged for 1 min to remove the photocatalysts before measurement. The peak absorbance of RhB at 552 nm was used to determine its concentration. The

photocatalytic activity was analyzed by the time profiles of C_0/C , where C is the concentration of RhB at the irradiation time t and C_0 the concentration just after the absorption equilibrium before irradiation, respectively.

1.5 Fabrication of thin film electrodes and electrochemical measurements

5 mg of photocatalysts and 10 μL of Nafion solution (5 wt%) were dispersed in 1 mL water/isopropanol mixed solvent (3:1 v/v) by at least 30 min sonication to form a homogeneous catalyst colloid. For the measurements, 100 μL of the catalyst colloid was deposited onto areas of ca. 1 cm^2 of the FTO conductive glass to form the working electrode. A platinum wire was used as a counter electrode while an Ag/AgCl electrode worked as the reference electrode in the three electrode electrochemical system. The electrolyte was 0.5 M Na_2SO_4 aqueous solution degassed with Ar. Electrochemical impedance spectra (EIS) were recorded under an ac perturbation signal of 10 mV over the frequency range from 1 MHz to 100mHz.

2. Additional NP Characterization

2.1. XPS

High-resolution XPS spectra of Zn 2p, Cu 2p, Sn 3d, and S 2p were measured to determine the oxidation states of the constituent elements and determine the potential presence of secondary phases (Figure S1). The narrow doublet peaks in the Cu 2p spectrum appeared at 932.1 eV ($2p_{3/2}$) and 951.9 eV ($2p_{1/2}$), confirming the Cu(I) state. The peaks of Zn 2p appeared at binding energies of 1021.6 and 1044.7 eV, which can be assigned to Zn(II) with a peak splitting of 23.1 eV. The Sn(IV) state was confirmed by peaks located at 486.4 and 494.8 eV with its characteristic peak separation of 8.4 eV. The sulfur spectrum can be assigned to the presence of sulfide at binding energies of 161.7 and 162.9 eV with a doublet separation of 1.2 eV.^[1,2] On the other hand, XPS analysis of the heterostructured nanoparticles unambiguously showed that noble metals were present only in the metallic form (Figure S2).

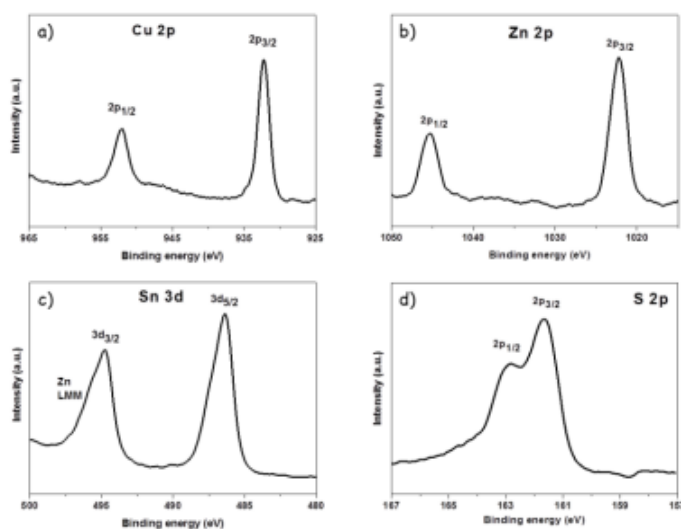


Figure S1. XPS spectra of CZTS nanocrystals.

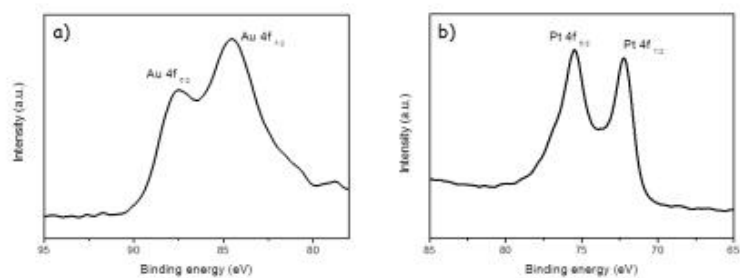


Figure S2. Au 4f (a) and Pt 4f (b) XPS spectra of CZTS-Au and CZTS-Pt nanoparticles.

2.2. UV-vis

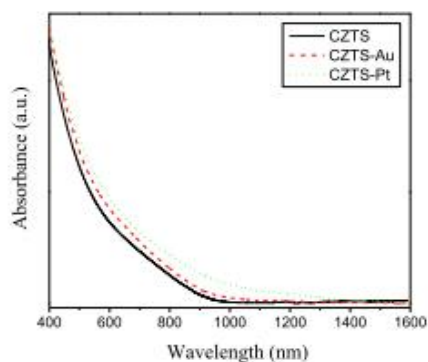


Figure S3. UV-vis absorbance spectra of CZTS, CZTS-Au and CZTS-Pt nanoparticles.

2.3. TEM

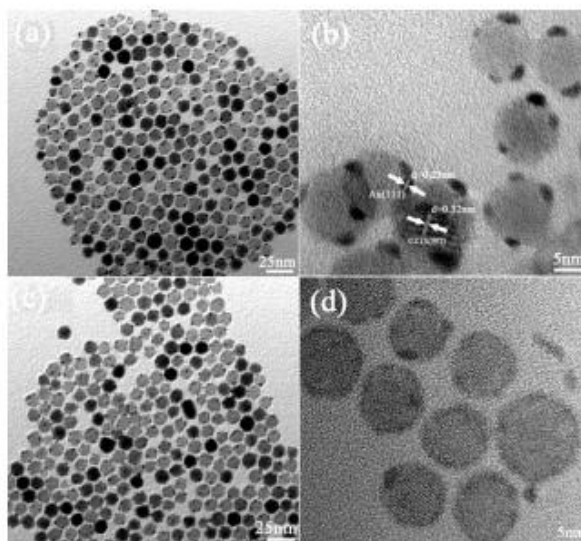


Figure S4. TEM and HRTEM images for CZTS-Au (a-b) and CZTS-Pt(c-d) heterostructured nanoparticles.

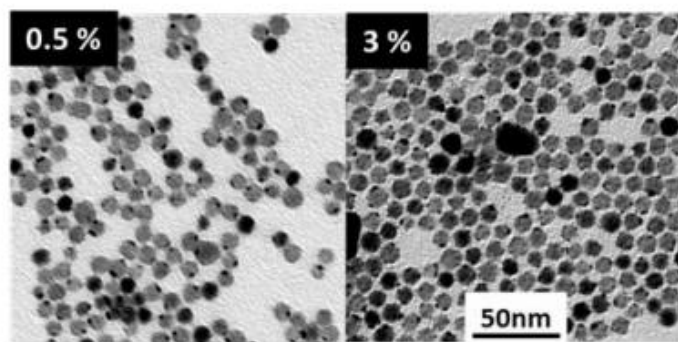


Figure S5. TEM images of CZTS-Au nanoparticles with different gold concentrations.

As we increased the metal concentration in the precursor solution, the number of tips increased. No clear differences on the tip size were observed. Notice that the concentration of metal at the CZTS surface was limited. Large concentrations of the gold precursor in the initial solution translated in small deposition yields, easily evidenced by the yellow color of the final solution (Figure S6). Large concentrations of Pt precursor on the initial solution translated into the nucleation of independent Pt particles (Figure S7).

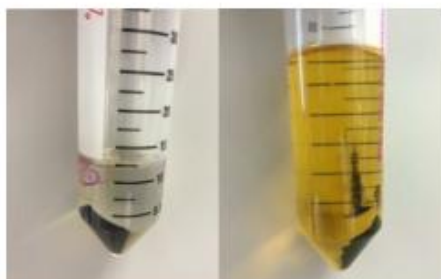


Figure S6. Photographs of the centrifuge tubes containing CZTS-Au nanoparticles with 1 % and 10 % nominal Au concentrations after reaction.

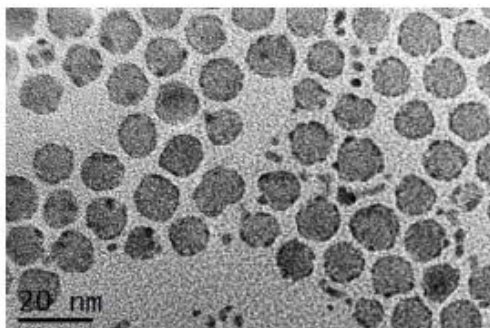


Figure S7. TEM image of 1.5 wt% CZTS-Pt nanostructures, showing the presence of independent Pt nanoparticles.

3. Additional Photocatalytic characterization

3.1. Unsupported Pt

As a control experiment, we determined the H_2 evolution rate of unsupported Pt nanoparticles. The evolution rate obtained for Pt nanoparticles without CZTS was a 4 fold lower than that obtained with CZTS particles and a 34 fold lower than that obtained for CZTS-Pt nanoparticles with 1 % of Pt.

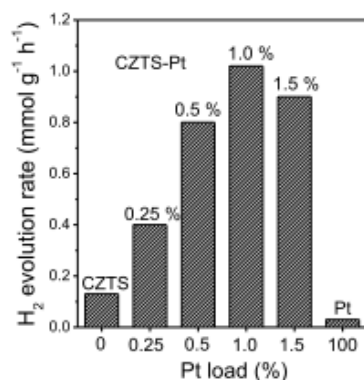


Figure S8. H₂ evolution rate of Pt nanoparticles compared with that of CZTS and CZTS-Pt nanoparticles.

3.2. Comparison of kesterite vs wurtzite CZTS nanoparticles

For a preliminary comparison the photocatalytic properties of kesterite vs. wurtzite nanoparticles, we prepared kesterite CZTS nanoparticles, grew Pt on their surface in the same conditions as we did over wurtzite CZTS and measured their photocatalytic properties. Two conclusions were extracted from this preliminary experiment: 1) The yield of the Pt deposition over the CZTS surface is lower in the case of kesterite CZTS nanoparticles than over wurtzite CZTS. This experimental fact should be associated to a higher density of nucleation sites at the wurtzite CZTS surface, possibly related to the higher faceting degree and the larger amount of vertex of the wurtzite CZTS nanoparticles; 2) At similar Pt concentrations, kesterite CZTS-Pt showed slightly lower hydrogen generation rates than wurtzite CZTS-Pt. While intrinsic differences related to the dissimilar crystal phase cannot be ruled out, the lower activity of the kesterite CZTS nanoparticles may be in part related to the slightly larger size of the kesterite CZTS nanoparticles and to their slightly higher agglomeration, which results in relatively lower surface areas.

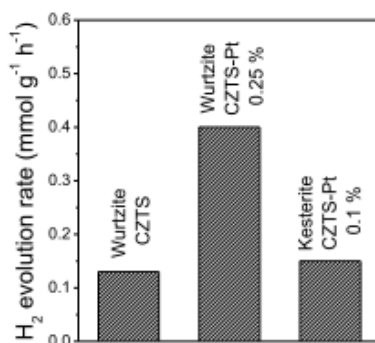


Figure S9. H₂ evolution rate of wurtzite CZTS, wurtzite CZTS-Pt (0.25 %) and kesterite CZTS-Pt (0.1 %).

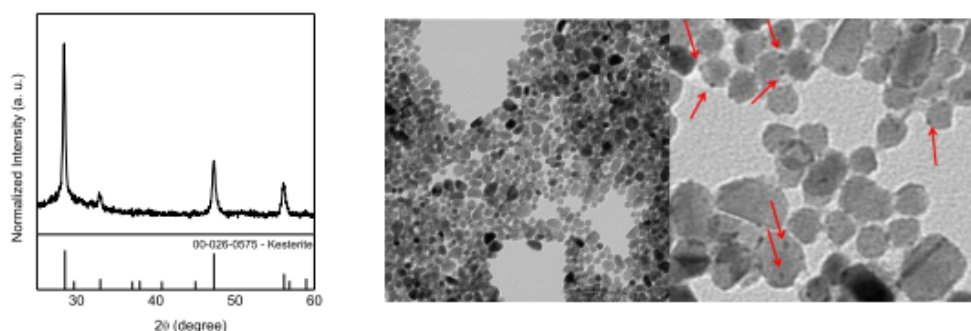


Figure S10. XRD pattern (left) and TEM images (right) of the kesterite CZTS-Pt nanoparticles used for photocatalytic experiments (few examples of Pt nanoparticles are pointed out with red arrows in the top-right TEM image).

3.3. Influence of the ligand exchange molecule

To determine the influence of the ligand on the photocatalytic properties of the material, we compared the photocatalytic activity of the materials after two different ligand exchange processes. We measured the hydrogen evolution rate of CZTS-Pt nanoparticles rendered water soluble by means of $(\text{NH}_4)_2\text{S}$ or mercaptopropionic acid (MPA). A slight increase of the hydrogen evolution rate was obtained when using MPA (Figure S11).

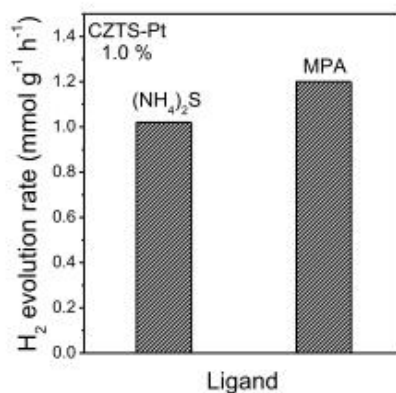


Figure S11. Hydrogen evolution rate as a function of the ligand used to render the CZTS-Pt nanoparticles water soluble.

3.4. Influence of the CZTS composition

By tuning the ratio of the different elements within the initial precursor solution, we further prepared CZTS nanoparticles with different compositions: i) $\text{Cu}_2\text{Zn}_{0.87}\text{Sn}_{0.95}\text{S}_4$; ii) $\text{Cu}_2\text{Zn}_{1.03}\text{Sn}_{1.15}\text{S}_4$; iii) $\text{Cu}_2\text{Zn}_{0.81}\text{Sn}_{1.06}\text{S}_4$; iv) $\text{Cu}_2\text{Zn}_{0.98}\text{Sn}_{1.05}\text{S}_4$, and we analyzed their photocatalytic activity. We observed an increase of the H₂ evolution rate with the Cu(Zn+Sn) ratio. Surprisingly, this is the opposite trend as the one observed in the photovoltaics field, where Cu-poor and Zn-rich materials generally result in higher efficiencies. On the other hand, no dependence of the photocatalytic activity on the Zn/Sn ratio was observed.

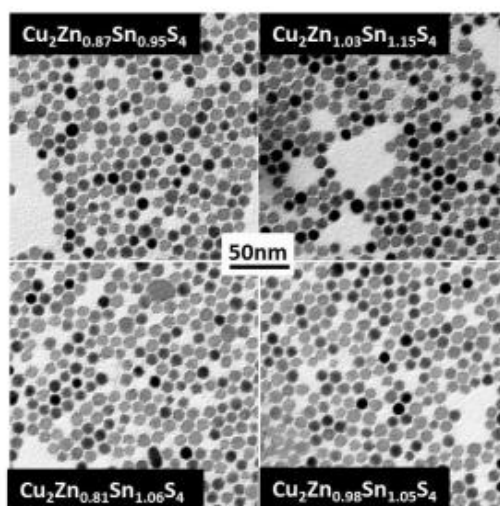


Figure S12. TEM images of CZTS-Pt (1%) nanoparticles with different CZTS compositions.

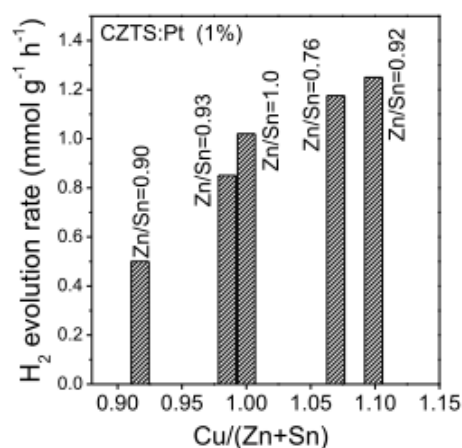


Figure S13. Hydrogen evolution rate of CZTS-Pt as a function of the CZTS composition.

3.5. Electrochemical tests:

Nyquist spectra obtained by electrochemical impedance spectra measurements for CZTS, CZTS-Au and CZTS-Pt electrodes are depicted in Figure S14. With the introduction of noble metals, the semicircles of both electrodes in the plot become narrower, which indicates an increase of the electrical conductivity of the system. Being all the other parameters the same, the lower conductivities are associated to a decrease of the charge transfer resistance between the material and the species in solution, which is associated to a reduction of the barrier for charge carrier transfer from the CZTS to the water molecules.

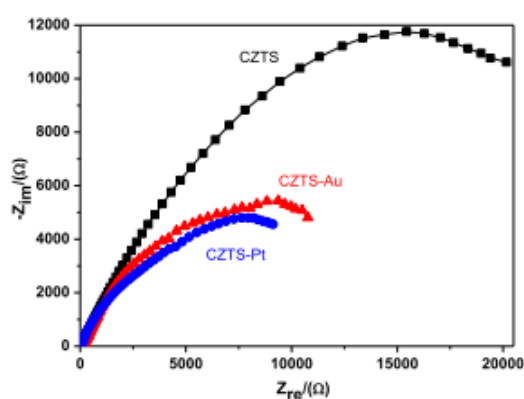


Figure S14. Electrochemical impedance spectra of CZTS, CZTS-Au and CZTS-Pt nanoparticles supported on a FTO-coated glass substrate.

References

- (1) NIST-XPS database, version 3.5. <http://srdata.nist.gov/xps/>.
- (2) Moulder, J. F.; Stickle, W. F.; Sobol, P. E.; Bomben, K. D. Handbook of X-Ray Photoelectron Spectroscopy; Perkin-Elmer: Eden Prairie, MN, 1992.

2.2.2 $\text{Cu}_2\text{ZnSnS}_4\text{-Ag}_2\text{S}$ Nanoscale p-n Heterostructures as Sensitizers for Photoelectrochemical Water Splitting

“ *$\text{Cu}_2\text{ZnSnS}_4\text{-Ag}_2\text{S}$ Nanoscale p-n Heterostructures as Sensitizers for Photoelectrochemical Water Splitting*” is the title of the fourth article presented on this thesis for the graduation requirements. The article was published in *Langmuir* **2015**, 31 (38), 10555-10561. As showed in the end of this part, it presented a detailed study of the formation of CZTS- Ag_2S heterodimers via a cation exchange-reaction. This reaction occurs when controlled amounts of Ag^+ ions are added to a solution containing CZTS NPs at 120 °C. TEM, HRTEM and XRD analysis of CZTS- Ag_2S p-n NPs with different ratio of CZTS and Ag_2S demonstrated that the HNP had coincident site epitaxial. Such CZTS- Ag_2S HNP exhibited significantly enhanced photoelectrochemical current response under visible-light illumination compared to pure CZTS. The ability to synthesize such structures with controlled composition and suitable band alignment promoting charge separation provided a better insight into fundamental synthetic chemistry as well as opening avenues for diverse optoelectronic application. Figure 2.11 shows the scheme of energy band gap of HNPs and water splitting reaction in the photoelectrochemical cell.

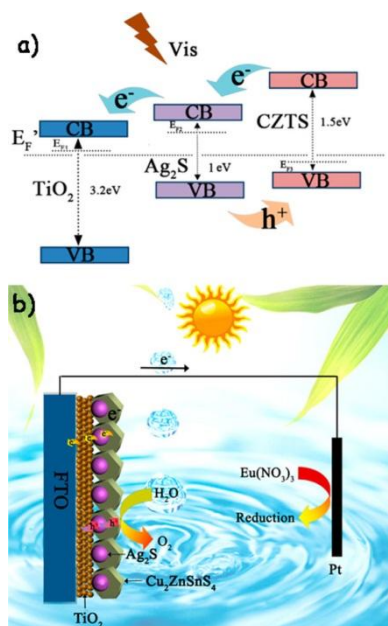


Figure 2.11 (a) Schematic of the energy band diagram of the heterostructures and the possible model of electron transfer. (b) Schematic diagram of water splitting reaction in the photoelectrochemical cell.

Cu₂ZnSnS₄–Ag₂S Nanoscale p–n Heterostructures as Sensitizers for Photoelectrochemical Water Splitting

Xuelian Yu,^{†,‡} Jingjing Liu,[§] Aziz Genç,^{||} Maria Ibáñez,[‡] Zhishan Luo,[‡] Alexey Shavel,[‡] Jordi Arbiol,^{||,⊥} Guangjin Zhang,[§] Yihe Zhang,^{*,†} and Andreu Cabot^{*,‡,⊥}

[†]Beijing Key Laboratory of Materials Utilization of Nonmetallic Minerals and Solid Wastes, National Laboratory of Mineral Materials, School of Materials Science and Technology, China University of Geosciences, 100083 Beijing, P. R. China

[‡]Catalonia Energy Research Institute - IREC, 08930 Sant Adria del Besos, Barcelona, Spain

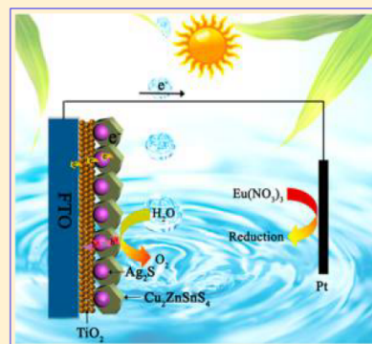
[§]Key Laboratory of Green Process and Engineering, Chinese Academy of Sciences, 100190 Beijing, P. R. China

^{||}Institut Català de Nanociència i Nanotecnologia, ICN2, Campus de la UAB, 08193 Bellaterra, Spain

[⊥]Institució Catalana de Recerca i Estudis Avançats - ICREA, 08010 Barcelona, Spain

Supporting Information

ABSTRACT: A cation exchange-based route was used to produce Cu₂ZnSnS₄ (CZTS)–Ag₂S nanoparticles with controlled composition. We report a detailed study of the formation of such CZTS–Ag₂S nanoheterostructures and of their photocatalytic properties. When compared to pure CZTS, the use of nanoscale p–n heterostructures as light absorbers for photocatalytic water splitting provides superior photocurrents. We associate this experimental fact to a higher separation efficiency of the photogenerated electron–hole pairs. We believe this and other type-II nanoheterostructures will open the door to the use of CZTS, with excellent light absorption properties and made of abundant and environmental friendly elements, to the field of photocatalysis.



INTRODUCTION

Colloidal nanocrystals are highly suitable building blocks for the fabrication of energy conversion and storage devices. Their solution processability and the precise control that can be achieved over their chemical and structural parameters, which control their optical and electronic properties, make nanocrystal-based solution processing approaches highly advantageous when compared with conventional vacuum-based thin film technologies.^{1–4} However, current functional nanomaterials must meet too many very demanding properties not realizable with a unique compound. Thus, the design of multicomponent nanostructures with improved, multiple, and/or new physical-chemical properties, such as enhanced photoluminescence,^{5,6} modified magnetic behavior,⁷ improved (photo)catalytic performances,^{8–10} and superior thermoelectric efficiencies,¹¹ is essential. In particular, p–n junction heterostructured nanoparticles provide new ways to manipulate electron and hole wave functions.¹² Among them, type-II nanoparticles, with a staggered alignment of band edges at the heterointerface, promote the spatial separation of electrons and holes.^{13–16}

Several synthesis strategies have been developed to produce type-II nanoheterostructures. Among them, ion-exchange methods based on solubility constant difference have been proven as particularly suitable.¹⁷ They provide versatility, high

degree of control over composition of each compound, and high selectivity toward the formation of dimers with an epitaxial heterointerface while keeping the geometry of the initial nanoparticles and preventing the nucleation of secondary phases.^{18,19}

While most of the effort oriented to produce nanoheterostructures by cation exchange methods has been carried out with Cd-based chalcogenides,²⁰ very recently, this strategy has also been applied to the total or partial conversion of more environmental friendly Cu-based chalcogenides.^{21–23} Within this group of materials, a particularly environmental friendly direct band gap semiconductor is Cu₂ZnSnS₄ (CZTS). In the past decade, CZTS has attracted much attention in the field of thin film photovoltaics as alternative to CdTe and CuIn_{1–x}Ga_xSe₂. CZTS uniquely combines both outstanding optoelectronic properties and a composition based on elements that are abundant in the Earth's crust. Particularly, its direct band gap at 1.5 eV matches well with the energy requirement for solar water splitting, which makes CZTS a strong candidate for water splitting.²⁴ However, in spite of its outstanding properties, and except for few examples on the photocatalytic

Received: July 6, 2015

Revised: August 28, 2015

Published: September 7, 2015

generation of hydrogen and other value-added chemicals,^{25–29} this material has been mostly ignored in the photocatalysis field. This is in part due to its high surface charge carrier recombination, which becomes critical in high surface area materials as those required for photocatalysis.

One solution to minimize recombination of photogenerated charge carriers is the rapid spatial separation of electrons and holes in heterostructures. CZTS and related quaternary nanocrystals can be nowadays produced by different synthetic approaches.^{30–36} However, due to the difficulties in tuning the composition, phase, size and shape of such complex materials, the preparation of CZTS-based nanoscale p–n junction heterostructures still remains challenging.

In this work, we demonstrate that partial cation exchange is an excellent strategy to produce CZTS-based nanoheterostructures due to the high mobility of cations in the CZTS lattice. In particular, we describe the preparation of CZTS-based type-II nanoheterostructures via cation exchange of CZTS with Ag⁺ ions to form CZTS–Ag₂S nanoparticles. The progressive exchange in the initial CZTS nanoparticles by Ag⁺ ions allows controlling the relative ratio between the two compounds. We further demonstrate here that the use of CZTS–Ag₂S nanoheterostructures as sensitizers provides significantly enhanced photocurrent response for photoelectrochemical water splitting under visible-light illumination.

EXPERIMENTAL SECTION

Chemicals and Solvents. *tert*-Dodecylmercaptan, dodecanethiol, tin(IV)chloride (SnCl₄·5H₂O), zinc oxide(ZnO), copper(II) chloride (CuCl₂·2H₂O), silver nitrate (AgNO₃), 1-octadecene (ODE), oleylamine (OLA, 70%), and oleic acid (OA, 90%) were purchased from Aldrich. Chloroform, isopropanol, tetrahydrofuran (THF), toluene, and methanol were of analytical grade and obtained from various sources. OLA was distilled before its use. The rest of the precursors and solvents were used without further purification.

Synthesis of CZTS–Ag₂S Heterostructures. Quasi-spherical CZTS nanoparticles with wurtzite structure were prepared using the method we described before²⁶ by the reaction of copper, tin, and zinc salts with a mixture of *tert*-dodecylmercaptan and dodecanethiol in the presence of OLA. In a typical synthesis, 5.4 mmol of CuCl₂·2H₂O, 4.8 mmol of ZnO, and 1.8 mmol of SnCl₄·5H₂O were dissolved in THF. Then, 24 mmol of distilled OLA and 20 g of ODE were added to the reaction mixture. The solution was heated to 175 °C under argon flow and maintained at this temperature for 1 h. After purging, the mixture was cooled to 100 °C, and 50 mmol of *tert*-dodecylmercaptan and 5 mmol of dodecanethiol were added. The solution was then heated to 250 °C and kept for 1 h. The obtained CZTS nanocrystals were thoroughly purified by multiple precipitation and redispersion steps using 2-propanol and chloroform.

To produce CZTS–Ag₂S heterostructures, first, a stock precursor solution of AgNO₃ in OLA was made by dissolving 0.34 g of AgNO₃ (2.0 mmol) in 10.0 mL of OLA at 60 °C. Dissolution took ~15 min under magnetic stirring and N₂ atmosphere. When cooled down to room temperature, the colorless solution gradually turned into a white waxy paste. Then, 1 mL of THF dispersion of the CZTS nanoparticles (~40 mg) was mixed with 10 mL of ODE and 0.5 mL of OLA under N₂ atmosphere. The solution was maintained under N₂ flow at 120 °C for 30 min to remove THF. Depending on the relative CZTS/Ag₂S ratio targeted, between 2 and 6 mL of AgNO₃ stock solution was quickly injected into the CZTS nanoparticle dispersion at 120 °C. The reaction was maintained at this temperature for 30 s before it was rapidly cooled down to room temperature using a water bath. Nanoparticles were finally washed by multiple precipitation and redispersion steps using toluene and ethanol.

Characterization Techniques. The morphological, chemical, and structural characterization of the nanoparticles was carried out by transmission electron microscopy (TEM) and high-resolution TEM

(HRTEM). Carbon-coated TEM grids from Ted-Pella were used as substrates. HRTEM images were obtained using a JEOL 2010F field-emission gun microscope with a 0.19 nm point-to-point resolution at 200 keV with an embedded Gatan image filter for EELS analyses. Images were analyzed by means of Gatan Digital micrograph software.

Powder X-ray diffraction (XRD) patterns were obtained with Cu K α ($\lambda = 1.5406 \text{ \AA}$) radiation in a reflection geometry on a Bruker D8 operating at 40 kV and 40 mA. UV–vis optical absorption spectra were recorded on a LAMBDA 950 UV–vis spectrophotometer from PerkinElmer. X-ray photoelectron spectroscopic (XPS) measurements were performed on a Thermo Scientific XPS spectrometer.

Photoelectrochemical response was measured using a CHI852C electrochemical workstation with conventional three-electrode setup under visible-light illumination. Fluorine doped tin oxide (FTO) glass substrates were cleaned with acetone and ethanol, and dried with pure nitrogen. To prepare the electrode, aqueous TiO₂ paste (25% w/w TiO₂, 10% w/w polyethylene glycol (MW 20 000)) was doctor bladed onto 1 × 1 cm² FTO substrates. The films were then calcined at 450 °C for 2 h. Then, the as-prepared CZTS–Ag₂S were first dispersed in 1 mL toluene with concentration of 1 mg/mL followed by sonication. After that, the solution was deposited on the working electrode substrate by spin-coating (rotation speed: 3000 rpm). A platinum wire and Ag/AgCl were used as the counter and reference electrodes, respectively. Eu(NO₃)₃ aqueous solution (1 M) was used as electrolyte. The illumination source was a 300 W xenon lamp with a cutoff filter ($\lambda > 420 \text{ nm}$) to provide visible light illumination.

RESULTS AND DISCUSSION

Figure 1a shows a representative TEM micrograph of the CZTS nanocrystals used to produce CZTS-based nano-

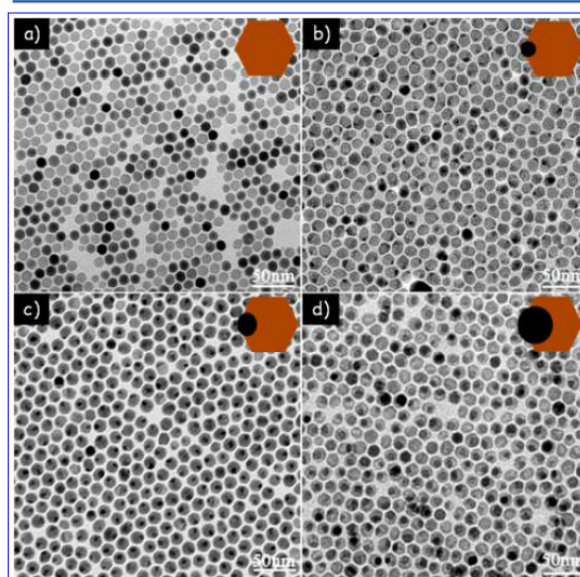


Figure 1. TEM images of CZTS nanocrystals (a) and CZTS–Ag₂S heterostructures with different amounts of AgNO₃ precursor: 0.4 mmol (b, sample H1), 0.8 mmol (c, sample H2), and 1.2 mmol (d, sample H3).

heterostructures. CZTS nanocrystals were highly monodisperse, with an average size of $12 \pm 1 \text{ nm}$, and presented quasi-spherical geometries with faceted surfaces. CZTS–Ag₂S heterostructures were obtained by adding Ag⁺ ions to a solution containing CZTS nanoparticles at 120 °C. CZTS–Ag₂S heterodimers were formed by the preferential cation exchange at the vertexes of the hexagonal structures, which are

the most reactive sites (Figure 1b–d). A similar preferential partial cation exchange reaction was observed with CdS rods that were progressively transformed into Cu_2S rods, starting at the nanorod tip as the most reactive regions.³⁷

When increasing the amount of Ag^+ precursor added, the interface between the two compounds, CZTS and Ag_2S , moved inward the CZTS nanoparticle. The diameter of the Ag_2S nanocrystal increased from ~ 2 nm (Figure 1b, sample H1), to ~ 4 nm (Figure 1c, sample H2), and ~ 7 nm (Figure 1d, sample H3) when the amount of Ag^+ precursor used increased from 0.4, 0.8, and 1.2 mmol, respectively. In accordance with the rapid kinetics characterizing cation exchange reactions,³⁸ the reaction was completed in less than 5 s and a further prolongation of the reaction time did not translate in any morphology change.

XRD patterns of the CZTS nanocrystals before and after the addition of increasing amounts of Ag^+ cations are shown in Figure 2. Initial CZTS nanoparticles presented a wurtzite

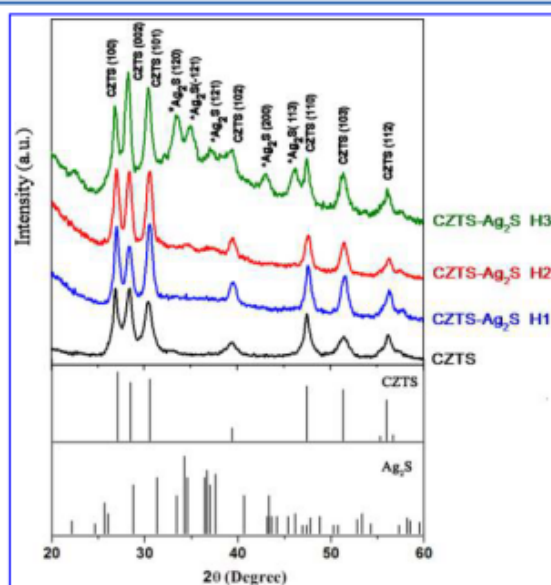


Figure 2. XRD patterns of CZTS nanocrystals and CZTS– Ag_2S nanoheterostructures obtained with the increasing amount of AgNO_3 added (H1, 0.4 mmol; H2, 0.8 mmol; H3, 1.2 mmol).

crystallographic structure.³⁹ As increasing amounts of Ag^+ were added, monoclinic Ag_2S (JCPDS card no. 14-0072) was formed, as it can be observed by the higher intensities of the peaks associated with Ag_2S crystallographic phase. Energy-dispersive X-ray spectroscopy (EDX) analysis (Table S1) verified the increasing ratio of $[\text{Ag}]/[\text{Cu} + \text{Zn} + \text{Sn}]$ when increasing the amount of Ag^+ ions introduced. Further confirmation of the element oxidation states was obtained by XPS. Besides the existence of Cu, Zn, Sn, and S, the XPS spectrum for both sample H1 and H3 (Figure S1) also showed the components at 368.0 and 374.0 eV, which were attributed to $\text{Ag } 3d_{5/2}$ and $\text{Ag } 3d_{3/2}$, respectively, of Ag^+ ions in the Ag_2S phase.

Based on these results, we believe Cu, Zn, and Sn atoms in CZTS behave virtually like a “fluid”, which diffuses toward the solid–liquid interface through the anion sublattice and is replaced by Ag^+ , with a slight preferential exchange of Zn^{2+} ions by Ag^+ . The exchange is in part driven by the extremely small

solubility constant of Ag^+ , $K_{sp} = 1.0 \times 10^{-49}$ at 18 °C.⁴⁰ CZTS– Ag_2S nanoparticles formed did not conserve the quasi-spherical geometry, but became slightly elongated (Figure S2). This slight shape modification is explained by the different crystallographic structures of the initial CZTS nanoparticles and the growing Ag_2S nanocrystals, what does not allow conservation of the anion sublattice during the cation exchange process.

As a final evidence of the cation exchange mechanism, CZTS nanoparticles were reacted with an excess of Ag^+ ions. As a result, a full exchange of Cu, Zn and Sn ions within CZTS by Ag^+ ions took place and Ag_2S nanoparticles were obtained (Figures S3 and S4). Final Ag_2S nanoparticles were mostly polycrystalline, indicating the presence of multiple Ag_2S nucleation points within each CZTS. Furthermore, Ag_2S nanoparticles did not conserve the very narrow size distribution of the initial CZTS nanoparticles, which indicates a coalescence or Ostwald ripening of the final Ag_2S nanoparticles (Figure S4). At the same time, the excess amount of Ag^+ most probably was reduced by OLA in the reaction conditions used, forming a broad size distribution of metal Ag nanoparticles (Figure S3).

HRTEM analysis confirmed the crystallographic phases, wurtzite and monoclinic, of both compounds within the CZTS– Ag_2S nanoheterostructure although some orthorhombic Ag_2S crystals were also identified (Figure S5). HRTEM analysis also allowed determining the structural relationship at the interface. Figure 3 shows HRTEM, fast Fourier transform

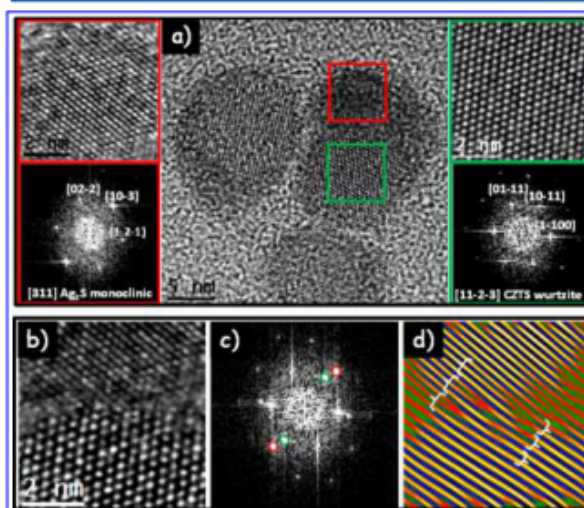


Figure 3. (a) HRTEM micrograph of CZTS– Ag_2S heterostructures. The closer look of the HRTEM image of CZTS and Ag_2S areas and its corresponding power spectrum analysis are shown in the left (Ag_2S , red) and right (CZTS, green) panels, respectively. (b) HRTEM image of the interface between CZTS and Ag_2S within a single CZTS– Ag_2S nanoparticle. (c) Corresponding power spectrum and (d) inverse FFT of the circled diffraction spots showing the epitaxial relation.

(FFT), and simulated HRTEM images of CZTS– Ag_2S heterostructures. In Figure 3a, details of each crystal structure (CZTS in green and Ag_2S in red) are shown along with their corresponding power spectra (FFTs). The Ag_2S crystal is visualized along the [311] axis of its monoclinic phase, with lattice parameters $a = 0.4127$ nm, $b = 0.6699$ nm, $c = 0.7838$ nm (space group = $P21/c$), $\alpha = \gamma = 90^\circ$, and $\beta = 99.67^\circ$. Power spectrum of the CZTS crystal unambiguously revealed that it

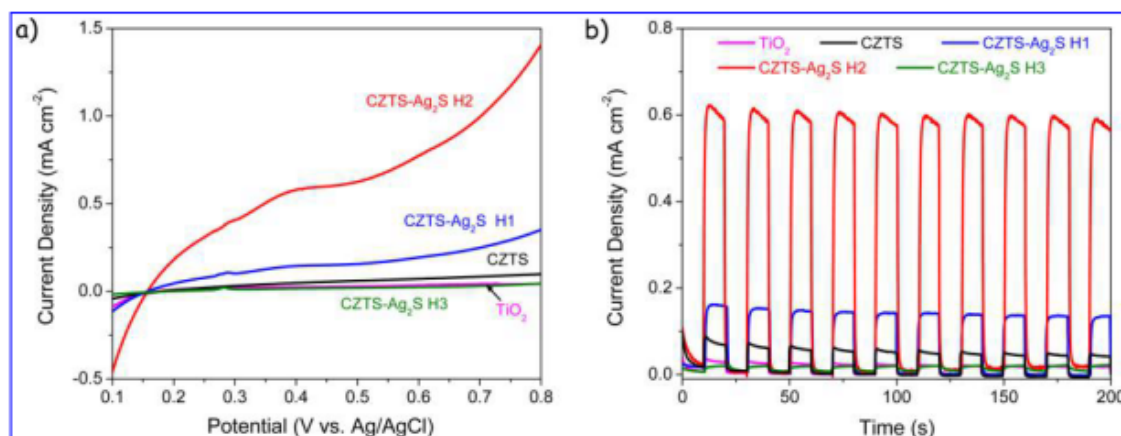


Figure 4. (a) Linear sweep voltammograms curves under visible light illumination for PECs. (b) Corresponding amperometric $I-t$ curves under switching light ON–OFF at the applied potential of 0.5 V.

had a wurtzite phase visualized along its $[11-2-3]$ axis and with lattice parameters of $a = b = 0.3839$ nm, and $c = 0.6339$ nm (space group = $P63mc$). Figure 3b shows a close-up HRTEM micrograph of the CZTS–Ag₂S interface. Its corresponding FFT power spectrum reveals a possible epitaxial relationship with a certain misorientation and lattice mismatch. In Figure 3c, green circled diffraction spots belong to the (10–11) plane of the wurtzite CZTS phase which has a d -spacing value of 0.2944 nm, and red circled diffraction spots belong to the (10–3) plane of monoclinic Ag₂S phase that has a d -spacing value of 0.2363 nm. For clarity, Figure 3d shows the inverse FFT of selected diffraction spots. Although they are slightly misoriented and the lattice mismatch between them is about 20%, the inverse FFT image shows an epitaxial relationship where there are three Ag₂S planes for every 2 CZTS plane (marked with white parentheses in the image, showing the expected misfit dislocations). Similar epitaxial relations were observed on CZTS–Au nanoheterostructures by Pradhan's group.⁴¹

As a proof-of-concept application, CZTS–Ag₂S nanoparticles were used as sensitizers in a photoelectrochemical (PEC) cell for water splitting. Within the PEC cell, electron–hole pairs are generated under visible light illumination. Photogenerated holes are used to oxidize H₂O and produce O₂ and the photogenerated electrons are driven toward the Pt electrode to produce hydrogen. As shown in Figure 4a, the photocurrent of TiO₂/CZTS–Ag₂S nanoheterostructures (H1) at 0.5 V is 0.15 mA/cm², what is much higher than that of the electrode made from pure TiO₂ (0.03 mA/cm²) or that of the one incorporating CZTS nanocrystals (TiO₂/CZTS, 0.06 mA/cm²). These values indicate that the CZTS–Ag₂S heterostructure promotes photocatalytic activity under visible light illumination. This result was further supported by the corresponding amperometric $I-t$ cycles. Figure 4b shows the rapid and consistent photocurrent responses for each switch-on and -off event in multiple 10 s on–off cycles under visible-light illumination. The sample H2 showed the highest photocurrent density (ca. 0.58 mA/cm²), which was about 10 times higher than that of the pure CZTS electrode (ca. 0.06 mA/cm²). However, the photocurrent decreased when further increasing the amount of Ag₂S (sample H3). This indicates that an optimal compositional ratio of the two phases exist that

provides the highest photocatalytic activity as will be discussed below.

The main key parameters determining the PEC activity are charge carriers photogeneration, separation, and transport efficiency.⁴² To be able to account for the performance enhancement, light absorption and charge separation and transfer properties of the CZTS–Ag₂S (H2) heterostructures were studied. As shown in Figure S6, just a slight extension of the absorbance edge toward the infrared was observed after coupling CZTS (1.5 eV) with Ag₂S. This observation agrees well with the fact that 4 nm Ag₂S nanocrystals do not exhibit quantum confinement effects and thus possess a bulk-like band gap (~ 1.0 eV).⁴³ To better understand the electronic properties of CZTS–Ag₂S heterostructures, Mott–Schottky (M–S) measurements were performed in dark using impedance spectroscopy. Figure S7 shows M–S plots of TiO₂ and CZTS–Ag₂S (H2) sensitized TiO₂. The flat band potential for TiO₂, calculated from the x intercept of the linear region, was found to be -0.8 V vs Ag/AgCl. Just a slight positive shift of potential was found for the TiO₂–CZTS–Ag₂S sample. This sample was also characterized by a lower slope of the linear region, which suggested a much higher donor density. The energy band structures of TiO₂, Ag₂S, and CZTS are plotted in Figure 5a. The Fermi level in n-type TiO₂ and Ag₂S are close to their conduction band minimum (CBM), while that of p-type CZTS are close to its valence band maximum (VBM). As the CBM and VBM of p-type CZTS are situated at higher energy levels than Ag₂S,⁴⁴ under visible-light irradiation, photogenerated electrons in the CB of CZTS will transfer to the CB of Ag₂S, while holes travel in the opposite direction within the VB, as shown in Figure 5a. This type-II band alignment in the CZTS–Ag₂S nanoscale p–n heterostructure increases the driving force for photogenerated charge carrier separation, thus reducing the chance for their recombination, increasing their lifetime and enhancing the overall material photocatalytic performance.⁴⁵ Besides, the relatively low CBM of Ag₂S still facilitates the electron transfer to the CB of TiO₂. In a third step, as shown in Figure 5b, the efficiently separated electrons are collected on the surface of electrodes and injected into the external circuit, which are subsequently consumed in the reduction of water into hydrogen,⁴⁶ while holes participate in the oxidation reaction taking place at the CZTS surface.

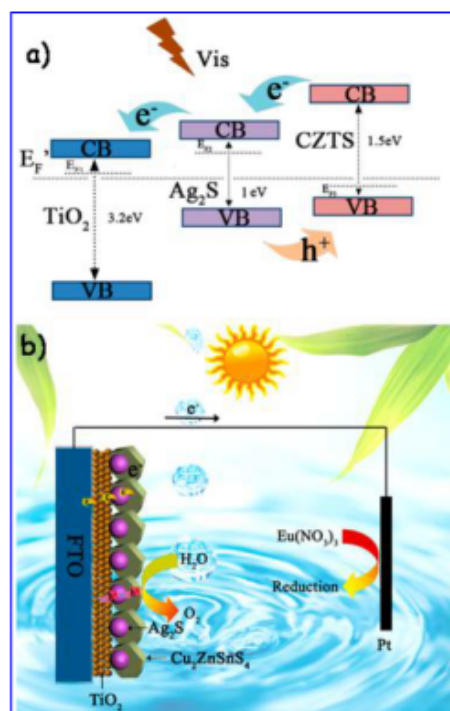


Figure 5. (a) Schematic of the energy band diagram of the heterostructures and the possible model of electron transfer. (b) Schematic diagram of water splitting reaction in the photoelectrochemical cell.

While the combination of CZTS and Ag_2S clearly results in an enhancement of the photocatalytic properties, it is also clear that an optimum composition exist. One possible explanation for the composition-dependent PEC activities measured might be ascribed to the structural change of CZTS in the presence of different concentration of Ag^+ . Along with the increase of Ag^+ concentration, the molar ratio of $\text{Zn}/(\text{Cu} + \text{Sn})$ decreases from 0.32 to 0.17. As previously reported, the content of Zn can affect the CBM of the particles. In this direction, usually Zn-rich CZTS nanocrystals exhibit better photovoltaic conversion efficiency.^{47,48} For CZTS– Ag_2S nanoheterostructures, a narrowing of the CZTS band gap from 1.5 to 1.37 eV was observed when increasing the Ag^+ concentration (Figure S8), which may make the transfer of electrons from CZTS to Ag_2S difficult. A second explanation for the PEC activity decrease with the increase of Ag^+ is related to the loss of effective donors for the oxidation reaction. The decreased amount of CZTS with good hole transport ability results in a lower donor density. Furthermore, excessive Ag_2S in the heterostructures surface might reduce the CZTS reactive sites for the oxidation reaction, thus deteriorating the hole extraction from CZTS. This is consistent with the fact that, for type-II nanoparticles, the use of linear heterostructures is more favorable than the use of core–shells to extract charge from both semiconductor phases.

CONCLUSIONS

In summary, a series of CZTS– Ag_2S nanoscale p–n heterostructures with different CZTS/ Ag_2S ratios was obtained by partial cation exchange. From HRTEM characterization, we conclude that the heterojunction has coincident site epitaxy.

Such CZTS– Ag_2S nanoheterostructures exhibited significantly enhanced photoelectrochemical current response under visible-light illumination compared to pure CZTS. The ability to synthesize such structures with controlled composition and suitable band alignment promoting charge separation provides a better insight into fundamental synthetic chemistry as well as opening avenues for diverse optoelectronic applications.

ASSOCIATED CONTENT

Supporting Information

The Supporting Information is available free of charge on the ACS Publications website at DOI: 10.1021/acs.langmuir.5b02490.

Atomic compositions of CZTS AND CZTS– Ag_2S structures, XPS spectra, HRTEM and TEM micrographs, XRD patterns, UV–vis absorbance spectra, Mott–Schottky plots, and linear extrapolation plots (PDF)

AUTHOR INFORMATION

Corresponding Authors

*E-mail: acabot@irec.cat.

*E-mail: zyh@cugb.edu.cn.

Notes

The authors declare no competing financial interest.

ACKNOWLEDGMENTS

This work was supported by the European Regional Development Funds, the Framework 7 program under project SCALENANO (FP7-NMP-ENERGY-2011-284486), the Spanish MINECO under Contract ENE2013-46624-C4-3-R and Fundamental Research Funds for the Central Universities (2652015086). Authors acknowledge the funding from Generalitat de Catalunya 2014 SGR 1638.

REFERENCES

- (1) Zhang, H.; Jang, J.; Liu, W.; Talapin, D. V. Colloidal Nanocrystals with Inorganic Halide, Pseudohalide, and Halometallate Ligands. *ACS Nano* **2014**, *8*, 7359–7369.
- (2) Zhang, L.; Xia, Y. Scaling up the Production of Colloidal Nanocrystals: Should We Increase or Decrease the Reaction Volume? *Adv. Mater.* **2014**, *26*, 2600–2606.
- (3) Park, J.; An, K.; Hwang, Y.; Park, J.-G.; Noh, H.-J.; Kim, J.-Y.; Park, J.-H.; Hwang, N.-M.; Hyeon, T. Ultra-Large-Scale Syntheses of Monodisperse Nanocrystals. *Nat. Mater.* **2004**, *3*, 891–895.
- (4) Kovalenko, M. V.; Manna, L.; Cabot, A.; Hens, Z.; Talapin, D. V.; Kagan, C. R.; Klimov, V. I.; Rogach, A. L.; Reiss, P.; Milliron, D. J.; et al. Prospects of Nanoscience with Nanocrystals. *ACS Nano* **2015**, *9*, 1012–1057.
- (5) Reiss, P.; Bleuse, J.; Pron, A. Highly Luminescent CdSe/ZnSe Core/Shell Nanocrystals of Low Size Dispersion. *Nano Lett.* **2002**, *2*, 781–784.
- (6) Li, L.; Daou, T. J.; Texier, I.; Kim Chi, T. T.; Liem, N. Q.; Reiss, P. Highly Luminescent CuInS₂/ZnS Core/Shell Nanocrystals: Cadmium-Free Quantum Dots for in Vivo Imaging. *Chem. Mater.* **2009**, *21*, 2422–2429.
- (7) Lee, J.-S.; Bodnarchuk, M. I.; Shevchenko, E. V.; Talapin, D. V. Magnet-in-the-Semiconductor" FePt–PbS and FePt–Pbse Nanostructures: Magnetic Properties, Charge Transport, and Magnetoresistance. *J. Am. Chem. Soc.* **2010**, *132*, 6382–6391.
- (8) Zhao, Q.; Ji, M.; Qian, H.; Dai, B.; Weng, L.; Gui, J.; Zhang, J.; Ouyang, M.; Zhu, H. Controlling Structural Symmetry of a Hybrid Nanostructure and Its Effect on Efficient Photocatalytic Hydrogen Evolution. *Adv. Mater.* **2014**, *26*, 1387–1392.

- (9) Chen, J.; Wu, X.; Yin, L.; Li, B.; Hong, X.; Fan, Z.; Chen, B.; Xue, C.; Zhang, H. One-pot Synthesis of CdS Nanocrystals Hybridized with Single-Layer Transition-Metal Dichalcogenide Nanosheets for Efficient Photocatalytic Hydrogen Evolution. *Angew. Chem., Int. Ed.* **2015**, *54*, 1210–1214.
- (10) Zhou, W.; Yin, Z.; Du, Y.; Huang, X.; Zeng, Z.; Fan, Z.; Liu, H.; Wang, J.; Zhang, H. Synthesis of Few-Layer MoS₂ Nanosheet-Coated TiO₂ Nanobelt Heterostructures for Enhanced Photocatalytic Activities. *Small* **2013**, *9*, 140–147.
- (11) Ibáñez, M.; Zamani, R.; Gorse, S.; Fan, J.; Ortega, S.; Cadavid, D.; Morante, J. R.; Arbiol, J.; Cabot, A. Core-Shell Nanoparticles as Building Blocks for the Bottom-up Production of Functional Nanocomposites: PbTe–PbS Thermoelectric Properties. *ACS Nano* **2013**, *7*, 2573–2586.
- (12) Meng, F.; Li, J.; Cushing, S. K.; Zhi, M.; Wu, N. Solar Hydrogen Generation by Nanoscale P–N Junction of P-Type Molybdenum Disulfide/N-Type Nitrogen-Doped Reduced Graphene Oxide. *J. Am. Chem. Soc.* **2013**, *135*, 10286–10289.
- (13) Kumar, S.; Jones, M.; Lo, S. S.; Scholes, G. D. Nanorod Heterostructures Showing Photoinduced Charge Separation. *Small* **2007**, *3*, 1633–1639.
- (14) Steiner, D.; Dorfs, D.; Banin, U.; Della Sala, F.; Manna, L.; Millo, O. Determination of Band Offsets in Heterostructured Colloidal Nanorods Using Scanning Tunneling Spectroscopy. *Nano Lett.* **2008**, *8*, 2954–2958.
- (15) Rivest, J. B.; Swisher, S. L.; Fong, L.-K.; Zheng, H.; Alivisatos, A. P. Assembled Monolayer Nanorod Heterojunctions. *ACS Nano* **2011**, *5*, 3811–3816.
- (16) Teranishi, T.; Sakamoto, M. Charge Separation in Type-II Semiconductor Heterodimers. *J. Phys. Chem. Lett.* **2013**, *4*, 2867–2873.
- (17) Rivest, J. B.; Jain, P. K. Cation Exchange on the Nanoscale: An Emerging Technique for New Material Synthesis, Device Fabrication, and Chemical Sensing. *Chem. Soc. Rev.* **2013**, *42*, 89–96.
- (18) Son, D. H.; Hughes, S. M.; Yin, Y.; Alivisatos, A. P. Cation Exchange Reactions in Ionic Nanocrystals. *Science* **2004**, *306*, 1009–1012.
- (19) De Trizio, L.; Li, H.; Casu, A.; Genovese, A.; Sathya, A.; Messina, G. C.; Manna, L. Sn Cation Valency Dependence in Cation Exchange Reactions Involving Cu₂xSe Nanocrystals. *J. Am. Chem. Soc.* **2014**, *136*, 16277–16284.
- (20) Bera, A.; Dey, S.; Pal, A. J. Band Mapping across a PN-Junction in a Nanorod by Scanning Tunneling Microscopy. *Nano Lett.* **2014**, *14*, 2000–2005.
- (21) Wu, X. J.; Huang, X.; Qi, X.; Li, H.; Li, B.; Zhang, H. Copper-Based Ternary and Quaternary Semiconductor Nanoplates: Templated Synthesis, Characterization, and Photoelectrochemical Properties. *Angew. Chem.* **2014**, *126*, 9075–9079.
- (22) De Trizio, L.; Gaspari, R.; Bertoni, G.; Kriegel, I.; Moretti, L.; Scotognella, F.; Maserati, L.; Zhang, Y.; Messina, G. C.; Prato, M.; et al. Cu₃xP Nanocrystals as a Material Platform for near-Infrared Plasmonics and Cation Exchange Reactions. *Chem. Mater.* **2015**, *27*, 1120–1128.
- (23) Lesnyak, V.; George, C.; Genovese, A.; Prato, M.; Casu, A.; Ayyappan, S.; Scarpellini, A.; Manna, L. Alloyed Copper Chalcogenide Nanoplatelets Via Partial Cation Exchange Reactions. *ACS Nano* **2014**, *8*, 8407–8418.
- (24) Park, Y.; McDonald, K. J.; Choi, K.-S. Progress in Bismuth Vanadate Photoanodes for Use in Solar Water Oxidation. *Chem. Soc. Rev.* **2013**, *42*, 2321–2337.
- (25) Ha, E.; Lee, L. Y. S.; Wang, J.; Li, F.; Wong, K. Y.; Tsang, S. C. E. Significant Enhancement in Photocatalytic Reduction of Water to Hydrogen by Au/Cu₂ZnSnS₄ Nanostructure. *Adv. Mater.* **2014**, *26*, 3496–3500.
- (26) Yu, X.; Shavel, A.; An, X.; Luo, Z.; Ibáñez, M.; Cabot, A. Cu₂ZnSnS₄-Pt and Cu₂ZnSnS₄-Au Heterostructured Nanoparticles for Photocatalytic Water Splitting and Pollutant Degradation. *J. Am. Chem. Soc.* **2014**, *136*, 9236–9239.
- (27) Moriya, M.; Minegishi, T.; Kumagai, H.; Katayama, M.; Kubota, J.; Domen, K. Stable Hydrogen Evolution from CdS-Modified CuGaSe₂ Photoelectrode under Visible-Light Irradiation. *J. Am. Chem. Soc.* **2013**, *135*, 3733–3735.
- (28) Dilsaver, P. S.; Reichert, M. D.; Hallmark, B. L.; Thompson, M. J.; Vela, J. Cu₂ZnSnS₄-Au Heterostructures: Toward Greener Chalcogenide Based Photocatalysts. *J. Phys. Chem. C* **2014**, *118*, 21226–21234.
- (29) Kush, P.; Deori, K.; Kumar, A.; Deka, S. Efficient Hydrogen/Oxygen Evolution and Photocatalytic Dye Degradation and Reduction of Aqueous Cr(VI) by Surfactant Free Hydrophilic Cu₂ZnSnS₄ Nanoparticles. *J. Mater. Chem. A* **2015**, *3*, 8098–8106.
- (30) Shavel, A.; Cadavid, D.; Ibáñez, M.; Carrete, A.; Cabot, A. Continuous Production of Cu₂ZnSnS₄ Nanocrystals in a Flow Reactor. *J. Am. Chem. Soc.* **2012**, *134*, 1438–1441.
- (31) Singh, A.; Geaney, H.; Laffir, F.; Ryan, K. M. Colloidal Synthesis of Wurtzite Cu₂ZnSnS₄ Nanorods and Their Perpendicular Assembly. *J. Am. Chem. Soc.* **2012**, *134*, 2910–2913.
- (32) Singh, A.; Singh, S.; Levchenko, S.; Unold, T.; Laffir, F.; Ryan, K. M. Compositionally Tunable Photoluminescence Emission in Cu₂ZnSn(S_{1-x}Se_x)₄ Nanocrystals. *Angew. Chem., Int. Ed.* **2013**, *52*, 9120–9124.
- (33) Ibáñez, M.; Zamani, R.; Li, W.; Shavel, A.; Arbiol, J.; Morante, J. R.; Cabot, A. Extending the Nanocrystal Synthesis Control to Quaternary Compositions. *Cryst. Growth Des.* **2012**, *12*, 1085–1090.
- (34) Ibáñez, M.; Zamani, R.; Li, W.; Cadavid, D.; Gorse, S.; Katcho, N. A.; Shavel, A.; López, A. M.; Morante, J. R.; Arbiol, J.; Cabot, A. Crystallographic Control at the Nanoscale to Enhance Functionality: Polytropic Cu₂GeSe₃ Nanoparticles as Thermoelectric Materials. *Chem. Mater.* **2012**, *24*, 4615–4622.
- (35) Ibáñez, M.; Cadavid, D.; Zamani, R.; García-Castelló, N.; Izquierdo-Roca, V.; Li, W.; Fairbrother, A.; Prades, J. D.; Shavel, A.; Arbiol, J.; et al. Composition Control and Thermoelectric Properties of Quaternary Chalcogenide Nanocrystals: The Case of Stannite Cu₂CdSnSe₄. *Chem. Mater.* **2012**, *24*, 562–570.
- (36) Ibáñez, M.; Zamani, R.; LaLonde, A.; Cadavid, D.; Li, W.; Shavel, A.; Arbiol, J.; Morante, J. R.; Gorse, S.; Snyder, G. J.; Cabot, A. Cu₂ZnGeSe₄ Nanocrystals: Synthesis and Thermoelectric Properties. *J. Am. Chem. Soc.* **2012**, *134*, 4060–4063.
- (37) Sadtler, B.; Demchenko, D. O.; Zheng, H. M.; Hughes, S. M.; Merkle, M. G.; Dahmen, U.; Wang, Z. L.; Alivisatos, A. P. Selective Facet Reactivity during Cation Exchange in Cadmium Sulfide Nanorods. *J. Am. Chem. Soc.* **2009**, *131*, 5285–5293.
- (38) Gupta, S.; Kershaw, S. V.; Rogach, A. L. 25th Anniversary Article: Ion Exchange in Colloidal Nanocrystals. *Adv. Mater.* **2013**, *25*, 6923–6944.
- (39) Lu, X.; Zhuang, Z.; Peng, Q.; Li, Y. Wurtzite Cu₂ZnSnS₄ Nanocrystals: A Novel Quaternary Semiconductor. *Chem. Commun.* **2011**, *47*, 3141–3143.
- (40) Pang, M.; Hu, J.; Zeng, H. C. Synthesis, Morphological Control, and Antibacterial Properties of Hollow/Solid Ag₂S/Ag Heterodimers. *J. Am. Chem. Soc.* **2010**, *132*, 10771–10785.
- (41) Patra, B. K.; Shit, A.; Guria, A. K.; Sarkar, S.; Prusty, G.; Pradhan, N. Coincident Site Epitaxy at the Junction of Au–Cu₂ZnSnS₄ Heteronanostructures. *Chem. Mater.* **2015**, *27*, 650–657.
- (42) Liu, J.; Yu, X.; Liu, Q.; Liu, R.; Shang, X.; Zhang, S.; Li, W.; Zheng, W.; Zhang, G.; Cao, H.; Gu, Z. Surface-Phase Junctions of Branched TiO₂ Nanorod Arrays for Efficient Photoelectrochemical Water Splitting. *Appl. Catal., B* **2014**, *158*, 296–300.
- (43) Huxter, V. M.; Mirkovic, T.; Nair, P. S.; Scholes, G. D. Demonstration of Bulk Semiconductor Optical Properties in Processable Ag₂S and Eus Nanocrystalline Systems. *Adv. Mater.* **2008**, *20*, 2439–2443.
- (44) Yang, X.; Xue, H.; Xu, J.; Huang, X.; Zhang, J.; Tang, Y.-B.; Ng, T.-W.; Kwong, H.-L.; Meng, X.-M.; Lee, C.-S. Synthesis of Porous ZnS: Ag₂S Nanosheets by Ion Exchange for Photocatalytic H₂ Generation. *ACS Appl. Mater. Interfaces* **2014**, *6*, 9078–9084.
- (45) Gao, X.; Wu, H. B.; Zheng, L.; Zhong, Y.; Hu, Y.; Lou, X. W. D. Formation of Mesoporous Heterostructured BiVO₄/Bi₂S₃ Hollow

Discoids with Enhanced Photoactivity. *Angew. Chem.* **2014**, *126*, 6027–6031.

(46) Shen, H.; Jiao, X.; Oron, D.; Li, J.; Lin, H. Efficient Electron Injection in Non-Toxic Silver Sulfide (Ag_2S) Sensitized Solar Cells. *J. Power Sources* **2013**, *240*, 8–13.

(47) Riha, S. C.; Fredrick, S. J.; Sambur, J. B.; Liu, Y.; Prieto, A. L.; Parkinson, B. Photoelectrochemical Characterization of Nanocrystalline Thin-Film $\text{Cu}_2\text{ZnSnS}_4$ Photocathodes. *ACS Appl. Mater. Interfaces* **2011**, *3*, 58–66.

(48) Wang, Y.-X.; Wei, M.; Fan, F.-J.; Zhuang, T.-T.; Wu, L.; Yu, S.-H.; Zhu, C.-F. Phase-Selective Synthesis of $\text{Cu}_2\text{ZnSnS}_4$ Nanocrystals through Cation Exchange for Photovoltaic Devices. *Chem. Mater.* **2014**, *26*, 5492–5498.

Cu₂ZnSnS₄-Ag₂S Nanoscale p-n Heterostructures as Sensitizers for Photoelectrochemical Water Splitting

Supporting Information

Xuelian Yu,^{a,b} Jingjing Liu,^c Aziz Genç,^d Maria Ibáñez,^b Zhishan Luo,^b Alexey Shavel,^b Jordi Arbiol,^d

^eGuangjin Zhang,^c Yihe Zhang^{*a} and Andreu Cabot^{*b,e}

a. Beijing Key Laboratory of Materials Utilization of Nonmetallic Minerals and Solid Wastes, National Laboratory of Mineral Materials, School of Materials Science and Technology, China University of Geosciences, 100083, Beijing, P. R. China

b. Catalonia Energy Research Institute - IREC, 08930, Sant Adria del Besos, Barcelona, Spain

c. Key Laboratory of Green Process and Engineering, Chinese Academy of Sciences, 100190, Beijing, P. R. China

d. Institut Català de Nanociència i Nanotecnologia, ICN2, Campus de la UAB, 08193 Bellaterra, Spain

e. Institució Catalana de Recerca i Estudis Avançats - ICREA, 08010, Barcelona, Spain

Table S1. CZTS and CZTS-Ag₂S atomic composition obtained from EDX analysis.

	Cu (%)	Zn (%)	Sn (%)	S (%)	Ag (%)	Zn/(Cu+Sn)
CZTS	22	11	12	55	0	0.32
CZTS-Ag ₂ S (Sample H1)	22	8	12	53	5	0.23
CZTS-Ag ₂ S (Sample H2)	17	5	9	57	12	0.19
CZTS-Ag ₂ S (Sample H3)	16	4	7	50	23	0.17

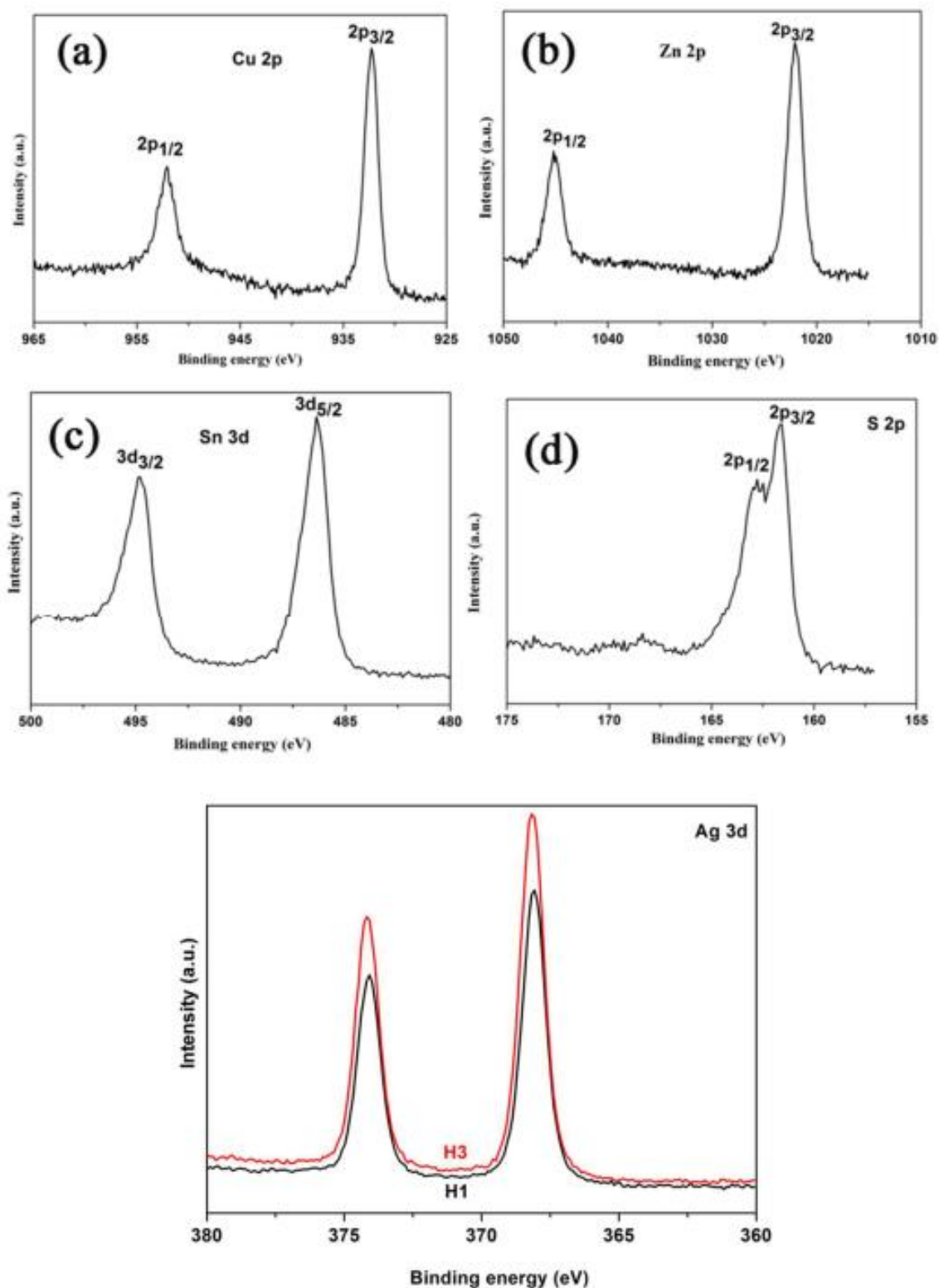


Figure S1. XPS spectra of CZTS-Ag₂S nano-heterostructures.

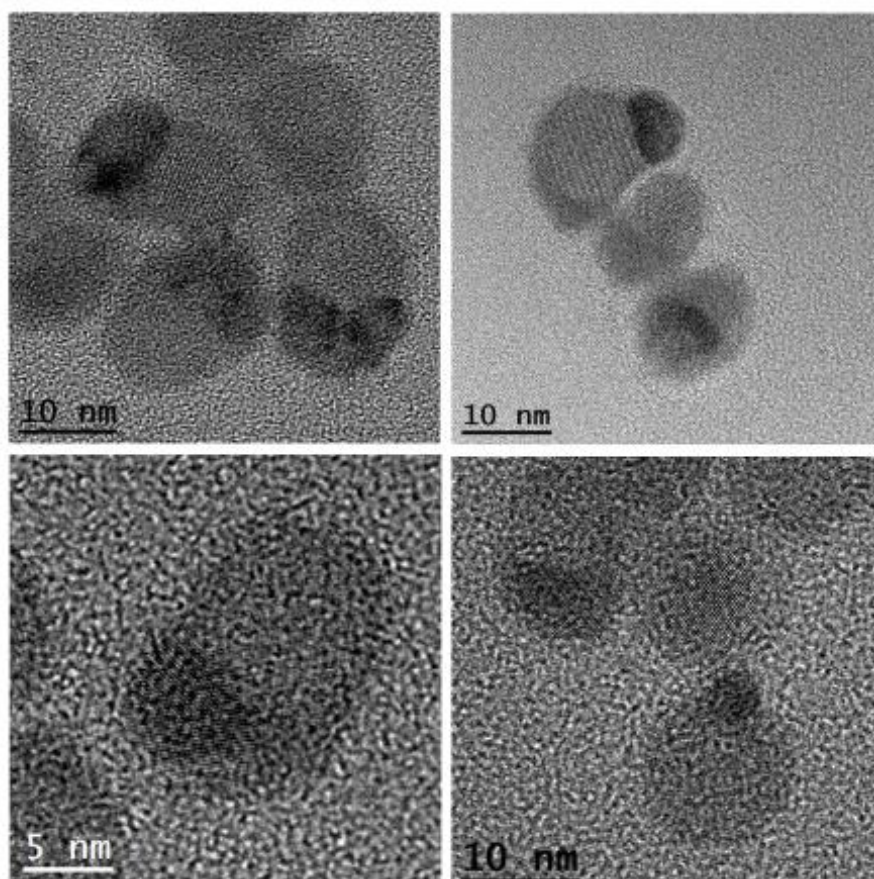


Figure S2. Selection of HRTEM micrographs showing some single crystalline and polycrystalline Ag₂S NPs attached to CZTS NPs. They all seem to have the epitaxial relation.

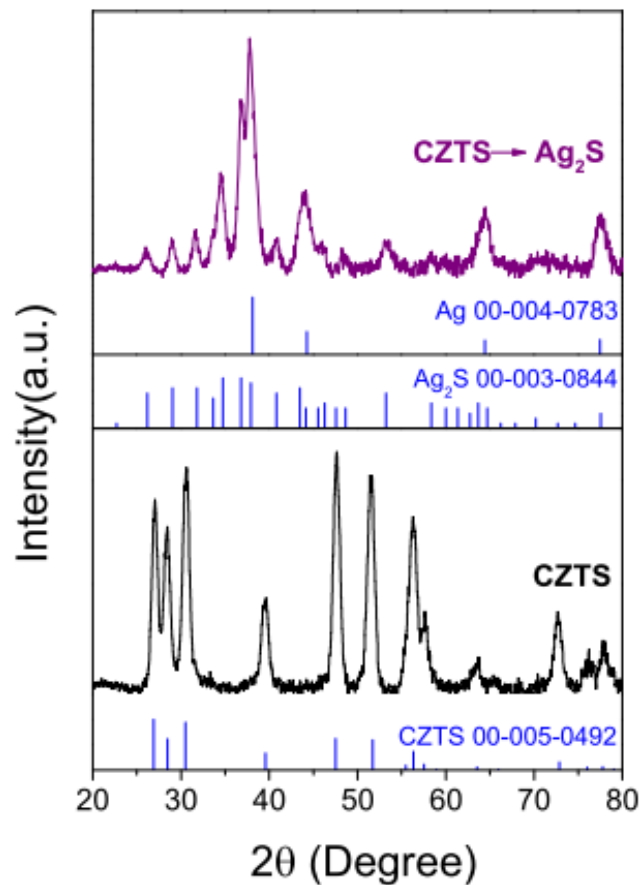


Figure S3. XRD patterns of CZTS nanoparticles and CZTS-Ag₂S nanoparticles obtained with an excess amount of Ag⁺. Only the XRD peaks corresponding to the Ag₂S and most probably also metal Ag crystal structures were obtained after the full cation exchange reaction. Reference patterns of wurtzite CZTS (JCPDS: 00-005-0492), Ag₂S (JCPDS: 00-003-0844) and Ag (JCPDS: 00-004-0783) are also shown as reference.

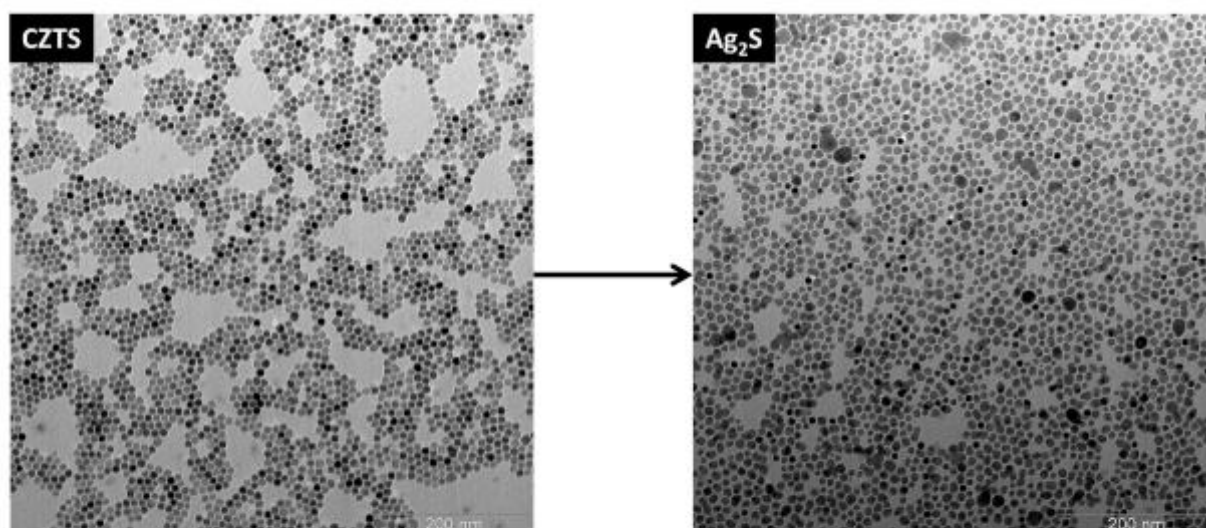


Figure S4. TEM micrographs of CZTS nanoparticles before (left) and after (right) full cation exchange with Ag^+ ions.

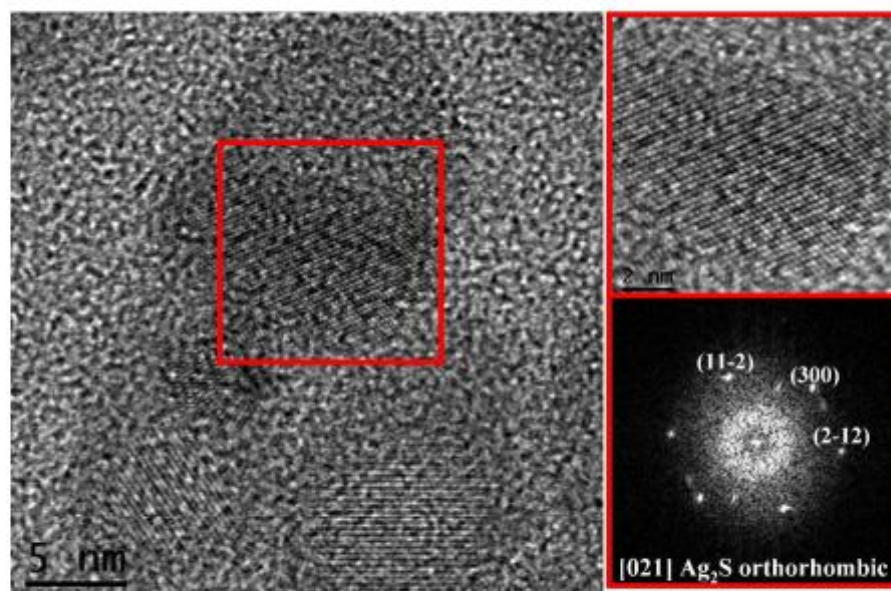


Figure S5. HRTEM micrograph showing the presence of several NPs, detail of the single crystalline NP indicated with red square and its corresponding power spectrum.

We identified another phase of Ag_2S , which has a primitive orthorhombic lattice (space group = $P2_12_12_1$) with lattice parameters of $a = 0.6725$ nm, $b = 0.4148$ nm and $c = 0.7294$ nm. The abundance of this phase is about the same with the above presented monoclinic Ag_2S phase. A HRTEM micrograph showing the presence of a single crystalline Ag_2S attachment is presented in Fig. S5. On the right, detail of the red squared region and its corresponding power spectrum, which reveals that this NP has the orthorhombic Ag_2S phase and visualized along its [021] axis, are shown.

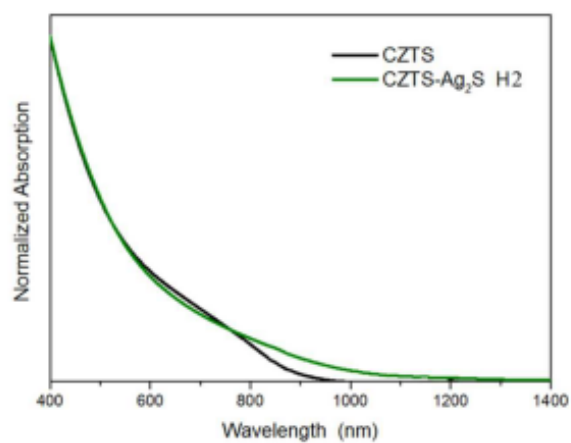


Figure S6. UV-vis absorbance spectra of CZTS nanocrystals and CZTS-Ag₂S nanoheterostructures (Sample H2).

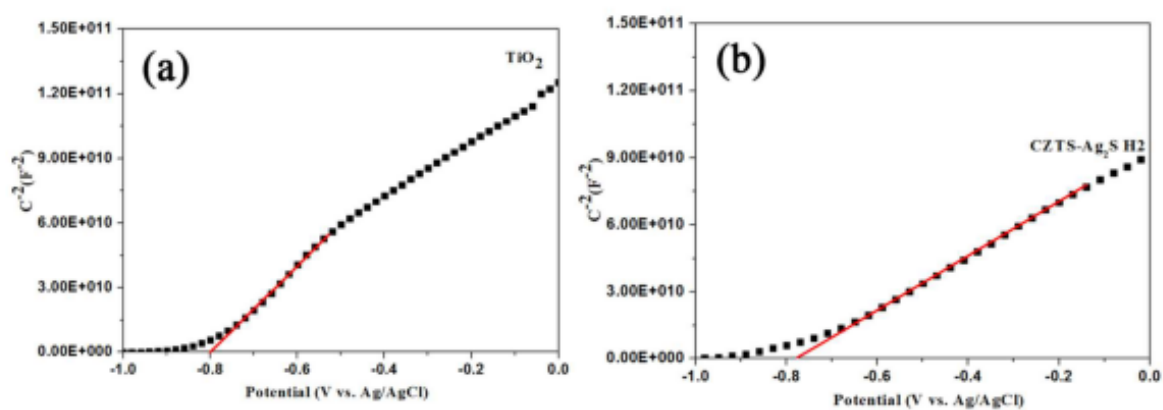


Figure S7. (a) Mott-Schottky plot of TiO₂; (b) Mott-Schottky plot of CZTS-Ag₂S-sensitized TiO₂.

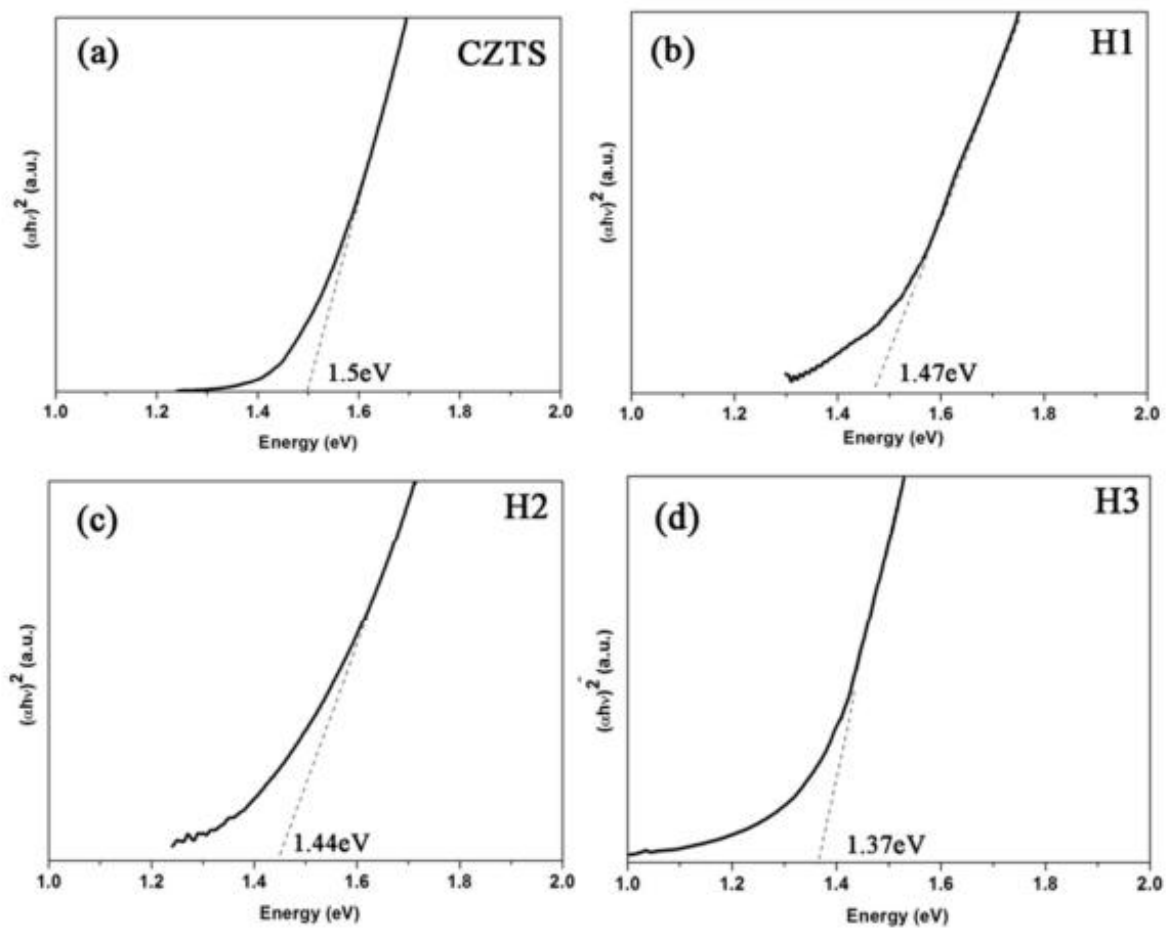


Figure S8. The linear extrapolations of plots of $(\alpha h\nu)^2$ vs. photon energy for CZTS (a), CZTS-Ag₂S H1 (b), CZTS-Ag₂S H2 (c) and CZTS-Ag₂S H3.

Chapter 3

Multimetallic NPs and Their Catalytic Property

3.1 Multimetallic NPs and their catalytic property

This chapter is about multimetallic NPs, including synthesis, structural and catalytic properties. The combination of two or more metals provides novel catalysts for energy conversion application. This chapter is based on the papers: "Size and Aspect Ratio Control of Pd₂Sn Nanorods and Their Water Denitration Properties", "Pd₂Sn Nanorods as Highly Active and Stable Catalyst for Ethanol Oxidation Reaction" and "Pd₂Sn and Au-Pd₂Sn Nanorods in Catalytic Hydrogenation and Sonogashira Coupling Reactions". The first is published in *Langmuir* **2015**, *31* (13), 3952-3957, and the later two part are under revision (we already submitted comments from the second one). In the first paper we report a synthesis of monodisperse Pd₂Sn NRs and their catalytic properties for reduction of nitrophenol and water denitration. The second is a study of Pd₂Sn NRs as electrocatalyst for EOR. In the final part of the chapter we detail the preparation of Pd₂Sn-based HNPs and their potential catalytic applications.

3.1.1 Synthesis of multimetallic NPs

The synthesis of multimetallic NPs is attracting large interest due to their unique physical and chemical properties. In particular, the synergic and co-operative effects of bimetallic NPs could lead to a more useful functionality and can ease the addressability of the particles with extensively studied surface states.⁹⁵⁻⁹⁸ Another merit of bimetallic, such as an alloy, core-shell, or Janus NPs, has been the possibility of lowering cost while maintaining performance through the use of a precious metal in combination with a more abundant, cheaper metal, with the properties of the former still being retained or sometimes even enhanced.^{99,100} Figure 3.1 shows the main four routes to prepare bimetallic NPs: (1) continuous growth, (2) crystallites coalescence, (3) seeded growth and (4) galvanic replacement reaction. There are some key factors for these synthetic routes:¹⁰¹

a) Different redox potentials between the different metals. Different standard reduction potential of metal is the driving force for the galvanic replacement reaction. In our group, we reported that a procedure to produce monodisperse Co@Cu core-shell NPs with control size and composition distributions involving galvanic replacement reaction.¹⁰²

b) Different reduction rate. Different reduction agents can decide reduction rate, further influence the shape and composition of bimetallic NPs. For instance, Au-Pd bimetallic NPs, such as core-shell octahedrons, alloy octahedron, rhombic dodecahedron and nano-dendrite, could be obtained through different reduction rate via controlling reductant.¹⁰³

c) Different capping agent. Facet-specific capping agents are essential for well-defined morphology of bimetallic NPs. Among them, halide ions and PVP are often used in aqueous system. Organic amines and acids (e.g. OLA and OA) are often used in organic solvent systems. In addition, citric acid, NO₂, C₂O₄, CO etc. can serve for special facet bimetallic NPs.¹⁰⁴⁻¹⁰⁶

d) Different interfacial energy. The interfacial energy between two metals plays a main role on the thermodynamic stability of bimetallic core-shell NPs. Two main factors determine the interfacial energy: the lattice mismatch, and the bond between atoms in the overlayer. Xia et al. reported the synthesis of Pd@Cu core-shell nanocubes via Cu epitaxial growth on Pd NCs, where the lattice mismatch is 7.1%. The results may be due to the decrease of the interfacial energy of NPs.¹⁰⁷

e) Temperature and reaction time. The reaction temperature and the time also play crucial roles to control the size and shape evolution of bimetallic NPs. A high temperature implies a high reduction rate during the reaction, which decreased the size of final products. Moreover, the thermodynamic stability of bimetallic NPs can be reached at high temperature easier with spheres or convex polygons structures. The reaction time should be determined to match the decomposition and reduction rates of the precursors. In general, the longer reaction time favors to obtain thermodynamically stable bimetallic NPs.

These factors provide us with the appropriated tools to design rationally well-defined bimetallic NPs with size, shape and composition control. Table 3.1 summarizes some cases of bimetallic NPs prepared by the four routes, including the geometric structure, synthetic route, and key factor in synthetic process.

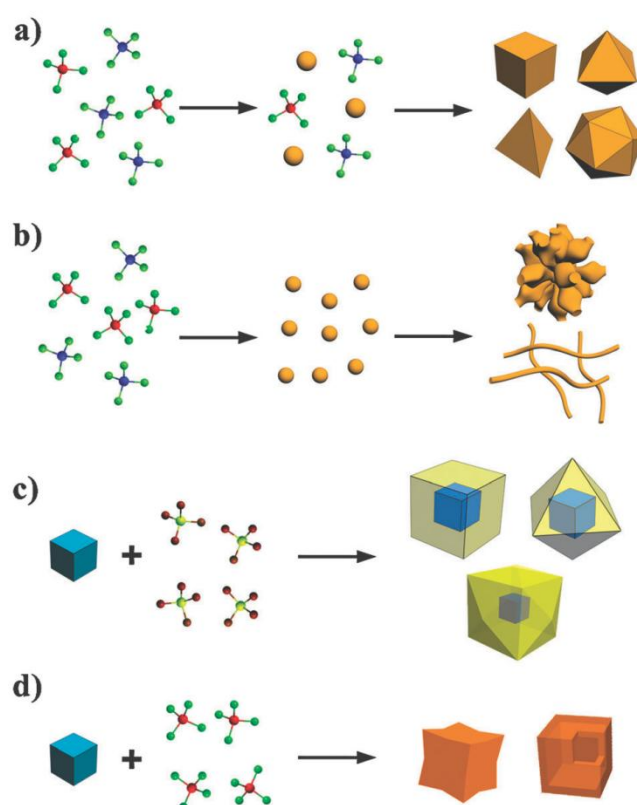


Figure 3.1 Four routes towards shape-controlled bimetallic NCs:¹⁰¹ (a) continuous growth, (b) crystallites coalescence, (c) seeded growth and (d) galvanic replacement reaction. Blue, red and yellow parts stand for mono-metal and orange parts stand for alloy.

Table 3.1 Summary of bimetallic NPs that have been successfully synthesized through routes of continuous growth, crystallites coalescence, seeded growth and galvanic replacement reaction, including alloy, core–shell and heterostructure bimetallic NPs

	nanostructure	Synthetic route	Key factors in the synthetic process	Synthetic cases
Alloy	Shpere	Continuous growth	Capping agents	Pd-Sn ¹⁰⁸
	Cube	Continuous growth	Capping agents	Pt-Ni ¹⁰⁹
	Terahedron	Continuous growth	Capping agents	Pt-Co ¹¹⁰
	Icosahedron	Continuous growth	Slow reduction rate; capping agents	Pt-Pd ¹¹¹
	Rod	Continuous growth	Capping agents	Pd-Sn ¹⁰⁸
	Dendritic structure	Crystallites coalescence	Rapid reduction; polymer-formed templates	Au-Pd ¹¹²
	Wires	Crystallites coalescence	Facet-oriented attachment of crystallites	Au-Ag ¹¹³
	Hollow structure	Galvanic replacement reaction	Kirkendall effect	Pt-Pd ¹¹⁴
Core-shell	Concave stucture	Galvanic replacement reaction	Underpotential deposition followed by galvanic replacement reaction	Pt-Cu ¹¹⁵
	Shpere	Galvanic replacement	Facet-specific galvanic replacement reaction	Co@Cu ¹⁰²

		reaction		
	Cube	Seeded growth	Capping agents	Pd@Pt ¹¹⁶
	Core-dendritic shell	Crystallites coalescence	Rapid reduction; polymer-formed templates	Pd@Rh ¹¹⁷
	Tetrahexahedron	Seeded growth	Large lattice mismatch; oxidative etching	Pd@Au ¹¹⁷
	Concave cube	Seeded growth	Growth rate control on different facets	Pt@Rh ¹¹⁸
heterostructure	Binary structure	Seeded growth	Island growth caused by large lattice mismatch or rapid reduction	Au-Pt ¹¹⁹
	Multi-pod	Galvanic replacement reaction	Facet-specific galvanic replacement reaction	Pd-Pt ¹²⁰

Recently, alloying Pd with a second element like Sn, Co, Cu or Bi is effective for increasing the electrocatalytic activity and CO tolerance through tuning the chemical composition, size and morphology between the two metals.^{108, 121-123} Besides, electronic states and synergy between the different components are playing a vital role to determine the electrocatalyst performance. Among the various Pd-based bimetallic NPs, Pd-Sn is a particularly interesting candidate for some catalytic application. However, the preparation of Pd-Sn NPs is still challenge. Liu X. et al. presented a study about synthesis of Pd-Sn bimetallic single-crystalline hollow nanospheres using a fast one-pot strategy in OLA.¹²⁴ In this system, didodecyldimethyl-ammonium bromide (DDAB) as one kind of surfactants played a key role to create hollow nanostructures (Figure 3.2). Such bimetallic NPs of special hollow structure may be expected to possess particular electronic, mechanical and optical properties. Freakley S. J. et al. reported a simple impregnation method to synthesize palladium-tin catalysts onto supports and then used an

appropriate heat treatment reaction, which enabling selectivity of >95% toward H_2O_2 synthesis directly from H_2 and O_2 .¹²⁵ In addition, they could synthesize a series of Pd-based bimetallic catalysts. All of these catalysts showed activity for H_2O_2 synthesis and no activity for H_2O_2 degradation (Figure 3.3). Du W. et al. presented a study of a series of Pd-Sn binary alloy support carbon catalysts as anode electrocatalysts for the ethanol oxidation reaction in alkaline medium.¹²⁶ Among various Pd-Sn/C catalysts, $\text{Pd}_{86}\text{Sn}_{14}/\text{C}$ showed much enhanced current densities in cyclic voltammetric and chronoamperometric measurements while compared to commercial Pd/C. Furthermore, such $\text{Pd}_{86}\text{Sn}_{14}/\text{C}$ was more favorable in high ethanol concentration and high pH environment. In addition, density functional theory calculations confirmed that Pd-Sn alloy nanostructures have lower reaction energy for the dehydrogenation of ethanol, compared to the Pd.

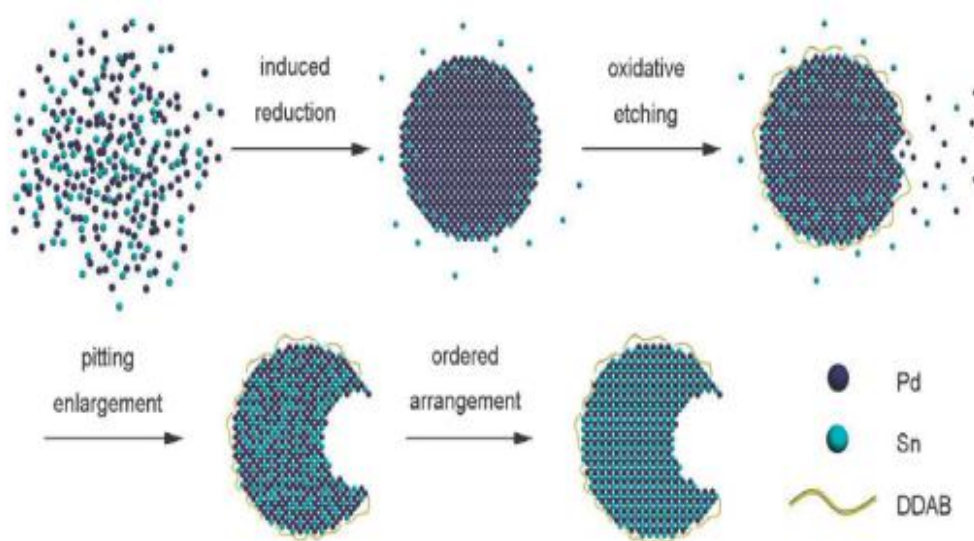


Figure 3.2 Proposed mechanism for the formation of hollow Pd/Sn bimetallic nanospheres.¹²⁴

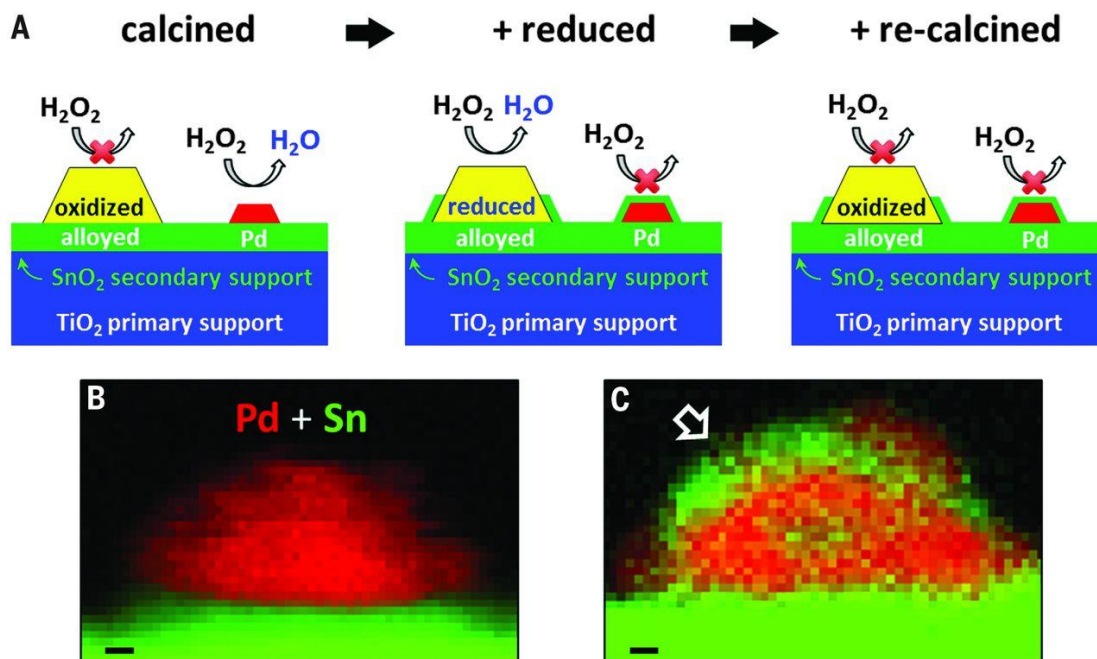


Figure 3.3 Evolution of catalyst through oxidation-reduction-oxidation cycle.¹²⁵ (A) Proposed mechanism for switching off H₂O₂ hydrogenation by small Pd-rich NPs through a strong metal-support interaction (SMSI). The secondary metal must both form an alloy with Pd and oxidize to form a secondary support (i.e., SnO_x) that can encapsulate the relatively small, poorly alloyed, Pd-rich NPs after an O-R-O cycle. This step prevents these NPs from decomposing and hydrogenating the H₂O₂ product. (B and C) STEM-EELS mapping of a 5 wt % Pd/SnO₂ model catalyst at the oxidized (B) and O-R-O (C) stages, showing partial encapsulation of the Pd NP (red) by SnO_x (green) after the O-R-O heat treatment cycle. The Sn intensities in the SnO₂ support area were deliberately saturated to reveal any relatively weak signals in the particle region. Scale bars, 1 nm.

3.1.2 Size and Aspect Ratio Control of Pd₂Sn Nanorods and Their Water Denitration Properties

The paper entitled “*Size and Aspect Ratio Control of Pd₂Sn Nanorods and Their Water Denitration Properties*” was published in *Langmuir* **2015**, *31* (13), 3952-3957 and can be found with the corresponding supporting information file after this brief summary. In this paper, we study the synthesis and catalytic properties of monodisperse Pd₂Sn NPs with different morphologies, sizes and aspect ratios. Pd-Sn NPs were prepared by co-reducing Pd(acac)₂ and Sn(acac)₂ in the presence of amines, TOP, and chlorine ions (Figure 3.4). The growth mechanism of the NRs was based on the selective desorption of TOP by chlorine ions at the NR tips. A preliminary evaluation of the geometry influence on catalytic properties evidenced Pd₂Sn NRs to have higher catalytic performance than spherical Pd₂Sn and Pd NPs toward reduction of nitrophenol and water denitration due to the more active surface facets of NRs.

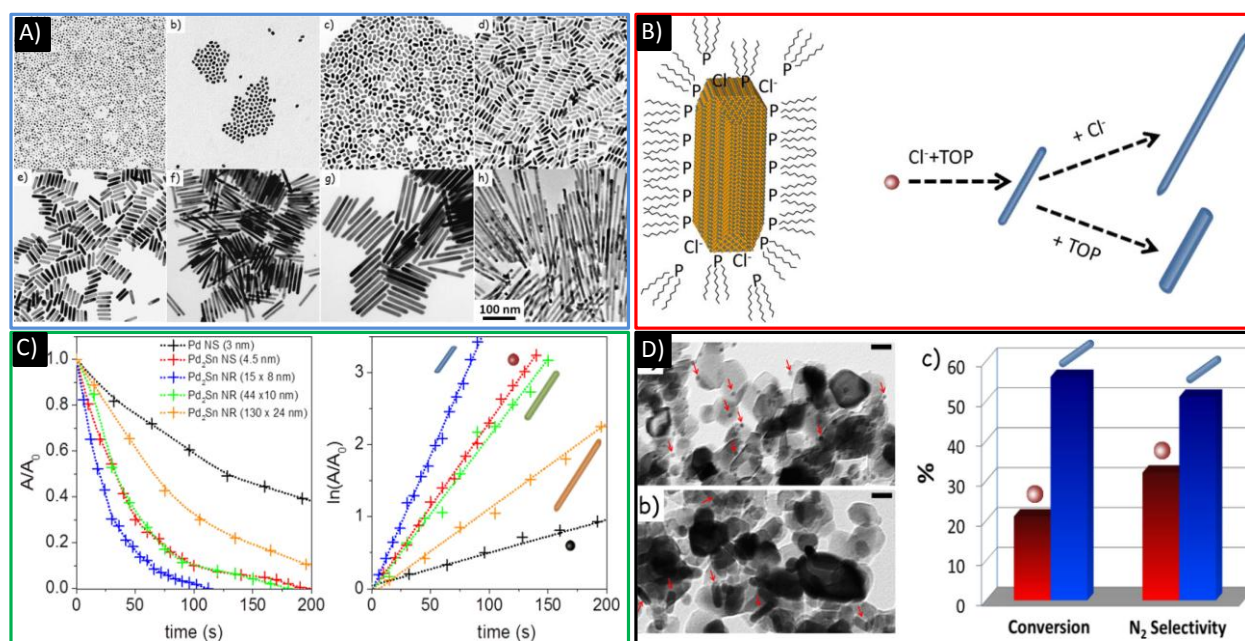
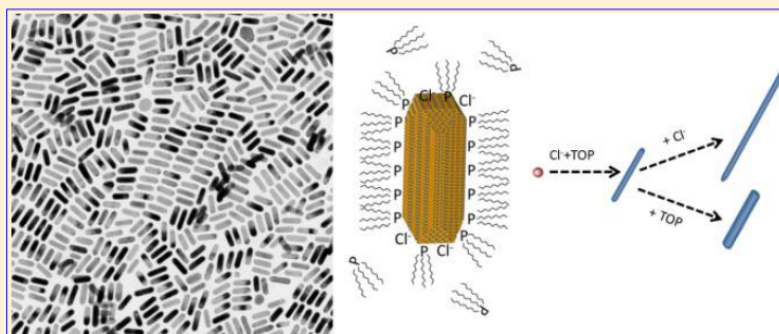


Figure 3.4 **A)** TEM micrographs of Pd₂Sn NPs with different aspect ratios. **B)** Schematic illustration of the influence of the TOP and chloride ions on the shape and size of the Pd₂Sn NRs. **c)** Sodium borohydride-driven degradation of *p*-nitrophenol over 3.0 nm Pd (black) and 4.3 nm Pd₂Sn (red) spheres, and 15 nm x 8 nm Pd₂Sn NRs (blue). **d)** TEM images of Pd₂Sn spherical NPs (a) and NRs (b) supported on TiO₂. Scale bars correspond to 20 nm. c) Nitrate conversion after 24h reaction and N₂ selectivity measured from TiO₂:Pd₂Sn spherical NPs (red) and TiO₂:Pd₂Sn NRs (blue).

Size and Aspect Ratio Control of Pd₂Sn Nanorods and Their Water Denitration PropertiesZhiShan Luo,[†] Maria Ibáñez,[†] Ana M. Antolín,[‡] Aziz Genç,[§] Alexey Shavel,[†] Sandra Contreras,[‡] Francesc Medina,[‡] Jordi Arbiol,^{§,||,⊥} and Andreu Cabot^{*,†,||}[†]Catalonia Institute for Energy Research (IREC), 08930 Sant Adrià del Besòs, Barcelona, Spain[‡]Departament d'Enginyeria Química, Universitat Rovira i Virgili, Campus Sescelades, Av. Països Catalans, 26, 43007 Tarragona, Tarragona, Spain[§]Institut de Ciència de Materials de Barcelona (ICMAB), Consejo Superior de Investigaciones Científicas (CSIC), Campus de la Universitat Autònoma de Barcelona (UAB), 08193 Bellaterra, Barcelona, Spain[⊥]Institut Català de Nanociència i Nanotecnologia, ICN2 Campus de la UAB, 08193 Bellaterra, CAT, Spain^{||}Institució Catalana de Recerca i Estudis Avançats (ICREA), 08010 Barcelona, Barcelona, Spain

Supporting Information



ABSTRACT: Monodisperse Pd₂Sn nanorods with tuned size and aspect ratio were prepared by co-reduction of metal salts in the presence of trioctylphosphine, amine, and chloride ions. Asymmetric Pd₂Sn nanostructures were achieved by the selective desorption of a surfactant mediated by chlorine ions. A preliminary evaluation of the geometry influence on catalytic properties evidenced Pd₂Sn nanorods to have improved catalytic performance. In view of these results, Pd₂Sn nanorods were also evaluated for water denitration.

INTRODUCTION

The development of alternative Pt-free catalysts with comparable or improved activities, selectivities, and stabilities is critical to reduce the cost of catalytic materials and processes. In this direction, bimetallic catalysts, including abundant elements, are one first step toward cost reduction.^{1–3} In particular, Pd-based bimetallic particles with tuned chemical composition, electronic states, and synergy between the two metals have allowed for not only the reduction of material costs but also the improvement of performance and stability with respect to Pt-based and pure Pd catalysts.^{4–6} As an example, Pd and Pd-based bimetallic catalysts are particularly suitable for hydrogenation and dehydrogenation reactions, carbon–carbon bond-forming reactions, such as Heck or Suzuki, and electrooxidation of primary alcohols.^{7–11} Pd alloys with metals that bind strongly to oxygen also provide greater resistance to CO, C, and S poisoning.^{12–17}

Besides composition, the shape of catalytic nanoparticles (NPs), which dictates surface facets and active reaction sites, is

the other key parameter determining a catalyst performance.^{18–20} However, because of the limitations of conventional impregnation methods to control NP geometry, this parameter is generally neglected during catalyst optimization. Colloidal synthesis methods allow for adjusting catalytic NP properties beyond conventional impregnation methods, offering the opportunity to design and engineer well-controlled model systems. In this direction, the development of synthetic routes to produce Pd-based bimetallic NPs with tuned size and shape has attracted significant effort in the past decade.^{5,12–17,21} Among the various bimetallic NPs, Pd–Sn is a particularly interesting candidate for the ethanol oxidation reaction^{22,23} and water denitration.^{24,25} However, despite its interest, the synthesis of Pd–Sn NPs with controlled morphology still remains a major challenge.

Received: December 18, 2014

Revised: March 7, 2015

Published: March 9, 2015

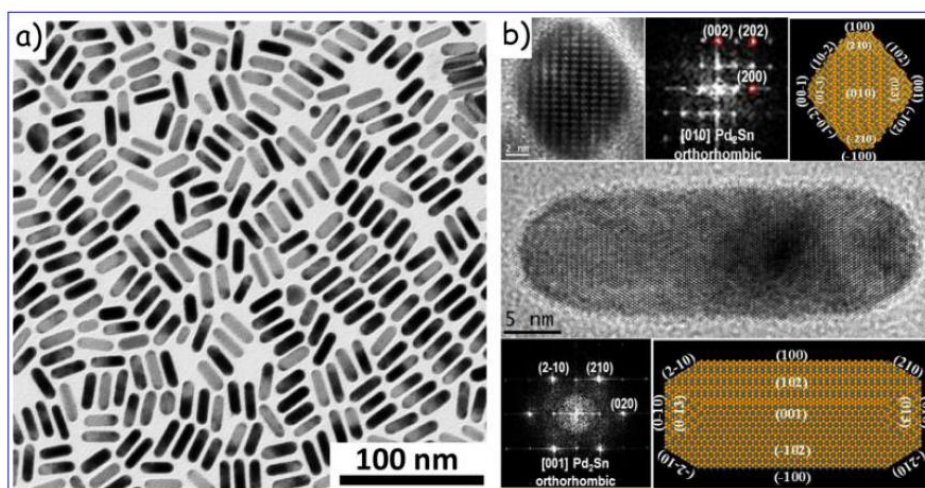


Figure 1. (a) TEM micrograph of 27 nm long and 9 nm wide Pd₂Sn NRs. (b) HRTEM micrographs, power spectra, and 3D atomic models of vertically and horizontally aligned Pd₂Sn NRs.

Herein, we describe a synthetic route to produce highly monodisperse Pd₂Sn NPs with tuned size and morphology. Besides, we present here results from the functional characterization of the new materials produced. We preliminarily tested the catalytic properties of Pd₂Sn NPs using the reduction of *p*-nitrophenol by NaBH₄ as a model reaction.²⁶ Furthermore, the performance of TiO₂-supported Pd₂Sn nanorods (NRs) and nanospheres toward water denitration was also evaluated.

EXPERIMENTAL SECTION

Chemicals. Palladium(II) acetylacetonate [Pd(acac)₂, 99%], tin(II) acetylacetonate [Sn(acac)₂, 99.9%], oleylamine (OLA, >70%), 3-mercaptopropionic acid (MPA, ≥99%), oleic acid (OA, 90%), hexadecylamine (HDA, 90%), cyclohexanone (C₆H₁₀O, 99.8%), sodium hydroxide pellets (NaOH, ≥97%), and hydrochloric acid (37% in water) were purchased from Sigma-Aldrich. Tri-*n*-octylphosphine (TOP, 97%) was purchased from Strem. Sodium nitrate (NaNO₃, 99%) was purchased Riser S.A. Aeroxide P25 (TiO₂) was purchased from Acros Organics. Hexane, chloroform, and ethanol were of analytical grade and obtained from various sources. Milli-Q water was supplied by the PURELAB flex from ELGA. All chemicals were used as received without further purification, except OLA, which was purified by distillation. All syntheses were carried out using standard airless techniques: a vacuum/dry argon gas Schlenk line was used for the syntheses, and an argon glovebox was used for storing and handling air and moisture-sensitive chemicals.

Preparation of Hexadecylammonium Chloride (HDA-HCl). HDA-HCl was prepared by the direct reaction of HDA with an aqueous solution of hydrochloric acid. A total of 20 mmol (4.83 g) of HDA was dissolved in 50 mL of acetone, and 30 mmol (2.96 g) of HCl (37% in water) was added dropwise to the solution. The white precipitate was kept stirring in solution overnight. The HDA-HCl precipitate was filtered out, thoroughly washed with Milli-Q water, and dried under vacuum.

Synthesis of Pd₂Sn Nanorods. In a typical synthesis, 5 mL of OLA, 0.2 mmol of HDA-HCl, and 0.075 mmol of Pd(acac)₂ were placed in a 25 mL four-neck flask and purged under argon flow for 30 min at 60 °C. Next, 0.25 mL of 0.1 M Sn(acac)₂ in TOP was injected. Upon injection, the solution color changed to dark yellow. The solution was heated to 200 °C at 12 °C/min and maintained at this temperature for 30 min. Afterward, the temperature was further increased to 300 °C at 2.5 °C/min and kept for an additional 30 min. During heating, the color changed gradually to black. Then, the solution was cooled to room temperature. While cooling, when the

temperature reached approximately 70 °C, 1 mL of OA was added to improve nanoparticle (NP) solubility. Pd₂Sn NPs were separated from the reaction mixture by adding 20 mL of ethanol and centrifuging at 3000 rpm for 5 min. NPs were washed with chloroform as the solvent and ethanol as the non-solvent by multiple precipitation/redispersion steps.

Synthesis of Pd₂Sn Spherical NPs for Catalytic Performance Evaluation. Pd₂Sn spherical NPs were obtained following the same procedure used to produce Pd₂Sn NRs but without introducing HDA-HCl.

Synthesis of Pd Spherical NPs for Catalytic Performance Evaluation. Pd spherical NPs were prepared following the same procedure used to produce Pd₂Sn NRs but without introducing HDA-HCl and Sn(acac)₂ and setting the growth temperature to 200 °C and growth time to 30 min.

Ligand Exchange with Mercaptopropionic Acid (MPA). Pd₂Sn NPs dispersed in hexane (~50 mg in 5 mL) were mixed with 5 mL of MPA and 5 mL of cyclohexanone. The mixture was sonicated for 30 min. Subsequently, NPs were centrifuged, and the precipitate was further washed with 10 mL of cyclohexanone, chloroform, and ethanol, successively. Finally, NPs were dissolved in 2.25 mL of deionized water with 0.25 mL of 0.2 M NaOH solution.

***p*-Nitrophenol Reduction.** The kinetics of catalytic reduction of *p*-nitrophenol to *p*-aminophenol was monitored by the color change involved in the reaction. Aqueous solutions of *p*-nitrophenol (1.4 mM) and NaBH₄ (0.42 M) were freshly prepared as separate stock solutions. Deionized water (13.0 mL) was mixed with 1.5 mL of *p*-nitrophenol stock solution. Then, 5 mL of MPA-coated Pd₂Sn NR catalysts in water containing 0.1 mL of 0.2 M NaOH solution was added to the mixture with a final concentration of 0.05 mg/mL or 1.4 × 10⁸ NRs/mL. After mixing, 19.5 mL of the reaction solution was quickly transferred to a quartz cuvette. Then, 0.5 mL of NaBH₄ stock solution was injected into the quartz cuvette, and the absorbance spectra were successively recorded with a 5 s period using an ultraviolet–visible (UV–vis) spectrometer until the pale brown solution became colorless. To properly compare each type of catalyst, we keep the same amount for all catalysts (0.05 mg/mL). A total of 5 mL of Pd (3.1 nm in size) and Pd₂Sn (4.9 nm in size) NP catalyst aqueous solution separately was used with a final concentration of 3.4 × 10¹¹ and 6.8 × 10¹¹ NPs/mL, respectively (see the Supporting Information).

Water Denitration. For the nitrate heterogeneous catalytic reduction reaction, 5% Pd₂Sn spherical NPs and NRs were supported on Aeroxide TiO₂ P25 powder form. A constant hydrogen flow (150 mL/min) was used as a reducing agent to transform nitrate into nitrogen gas as the desirable product.

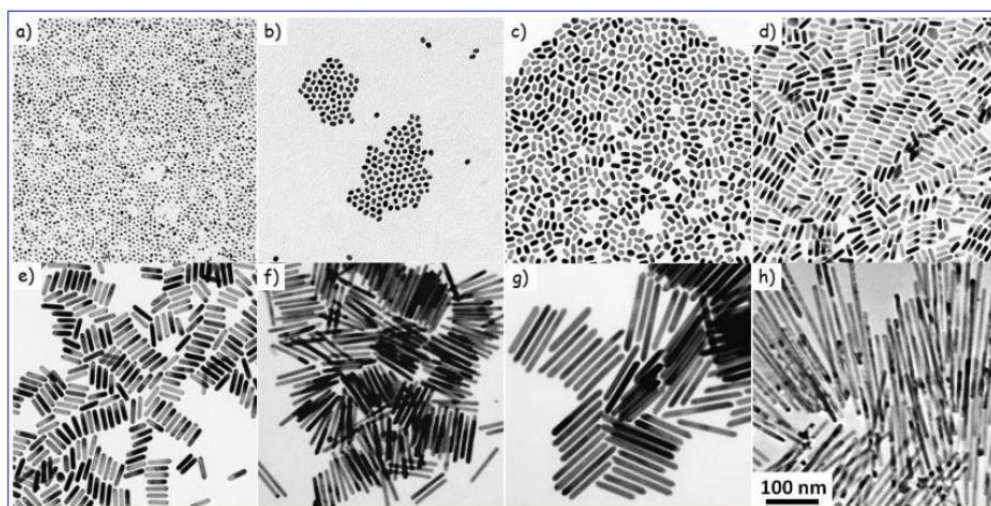


Figure 2. TEM micrographs of Pd₂Sn NPs with different aspect ratios (AR): (a) 4.3 ± 0.2 nm, AR = 1; (b) 9 ± 1 nm \times 6.8 ± 0.6 nm, AR = 1.3; (c) 15 ± 1 nm \times 7 ± 1 nm, AR = 2.1; (d) 24 ± 2 nm \times 7 ± 1 nm, AR = 3.4; (e) 44 ± 4 nm \times 10 ± 2 nm, AR = 4.4; (f) 98 ± 8 nm \times 9 ± 1 nm, AR = 10.8; (g) 130 ± 10 nm \times 24 ± 4 nm, AR = 5.4; and (h) 290 ± 20 nm \times 12 ± 3 nm, AR = 24.2.

Denitration experiments were performed in a 350 mL polytetrafluoroethylene (PTFE) batch reactor under standard operational conditions (atmospheric pressure and room temperature). Sodium nitrate (NaNO₃) was used as the nitrate source in ultrapure water. The amount of 0.2 g of catalyst was introduced in the 100 ppm nitrate (NO₃⁻) solution and remained in suspension by continuously stirring at 500 rpm. Samples were periodically withdrawn to analyze NO₃⁻ and reaction byproducts, such as nitrite (NO₂⁻) and ammonia (NH₄⁺) ions, which were quantified by photometry (PC MultiDirect Lovibond).

RESULTS AND DISCUSSION

Pd–Sn NPs were prepared by co-reducing Pd(acac)₂ and Sn(acac)₂ in the presence of amines, TOP, and chloride ions. In a typical synthesis, 5 mL of OLA, 0.2 mmol of HDA·HCl, and 0.075 mmol of Pd(acac)₂ were placed in a 25 mL four-neck flask and purged under argon flow for 30 min. Next, 0.25 mL of a 0.1 M Sn(acac)₂ solution in TOP was injected, and the mixture was heated to 200 °C at 12 °C/min and maintained at this temperature for 30 min. Finally, the solution was heated to 300 °C at 2.5 °C/min, and NPs were allowed to grow for 30 min before cooling to room temperature. Finally, NPs were purified by multiple precipitation/redispersion steps.

Figure 1 displays representative transmission electron microscopy (TEM) and high-resolution transmission electron microscopy (HRTEM) micrographs of Pd–Sn NPs obtained by the procedure described above. Pd–Sn NPs were characterized by very narrow size distributions and rod-like geometry.

Power spectrum analysis revealed Pd–Sn NRs to have an orthorhombic Pd₂Sn phase (space group *Pnma*) with lattice parameters $a = 0.5635$ nm, $b = 0.4283$ nm, and $c = 0.8091$ nm. The NR growth direction was identified as [010]. HRTEM micrographs taken from vertically (along the growth axis) and horizontally (lateral view) aligned NRs showed them to have eight facets, {100} and {102}, forming a rhombitruncated hexahedron.²⁷ Pd₂Sn NR tips were also faceted, as shown in Figure 1b, and three-dimensional (3D) models were obtained using Rhodius software²⁸ (see animated 3D models in ref 29). The Pd/Sn ratio within Pd–Sn NPs was 2:1, as determined by

energy-dispersive X-ray spectroscopy within scanning electron microscopy and confirmed by inductively coupled plasma spectrometry. X-ray diffraction analysis further confirmed Pd–Sn NRs to have a Pd₂Sn orthorhombic crystal structure [Joint Committee on Powder Diffraction Standards (JCPDS) number 00-026-1297; see Figure S2 of the Supporting Information].

The presence of both chloride ions and TOP was critical to produce rod-shaped Pd₂Sn NPs. Moreover, the chlorine and TOP concentrations determined NR size and aspect ratio. Experimental results pointed out that the NR thickness was mainly influenced by the TOP concentration, while the length mainly depended upon the amount of chloride ions (Figure 3).

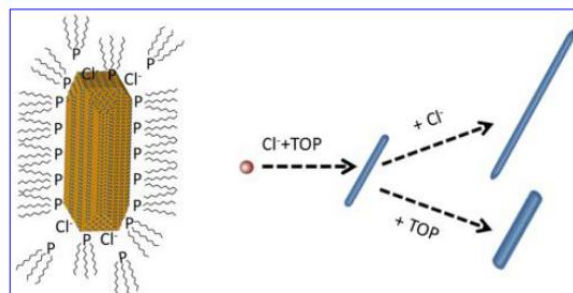


Figure 3. Schematic illustration of the influence of TOP and chloride ions on the shape and size of the Pd₂Sn NRs.

With adjustment of the synthetic conditions (details in section 4 of the Supporting Information), the average NR length could be tuned in the range from 20 to 600 nm and its diameter could be tuned in the range between 6 and 40 nm (Figure 2).

Several theories have been proposed to explain the influence of halide ions on the shape control of Pd,³⁰ Ag,^{31,32} Au,^{33–35} and CdSe^{36–39} NPs. Halides may modify the reduction potential of the metal ions, passivate specific NP surfaces, or control surface passivation by modulating the concentration of surface ligands.^{31–34,40,41} In our system, while OLA played an essential role as coordinating solvent in controlling NP size, TOP and chloride ions were the key compounds directing

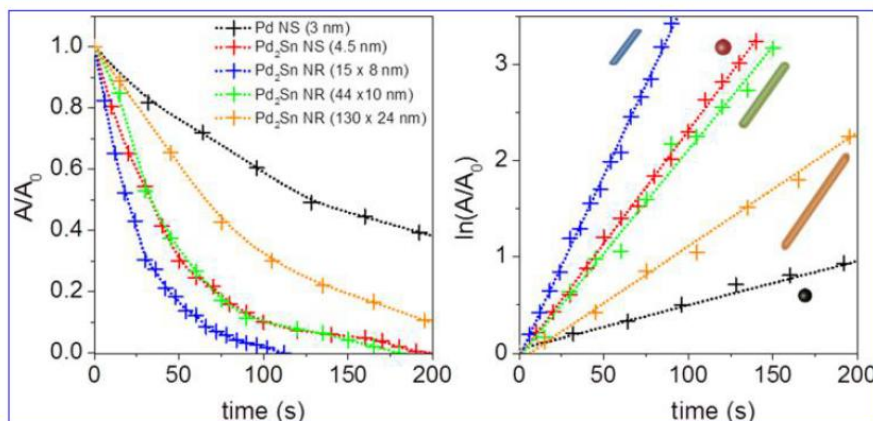


Figure 4. Sodium-borohydride-driven degradation of *p*-nitrophenol over 3.0 nm Pd and 4.3 nm Pd₂Sn spheres, 15 × 8 nm Pd₂Sn NRs, 44 × 10 nm Pd₂Sn NRs, and 130 × 24 nm Pd₂Sn NRs.

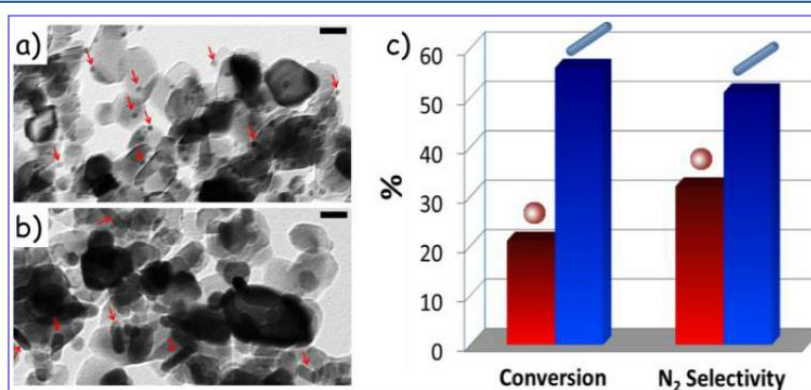


Figure 5. (a and b) TEM images of Pd₂Sn (a) spherical NPs and (b) NRs, supported on TiO₂. Scale bars correspond to 20 nm. (c) Nitrate conversion after 24 h of reaction and N₂ selectivity measured from TiO₂/Pd₂Sn spherical NPs (red) and TiO₂/Pd₂Sn NRs (blue).

Pd₂Sn NP asymmetric growth and determining its aspect ratio. Experimental results evidenced that both TOP and chlorine ions were necessary to produce Pd₂Sn NRs and that they both competed for the passivation of the NR tips (see control experiments in section 5 of the Supporting Information). We believe that a preferential organic ligand desorption from Pd₂Sn NP tip facets directs the growth of asymmetric Pd₂Sn NPs. We hypothesize that, while TOP bonded across the whole NP surface, chlorine ions (harder base than phosphine) induced TOP desorption at the NP tip facets, where a larger density of Sn ions (harder acid than Pd ions) was probably found. From another point of view, rods were formed in the presence of Cl⁻ because the surface energy differences among the various facets allowed Cl⁻ to selectively desorb TOP from the (010) facets. These hypotheses are consistent with the larger amounts of TOP providing a more efficient protection of the NR tips, thus resulting in thicker NRs. At the same time, larger amounts of Cl⁻ displace TOP from the NR tips more efficiently, resulting in longer Pd₂Sn NRs.

An initial evaluation of the functional properties of the new Pd₂Sn NP geometry detailed here was obtained using the reduction of *p*-nitrophenol by sodium borohydride as a model catalytic system.²⁶ To evaluate and compare NP activity, spherical Pd₂Sn and Pd NPs and Pd₂Sn NRs with three different lengths were rendered soluble in water through ligand exchange with MPA (see the Supporting Information). Figure

4a displays the kinetic of *p*-nitrophenol reduction to *p*-aminophenol in the presence of 3.0 nm Pd (160 m²/g), 4.3 nm Pd₂Sn spheres (110 m²/g), 15 × 8 nm Pd₂Sn NRs (50 m²/g), 44 × 10 nm Pd₂Sn NRs (37 m²/g), and 130 × 24 nm Pd₂Sn NRs (15 m²/g).⁴² In the presence of an excess of sodium borohydride and sufficient catalysts, the reaction rate could be fitted to a pseudo-first-order reaction, $\ln(A_0/A) = kt$, where k is the apparent rate constant (Figure 4b).⁴³ Using the exact same total amount (5 mg) and concentration (0.05 mg/mL) of catalytic NPs, 15 × 8 nm Pd₂Sn NRs showed the highest reaction rates, 38 s⁻¹ g⁻¹ (0.7 s⁻¹ m⁻²). This value was clearly above that measured for spherical Pd₂Sn (23 s⁻¹ g⁻¹; 0.2 s⁻¹ m⁻²) and spherical Pd (4.6 s⁻¹ g⁻¹; 0.03 s⁻¹ m⁻²) NPs. With normalization for the different surface areas of NRs and spherical NPs, the performance enhancement associated with Pd₂Sn NRs was even more notable, with 3.5- and 28-fold reaction rate increases over spherical Pd₂Sn and Pd NPs, respectively. Such an enhancement of the reaction rates with this particular NR geometry indicates that highly active catalytic sites are located at the NR (100) and/or (102) facets or at the corners between these facets. The reaction rates for longer NRs were 22 s⁻¹ g⁻¹ (0.6 s⁻¹ m⁻²) for 44 × 10 nm Pd₂Sn NRs and 11 s⁻¹ g⁻¹ (0.8 s⁻¹ m⁻²) for 130 × 24 nm Pd₂Sn NRs. When the NR length was increased, similar reaction rates per surface area unit were obtained (see Figure S17 of the Supporting Information). However, when the decrease of the surface area is

taken into account with the increase of the NR size, lower reaction rates per mass unit were measured when increasing the NR size.

We further compared the activity and selectivity of Pd₂Sn NRs (AR = 1.9) and Pd₂Sn spherical NPs toward water denitration. The removal of nitrate is becoming a major social and environmental challenge because nitrate is growing to be one main pollutant of natural aquifers and drinking water produced from groundwater. The catalytic hydrogenation of nitrate to nitrogen is a potential cost-effective and ecological alternative to biological and physicochemical processes of denitrification.^{44–46} However, an efficient and selective nitrate hydrogenation requires the synergy between different metals, complicating the catalyst optimization by conventional impregnation methods. Among the different materials tested, Pd-based bimetallic catalysts have shown some of the best conversion rates and selectivities.^{25,47,48}

To evaluate Pd₂Sn NP activity toward water denitration, water-soluble spherical Pd₂Sn NPs and Pd₂Sn NRs were supported on Aeroxide TiO₂ P25 with a 5% weight load. Panels a and b of Figure 5 show TEM images of 4.3 ± 0.2 nm Pd₂Sn spherical NPs and 27 ± 2 nm long and 9 ± 1 nm Pd₂Sn NRs, respectively, supported on TiO₂. A constant hydrogen gas flow (150 mL/min) was used as a reducing agent to transform nitrate into nitrogen gas.

Figure 5c shows the percentage of nitrate conversion and the selectivity to N₂ obtained after 24 h of reaction. The catalyst containing 5 wt % Pd₂Sn NRs showed much higher catalytic activity than the spherical NPs; around 3 times higher nitrate conversion was observed. The initial reaction rate for nitrate removal was 21.7 mg h⁻¹ g⁻¹ (0.5 mg h⁻¹ m⁻²) of metal and 7.4 mg h⁻¹ g⁻¹ (0.06 mg h⁻¹ m⁻²) of metal for NRs and spherical NPs, respectively (SI). The selectivity to nitrogen for NRs was higher (51%) than that for spherical NPs (32%). Furthermore, the NH₄⁺ formation (5% of selectivity) was lower than other reported Pd–Sn catalysts, e.g., the catalyst reported by Palomares et al.⁴⁹ (around 40% of selectivity to NH₄⁺). The hydrogen chemisorption technique (see the Supporting Information) was applied on both catalysts to determine palladium dispersion. The 5% Pd₂Sn NRs exhibited a dispersion of 0.37%, while the 5% Pd₂Sn spherical NPs showed a lower dispersion (0.16%). These very low values of metal dispersion indicate that the formation of the PdSn alloy inhibits the hydrogen chemisorption, as reported by other authors.^{50,51} Consequently, the alloy formation could be responsible for the lower selectivity to NH₄⁺, reducing the over-hydrogenation reaction.

CONCLUSION

In summary, we detailed a procedure to produce Pd₂Sn NRs with controlled size and aspect ratio. The growth mechanism was based on the selective desorption of TOP by chlorine ions. Pd₂Sn NRs showed higher catalytic performance than smaller spherical NPs toward reduction of *p*-nitrophenol by sodium borohydride and water denitration. Enhanced catalytic properties must be associated with the more active surface facets of Pd₂Sn NRs. A systematic optimization of the catalyst, which should probably involve the decrease of the NR dimensions, is now required to maximize its catalytic activity and selectivity in several potential applications of this material.

ASSOCIATED CONTENT

Supporting Information

TEM micrograph of spherical Pd NPs, geometric and crystal structure characterization, control experiments, and details of the *p*-nitrophenol reduction, EOR, and water denitration experiments. This material is available free of charge via the Internet at <http://pubs.acs.org>.

AUTHOR INFORMATION

Corresponding Author

*E-mail: acabot@irec.cat.

Notes

The authors declare no competing financial interest.

ACKNOWLEDGMENTS

This work was supported by the European Regional Development Funds, Generalitat de Catalunya 2014SGR1638, and Spanish MINECO for ENE2013-46624-C4-3-R, 2014 SGR 1640, CTQ2012-35789-C02-02, and CSD2009-00050. ZhiShan Luo thanks the China Scholarship Council (CSC 201206740024) for scholarship support. Maria Ibáñez thanks AGAUR for her Beatriu i Pinós (2013 BP-A 00344) postdoctoral grant. Aziz Genç acknowledges the scholarship from the Ministry of National Education of Turkey. J.A. acknowledges ICN2 Severo Ochoa Excellence grant.

REFERENCES

- (1) Herranz, T.; Ibáñez, M.; Gómez de la Fuente, J. L.; Pérez-Alonso, F. J.; Peña, M. A.; Cabot, A.; Rojas, S. *In situ* study of ethanol electrooxidation on monodispersed Pt₃Sn nanoparticles. *ChemElectroChem* **2014**, *1*, 885–895.
- (2) Flox, C.; Rubio-Garcia, J.; Nafria, R.; Zamani, R.; Skoumal, M.; Andreu, T.; Arbiol, J.; Cabot, A.; Morante, J. R. Active nano-CuPt₃ electrocatalyst supported on graphene for enhancing reactions at the cathode in all-vanadium redox flow batteries. *Carbon* **2012**, *50*, 2372–2374.
- (3) Porter, N. S.; Wu, H.; Quan, Z.; Fang, J. Shape-control and electrocatalytic activity-enhancement of Pt-based bimetallic nanocrystals. *Acc. Chem. Res.* **2013**, *46*, 1867–1877.
- (4) Shao, M.; Liu, P.; Zhang, J.; Adzic, R. Origin of enhanced activity in palladium alloy electrocatalysts for oxygen reduction reaction. *J. Phys. Chem. B* **2007**, *111*, 6772–6775.
- (5) Yang, X.; Hu, J.; Fu, J.; Wu, R.; Koel, B. E. Role of surface iron in enhanced activity for the oxygen reduction reaction on a Pd₃Fe(111) single-crystal alloy. *Angew. Chem., Int. Ed.* **2011**, *50*, 10182–10185.
- (6) Shao, M.-H.; Sasaki, K.; Adzic, R. R. Pd–Fe nanoparticles as electrocatalysts for oxygen reduction. *J. Am. Chem. Soc.* **2006**, *128*, 3526–3527.
- (7) Kim, S.-W.; Kim, M.; Lee, W. Y.; Hyeon, T. Fabrication of hollow palladium spheres and their successful application to the recyclable heterogeneous catalyst for Suzuki coupling reactions. *J. Am. Chem. Soc.* **2002**, *124*, 7642–7643.
- (8) Son, S. U.; Jang, Y.; Park, J.; Na, H. B.; Park, H. M.; Yun, H. J.; Lee, J.; Hyeon, T. Designed synthesis of atom-economical Pd/Ni bimetallic nanoparticle-based catalysts for Sonogashira coupling reactions. *J. Am. Chem. Soc.* **2004**, *126*, 5026–5027.
- (9) Yin; Liebscher, J. Carbon–carbon coupling reactions catalyzed by heterogeneous palladium catalysts. *Chem. Rev.* **2006**, *107*, 133–173.
- (10) Xia, Y.; Xiong, Y.; Lim, B.; Skrabalak, S. E. Shape-controlled synthesis of metal nanocrystals: Simple chemistry meets complex physics? *Angew. Chem., Int. Ed.* **2009**, *48*, 60–103.
- (11) Kariuki, N. N.; Wang, X.; Mawdsley, J. R.; Ferrandon, M. S.; Niyogi, S. G.; Vaughney, J. T.; Myers, D. J. Colloidal synthesis and characterization of carbon-supported Pd–Cu nanoparticle oxygen reduction electrocatalysts. *Chem. Mater.* **2010**, *22*, 4144–4152.

- (12) Zhang, L.; Hou, F.; Tan, Y. Shape-tailoring of CuPd nanocrystals for enhancement of electro-catalytic activity in oxygen reduction reaction. *Chem. Commun.* **2012**, *48*, 7152–7154.
- (13) Tang, W.; Zhang, L.; Henkelman, G. Catalytic activity of Pd/Cu random alloy nanoparticles for oxygen reduction. *J. Phys. Chem. Lett.* **2011**, *2*, 1328–1331.
- (14) Jin, M.; Zhang, H.; Wang, J.; Zhong, X.; Lu, N.; Li, Z.; Xie, Z.; Kim, M. J.; Xia, Y. Copper can still be epitaxially deposited on palladium nanocrystals to generate core–shell nanocubes despite their large lattice mismatch. *ACS Nano* **2012**, *6*, 2566–2573.
- (15) Gao, Q.; Ju, Y.-M.; An, D.; Gao, M.-R.; Cui, C.-H.; Liu, J.-W.; Cong, H.-P.; Yu, S.-H. Shape-controlled synthesis of monodisperse PdCu nanocubes and their electrocatalytic properties. *ChemSusChem* **2013**, *6*, 1878–1882.
- (16) Mazumder, V.; Chi, M.; Mankin, M. N.; Liu, Y.; Metin, Ö.; Sun, D.; More, K. L.; Sun, S. A facile synthesis of MPd (M = Co, Cu) nanoparticles and their catalysis for formic acid oxidation. *Nano Lett.* **2012**, *12*, 1102–1106.
- (17) Hokenek, S.; Bennett, C.; Kuhn, J. N. Synthesis of Ni–Pd nanocubes and nanorods with high selectivity through a modified polyol process. *J. Cryst. Growth* **2013**, *374*, 18–22.
- (18) Rupprechter, G.; Weilach, C. Mind the gap! Spectroscopy of catalytically active phases. *Nano Today* **2007**, *2*, 20–29.
- (19) Long, R.; Mao, K.; Ye, X.; Yan, W.; Huang, Y.; Wang, J.; Fu, Y.; Wang, X.; Wu, X.; Xie, Y.; Xiong, Y. Surface facet of palladium nanocrystals: A key parameter to the activation of molecular oxygen for organic catalysis and cancer treatment. *J. Am. Chem. Soc.* **2013**, *135*, 3200–3207.
- (20) Narayanan, R.; El-Sayed, M. A. Effect of colloidal nanocatalysis on the metallic nanoparticle shape: The Suzuki reaction. *Langmuir* **2005**, *21*, 2027–2033.
- (21) Heemeier, M.; Carlsson, A. F.; Naschitzki, M.; Schmal, M.; Bäumer, M.; Freund, H.-J. Preparation and characterization of a model bimetallic catalyst: Co–Pd nanoparticles supported on Al₂O₃. *Angew. Chem., Int. Ed.* **2002**, *41*, 4073–4076.
- (22) Du, W.; Mackenzie, K. E.; Milano, D. F.; Deskins, N. A.; Su, D.; Teng, X. Palladium–tin alloyed catalysts for the ethanol oxidation reaction in an alkaline medium. *ACS Catal.* **2012**, *2*, 287–297.
- (23) Jou, L.-H.; Chang, J.-K.; Whanga, T.-J.; Sun, I.-W. Electrodeposition of palladium–tin alloys from 1-ethyl-3-methylimidazolium chloride–tetrafluoroborate ionic liquid for ethanol electro-oxidation. *J. Electrochem. Soc.* **2010**, *157*, D443–D449.
- (24) Barbosa, D. P.; Tchiéta, P.; Rangel, M. d. C.; Epron, F. The use of a cation exchange resin for palladium–tin and palladium–indium catalysts for nitrate removal in water. *J. Mol. Catal. A: Chem.* **2013**, *366*, 294–302.
- (25) Garron, A.; Lázár, K.; Epron, F. Effect of the support on tin distribution in Pd–Sn/Al₂O₃ and Pd–Sn/SiO₂ catalysts for application in water denitration. *Appl. Catal., B* **2005**, *59*, 57–69.
- (26) Hayakawa, K.; Yoshimura, T.; Esumi, K. Preparation of gold–dendrimer nanocomposites by laser irradiation and their catalytic reduction of 4-nitrophenol. *Langmuir* **2003**, *19*, 5517–5521.
- (27) Barnard, A. S.; Osawa, E. The impact of structural polydispersity on the surface electrostatic potential of nanodiamond. *Nanoscale* **2014**, *6*, 1188–1194.
- (28) Bernal, S.; Botana, F. J.; Calvino, J. J.; López-Cartes, C.; Pérez-Omil, J. A.; Rodríguez-Izquierdo, J. M. The interpretation of HREM images of supported metal catalysts using image simulation: Profile view images. *Ultramicroscopy* **1998**, *72*, 135–164.
- (29) www.gaen.cat/research/240.
- (30) Zhang, H.; Jin, M.; Xiong, Y.; Lim, B.; Xia, Y. Shape-controlled synthesis of Pd nanocrystals and their catalytic applications. *Acc. Chem. Res.* **2012**, *46*, 1783–1794.
- (31) Wiley, B.; Herricks, T.; Sun, Y.; Xia, Y. Polyol synthesis of silver nanoparticles: Use of chloride and oxygen to promote the formation of single-crystal, truncated cubes and tetrahedrons. *Nano Lett.* **2004**, *4*, 1733–1739.
- (32) Cathcart, N.; Frank, A. J.; Kitaev, V. Silver nanoparticles with planar twinned defects: Effect of halides for precise tuning of plasmon resonance maxima from 400 to >900 nm. *Chem. Commun.* **2009**, 7170–7172.
- (33) Millstone, J. E.; Wei, W.; Jones, M. R.; Yoo, H.; Mirkin, C. A. Iodide ions control seed-mediated growth of anisotropic gold nanoparticles. *Nano Lett.* **2008**, *8*, 2526–2529.
- (34) DuChene, J. S.; Niu, W.; Abendroth, J. M.; Sun, Q.; Zhao, W.; Huo, F.; Wei, W. D. Halide anions as shape-directing agents for obtaining high-quality anisotropic gold nanostructures. *Chem. Mater.* **2012**, *25*, 1392–1399.
- (35) Gómez-Graña, S.; Goris, B.; Altantzis, T.; Fernández-López, C.; Carbó-Argibay, E.; Guerrero-Martínez, A.; Almora-Barrios, N.; López, N.; Pastoriza-Santos, I.; Pérez-Juste, J.; Bals, S.; Van Tendeloo, G.; Liz-Marzán, L. M. Au@Ag nanoparticles: Halides stabilize {100} facets. *J. Phys. Chem. Lett.* **2013**, *4*, 2209–2216.
- (36) Lim, S. J.; Kim, W.; Jung, S.; Seo, J.; Shin, S. K. Anisotropic etching of semiconductor nanocrystals. *Chem. Mater.* **2011**, *23*, 5029–5036.
- (37) Iacono, F.; Palencia, C.; de la Cueva, L.; Meyns, M.; Terracciano, L.; Vollmer, A.; de la Mata, M. J.; Klinke, C.; Gallego, J. M.; Juarez, B. H.; Otero, R. Interfacing quantum dots and graphitic surfaces with chlorine atomic ligands. *ACS Nano* **2013**, *7*, 2559–2565.
- (38) Meyns, M.; Bastus, N. G.; Cai, Y.; Kornowski, A.; Juarez, B. H.; Weller, H.; Klinke, C. Growth and reductive transformation of a gold shell around pyramidal cadmium selenide nanocrystals. *J. Mater. Chem.* **2010**, *20*, 10602–10605.
- (39) Palencia, C.; Lauwaet, K.; de la Cueva, L.; Acebron, M.; Conde, J. J.; Meyns, M.; Klinke, C.; Gallego, J. M.; Otero, R.; Juarez, B. H. Cl-Capped CdSe nanocrystals via *in situ* generation of chloride anions. *Nanoscale* **2014**, *6*, 6812–6818.
- (40) Kim, M. R.; Miszta, K.; Povia, M.; Brescia, R.; Christodoulou, S.; Prato, M.; Marras, S.; Manna, L. Influence of chloride ions on the synthesis of colloidal branched CdSe/CdS nanocrystals by seeded growth. *ACS Nano* **2012**, *6*, 11088–11096.
- (41) Lohse, S. E.; Burrows, N. D.; Scarabelli, L.; Liz-Marzán, L. M.; Murphy, C. J. Anisotropic noble metal nanocrystal growth: The role of halides. *Chem. Mater.* **2013**, *26*, 34–43.
- (42) Zeng, J.; Zhang, Q.; Chen, J.; Xia, Y. A comparison study of the catalytic properties of Au-based nanocages, nanoboxes, and nanoparticles. *Nano Lett.* **2009**, *10*, 30–35.
- (43) Lee, J.; Park, J. C.; Song, H. A nanoreactor framework of a Au@SiO₂ yolk/shell structure for catalytic reduction of *p*-nitrophenol. *Adv. Mater.* **2008**, *20*, 1523–1528.
- (44) Aristizábal, A.; Contreras, S.; Divins, N. J.; Llorca, J.; Medina, F. Pt–Ag/activated carbon catalysts for water denitration in a continuous reactor: Incidence of the metal loading, Pt/Ag atomic ratio and Pt metal precursor. *Appl. Catal., B* **2012**, *127*, 351–362.
- (45) Aristizábal, A.; Contreras, S.; Divins, N. J.; Llorca, J.; Medina, F. Effect of impregnation protocol in the metallic sites of Pt–Ag/activated carbon catalysts for water denitration. *Appl. Surf. Sci.* **2014**, *298*, 75–89.
- (46) Prüsse, U.; Hähnlein, M.; Daum, J.; Vorlop, K.-D. Improving the catalytic nitrate reduction. *Catal. Today* **2000**, *55*, 79–90.
- (47) Dodouche, I.; Barbosa, D. P.; Rangel, M. d. C.; Epron, F. Palladium–tin catalysts on conducting polymers for nitrate removal. *Appl. Catal., B* **2009**, *93*, 50–55.
- (48) Lemaigen, L.; Tong, C.; Begon, V.; Burch, R.; Chadwick, D. Catalytic denitrification of water with palladium-based catalysts supported on activated carbons. *Catal. Today* **2002**, *75*, 43–48.
- (49) Palomares, A. E.; Franch, C.; Corma, A. A study of different supports for the catalytic reduction of nitrates from natural water with a continuous reactor. *Catal. Today* **2011**, *172*, 90–94.
- (50) Tanielyan, S. K.; Augustine, R. L. Acetoxylation of toluene catalyzed by supported Pd–Sn catalysts. *J. Mol. Catal.* **1994**, *87*, 311–328.
- (51) Rochefort, A.; Andzelm, J.; Russo, N.; Salahub, D. R. Chemisorption and diffusion of atomic hydrogen in and on cluster models of palladium, rhodium and bimetallic palladium tin, rhodium tin, and rhodium zinc catalysts. *J. Am. Chem. Soc.* **1990**, *112*, 8239–8247.

Size and Aspect Ratio Control of Pd₂Sn Nanorods and their Water Denitration Properties

Supporting Information

ZhiShan Luo,[†] Maria Ibáñez,[†] Ana M. Antolín,[‡] Aziz Genç,[¥] Alexey Shavel,[†] Sandra Contreras,[‡]
Francesc Medina,[‡] Jordi Arbiol^{¶,Ψ} and Andreu Cabot^{†,Ψ,*}

[†] Catalonia Energy Research Institute - IREC, Sant Adria del Besos, 08930 Barcelona, Spain

[‡] Departament d'Enginyeria Química, Universitat Rovira i Virgili, Campus Sescelades, 43007 Tarragona, Spain

[¥] Institut de Ciència de Materials de Barcelona, ICMAB-CSIC, Campus de la UAB, Bellaterra, 08193, Spain

^Ψ Institució Catalana de Recerca i Estudis Avançats - ICREA, 08010 Barcelona, Spain

Contents

1. Characterization Techniques.....	2
2. TEM micrograph spherical Pd NPs	2
3. Geometric and crystal structure characterization.....	2
4. Summary of synthesis conditions of samples presented in figure 2	6
5. Control experiments.....	6
6. Ligand exchange with mercaptopropionic acid	10
7. Estimation of nanorods and nanospheres concentration in NPs/ml.....	10
8. P-nitrophenol reaction.....	10
9. Water denitration	11
10. References	13

1. Characterization Techniques

Transmission electron microscopy (TEM) studies. Size and shape of initial nanoparticles were examined by transmission electron microscopy (TEM) using a ZEISS LIBRA 120, operating at 120 kV. Structural and compositional characterization of the nanocomposites were also examined under TEM. High resolution TEM (HRTEM) studies are conducted by using a field emission gun FEI™ Tecnai F20 microscope at 200 kV with a point-to-point resolution of 0.19 nm.

X-ray power diffraction (XRD) analyses were collected directly from the as-synthesized NPs dropped on Si(501) substrate on a Bruker AXS D8 Advance X-ray diffractometer with Ni-filtered (2 μm thickness) Cu K α radiation ($\lambda = 1.5406 \text{ \AA}$) operating at 40kV and 40mA. A LynxEye linear position-sensitive detector was used in reflection geometry.

2. TEM micrograph spherical Pd NPs



Figure S1. TEM micrograph of spherical Pd NPs.

3. Geometric and crystal structure characterization

As shown in figure S2 and S3, X-ray diffraction confirmed the Pd₂Sn spherical NPs and NRs to have the orthorhombic Pd₂Sn phase (space group Pnma, JCPDS no. 00-026-1297). Which was further verified by HRTEM studied performed either in the Pd₂Sn nanorods and Pd₂Sn spherical nanoparticles.

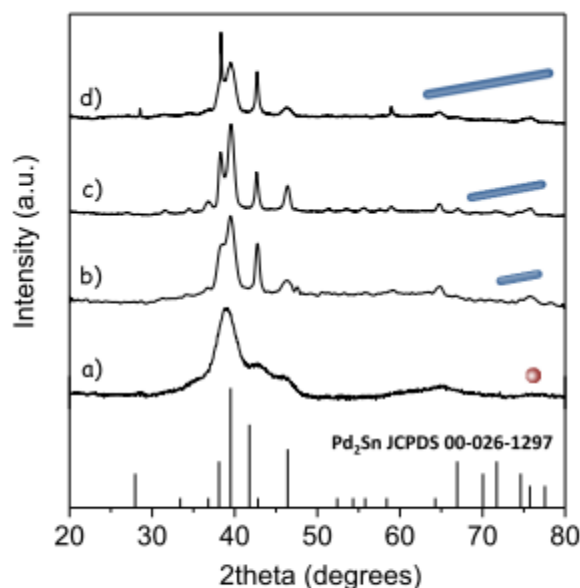


Figure S2 XRD pattern of a) 4.3 ± 0.2 nm diameter Pd_2Sn spherical NPs, b) 83 ± 9 nm long and 9 ± 2 nm wide NRs, c) 276 ± 28 nm long and 15 ± 2 nm wide NRs, d) 603 ± 65 nm long and 32 ± 3 nm wide NRs, and reference pattern corresponding to orthorhombic Pd_2Sn phase Pnma space group (JCPDS no. 00-026-1297).

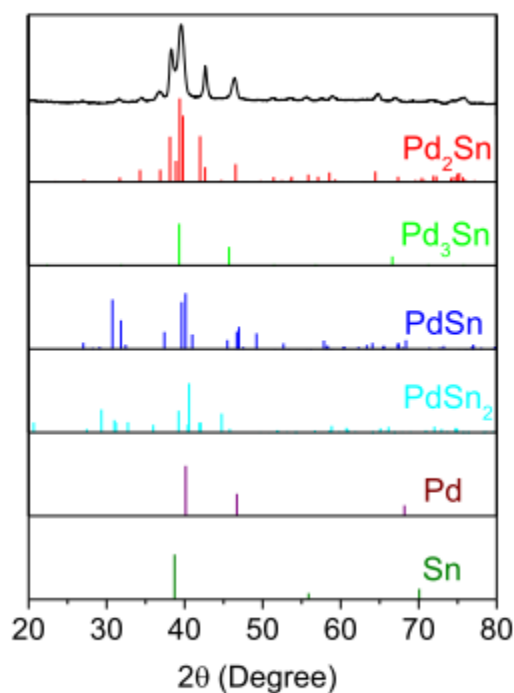


Figure S3 XRD pattern of 276 ± 28 nm long and 15 ± 2 nm wide NRs and reference pattern corresponding to orthorhombic Pd_2Sn (red) phase Pnma space group (JCPDS no. 00-026-1297), cubic Pd_3Sn (green) phase Pm-3m space group (JCPDS no. 03-065-8225), orthorhombic PdSn (dark blue) phase Pnma space group (JCPDS no. 03-065-2603), tetragonal PdSn_2 (light blue) phase space group (JCPDS no. 01-075-0892), cubic Pd (purple) phase Fm-3m space group (JCPDS no. 03-065-6174), and cubic Sn (dark green) phase Im-3m space group (JCPDS no. 03-065-0298).

TEM, HRTEM and STEM-HAADF micrographs of vertically aligned NRs probed NRs to be faceted and to show a rhombitruncated hexahedron geometry. Figure S4 and S5 display TEM and HAADF-STEM micrographs of vertically aligned Pd₂Sn NRs where it is clearly appreciated their non-circular cross section.

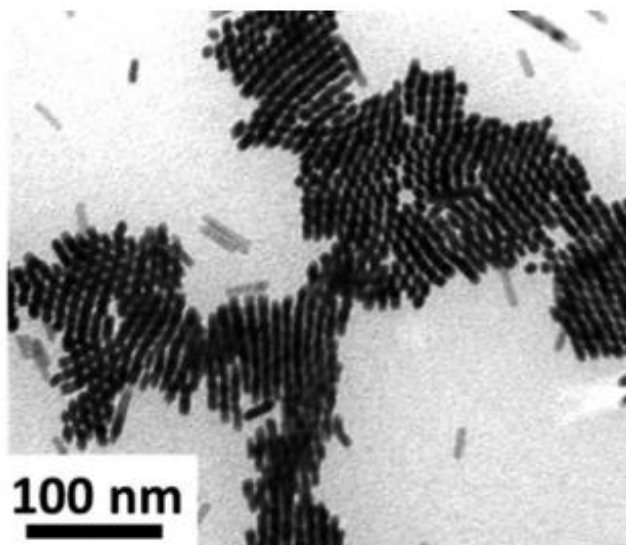


Figure S4 TEM micrograph of vertically aligned Pd₂Sn NRs.

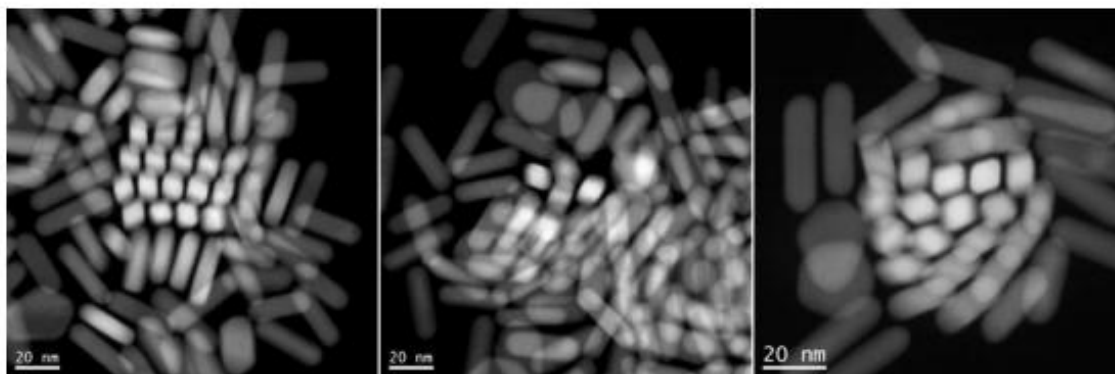


Figure S5 General STEM-HAADF micrographs showing Pd₂Sn NRs aligned along the growth axis.

The crystal phase, shape and faceting of the NRs were studied in more detail by HRTEM. Figure 1b in the main text shows HRTEM micrographs taken from vertically (along the growth axis) and horizontally aligned (lateral view) NRs, their corresponding power spectra and 3D structural models. As seen in the HRTEM micrograph taken from the vertically aligned NR, Pd₂Sn NRs have at least 8 facets. This kind of structure is called rhombitruncated hexahedron and comprises {100} and {110} facets for cubic structures.¹ The power spectrum of the Pd₂Sn NR revealed that it has an orthorhombic Pd₂Sn phase (space group Pnma) with lattice parameters of $a = 0.5635$ nm, $b = 0.4283$ nm and $c = 0.8091$ nm. The NR vertical view is visualized along its [010] zone axis, which is also the growth direction of the NR. For the orthorhombic system, {110} planes of the cubic rhombitruncated hexahedron structures are replaced by {102} planes, which are perpendicular planes to the <101> zone axes. Notice that the tips of the NR are also faceted. We could identify the Pd₂Sn NR tip facets using different power spectra of Pd₂Sn NRs aligned along [001] and [101] lateral zone axes. We created 3D structural models with the observed facets using the Rhodius software² (Figure S6). It should be noted here that the experimentally observed facets are mostly truncated and in some cases may contain other high index facets. Power spectrum of

horizontally aligned NR was also in good agreement with the orthorhombic Pd₂Sn phase and confirmed the growth direction of the Pd₂Sn NR as [010].

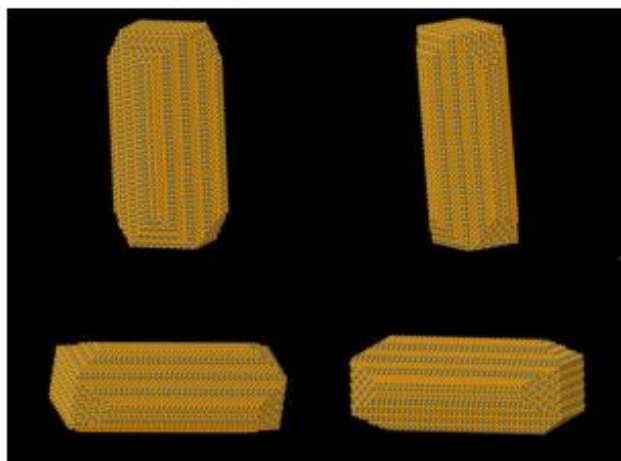


Figure S6 Additional images of the 3D structural model of a Pd₂Sn NR.

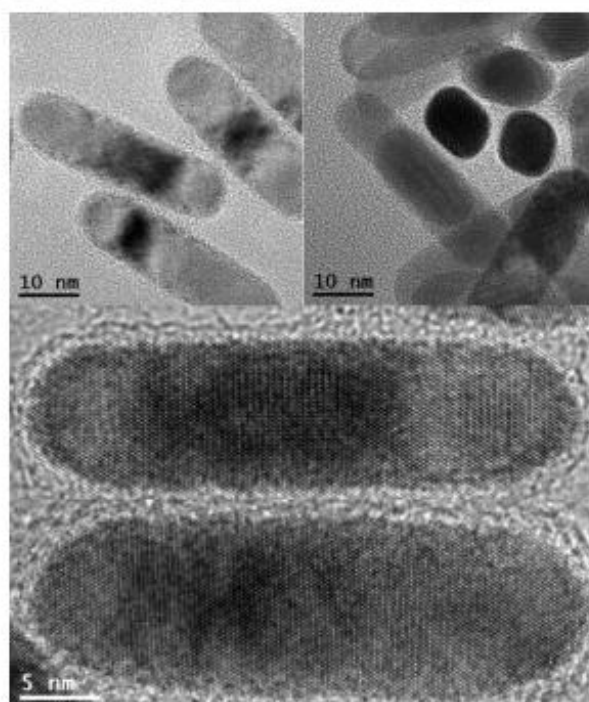
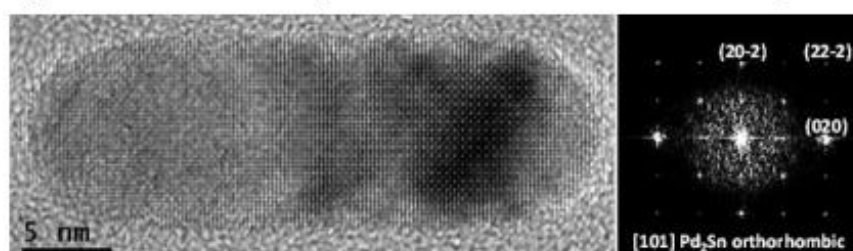


Figure S7 Additional HRTEM micrographs of orthorhombic Pd₂Sn NRs.

Figure S8 shows a HRTEM micrograph revealing the presence of mostly single crystalline nanoparticles, where the presence of several twinned nanoparticles is also observed. Detail of the red squared nanoparticle and its corresponding power spectrum (FFT) are presented on the right. The power spectrum

reveals that this 4.5 nm nanoparticle is composed of an orthorhombic Pd₂Sn phase (space group Pnma) with lattice parameters of a = 0.5635 nm, b = 0.4283 nm and c = 0.8091 nm and it is visualized along its [010] zone axis. The phase is in good agreement with the previously studied Pd₂Sn nanorods.

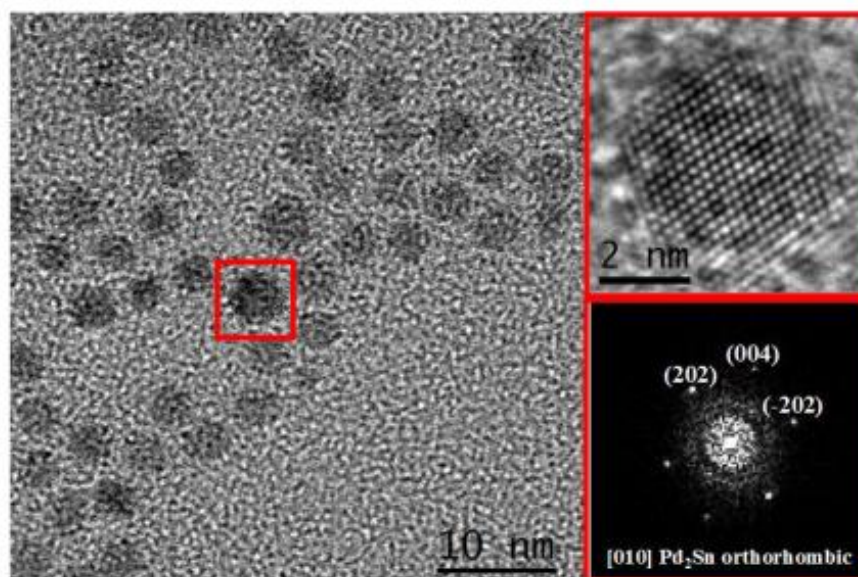


Figure S8 HRTEM micrograph showing several nanoparticles, detail of the red squared nanoparticle and its corresponding power spectrum.

4. Summary of synthesis conditions of samples presented in figure 2

Table S1. Synthesis conditions and geometrical parameters of the Pd₂Sn NPs obtained

Sample	Pd(acac) ₂ (mmol)	Sn(acac) ₂ (mmol)	TOP (ml)	OLA (ml)	Cl- precursor	Cl content (mmol)	Length (nm)	Width (nm)	Aspect Ratio (nm)
a	0.075	0.025	0.25	5	-----	0	$\delta=4.3 \pm 0.2$		1
b	0.075	0.025	0.25	5	HDA·HCl	0.15	9 ± 1	6.8 ± 0.6	1.3
c	0.075	0.025	0.25	5	HDA·HCl	0.18	15 ± 1	7 ± 1	2.1
d	0.075	0.025	0.25	5	MAH	0.2	24 ± 2	7 ± 1	3.4
e	0.075	0.025	0.5	5	HDA·HCl	0.2	44 ± 4	10 ± 2	4.4
f	0.075	0.025	0.25	5	HDA·HCl	0.25	98 ± 8	9 ± 1	10.8
g	0.075	0.025	0.50	5	HDA·HCl	0.5	130 ± 10	24 ± 4	5.4
h	0.075	0.025	0.25	5	HDA·HCl	0.5	290 ± 20	12 ± 3	24.2

5. Control experiments

To understand the role of each compound in the reaction mixture, a series of control experiments was carried out. We observed that the presence of chlorine ions and TOP was essential to obtain Pd₂Sn NRs.

In the absence of any of these two compounds, no NRs were produced. As a source of chlorine ions, we initially tested the use of CHCl_3 . The addition of chloroform in the reaction mixture containing an amine resulted in elongated Pd_2Sn NPs, but repetitivity was very poor due to a lack of control on the chlorine ion concentration in solution. In this regard, chloroform decomposes to give a number of chlorine substituted organic compounds (mostly C_2Cl_4 , C_2HCl_3 , etc.) and HCl as a main product.³ Subsequently, HCl reacts with amine to provide the chlorine ions. Note that the yield of CHCl_3 decomposition to HCl is quite low at relatively high temperatures, although CHCl_3 decomposition can be catalyzed by the presence of the small Pd_2Sn NPs. Instability of the Ar flow rate adds an additional uncertainty in the final hydrochloride concentration and thus the corresponding amount of chlorine ions present in the solution. A much more convenient strategy to introduce controlled amounts of chlorine ions was the addition of amine hydrochlorides. Different amine hydrochlorides were prepared as detailed in the previous section. The introduction of controlled amounts of amine hydrochloride allowed a precise control of the NR dimensions with a relatively high repetitivity from batch to batch. It should be pointed out that we observed no large differences on the results obtained using different amine hydrochlorides as chloride sources.

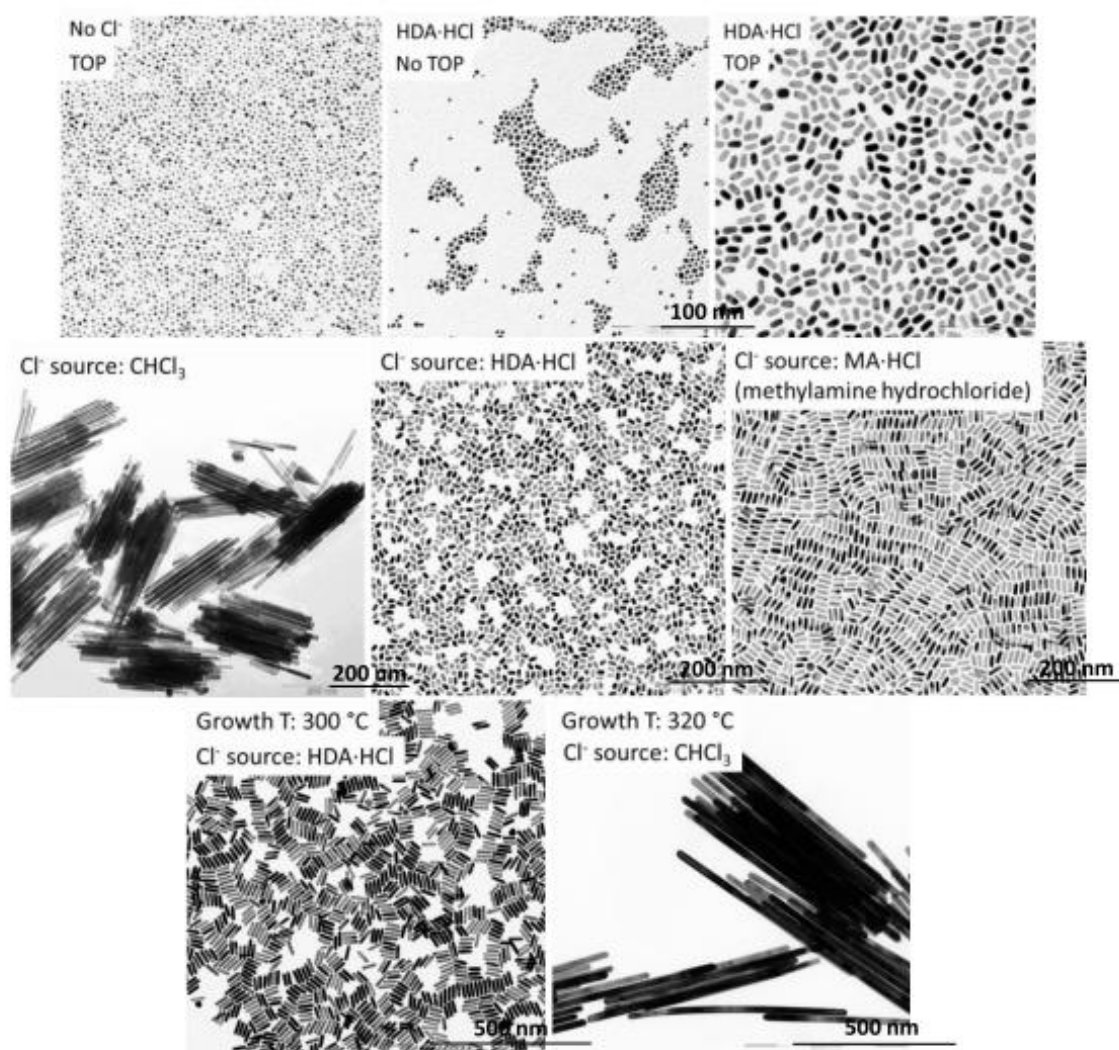


Figure S9 TEM micrographs of the Pd_2Sn NPS obtained from the control experiments. In each TEM image the parameter changed with respect to the standard Pd_2Sn NR synthesis conditions is pointed out.

The reaction temperature also played an important role in the control of the size of the NRs obtained. Larger temperatures and chloroform as a chlorine ion source resulted in the largest NRs, 600 ± 65 nm x 32 ± 3 nm.

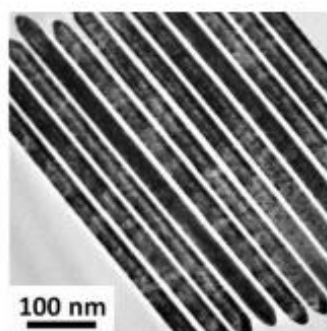


Figure S10 TEM micrograph of $\sim 600 \pm 60$ nm x 32 ± 3 nm Pd₂Sn NRs.

The use of OLA as a coordinating solvent systematically resulted in much better quality NP ensembles. As pointed out before, the presence of amines was also key to introduce chlorine ions when using CHCl₃ as the chlorine source. Thus the use of absolutely no amines resulted in spherical nanoparticles (Fig. S11).

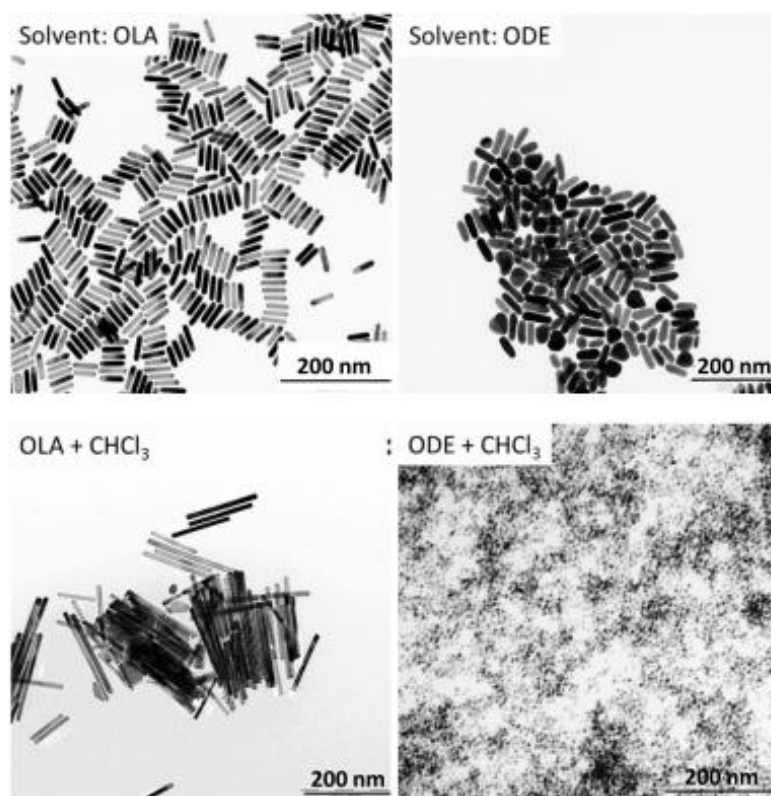


Figure S11 TEM micrographs of the Pd₂Sn NPs obtained from control experiments. Noted in each TEM image the parameter changed with respect to the standard Pd₂Sn NR synthesis conditions.

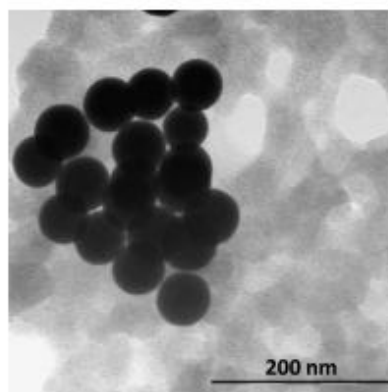


Figure S12 TEM micrograph of the Pd NPs obtained when no $\text{Sn}(\text{acac})_2$ and $\text{HDA}\cdot\text{HCl}$ were added.

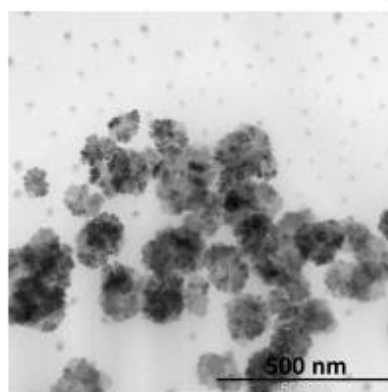


Figure S13 TEM micrograph of the NPs obtained when no $\text{Pn}(\text{acac})_2$ and $\text{HDA}\cdot\text{HCl}$ were added.

Note Pd/Sn ratio: Different ratios of Pd/Sn precursor did not allow to control composition or crystallographic phase of the nanoparticles. The only effect we observed is that highest monodispersity was obtained when Pd-complex concentration was higher than the stoichiometric amount.

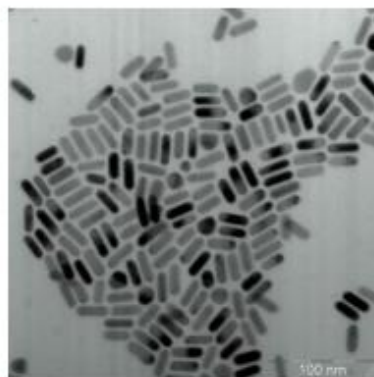


Figure S14 TEM micrograph of the NPs obtained for Pd/Sn ratio equal to 2.

6. Ligand exchange with mercaptopropionic acid

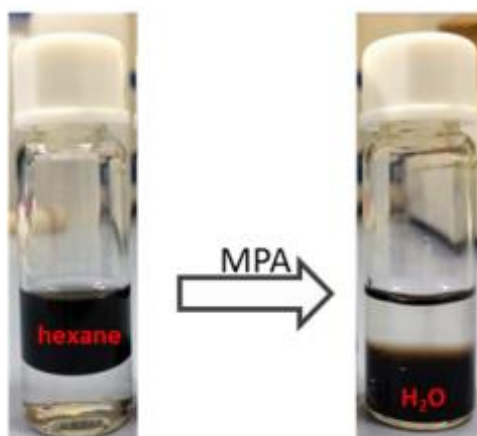


Figure S15 Picture of the solution of Pd₂Sn NRs before and after the MPA treatment.

7. Estimation of nanorods and nanospheres concentration in NPs/ml

Concentrations of NPs per ml were estimated considering the NPs geometry and the density for bulk Pd₂Sn and Pd. NRs geometry was approximated as cylinders. The length and radius of the cylinder were obtained from TEM analysis and correspond to the length and the half width of the NR respectively. In the case of spheres, the radius was also estimated by means of TEM analysis

Pd₂Sn NRs volume (V) is $V_{NR} = L \pi r^2$, where r is the radius and L is the length. Pd and Pd₂Sn nanospheres (NE) volume: $V_{NE} = 4/3 \cdot \pi \cdot r^3$, where r is radius.

To estimate the amount of NPs (n) in a certain mass we used the values provide in literature for the density (ρ) of Pd₂Sn and Pd: $n = m / \rho \cdot V$.

8. P-nitrophenol reaction

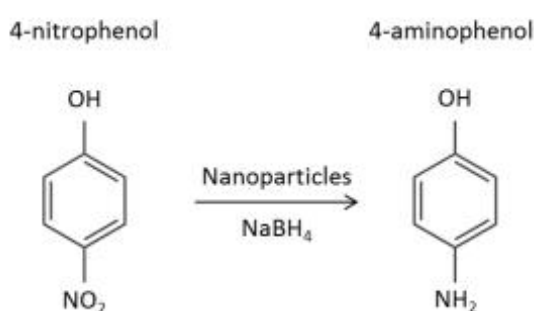


Figure S16 Scheme of the p-nitrophenol reaction

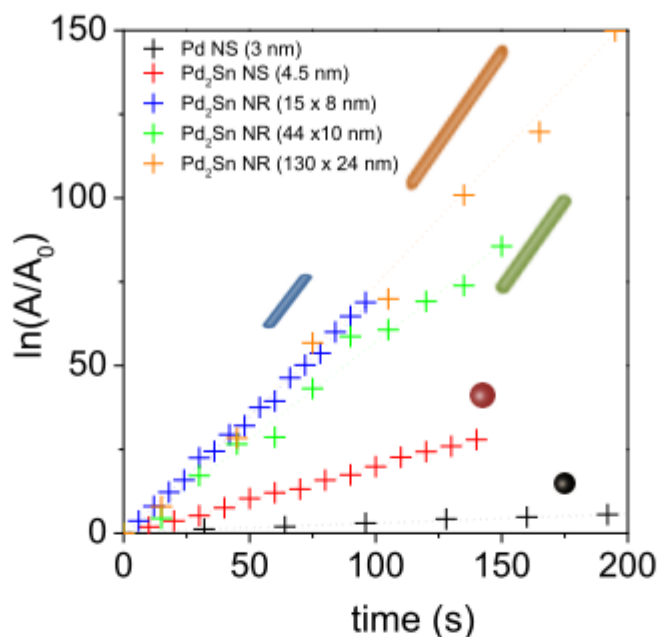


Figure S17 Sodium borohydride-driven degradation of *p*-nitrophenol over 3.0 nm Pd (black) and 4.3 nm Pd₂Sn spheres, 15 nm x 8 nm Pd₂Sn NRs, 44 nm x 10 nm Pd₂Sn NRs and, 130 nm x 24 nm Pd₂Sn NRs.

9. Water denitration

A general mechanism for nitrate reduction in aqueous solution⁴ is shown in Figure S13:

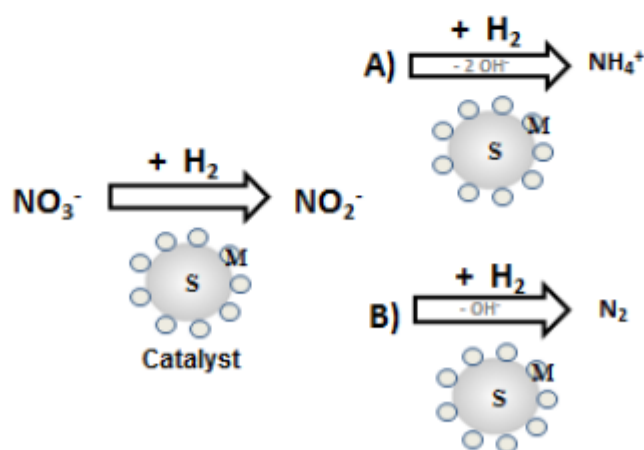


Figure S18 Mechanism of nitrate reduction by catalyzed hydrogenation to final product A) Ammonia and/or B) Nitrogen. The letter S represents the support of the catalyst, and the M, its metal phase.

In the pathway of nitrate reduction into nitrogen by hydrogenation, it is accepted that nitrite is obtained as an intermediate and ammonia as a by-product if the reaction is over-hydrogenated.

Figure S19 shows the percentage of nitrate conversion and the selectivity to N_2 , NO_2^- and NH_4^+ obtained after 24 hours of reaction. The 5% wt $Pd_2Sn/P25$ NRs catalyst showed around three times higher nitrate conversion than the NPs. Moreover, the selectivity to nitrogen was higher for the Pd_2Sn NRs.

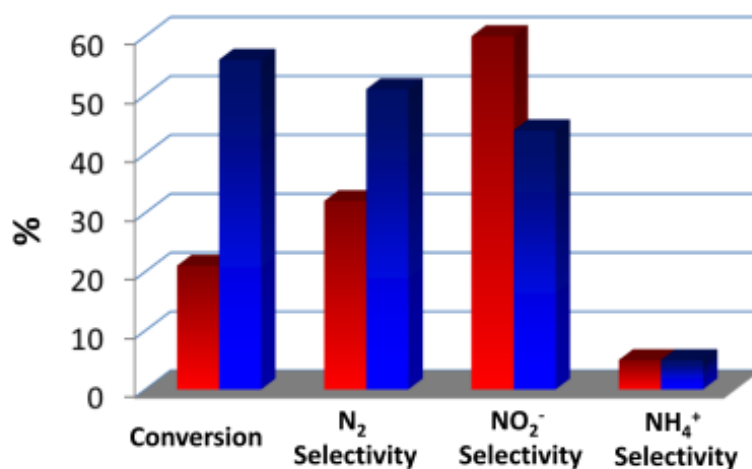


Figure S19 Nitrate conversion and selectivity towards nitrogen, nitrite and ammonia measured from $TiO_2:Pd_2Sn$ spherical NPs (red) and $TiO_2:Pd_2Sn$ NRs (blue), after 24 hours reaction.

Although the amount of nitrate obtained is under the legal limit (50 ppm), the European limits of drinking water for nitrite and ammonia are not reached (0.1 ppm and 0.5 ppm, respectively).⁵ Further optimization has to be done.

To determine the palladium dispersion (%) and metallic surface area (m^2/g) in each catalyst, hydrogen chemisorption studies were carried out with a Micromeritics ASAP 2010 equipment. The H/Pd hydrogen adsorption stoichiometry factor has been considered as 1,⁶ and the amount of catalyst sample introduced was 0.6 g. The study consisted on one cycle of Helium, two cycles of O_2 flow followed by two cycles of H_2 flow at 350 °C. Afterwards, the chemisorption analysis took place at 100 °C. Table 1 shows the hydrogen chemisorption results, which are so far under the expected values. It is concluded that Pd-Sn alloy formation strongly decreases the hydrogen adsorption over palladium.

In the main text, the reaction rates for nitrate removal per surface area unit were calculated taking into account the total surface area of the nanorods, not taking into account the support or a possible aggregation. Metal dispersion values were calculated using hydrogen chemisorption, but results obtained are a clear underestimation taking into account that the formation of the PdSn alloy inhibits hydrogen chemisorption.

Table 2 Hydrogen chemisorption results for 5% wt Pd₂Sn NPs and 5% wt Pd₂SnNRs.

Catalyst	Metal (%)		Metal Dispersion (%)	Metallic Surface Area (m ² /g)		Volume of H ₂ adsorbed (cm ³ /g catalyst STP)
	Pd	Sn		Sample (m ² /g sample)	Metal (m ² /g Metal)	
NPs	3	2	0.1604	0.0214	0.7148	0.010140 ± 0.004332
NRs	3	2	0.3731	0.0499	1.6622	0.000280 ± 0.000039

10. References

- (1) Barnard, A. S.; Osawa, E. *Nanoscale* **2014**, *6*, 1188-1194.
- (2) Bernal, S.; Botana, F. J.; Calvino, J. J.; López-Cartes, C.; Pérez-Omil, J. A.; Rodríguez-Izquierdo, J. M. *Ultramicroscopy* **1998**, *72*, 135-164.
- (3) (a) Semeluk, G. P.; Bernstein, R. B. *J. Am. Chem. Soc.* **1954**, *76*, 3793-3796; (b) Semeluk, G. P.; Bernstein, R. B. *J. Am. Chem. Soc.* **1957**, *79*, 46-49.
- (4) Hörold, S.; Vorlop, K. D.; Tacke, T.; Sell, M. *Catal. Today* **1993**, *17*, 21-30.
- (5) Council, T. H. E.; The, O. F.; Union, E. *Off. J. Eur. Communities* **1998**, *L 330*, 32-54.
- (6) Berndt, H.; Mönnich, I.; Lücke, B.; Menzel, M. *Appl. Catal., B- Environ.* **2001**, *30*, 111-122.

3.1.3 Pd₂Sn nanorods as Highly Active and Stable Catalyst for Ethanol Oxidation Reaction

This article with title “Pd₂Sn [010] Nanorods as a Highly Active and Stable Ethanol Oxidation Catalyst” is a submitted to Journal of Materials Chemistry A, currently under review with major corrections required. This work is about to study Pd₂Sn NRs as electrocatalyst for EOR, detail information is presented in the end of this section. In this work, the superior EOR catalytic properties were observed using Pd₂Sn NRs as anode electrocatalyst for EOR in alkaline medium. We demonstrated an effective approach to remove organic ligands with hydrazine hydrate treatment. We also demonstrated the organic-free Pd₂Sn NRs with tuned size and aspect ratio exhibited improved EOR performance and durability while comparing with Pd₂Sn nanospheres and Pd NPs electrocatalysts. Pd₂Sn NRs provided 3 fold higher peak current densities than spherical Pd₂Sn NPs, a 10 fold increase over Pd NPs. We presented DFT analysis results in showing (100) and (001) facets of orthorhombic Pd₂Sn to be more favourable for EOR than (010). The stability measurements exhibited NRs was a more effect electrocatalysts in potential practical application in direct alcohol fuel cells. Figure 3.5 shows that summary of TEM images of different aspect ratio of Pd and Pd₂Sn NPs, FTIR spectrum of before and after Pd₂Sn NRs ligand removed and performance EOR of Pd₂Sn and Pd NPs.

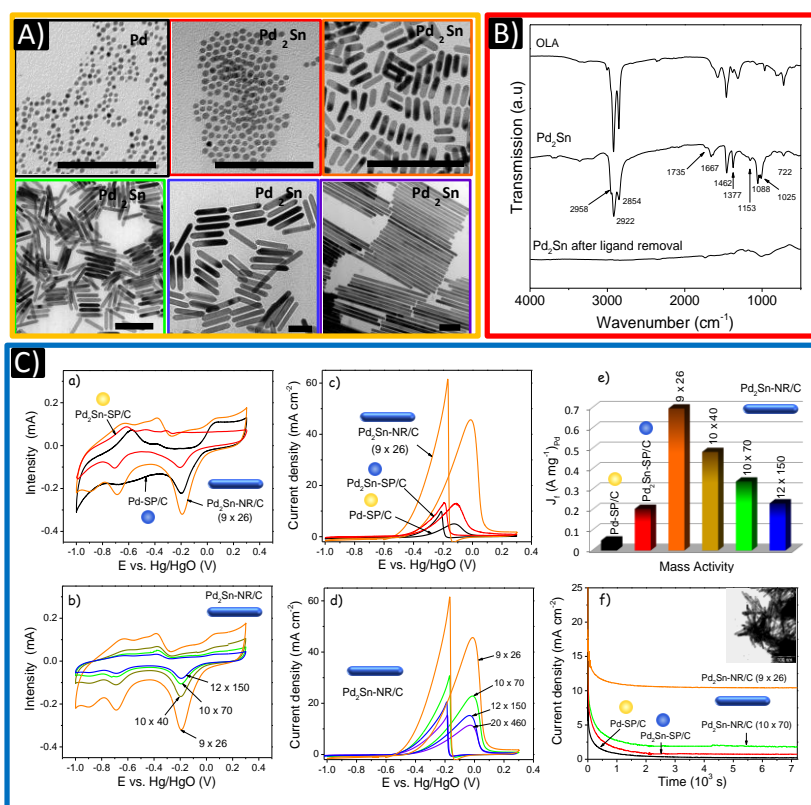


Figure 3.5 A) TEM micrographs of Pd₂Sn NPs with different aspect ratios. B) FTIR spectra of before and after of removing ligand of Pd₂Sn NRs. C) Performance EOR of Pd₂Sn and Pd NPs including cyclic voltammetric and chronoamperometric in 0.5 M KOH and 0.5 M KOH + 0.5 M ethanol solution.

Pd₂Sn [010] Nanorods as a Highly Active and Stable Ethanol Oxidation Catalyst

Zhishan Luo,^{a,†} Jianmin Lu,^{b,†} Cristina Flox,^{a,*} Raquel Nafria,^a Aziz Genç,^c Jordi Arbiol^{c,d}
Jordi Llorca,^c Maria Ibáñez,^a Joan Ramon Morante^{a,f}, Andreu Cabot^{a,d,*}

Received 00th January 20xx,
Accepted 00th January 20xx

DOI: 10.1039/x0xx00000x

www.rsc.org/

The development of highly active, low cost and stable electrocatalysts for direct alcohol fuel cell remains as a critical challenge. While Pd₂Sn has been reported as an excellent catalyst for the ethanol oxidation reaction (EOR), here we present DFT analysis results showing (100) and (001) facets of orthorhombic Pd₂Sn to be more favourable for EOR than (010). Accordingly, using tri-*n*-octylphosphine, oleylamine (OLA) and methylamine hydrochloride as size and shape directing agents, we produced colloidal Pd₂Sn nanorods (NRs) grown on the [010] direction. Such Pd₂Sn NRs, supported on graphitic carbon, showed excellent performance and stability as anode electrocatalyst for the EOR in alkaline medium, exhibiting 3-fold and 10-fold higher EOR current densities than that of Pd₂Sn and Pd nanospheres, respectively. We associate this improved performance with the favourable faceting of the NRs.

Introduction

Ethanol is a particular appealing fuel. Ethanol (24 MJ/L) has higher energy density than hydrogen (liquid, 8.5 MJ/L), methanol (15.6 MJ/L) or formic acid (6.4 MJ/L). It has a low toxicity, is safe to store due to its relatively high boiling point and it can be bio-sourced by fermentation of sugar- or cellulose-containing compounds.¹⁻⁶ Therefore, direct ethanol fuel cells (DEFCs), with low operation temperature operation, high potential energy density, and safe storage and operation, are considered as one of the main candidate technologies to supply electric power in electric vehicles and portable electronics.⁷ However, several limitations still hinder the large scale implementation of DEFCs, most of them being related to the ethanol oxidation electrocatalyst. Current electrocatalysts for the ethanol oxidation reaction (EOR) show relatively slow kinetics and low stability associated with the poisoning of the surface active sites. The use of alkaline media represents an advantage in these two directions. Compared with acid electrolytes, alkaline solutions

provide faster reaction kinetics for both alcohol oxidation and oxygen reduction, enabling use of less expensive catalysts or higher efficiencies in the use of precious metals, easier electrolyte management and a wider fuel product selection.^{6,8-11} Pt has been widely used as the most active electrocatalysts for DEFC.¹²⁻¹⁷ However, its scarcity and related high price limits the cost-effectiveness of this technology. Recently, increasing attention has been paid to less expensive Pd and Pd-based compounds which show comparable or even better electrocatalytic activities than Pt-based catalysts for alcohol oxidation.¹⁸⁻²⁰ Specifically, alloying Pd with elements such as Sn,²¹⁻²⁴ Co,²⁵ Cu^{26, 27} or Bi²⁸ is effective in increasing electrocatalytic activity and CO tolerance, particularly for the EOR.

Currently, electrocatalysts are mainly produced by the impregnation, electrodeposition or evaporation of one or several active phases on a large surface support. These methodologies provide very limited control over the size, shape and distribution of the different phases, which generally makes the development of new catalysts a slow trial and error process, especially in structural sensitive reactions such as EOR. Alternatively, colloidal synthesis routes and bottom-up assembly procedures allow an unmatched precise tuning over material properties at the nanometer scale. Moreover, such control of material parameters at its lowest organization level does not require high capital cost equipment or extremely complex procedures, but can be reached using high-throughputs and high yield chemical routes at ambient pressure and low temperature. The huge potential of such solution-based strategies to tune material properties resides in the ability to chemically manipulate material formation, from the very initial

^a Catalonia Institute for Energy Research-IREC, 08930 Sant Adrià del Besos (Barcelona), Spain. Email: cflox@irec.cat, acabot@irec.cat.

^b State Key Laboratory of Catalysis, Dalian National Laboratory for Clean Energy, Dalian Institute of Chemical Physics, Chinese Academy of Sciences, Dalian 116023, China.

^c Catalan Institute of Nanoscience and Nanotechnology (ICN2), CSIC and The Barcelona Institute of Science and Technology (BIST), Campus UAB, Bellaterra, 08193 Barcelona, Spain

^d ICREA, Pg. Lluís Companys 23, 08010 Barcelona, Spain.

^e Institut de Tècniques Energètiques, Universitat Politècnica de Catalunya, 08028 Barcelona, Spain

^f Departament d'Electrònica, Universitat de Barcelona, 08028 Barcelona, Spain.

† These authors contributed equally.

combination of atoms into cluster to the growth of nanometer scale entities. Chemical manipulation is accomplished through the use of surfactants, which regulate the incorporation of atom/ions at each surface site by locally determining surface energy and charge. This strategy allows huge amounts of colloidal nanoparticles (NPs) to simultaneously nucleate and grow, all evolving at the same rate in the same conditions. Thus, massive amounts of particles with precisely tuned properties can be produced in a simple, fast and cost-effective manner. Colloidal synthesis routes are also extremely versatile, allowing production of elemental, multinary and heterostructured NPs with metallic, semiconductor, magnetic, plasmonic, etc. character and with unmatched composition, size, shapes and phases control.²⁹⁻³⁷

In the present work, using DFT calculations, we show the (100) and (001) facets of orthorhombic Pd₂Sn to be more favorable for EOR than (010). We subsequently produce colloidal Pd₂Sn NRs grown on the [010] direction and assess their electrocatalytic performance as anode EOR electrocatalyst for DEFC in alkaline medium, comparing it with that of Pd₂Sn and Pd spherical NPs.

Experimental

Chemicals: Palladium (II) acetylacetonate (Pd(acac)₂, 99%), tin(II) acetate (Sn(OAc)₂), oleylamine (OLA, >70%), oleic acid (OA, 90%), methylamine hydrochloride (MAHC), hydrazine hydrate (N₂H₄, 50-60% in water) were purchased from Sigma Aldrich. Tri-n-octylphosphine (TOP, 97 %) was purchased from Strem. Hexane, chloroform and ethanol were of analytical grade and obtained from various sources. MilliQ water was supplied by the PURELAB flex from ELGA. All chemicals were used as received without further purification, except OLA, which was purified by distillation. All syntheses were carried out using standard airless techniques: a vacuum/dry argon Schlenk line was used for the syntheses and an argon glove-box for storing and handling sensitive chemicals.

Pd₂Sn NRs: Pd₂Sn NRs were prepared following the protocol we previously reported with slight modifications.²⁴ Briefly, 20 mL of OLA, a certain amount of MAHC, 0.3 mmol of Pd(acac)₂ and 0.15 mmol Sn(OAc)₂ were placed in a 100 mL four-neck flask and purged under argon flow for 30 minutes at 60 °C. Then 1 mL of TOP was injected into the solution was heated to 200 °C in 10 min and kept for 30 min. Then, the temperature was further increased to 300 °C in 40 min and maintained for additional 30 min. Finally, the solution was cooled to room temperature. Pd₂Sn NPs were collected by centrifuging and washing with ethanol and chloroform. When different amount of MAHC was used, different size and aspect ratio of NRs were obtained.

Pd₂Sn and Pd spherical NPs were also produced following previously reported procedures with slight modifications.²⁴ Briefly, Pd₂Sn spherical NPs were obtained by mixing 20 mL of OLA, 0.3 mmol of Pd(acac)₂, 0.15 mmol of Sn(OAc)₂ and 1 mL of TOP under argon flow but without MAHC. The rest of the procedure was the same as that used to produce Pd₂Sn NRs. Pd spherical NPs were prepared by mixing OLA, Pd(acac)₂ and TOP under argon flow but without

Sn(OAc)₂ and MAHC precursors, then setting the growth temperature to 200 °C and growth time to 30 min.

Organic ligand removal: Pd₂Sn NPs dispersed in hexane (~50 mg in 5 ml) were mixed with an equal volume fraction of a 1 M hydrazine hydrate aqueous solution to form two phase system. The mixture was stirred until the black NPs turned into aqueous phase. NPs were collected by centrifugation and washed with hexane and ethanol.

Characterization: Size and shape of initial NPs were examined by transmission electron microscopy (TEM) using a ZEISS LIBRA 120, operating at 120 kV. Structural and compositional properties of the nanocomposites were also examined under TEM. High resolution TEM (HRTEM) studies were conducted using a field emission gun FEI™ Tecnai F20 microscope at 200 kV with a point-to-point resolution of 0.19 nm. Scanning electron microscopy (SEM) analysis was done in a ZEISS Auriga SEM with an energy dispersive X-ray spectroscopy (EDS) detector at 20 kV to study the composition of nanoparticles. For SEM characterization, NPs were dissolved in chloroform and were drop casted on silicon substrates. Powder X-ray diffraction (XRD) patterns were collected directly from the as-synthesized NPs dropped on Si(501) substrate on a Bruker AXS D8 Advance X-ray diffractometer with Ni-filtered (2 μm thickness) Cu K radiation (λ = 1.5406 Å) operating at 40kV and 40mA. A LynxEye linear position-sensitive detector was used in reflection geometry. X-ray photoelectron spectroscopy (XPS) was done on a SPECS system equipped with an Al anode XR50 source operating at 150 mW and a Phoibos 150 MCD-9 detector. The pressure in the analysis chamber was always below 10⁻⁷ Pa. The area analyzed was about 2 mm × 2 mm. The pass energy of the hemispherical analyzer was set at 25 eV and the energy step was set at 0.1 eV. Data processing was performed with the CasaXPS program (Casa Software Ltd., UK). Binding energy (BE) values were centered using the C 1s peak at 284.8 eV. The atomic fractions (%) were calculated using peak areas normalized on the basis of acquisition parameters after background subtraction, experimental sensitivity factors and transmission factors provided by the manufacturer. Fourier transform infrared spectroscopy (FTIR) was measured on Alpha Bruker FTIR spectrometer with a platinum attenuated total reflectance (ATR) single reflection module. FTIR data were typically averaged over 64 scans.

Electrochemical measurements: All electrochemical measurements were performed at room temperature in a standard three-electrode cell using a rotating disc electrode from Pine Instruments connected to a Bio-Logic VMP-3 multipotentiostat controlled by EC-lab software. A Pt foil and Hg/HgO (1 M KOH) were used as counter and reference electrode, respectively. The working electrode was prepared using a glassy carbon (GC) disc measuring 5 mm in diameter, which was previously polished with diamond (1 μm) and alumina (0.05 μm), sonicated for 10 min and washed with deionized water. Catalytic electrodes were produced by drop-casting 10 μL of a 2 mg/ml suspension of NPs in deionized water on the GC. To immobilize the Pd or Pd₂Sn NPs on the GC, 10 μL of 0.5 wt% Nafion was dropped on the surface electrode. The background was obtained by cyclic voltammetry (CV) in an Argon-purged aqueous

solutions of 0.5 M KOH without ethanol solution from -1 to 0.3 V vs. Hg/HgO at 50 mV s⁻¹ and 1000 rpm. The electrochemically active surface areas (ECSA) were evaluated from integration of the charges during PdO reduction in the cathode scan, assuming a value of 405 μC/cm² for the reduction of PdO monolayer. Electrochemical activity of the Pd- and PdSn-based catalysts was conducted in 0.5M KOH with 0.5M ethanol solution at the same condition. The chronoamperometric (CA) analysis was conducted at -0.1 V during 2 hour in 0.5 M ethanol/0.5 M KOH electrolyte in order to elucidate the stability of the NPs. The quasi-steady state polarization curves recorded at a sweep rate of 1 mV s⁻¹ by using the Linear Sweep Voltammetry (LSV) technique in 0.5M ethanol/ 0.5M KOH solutions were used to derive the Tafel plots. Current densities were calculated taking into account the geometrical area of the electrode (0.196 cm²). Electrochemical impedance spectroscopy (EIS) measurements were carried out from 100 kHz to 10 mHz with a 5 mV Ac amplitude at -0.4 and -0.1 V.

DFT calculations: All DFT calculations were performed using the Vienna Ab Initio Simulation Package (VASP),^{38,39} a periodic plane-wave-based density functional theory (DFT) package. The electron-ion interactions were described by the projector-augmented wave method (PAW).⁴⁰ The exchange correlation energy has been calculated within the generalized gradient approximation by the Perdew-Burke-Ernzerhof formulation (GGA-PBE).^{41,42} The kinetic

energy cutoff of plane-wave basis sets was fixed to 400 eV for all calculations. Dispersion (van der Waals forces) corrections were included by the DFT-D3 methodology.⁴³ The lattice constants of bulk orthorhombic Pd₂Sn were calculated to be a=5.616 Å, b=4.333 Å, c=8.203 Å, which are in reasonable agreements with experimental values (a=5.635 Å, b=4.283 Å, c=8.091 Å).²⁴ These lattice constants are used to construct 3 periodic Pd₂Sn slabs ((010), (001) and (100) surfaces) the parameters of which are listed in table 1. For each slab, 15 Å of vacuum layer was added to mitigate the interactions between the slab and its periodic replica. For the 3 slabs, the bottom half atomic layers were fixed to their optimized bulk configuration during all computations, and the top half atomic layers and surface intermediates are fully relaxed. All atomic coordinates of the adsorbates and the atoms in the relaxed layers were optimized to a force of <0.03 eV/Å on each atom. All self-consistent field calculations were converged to 1×10⁻⁵ eV. Brillouin zone integration was performed with a Methfessel-Paxton smearing order of 2 with a broadening of 0.2 eV. The adsorption energy of ethanol, E_{ads}, was calculated by the following equation:

$$E_{\text{ads}} = E_{\text{slab+ethanol}} - E_{\text{slab}} - E_{\text{ethanol(g)}}$$

where E_{slab+ethanol} is the total energy of the slab with an ethanol bound to it, E_{slab} is the total energy of the clean Pd₂Sn slab, and E_{ethanol(g)} is the total energy of ethanol in gas phase.

Table 1. Parameters of 3 Pd₂Sn surface slabs for the DFT calculations. The (010), (001) and (100) slabs are orthorhombic.

Surface	Periodicity	a (Å)	b (Å)	c (Å)	Pd atoms	Sn atoms	k-point mesh
(010)	1×1×2	8.203	5.616	21.500	16	8	5×7×1
(001)	1×1×2	11.230	8.667	22.305	32	16	3×4×1
(100)	2×1×1.5	8.667	8.203	22.733	24	12	4×5×1

Results and discussion

While the mechanism of electrochemical oxidation of ethanol is still controversial, it is generally accepted that the first step involves the dissociative adsorption of ethanol on the catalyst surface aided by hydroxide groups.^{6,44-47} We carried out a DFT investigation of the interaction between the ethanol molecule and different Pd₂Sn surfaces to understand the role of Pd and Sn and different facets on this reaction. Figure 1 shows the ethanol adsorption configurations on Pd₂Sn (001), (010) and (100) surfaces. The adsorption energies of ethanol (E_{ads}) on Pd, obtained for each surface were -0.52, -0.45 and -0.51 eV for Pd₂Sn (001), Pd₂Sn (010) and Pd₂Sn (100), respectively. The corresponding E_{ads} of Sn were -0.35, -0.42 and -0.45 eV, respectively. The higher absolute values of E_{ads} on Pd indicate that ethanol molecules prefer to adsorb on Pd atom instead of Sn, in which cases, the O atom of ethanol binds on top of Pd atoms. However, the presence of Sn clearly changes E_{ads} of Pd by means of an electronic and also geometrical effect. Our DFT results also show that among the studied surfaces and taking into account just the first ethanol adsorption step, the (001) and (100) are more favorable for EOR than the (010). We also investigated the OH⁻ adsorption on the different elements and

facets. DFT calculations showed that OH⁻ preferentially adsorbs on Sn atoms at (001) and (100) facets, with E_{ads} values -2.91 and -2.92, respectively. E_{ads} on Sn at a (010) facet was just -2.83 and E_{ads} on Pd sites ranged from -2.61 for (010) to -2.27 and -2.25 for (001) and (100) facets, respectively.

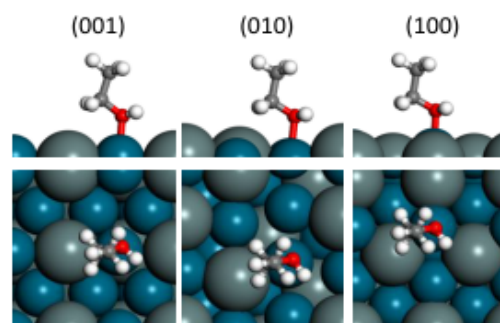


Figure 1. Side (upper panel) and top view (lower panel) of preferred adsorption structure of ethanol on Pd atoms over the Pd₂Sn (001), Pd₂Sn (010) and Pd₂Sn (100) surfaces. Blue and dark silver spheres represent Pd and Sn atoms, respectively.

Figure 2a and 2c show representative TEM micrograph and size distribution histograms of 4 nm spherical Pd NPs, 5 nm spherical Pd₂Sn NPs and different aspect ratio Pd₂Sn NRs produced following the above detailed procedure.²⁴ Pd₂Sn NRs were synthesized from the reaction of Pd(acac)₂ and Sn(OAc)₂ in the presence of OLA, TOP

and MAHC.²⁴ Increasingly larger sizes and aspect ratios were obtained by increasing the amount of MAHC added: 9 nm x 26 nm (0.85 mmol MAHC); 10 nm x 70 nm (0.95 mmol MAHC); 12 nm x 150 nm (1.8 mmol MAHC); 20 nm x 460 nm (2.75 mmol MAHC).

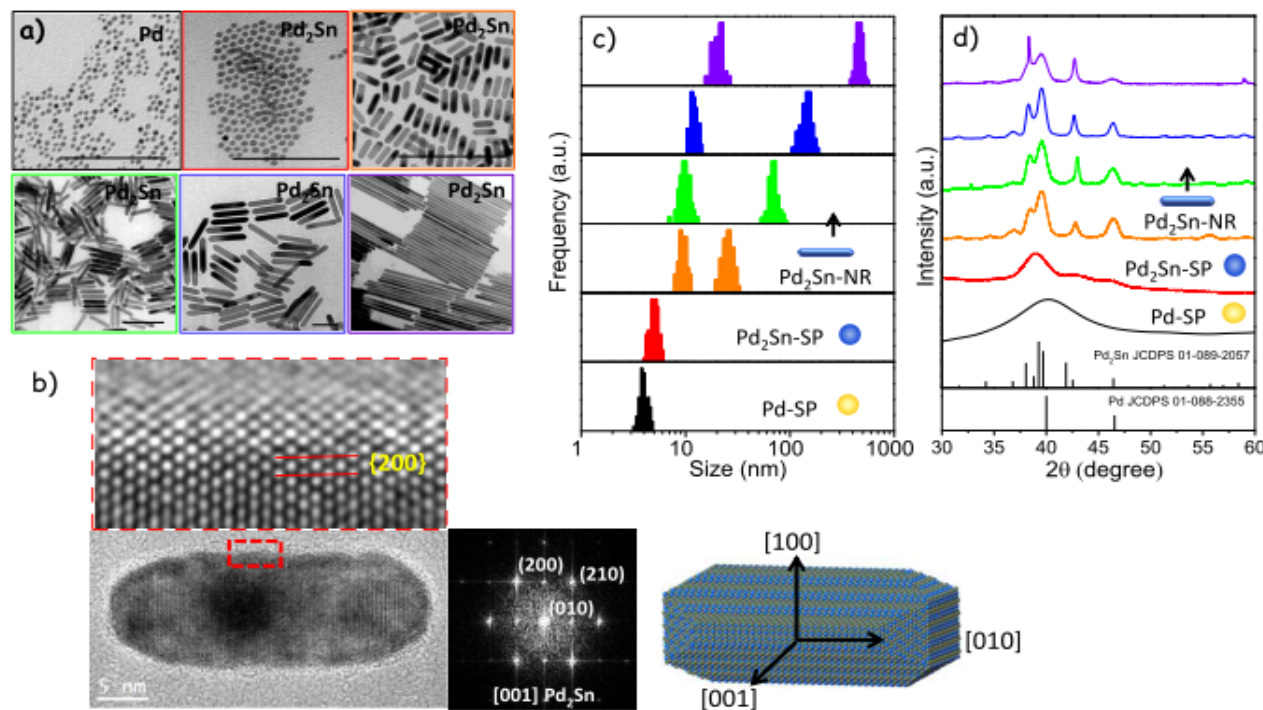


Figure 2. a) Representative TEM micrographs of spherical Pd NPs (4 nm), spherical Pd₂Sn NPs (5 nm) and Pd₂Sn NRs with different sizes: 9 nm x 26 nm; 10 nm x 70 nm; 12 nm x 150 nm; 20 nm x 460 nm. b) HRTEM micrograph of a Pd₂Sn NR visualized along the [001] axis and its corresponding power spectrum, which shows that it has the orthorhombic Pd₂Sn phase. An atomic model of a Pd₂Sn NR is also displayed. c) Size distribution histograms of the same samples; d) XRD patterns including reference patterns for Pd (JCPDS 01-088-2355) and Pd₂Sn (JCPDS 01-089-2057).

HRTEM analysis showed Pd₂Sn NRs to be crystalline with an orthorhombic structure (space group Pnma) with $a = 0.56 \text{ \AA}$, $b = 0.431 \text{ \AA}$ and $c = 0.812 \text{ \AA}$ and to grow along the [010] direction (Figure 2b). XRD analysis (Figure 1d) confirmed the Pd₂Sn NRs and spherical NPs to have the orthorhombic crystal structure (JCPDS 00-026-1297) and showed Pd NPs to have the cubic phase (JCPDS 01-088-2335). Within its experimental error, EDS analysis revealed metal ratios of Pd and Sn to be $[\text{Pd}]/[\text{Sn}] = 2.0 \pm 0.1$. On the contrary, XPS analysis systematically provided significantly higher Sn contents, $[\text{Pd}]/[\text{Sn}] = 1.25 \pm 0.05$, which pointed toward a partial surface segregation of Sn.

Figure 3 shows the Pd 3d and Sn 3d regions of the XPS spectrum of Pd₂Sn NRs. Pd 3d peaks could be deconvoluted into a pair of doublets, pointing to the presence of two Pd chemical states. The main component, Pd⁰, appeared at binding energies of 335.6 eV (3d_{5/2}) and 340.9 eV (3d_{3/2}), which represents a positive shift of ~0.5 eV compared with Pd metal, at 335.1 eV (3d_{5/2}) and 340.4 eV

(3d_{3/2}). This result revealed that the electronic structure of Pd changed with the incorporation of Sn, which is a common observation considered to have a positive effect on catalytic activity by reducing the adsorption strength of poisonous intermediates.⁴⁸ On the other hand, the minority Pd²⁺ state provided peaks located at 337.6 eV (3d_{5/2}) and 342.9 eV (3d_{3/2}). In addition, three pairs of doublets were fitted to the Sn 3d binding energy region. The peaks at 488.4 eV (3d_{5/2}), and 496.8 eV (3d_{3/2}), were associated to Sn⁴⁺, the stronger peaks at 486.3 eV (3d_{5/2}), and 494.9 eV (3d_{3/2}), could be associated with Sn²⁺, and the minority component at 484.8 eV (3d_{5/2}) and 493.3 eV (3d_{3/2}) corresponded to metallic Sn. Thus Sn atoms on the Pd₂Sn NR surface appeared to be significantly oxidized as commonly observed in previous works on Sn-based alloys.^{21, 49}

Control over NP size and shape rely on the use of organic ligands adjusting surface energy and providing stability in solution. Such ligands may block catalytic active sites and hinder charge transfer, thus they must be removed before testing the material

electrocatalytic performance.^{50, 51} Several strategies have been proposed to clean colloidal NP surfaces, including the ligand decomposition by means of a thermal annealing⁵² or UV-ozone irradiation, surface etching and ligand exchange procedures.⁵³ In the present work, to remove the loosely bond OLA from the NP surface, NPs were suspended in a hydrazine hydrate aqueous/hexane two phase mixture. After shaking, the NPs moved into the polar phase leaving surfactants in the organic phase, as confirmed by FTIR analysis (Figure 4).

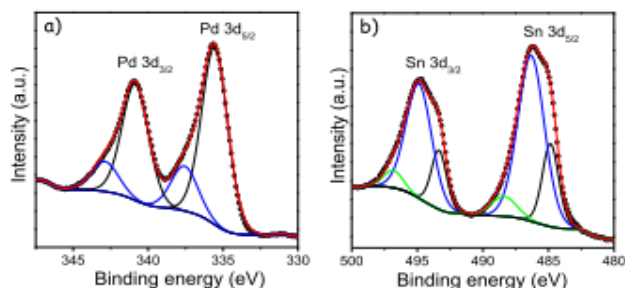


Figure 3. Pd 3d and Sn 3d regions of the XPS spectrum of Pd₂Sn NRs.

For electrocatalytic measurements, Pd and Pd₂Sn NPs were supported on GC. CV of the electrocatalysts prepared from Pd and Pd₂Sn spheres (Pd-SP/C, Pd₂Sn-SP/C) and from Pd₂Sn NRs (Pd₂Sn-NRs/C) was first investigated in 0.5 M KOH without ethanol (Figure 5a,b). All NPs showed similar voltammetric profiles, although small differences in relevant regions of the voltammograms were observed. The peaks in the region between -0.6 V and -0.8 V vs. Hg/HgO are attributed to the absorption/adsorption and desorption of hydrogen. In the anodic sweep, the cyclic voltammetry of Pd₂Sn-NRs/C shows two peaks centered in -0.65 V and -0.41 V vs. Hg/HgO, attributed to the desorption of weakly and strongly bond hydrogen, respectively.

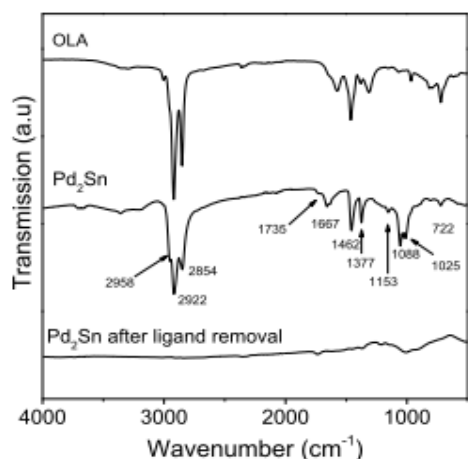


Figure 4. FTIR spectra of OLA and Pd₂Sn NRs before and after ligand removal.

Moving to higher potentials, oxidation peaks associated to the formation of surface oxides appeared (from -0.4 to 0.1 V vs. Hg/HgO). Subsequently, oxide reduction peaks showed up during the negative scans (from 0 to -0.4 V vs. Hg/HgO). Comparing the cathodic peak potentials of Pd₂Sn- and Pd-based electrocatalysts, Pd₂Sn-NR/C samples showed positive shifts, indicating that the electronic structure of Pd atoms on the Pd₂Sn surface had changed, as observed from XPS analysis. The electrochemically active surface area (ECSA) was estimated for all catalysts using the area over the voltammetry curve in the PdO_x reduction peak region (Table 2). ECSA values increased when decreasing the NR length in Pd₂Sn-NRs/C catalysts, consistently with the increase of surface area. Moreover, higher ECSA values were obtained for Pd-SP/C compared with most Pd₂Sn-based catalysts.

The EOR electrocatalytic activities were characterized by CV technique in a mixture of 0.5 M KOH and 0.5 M ethanol aqueous solution (Figure 5c,d). The hydrogen absorption-desorption peaks disappeared in presence of the ethanol due to the dominant adsorption of the ethanol in the low-potential region. All CVs yielded a pair of well-defined peaks characteristic for the ethanol electro-oxidation. In the anodic scan, the forward oxidation peak at around 0.0 V vs. Hg/HgO is assigned to the oxidation of freshly chemisorbed species derived from ethanol adsorption. The current density decrease at high potentials is associated to the oxidation of the Pd surface blocking the EOR electrocatalytic activity. During the reverse scan, the catalyst reactivates when reaching the Pd reduction potentials (around -0.2 V vs. Hg/HgO). While the forward peak is associated to the dehydrogenation and dissociative adsorption of ethanol, the oxidation peak in the reverse scan has an additional strong contribution from the oxidation of carbonaceous species.⁴⁶

To quantify the electrocatalytic performance, the redox onset potential (E_o), the forward oxidation current density peak (j_f), the potential at j_f (E_f), the backward anodic peak current (j_b) and the j_f/j_b ratio were determined (table 2). Lower overpotentials and much higher current densities were generally obtained for EOR in Pd₂Sn-based catalyst compared with Pd-SP/C. The overall EOR mechanism in alkaline media involves the reaction of ethanol with 4 OH⁻ groups to produce acetic acid and water. In Pd-based alloys, ethanol is generally accepted to adsorb at Pd sites. In Sn-based alloys, the formation of Sn(OH)_x increases the surface density of OH⁻ groups available for ethanol oxidation, enhancing in this way the electrocatalytic activity.²¹ On top of the alloying benefits, the rod geometry further reduced the overpotentials required, down to -0.47 V vs Hg/HgO for Pd₂Sn-SP/C (9 x 26 nm) as compared with -0.39 for Pd-SP/C, and increased the peak current densities, up to 45.6 mA·cm⁻² (9 x 26 nm) as compared with 5.0 mA·cm⁻² and 13.1 mA·cm⁻² for Pd-SP/C and Pd₂Sn-SP/C, respectively. The lower onset potential measured from Pd₂Sn NRs compared with spherical Pd₂Sn NPs suggests lower activation energy for ethanol oxidation at the facets of Pd₂Sn NRs. Nevertheless, as the NR size increased, the current density decreased due to a reduction of the surface-to-bulk ratio as the thickness of the NRs also increased with the length. A decrease of the overall concentration of NR tips, potentially

providing high activity sites, with the NR size increase may also contribute to the observed activity reduction. Overall the highest mass activity was obtained for the smallest Pd₂Sn NRs (9 x 26 nm Pd₂Sn-NRs/C), being 3-fold higher than Pd₂Sn-SP/C and close to 10-fold higher than Pd-SP/C (Table 2, Figure 5e).

Higher j_f/j_b ratios were obtained for all the Pd₂Sn-based catalysts when compared with Pd-SP/C, which is indicative of a more efficient oxidation of ethanol and less accumulation of carbonaceous species to the catalyst. The long-term stability of the electrocatalyst was determined by chronoamperometric techniques (Figure 5f) at -0.1 V vs Hg/HgO during 2 h. The current density of ethanol oxidation dropped quickly within the first seconds presumably due to the formation of strongly adsorbed intermediates onto the surface of reactive sites. After that, the current decreased slowly and reached a pseudo-steady state. Current densities decayed faster on Pd NP-based electrodes than on Pd₂Sn NRs. After 2 h of reaction, the current obtained for Pd₂Sn-NR/C (10.4 mA cm⁻²) was up to an order of magnitude higher than Pd₂Sn-SP/C (0.8 mA cm⁻²) and Pd-SP/C (0.35 mA cm⁻²), proving the

potential of Pd₂Sn NRs to enhance both performance and stability. TEM analysis of the NRs after stability test showed no change on their size and geometry (Figure 5f inset). Additional SEM-EDX analysis showed no change of composition.

The linear region of the Tafel plots stretched from -0.4 to -0.1 V. As the potential is further increased above -0.2 V, the Tafel plot becomes curved, indicating the EORs are no longer charge transfer controlled reactions. Similar Tafel slopes were obtained for the different Pd₂Sn-based catalysts, around 130 mV·dec⁻¹, denoting similar ethanol oxidation mechanism. These values significantly differed from that of Pd-SP/C (167 mV·dec⁻¹) which also showed a clear change of slope denoting a variation of the EOR mechanism. The lowest Tafel slopes obtained for the Pd₂Sn-based catalysts compared with Pd-SP/C can be explained by the contribution of Sn to form oxygenated species (e.g., OH_{ads}) that participate to the EOR accelerating the oxidation of the reaction intermediates adsorbed on the Pd sites.

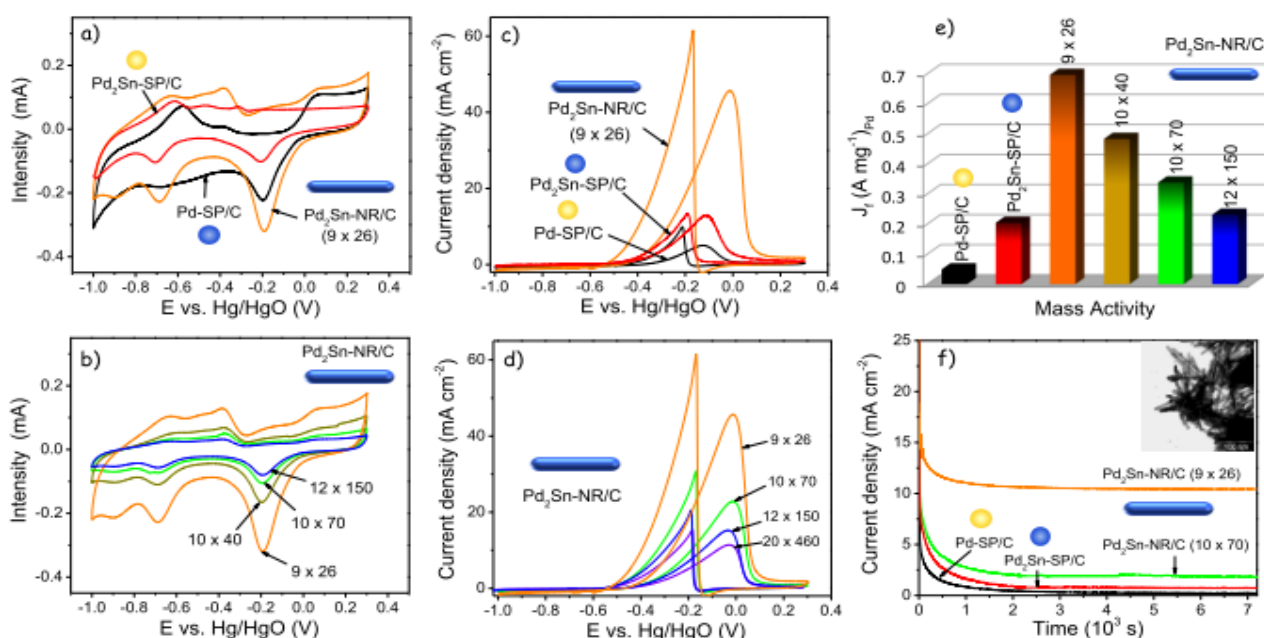


Figure 5. a-d) Cyclic voltammetric measurements of Pd and Pd₂Sn spheres and Pd₂Sn NRs with different sizes supported on GC in a 0.5 M KOH solution (a,b) and in a 0.5 M KOH + 0.5 M ethanol solution (c,d). e) Mass activity at the ethanol oxidation peak calculated per mass of palladium. f) Chronoamperometric measurements for the different samples in a 0.5 M KOH + 0.5 M ethanol solution at -0.1 V vs Hg/HgO. Inset shows a TEM image of the 10x70 nm Pd₂Sn NRs after the stability test.

Table 2. Summary of the electrochemical parameters measured for Pd₂Sn-NR/C, Pd₂Sn-SP/C and Pd-SP/C electrocatalysts

Catalyst	ECSA (m ² g ⁻¹)	E _o (V vs. Hg/HgO)	E _f (V vs. Hg/HgO)	j_f (mA cm ⁻²)	j_f mass activity (A g ⁻¹)	$j_{-0.1V}$ (mA cm ⁻²)	j_f/j_b	$j_{-0.1V}$ at 2h (mA cm ⁻²)	Tafel slope (mV dec ⁻¹)
Pd-SP/C	52.0	-0.39	-0.12	5.0	49	4.7	0.54	0.3	167

PdSn-SP/C	27.1	-0.51	0.11	13.1	131	12.8	0.98	0.8	128
Pd ₂ Sn-NR/C (9x26)	99.4	-0.47	-0.01	45.6	447	33.1	0.75	10.4	131
Pd ₂ Sn-NR/C (10x40)	54.3	-0.48	0.04	31.6	310	19.3	0.77	-	-
Pd ₂ Sn-NR/C (10x70)	33.9	-0.49	0.03	22.1	217	18.4	0.73	1.9	-
Pd ₂ Sn-NR/C (12x150)	22.6	-0.54	-0.04	15.1	148	17.1	0.75	-	-

Figure 6 displays the Nyquist impedance spectra of ethanol oxidation on Pd-SP/C, Pd₂Sn-SP/C and Pd₂Sn-NR/C electrodes. The measurements were made in 0.5 M KOH + 0.5 M ethanol solution at -0.1 V vs. Hg/HgO. We observed the electron-transfer resistance for ethanol electrochemical oxidation to decrease in the following order: Pd-SP/C >> Pd₂Sn-SP/C >> Pd₂Sn-NR/C, demonstrating the enhanced electron-transfer kinetics of Pd₂Sn-NR/C catalysts, in good agreement with voltammetric results presented above.

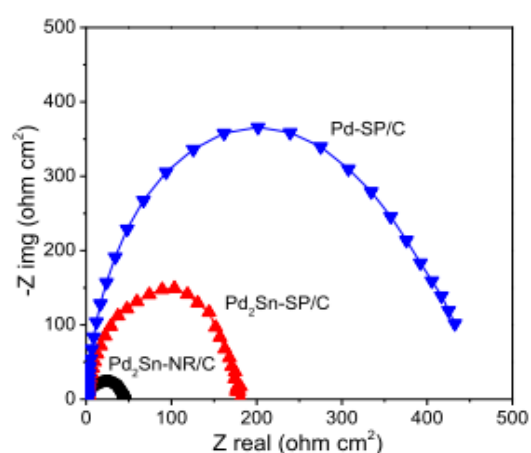


Figure 6. Nyquist plot of the ethanol oxidation on Pd-SP/C, Pd₂Sn-SP/C and Pd₂Sn-NRs/C electrodes in 0.5 M KOH + 0.5 M ethanol solution at -0.1 V vs. Hg/HgO.

Conclusions

In summary, a series of Pd₂Sn NRs grown in the [010] direction were produced via colloidal synthesis routes. Their surface chemistry was characterized by XPS, which discerned a loosely bonded organic shell that could be easily removed. Such NRs were employed as electrocatalyst for EOR in alkaline solution. Pd₂Sn NR-based electrocatalysts showed superior electrocatalytic activity and durability toward EOR over Pd₂Sn and Pd nanospheres. The excellent electrocatalytic performance correlates with DFT calculations showing (001) and (100) facets to be more favorable than (010) facets for ethanol and OH adsorption, although further detailed surface analysis and much more meticulous DFT calculations taking into account all the reaction steps and the real Pd₂Sn NR surface, i.e. taking into account the higher amount of Sn observed and its possible surface ordering with Pd, are

required to determine the exact EOR mechanism on this material.

Acknowledgements

This work was supported by the European Regional Development Funds and the Spanish MINECO project BOOSTER, TNT-FUELS, and PEC-CO₂. ZL thanks the China Scholarship Council for scholarship support. MI thanks AGAUR for Beatriu de Pinós postdoctoral grant (2013 BP-A00344). JL is Serra Hünter Fellow and is grateful to ICREA Academia program. Authors also acknowledge the funding from Generalitat de Catalunya 2014 SGR 1638.

Notes and references

1. Y.-J. Wang, J. Qiao, R. Baker and J. Zhang, *Chem. Soc. Rev.*, 2013, **42**, 5768-5787.
2. M. Akhairi and S. K. Kamarudin, *Int. J. Hydrogen Energy*, 2016, **41**, 4214-4228.
3. Y. Chen, M. Bellini, M. Bevilacqua, P. Fornasiero, A. Lavacchi, H. A. Miller, L. Wang and F. Vizza, *ChemSusChem*, 2015, **8**, 524-533.
4. M. Kamarudin, S. K. Kamarudin, M. Masdar and W. R. W. Daud, *Int. J. Hydrogen Energy*, 2013, **38**, 9438-9453.
5. L. An and T. Zhao, *Energy Environ. Sci.*, 2011, **4**, 2213-2217.
6. E. Antolini and E. R. Gonzalez, *J. Power Sources*, 2010, **195**, 3431-3450.
7. S. Badwal, S. Giddey, A. Kulkarni, J. Goel and S. Basu, *Appl. Energy*, 2015, **145**, 80-103.
8. J. R. Varcoe, R. C. Slade, E. L. H. Yee, S. D. Poynton and D. J. Driscoll, *J. Power Sources*, 2007, **173**, 194-199.
9. N. J. Robertson, H. A. Kostalik IV, T. J. Clark, P. F. Mutolo, H. D. Abruña and G. W. Coates, *J. Am. Chem. Soc.*, 2010, **132**, 3400-3404.
10. R. B. Kutz, B. r. Braunschweig, P. Mukherjee, D. D. Dlott and A. Wieckowski, *J. Phys. Chem. Lett.*, 2011, **2**, 2236-2240.
11. V. Rao, C. Cremers and U. Stimming, *Fuel Cells*, 2007, **7**, 417-423.
12. C. Busó-Rogero, S. Brimaud, J. Solla-Gullon, F. J. Vidal-Iglesias, E. Herrero, R. J. Behm and J. M. Feliu, *J. Electroanal. Chem.*, 2016, **763**, 116-124.
13. A. Bach Delpeuch, F. Maillard, M. Chatenet, P. Soudant and C. Cremers, *Appl. Catal., B* 2016, **181**, 672-680.
14. Y. Wang, S. Zou and W.-B. Cai, *Catalysts*, 2015, **5**, 1507.
15. D. A. Cantane, W. F. Ambrosio, M. Chatenet and F. H. B. Lima, *J. Electroanal. Chem.*, 2012, **681**, 56-65.
16. Y.-J. Wang, N. Zhao, B. Fang, H. Li, X. T. Bi and H. Wang, *Chem. Rev.*, 2015, **115**, 3433-3467.

17. W. J. Zhou, S. Q. Song, W. Z. Li, G. Q. Sun, Q. Xin, S. Kontou, K. Poullianitis and P. Tsiakaras, *Solid State Ionics*, 2004, **175**, 797-803.
18. S. Carrión-Satorre, M. Montiel, R. Escudero-Cid, J. L. G. Fierro, E. Fatás and P. Ocón, *Int. J. Hydrogen Energy*, 2016, **41**, 8954-8962.
19. C. Bianchini and P. K. Shen, *Chem. Rev.*, 2009, **109**, 4183-4206.
20. H. An, L. Pan, H. Cui, B. Li, D. Zhou, J. Zhai and Q. Li, *Electrochim. Acta*, 2013, **102**, 79-87.
21. W. Du, K. E. Mackenzie, D. F. Milano, N. A. Deskins, D. Su and X. Teng, *ACS Catal.*, 2012, **2**, 287-297.
22. L.-X. Ding, A.-L. Wang, Y.-N. Ou, Q. Li, R. Guo, W.-X. Zhao, Y.-X. Tong and G.-R. Li, *Sci. Rep.*, 2013, **3**, 1181.
23. A. N. Geraldes, D. Furtunato da Silva, J. C. Martins da Silva, O. Antonio de Sá, E. V. Spinacé, A. O. Neto and M. Coelho dos Santos, *J. Power Sources*, 2015, **275**, 189-199.
24. Z. Luo, M. Ibáñez, A. M. Antolín, A. Genç, A. Shavel, S. Contreras, F. Medina, J. Arbiol and A. Cabot, *Langmuir*, 2015, **31**, 3952-3957.
25. A.-L. Wang, X.-J. He, X.-F. Lu, H. Xu, Y.-X. Tong and G.-R. Li, *Angew. Chem. Int. Ed.*, 2015, **54**, 3669-3673.
26. H. Na, L. Zhang, H. Qiu, T. Wu, M. Chen, N. Yang, L. Li, F. Xing and J. Gao, *J. Power Sources*, 2015, **288**, 160-167.
27. J. Yin, S. Shan, M. S. Ng, L. Yang, D. Mott, W. Fang, N. Kang, J. Luo and C.-J. Zhong, *Langmuir*, 2013, **29**, 9249-9258.
28. J. Cai, Y. Huang and Y. Guo, *Electrochim. Acta*, 2013, **99**, 22-29.
29. A. Shavel, M. Ibáñez, Z. Luo, J. De Roo, A. Carrete, M. Dimitrievska, A. Genç, M. Meyns, A. Pérez-Rodríguez and M. V. Kovalenko, *Chem. Mater.*, 2016, **28**, 720-726.
30. W. Li, R. Zamani, P. Rivera Gil, B. Pelaz, M. Ibáñez, D. Cadavid, A. Shavel, R. A. Alvarez-Puebla, W. J. Parak and J. Arbiol, *J. Am. Chem. Soc.*, 2013, **135**, 7098-7101.
31. M. Ibáñez and A. Cabot, *Science*, 2013, **340**, 935-936.
32. M. Ibáñez, R. Zamani, S. Gorsse, J. Fan, S. Ortega, D. Cadavid, J. R. Morante, J. Arbiol and A. Cabot, *ACS nano*, 2013, **7**, 2573-2586.
33. R. Nafria, A. Genç, M. Ibáñez, J. Arbiol, P. Ramírez de la Piscina, N. Homs and A. Cabot, *Langmuir*, 2016, **32**, 2267-2276.
34. X. Yu, J. Liu, A. Genç, M. Ibáñez, Z. Luo, A. Shavel, J. Arbiol, G. Zhang, Y. Zhang and A. Cabot, *Langmuir*, 2015, **31**, 10555-10561.
35. X. Yu, A. Shavel, X. An, Z. Luo, M. Ibáñez and A. Cabot, *J. Am. Chem. Soc.*, 2014, **136**, 9236-9239.
36. Z. Luo, E. Irtem, M. Ibáñez, R. Nafria, S. Martí-Sánchez, A. Genç, M. de la Mata, Y. Liu, D. Cadavid, J. Llorca, J. Arbiol, T. Andreu, J. R. Morante and A. Cabot, *ACS Appl. Mat. Interfaces*, 2016, **8**, 17435-17444.
37. R. R. Zamani, M. Ibáñez, M. Luysberg, N. García-Castelló, L. Houben, J. D. Prades, V. Grillo, R. E. Dunin-Borkowski, J. R. Morante, A. Cabot and J. Arbiol, *ACS Nano*, 2014, **8**, 2290-2301.
38. G. Kresse and J. Hafner, *Phys. Rev. B*, 1993, **47**, 558-561.
39. G. Kresse and J. Furthmüller, *Comput. Mater. Sci.*, 1996, **6**, 15-50.
40. G. Kresse and D. Joubert, *Phys. Rev. B*, 1999, **59**, 1758-1775.
41. J. P. Perdew and Y. Wang, *Phys. Rev. B*, 1986, **33**, 8800-8802.
42. J. P. Perdew and Y. Wang, *Phys. Rev. B*, 1992, **45**, 13244-13249.
43. S. Grimme, J. Antony, S. Ehrlich and H. Krieg, *J. Chem. Phys.*, 2010, **132**, 154104.
44. S. A. Kirillov, P. E. Tsiakaras and I. V. Romanova, *J. Mol. Struct.*, 2003, **651-653**, 365-370.
45. E. D. Wang, J. B. Xu and T. S. Zhao, *J. Phys. Chem. C*, 2010, **114**, 10489-10497.
46. Z. Liang, T. Zhao, J. Xu and L. Zhu, *Electrochim. Acta*, 2009, **54**, 2203-2208.
47. A. Kowal, M. Li, M. Shao, K. Sasaki, M. Vukmirovic, J. h. Zhang, N. Marinkovic, P. Liu, A. Frenkel and R. Adzic, *Nat. Mater.*, 2009, **8**, 325-330.
48. Z. Zhang, J. Ge, L. Ma, J. Liao, T. Lu and W. Xing, *Fuel Cells*, 2009, **9**, 114-120.
49. Y. Feng, D. Bin, K. Zhang, F. Ren, J. Wang and Y. Du, *RSC Adv.*, 2016, **6**, 19314-19321.
50. D. V. Talapin, J.-S. Lee, M. V. Kovalenko and E. V. Shevchenko, *Chem. Rev.*, 2010, **110**, 389-458.
51. T. Chen and V. O. Rodionov, *ACS Catal.*, 2016, **6**, 4025-4033.
52. M. Ibáñez, Z. Luo, A. Genç, L. Piveteau, S. Ortega, D. Cadavid, O. Dobrozhan, Y. Liu, M. Nachtegaal and M. Zabarjadi, *Nat. Commun.*, 2016, **7**:10766.
53. Z. Niu and Y. Li, *Chem. Mater.*, 2014, **26**, 72-83.

3.1.4 Au-Pd₂Sn heterostructures nanoalloy: tuning alloy composition and catalytic property

This section contains the manuscript submitted for publication with the title “Pd₂Sn and Au-Pd₂Sn Nanorods in Catalytic Hydrogenation and Sonogashira Coupling Reactions”. Pd₂Sn NCs with tuned sizes, shapes and compositions are good candidates for several applications, such as fuel cell catalysis, water denitration and oxidative dehydrogenation of organic molecule. Meanwhile, to achieve multifunctionality, synergetic effects or enhanced performance Pd₂Sn-based HNPs could be developed.

On the other hand, Au NCs are well-known for their wide use in optical devices, catalysts and SERS. Moreover, Au domains can be introduced into HNPs to improve catalytic activity, stability and biocompatibility. In this section we present for the first time a synthetic method to produce novel hybrid Au-Pd₂Sn NPs with tuning composition. Au-Pd₂Sn heterostructured NRs were synthesized by a seed-mediated growth method involving a galvanic replacement reaction. Different size and aspect ratio of Pd₂Sn NRs were used as seeds. Au domains were selectively grown in the presence of OLA at room temperature. TEM, HRTEM, UV-vis and XRD confirmed such HNPs (Figure 3.6). Both Pd₂Sn and Au-Pd₂Sn NRs were found to be very active in the hydrogenation of aromatic and aliphatic alkenes and alkynes under mild conditions, also active in the Sonogashira coupling between PhA and PhI to yield tolan in good selectivity, especially with Au-Pd₂Sn NRs, when the reaction was performed at high dilution. In addition, the novel synthetic strategy offers an important tool towards the development of multifunctional nanomaterial applicable in photocatalysis, chemical sensing, and fabrication of photovoltaic devices.

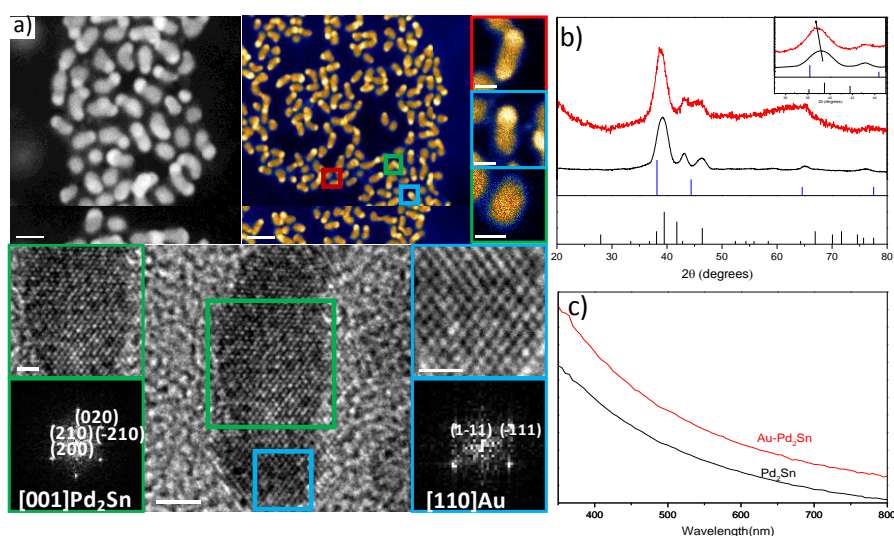


Figure 3.6 (a) TEM and HRTEM micrographs of Au-Pd₂Sn HNPs (b) XRD pattern of Pd₂Sn and Au-Pd₂Sn HNPs, inset showed angle shift before and after Au growth on surface of Pd₂Sn NRs (c) UV-vis spectra of Pd₂Sn and Au-Pd₂Sn HNPs.

Pd₂Sn and Au-Pd₂Sn Nanorods in Catalytic Hydrogenation and Sonogashira Coupling

Reactions

Raquel Nafria,^{a, ‡} ZhiShan Luo,^{a, ‡} Maria Ibañez,^{b,c} Sara Martí-Sánchez,^d María de la Mata,^d Jordi Llorca,^c Jordi Arbiol,^{d,f} Maksym V. Kovalenko,^{b,c} Arnald Grabulosa,^{*,g} Guillermo Muller^g and Andreu Cabot^{*,a,f}

^a Catalonia Institute for Energy Research (IREC), 08930 Sant Adrià de Besòs, Barcelona, Spain

^b Institute of Inorganic Chemistry, Department of Chemistry and Applied Biosciences, ETH Zürich, CH-8093, Switzerland

^c Empa-Swiss Federal Laboratories for Materials Science and Technology, Dübendorf, CH-8600, Switzerland

^d Catalan Institute of Nanoscience and Nanotechnology (ICN2), CSIC and the Barcelona Institute of Science and Technology (BIST), Campus UAB, Bellaterra, 08193 Barcelona, Spain

^e Institut de Tècniques Energètiques, Universitat Politècnica de Catalunya, 08028 Barcelona, Spain

^f ICREA, Pg. Lluís Companys 23, 08010 Barcelona, Spain

^g Departament de Química Inorgànica i Orgànica, Secció de Química Inorgànica, Universitat de Barcelona, Martí i Franquès 1-11, 08028 Barcelona, Spain.

‡ These authors contributed equally

ABSTRACT

Colloidal Pd₂Sn and Au-Pd₂Sn nanorods (NRs) with tuned size were produced by the reduction of Pd and Sn salts in the presence of size- and shape-controlling agents and the posterior growth of Au tips through a galvanic replacement reaction. ¹H nuclear magnetic resonance (NMR) and diffusion ordered NMR spectroscopy (DOSY) analysis revealed a highly dynamic binding of surfactants to these colloidal nanoparticles (NPs). Such dynamics allowed Pd₂Sn and Au-Pd₂Sn NRs to exhibit a high catalytic activity in the quasi-homogeneous hydrogenation of alkenes (styrene and 1-octene) and alkynes (phenylacetylene and 1-octyne) in dichloromethane (DCM). In Au-Pd₂Sn heterostructures, XPS evidenced an electron donation from the Pd₂Sn NR to the Au tips. Such heterostructures showed distinct catalytic behaviour in the

hydrogenation of compounds containing a triple bond such as tolan. This can be explained by the aurophilicity of triple bonds. Pd₂Sn and Au-Pd₂Sn NRs were also tested in the Sonogashira coupling reaction between iodobenzene and phenylacetylene in DMF. At low concentration, this reaction provided the expected product (tolan). However, at high concentration, more reduced products such as stilbene and 1,2-diphenylethane could be also obtained, even without the addition of H₂. A mechanism for this unexpected reduction is proposed as well.

INTRODUCTION

The development of homogeneous and heterogeneous catalysts for organic reactions is driven by the search of cost-effective and environmentally-friendly processes suitable for a sustainable society. From the myriad of currently exploited catalytic reactions, hydrogenation and cross-coupling are among the most heavily studied. Hydrogenation comprises an exceedingly important group of reactions, including the Haber-Bosch process as well as the reduction of alkenes, aldehydes, ketones and imines.^[1] On the other hand, cross-coupling reactions comprise several essential mechanistically-related reactions, including Suzuki, Stille, Heck and Sonogashira couplings among others.^[2]

While numerous homo- and heterogeneous catalysts have been successfully applied in these reactions, several performance, economic and impact parameters, such as activity, selectivity, substrate scope, durability/recyclability, cost-effectiveness, environmental friendliness and sustainability require further improvement, making the design of better hydrogenation and cross-coupling catalysts a worthy endeavour.

The recent years have witnessed an intense activity on Pd hydrogenation catalysts for a wide range of applications.^[3] Pd-based catalysts have been also explored for the Sonogashira reaction,^[2] which is ideally suited to install an alkyne unit in molecules intended for use in drugs, natural products, molecular wires and other organic functional materials. In particular, Pd-based bimetallic catalysts and specifically Pd-Sn alloys for hydrogenation and alkynylation reactions,^[2a,5,6,7] have raised especial attention owing to their reduced cost and improved performance compared to bare Pt or Pd catalysts. While cost is reduced by decreasing the use of expensive noble metals, bimetallic catalysts can also improve performance by a fine tuning the structural and electronic properties of the resulting alloy. The presence of two different metals may also

allow the development of tandem reactions or alternative multisite reaction paths that are faster, more selective and/or prevent poisoning species to be formed or to remain at the catalyst surface. Moreover, tandem reactions can reduce the number of synthetic steps toward a specific product in one-pot procedures.^[8] Bimetallic catalysts can be realised by incorporating the two metal centres within a molecule, by producing alloyed particles or by supporting the two metals on a substrate. Among the different options, monodisperse and shape-engineered colloidal inorganic NPs are an interesting but clearly underexploited class of catalysts. Being unsupported, essentially solution-dispersed, they combine the advantages of classic homogeneous and heterogeneous catalysts.^[9] Like organic synthesis methods, colloidal synthesis routes allow preparing materials with extraordinary control over main parameters relevant to catalysis, composition, size, phase organization and surface sites/facets, potentially allowing to rationally tune or even program the catalytic performance and especially selectivity in sensitive reactions.^[10] Colloidal NPs can also have extremely high surface-to-volume ratio, what makes them potentially very active, as molecular catalysts. Additionally, unlike molecular catalysts, NPs can be easily separated from reactants and products, and used in multiple cycles.

We recently described the synthesis of Pd₂Sn NRs with narrow size distribution and geometry control.^[10d] In the present paper we report a procedure for the growth of Au tips onto Pd₂Sn NRs to produce Au-Pd₂Sn NRs. With both types of NRs in hand, we compare the performance of Pd₂Sn and Au-Pd₂Sn NPs in alkene and alkyne hydrogenations and in Sonogashira couplings. These reactions have been chosen because Pd-Sn systems have been previously shown excellent performance used in cross-couplings^[2a] and there is also literature precedents demonstrating that supported Au NPs are active both in hydrogenation^[11] and Sonogashira^[12] couplings due the aurophilicity of alkynes.^[13]

EXPERIMENTAL

Chemicals: Palladium(II) acetylacetonate ($[\text{Pd}(\text{acac})_2]$, 99%), tin(II) acetate ($\text{Sn}(\text{OAc})_2$), gold(III) chloride (AuCl_3 , 99,99%), 1-octadecene (ODE, 90%), oleylamine (OLA, > 70%), oleic acid (OA, 90%), methylamine hydrochloride (MAH), hydrochloric acid (37% in water), styrene, 1-octene, phenylacetylene (PhA), 1-octyne, iodobenzene (PhI), tolan, potassium carbonate and potassium hydroxide were purchased from Sigma Aldrich. Tri-*n*-octylphosphine (TOP, 97%) was acquired from Strem. Hexane, chloroform, *N,N*-dimethylformamide, toluene and ethanol were of analytical grade and obtained from various sources. MilliQ water was supplied by the PURELAB flex from ELGA. All chemicals were used as received without further purification, except OLA, which was purified by distillation.

Synthesis of Pd_2Sn NRs: Pd_2Sn NRs were produced following our previous report^[10d] with a slight modification to improve the yield of the synthesis while simultaneously using an air stable reactant, $\text{Sn}(\text{OAc})_2$. In a typical synthesis, 20 mL of OLA, 0.8 mmol of MAH, 0.3 mmol of $[\text{Pd}(\text{acac})_2]$ and 0.15 mmol $\text{Sn}(\text{OAc})_2$ were placed in a 100 mL four-neck flask and purged under argon flow for 30 minutes at 60 °C. Then 1 mL of TOP was injected into the solution and the mixture was heated to 200 °C at 12 °C/min. After maintaining the reaction mixture at 200 °C for 30 min, the solution was heated to 300 °C at 2.5 °C/min and kept for additional 30 min at this temperature. Finally, the solution was cooled down and Pd_2Sn NRs were separated from the reaction mixture by adding 20 mL of ethanol and centrifuging at 3000 rpm for 5 min. NRs were washed with chloroform as solvent and ethanol as non-solvent by multiple precipitation/redispersion steps.

Synthesis of $\text{Au-Pd}_2\text{Sn}$ NRs: $\text{Au-Pd}_2\text{Sn}$ NRs were prepared by growing Au over Pd_2Sn NRs produced following the procedure described above. Initially, a stock solution containing 0.02 mmol of AuCl_3 in 50 μL of OLA and 2 mL of ODE was prepared. Then, this Au stock solution was injected at room temperature into 5 mL of Pd_2Sn NRs dispersed in toluene (5 mg/mL) under strong stirring, and maintained in these conditions for 60 min. Finally, $\text{Au-Pd}_2\text{Sn}$ NRs were washed by multiple precipitation/redispersion using toluene and ethanol.

Procedures for the catalytic runs:

A) Hydrogenation reactions. An exactly weighted quantity of 12 nm Pd₂Sn or Au-Pd₂Sn NRs (usually 10.0 mg) and the allotted quantity of substrate (styrene, 1-octene, PhA, 1-octyne or tolan) were dissolved in 20 mL of the solvent of choice under nitrogen atmosphere, sonicated for 10 minutes and transferred by syringe to a Fischer-Porter flask, which was then purged with H₂ three times, pressurised to the desired H₂ pressure (usually 3 bar) and left stirring for the selected time.

B) Sonogashira coupling reactions. An exactly weighted quantity of 12 nm Pd₂Sn or Au-Pd₂Sn NRs (usually 10.0 mg), PhI (204 mg, 1.0 mmol), PhA (153 mg, 1.5 mmol) and base (2 mmol) were dissolved in 10 mL of dry DMF under nitrogen atmosphere, sonicated for 10 minutes and transferred by syringe to a microwave tube. The reaction was heated 130 °C for the allotted time.

The conversions in Sonogashira coupling reactions were calculated with respect to the limiting agent (PhI). The Turnover Frequencies (TOF) were calculated from the amount of product produced in a specific time interval in hours by considering the total Pd amount according to:

$$TOF = \frac{mol\ product}{mol\ Pd \cdot t}$$

Gas chromatography (GC) analyses after catalytic runs were performed with an Agilent Technologies 6890N chromatograph equipped with a HP5-5MS capillary column (30 m x 0.32 mm size) and a FID detector, with He as a carrier gas. Additionally some compounds were characterized by GC-MS analyses in an Agilent Technologies chromatograph 7820A with a mass detector 5975 using the same column.

Characterisation:

Size and shape of initial NPs were examined by transmission electron microscopy (TEM) using a ZEISS LIBRA 120, operating at 120 kV. Structural and compositional characterization of the nanocomposites were analysed by high resolution TEM (HRTEM) and high angle annular dark field (HAADF) scanning TEM (STEM) using a field emission gun FEI™ Tecnai F20 microscope at 200 kV with a point-to-point resolution of 0.19 nm. Scanning electron microscopy (SEM) analysis was done in a ZEISS Auriga microscope with an energy dispersive X-ray spectroscopy (EDS) detector at 20 kV to study the chemical composition of NPs. For SEM characterization, NPs were dissolved in chloroform and were drop casted on silicon substrates. X-ray power diffraction (XRD) patterns were obtained on a Bruker AXS D8 Advance diffractometer, using CuK radiation ($\lambda = 1.5406 \text{ \AA}$), operating at 40 kV and 40 mA, and with a LynxEye linear position-sensitive

detector used in reflection geometry. For XRD characterization, samples were deposited on a Si substrate. Ultraviolet-visible (UV-Vis) spectra were recorded on a LAMBDA 950 UV-Vis spectrophotometer from PerkinElmer. X-ray photoelectron spectroscopy (XPS) was done on a SPECS system equipped with an Al anode XR50 source operating at 150 mW and a Phoibos 150 MCD-9 detector. The pressure in the analysis chamber was always below 10^{-7} Pa. The area analysed was about 2 mm \times 2 mm. The pass energy of the hemispherical analyser was set at 25 eV and the energy step was set at 0.1 eV. Data processing was performed with the CasaXPS program (Casa Software Ltd., UK). Binding energy (BE) values were centered using the C 1s peak at 284.8 eV. The atomic fractions (%) were calculated using peak areas normalized on the basis of acquisition parameters after background subtraction, experimental sensitivity factors and transmission factors provided by the manufacturer.

Thermogravimetric analyses (TGA) were performed in the temperature range of 30–500 °C at a heating rate of 10 °C min⁻¹ under Ar using a PerkinElmer TGA4000. Nuclear Magnetic Resonance (NMR) measurements were recorded on a Bruker Avance III HD Spectrometer operating at a ¹H frequency of 500.26 MHz and equipped with a BBFO-Z probe. The sample temperature was set to 298.2 K. One dimensional (1D) ¹H and 2D NOESY (Nuclear Overhauser Effect Spectroscopy) spectra were acquired using standard pulse sequences from the Bruker library. For the quantitative 1D ¹H measurements, 64k data points were sampled with the spectral width set to 20 ppm and a relaxation delay of 30 s. NOESY mixing time was set to 300 ms and 4096 data points in the direct dimension for 512 data points in the indirect dimension were typically sampled, with the spectral width set to 10 ppm. Diffusion measurements (2D DOSY) were performed using a double stimulated echo sequence for convection compensation and with monopolar gradient pulses.^[14] Smoothed rectangle gradient pulse shapes were used throughout. The gradient strength was varied linearly from 2 to 95% of the probe's maximum value in 64 increments, with the gradient pulse duration and diffusion delay optimized to ensure a final attenuation of the signal in the final increment of less than 10% relative to the first increment. For 2D processing, the spectra were zero filled until a 4096–2048 real data matrix. Before Fourier transformation, the 2D spectra were multiplied with a squared cosine bell function in both dimensions, the 1D spectra were multiplied with an exponential window function. The diffusion coefficients were obtained by fitting the appropriate Stejskal-Tanner (ST) equation to the signal intensity decay.^[15]

Diffusion measurements (2D DOSY) were performed using a double stimulated echo sequence for convection compensation and with monopolar gradient pulses.^[14] Smoothed rectangle gradient pulse shapes were used throughout. The gradient strength was varied linearly from 2-95% of the probe's maximum value (calibrated at 50.2 G/cm) in 64 steps, with the gradient pulse duration and diffusion delay optimized to ensure a final attenuation of the signal in the final increment of less than 10% relative to the first increment. The diffusion coefficients were obtained by fitting the Stejskal-Tanner (ST) equation to the signal intensity decay. For the pulse sequence at hand, the appropriate ST equation is:^[15]

$$I = I_0 e^{-D\gamma^2 \delta^2 g^2 (\Delta - \delta/3)}$$

with the gyromagnetic ratio of the observed ¹H nucleus γ , the gradient pulse length δ , the gradient strength g , the diffusion time Δ and the diffusion coefficient D .

RESULTS AND DISCUSSION

Structural and chemical characterisation of Pd₂Sn and Au-Pd₂Sn NRs

Representative TEM micrographs of rod-shaped Pd₂Sn NPs with three different sizes [(10 ± 2 nm) × (4 ± 1 nm); (26 ± 2 nm) × (9 ± 1 nm); (40 ± 5 nm) × (11 ± 2 nm)] produced following the methodology detailed above are shown in Figure 1a, 1c, 1e. NPs showed narrow size distributions and no apparent aggregation. After the Au growth stage, multiple Au dots with higher contrast and average size of ca. 2 nm were grown along the whole NR surface for the larger NRs and preferentially at the NR ends in the smallest ones (Figures 1b, 1d, 1f). Figure 1g shows the size distribution histograms for the smallest Pd₂Sn and Au-Pd₂Sn NRs produced. Due to the preferential growth of the Au domains at the NR tips, a slight increase of the NR length was obtained in this sample, from (10 ± 2 nm) × (4 ± 1 nm) to (12 ± 2 nm) × (4 ± 1 nm). EDX spectra of single NRs that contained a contrast difference confirmed the presence of the three elements, Pd, Sn and Au (Figure 2a). Moreover UV-vis spectroscopy showed the disappearance of the characteristic Au plasmonic peak, suggesting a strong electronic interaction between Au and Pd₂Sn nanodomains (Figure 1h).

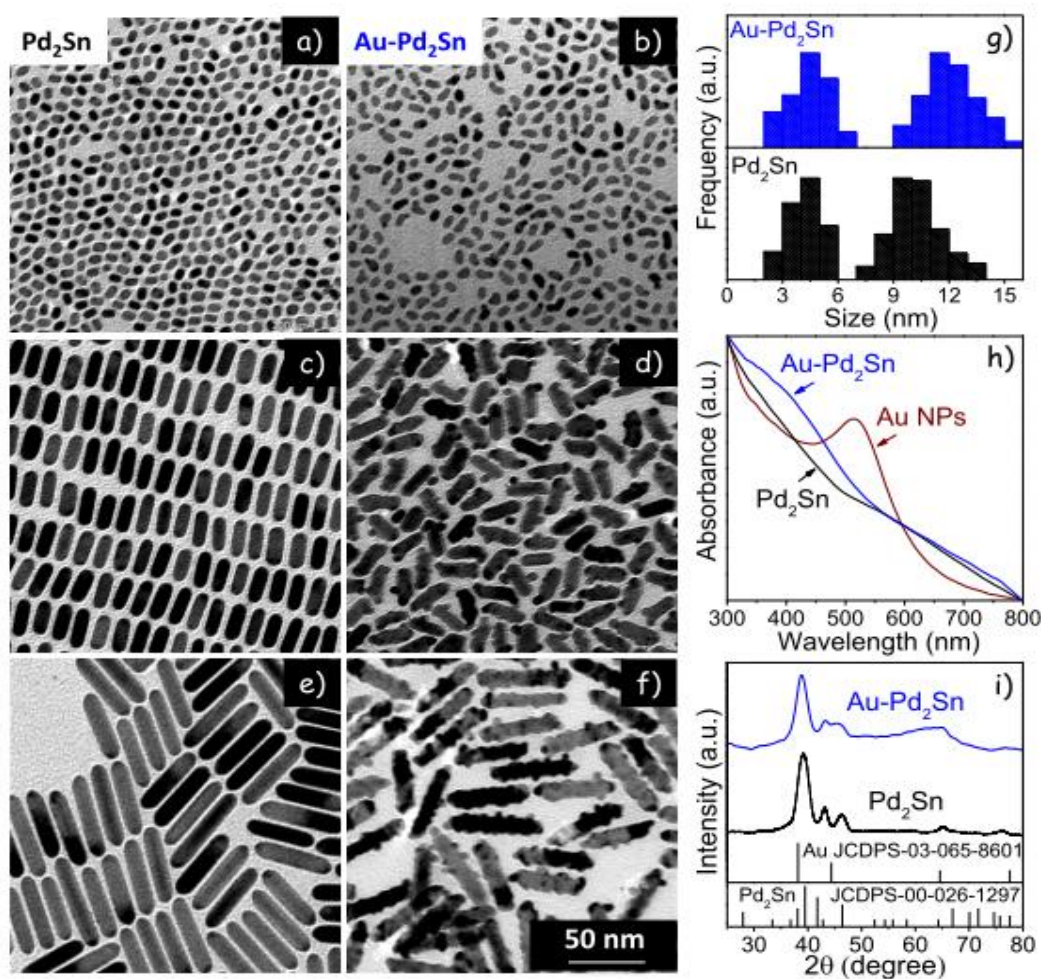


Figure 1. a)-f) TEM micrographs of Pd₂Sn (a,c,e) and Au-Pd₂Sn (b,d,f) NRs with three different sizes: 10 ± 2 nm x 4 ± 1 nm (a,b); 26 ± 2 nm x 9 ± 1 nm (c,d); 40 ± 5 nm x 11 ± 2 nm (e,f). All TEM micrographs have the same scale. g) Size distribution histograms of the smallest Pd₂Sn and Au-Pd₂Sn NRs (10 ± 2 nm x 4 ± 1 nm). h) UV-vis spectra of independent colloidal Au NPs, and Pd₂Sn and Au-Pd₂Sn NRs. i) XRD patterns of Pd₂Sn NRs and Au-Pd₂Sn NRs, including reference patterns for Pd₂Sn and Au.

HAADF-STEM images of the smallest Au-Pd₂Sn NRs further confirmed the presence of Au dots at the Pd₂Sn NR tips, as deduced by the brighter dots associated to the higher Z contrast of Au (Figure 2). Even though most of the NRs showed the presence of Au in just one tip, a few contained Au on both sides of the NR while a few other displayed no contrast difference. XRD patterns showed Pd₂Sn NRs to have an orthorhombic crystal structure (JCPDS No. 00-026-1297). While the Au XRD reflections were mostly

hidden by the Pd₂Sn peaks, slight shoulders at $2\theta = 44.5^\circ$ and 64.5° and a shift of the main Pd₂Sn diffraction peak to lower angles clearly suggested the presence of Au crystalline domains (Figure 1i).^[16] HRTEM analysis confirmed the orthorhombic crystal structure of Pd₂Sn NRs (space group Pnma) with $a = 5.65 \text{ \AA}$, $b = 4.31 \text{ \AA}$ and $c = 8.12 \text{ \AA}$, showed the [010] as the NR growth direction and revealed the presence of Au crystal domains at the Pd₂Sn NR tips forming almost perfect epitaxy (Figure 2c). The Au crystal phase was identified as cubic Fm-3m with $a = b = c = 4.09 \text{ \AA}$. It has to be noticed that the Au{111} and Pd₂Sn{210} planes, as well as Au{002} and Pd₂Sn{020} present almost identical lattice parameters, which difficult distinguishing between them.

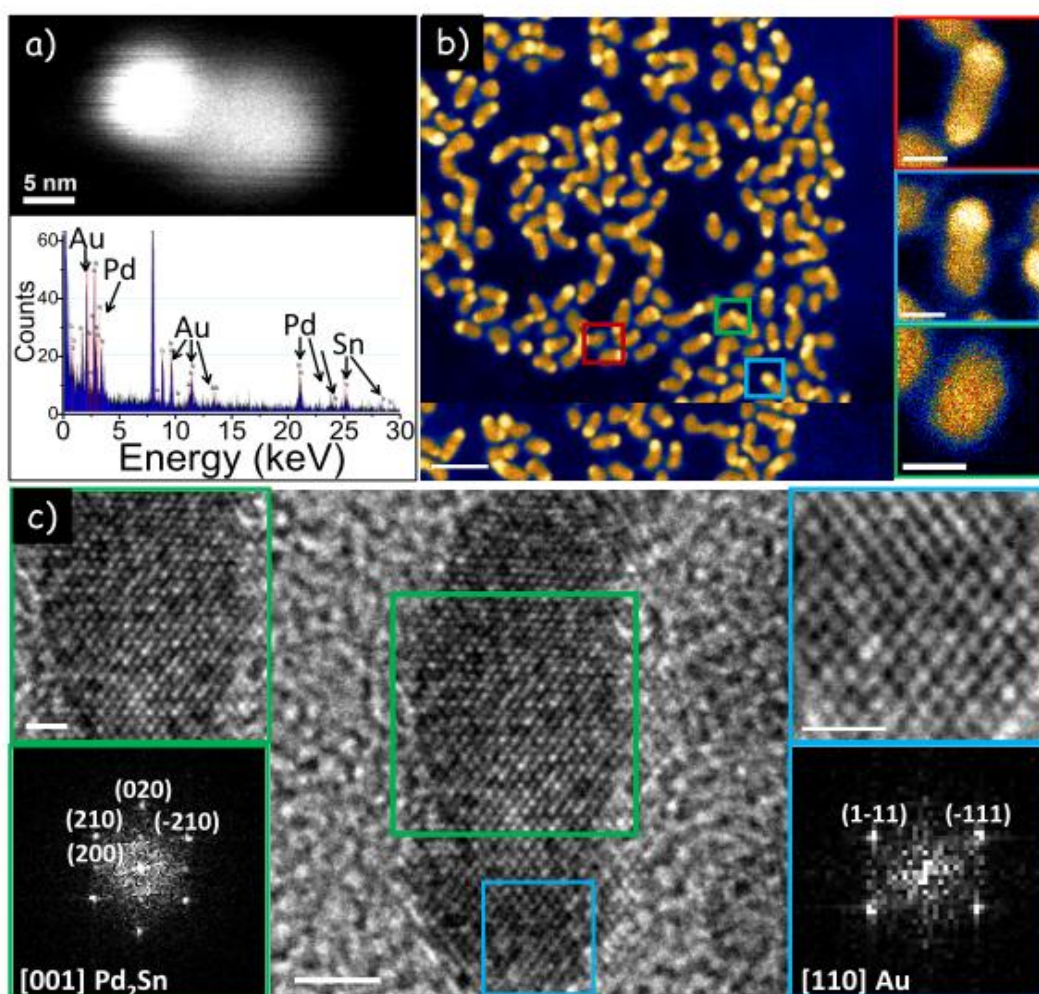


Figure 2. a) HAADF-STEM image of a single Au-Pd₂Sn NR and its corresponding EDX spectrum. b) False coloured HAADF-STEM image of Au-Pd₂Sn NRs and details of three different particles one containing a higher contrast dot at

both ends, another at only one end (most common case) and another without any higher contrast region. c) HRTEM micrograph of a Au-Pd₂Sn NRs, details of the squared regions and their corresponding power spectra.

Within its experimental error, EDX analysis showed the atomic ratio of Pd and Sn to be consistent with stoichiometric Pd₂Sn ([Pd]/[Sn] = 2.0 ± 0.1). However, with the introduction of Au, higher Pd ratios were systematically obtained as detailed in Table 1. We associate this experimental observation to a possible galvanic replacement of Sn by Au. We speculate that when adding AuCl₃ to the solution containing Pd₂Sn NRs, Au³⁺ ions in solution could be reduced to Au⁺ or even Au⁰ at the NR surface through the simultaneous oxidation of Sn or Sn²⁺ ions to Sn⁴⁺ and the subsequent solvation of Sn⁴⁺ ions in the solution containing the remaining chlorine ions. Au⁺ could be also further reduced to Au⁰ through charge transfer from Pd atoms (Figure 3a).^[17]

Table 1. Atomic ratios of Pd₂Sn and Au-Pd₂Sn NRs as obtained by EDX and XPS analyses, and atomic percentage of each oxidation state as obtained from the fitting of the XPS spectra

[AuCl ₃] M	EDX		XPS									
	[Pd]/[Sn]	[Au]/[Pd]	[Pd]/[Sn]	[Au]/[Pd]	Pd ⁰ at%	Pd ²⁺ at%	Sn ⁰ at%	Sn ²⁺ at%	Sn ⁴⁺ at%	Au ⁰ at%	Au ^{δ+} at%	
-	2.0	-	1.25	-	79.4	20.6	21.7	70.2	8.0	-	-	
0.01	2.2	0.07										
0.02	2.3	0.14	5.5	0.5	86.2	13.8	18.4	81.7		61.9	38.1	
0.04	2.4	0.26										

To further clarify the composition and oxidation states of the different elements within Pd₂Sn and Au-Pd₂Sn NRs, samples were analysed using XPS (Figure 3b-f). In Pd₂Sn NRs, the atomic ratio of Pd and Sn was measured as [Pd]/[Sn] = 1.25, pointing at a surface segregation of Sn. However, this ratio was much higher in Au-Pd₂Sn NRs, up to [Pd]/[Sn] = 5.5 when using a 0.02 M AuCl₃ concentration (Table 1), which further points toward a galvanic replacement of surface Sn by Au. Fitting each region of the XPS spectra, it can be observed that in Pd₂Sn and Au-Pd₂Sn NRs the deconvolution of the Pd 3d spectra indicated the presence of two Pd oxidation states, a dominant Pd⁰ state with a doublet at around 335.6 eV (Pd 3d_{5/2}) and 340.9 eV (Pd 3d_{3/2}), and a Pd²⁺ state with a doublet at 337.6 eV (Pd 3d_{5/2}) and 342.9 eV (Pd 3d_{3/2}). With the Au introduction, these two doublets were slightly shifted to lower binding energies (ΔE = -0.5 eV) and an increase of the Pd⁰ contribution was observed, which is in good agreement with previous reports.^[17b] Larger changes were obtained in the Sn 3d spectral region, which showed three main Sn contributions in Pd₂Sn NRs: a main Sn²⁺ state (486.3 eV and 494.9 eV) and minor Sn⁴⁺ (488.4 eV and 496.8 eV) and Sn⁰ (484.8 eV and 493.3 eV) states. Oxidised surface Sn phases, related either to the Sn reaction with oxygen or its coordination with ligands, are a

common observation on Pd-Sn and Pt-Sn alloys.^[17a,18] With the introduction of Au, on top of the decrease of the Sn signal described above, the main Sn²⁺ contribution was further oxidized, shifting its doublet peak position more than 1 eV toward higher binding energies. Finally, the deconvolution of the Au 4f spectrum in Au-Pd₂Sn showed 2 doublets. The major contribution corresponded to metallic Au (83.3 eV and 87.0 eV), and the other contribution at higher binding energy (84.5 eV and 88.2 eV) indicated the presence of positively charged gold atoms, Au^{δ+}, which can be attributed to Au surface atoms with different environments.^{[17a]6a}

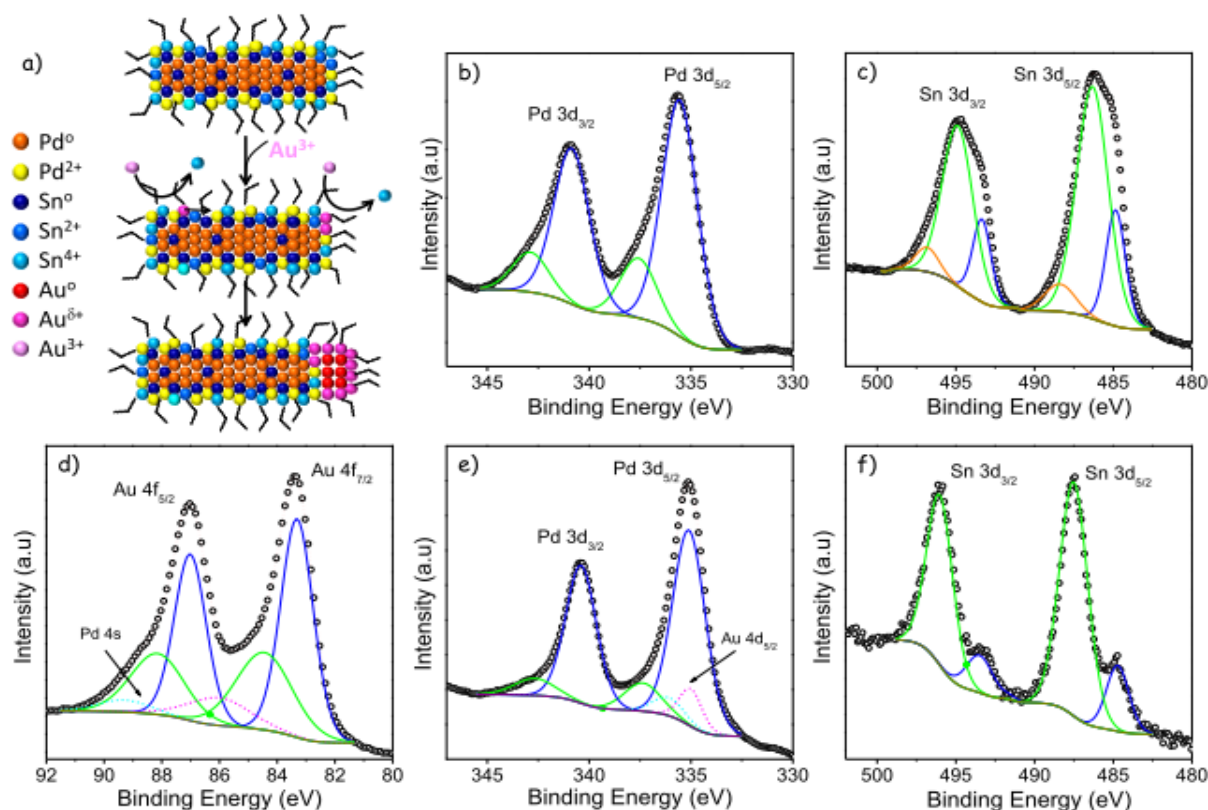


Figure 3. a) Scheme of the proposed Au-Pd₂Sn formation mechanism. b-f) Detailed regions of the XPS spectra of Pd₂Sn (b, c) and Au-Pd₂Sn NRs (d-f): Pd 3d (b,e), Sn 3d (c,f) and Au 4f (d), as indicated within each graph.

Thermogravimetric analysis showed the presence of a 13% of organics at the NR surface in the smallest 10 nm x 4 nm Pd₂Sn NRs subsequently used in catalytic tests (Figure S1).

The Pd₂Sn NR surface chemistry was further elucidated by solution ¹H NMR techniques. Prior to solution ¹H NMR characterization, Pd₂Sn NRs were washed by different precipitation and redispersion steps. Initial washing step was performed without adding any non-solvent. Further purifications were carried out using

chloroform as solvent and acetone as non-solvent. For NMR measurements NRs were dissolved in deuterated chloroform. After a second purification step, NR colloidal stability was compromised and concentration of NRs stable in solution decreased abruptly. The resonance at chemical shift around 5.3 ppm characteristic of the alkene group indicated the presence of OLA (Figure 4a). The other organic molecules used during the NR synthesis could not be identified in the ^1H NMR spectra. Further analysis to determine the characteristic of the interaction between OLA and the NR surface was performed by observing this resonance. The alkene group displayed slightly shifted sharp resonances in the ^1H NMR spectra, in contrast to the broad resonances typically characteristic of tightly bound ligands.^[19] In parallel, NOESY spectra presented negative cross peaks corroborating the interaction of OLA with the surface (Figure 4b). These data pointed us toward the possibility of a highly dynamic surface stabilization, as previously reported for other systems.^[20] Hence, we studied the diffusion coefficient of our system (NR plus the ligand shell) using DOSY. Generally, once the diffusion coefficient is found the solvodynamic size can be estimated via the Stokes-Einstein equation:

$$D = \frac{k_B T}{f}$$

where k_B is the Boltzmann constant, T the absolute temperature and f the friction coefficient. The friction coefficient depends on the object size and shape, $f = 6\pi\eta C$ where η solvent's viscosity and C the so-called capacity of the object. For spherical NRs C is equal to the solvodynamic radius (r_s) and for cubes $C = 0.66d$ with d the cube edge length.^[21] Both of these expressions have been used to determine the solvodynamic size of the different NPs from DOSY data.^[20,22] To the best of our knowledge, there are no studies of the DOSY NMR on rod-shape NPs. Mansfield and Douglas determined an approximation to calculate C for rods.^[23] We used their expression for rods with rounded ends (r radius of the circular cross section of the NR, $A = L/r$ aspect ratio with L being the length), $t = 1/\ln A$):

$$\frac{C}{r} = A \left[\ln \left(\frac{4A}{e} \right) \right]^{-1} \left[\frac{1 - 0.782t + 0.691t^{1.67} + 0.622t^{1.77} + 0.481t^{2.16}}{1 - 0.677t + 1.601t^{2.07} + 0.178t^{2.26}} \right]$$

Using this expression, we estimated the diffusion coefficient of 26 x 9 nm NRs to be $26 \mu\text{m}^2\text{s}^{-1}$; from DOSY data we found $D = 120 \pm 12 \mu\text{m}^2\text{s}^{-1}$. The larger experimental value can be ascribed to the highly dynamic stabilization of OLA on the NRs surface.

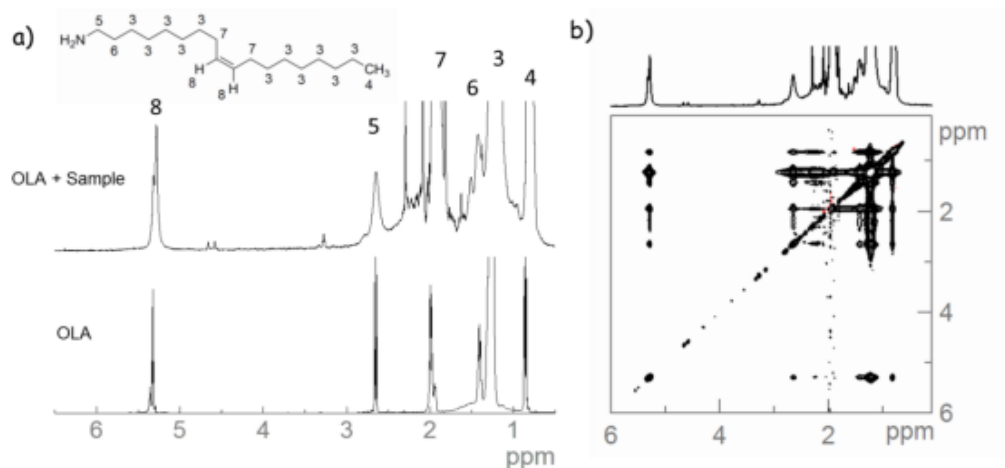


Figure 4. a) ^1H NMR spectra of 26 x 9 nm Pd_2Sn NRs in CDCl_3 after 2 purification steps (OLA + sample) and reference spectrum of OLA; b) NOESY spectrum of the Pd_2Sn NRs.

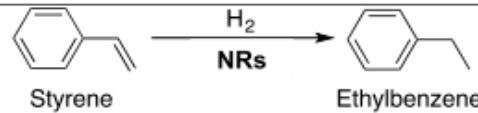
Hydrogenation reactions

The exploration of the catalytic potential of Pd_2Sn and $\text{Au-Pd}_2\text{Sn}$ NRs was started with the hydrogenation of styrene to ethylbenzene (Table 2). The smallest Pd_2Sn NRs were active in the hydrogenation reaction when DCM was used as solvent and H_2 pressure was set at 3 bar, achieving conversions above 70% at large loadings (100 g styrene/g Pd_2Sn) even under mild reaction conditions (25°C, Table 2, entry 1). Larger Pd_2Sn systematically resulted in lower activities (Table 2, entry 2) due to their lower surface-to-bulk ratio and possibly to the reduced number of higher active sites such as tips, thus the shortest Pd_2Sn (10 ± 2 nm x 4 ± 1 nm) NRs were used for all following catalytic tests. The activity of Pd_2Sn NRs toward the hydrogenation of styrene was higher than that of $\text{Au-Pd}_2\text{Sn}$ NRs (Table 2, entry 3). Notice in this regard that all the comparisons carried out between Pd_2Sn and $\text{Au-Pd}_2\text{Sn}$ NRs were based on results obtained from the exact same batch of Pd_2Sn NRs.

Activity was lower at 1 bar of hydrogen pressure (Table 2, entry 4) and when using methanol as solvent (Table 2, entry 5) due to the low solubility of the NRs in this solvent.

Even at much harsher conditions (Table 2, entry 6) the reaction yielded just ethylbenzene, without any trace of phenyl group hydrogenation. Finally, it is also worth noting that the reaction could be carried out without solvent, in neat styrene (Table 2, entry 7), achieving the highest TOF values up to 286 h^{-1} .

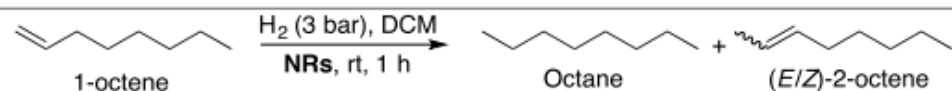
Table 2. Results of the styrene hydrogenation with Pd₂Sn NRs.

								
Entry	Catalyst (size/nm)	Solvent	T/°C	P/bar	t/h	Loading ^a	Conv/%	TOF/h ⁻¹
1	Pd ₂ Sn (10 x 4)	DCM	25	3	1	100	73.3	114
2	Pd ₂ Sn (40 x 12)	DCM	25	3	1	99	53.3	84
3	Au-Pd ₂ Sn (12 x 4)	DCM	25	3	1	100	48.3	86
4	Pd ₂ Sn (10 x 4)	DCM	25	1	1	104	12.8	21
5 ^b	Pd ₂ Sn (10 x 4)	MeOH	25	3	1	103	58.0	96
6	Pd ₂ Sn (10 x 4)	Toluene	70	50	4	30	100	–
7 ^c	Pd ₂ Sn (10 x 4)	–	25	3	1	436	41.3	287

^ag styrene/g NRs. ^bNRs were poorly soluble in methanol. ^cThe reaction was carried out in neat styrene.

The hydrogenation of 1-octene under the optimised conditions was then pursued (Table 3). Apart from the hydrogenated product, octane, isomerisation of the substrate to the two geometric isomers of 2-octene was observed. In this case, Au-Pd₂Sn NRs were more active than Pd₂Sn NRs, achieving almost full conversion after 1 h, and were slightly more selective towards the formation of the hydrogenated product. The isomerisation of 1-octene to 2-octene can be explained by a sequence of insertion and β-hydride elimination on the NR surface (Figure 5). It is interesting to note that no further isomerisation of 2-octene to more internal olefins was observed, suggesting that such reaction was very slow.

Table 3. Results of 1-octene hydrogenation with Pd₂Sn and Au-Pd₂Sn NRs.^a

					
Catalyst	Conv/%	TOF/h ⁻¹	Selectivity/%		
			Octane	(E)-2-octene	(Z)-2-octene
Pd ₂ Sn	70.6	110.2	52.7	27.6	19.7
Au-Pd ₂ Sn	98.1	157.2	56.7	32.7	10.6

^a The catalyst loading (g 1-octene/g NRs) was 106.

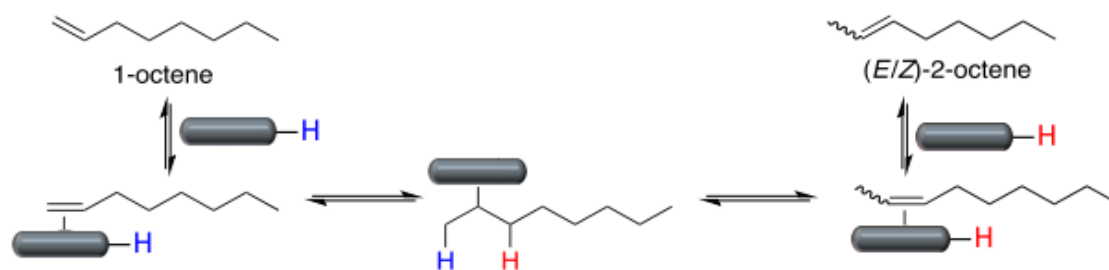


Figure 5. Mechanism of isomerisation of 1-octene to 2-octenes.

In Table 4, the results obtained in the hydrogenation of alkynes, namely phenylacetylene and 1-octyne, are presented. In this case, a clearer gold effect was expected on the grounds of the known affinity of Au for triple bonds.^[13a] In the hydrogenation of phenylacetylene, a slightly higher activity of the Au-Pd₂Sn NRs was observed. Regarding the selectivity, very little amounts of ethylbenzene were formed, evidencing the higher reactivity of phenylacetylene compared to styrene in hydrogenation. Similar results and tendencies were obtained for the hydrogenation of 1-octyne. In this case, both Pd₂Sn and Au-Pd₂Sn NRs were very selective towards hydrogenation to 1-octene. The small amount of 2-octenes yielded showed that the hydrogenation of 1-octyne was also faster than the isomerisation of the 1-octene formed. In the case of styrene, Pd₂Sn NRs were considerably more active than Au-Pd₂Sn NRs, whereas the opposite trend was observed for 1-octene. The more electron-rich nature and the lesser steric shielding of 1-octene compared to styrene could explain this effect. In contrast, the differences in performance were less important for phenylacetylene and 1-octyne, with the Au-Pd₂Sn being more active for both substrates. These trends could be understood by the known alkynophilicity of Au.^[13a,b,24] The high electron rich character of the triple bond probably masked the effect of the substituent.

Table 4. Results of alkyne hydrogenation with Pd₂Sn and Au-Pd₂Sn NRs.^a

Phenylacetylene		Styrene	Ethylbenzene	
Catalyst	Conv/%	TOF/h ⁻¹	Selectivity/%	
			Styrene	Ethylbenzene
Pd ₂ Sn	46.4	78.9	96.6	3.4
Au-Pd ₂ Sn	54.8	90.7	96.7	3.3
1-octyne		Octane	1-octene	(E/Z)-2-octene

NR	Conv/%	TOF/h ⁻¹	Selectivity/%			
			Octane	1-octene	(E)-2-octene	(Z)-2-octene
Pd ₂ Sn	47.4	75.5	0.0	98.1	1.9	0.0
Au-Pd ₂ Sn	58.7	93.9	0.7	94.4	4.0	0.9

^aThe catalyst loading (g alkyne/g NRs) was 106.

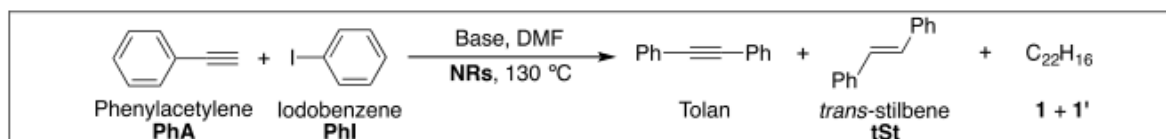
Sonogashira coupling reactions

The Pd₂Sn and Au-Pd₂Sn NR performance in the Sonogashira reaction between phenylacetylene (PhA) and iodobenzene (phenyl iodide, PhI) to give diphenylacetylene (tolan) is displayed in Table 5. Using Pd₂Sn NRs and K₂CO₃ as base (Table 5, entries 1-4) very high conversions could be attained at 2 h (Table 5, entry 2) leading mainly to tolan, although products 1 and 1' were also formed. Both products were characterised by GC-MS, with a peak at m/z of 280 units, proving that they are isomeric. These compounds arose from the condensation of two molecules of PhA and one molecule of PhI, which gave a pair of geometric isomers of a 1,3-enyne (Figure 6). The decrease of the catalyst loading (Table 5, entry 3) produced a drop on the conversion and selectivity to tolan. Comparison of entries 1 and 4 shows that Pd₂Sn NRs were more active than Au-Pd₂Sn NRs.

When the base was changed to KOH (Table 5, entries 5-8) the activity was higher, achieving full conversion at 1 h (Table 5, entries 5 and 7). However, the selectivity toward tolan was not improved, because apart from 1 and 1', *trans*-stilbene (tSt) was also produced. This compound is the product of the formal addition of H₂ to tolan. Interestingly, not even trace amounts of *cis*-stilbene (cSt) were detected. Additionally, in all the essays with KOH, a trace quantity of triphenylethene (TPE) was formed, which arises from the combination of a molecule of PhA and two molecules of PhI.

It is widely accepted that the Sonogashira reaction mechanism starts with an oxidative addition of the Ph-I bond to Pd(0). Therefore, the higher activity of Au-containing NRs (Table 5, entries 6 and 8) can be due to the larger content of catalytically active Pd(0) of these NRs, as demonstrated by XPS.

Table 5. Results of Sonogashira with Pd₂Sn and Au-Pd₂Sn NRs.



Entry	Catalyst	Base	t/h	Conv/%	Tolan/%	tSt/%	1+1'/%
1	Pd ₂ Sn	K ₂ CO ₃	1.0	47.2	70.6	–	29.4
2	Pd ₂ Sn	K ₂ CO ₃	2.0	97.3	65.7	–	34.7
3 ^a	Pd ₂ Sn	K ₂ CO ₃	1.0	10.9	40.6	–	59.4
4	Au-Pd ₂ Sn	K ₂ CO ₃	1.0	20.9	60.9	–	39.1
5	Pd ₂ Sn	KOH	1.0	100	60.8	17.6	21.6
6	Pd ₂ Sn	KOH	0.5	88.3	66.7	17.9	15.4
7	Au-Pd ₂ Sn	KOH	1.0	100	65.0	17.0	18.0
8	Au-Pd ₂ Sn	KOH	0.5	100	67.0	14.1	18.9

^a5.3 mg of NR were used.

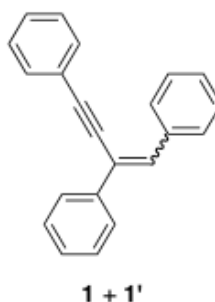


Figure 6. Proposed structures of 1 and 1'.

The recyclability of the Pd₂Sn NR catalyst was studied under the conditions of entry 5 in Table 5. After each catalytic run, NRs were separated by centrifugation. To the recovered NRs, a new batch of fresh reagents was added to carry out a second catalytic run under the same conditions. The process was repeated three times. Figure 7 represents the conversions referred to PhI after each catalytic run (blue bars) and also the activity of the first supernatant after the addition of one batch of fresh reagents. A drop in the conversion, but no change in the selectivity, was observed in each catalytic run. We associate this drop to the non-full recovery of the material in each precipitation step, what would also explain the relatively high supernatant activity obtained. A partial NR aggregation during the recovery and their degradation by leaching and/or surface modification could also reduce the NR catalytic activity.

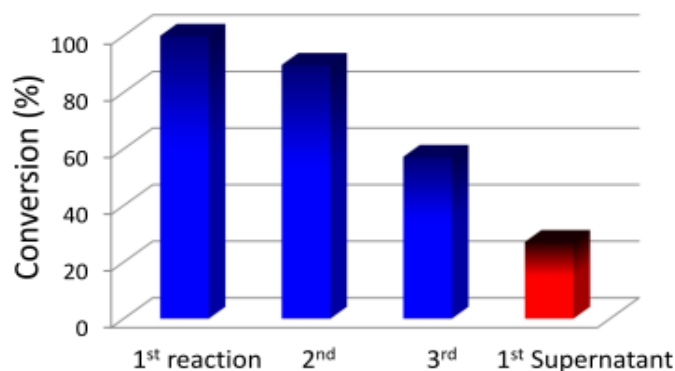


Figure 7. Recycling test for the Sonogashira reaction. Blue bars show the conversion obtained from the first to the third reaction. The red bar corresponds to the conversion obtained with the first supernatant.

An interesting aspect of the catalytic runs was the unexpected formation of the products *tSt*, *1*, *1'* and TPE. To shed light into the formation of these products, we carried out a set of experiments at different conditions (Table 6). It was found that reducing the concentration of PhI fivefold with respect to the 0.1 M used in previous experiments improved the selectivity to tolan (Table 6, cf. entries 1 with 2 and 4 with 5) by diminishing the quantity of *1* and *1'* or eliminating it completely in the case of Au-Pd₂Sn NRs (Table 6, entry 4). Unexpectedly, with Pd₂Sn NRs, increasing the concentration to 0.5 M (Table 6, entry 3) resulted in no trace of tolan but the formation of new products *cSt*, 1,2-diphenylethane (DPE), TPE and *2* (Figure S2). A similar result was obtained with Au-Pd₂Sn NRs (Table 6, entry 6), but in this case only traces of DPE were formed, what improved the selectivity toward *cSt*.

Table 6. Effect of the concentration on the Sonogashira reaction with NRs.^a

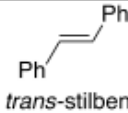
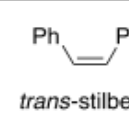
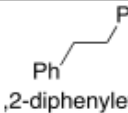
Entry	NRs	[PhI]/M	Tolan/%	<i>tSt</i> /%	<i>cSt</i> /%	TPE/%	DPE/%	<i>1+1'</i> /%	<i>2</i> /%
1	Pd ₂ Sn	0.02	66.7	16.9	–	–	–	16.4	–
2	Pd ₂ Sn	0.1	60.8	17.6	–	–	–	21.6	–
3	Pd ₂ Sn	0.5	–	10.1	49.2	6.2	9.8	15.2	9.5
4	Au-Pd ₂ Sn	0.02	88.7	11.3	–	–	–	–	–
5	Au-Pd ₂ Sn	0.1	65.0	17.0	–	–	–	18.0	–
6	Au-Pd ₂ Sn	0.5	–	11.9	63.7	3.8	–	17.5	3.1

DPE and 2 come from the formal addition of hydrogen to St and to 1/1' respectively whereas St comes from the formal addition of hydrogen to tolan. To understand the origin of the reduced products and the different selectivity of Pd₂Sn and Au-Pd₂Sn NRs, a sample of tolan was subjected to the catalytic conditions of the Sonogashira coupling and also to standard reduction with H₂ (Table 7).

Pd₂Sn and Au-Pd₂Sn NRs catalysed the reduction of tolan to St (but not to DPE) under Sonogashira conditions. The reduction was quite selective to the formation of cSt, as it happened when the Sonogashira coupling was carried out at high concentration (Table 6). As no trace of 1/1' or 2 was detected, it can be concluded that the formation of these molecules needs PhI and PhA. Au-Pd₂Sn NRs were less active for the reduction of tolan, possibly due to the major adsorption of the triple bond to Au.^[13b,24]

Pd₂Sn and Au-Pd₂Sn NRs were also active in the reduction of tolan by hydrogenation. While Pd₂Sn NRs gave mainly cSt and DPE, Au-Pd₂Sn NRs were more active and gave full conversion to DPE. In both cases, however, the product distribution was rather different from that obtained under the Sonogashira reaction conditions.

Table 7. Results of tolan reduction with NRs.

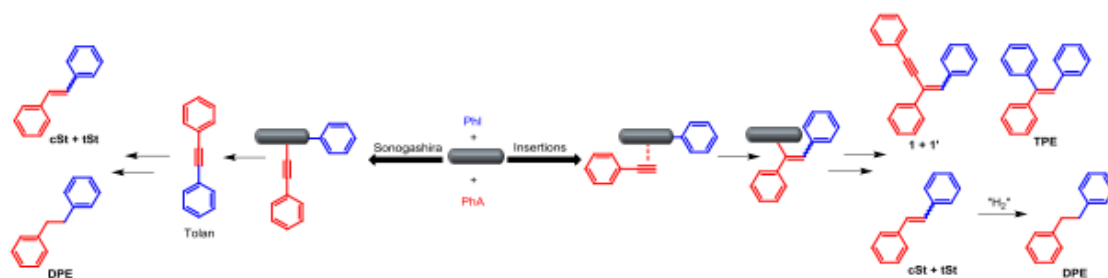
$\text{Ph}-\text{C}\equiv\text{C}-\text{Ph} \xrightarrow[\text{NRs, 130 }^\circ\text{C, 1 h}]{\text{KOH, DMF}}$				
$\text{Ph}-\text{C}\equiv\text{C}-\text{Ph} \xrightarrow[\text{NRs, rt, 1 h}]{\text{H}_2 (3 \text{ bar}), \text{DMF}}$				
Tolan			+ 	+ 
		<i>trans</i> -stilbene tSt	<i>trans</i> -stilbene cSt	1,2-diphenylethane DPE
<i>NR</i> ^a	<i>Tolan</i> /%	<i>tSt</i> /%	<i>cSt</i> /%	<i>DPE</i> /%
Pd ₂ Sn	–	10.7	89.3	–
Au-Pd ₂ Sn	33.6	7.1	59.2	–
<i>NR</i> ^b	<i>Tolan</i> /%	<i>tSt</i> /%	<i>cSt</i> /%	<i>DPE</i> /%
Pd ₂ Sn	–	5.0	44.3	50.7
Au-Pd ₂ Sn	–	–	–	100.0
^{a,b} The catalyst loading (g tolan/ g NRs) was 18.				
^a Conditions as in Table 5.				

From the above data, a mechanism for the formation of the different products can be envisaged (Scheme 1). The formation of the expected tolan through Sonogashira coupling (left in Scheme 1) involves oxidative addition of PhI, transmetalation with PhA and reductive elimination. The reduction of tolan catalysed by the

Pd₂Sn or Au-Pd₂Sn NRs leads to the formation of mainly cSt as shown by the data of Table 6 at high concentration and also by experiments of Table 7. An alternative mechanism (right in Scheme 1) might start with an initial insertion of PhA into the Ph–NR bond forming an intermediate. From this intermediate, 1, 1', St and TPE can be produced by functionalization of the NRs and reductive elimination (see Scheme 1 of the Supporting Information). It is interesting to note that by this mechanism, tSt, the most thermodynamically stable compound, is mainly formed as shown in the data given in Table 5 and Table 6.

Although the reduction of both isomers St produces DPE, the selectivity to cSt observed when performing the reactions at high concentration (Table 6) suggests that most of the DPE was formed by the reduction of cSt, shown in the left-hand side of Scheme 1.

Under the Sonogashira catalytic conditions the formal addition of a molecule of hydrogen to tolan, St, 1 and 1' is observed. This pointed out that molecular hydrogen, formed by decomposition of DMF, [25] was probably involved in the reductions. To explore the origin of the added hydrogen atoms an experiment with DMF-*d*₇ was performed, under analogous conditions to entry 3 of Table 6. It was found that no deuterium was incorporated to product 1 but its reduction product (2) was formed in 30% as monodeuterated and 10% as dideuterated. In the case of St, both isomers were formed with similar ratios of mono- and dideuterated form. These facts pointed out that 1 was formed by an insertion reductive elimination steps (see Scheme 1 of Supporting Information) not involving hydrogen or deuterium adsorbed on the Pd₂Sn or Au-Pd₂Sn NR. In contrast, St (either formed from tolan or by the insertion mechanism) required the adsorption of hydrogen on the NR. The detection of a mixture of hydrogenated and deuterated reduction products indicates that the solvent provided the required H or D atoms. [25]



CONCLUSIONS

Au nanodomains were grown at the surface of Pd₂Sn NRs through a process involving a galvanic replacement with Sn ions. The surface chemistry of Pd₂Sn and Au-Pd₂Sn NRs was characterized by XPS and NMR. XPS results evidenced an electron donation from the Pd₂Sn NR to the Au tips. ¹H NMR and DOSY allowed demonstrating for the first time in NRs a highly dynamically binding of the surfactant. Both Pd₂Sn and Au-Pd₂Sn NRs were found to be very active in the hydrogenation of aromatic and aliphatic alkenes and alkynes under mild conditions. While Pd₂Sn NRs were more active in the hydrogenation of styrene, Au-Pd₂Sn NRs performed better for the hydrogenation of alkynes, probably due to their aurophilicity. Pd₂Sn and Au-Pd₂Sn NRs were also active in the Sonogashira coupling between PhA and PhI to yield tolan in good selectivity, especially with Au-Pd₂Sn NRs, when the reaction was performed at high dilution. An advantage of our system over traditional Cu-cocatalyzed Sonogashira couplings is that the catalytic system does contain the catalyst and the cocatalyst in a single unit. Interestingly, St was produced at higher concentration either by reduction of tolan or by a mechanism involving insertion of PhA into the NR-Ph bond. In this regard, the production of St can be considered a cascade or tandem reaction, which was performed with a better selectivity using Au-Pd₂Sn NRS as a catalyst. Additionally the deuterated experiments confirmed that the solvent (DMF) play a role in this cascade reaction. We are currently investigating the implications of this methodology with other substrates.

Supporting information

Thermogravimetric profile of Pd₂Sn NRs, chromatogram of the products obtained in the Sonogashira reaction and possible mechanism of formation of St, 1, 1', 2, DPTE and TPE. This material is available free of charge via the Internet at <http://pubs.acs.org>.

Acknowledgements

This work was supported by the European Regional Development Funds and the Spanish MINECO projects ENE2013-46624-C4-3-R, MAT2014-59961-C2-2-R and CTQ2015-65040-P respectively. Z.L. thanks the China Scholarship Council for scholarship support. M.I. thanks AGAUR for Beatriu

de Pinós postdoctoral grant (2013 BP-A00344). J.L. is Serra Hünter Fellow and is grateful to ICREA Academia program. Authors also acknowledge the funding from Generalitat de Catalunya 2014 SGR 1638. SMS acknowledges funding from "Programa Internacional de Becas "la Caixa"-Severo Ochoa". ICN2 acknowledges support from the Severo Ochoa Program (MINECO, Grant SEV-2013-0295). Part of the present work has been performed in the framework of Universitat Autònoma de Barcelona Materials Science PhD program. We would like to thank Michaela Meyns for fruitful discussions.

References

- (1) *Handbook of Homogeneous Hydrogenation*; de Vries, J. G.; Elsevier, C. J., Eds.; Wiley-VCH: Weinheim, 2007.
- (2) (a) Negishi, E.-i.; Anastasia, L. *Chem. Rev.* **2003**, *103*, 1979-2018 (b) Karak, M.; Barbosa, L. C. A.; Hargaden, G. C. *RSC Adv.* **2014**, *4*, 53442-53466.
- (3) (a) Červený, L. *Palladium Catalysts in Hydrogenation Reactions*; 1989; Vol. 83. (b)Tungler, a; (c) Tarnai, T.; Hegedus, L. *Platin. Met. Rev.* **1998**, *42* (3), 108–115.(d)Teschner, D.; Révay, Z.; Borsodi, J.; Hävecker, M.; Knop-Gericke, A.; Schlögl, R.; Milroy, D.; Jackson, S. D.; Torres, D.; Sautet, P. *Angew. Chemie - Int. Ed.* **2008**, *47* (48), 9274–9278.
- (4) (a) Sengupta, D.; Saha, J.; De, G.; Basu, B. *J. Mater. Chem A*, **2014**, *2*, 3986-3992. (b) Son, S. U.; Jang, Y.; Park, J.; Na, H. B.; Park, H. M.; Yun, H. J.; Lee, J.; Hyeon, T. *J. Am. Chem. Soc.* **2004**, *126*, 5026-5027. (c) Jiang, H.-L.; Xu, Q. *J. Mater. Chem.*, **2011**, *21*, 13705 .
- (5) López, N.; Vargas-Fuentes, C. *Chem. Commun. (Camb)*. **2012**, *48* (10), 1379–1391.
- (6) Kosugi, M.; Fugami, K. *Reactions* **2002**, 263–283.
- (7) (a) Sales, E. A.; Jove, J.; Mendes, M. D.; Bozon-Verduraz, F. *J. Catal.* **2000**, *195* (1), 88–95. (b) Pattamakomsan, K.; Ehret, E.; Morfin, F.; Gélin, P.; Jugnet, Y.; Prakash, S.; Bertolini, J. C.; Panpranot, J.; Aires, F. J. C. S. *Catal. Today* **2011**, *164* (1), 28–33. (c) Stassi, J. P.; Zgoliecz, P. D.; De Miguel, S. R.; Scelza, O. A. *J. Catal.* **2013**, *306*, 11–29. (d) Freakley, S. J.; He, Q.; Harrhy, J. H.; Lu, L.; Crole, D. A.; Morgan, D. J.; Ntainjua, E. N.; Edwards, J. K.; Carley, A. F.; Borisevich, A. Y.; Kiely, C. J.; Hutchings, G. J. *Science* **2015**, *351* (6276), 279–296.
- (8) (a) Parsons, P. J.; Penkett, C. S.; Shell, A. J. *Chem. Rev.* **1996**, *96*, 195-206 (b) Climent, M. J.; Corma, A.; Iborra, S.; Sabater, M. J. *ACS Catal.* **2014**, *4*, 870-891.
- (9) (a) Astruc, D. *Inorg. Chem.* **2007**, *46*, 1884-1894. (b) Balanta, A.; Godard, C.; Claver, C. *Chem. Soc. Rev. Chem. Soc. Rev* **2011**, *40* (40), 4973–4985. (c) Chu, Y. T.; Chanda, K.; Lin, P. H.; Huang, M. H. *Langmuir* **2012**, *28*, 11258-11264. (d) Pérez-Lorenzo, M. *J. Phys. Chem. Lett.* **2012**, *3*, 167-174. (e) De Roo, J.; Van Driessche, I.; Martins, J. C.; Hens, Z. *Nat. Mater.* **2016**, *15*, 517–521.
- (10) (a) Flox, C.; Rubio-Garcia, J.; Nafria, R.; Zamani, R.; Skoumal, M.; Andreu, T.; Arbiol, J.; Cabot, A.; Morante, J. R. *Carbon.* **2012**, *50* (6), 2372–2374. (b) Yu, X.; Shavel, A.; An, X.; Luo, Z.; Ibáñez, M.; Cabot, A. *J. Am. Chem. Soc.* **2014**, *136* (26), 9236–9239. (c) Yu, X.; Liu, J.; Genç, A.; Ibáñez, M.;

- Luo, Z.; Shavel, A.; Arbiol, J.; Zhang, G.; Zhang, Y.; Cabot, A. *Langmuir* **2015**, *31* (38), 10555–10561. (d) Luo, Z.; Ibáñez, M.; Antolín, A. M.; Genç, A.; Shavel, A.; Contreras, S.; Medina, F.; Arbiol, J.; Cabot, A. *Langmuir* **2015**, *31*, 3952–3957. (e) Nafria, R.; Genç, A.; Ibáñez, M.; Arbiol, J.; Ramírez de la Piscina, P.; Homs, N.; Cabot, A. *Langmuir* **2016**, *32*, 2267–2276. (f) Luo, Z.; Irtem, E.; Ibáñez, M.; Nafria, R.; Martí-Sánchez, S.; Genç, A.; de la Mata, M.; Liu, Y.; Cadavid, D.; Llorca, J.; Arbiol, J.; Andreu, T.; Morante, J. R.; Cabot, A. *ACS Appl. Mater. Interfaces* **2016**, *8*, 17435–17444.
- (11) Hugon, A.; Delannoy, L.; Louis, C. *Gold Bull.* **2008**, *41*, 127–138.
- (12) (a) González-Arellano, C.; Abad, A.; Corma, A.; García, H.; Iglesias, M.; Sánchez, F. *Angew. Chem. Int. Ed.* **2007**, *46*, 1536–1538 (b) de Souza, R. O. M. A.; Bittar, M. S.; Mendes, L. V. P.; da Silva, C. M. F.; da Silva, V. T.; Antunes, O. A. C. *Synlett* **2008**, 1777–1780 (c) Beaumont, S. K.; Kyriakou, G.; Lambert, R. M. *J. Am. Chem. Soc.* **2010**, *132*, 12246–12248 (d) Kanuru, V. K.; Kyriakou, G.; Beaumont, S. K.; Papageorgiou, A. C.; Watson, D. J.; Lambert, R. M. *J. Am. Chem. Soc.* **2010**, *132*, 8081–8086 (e) Venkatesan, P.; Santhanalakshmi, J. *Langmuir* **2010**, *26*, 12225–12229 (f) Corma, A.; Juarez, R.; Boronat, M.; Sanchez, F.; Iglesias, M.; Garcia, H. *Chem. Commun.* **2011**, *47*, 1446–1448.
- (13) (a) Corma, A.; Garcia, H. *Chem. Soc. Rev.* **2008**, *37*, 2096–2126 (b) García-Mota, M.; Cabello, N.; Maseras, F.; Echavarren, A. M.; Pérez-Ramírez, J.; Lopez, N. *ChemPhysChem* **2008**, *9*, 1624–1629 (c) Stratakis, M.; Garcia, H. *Chem. Rev.* **2012**, *112*, 4469–4506.
- (14) Connell, M. A.; Bowyer, P. J.; Adam Bone, P.; Davis, A. L.; Swanson, A. G.; Nilsson, M.; Morris, G. A. *J. Magn. Reson.* **2009**, *198*, 121–131.
- (15) Sinnave, D. *Concepts Magn. Reson., Part A* **2012**, *40A*, 39–65.
- (16) Kwon, S. G.; Krylova, G.; Phillips, P. J.; Klie, R. F.; Chattopadhyay, S.; Shibata, T.; Bunel, E. E.; Liu, Y.; Prakapenka, V. B.; Lee, B.; Shevchenko, E. V. *Nat. Mater.* **2015**, *14*, 215–223.
- (17) (a) de la Cueva, L.; Meyns, M.; Bastús, N. G.; Rodríguez-Fernández, J.; Otero, R.; Gallego, J. M.; Alonso, C.; Klinke, C.; Juárez, B. H. *Chem. Mater.* **2016**, *28*, 2704–2714 (b) Krylova, G.; Giovanetti, L. J.; Requejo, F. G.; Dimitrijevic, N. M.; Prakapenka, A.; Shevchenko, E. V. *J. Am. Chem. Soc.* **2012**, *134*, 4384–4392.
- (18) (a) Du, W.; Mackenzie, K. E.; Milano, D. F.; Deskins, N. A.; Su, D.; Teng, X. *ACS Catal.* **2012**, *2*, 287–297 (b) Lee, A. F.; Baddeley, C. J.; Hardacre, C.; Moggridge, G. D.; Ormerod, R. M.; Lambert, R. M.; Candy, J. P.; Basset, J.-M. *J. Phys. Chem. B* **1997**, *101*, 2797–2805.
- (19) Hens, Z.; Martins, J. C. *Chem. Mater.* **2013**, *25*, 1211–1221.
- (20) (a) De Roo, J.; Ibáñez, M.; Geiregat, P.; Nedelcu, G.; Walravens, W.; Maes, J.; Martins, J. C.; Van Driessche, I.; Kovalenko, M. V.; Hens, Z. *ACS Nano* **2016**, *10*, 2071–2081. (b) Liu, Y.; Cadavid, D.; Ibáñez, M.; De Roo, J.; Ortega, S.; Dobrozhan, O.; Kovalenko, M.; Cabot, A. *J. Mat. Chem. C* **2016**, *4*(21), 4756–4762
- (21) Douglas, J. F.; Zhou, H.-X.; Hubbard, J. B. *Phys. Rev. E* **1994**, *49*, 5319–5331.
- (22) De Roo, J.; Van den Broeck, F.; De Keukeleere, K.; Martins, J. C.; Van Driessche, I.; Hens, Z. *J. Am. Chem. Soc.* **2014**, *136*, 9650–9657.
- (23) Mansfield, M. L.; Douglas, J. F. *Macromolecules* **2008**, *41*, 5422–5432.
- (24) Segura, Y.; López, N.; Pérez-Ramírez, J. *J. Catal.* **2007**, *247*, 383–386.
- (25) (a) Yu, J. Y.; Schreiner, S.; Vaska, L. *Inorg. Chim. Acta* **1990**, *170*, 145–147 (b) Wang, H.-S.; Wang, Y.-C.; Pan, Y.-M.; Zhao, S.-L.; Chen, Z.-F. *Tetrahedron Lett.* **2008**, *49*, 2634–2637.

Supporting Information

Pd₂Sn and Au-Pd₂Sn Nanorods in Catalytic Hydrogenation and Sonogashira Coupling Reactions

Raquel Nafria,^a ZhiShan Luo,^a Maria Ibañez,^{b,c} Sara Martí-Sánchez,^d María de la Mata,^d Jordi Llorca,^e Jordi Arbiol,^{d,f} Maksym V. Kovalenko,^{b,c} Arnald Grabulosa,^{*g} Guillermo Muller^g and Andreu Cabot^{*a,f}

^a Catalonia Institute for Energy Research (IREC), 08930 Sant Adrià de Besòs, Barcelona, Spain

^b Institute of Inorganic Chemistry, Department of Chemistry and Applied Biosciences, ETH Zürich, CH-8093, Switzerland

^c Empa-Swiss Federal Laboratories for Materials Science and Technology, Dübendorf, CH-8600, Switzerland

^d Catalan Institute of Nanoscience and Nanotechnology (ICN2), CSIC and the Barcelona Institute of Science and Technology (BIST), Campus UAB, Bellaterra, 08193 Barcelona, Spain

^e Institut de Tècniques Energètiques, Universitat Politècnica de Catalunya, 08028 Barcelona, Spain

^f ICREA, Pg. Lluís Companys 23, 08010 Barcelona, Spain

^g Departament de Química Inorgànica i Orgànica, Secció de Química Inorgànica, Universitat de Barcelona, Martí i Franquès 1-11, 08028 Barcelona, Spain.

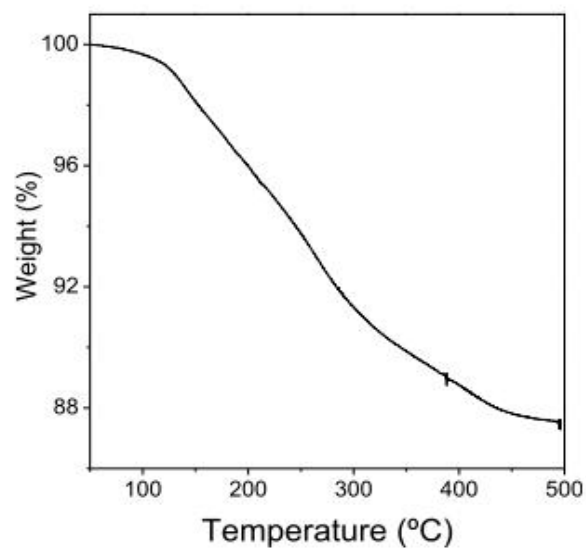


Figure S1. Thermogravimetric profile of Pd₂Sn NRs.

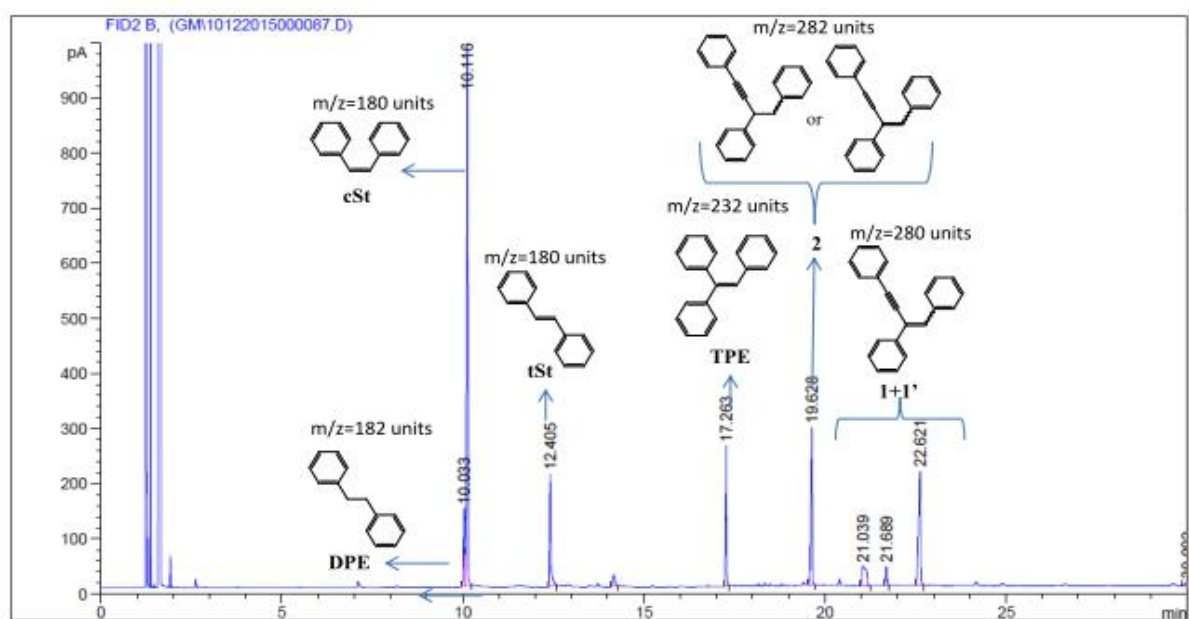
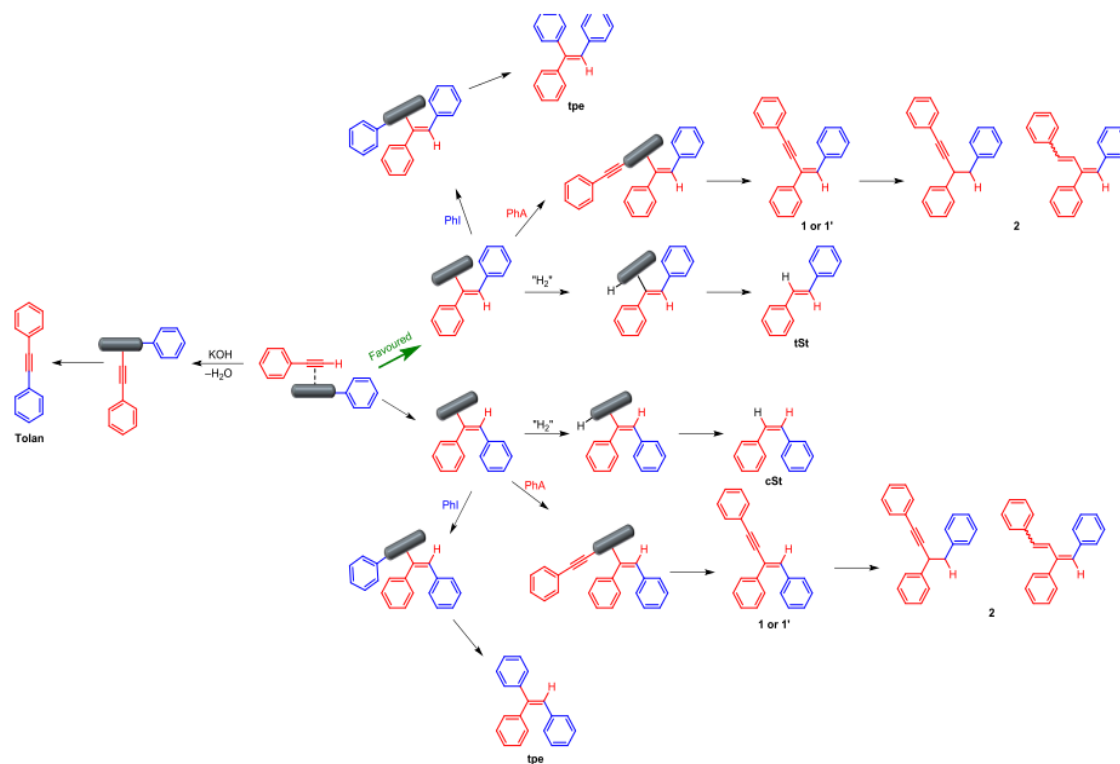


Figure S2. Chromatogram of the products obtained with Pd₂Sn NRs in the Sonogashira reaction when increasing the concentration to 0.5 M.



Scheme S1. Possible mechanism of formation of St, 1, 1', 2, DPE and TPE.

S1

Chapter 4

Heterostructured Metal Oxide NPs and Their Electrocatalytic Properties

4.1 Heterostructured metal oxide NPs and their electrocatalytic properties

This chapter focuses on heterostructured metal oxide NPs and their electrocatalytic properties. Cation exchange reaction is a simple and adjustable tool to design HNPs. In the first part of the chapter, we study $\text{Mn}_3\text{O}_4@\text{CoMn}_2\text{O}_4$ core-shell NPs formed by the partial cation exchange between Mn and Co in preformed Mn_3O_4 NPs. $\text{Mn}_3\text{O}_4@\text{CoMn}_2\text{O}_4\text{-CoO}$ NPs could be as well obtained when the proper cobalt precursor was selected. Such HNPs exhibited improved performance and stability as bifunctional catalysts for the ORR and OER in alkaline solution. The results obtained were published in *ACS Applied Materials & Interfaces* in 2016.

The cation exchange strategy was also applied to synthesize metal oxide shell onto iron oxide NPs. The second part of this chapter is based on the paper “ $\text{Fe}_3\text{O}_4@\text{NiFe}_x\text{O}_y$ Nanoparticles with Enhanced Electrocatalytic Properties for Oxygen Evolution in Carbonate Electrolyte”, which was just accepted by *ACS Applied Materials & Interfaces*. We demonstrated that monodisperse ultrathin transition metal oxide shell coating iron oxide HNPs are efficient electrocatalysts exhibiting high activity toward the OER in carbonate electrolyte.

4.1.1 HNPs based on colloidal NCs

One of the most active lines of research nowadays is the development of synthetic procedures that allow to form multicomponent NCs, such as core-shell or dumbbell-like NPs among others.¹²⁷⁻¹³⁴ There are very specific conditions to be able to growth such type of NPs and hence different types of growth mechanisms which are enumerated below these lines..^{80, 135, 136}

- a) Surface growth. Mainly seeds growth is applied to such reaction regime, to overcome energy barrier for surface nucleation and growth.
- b) Surface diffusion. In some systems, NCs grown at the surface may undergo a diffusion process. A transport process occurs via the merge of surface clusters at a single particle, either on the surface of the HNPs or within the center of the HNPs.
- c) Simultaneous nucleation and growth of both materials. One component forms a seed particle by homogeneous nucleation at the beginning state. Secondly, the other mater heterogeneously nucleates and grows on the initial seed particles.
- d) Replacement of a sacrificial domain. In some systems, HNPs obtained involve galvanic replacement reaction, cation exchange, anion exchange and chemical etching.
- e) Self-assembled HNPs.

Among HNPs, core-shell NPs have attracted numerous interests to the basis for widespread application in energy storage materials, fuel cell, solar cells and many important catalytic processes. These interesting properties between cores and shells arise depending on the interactions between the core and shell.^{78, 137-150} Several strategies for core-shell NPs have been used, as shown in Figure 4.1, including direct heterogeneous deposition on core to grow shell material (a-c, e and j), shell growth after chemical activation of the core surface involving cation exchange, redox replacement and Kirkendall effect (d, f and g), self-controlled nucleation growth shell (h and i).

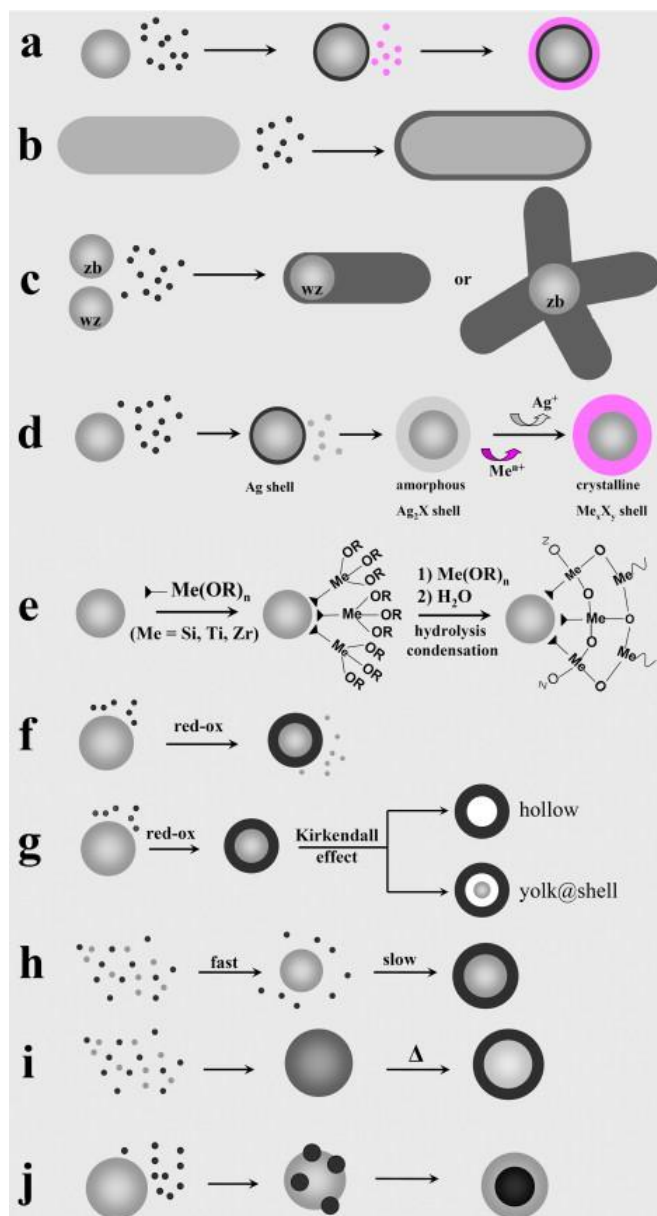


Figure 4.1 Sketch of mechanisms leading to the formation of core@shell HNPs⁸⁰: (a–c) direct heterogeneous nucleation and growth of the shell material onto preformed NC seeds with controlled shape and crystal structure; (d) sequential heterogeneous nucleation and growth steps onto preformed seeds, involving deposition of an

amorphous shell and its conversion to crystalline upon cation exchange; (e) silica shell growth by priming of the seed surface and subsequent polymerization; (f) sacrificial red-ox replacement of the outer seed layer; (g) surface-confined red-ox reaction followed by hollowing via the Kirkendall effect; (h) self-controlled nucleation-growth; (i) thermally driven crystal-phase segregation; (j) solid-state diffusion and coalescence

Table 4.1 List of reactant and core-shell structure product materials via cation exchange in NCs

Class	Reactant	product
oxides	FeO@CoFe ₂ O ₄	Fe _{1-x} Co _x O ₄ @CoFe ₂ O ₄ ¹⁵¹
	Mn ₃ O ₄	Mn ₃ O ₄ @CoMn ₂ O ₄
	Fe ₃ O ₄	Fe ₃ O ₄ @Ni _x Fe _{3-x} O ₄
selenides	CdSe	CdSe@PdSe ¹⁵²
	PbSe	PbSe@CdSe ¹⁵³
sulfides	PbS	PbS@CdS ¹⁵⁴⁻¹⁵⁶
	CdS	CdS@PbS, ¹⁵⁷ CdS@HgS, ¹⁵⁸ CdS@Cu _{2-x} S ¹⁵⁹
	CuInS ₂	CuInS ₂ @ZnS ¹⁶⁰
	Cu ₂ S	Cu ₂ S@Au ₂ S, ¹⁶¹ Cu ₂ S@ZnS, ¹⁶² Cu _{2-x} S@CuInS ₂ ¹⁶³
	TiS ₂	TiS ₂ @Cu ₂ S ¹⁶⁴
	CZTS	CZTS@Ag ₂ S ⁹⁴
lanthanide fluorides	NaYF ₄ : Yb, Tm	NaYF ₄ : Yb, Tm@NaGdF ₄ ¹⁶⁵
tellurides	PbTe	PbTe@CdTe ¹⁶⁶
	Cu _{2-x} Te	Cu _{2-x} Te@PbTe, ¹⁶⁷ Cu _{2-x} Te@SnTe ¹⁶⁷
Selenide-sulfide	CuInSe _x S _{2-x}	CuInSe _x S _{2-x} @CdSe _x S _{2-x} ¹⁶⁸
	CdSe@CdS	Cu ₂ Se@Cu ₂ S ¹⁶⁹⁻¹⁷¹
	Cu ₂ Se@Cu ₂ S	PbSe@PbS, ¹⁷¹ ZnSe@ZnS, ^{169, 172} CdSe@CdS ¹⁷⁰

Hybrid metal	Au@Fe ₃ O ₄	Au@Co _x Fe _{1-x} O ₄ ¹⁵¹
chalcogenide	Au@Ag ₂ S	Au@CdS ¹⁷³
	Se@Ag ₂ Se	Se@ZnSe, Se@CdSe, Se@PbSe ^{174, 175}
	Au@Ag ₂ X(X = S, Se, Te)	Au@CdS, Au@CdTe, Au@PbS, Au@ZnS ¹⁷⁶

Among all these methods, cation exchange reactions have been increasingly utilized as a synthetic tool for core-shell NPs with unique composition and morphology. Table 4.1 shows a list of core-shell NPs that were prepared via cation exchange reactions. For instance, Sytnyk et al. reported that cation exchange process is a valuable tool for tuning of the magnetic properties of 3 different metal oxides based colloidal NCs, such as Fe₃O₄, Au@Fe₃O₄ and FeO@CoFe₂O₄ NCs.¹⁵¹ They demonstrated ferrite-based NCs were subjected to a Fe²⁺ to Co²⁺ cation exchange procedure (Figure 4.2). Such cation exchange process enables to obtain novel nanoheterostructures, which are not achievable by conventional synthetic routes. While Lee et al. demonstrated an innovative and universal strategy for Cu_{2-x}S@CuInS₂ core-shell nanodisks by involving cation exchange reaction, introducing In into Cu_{2-x}S nanoplates with controlling shell thickness and composition.¹⁶³ In addition, they also showed AuS@CuInS₂ core-shell nanodisk obtained from Cu_{2-x}S@CuInS₂ by replacing Cu with Au. Similarly, our group has been reported the partial ation exchange reaction to produce Mn₃O₄@CoMn₂O₄ core-shell NPs at low temperature and ambient atmosphere. Furthermore, by using a cobalt perchlorate instead of cobalt chloride, Mn₃O₄@CoMn₂O₄-CoO NPs were obtained due to a simultaneous nucleation on the core-shell surface in addition to the cation exchange reaction (Figure 4.3). Such HNPs were investigated for ORR and OER in alkaline solution and improved performance with respect to commercial Pt, IrO₂-based and previously reported transition metal oxides as bifunctional catalysts.

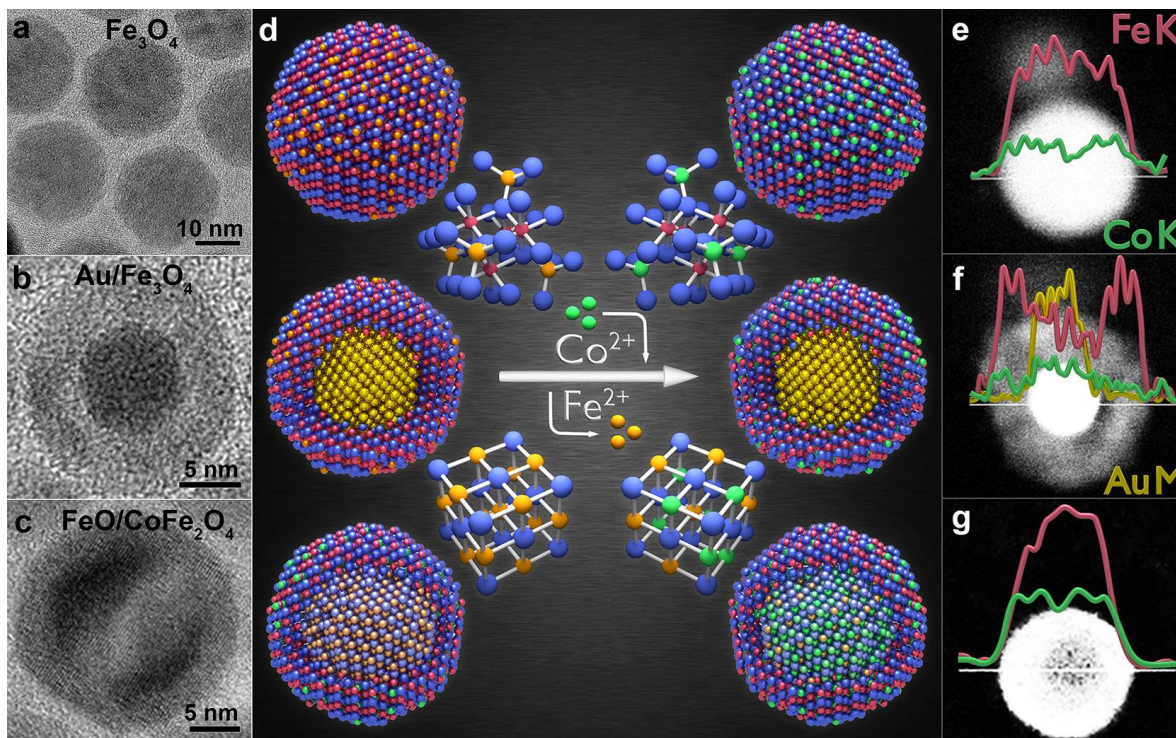


Figure 4.2 Three classes of magnetic NCs are investigated:¹⁵¹ (a, e) homogeneous spherical magnetite (Fe_3O_4) NCs, (b, f) gold-magnetite core-shell NCs, and (c, g) wüstite (FeO)-magnetite core-shell NCs. (a-c) TEM images of the starting materials. (d) Scheme of the cation exchange procedure in the three different NC types with inverse spinel or rock-salt crystal structure, (blue balls represent oxygen atoms; red balls, Fe^{3+} ; orange, Fe^{2+} ; green, Co^{2+} ; gold, Au atoms). (e, f) are high-angle annular dark field STEM images of NCs after the Fe^{2+} to Co^{2+} cation exchange procedure is performed. The ion concentration distributions for Fe (red) and Co (green), and Au (golden) across the NCs, shown by the EDX line scans (obtained for transitions from the K or M shell respectively), evidence the Co doping after the cation exchange treatment.

Currently, core-shell NPs catalysts have been used in many areas of electrocatalysis, such as ORR, OER and alcohol oxidation.^{139, 142, 146} Their electrocatalytic activity depends on their structure and composition. Core-shell NPs show remarkable catalytic activity compared with single-component NPs because of the synergistic effect between the core and shell. In Zhuang et al. report, monodisperse $\text{Au}@ \text{Co}_3\text{O}_4$ core-shell NCs were prepared by seeds growth method to deposit Co shells on surface of the Au core and their conversion to Co_3O_4 shells.¹⁷⁷ Such $\text{Au}@ \text{Co}_3\text{O}_4$ core-shell as a OER catalysts has 7 times higher activity than Au and Co_3O_4 mixture or Co_3O_4 alone and 55 times higher than Au alone due to synergistic between the Au core and Co_3O_4 shell (Figure 4.4) at overpotential of 0.35 V. Guo et al. reported a seed-mediated growth method to prepare core-shell $\text{FePtM}@ \text{FePt}$ ($\text{M} = \text{Pd}, \text{Au}$) nanowires.¹⁷⁸ These $\text{FePtM}@ \text{FePt}$ nanowires were used as electrocatalysts for ORR and displayed excellent performance and significant stability dependent on core composition and shell thickness. A general synthetic approach to synthesize core-shell metal oxide hybrid ($\text{M}_1\text{M}_2@ \text{M}_1\text{O}_x$) NPs was demonstrated by Nong and co-

workers.¹⁷⁹ They took IrNi@IrO_x NPs as example to exhibit these kinds of core-shell NPs and showed that they possess improved OER catalytic activity when compare with benchmark catalysts. Hu et al. also demonstrated that Co₃O₄@NiCo₂O₄ double-shelled nanocages had superior performance when evaluated as electrocatalysts for OER and compared with many other related work.¹⁸⁰

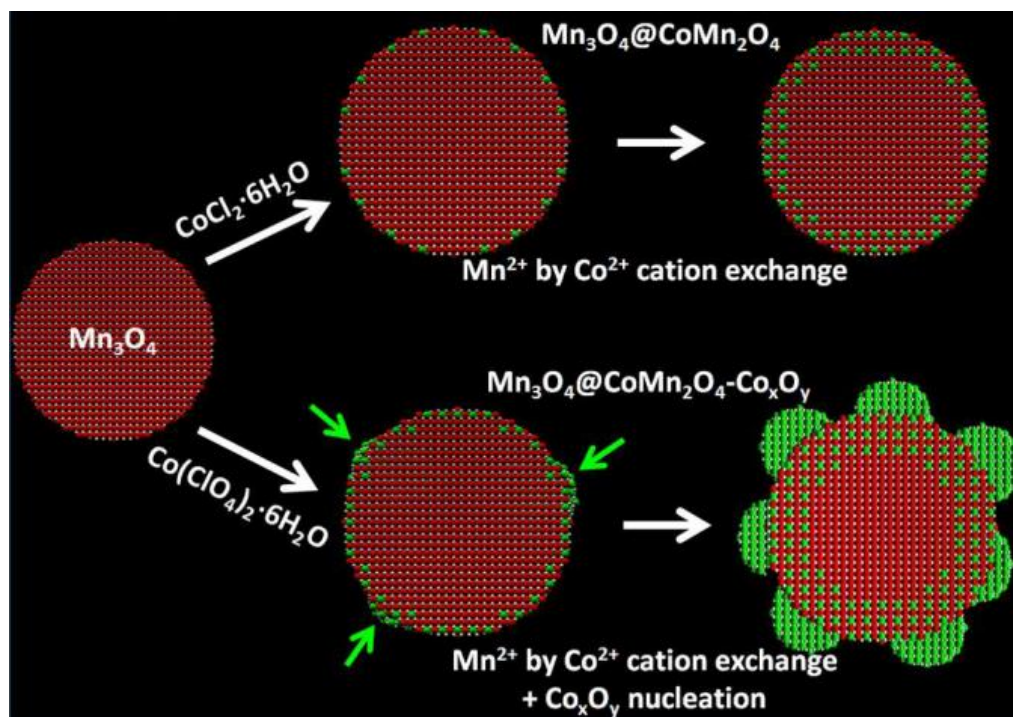


Figure 4.3 Scheme of the formation of the Mn₃O₄@CoMn₂O₄ and Mn₃O₄@CoMn₂O₄-Co_xO_y nanoheterostructures when using either a cobalt chloride or a cobalt perchlorate solution. Mn₃O₄@CoMn₂O₄ was obtained by partial cation exchange between Mn²⁺ and Co²⁺ when using a cobalt chloride precursor. Mn₃O₄@CoMn₂O₄-Co_xO_y were obtained by the same cation exchange reaction and the additional and simultaneous nucleation of a Co_xO_y phase when using a cobalt perchlorate. Green arrows in the bottom cartoon point at Co_xO_y NC nucleation sites of the Mn₃O₄@CoMn₂O₄.

In summary, the works specify above are just some examples of the fact that core-shell nanostructures as electrocatalyst exhibit many unique properties providing an exceptional way to increase active surface energy on the shell surface and decrease the reactions overpotential.

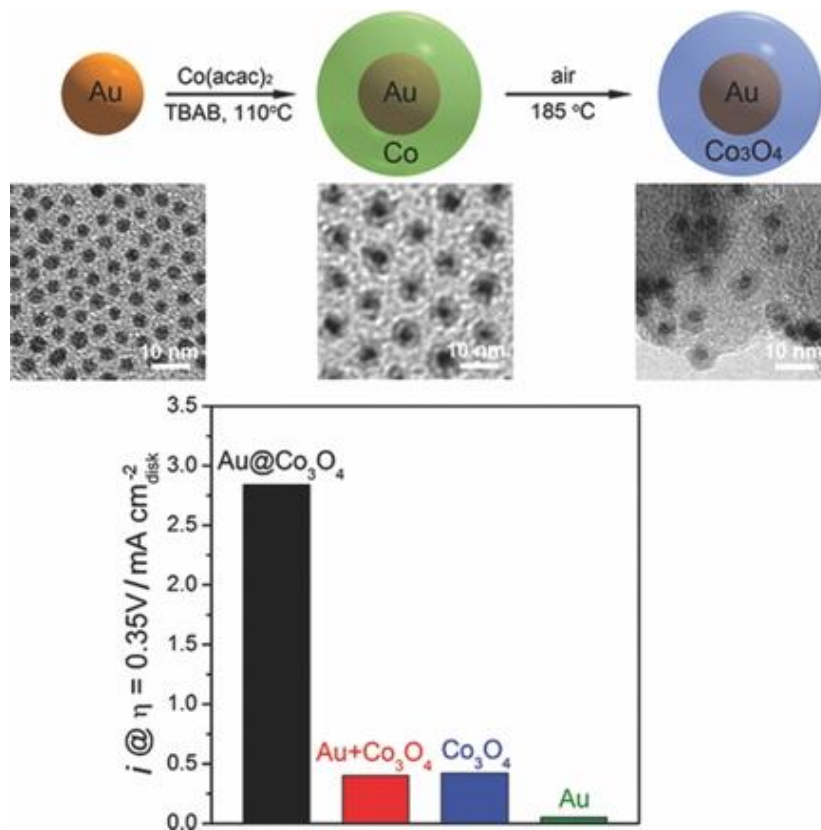


Figure 4.4 Scheme of the synthetic route to Au@Co₃O₄ core-shell NPs (top), and TEM micrographs of Au, Au@Co and to Au@Co₃O₄ (middle), and corresponding activity of the catalysts at an overpotential of 0.35 V (bottom).¹⁷⁷

4.1.2 Mn₃O₄@CoMn₂O₄-Co_xO_y Nanoparticles: Partial Cation Exchange Synthesis and Electrocatalytic Properties Toward the Oxygen Reduction and Evolution Reactions

This paper of the thesis is based on the paper entitled “*Mn₃O₄@CoMn₂O₄-Co_xO_y Nanoparticles: Partial Cation Exchange Synthesis and Electrocatalytic Properties Toward the Oxygen Reduction and Evolution Reactions*” published in ACS Applied Materials & Interfaces, 2016, 8, 17435-17444. This paper is based on partial cation exchange reaction between Mn ions and Co ions in preformed Mn₃O₄ seeds NPs to produce Mn₃O₄@CoMn₂O₄ NPs. Additionally Mn₃O₄@CoMn₂O₄-CoO were obtained by different using a different cobalt precursor that promoted a simultaneous nucleation on the Mn₃O₄@CoMn₂O₄ surface. Such a seeds-mediated growth method offers a scalable, low temperature and ambient pressure protocol to control composition and phase distribution of core-shell HNPs. The growth mechanism was discussed in the article. The different coordination ability of the cobalt precursors was the key behind the formation of this two distinct HNPs. Cobalt chloride was used for Mn₃O₄@CoMn₂O₄ and cobalt perchlorate for Mn₃O₄@CoMn₂O₄-CoO. These HNPs were tested as electrocatalysts for ORR and OER in alkaline solution and displayed superior activity and durability versus to state-of-the-art electrocatalysts. For instance, MC1 composition showed low overpotentials of 0.31 V at -3 mA·cm⁻² and a small Tafel slope of 52 mV/dec for ORR, and overpotentials of 0.31 V at 10 mA·cm⁻² and a Tafel slope of 81 mV/dec for OER. These properties outperformed commercial Pt, IrO₂-based and previously reported transition metal oxides as bifunctional catalysts. In addition, the different potential of ORR current density of -3 mA·cm⁻² and that at OER current density of 10 mA·cm⁻² is a main figure of merit for potential practical applications. The value was 0.85 V for MC1/C is among the best values reported. Figure 4.5 shown, a clear nanoheterostructure of MC1 where the CoO (green part) grew on the surface of core-shell NPs (red and yellow part), and the spider graphic showed some electrocatalytic performance of ORR and OER in onset potential, Tafel and overpotential, and a comparison with commercial Pt and IrO_x electrocatalysts.

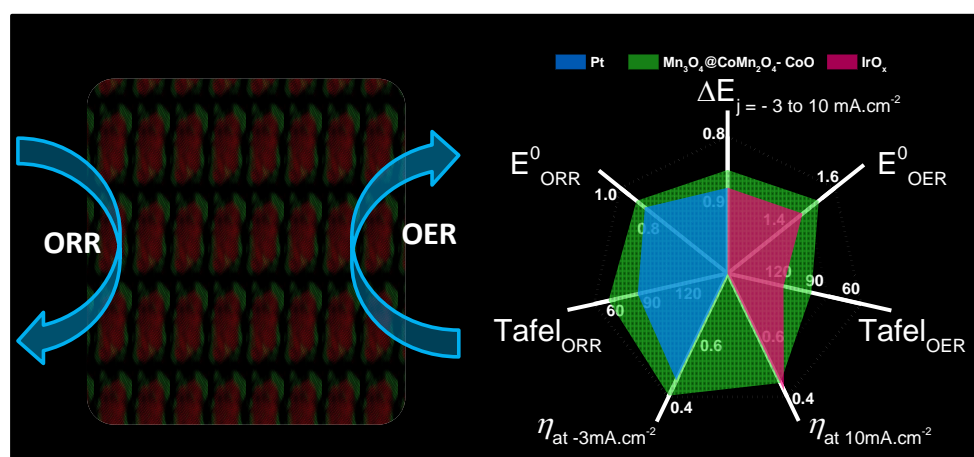


Figure 4.5 HRTEM micrograph of Mn-Co oxide HNPs (left) and some electrocatalytic performance Mn-Co oxide HNPs and commercial noble catalysts.

Mn₃O₄@CoMn₂O₄-Co_xO_y Nanoparticles: Partial Cation Exchange Synthesis and Electrocatalytic Properties toward the Oxygen Reduction and Evolution Reactions

Zhishan Luo,^{†,○} Erdem Irtem,^{†,○} Maria Ibáñez,[†] Raquel Nafria,[†] Sara Martí-Sánchez,[⊥] Aziz Genç,[⊥] Maria de la Mata,[⊥] Yu Liu,[†] Doris Cadavid,[†] Jordi Llorca,^{||} Jordi Arbiol,^{⊥,▽} Teresa Andreu,[†] Joan Ramon Morante,^{†,#} and Andreu Cabot^{*,†,▽}

[†]Catalonia Institute for Energy Research—IREC, Sant Adrià del Besòs, 08930 Barcelona, Spain

^{||}Institut de Tècniques Energètiques, Universitat Politècnica de Catalunya, 08028 Barcelona, Spain

[⊥]Catalan Institute of Nanoscience and Nanotechnology (ICN2), CSIC and The Barcelona Institute of Science and Technology (BIST), Campus UAB, Bellaterra, 08193 Barcelona, Spain

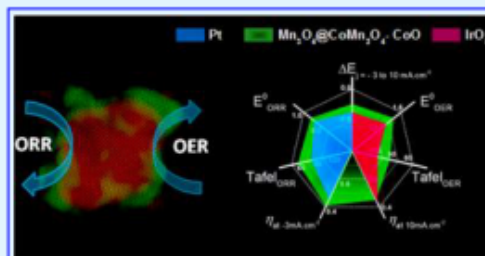
[#]Departament d'Electronica, Universitat de Barcelona, 08028 Barcelona, Spain

[▽]ICREA, Pg. Lluís Companys 23, 08010 Barcelona, Spain

Supporting Information

ABSTRACT: Mn₃O₄@CoMn₂O₄ nanoparticles (NPs) were produced at low temperature and ambient atmosphere using a one-pot two-step synthesis protocol involving the cation exchange of Mn by Co in preformed Mn₃O₄ NPs. Selecting the proper cobalt precursor, the nucleation of Co_xO_y crystallites at the Mn₃O₄@CoMn₂O₄ surface could be simultaneously promoted to form Mn₃O₄@CoMn₂O₄-Co_xO_y NPs. Such heterostructured NPs were investigated for oxygen reduction and evolution reactions (ORR, OER) in alkaline solution. Mn₃O₄@CoMn₂O₄-Co_xO_y NPs with [Co]/[Mn] = 1 showed low overpotentials of 0.31 V at -3 mA·cm⁻² and a small Tafel slope of 52 mV·dec⁻¹ for ORR, and overpotentials of 0.31 V at 10 mA·cm⁻² and a Tafel slope of 81 mV·dec⁻¹ for OER, thus outperforming commercial Pt-, IrO₂-based and previously reported transition metal oxides. This cation-exchange-based synthesis protocol opens up a new approach to design novel heterostructured NPs as efficient nonprecious metal bifunctional oxygen catalysts.

KEYWORDS: nanoparticle, ORR, OER, manganese oxide, cobalt oxide, colloidal, electrocatalysis, cation exchange



1. INTRODUCTION

The development of highly active, low-overpotential, stable, and low-cost electrocatalysts based on abundant and conflict-free raw materials is a critical challenge in several energy conversion technologies. In particular, high-performance bifunctional electrocatalysts for oxygen reduction and evolution reactions (ORR and OER) are an essential component in rechargeable metal–air batteries and regenerative low-temperature fuel cells.^{1–6} In these devices, the use of a catalyst based on scarce and high-cost platinum group metals represents a severe cost constraint that strongly limits deployment. Alternative cost-effective and abundant transition metal oxides have been recently shown as outstanding candidates for ORR and/or OER in alkaline media. Some transition metal oxides show excellent stability, very high activity, low overpotential, and large roundtrip efficiency associated with their multiple possible oxidation states, off-stoichiometric compositions, defects, and vacancies.^{7–14}

Among transition metal oxides, Mn-based oxides and particularly spinels have shown outstanding performance for ORR and, to a minor extent, for OER.^{7,15–21} Besides, Co-based

oxides are excellent electrocatalysts for OER,^{22–25} although particular Co-based catalysts have also shown excellent properties as bifunctional OER/ORR catalysts.^{26–29} For instance, Co₃O₄ NPs supported on graphene demonstrated excellent electrocatalyst not only for OER but also for ORR.⁸ Outstanding performances were also demonstrated from Co₃O₄ nanoparticles (NPs) on carbon nanofibers and Vulcan carbon as oxygen catalysts in zinc–air batteries.³⁰

The combination of Mn and Co oxides, among other applications,^{31–34} may thus provide excellent ORR/OER activities useful for a range of technologies.^{35–43} In this direction, Cheng et al. demonstrated that Co_xMn_{3-x}O₄ NPs have considerable catalytic activity toward ORR and OER.⁹ Liang et al. demonstrated MnCo₂O₄–graphene hybrids to be excellent electrocatalysts for ORR.³⁵ D. Wang et al. produced Co₂MnO₄–Co₃O₄ nanocomposites and demonstrated their excellent performance as bifunctional oxygen electrocatalyst.²²

Received: March 5, 2016

Accepted: June 20, 2016

Published: June 20, 2016

Y. Wang et al. showed $\text{MnO}_x\text{-Co}_3\text{O}_4$ supported on carbon to outperform MnO_x/C and $\text{Co}_3\text{O}_4/\text{C}$ catalysts in the ORR.³⁶ Xiao et al. produced $\text{Mn}_3\text{O}_4\text{-CoO}$ core-shell structures and demonstrated that they have high performance in the ORR.³⁷ $\text{Mn}_{1.5}\text{Co}_{1.5}\text{O}_4$ oxides were produced by Xu et al., who also evaluated their electrocatalytic ORR performance.³⁸ In another excellent work, Menezes et al. demonstrated that tetragonal CoMn_2O_4 catalyst outperforms MnCo_2O_4 in the ORR but MnCo_2O_4 outperforms CoMn_2O_4 in the OER.³⁹ Zhao et al. also produced spinel Mn-Co oxides and demonstrated their superior bifunctional electrocatalytic properties when supported on N-doped carbon nanotubes.¹⁰ Recently, C. Li et al. demonstrated the phase and composition control of cobalt manganese spinel NPs to provide improved oxygen electrocatalysis performances.¹⁴ G. Li et al. probed $\text{Co}_3\text{O}_4\text{-Mn}_3\text{O}_4$ composites having discovered their excellent performance as oxygen electrocatalysts in zinc-air batteries.⁴⁰ $\text{MnO}_2\text{-CoO}$ supported on reduced graphene oxide was also demonstrated as an excellent catalyst for ORR,⁴¹ and CoMn_2O_4 nanodots on graphene showed efficient ORR and OER.⁴² Interestingly, ordered CoMnO NPs within a nitrogen carbon framework also showed excellent OER activity.¹¹ Ge et al. also showed MnCo_2O_4 supported on nanocarbon supports to be an excellent electrocatalyst for ORR and OER.⁴³

However, the multiple valence and related structural variability of transition metal oxides, which is at the origin of their exceptional electrocatalytic performance, is also behind the difficulty to produce these compounds in a reproducible and controlled manner. This is a particularly important limitation when taking into account the strong dependence of the physicochemical properties of transition metal oxides on composition, structural parameters, and distribution and oxidation state of cations. Besides, beyond performance and reproducibility, to ensure technological relevance, materials with large surface areas to maximize activity need to be produced in a cost-effective manner, what requires the synthesis of NPs using low reaction temperatures and ambient pressures.

In this work, we detail a scalable, low-temperature, and ambient pressure protocol to produce monodisperse $\text{Mn}_3\text{O}_4@ \text{CoMn}_2\text{O}_4$ and $\text{Mn}_3\text{O}_4@ \text{CoMn}_2\text{O}_4\text{-Co}_x\text{O}_y$ NPs with controlled composition and phase distribution. We characterized the ORR and OER performance in alkaline solution of such heterostructured NPs performance to demonstrate their superior activity and durability when compared with benchmark electrocatalysts.

2. EXPERIMENTAL SECTION

Chemicals. Manganese(II) acetate ($\text{Mn}(\text{OAc})_2$, 98%), cobalt(II) perchlorate hexahydrate ($\text{Co}(\text{ClO}_4)_2 \cdot 6\text{H}_2\text{O}$), xylenes ($\geq 98.5\%$), cobalt(II) chloride hexahydrate ($\text{CoCl}_2 \cdot 6\text{H}_2\text{O}$, 98%), oleylamine (OLA, $>70\%$), oleic acid (OA, 90%), Nafion (5%), and carbon-supported Pt nanoparticles (Pt/C, 10 wt % Pt) were purchased from Sigma-Aldrich. The reference IrOx/Ti dimensionally stable anode (DSA) electrocatalyst was obtained from ElectroCell Systems. Toluene, chloroform, and ethanol were of analytical grade and obtained from various sources. Milli-Q water was supplied by the PURELAB flex from ELGA. All chemicals were used as received without further purification, except OLA, which was purified by distillation.

Synthesis of $\text{Mn}_3\text{O}_4@ \text{CoMn}_2\text{O}_4$ Core-Shell NPs. $\text{Mn}_3\text{O}_4@ \text{CoMn}_2\text{O}_4$ core-shell NPs were synthesized by means of a one-pot two-step procedure. First Mn_3O_4 NPs were prepared similarly to previously reported procedures.³⁴ Briefly, xylene (15 mL), OLA (0.82 mL), OA (0.16 mL), and $\text{Mn}(\text{OAc})_2$ (1 mmol) were placed in a 50

mL three-neck flask. Under air conditions, the solution was heated to 90 °C at 5 °C/min, the temperature at which deionized water (1 mL) was injected. The reaction mixture was maintained at 90 °C for 100 min to form Mn_3O_4 NPs. At this point, 1.0 M $\text{CoCl}_2 \cdot 6\text{H}_2\text{O}$ aqueous solution (1 mL) was added and the reaction was continued for an additional 300 min. Finally, the solution was cooled to room temperature, and NPs were purified by multiple precipitation/redispersion steps using toluene as solvent and ethanol as nonsolvent.

Synthesis of $\text{Mn}_3\text{O}_4@ \text{CoMn}_2\text{O}_4\text{-Co}_x\text{O}_y$ NPs. $\text{Mn}_3\text{O}_4@ \text{CoMn}_2\text{O}_4\text{-Co}_x\text{O}_y$ NPs were prepared following the exact same procedure but using a different cobalt precursor: $\text{Co}(\text{ClO}_4)_2 \cdot 6\text{H}_2\text{O}$. By tuning the Co:Mn molar ratio, NPs with different sizes and different compositions were obtained. In order to tune the Co:Mn molar ratio, we modified the concentration of the $\text{Co}(\text{ClO}_4)_2 \cdot 6\text{H}_2\text{O}$ aqueous solution between 0.5 and 2 M. The obtained $\text{Mn}_3\text{O}_4@ \text{CoMn}_2\text{O}_4\text{-CoO}$ NPs were denoted MC0.5, MC1, and MC2 referring to the Co:Mn molar ratios of 0.5, 1, and 2, respectively.

Structural and Chemical Characterization. Sizes and shapes of the initial NPs were examined by transmission electron microscopy (TEM) using a ZEISS LIBRA 120, operating at 120 kV. High-resolution TEM (HRTEM) studies were conducted using a field emission gun FEI Tecnai F20 microscope at 200 kV with a point-to-point resolution of 0.19 nm. Scanning electron microscopy (SEM) analyses were done in a ZEISS Auriga microscope with an energy dispersive X-ray spectroscopy (EDS) detector operating at 20 kV that allowed studying the NP composition. For SEM characterization, the materials were dispersed in chloroform and drop cast on silicon substrates. Powder X-ray diffraction (XRD) patterns were collected directly from the as-synthesized NPs dropped on Si(501) substrate on a Bruker AXS D8 Advance X-ray diffractometer with Ni-filtered ($2 \mu\text{m}$ thickness) $\text{Cu K}\alpha$ radiation ($\lambda = 1.5406 \text{ \AA}$) operating at 40 kV and 40 mA. A LynxEye linear position-sensitive detector was used in reflection geometry. Nitrogen adsorption-desorption events were performed on a BEL-Mini adsorption analyzer. Thermogravimetric analysis was carried out on a Netzsch STA 449 F3 Jupiter analyzer. Hydrogen temperature-programmed reduction (TPR) was performed using a Micromeritics AutoChem HP 2950 chemisorption analyzer. A 20 mg amount of sample was pretreated at 100 °C for 30 min under an He flow of 50 mL/min. After cooling to room temperature, the samples were reduced in a flow of 12 vol % H_2/Ar (50 mL/min), and temperature was linearly increased at a rate of 10 °C/min up to 600 °C. X-ray photoelectron spectroscopy (XPS) was done on a SPECS system equipped with an Al anode XRS0 source operating at 150 mW and a Phoibos 150 MCD-9 detector. The pressure in the analysis chamber was always below 10^{-7} Pa. The area analyzed was about $2 \text{ mm} \times 2 \text{ mm}$. The pass energy of the hemispherical analyzer was set at 25 eV and the energy step was set at 0.1 eV. Data processing was performed with the CasaXPS program (Casa Software Ltd., Teignmouth, U.K.). Binding energy (BE) values were centered using the C 1s peak at 284.8 eV. The atomic fractions (%) were calculated using peak areas.

Catalyst Preparation. The as-synthesized Mn-Co oxide NPs were mixed with carbon powder (Vulcan XC-72) with a weight ratio of 30% through sonication of NPs and carbon in chloroform and ethanol mixture (1:1). The NP/C composite was washed several times with chloroform and acetone. As formed NP/C nanocomposites were treated under air atmosphere at 180 °C for 5 h to remove surface organic ligands.⁷ The catalyst ink for electrochemical measurements was prepared by mixing 5 mg of NP/C, 0.5 mL of deionized water, 0.5 mL of isopropanol, and 17.5 μL of 5 wt % of Nafion solution. The electrode was prepared by drop casting 10 μL of the catalyst ink on glassy carbon electrode, to afford a catalyst mass loading of approximately $275 \text{ mg}\cdot\text{cm}^{-2}$. For comparison, electrodes with commercial Pt/C and an IrO_x-based catalyst (DSA, ElectroCell A/S) were also prepared following the same experimental procedure.

Electrochemical Measurements. Electrochemical measurements were performed with a computer-controlled workstation bipotentiostat (VMP3 multichannel, BioLogic Instruments). A three-electrode system and rotator assembly (Pine rotator, AFMSRCE Pine Instruments) were used for electrochemical measurements containing

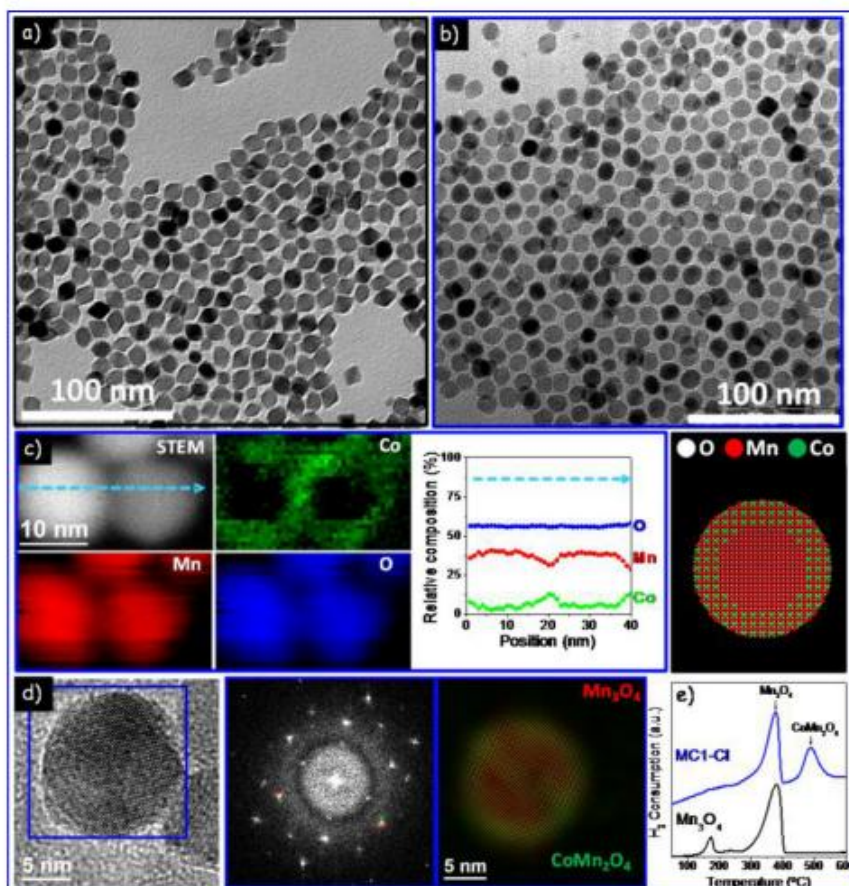


Figure 1. TEM micrographs of Mn_3O_4 NPs (a) and MC1-Cl NPs (b). (c) ADF-STEM image and EELS elemental mapping of MC1-Cl NPs and compositional line profile of Mn, Co, and O elements recorded along the arrow in the STEM images. (d) HRTEM micrograph of a MC1-Cl NP, power spectra of the blue squared region, and colorful structural map showing the distribution of Mn_3O_4 (red) and CoMn_2O_4 (green) phases. (e) H_2 TPR profile of Mn_3O_4 and MC1-Cl NPs.

a Teflon surrounded glassy carbon working electrode (5 mm in diameter), a silver–silver chloride reference electrode (Ag/AgCl with 3.5 M KCl encapsulated, 012167 RE-1B, ALS Co. Ltd.-BAS Inc.), and a platinum wire for the counter electrode. The Ag/AgCl electrode was calibrated in a standard three-electrode system with two Pt wires used as working and counter electrodes and the Ag/AgCl electrode as reference electrode, using a 0.1 M KOH electrolyte saturated with pure H_2 .⁴⁵ From linear scanning voltammetry at a scan rate of $0.1 \text{ mV}\cdot\text{s}^{-1}$, the thermodynamic potential (versus Ag/AgCl) for the hydrogen electrode reaction (potential at which the current crossed zero) was measured as -0.9863 V (Supporting Information Figure S8). Then, potential was transformed to the reversible hydrogen electrode (RHE) scale as follows: $E_{\text{RHE}} = E_{\text{Ag/AgCl}} + 0.9863 \text{ V}$. Both ORR and OER polarization curves were obtained in O_2 -saturated 0.1 M KOH electrolyte. ORR experiments were tested from 0.1 to -0.55 V versus Ag/AgCl (i.e., 1.09 to 0.44 V versus RHE) at a scan rate of $5 \text{ mV}\cdot\text{s}^{-1}$ with different rotating rates (400–2000 rpm). OER polarization curves were obtained at potentials from 0.1 V versus Ag/AgCl (i.e., 1.09 V versus RHE) until current density reached $15 \text{ mA}\cdot\text{cm}^{-2}$ at a scan rate of $5 \text{ mV}\cdot\text{s}^{-1}$. To evaluate the catalyst durability, chronoamperometry was collected at 0.79 V versus RHE without rotation (0 rpm) in O_2 -saturated 0.1 M KOH solution. For all measurements, the current density was iR -corrected ($R \approx 45 \Omega$) using the solution resistance measured by EIS (electrochemical impedance spectroscopy) at open circuit potential with 5 mV amplitude over the frequency range of 200 kHz to 100 mHz.

3. RESULTS AND DISCUSSION

Mn–Co oxide (MC) NPs were prepared by a one-pot, two-step process. First Mn_3O_4 NPs with octahedral geometries were produced by decomposing $\text{Mn}(\text{OAc})_2$ at 90°C in the presence of OLA, OA, and water.⁴⁴ In a second step, within the same flask and at the same temperature, an aqueous cobalt chloride ($\text{CoCl}_2\cdot 6\text{H}_2\text{O}$) solution was added and allowed to react for 300 min. Panels a and b of Figure 1 show representative transmission electron microscopy (TEM) micrographs of the initial Mn_3O_4 NPs and those produced after adding an equivalent molar amount of Co chloride ($[\text{Co}]/[\text{Mn}] = 1$; MC1-Cl). Upon Co addition, the initial octahedral-shaped Mn_3O_4 NPs were slightly rounded (Figure 1a,b) without undergoing significant growth even for $[\text{Co}]/[\text{Mn}]$ ratios up to 5. Annular dark field scanning TEM (ADF-STEM) in combination with electron energy loss spectroscopy (EELS) showed a core–shell type Co and Mn distribution with core and shell compositions compatible with Mn_3O_4 and CoMn_2O_4 stoichiometries (Figure 1c). We observed no modification of the shell thickness when increasing the $[\text{Co}]/[\text{Mn}]$ ratios above one, what points toward a self-limited reaction. High-resolution TEM (HRTEM) analysis showed Bragg reflections from two body centered tetragonal Mn_3O_4 phases (space group = $I4_1/amd$) with close lattice parameters. Upon filtering, a crystallo-

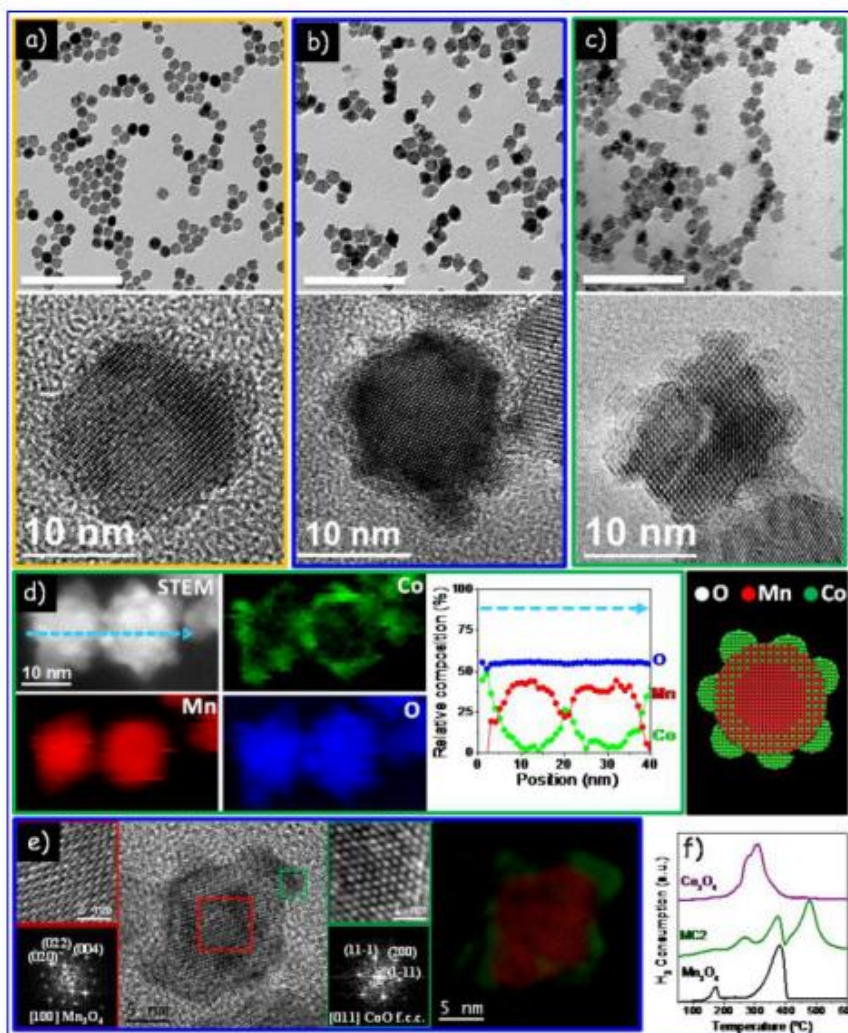


Figure 2. TEM (scale bar = 100 nm) and HRTEM micrographs of MC0.5 (a), MC1 (b), and MC2 (c) NPs. (d) ADF-STEM image and EELS elemental mapping of MC2 NPs and compositional line profile of Mn, Co, and O elements recorded along the arrow in the STEM image. (e) HRTEM micrographs of a MC1 NP, details of the red and green squared regions with the corresponding power spectra, and colorful structural map showing the distribution of body centered tetragonal Mn₃O₄ (red) and face centered cubic CoO (green) phases. (f) H₂ TPR profile of Mn₃O₄, MC2, and Co₃O₄ NPs.

graphic epitaxial core–shell distribution was identified (Figure 1d). H₂ temperature-programmed reduction (TPR) profiles of Mn₃O₄ and MC1-Cl NPs were performed after ligand removal at 180 °C. H₂ TPR profile of Mn₃O₄ NPs showed two peaks, at 173 and 380 °C, which are associated with the reduction of low-coordinated surface and bulk Mn ions, respectively. MC1-Cl NPs did not present the 173 °C peak related to surface Mn ions in Mn₃O₄. However, it displayed the main Mn₃O₄ reduction peak at 380 °C and an additional peak at 490 °C, which can be associated with the reduction of a CoMn₂O₄ phase (Figure 1e).^{46,47}

When cobalt perchlorate (Co(ClO₄)₂·6H₂O) instead of chloride was used as cobalt precursor, NPs with rougher surfaces were produced (Figure 2a–c). Upon Co perchlorate addition, a clear increase of the NP size was observed, with a final diameter depending on the amount of Co precursor used (Figures S1–S3). HRTEM and EELS mapping (Figure 2d,e) displayed a clear core–shell type element distribution with a

central core phase and composition consistent with Mn₃O₄ and a Co-rich shell. At the NP surface, several crystallites with a CoO phase were evidenced (Figure 2e). H₂ TPR analysis of the MC/C samples after thermal treatment at 180 °C showed the main Mn₃O₄ and the CoMn₂O₄-related components and an additional peak at the reduction temperatures of Co₃O₄ (300 °C, Figure 2f).^{48–51}

From the structural and chemical characterization, we conclude that when reacting Mn₃O₄ with a solution of cobalt chloride or perchlorate in the above-defined conditions, a partial cation exchange between Mn²⁺ and Co²⁺ takes place at the Mn₃O₄ surfaces, to form a CoMn₂O₄ shell.⁵² Besides, when compared with the Co chloride, the lower coordination ability of the perchlorate translates in a relatively higher reactivity of the Co ions in solution.^{53–55} The higher propensity of Co²⁺ ions to incorporate to the oxide structure in the presence of the weaker perchlorate ion coordination makes the Co²⁺ ion uptake by cation exchange not fast enough, which results in the

simultaneous nucleation of a cobalt oxide phase at the surface of the growing $\text{Mn}_3\text{O}_4@CoMn_2O_4$ structure. The initially nucleated cobalt oxide phase was identified as CoO by HRTEM, but it oxidized to Co_3O_4 with time and/or under mild thermal treatment. On the other hand, the lower reactivity of Co^{2+} in the presence of the more strongly coordinating chlorine ions prevented the nucleation of a Co_xO_y phase and constrained the Co incorporation to a self-limited partial cation exchange reaction. Figure 3 shows a scheme of the growth mechanisms to produce either $\text{Mn}_3\text{O}_4@CoMn_2O_4$ or $\text{Mn}_3\text{O}_4@CoMn_2O_4-Co_xO_y$ NPs.

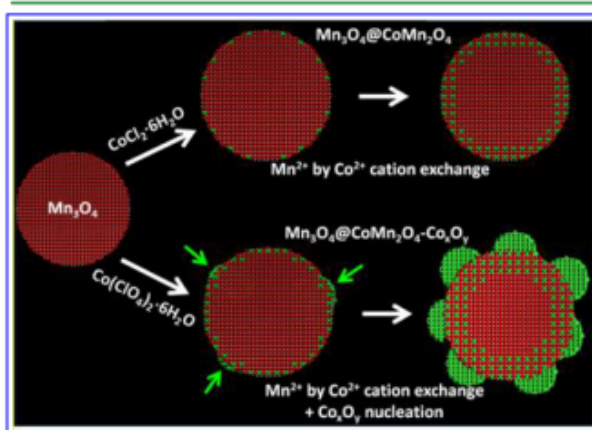


Figure 3. Scheme of the formation of the $\text{Mn}_3\text{O}_4@CoMn_2O_4$ and $\text{Mn}_3\text{O}_4@CoMn_2O_4-Co_xO_y$ nano-heterostructures when using either a cobalt chloride or a cobalt perchlorate solution. $\text{Mn}_3\text{O}_4@CoMn_2O_4$ NPs were obtained by partial cation exchange between Mn^{2+} and Co^{2+} when using a cobalt chloride precursor. $\text{Mn}_3\text{O}_4@CoMn_2O_4-Co_xO_y$ NPs were obtained by the same cation exchange reaction and the additional and simultaneous nucleation of a Co_xO_y phase when using a cobalt perchlorate. Green arrows in the bottom cartoon point at Co_xO_y nanocrystal nucleation sites.

Figure 4 shows the XRD pattern of as-synthesized Mn_3O_4 , MC1-Cl, and MC1 NPs. XRD patterns revealed NPs to have a body centered tetragonal phase. Due to the peak broadening associated with the small crystal domains and the very similar unit cell parameters of Mn_3O_4 and CoMn_2O_4 , XRD patterns were consistent with Mn_3O_4 (JCPDS No. 00-018-0803), Co_3O_4 (JCPDS No. 00-018-1538), and Mn–Co mixed oxides having spinel structure. On the other hand, CoO peaks (JCPDS No. 01-070-2856) could not be observed for any of the samples.

To study their electrocatalytic properties toward ORR and OER, NPs were supported on carbon powder (Vulcan XC-72) with a weight ratio of 30% through sonication of NPs and carbon in chloroform and ethanol (Figure S5). NP/C nanocomposites were then thermally treated under air atmosphere at 180 °C for 5 h to remove organic ligands. After this mild thermal treatment, no appreciable structural change was observed from TEM and XRD analyses (Figure S6). On the other hand, XPS analysis showed the presence of a main Co^{2+} component and an additional Co^{3+} contribution both before and after thermal treatment (Figure S7), which evidenced a partial oxidation of the cobalt ions at the CoMn_2O_4 and Co_xO_y surface. This oxidation was accentuated during the thermal treatment, with an increase of $[\text{Co}^{3+}]/[\text{Co}^{2+}]$ from 0.43 to 0.59. This oxidation is consistent with the H_2 TPR

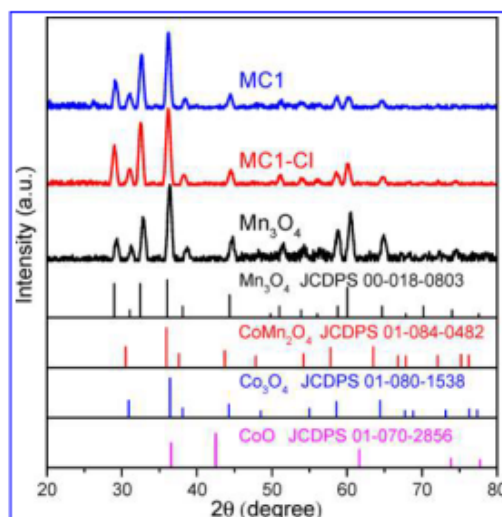


Figure 4. XRD patterns of as-synthesized, Mn_3O_4 and Mn–Co oxide NPs.

profiles also performed after the thermal treatment, since both CoO and Co_3O_4 phases show a similar reduction peak at 300 °C.^{48–51} The final NP/C composites had specific surface areas and average pore sizes of around 140 m^2/g and 20 nm, respectively (Table S1).

The ORR activity of NP/C was measured in O_2 -saturated 0.1 M KOH aqueous solution using a rotating disk electrode (RDE, Figures S9 and S10). Figure 5a shows linear sweep voltammograms (LSVs) of the different MC/C, and reference $\text{Mn}_3\text{O}_4/\text{C}$, $\text{Co}_3\text{O}_4/\text{C}$, and commercial Pt/C electrocatalysts. Figure 5b displays two ORR figures of merit, the current density at half-wave potential and the required overpotentials to reach $-3 \text{ mA}\cdot\text{cm}^{-2}$. Yet, an extended summary of the electrochemical data is presented in Tables S1–S4. When compared with $\text{Mn}_3\text{O}_4/\text{C}$ and $\text{Co}_3\text{O}_4/\text{C}$, the current density at half-wave potential and the required overpotentials to reach $-3 \text{ mA}\cdot\text{cm}^{-2}$ clearly improved with the presence of the CoMn_2O_4 shell (MC1-Cl). In addition, the overpotentials at $-3 \text{ mA}\cdot\text{cm}^{-2}$ of MC/C catalysts, including the Co_xO_y phase, were lower than those of MC1-Cl. In particular, the MC1/C catalyst outperformed the rest, showing the highest half-wave current densities, $-2.77 \text{ mA}\cdot\text{cm}^{-2}$, and the lowest overpotential, 0.4 V. Higher Co_xO_y concentrations (MC2/C) maintained the large current density in the diffusion limited region but with a slightly higher overpotential.

Electrochemical kinetics was evaluated from Tafel slopes obtained from the middle ORR current density range, where the limitation by O_2 diffusion in the active layer was negligible (Figure S11). MC1/C exhibited a Tafel value of $52 \text{ mV}\cdot\text{dec}^{-1}$, much lower than MC1-Cl/C ($95 \text{ mV}\cdot\text{dec}^{-1}$), $\text{Mn}_3\text{O}_4/\text{C}$ ($100 \text{ mV}\cdot\text{dec}^{-1}$), $\text{Co}_3\text{O}_4/\text{C}$ ($124 \text{ mV}\cdot\text{dec}^{-1}$), and even benchmark Pt/C ($76 \text{ mV}\cdot\text{dec}^{-1}$). The higher sensitivity of the electric current response to the applied potential for the MC1/C sample indicates this sample to have much more favorable kinetics. The lower Tafel slopes also indicate the ORR in this material to be most probably limited by a different reaction rate than in Mn_3O_4 or Co_3O_4 , showing Tafel slopes closer to the 120 mV predicted when the formation of O_2^- is the rate-determining step.⁵⁶ The values obtained for MC1/C coincide with some of the best ORR Tafel values found in the literature,

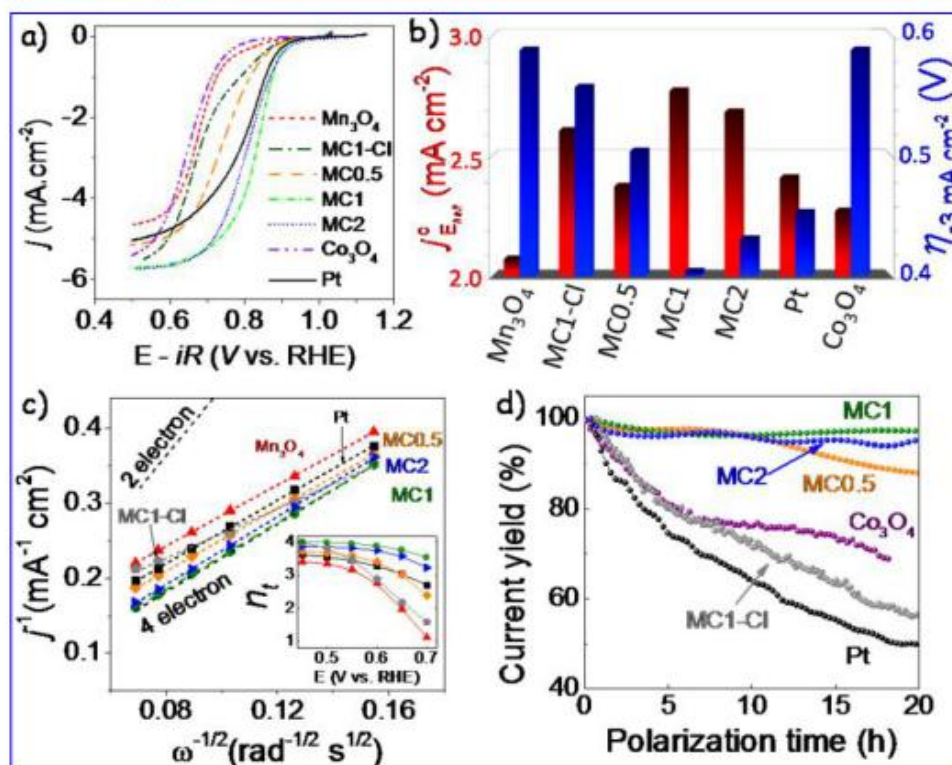


Figure 5. (a) ORR polarization curves of MC/C, $\text{Mn}_3\text{O}_4/\text{C}$, $\text{Co}_3\text{O}_4/\text{C}$, and Pt/C in O_2 -saturated 0.1 M KOH at 1600 rpm using a scan rate of 5 mV/s. (b) Kinetic current densities at half-wave potential (red) and overpotentials (blue). (c) K–L plots at 0.5 V versus RHE. The standard lines for two- and four-electron pathways are also plotted as a guideline. Inset shows n_t at different potentials. (d) Chronoamperometric data at 0.79 V in O_2 -saturated 0.1 M KOH.

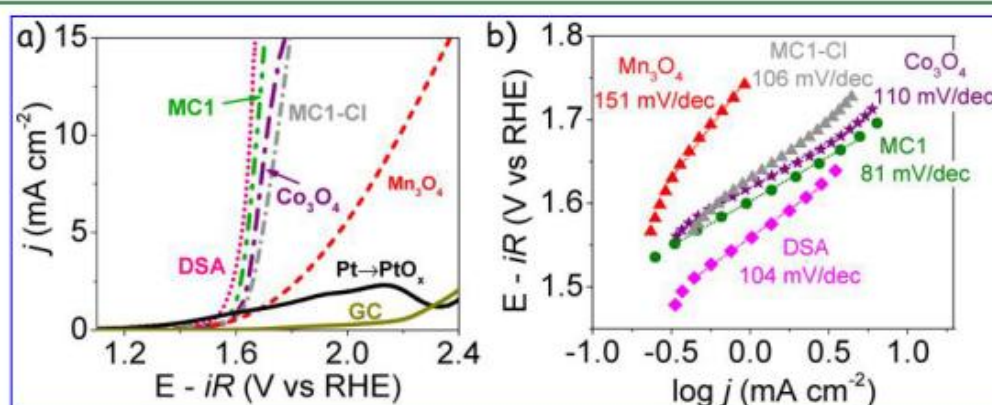


Figure 6. (a) OER polarization curves of $\text{Mn}_3\text{O}_4/\text{C}$, $\text{Co}_3\text{O}_4/\text{C}$, MC/C, Pt/C, DSA, and glassy carbon (GC) in O_2 -saturated 0.1 M KOH at a scan rate of 5 mV/s. (b) Tafel plots derived from OER polarization curves.

also associated with Mn-based oxide electrocatalysts under alkaline conditions.⁵⁷

The electron transfer number (n_t) was calculated by Koutecky–Levich (K–L) method from the RDE current–potential curves at various rotation speeds (Figure S12).⁵⁸ Figure 5c shows n_t as a function of electrode potential from the slope of the resulting best-fit line, i.e., 0.45–0.7 V. The presence of CoMn_2O_4 on the Mn_3O_4 surface had a minor influence on n_t , which increased just slightly from bare $\text{Mn}_3\text{O}_4/\text{C}$ to MC1-CI/C. However, the presence of Co_3O_4 at the $\text{Mn}_3\text{O}_4/\text{CoMn}_2\text{O}_4$ surface facilitated a rapid electron transfer, clearly

shifting the ORR mechanism toward the four-electron pathway as evidenced by the increase of n_t values up to 3.68, 3.98, and 3.86 for MC0.5/C, MC1/C, and MC2/C, respectively.

In terms of stability, a critical requirement for practical applications, MC1/C and MC2/C catalysts showed current retention above 95% of the initial current after 20 h (Figure 5d), well above that of $\text{Mn}_3\text{O}_4/\text{C}$, $\text{Co}_3\text{O}_4/\text{C}$, MC1-CI/C, and Pt/C catalyst, losing nearly half of its current density within the first 20 h (Figure 4d). Further, MC/C samples showed outstanding current retention 76% of the initial current compared to benchmark Pt/C catalyst, which lost 70% after

Table 1. Summary of the ORR/OER Catalytic Performance Revealed from Tafel Plots and Koutecky–Levich Plots

	ORR				OER			ORR-OER ΔE_{onset} , V
	$\eta_{E-E_{\text{onset}}}$, V	j_{LOR} , mA·cm ⁻²	n_1	Tafel, mV·dec ⁻¹	$\eta_{E-E_{\text{onset}}}$, V	$E_{j=10\text{mA}\cdot\text{cm}^{-2}}$, V	Tafel, mV·dec ⁻¹	
Mn ₃ O ₄	0.35	-4.64	3.2	100	0.43	2.19 ^b	151	1.53
Mn ₃ O ₄ @CoMn ₂ O ₄ (MC1-Cl)	0.34	-5.50	3.5	95	0.43	1.75	106	1.10
Mn ₃ O ₄ @CoMn ₂ O ₄ -Co _x O _y (MC0.5)	0.38	-5.14	3.6	81	0.38	1.72 ^b	95	0.99
Mn ₃ O ₄ @CoMn ₂ O ₄ -Co _x O _y (MC1)	0.31	-5.71	4.0	52	0.31	1.68	81	0.85
Mn ₃ O ₄ @CoMn ₂ O ₄ -Co _x O _y (MC2)	0.34	-5.73	3.8	83	0.35	2.01	83	1.21
Co ₃ O ₄	0.41	-5.40	3.4	124	0.39	1.71	110	1.07
Pt/DSA ^c	0.34	-5.25	3.5	76	0.25	1.65	104	0.88 ^d

^aDifference between the potential at ORR current density of -3 mA·cm⁻² and that at OER current density of 10 mA·cm⁻². ^bValues extrapolated from Tafel slopes. ^cORR values for Pt and OER values for DSA. ^dValue obtained from Pt ORR and DSA OER performance.

60 h durability test (Figure S13). For MC1/C and MC2/C, n_1 values close to 4 revealed a direct O₂ reduction path and an advanced decomposition activity against deteriorating peroxide species, which is beneficial for holding a stable catalytic activity. On the contrary, in reference catalysts, the four-electron O₂ reduction into OH⁻ competed with the two-electron pathway yielding HO₂⁻ species which can induce electrode corrosion.^{59,60} Besides, LSV before and after a 20 h test showed no significant change either in the onset voltage or in current density of both ORR and OER for MC0.5/C, MC1/C, and MC2/C electrocatalysts (Figure S14). A slight OER current density improvement was actually observed after a 20 h test, which we associate with the slow penetration of electrolyte into the film nanopores to meet additional catalytic sites.

Catalytic activities for OER are shown in Figure 6, including LSV driven to higher values than water oxidation standard potential, 1.23 V versus RHE and the corresponding Tafel plots. Co₃O₄/C showed state-of-the-art values, with an excellent catalytic activity, clearly outperforming that of Mn₃O₄/C. Since the Pt/C catalyst was not stable in OER, exhibiting an oxidation peak in the LSV,⁶¹ an IrO₂-based commercial anode (Ti/IrO₂:Ta₂O₅, DSA) was tested as OER benchmark catalyst. This material showed exceptionally low onset voltages (0.25 V) and high current densities. On the other hand, all MC/C catalysts showed excellent OER performances close to the Co₃O₄ and DSA references, with low overpotentials (e.g., 0.31 V for MC1/C) and sharp current density increases. MC1/C exhibited a Tafel value of 81 mV·dec⁻¹, clearly below that predicted for a single-electron rate-determining step, but slightly larger than lowest slopes obtained in literature, several of them using Ni-, Fe-, or Co-based electrocatalysts.^{62,63} Nevertheless, MC1/C showed the lowest Tafel slope from the materials tested here, with a value well below that of Mn₃O₄ (151 mV·dec⁻¹) and MC1-Cl (106 mV·dec⁻¹), but also of Co₃O₄ (110 mV·dec⁻¹) and even DSA (104 mV·dec⁻¹). This demonstrates the higher sensitivity to overpotential of the electrocatalytic activity of this material.

Overall, MC/C and MC-Cl/C composites clearly outperformed Mn₃O₄/C and Co₃O₄/C. We associate this fact with the presence of Co ions on the surface, which provide enhanced electron transfer capacity and strong coupling, thus resulting in more favorable reaction kinetics for OER. The better performance of MC/C over MC-Cl catalyst showed the addition of cobalt as a Co_xO_y phase to be particularly favorable. In particular, MC1/C exhibited the faster reaction kinetics, with a Tafel value of 81 mV·dec⁻¹, clearly below that of Mn₃O₄, but also of that of Co₃O₄ and even DSA.

A main figure of merit for practical electrochemical and photoelectrochemical applications is the difference between the

potential at ORR current density of -3 mA·cm⁻² and that at OER current density of 10 mA·cm⁻² ($\Delta E_{\text{ORR-OER}}$, Table 1). The smaller this difference, the closer a material is to being an ideal reversible catalyst. This value was 1.53 for Mn₃O₄/C and 1.07 for Co₃O₄. Lower $\Delta E_{\text{ORR-OER}}$ values were obtained for all the MC samples, especially for MC1/C, 0.85 V, which is among the best values reported (Tables S2–S4).

Electrocatalytic performance is boosted by enhancing charge transfer and increasing the number of available catalytic sites, i.e., proper energy band alignment and affinity for O₂/OH⁻ absorption. In this direction, cation ion doping and nanocrystallite surface decorating have provided relatively low onset potentials for spinel structures through increasing availability of catalytically active sites and their adsorption capabilities.^{9,15} In particular, the electrocatalytic activity of Co–Mn–O spinels was correlated with the oxygen binding ability on the catalyst surface.⁹ Obviously, in such a complex catalyst, composition should be carefully adjusted to optimize performance in the two reactions. As an example, J. Li et al. calculated the OH⁻ adsorption energy of Co–Mn oxide with 1:1 ratio to be larger than that of pristine CoO and MnO, yet the trend was the opposite for the corresponding adsorption energy of O₂ molecule, suggesting that an optimum ratio must be reached to bridge these two abilities (ORR + OER).¹¹ Consistently with previous works, we found Mn₃O₄@CoMn₂O₄ to outperform Mn₃O₄ and Co₃O₄ catalysts in the ORR, but to be outperformed by the Co₃O₄ catalyst in the OER. However, Mn₃O₄@CoMn₂O₄-Co_xO_y catalysts reached OER performances above those of Co₃O₄, while simultaneously further enhancing ORR. The higher performance of Mn₃O₄@CoMn₂O₄-Co_xO_y catalysts compared with Mn₃O₄@CoMn₂O₄ demonstrates Co_xO_y to play a key role in the electrocatalytic performance. Besides, the lower performances obtained for Mn₃O₄@CoMn₂O₄-Co_xO_y materials with too high cobalt concentrations (MC2) demonstrate the availability of MnCo₂O₄ surface sites to also play an important role in the overall performance. Such uniquely heterogeneous nanocomposite structure, making strong interface coupling between Co_xO_y and spinel, can not only provide intrinsic electronic structure but also a favorable electronic transport capability. We hypothesize these improvements to be related with (i) a higher surface site density on the much rougher NP surface after Co_xO_y nucleation; (ii) an enhanced charge transfer from the lower band gap Co_xO_y; and (iii) a modified adsorption affinity for O₂ and OH⁻ that requires extensive computational work to be elucidated.

4. CONCLUSION

In summary, $\text{Mn}_3\text{O}_4@\text{CoMn}_2\text{O}_4\text{-CoO}$ NPs were synthesized at low temperature and air atmosphere by the cation exchange of Mn by Co in preformed Mn_3O_4 NPs and the simultaneous growth of CoO crystallites at the $\text{Mn}_3\text{O}_4@\text{CoMn}_2\text{O}_4$ surface. Such heterostructured NPs showed electrocatalytic activities for both ORR and OER in alkaline media outperforming those of Mn_3O_4 , Co_3O_4 , and benchmark electrocatalysts. In particular, the optimized MC1 composition showed exceptionally low overpotentials, high current densities with excellent overall oxygen electrode activity and an improved durability. The cation-exchange-based synthesis protocol reported here with and without nucleation of secondary phases should be used as an additional tool to further aid precise engineering of complex heterostructured oxide catalysts directed toward optimizing their performance.

■ ASSOCIATED CONTENT

Supporting Information

The Supporting Information is available free of charge on the ACS Publications website at DOI: 10.1021/acsami.6b02786.

Additional experimental details and structural, chemical, and functional characterization results (PDF)

■ AUTHOR INFORMATION

Corresponding Author

*E-mail: acabot@irec.cat.

Author Contributions

[○]Z.L. and E.I. contributed equally to this work.

Notes

The authors declare no competing financial interest.

■ ACKNOWLEDGMENTS

This work was supported by the European Regional Development Funds and the Spanish MINECO projects BOOSTER (ENE2013-46624-C4-3-R), TNT-FUELS (MAT2014-59961), e-TNT (MAT2014-59961-C2-2-R) and PEC-CO₂ (ENE2012-3651). Z.L. and Y.L. thank the China Scholarship Council for scholarship support. E.I. thanks AGAUR for his Ph.D. grant (FI-2013-B-00769). M.I. thanks AGAUR for the Beatriu de Pinós postdoctoral grant (2013 BP-A00344). S.M. acknowledges funding from "Programa Internacional de Becas 'la Caixa'-Severo Ochoa". J.L. is a Serra Hünter Fellow and is grateful to ICREA Academia program. We also acknowledge the funding from Generalitat de Catalunya 2014 SGR 1638

■ REFERENCES

- (1) Kravtsov, A.; Ein-Eli, Y. The Impact of Nano-Scaled Materials on Advanced Metal–air Battery Systems. *Nano Energy* **2013**, *2*, 468–480.
- (2) He, Q.; Cairns, E. J. Review—Recent Progress in Electrocatalysts for Oxygen Reduction Suitable for Alkaline Anion Exchange Membrane Fuel Cells. *J. Electrochem. Soc.* **2015**, *162*, F1504–F1539.
- (3) Yang, Z.; Nie, H.; Chen, X.; Chen, X.; Huang, S. Recent Progress in Doped Carbon Nanomaterials as Effective Cathode Catalysts for Fuel Cell Oxygen Reduction Reaction. *J. Power Sources* **2013**, *236*, 238–249.
- (4) Cheng, F.; Chen, J. Metal–Air Batteries: From Oxygen Reduction Electrochemistry to Cathode Catalysts. *Chem. Soc. Rev.* **2012**, *41*, 2172–2192.
- (5) Neburchilov, V.; Wang, H.; Martin, J. J.; Qu, W. A Review on Air Cathodes for Zinc–air Fuel Cells. *J. Power Sources* **2010**, *195*, 1271–1291.

- (6) Jaouen, F.; Proietti, E.; Lefèvre, M.; Chenitz, R.; Dodelet, J.-P.; Wu, G.; Chung, H. T.; Johnston, C. M.; Zelenay, P. Recent Advances in Non-Precious Metal Catalysis for Oxygen-Reduction Reaction in Polymer Electrolyte Fuelcells. *Energy Environ. Sci.* **2011**, *4*, 114–130.
- (7) Zhu, H.; Zhang, S.; Huang, Y.-X.; Wu, L.; Sun, S. Monodisperse $\text{M}_x\text{Fe}_{3-x}\text{O}_4$ (M = Fe, Cu, Co, Mn) Nanoparticles and Their Electrocatalysis for Oxygen Reduction Reaction. *Nano Lett.* **2013**, *13*, 2947–2951.
- (8) Liang, Y.; Li, Y.; Wang, H.; Zhou, J.; Wang, J.; Regier, T.; Dai, H. Co_3O_4 Nanocrystals on Graphene as a Synergistic Catalyst for Oxygen Reduction Reaction. *Nat. Mater.* **2011**, *10*, 780–786.
- (9) Cheng, F.; Shen, J.; Peng, B.; Pan, Y.; Tao, Z.; Chen, J. Rapid Room-Temperature Synthesis of Nanocrystalline Spinel as Oxygen Reduction and Evolution Electrocatalysts. *Nat. Chem.* **2011**, *3*, 79–84.
- (10) Zhao, A.; Masa, J.; Xia, W.; Maljusch, A.; Willinger, M.-G.; Clavel, G.; Xie, K.; Schlögl, R.; Schuhmann, W.; Muhler, M. Spinel Mn-Co Oxide in N-Doped Carbon Nanotubes as a Bifunctional Electrocatalyst Synthesized by Oxidative Cutting. *J. Am. Chem. Soc.* **2014**, *136*, 7551–7554.
- (11) Li, J.; Wang, Y.; Zhou, T.; Zhang, H.; Sun, X.; Tang, J.; Zhang, L.; Al-Enizi, A. M.; Yang, Z.; Zheng, G. Nanoparticle Superlattices as Efficient Bifunctional Electrocatalysts for Water Splitting. *J. Am. Chem. Soc.* **2015**, *137*, 14305–14312.
- (12) Indra, A.; Menezes, P. W.; Driess, M. Uncovering Structure-Activity Relationships in Manganese-Oxide-Based Heterogeneous Catalysts for Efficient Water Oxidation. *ChemSusChem* **2015**, *8*, 776–785.
- (13) Chen, D.; Chen, C.; Baiye, Z. M.; Shao, Z.; Ciucci, F. Nonstoichiometric Oxides as Low-Cost and Highly-Efficient Oxygen Reduction/Evolution Catalysts for Low-Temperature Electrochemical Devices. *Chem. Rev.* **2015**, *115*, 9869–9921.
- (14) Li, C.; Han, X.; Cheng, F.; Hu, Y.; Chen, C.; Chen, J. Phase and Composition Controllable Synthesis of Cobalt Manganese Spinel Nanoparticles towards Efficient Oxygen Electrocatalysis. *Nat. Commun.* **2015**, *6*, 7345.
- (15) Cheng, F.; Shen, J.; Ji, W.; Tao, Z.; Chen, J. Selective Synthesis of Manganese Oxide Nanostructures for Electrocatalytic Oxygen Reduction. *ACS Appl. Mater. Interfaces* **2009**, *1*, 460–466.
- (16) Meng, Y.; Song, W.; Huang, H.; Ren, Z.; Chen, S.-Y.; Suib, S. L. Structure-Property Relationship of Bifunctional MnO_2 Nanostructures: Highly Efficient, Ultra-Stable Electrochemical Water Oxidation and Oxygen Reduction Reaction Catalysts Identified in Alkaline Media. *J. Am. Chem. Soc.* **2014**, *136*, 11452–11464.
- (17) Duan, J.; Chen, S.; Dai, S.; Qiao, S. Z. Shape Control of Mn_3O_4 Nanoparticles on Nitrogen-Doped Graphene for Enhanced Oxygen Reduction Activity. *Adv. Funct. Mater.* **2014**, *24*, 2072–2078.
- (18) Wu, G.; Zelenay, P. Nanostructured Nonprecious Metal Catalysts for Oxygen Reduction Reaction. *Acc. Chem. Res.* **2013**, *46*, 1878–1889.
- (19) Kuo, C.-H.; Mosa, I. M.; Thanneer, S.; Sharma, V.; Zhang, L.; Biswas, S.; Aindow, M.; Pamiir Alpay, S.; Rusling, J. F.; Suib, S. L.; et al. Facet-Dependent Catalytic Activity of MnO Electrocatalysts for Oxygen Reduction and Oxygen Evolution Reactions. *Chem. Commun.* **2015**, *51*, 5951–5954.
- (20) Zhang, K.; Han, X.; Hu, Z.; Zhang, X.; Tao, Z.; Chen, J. Nanostructured Mn-Based Oxides for Electrochemical Energy Storage and Conversion. *Chem. Soc. Rev.* **2015**, *44*, 699–728.
- (21) Huynh, M.; Shi, C.; Billinge, S. J. L.; Nocera, D. G. Nature of Activated Manganese Oxide for Oxygen Evolution. *J. Am. Chem. Soc.* **2015**, *137*, 14887–14904.
- (22) Wang, D.; Chen, X.; Evans, D. G.; Yang, W. Well-Dispersed $\text{Co}_3\text{O}_4/\text{Co}_2\text{MnO}_4$ Nanocomposites as a Synergistic Bifunctional Catalyst for Oxygen Reduction and Oxygen Evolution Reactions. *Nanoscale* **2013**, *5*, 5312–5315.
- (23) Deng, X.; Tüysüz, H. Cobalt-Oxide-Based Materials as Water Oxidation Catalyst: Recent Progress and Challenges. *ACS Catal.* **2014**, *4*, 3701–3714.

- (24) Deng, X.; Schmidt, W. N.; Tüysüz, H. Impacts of Geometry, Symmetry, and Morphology of Nanocast Co_3O_4 on Its Catalytic Activity for Water Oxidation. *Chem. Mater.* **2014**, *26*, 6127–6134.
- (25) Jin, H.; Wang, J.; Su, D.; Wei, Z.; Pang, Z.; Wang, Y. In Situ Cobalt-Cobalt oxide/N-Doped Carbon Hybrids as Superior Bifunctional Electrocatalysts for Hydrogen and Oxygen Evolution. *J. Am. Chem. Soc.* **2015**, *137*, 2688–2694.
- (26) Menezes, P. W.; Indra, A.; González-Flores, D.; Sahraie, N. R.; Zaharieva, I.; Schwarze, M.; Strasser, P.; Dau, H.; Driess, M. High-Performance Oxygen Redox Catalysis with Multifunctional Cobalt Oxide Nanochains: Morphology-Dependent Activity. *ACS Catal.* **2015**, *5*, 2017–2027.
- (27) Lu, X.; Chan, H. M.; Sun, C.-L.; Tseng, C.-M.; Zhao, C. Interconnected Core-shell Carbon Nanotube-graphene Nanoribbon Scaffolds for Anchoring Cobalt Oxides as Bifunctional Electrocatalysts for Oxygen Evolution and Reduction. *J. Mater. Chem. A* **2015**, *3*, 13371–13376.
- (28) Maiyalagan, T.; Jarvis, K. A.; Therese, S.; Ferreira, P. J.; Manthiram, A. Spinel-Type Lithium Cobalt Oxide as a Bifunctional Electrocatalyst for the Oxygen Evolution and Oxygen Reduction Reactions. *Nat. Commun.* **2014**, *5*, 3949.
- (29) Su, Y.; Zhu, Y.; Jiang, H.; Shen, J.; Yang, X.; Zou, W.; Chen, J.; Li, C. Cobalt Nanoparticles Embedded in N-Doped Carbon as an Efficient Bifunctional Electrocatalyst for Oxygen Reduction and Evolution Reactions. *Nanoscale* **2014**, *6*, 15080–15089.
- (30) Li, B.; Ge, X.; Goh, F. W. T.; Hor, T. S. A.; Geng, D.; Du, G.; Liu, Z.; Zhang, J.; Liu, X.; Zong, Y. Co_3O_4 Nanoparticles Decorated Carbon Nanofiber Mat as Binder-Free Air-Cathode for High Performance Rechargeable Zinc-Air Batteries. *Nanoscale* **2015**, *7*, 1830–1838.
- (31) Li, C.-S.; Melaet, G.; Ralston, W. T.; An, K.; Brooks, C.; Ye, Y.; Liu, Y.-S.; Zhu, J.; Guo, J.; Alayoglu, S.; et al. High-Performance Hybrid Oxide Catalyst of Manganese and Cobalt for Low-Pressure Methanol Synthesis. *Nat. Commun.* **2015**, *6*, 6538.
- (32) Dang, F.; Oaki, Y.; Kokubu, T.; Hosono, E.; Zhou, H.; Imai, H. Formation of Nanostructured $\text{MnO}/\text{Co}/\text{solid-Electrolyte}$ Interphase Ternary Composites as a Durable Anode Material for Lithium-Ion Batteries. *Chem. - Asian J.* **2013**, *8*, 760–764.
- (33) Liotta, L. F.; Wu, H.; Pantaleo, G.; Venezia, A. M. Co_3O_4 Nanocrystals and $\text{Co}_3\text{O}_4\text{-MO}_x$ Binary Oxides for CO, CH₄ and VOC Oxidation at Low Temperatures: A Review. *Catal. Sci. Technol.* **2013**, *3*, 3085.
- (34) Liang, H.; Sun, H.; Patel, A.; Shukla, P.; Zhu, Z. H.; Wang, S. Excellent Performance of Mesoporous $\text{Co}_3\text{O}_4/\text{MnO}_2$ Nanoparticles in Heterogeneous Activation of Peroxymonosulfate for Phenol Degradation in Aqueous Solutions. *Appl. Catal., B* **2012**, *127*, 330–335.
- (35) Liang, Y.; Wang, H.; Zhou, J.; Li, Y.; Wang, J.; Regier, T.; Dai, H. Covalent Hybrid of Spinel Manganese-Cobalt Oxide and Graphene as Advanced Oxygen Reduction Electrocatalysts. *J. Am. Chem. Soc.* **2012**, *134*, 3517–3523.
- (36) Wang, Y.; Ma, X.; Lu, L.; He, Y.; Qi, X.; Deng, Y. Carbon Supported $\text{MnO}_x\text{-Co}_3\text{O}_4$ as Cathode Catalyst for Oxygen Reduction Reaction in Alkaline Media. *Int. J. Hydrogen Energy* **2013**, *38*, 13611–13616.
- (37) Xiao, J.; Wan, L.; Wang, X.; Kuang, Q.; Dong, S.; Xiao, F.; Wang, S. Mesoporous $\text{Mn}_3\text{O}_4\text{-CoO}$ Core-shell Spheres Wrapped by Carbon Nanotubes: A High Performance Catalyst for the Oxygen Reduction Reaction and CO Oxidation. *J. Mater. Chem. A* **2014**, *2*, 3794–3800.
- (38) Xu, Y.; Jiang, H.; Li, X.; Xiao, H.; Xiao, W.; Wu, T. Synthesis and Characterization of Mn-Based Composite Oxides with Enhanced Electrocatalytic Activity for Oxygen Reduction. *J. Mater. Chem. A* **2014**, *2*, 13345–13351.
- (39) Menezes, P. W.; Indra, A.; Sahraie, N. R.; Bergmann, A.; Strasser, P.; Driess, M. Cobalt-Manganese-Based Spinels as Multifunctional Materials That Unify Catalytic Water Oxidation and Oxygen Reduction Reactions. *ChemSusChem* **2015**, *8*, 164–171.
- (40) Li, G.; Zhang, K.; Mezaal, M. A.; Lei, L. Synthesis and Electrocatalytic Performance of Co_3O_4 Modified Mn_3O_4 Composites for Zinc-Air Batteries Synthesis and Electrocatalytic Performance of NiO Modified Co_3O_4 Composites for Zinc-Air Batteries. *Int. J. Electrochem. Sci.* **2015**, *10*, 10554–10564.
- (41) Huang, W.; Zhong, H.; Li, D.; Tang, P.; Feng, Y. Reduced Graphene Oxide Supported CoO/MnO_2 Electrocatalysts from Layered Double Hydroxides for Oxygen Reduction Reaction. *Electrochim. Acta* **2015**, *173*, 575–580.
- (42) Du, J.; Chen, C.; Cheng, F.; Chen, J. Rapid Synthesis and Efficient Electrocatalytic Oxygen Reduction/Evolution Reaction of CoMn_2O_4 Nanodots Supported on Graphene. *Inorg. Chem.* **2015**, *54*, 5467–5474.
- (43) Ge, X.; Liu, Y.; Goh, F. W. T.; Hor, T. S. A.; Zong, Y.; Xiao, P.; Zhang, Z.; Lim, S. H.; Li, B.; Wang, X.; et al. Dual-Phase Spinel MnCo_2O_4 and Spinel $\text{MnCo}_2\text{O}_4/\text{nanocarbon}$ Hybrids for Electrocatalytic Oxygen Reduction and Evolution. *ACS Appl. Mater. Interfaces* **2014**, *6*, 12684–12691.
- (44) Yu, T.; Moon, J.; Park, J.; Park, Y. I.; Na, H. B.; Kim, B. H.; Song, I. C.; Moon, W. K.; Hyeon, T. Various-Shaped Uniform Mn_3O_4 Nanocrystals Synthesized at Low Temperature in Air Atmosphere. *Chem. Mater.* **2009**, *21*, 2272–2279.
- (45) Li, Y.; Zhou, W.; Wang, H.; Xie, L.; Liang, Y.; Wei, F.; Idrobo, J.-C.; Pennycook, S. J.; Dai, H. An Oxygen Reduction Electrocatalyst Based on Carbon Nanotube-graphene Complexes. *Nat. Nanotechnol.* **2012**, *7*, 394–400.
- (46) Hosseini, S. a.; Niaei, a.; Salari, D.; Nabavi, S. R. Nanocrystalline AMn_2O_4 (A = Co, Ni, Cu) Spinels for Remediation of Volatile Organic Compounds—synthesis, Characterization and Catalytic Performance. *Ceram. Int.* **2012**, *38*, 1655–1661.
- (47) Hosseini, S. A.; Salari, D.; Niaei, A.; Deganello, F.; Pantaleo, G.; Hojati, P. Chemical-Physical Properties of Spinel CoMn_2O_4 Nanopowders and Catalytic Activity in the 2-Propanol and Toluene Combustion: Effect of the Preparation Method. *J. Environ. Sci. Health, Part A: Toxic/Hazard. Subst. Environ. Eng.* **2011**, *46*, 291–297.
- (48) Sexton, B. A.; Hughes, A. E.; Turney, T. W. An XPS and TPR Study of the Reduction of Promoted Cobalt-Kieselguhr Fischer-Tropsch Catalysts. *J. Catal.* **1986**, *97*, 390–406.
- (49) Arnoldy, P. Temperature-Programmed Reduction of $\text{CoO}/\text{Al}_2\text{O}_3$ Catalysts. *J. Catal.* **1985**, *93*, 38–54.
- (50) Brown, R.; Cooper, M. E.; Whan, D. A. Temperature Programmed Reduction of Alumina-Supported Iron, Cobalt and Nickel Bimetallic Catalysts. *Appl. Catal.* **1982**, *3*, 177–186.
- (51) Lin, H. Y.; Chen, Y. W. The Mechanism of Reduction of Cobalt by Hydrogen. *Mater. Chem. Phys.* **2004**, *85*, 171–175.
- (52) Sytnyk, M.; Kirchschrager, R.; Bodnarchuk, M. I.; Primetzhofer, D.; Krieger, D.; Enser, H.; Stangl, J.; Bauer, P.; Voith, M.; Hassel, A.; et al. Tuning the Magnetic Properties of Metal-Oxide Nanocrystal Heterostructures by Cation Exchange. *Nano Lett.* **2013**, *13*, 586–593.
- (53) Gutmann, V. *Coordination Chemistry in Non-Aqueous Solutions*; Springer Vienna: Vienna, 1968.
- (54) Trutia, A. Optical Spectra of Divalent Cobalt Complexes. *J. Optoelectron. Adv. Mater.* **2005**, *7*, 2677–2686.
- (55) Fine, A. Halide Complexes of Cobalt (II) in Acetone Solution. *J. Am. Chem. Soc.* **1962**, *84*, 1139–1144.
- (56) Shinagawa, T.; Garcia-Esparza, A. T.; Takanabe, K. Insight on Tafel Slopes from a Microkinetic Analysis of Aqueous Electrocatalysis for Energy Conversion. *Sci. Rep.* **2015**, *5*, 13801.
- (57) Roche, L.; Chainet, E.; Chatenet, M.; Vondrák, J. Carbon-Supported Manganese Oxide Nanoparticles as Electrocatalysts for the Oxygen Reduction Reaction (ORR) in Alkaline Medium: Physical Characterizations and ORR Mechanism. *J. Phys. Chem. C* **2007**, *111*, 1434–1443.
- (58) Bard, A. J.; Faulkner, L. R. *Electrochemical Methods: Fundamentals and Applications*, 2nd ed.; Wiley: New York, 2001.
- (59) Chatenet, M.; Arousseau, M.; Durand, R.; Andolfatto, F. Silver-Platinum Bimetallic Catalysts for Oxygen Cathodes in Chlor-Alkali Electrolysis: Comparison with Pure Platinum. *J. Electrochem. Soc.* **2003**, *150*, D47–D55.
- (60) Chatenet, M.; Genies-Bultel, L.; Arousseau, M.; Durand, R.; Andolfatto, F. Oxygen Reduction on Silver Catalysts in Solutions

Containing Various Concentrations of Sodium Hydroxide - Comparison with Platinum. *J. Appl. Electrochem.* **2002**, *32*, 1131–1140.

(61) Cherevko, S.; Zeradjanin, A. R.; Keeley, G. P.; Mayrhofer, K. J. J. A Comparative Study on Gold and Platinum Dissolution in Acidic and Alkaline Media. *J. Electrochem. Soc.* **2014**, *161*, H822–H830.

(62) Gong, M.; Li, Y.; Wang, H.; Liang, Y.; Wu, J. Z.; Zhou, J.; Wang, J.; Regier, T.; Wei, F.; Dai, H. An Advanced Ni-Fe Layered Double Hydroxide Electrocatalyst for Water Oxidation. *J. Am. Chem. Soc.* **2013**, *135*, 8452–8455.

(63) Smith, R. D. L.; Prévot, M. S.; Fagan, R. D.; Zhang, Z.; Sedach, P. A.; Siu, M. K. J.; Trudel, S.; Berlinguette, C. P. Photochemical Route for Accessing Amorphous Metal Oxide Materials for Water Oxidation Catalysis. *Science* **2013**, *340*, 60–63.

SUPPORTING INFORMATION

Mn₃O₄@CoMn₂O₄-Co_xO_y Nanoparticles: Partial Cation Exchange Synthesis and Electrocatalytic Properties toward the Oxygen Reduction and Evolution Reactions

Zhishan Luo^{†,‡}, Erdem Irtem^{†,‡}, Maria Ibáñez[†], Raquel Nafria[†], Sara Martí-Sánchez[¶], Aziz Genç[¶], Maria de la Mata[¶], Yu Liu[†], Doris Cadavid[†], Jordi Llorca[□], Jordi Arbiol^{¶,‡}, Teresa Andreu[†], Joan Ramon Morante^{†,§}, Andreu Cabot^{†,‡,}*

[†] Catalonia Institute for Energy Research - IREC, Sant Adrià del Besòs, Barcelona, 08930, Spain

[□] Institut de Tècniques Energètiques, Universitat Politècnica de Catalunya, 08028 Barcelona, Spain

[¶] Catalan Institute of Nanoscience and Nanotechnology (ICN2), CSIC and The Barcelona Institute of Science and Technology (BIST), Campus UAB, Bellaterra, 08193 Barcelona, Spain

[§] Departament d'Electronica, Universitat de Barcelona, 08028 Barcelona, Spain

[‡] ICREA, Pg. Lluís Companys 23, 08010 Barcelona, Spain

* acabot@irec.cat

Contents

1. Additional nanoparticles characterization results	S-1
1.1 Additional TEM micrographs	S-2
1.2. Shape and size evolution of MC1 with different reaction time	S-4
1.3. Co LDH and High ratio of Co/Mn.....	S-5
1.4. TGA analysis of as-prepared MC1/C samples.....	S-6
1.5. TEM and XRD of MC1/C catalysts after thermal annealing.....	S-7
1.6. XPS of MC samples.....	S-8
1.7. Surface Area and texture parameters	S-9
2. Additional Electrochemical Measurements Discussion.....	S-10
2.1 Rotating-disk voltammograms of different samples	S-10
2.2 Different scan rates and quadratic curves of HNPs samples.....	S-13
2.3 ORR Tafel curves of different NPs/C and Pt/C	S-14
2.4 Koutecky-Levich (K-L) plots of different HNPs samples	S-15
2.5 Additional durability test and TEM images of MC and Pt samples after stability test.....	S-16
2.6 Comparison of ORR and OER activities of MC2 NPs	S-17
3. Summary of the ORR/OER Catalytic Performance.....	S-18
4. State-of-the-art values for bi-functional ORR/OER of non-precious oxide catalysts.....	S-19
5. REFERENCES	S-20

1. Additional nanoparticles characterization results

1.1 Additional TEM micrographs

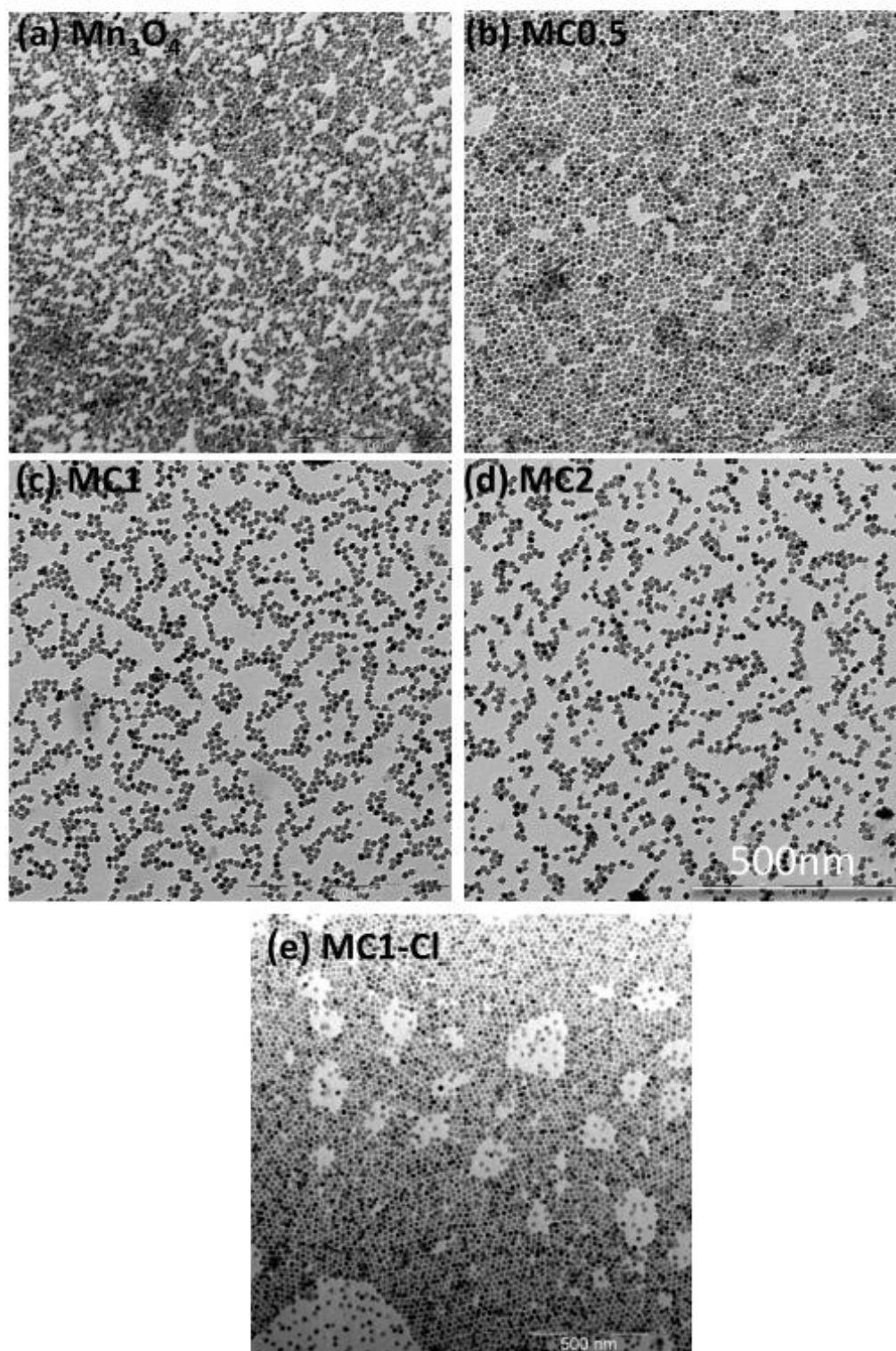


Figure S1. Additional TEM micrographs of Mn₃O₄ (a), MC0.5 (b), MC1 (c), MC2 (d) and MC1-Cl NPs (e).

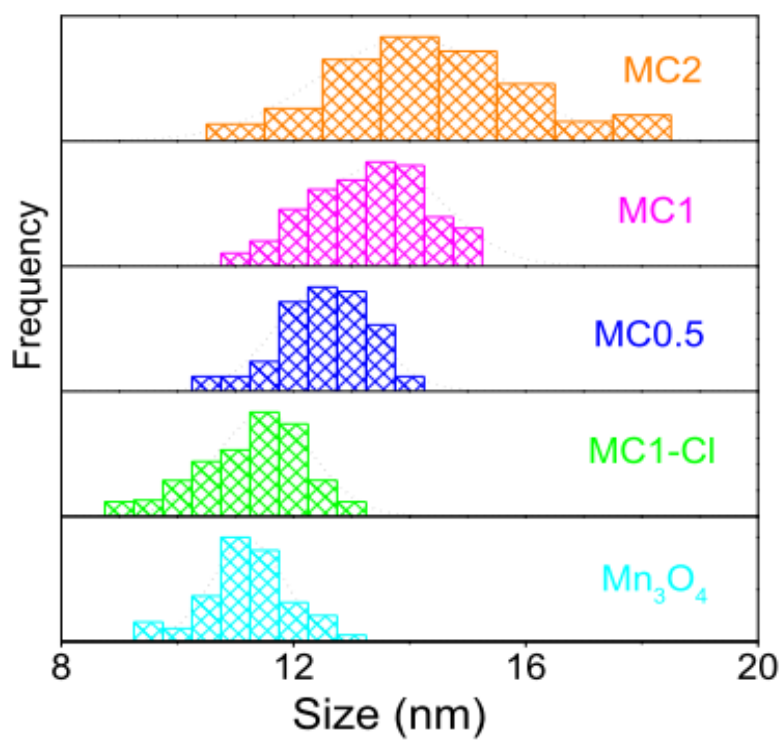


Figure S2. Histograms with NP size distribution of Mn₃O₄, MC0.5, MC1, MC2 and MC1-Cl NPs.

1.2. Shape and size evolution of MC1 with different reaction time

Long reaction times, up to 300 min, were necessary to achieve $\text{Mn}_3\text{O}_4@\text{CoMn}_2\text{O}_4\text{-CoO}$ NPs. MC1 NP size gradually increased with the reaction time, initially forming CoMn_2O_4 and later on the CoO satelletes (rougher surface).

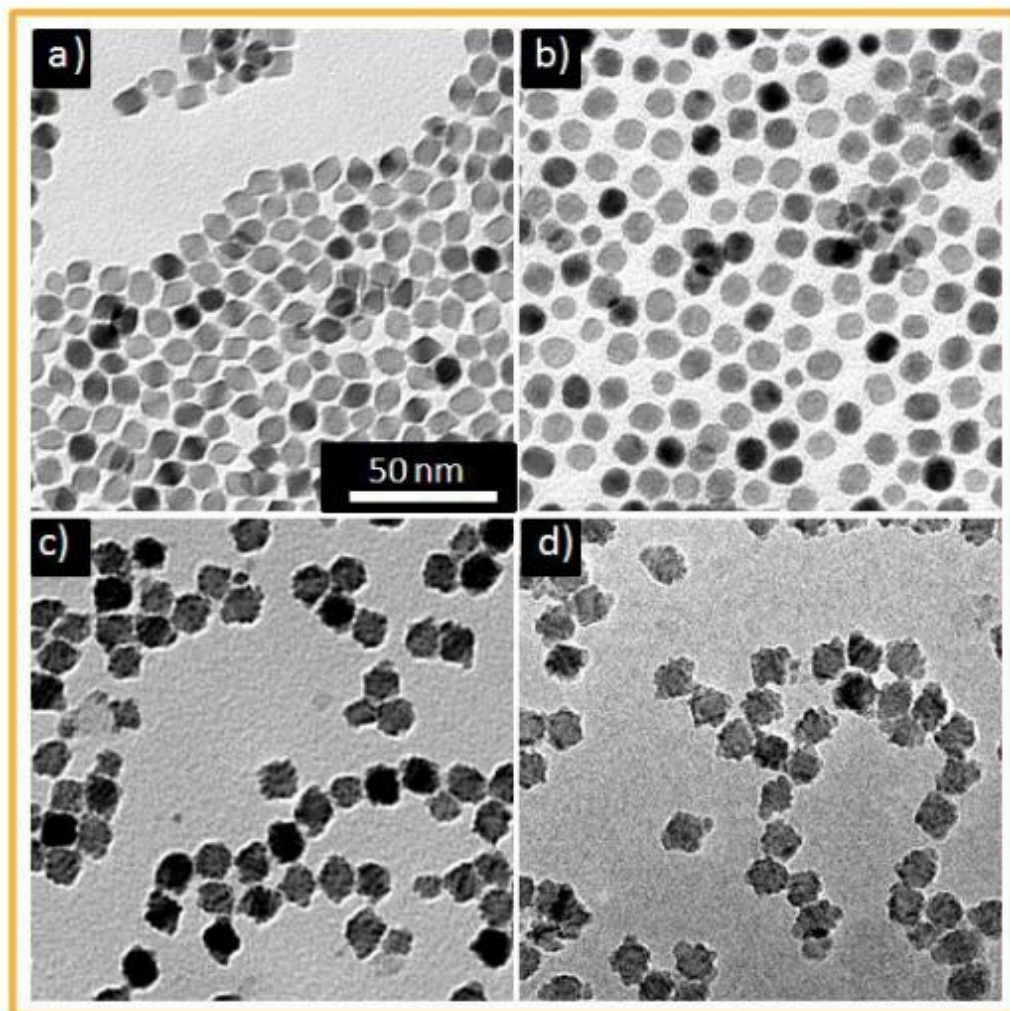


Figure S3. TEM micrographs showing the size and shape evolution of MC1 HNPs at reaction times of (a) 0 min, (b) 60min, (c) 180min and (d) 300min.

1.3. Co LDH and High ratio of Co/Mn

Ultrathin Co layered double hydroxide (LDH) nanoplates were obtained following the same procedure used to produce Mn-Co oxide NPs but in the absence of Mn_3O_4 . Figure S4 (a) and (b) show the corresponding TEM image and the XRD pattern respectively. When large Co:Mn molar ratios ($Co:Mn \geq 4$) were used, a mixture of Mn-Co oxide NPs and Co LDH was obtained (Figure S4 (c) and (d)).

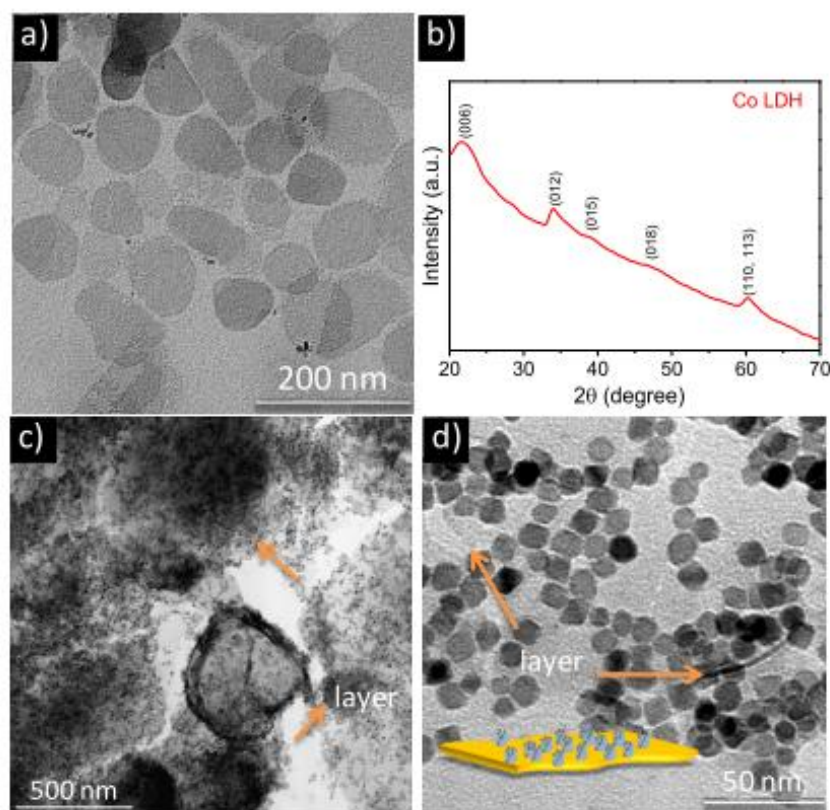


Figure S4. TEM image (a) and XRD pattern (b) of Co LDH obtained when injecting Co perchlorate in the same conditions than for the synthesis of Mn-Co oxide NPs, but in the absence of Mn_3O_4 NPs. c), d) TEM images of Mn-Co NPs obtained with a ratio $Co:Mn=4$. The inset shows a scheme of a Co LDH plate supporting several Mn-Co NPs. Orange arrows show the Co LDH layers.

1.4. TGA analysis of as-prepared MC1/C samples

As-prepared MC1/C was analyzed by TGA in air. The weight of the sample started to drop above 360 °C, as the carbon support started to oxidize. Above 570 °C all the carbon had been oxidized. The remaining weight, 28.4%, corresponds to the weight ratio of NPs introduced.

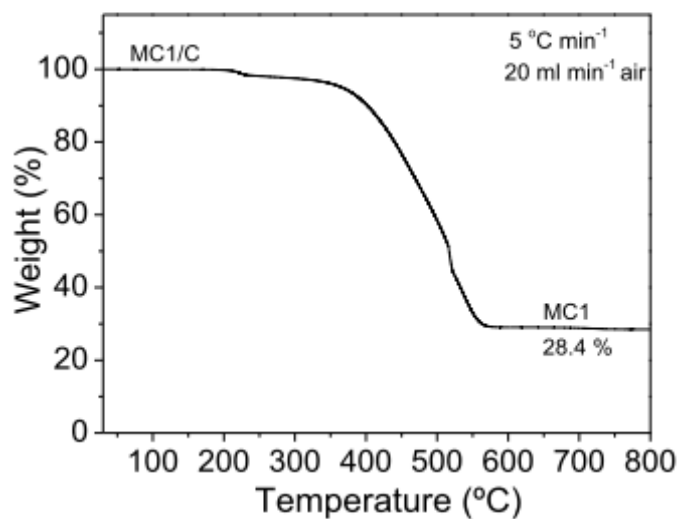


Figure S5. TGA profile of the as-prepared MC1/C.

1.5. TEM and XRD of MC1/C catalysts after thermal annealing

Figure S6 shows a representative TEM micrograph of the MC1/C composite, revealing that MC1 NPs were uniformly deposited on carbon in the loading-annealing process. Besides, no appreciable change was observed from XRD patterns, indicating insignificant NP structural variations.

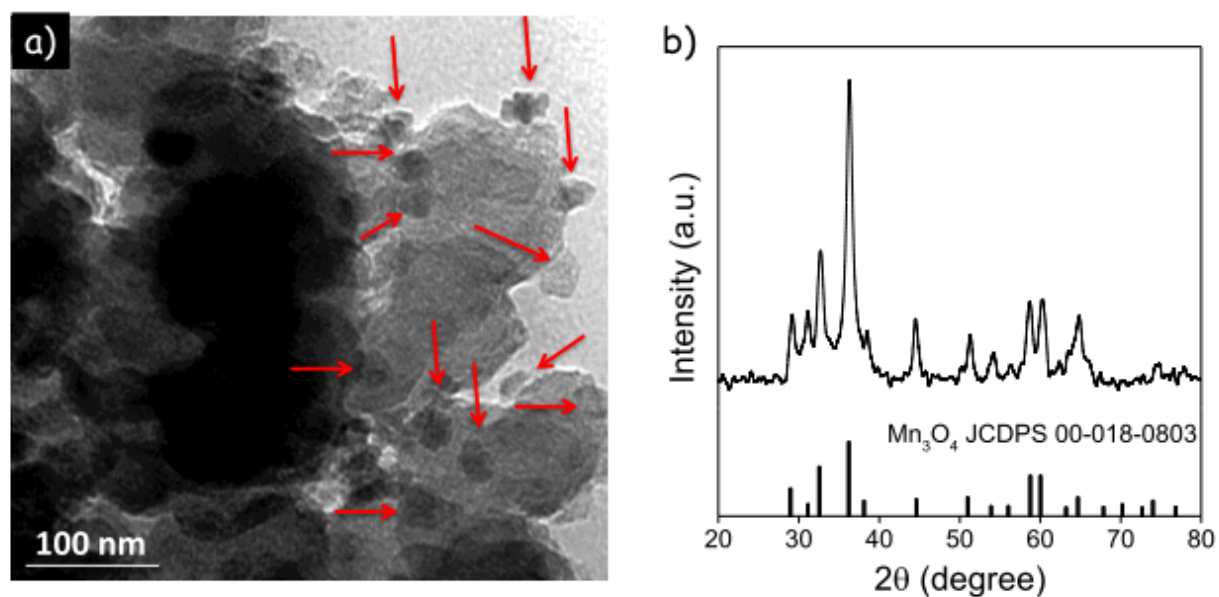


Figure S6. TEM micrograph (a) and XRD pattern (b) of MC1 NPs supported on carbon black (red arrows point at some of the NPs).

1.6. XPS of MC samples

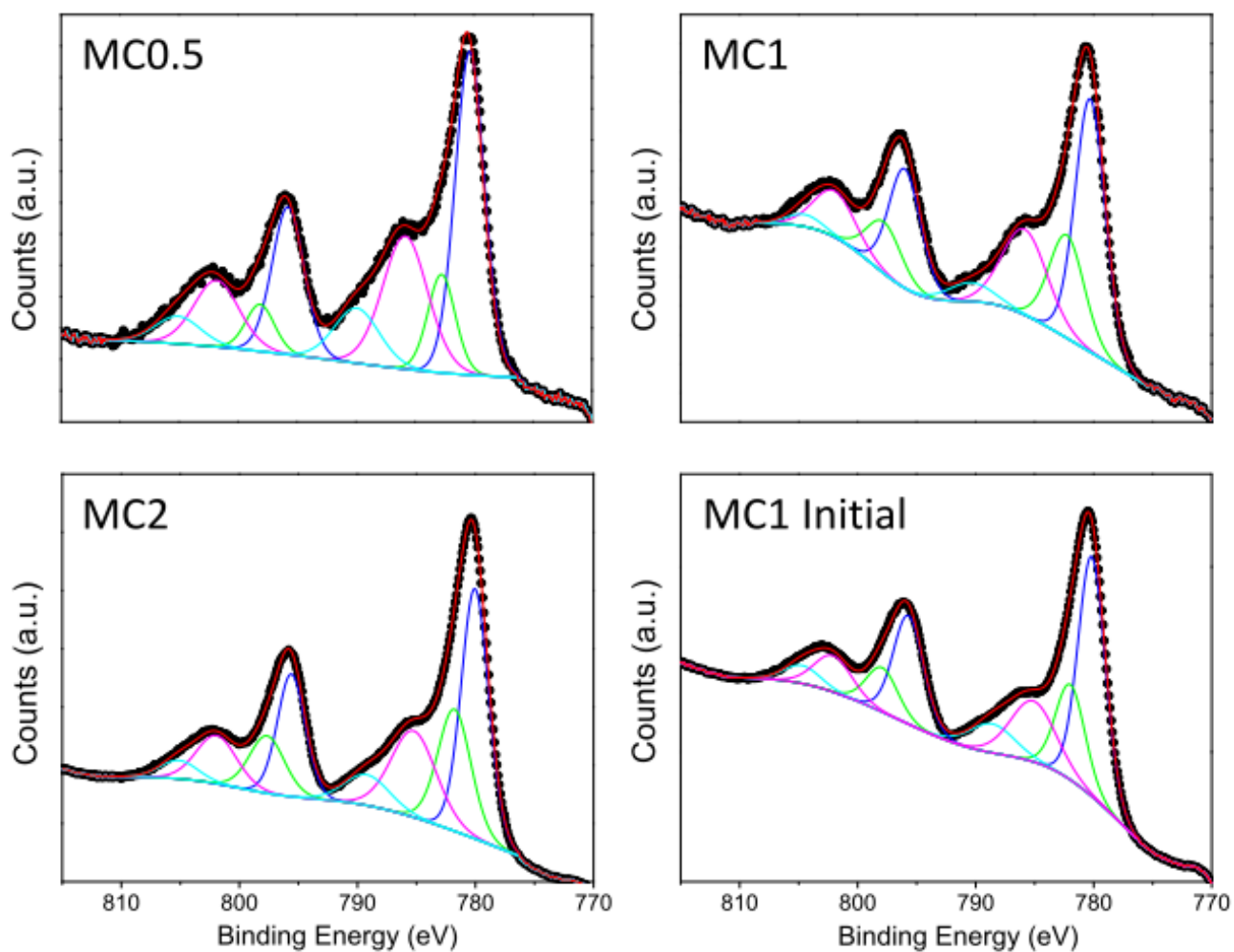


Figure S7. Co_{2p} region of the XPS spectra of MC0.5, MC1 and MC2 NPs after annealing at 180°C and of MC1 before the annealing (initial).

1.7. Surface Area and texture parameters

BET analysis showed NP/C nanocomposites to have specific surface areas around $140 \text{ m}^2 \text{ g}^{-1}$ and average pore size below 20 nm, but MC1-Cl/C.

Table S1. Surface area and texture parameters of the NP/C

Sample	$S_{\text{BET}}(\text{m}^2 \text{ g}^{-1})$	Average pore size (nm)	Pore volume ($\text{cm}^3 \text{ g}^{-1}$)
$\text{Mn}_3\text{O}_4/\text{C}$	150	18.1	0.543
MC0.5/C	135	17.8	0.485
MC1/C	137	17.4	0.487
MC2/C	162	16.4	0.545
MC1-Cl/C	101	21.52	0.489

2. Additional Electrochemical Measurements Discussion

2.1 Rotating-disk voltammograms of different samples

The electrocatalysts thin film of as-prepared NP/C composites was immobilized by drop casting a suspension of the electrocatalysts ink onto an inverted glassy carbon disk electrode followed by the rotational drying. The centrifugal force during rotational drying causes the ink to spread evenly from the center to edge of the substrate producing a uniform electrocatalyst thin-film free of “coffee rings” which has a great effect on electrochemical performance and reproducibility of RDE measurements.¹ Later on, catalyst loaded electrodes were left in Ar flushed low vacuum oven (25 mbar) at 40 °C for 1 hour for complete desorption of surface groups left from the ink on the NPs. Glassy carbon electrode introduced RDE rotator was set to at various rates, i.e. 400, 900, 1200, 1600, and 2000 rpm and voltage window was tuned to obtain a well-defined, steady state mass transport regime to investigate the electrocatalytic activity towards ORR. The electrochemical activity of nanostructured catalyst materials was investigated in 0.1 M KOH electrolyte pre-saturated with Ar or O₂ at least 30 min before each tests (pH = 13.3). The linear sweep voltammograms (LSV) for ORR/OER activity of catalyst thin-films were recorded at a scan rate of 5 mV s⁻¹ with 1600 rpm rotating rate. The Ag/AgCl reference electrode was calibrated as detailed in the experimental part in the manuscript and the calibration is shown in Figure S8. In order to highlight the change in activity towards ORR and/or OER, such conditions were selected to well eliminate the O₂ bubbles formed during the reaction and to instantly remove the products (LSV curves of all samples with varying rotation rates are listed in Figure S9).

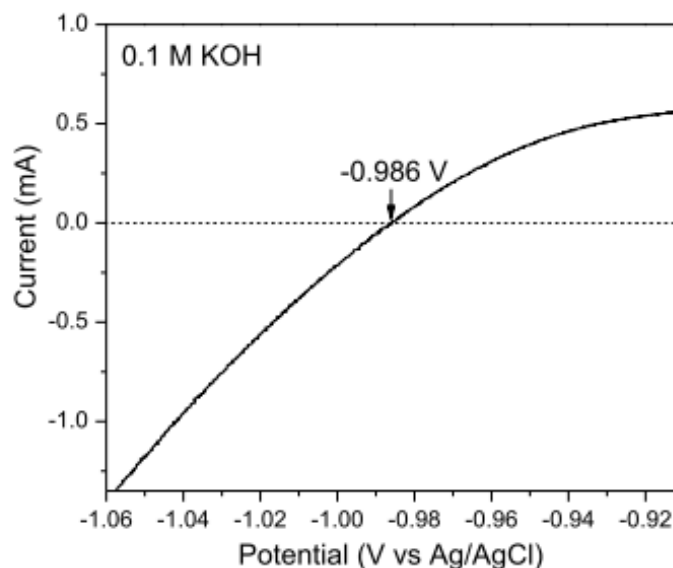


Figure S8. Calibration of the Ag/AgCl reference electrode for the transformation of the reference electrode potential to the reversible hydrogen electrode (RHE) scale.

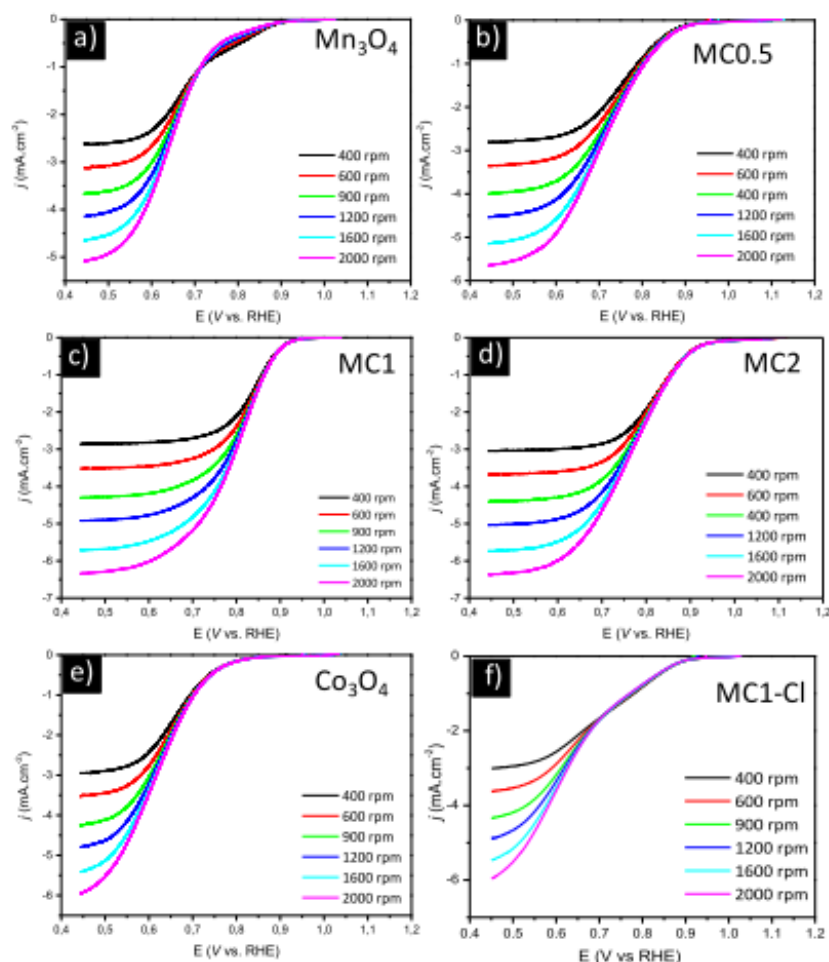


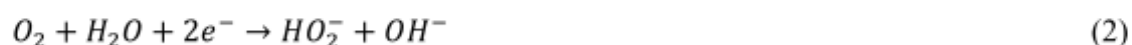
Figure S9. Rotating-disk electrode voltammograms recorded on different catalyst-modified electrodes in O_2 -saturated 0.1 M KOH solution at different rotation rates as indicated: (a) Mn_3O_4/C , (b) $MC0.5/C$, (c) $MC1/C$, (d) $MC2/C$, (e) Co_3O_4/C , (f) $MC1-Cl/C$. All those values for ORR and OER were calculated by interpolation and analysis of the wave form at both ends. The wave analysis was made according to two straight lines, defined using a linear regression fit. The software (EC Lab, Biologic Instruments) automatically finds the two parts of the curve with the shallowest slope for the fit. $E_{1/2}$ is the half-wave potential obtained by the intersection of the curve with the median between both linear regressions. I_L^c is defined as the current value for $E = E_{1/2}$ on the cathodic linear regression.

Though previous studies reported that MnO_x catalytic activity is mainly towards 2 x 2 electrons along with the peroxide decomposition reaction.² It is well-known that electrocatalytic ORR process involves multistep and multiple adsorbed intermediates which highly depend on the catalyst surface properties,³ i.e. specific adsorption of the reactant. Briefly, two main pathways govern ORR. Pathway A is the “ direct $4e^-$ ORR to H_2O ” (1) and Pathway B is so called “ 2 x $2e^-$ ORR ” that involve initially hydrogen peroxide (H_2O_2) formation by $2e^-$ (2) followed by either complete reduction to hydroxide with $2e^-$ (3) or disproportionation into hydroxide and oxygen, as shown below.

Pathway A.



Pathway B.



2.2 Different scan rates and quadratic curves of HNPs samples

Considering the capacitive effect of the NPs, we conducted LSVs of MC1 nanocatalyst film with different scan rates of 1, 2.5, 5 and 10 mV s^{-1} and did not observe any negligible difference between 1 to 5 mV s^{-1} . However a high capacitive contribution was found for 10 mV s^{-1} due to the shift of on-set potential and slight increment in current density so the tests were conducted under 5 mV s^{-1} scan rate speed. All the LSVs conducted under Ar bubbling did not display any significant activity in the tested potential window for ORR, suggesting no redox coupled reaction happens in the Ar saturated media (Figure S10).

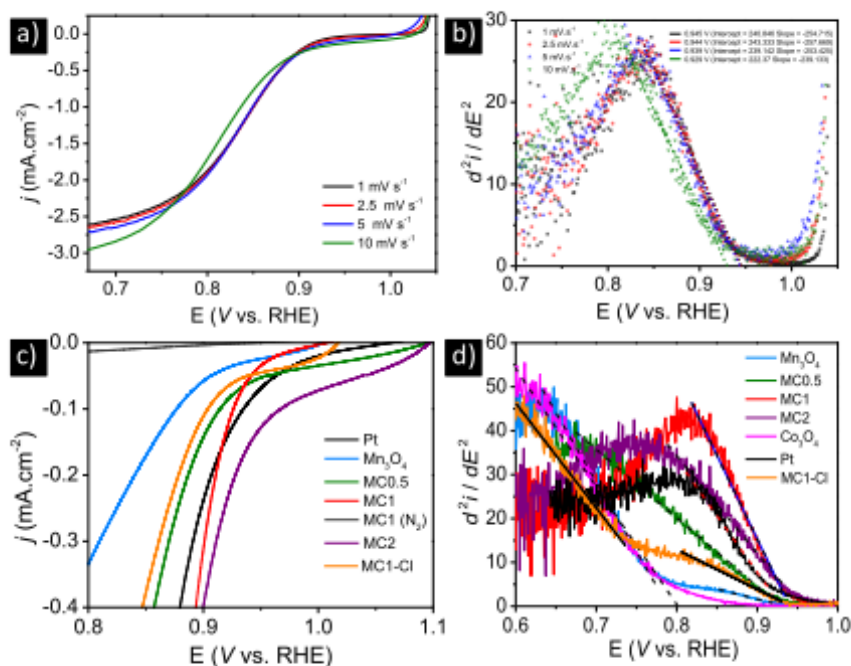


Figure S10. (a) Linear sweep voltammograms under different scan rates to exploit the capacitive response. Rotating disk electrode was adjusted to 400 rpm and 0.1M KOH solution was pre-saturated with O_2 gas for 30 min before the test. (b) The quadratic differential curves plotted from the corresponding LSVs. The on-set potential can be determined by the extrapolation of polynomial fit when its quadratic differential value is null on x-axis. (c) LSVs of nanocomposites of HNPs having Mn/Co ratio of 0.5, 1 and 2 with an emphasis on lower overvoltage area to highlight the on-set potentials. The activity under N_2 bubbling for the catalyst with the highest performance was also added (in grey) to show the inert and negligible background contribution. (d) The quadratic differential curves constructed from the LSVs and their polynomial fitting to indicate on-set potential of oxygen reduction.

2.3 ORR Tafel curves of different NPs/C and Pt/C

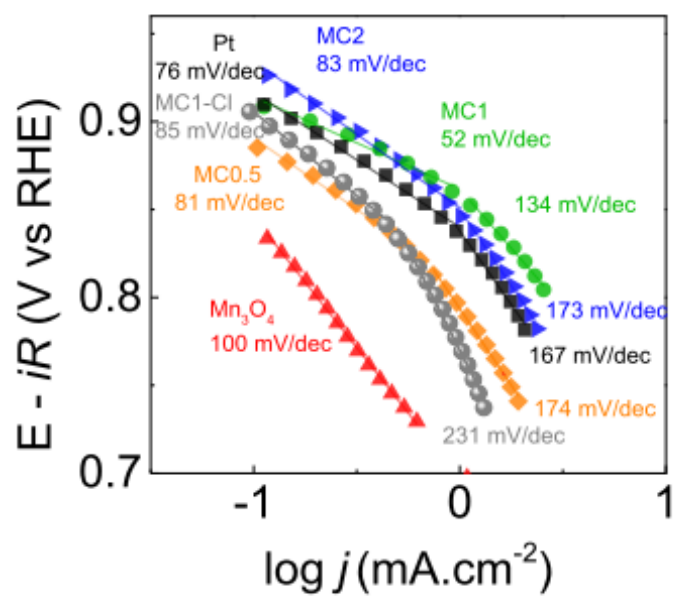


Figure S11. Tafel plots derived from ORR polarization curves

2.4 Koutecky-Levich (K-L) plots of different HNPs samples

The K-L curves are constructed following the K-L equation:⁴

$$\frac{1}{j} = \frac{1}{j_k} + \frac{1}{j_l} = \frac{1}{j_k} + \frac{1}{B\omega^{1/2}}$$

$$B = 0.62n_tFC_{O_2}D_{O_2}^{2/3}\nu^{-1/6}$$

where j , j_k and j_l are measured current, kinetic current and diffusion-limiting current respectively, ω is the angular velocity, n_t is the overall number of electrons transferred during oxygen reduction, F is the Faraday constant ($96500 \text{ C}\cdot\text{mol}^{-1}$), C_{O_2} is the concentration of dissolved O_2 ($1.2\times 10^{-6} \text{ mol}\cdot\text{cm}^{-3}$), D_{O_2} is the diffusion coefficient of O_2 ($1.9\times 10^{-5} \text{ cm}^2\cdot\text{s}^{-1}$) and ν is kinetic viscosity of the electrolyte ($0.01 \text{ cm}^2\cdot\text{s}^{-1}$). The constant 0.62 is applied when the rotation speed is expressed in radius per second (rad/s).

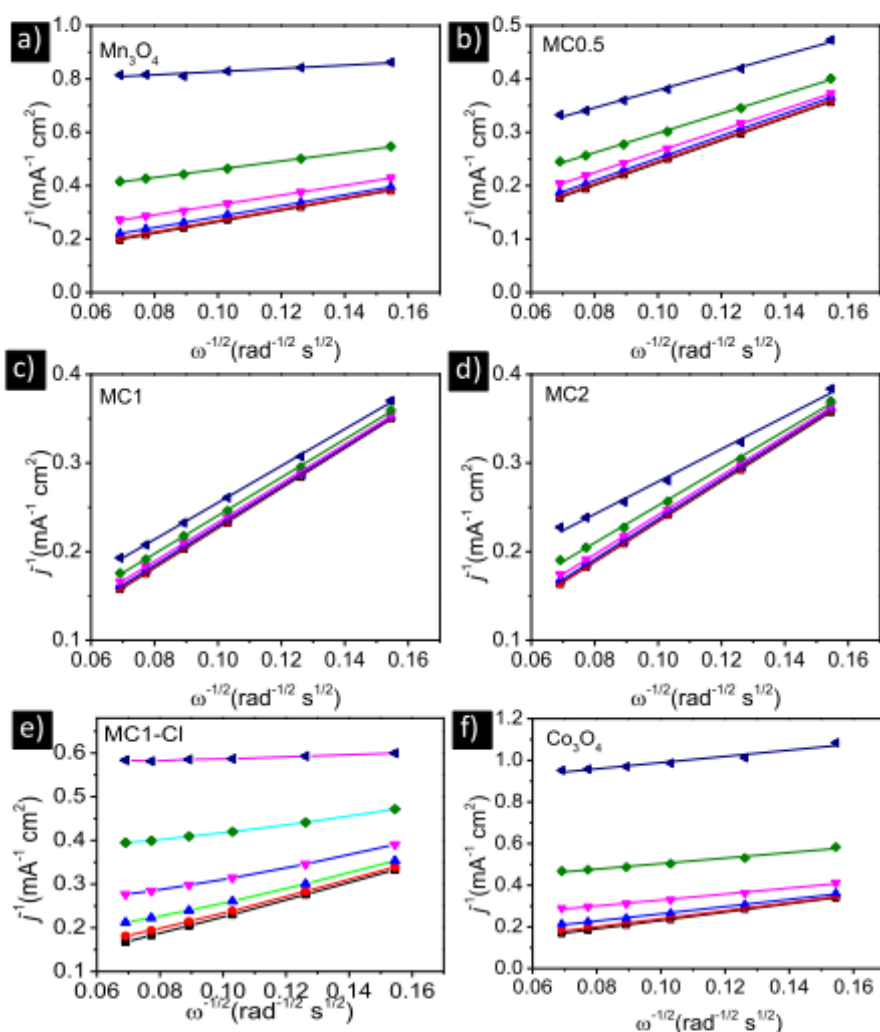


Figure S12. K-L plots of Mn_3O_4 (a), MC0.5 (b), MC1 (c), MC2 (d), MC1-Cl (e) and Co_3O_4 (f) at 0.5 V vs RHE.

2.5 Additional durability test and TEM images of MC and Pt samples after stability test

Figure S13 (a) shows long-term stability test was conducted for 60 hours of the MC0.5 and Pt/C samples. MC0.5 HNP catalyst showed outstanding current retention 76% of the initial current compared to benchmark Pt/C catalyst, which lost 70% after durability test. The MC0.5 HNPs kept the same morphology after stability test (Figure S13 c and d).

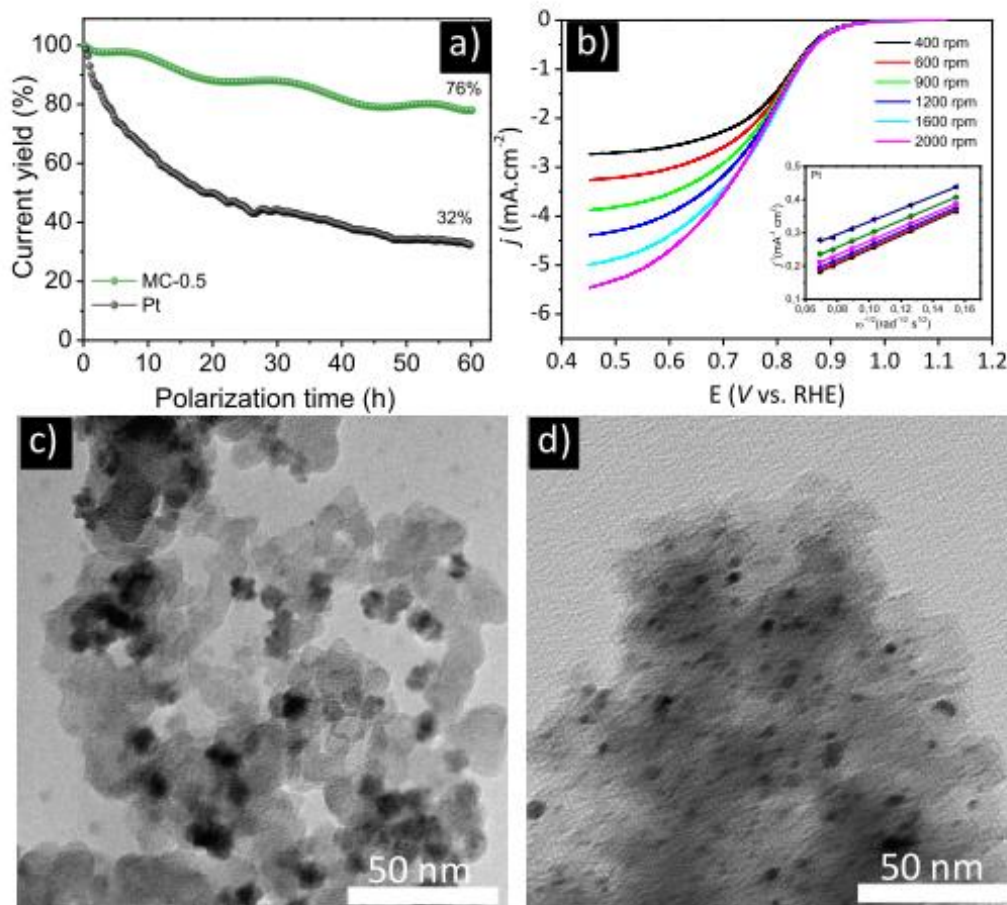


Figure S13. (a) Chronoamperometric responses of MC0.5 and Pt/C at 0.79 V in O₂-saturated 0.1 M KOH with 60h durability test. (b) Rotation-speed-dependent current-potential curves of Pt/C catalyst in O₂-saturated 0.1 M KOH solution, inset of K-L plots of Pt/C at 0.5V vs. RHE. (c) and (d) show TEM images of MC0.5/C catalyst and commercial Pt/C after 60h durability test.

2.6 Comparison of ORR and OER activities of MC2 NPs

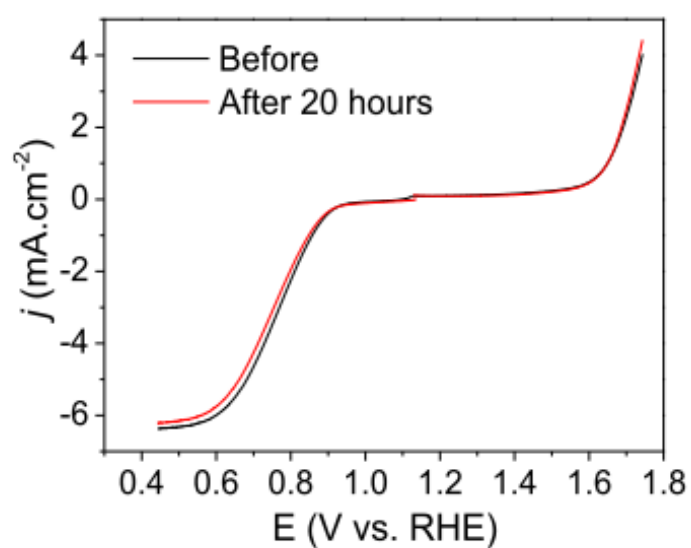


Figure S14. Comparison of ORR and OER activities of MC2 NPs before and after durability test in 0.1 M KOH solution. The rotation rate is 1600 rpm during the ORR.

3. Summary of the ORR/OER Catalytic Performance

Table S2. ORR catalytic performance parameters

	E^*/V vs RHE	E^0	η	E^*/V vs RHE	η	E^*/V vs RHE	η	j	$j/mA\cdot cm^{-2}$	$j/mA\cdot cm^{-2}$	$j_{,half}$	j	n	n	Tafel Slopes	
	-0.1mA.cm-2	1600rpm		-1mA.cm ⁻²	-1mA.cm ⁻²	-3mA.cm ⁻²	-3mA.cm ⁻²	at $\eta=-500mV$	at E_{half}	at E_{half}	A.g ⁻¹ 0.0148 g cat	1600rpm max	K-L 0.55V	K-L 0.6V	low	high
Mn ₃ O ₄	0.88	0.89	0.35	0.73	0.51	0.66	0.57	-4.1	-0.67	-2.1	27.4	-4.6	3.2	2.8	100	162
MC1-Cl	0.90	0.89	0.34	0.78	0.45	0.65	0.58	-5.2	-1.38	-2.6	34.5	-5.5	3.5	2.9	95	231
MC0.5	0.91	0.85	0.38	0.81	0.42	0.73	0.50	-4.7	-2.11	-2.4	31.4	-5.1	3.6	3.4	81	174
MC1	0.93	0.93	0.31	0.87	0.36	0.83	0.40	-5.5	-4.30	-2.8	36.7	-5.7	4.0	3.9	52	134
MC2	0.97	0.89	0.34	0.87	0.36	0.80	0.43	-5.4	-3.61	-2.7	35.5	-5.7	3.8	3.8	83	173
Co ₃ O ₄	0.82	0.82	0.41	0.71	0.52	0.64	0.59	-4.5	-0.51	-2.3	30.1	-5.4	3.4	2.8	124	212
Pt	0.94	0.89	0.34	0.84	0.39	0.78	0.45	-4.9	-2.87	-2.4	32.3	-5.3	3.5	3.3	76	167

Table S3. OER catalytic performance parameters

	E^*/V vs RHE	E^0	η	E^*/V vs RHE	η	E^*/V vs RHE	η/V	Tafel Slopes
	0.1mA.cm-2			1mA.cm-2	1mA.cm-2	10 mA.cm-2	for 10mA.cm-2	
Mn ₃ O ₄	1.46	1.66	0.43	1.75	0.52	2.19	0.96	151
MC1-Cl	1.08	1.66	0.43	1.63	0.40	1.75	0.52	106
MC0.5	1.39	1.61	0.38	1.67	0.44	1.72	0.49	95
MC1	1.45	1.54	0.31	1.59	0.36	1.68	0.45	81
MC2	1.48	1.58	0.35	1.64	0.41	2.01	0.78	83
Co ₃ O ₄	1.41	1.62	0.39	1.61	0.38	1.71	0.48	110
DSA	1.15	1.48	0.25	1.55	0.32	1.65	0.42	104

4. State-of-the-art values for bi-functional ORR/OER of non-precious oxide catalysts

Table S4. Comparison of bi-functional oxygen electrode activities of MC1 hybrid and non-precious oxide catalysts.

Catalyst material	ORR: E(V) at $j = -3 \text{ mA cm}^{-2}$	OER: E(V) at $j = 10 \text{ mA cm}^{-2}$	Oxygen electrode (OER-ORR) E(V)	References
MC1 NPs	0.83	1.68	0.85	This work
20 wt % Ir/C	0.69	1.61	0.92	5
Nanostructured Mn oxide	0.73	1.77	1.04	5
$\text{Co}_3\text{O}_4/2.7\text{Co}_2\text{MnO}_4$	0.68	1.77	1.09	6
$\alpha\text{-MnO}_2\text{-SF}$	0.76	1.72	0.96	7
$\text{MnO}_2/\text{Co}_3\text{O}_4$	0.28	1.90	1.62	8
c-CoMn ₂ /C*	0.82	1.78	0.96	9
MnCoFeO ₄	0.78	1.71	0.93	10
$\beta\text{-MnO}_2$ film	0.76	1.78	1.02	11
$\text{Ni}_{0.4}\text{Co}_{2.6}\text{O}_4$	0.75	1.79	0.96	12
$\text{NiCo}_2\text{O}_4/\text{Graphene}$	0.55	1.69	1.14	13
$\text{MnCo}_2\text{O}_4/\text{N-rGO}^*$	0.84	1.57	0.73(1M KOH)	14
CoO/N-GO	0.81	1.57	0.76(1 M KOH)	15
$\text{Mn}_x\text{O}_y/\text{NC}$	0.81 (1mA cm ⁻²)	1.68	0.87	16
Hollow CoFe ₂ O ₄	0.65(1mA cm ⁻²)	1.68	1.03	17
$\text{Fe}_3\text{O}_4/\text{Graphene}$	0.86(1mA cm ⁻²)	1.78	0.92	18

*The value of potential was directly estimated from Tafel slopes and LSVs of the ORR current density at -3 mA cm^{-2} and OER current density at 10 mA cm^{-2} .

5. REFERENCES

- (1) Garsany, Y.; Singer, I. L.; Swider-Lyons, K. E. Impact of Film Drying Procedures on RDE Characterization of Pt/VC Electrocatalysts. *J. Electroanal. Chem.* **2011**, *662*, 396–406.
- (2) Cheng, F.; Shen, J.; Ji, W.; Tao, Z.; Chen, J. Selective Synthesis of Manganese Oxide Nanostructures for Electrocatalytic Oxygen Reduction. *ACS Appl. Mater. Interfaces* **2009**, *1*, 460–466.
- (3) Bard, A. J. Inner-Sphere Heterogeneous Electrode Reactions. Electrocatalysis and Photocatalysis: The Challenge. *J. Am. Chem. Soc.* **2010**, *132*, 7559–7567.
- (4) Zhu, H.; Zhang, S.; Huang, Y.-X.; Wu, L.; Sun, S. Monodisperse $M_xFe_{3-x}O_4$ ($M = Fe, Cu, Co, Mn$) Nanoparticles and Their Electrocatalysis for Oxygen Reduction Reaction. *Nano Lett.* **2013**, *13*, 2947–2951.
- (5) Gorlin, Y.; Jaramillo, T. F. A Bifunctional Nonprecious Metal Catalyst for Oxygen Reduction and Water Oxidation. *J. Am. Chem. Soc.* **2010**, *132*, 13612–13614.
- (6) Wang, D.; Chen, X.; Evans, D. G.; Yang, W. Well-Dispersed Co_3O_4/Co_2MnO_4 Nanocomposites as a Synergistic Bifunctional Catalyst for Oxygen Reduction and Oxygen Evolution Reactions. *Nanoscale* **2013**, *5*, 5312–5315.
- (7) Meng, Y.; Song, W.; Huang, H.; Ren, Z.; Chen, S.-Y.; Suib, S. L. Structure-Property Relationship of Bifunctional MnO_2 Nanostructures: Highly Efficient, Ultra-Stable Electrochemical Water Oxidation and Oxygen Reduction Reaction Catalysts Identified in Alkaline Media. *J. Am. Chem. Soc.* **2014**, *136*, 11452–11464.
- (8) Zhan, Y.; Xu, C.; Lu, M.; Liu, Z.; Lee, J. Y. Mn and Co Co-Substituted Fe_3O_4 Nanoparticles on Nitrogen-Doped Reduced Graphene Oxide for Oxygen Electrocatalysis in Alkaline Solution. *J. Mater. Chem. A* **2014**, *2*, 16217–16223.
- (9) Li, C.; Han, X.; Cheng, F.; Hu, Y.; Chen, C.; Chen, J. Phase and Composition Controllable Synthesis of Cobalt Manganese Spinel Nanoparticles towards Efficient Oxygen Electrocatalysis. *Nat. Commun.* **2015**, *6*, 7345.
- (10) Du, G.; Liu, X.; Zong, Y.; Hor, T. S. A.; Yu, A.; Liu, Z. Co_3O_4 Nanoparticle-Modified MnO_2 Nanotube Bifunctional Oxygen Cathode Catalysts for Rechargeable Zinc-Air Batteries. *Nanoscale* **2013**, *5*, 4657–4661.
- (11) Fekete, M.; Hocking, R. K.; Chang, S. L. Y.; Italiano, C.; Patti, A. F.; Arena, F.; Spiccia, L. Highly Active Screen-Printed Electrocatalysts for Water Oxidation Based on β -Manganese Oxide. *Energy Environ. Sci.* **2013**, *6*, 2222.
- (12) Lambert, T. N.; Vigil, J. A.; White, S. E.; Davis, D. J.; Limmer, S. J.; Burton, P. D.; Coker, E. N.; Beechem, T. E.; Brumbach, M. T. Electrodeposited $Ni_xCo_{3-x}O_4$ Nanostructured Films as Bifunctional Oxygen Electrocatalysts. *Chem. Commun.* **2015**, *51*, 9511–9514.
- (13) Lee, D. U.; Kim, B. J.; Chen, Z. One-Pot Synthesis of a Mesoporous $NiCo_2O_4$ Nanoplatelet and Graphene Hybrid and Its Oxygen Reduction and Evolution Activities as an Efficient Bi-Functional Electrocatalyst. *J. Mater. Chem. A* **2013**, *1*, 4754–4762.

- (14) Liang, Y.; Wang, H.; Zhou, J.; Li, Y.; Wang, J.; Regier, T.; Dai, H. Covalent Hybrid of Spinel Manganese-Cobalt Oxide and Graphene as Advanced Oxygen Reduction Electrocatalysts. *J. Am. Chem. Soc.* **2012**, *134*, 3517–3523.
- (15) Mao, S.; Wen, Z.; Huang, T.; Hou, Y.; Chen, J. High-Performance Bi-Functional Electrocatalysts of 3D Crumpled Graphene–cobalt Oxide Nanohybrids for Oxygen Reduction and Evolution Reactions. *Energy Environ. Sci.* **2014**, *7*, 609–616.
- (16) Masa, J.; Xia, W.; Sinev, I.; Zhao, A.; Sun, Z.; Grütze, S.; Weide, P.; Muhler, M.; Schuhmann, W. Mn_xO_y/NC and Co_xO_y/NC Nanoparticles Embedded in a Nitrogen-Doped Carbon Matrix for High-Performance Bifunctional Oxygen Electrodes. *Angew. Chem. Int. Ed.* **2014**, *53*, 8508–8512.
- (17) Xu, Y.; Bian, W.; Wu, J.; Tian, J.-H.; Yang, R. Preparation and Electrocatalytic Activity of 3D Hierarchical Porous Spinel $CoFe_2O_4$ Hollow Nanospheres as Efficient Catalyst for Oxygen Reduction Reaction and Oxygen Evolution Reaction. *Electrochim. Acta* **2015**, *151*, 276–283.
- (18) Zhao, B.; Zheng, Y.; Ye, F.; Deng, X.; Xu, X.; Liu, M.; Shao, Z. Multifunctional Iron Oxide Nanoflake/Graphene Composites Derived from Mechanochemical Synthesis for Enhanced Lithium Storage and Electrocatalysis. *ACS Appl. Mater. Interfaces* **2015**, *7*, 14446–14455.

4.1.3 $\text{Fe}_3\text{O}_4@\text{NiFe}_x\text{O}_y$ Nanoparticles with Enhanced Electrocatalytic Properties for Oxygen Evolution in Carbonate Electrolyte

This section is based on the recently accepted paper " *$\text{Fe}_3\text{O}_4@\text{NiFe}_x\text{O}_y$ Nanoparticles with Enhanced Electrocatalytic Properties for Oxygen Evolution in Carbonate Electrolyte*" in ACS Applied Materials & Interfaces. We design an earth-abundant catalyst with cost-effective and high activity for water splitting. Herein, we report monodisperse Fe-Ni oxide based core-shell NPs containing Fe_3O_4 as core material and a NiFe_xO_y as shell. These HNP were efficient electrocatalyst for water oxidation. The core-shell nanostructures were synthesized by a simple and scalable protocol involving the diffusion of Ni cations to form NiFe_xO_y shell on iron oxide template. Significantly, the as-anodized core-shell catalyst film exhibit high activity towards the OER under near neutral pH conditions (pH is 9.75 in carbonate electrolyte), reaching a current density of 1 mA/cm^2 at 410 mV overpotential and the Tafel slope of 48 mV/dec. Such a simple strategy was applied to incorporate manganese and cobalt ions into Fe_3O_4 NPs for OER or for other applications. This method yielded efficient low cost catalyst inks that can be produce in large scale, at low temperature and ambient pressure for water oxidation. The graphical abstract is shown in Figure 4.6, and the article is found right below these lines.

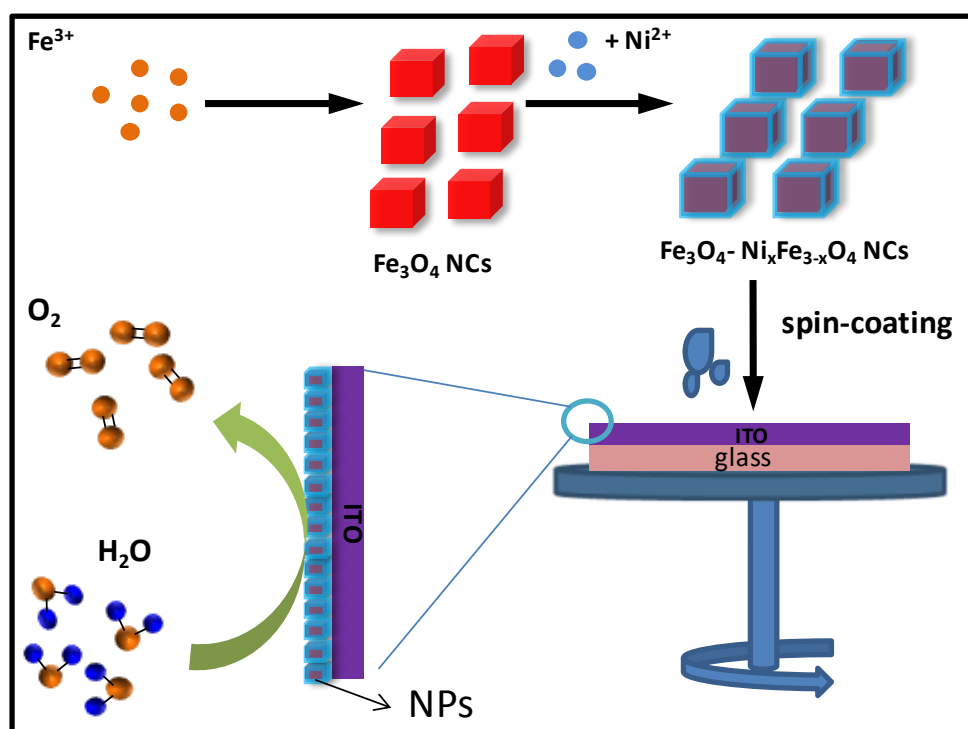


Figure 4.6 Scheme illustration of the synthesis of core-shell NPs and fabrication of electrocatalysts thin film to apply water oxidation.

$\text{Fe}_3\text{O}_4@\text{NiFe}_x\text{O}_y$ Nanoparticles with Enhanced Electrocatalytic Properties for Oxygen Evolution in Carbonate Electrolyte

Zhishan Luo,[†] Sara Martí,[¶] Raquel Nafria,[†] Gihan Joshua,[†] Maria de la Mata,[¶] Pablo Guardia,^{†,¶} Cristina Flox,[†] Carlos Martínez-Boubeta,[⊥] Konstantinos Simeonidis,[§] Jordi Llorca,[⊞] Joan Ramon Morante,[†] Jordi Arbiol,^{¶,¥} Maria Ibáñez,[†] Andreu Cabot^{†,¥,*}

[†] Catalonia Institute for Energy Research - IREC, Sant Adrià de Besòs, Barcelona, 08930, Spain

[¶] Catalan Institute of Nanoscience and Nanotechnology (ICN2), CSIC and The Barcelona Institute of Science and Technology (BIST), Campus UAB, Bellaterra, 08193 Barcelona, Spain

[⊞] Centre de Tecnologia Química de Catalunya and Universitat Rovira i Virgili, Carrer de Marcel·lí Domingo s/n, 43007 Tarragona, Spain

[⊥] Freelancer in Santiago de Compostela, Spain

[§] Department of Physics, Aristotle University Thessaloniki, 54124 Thessaloniki, Greece

[⊞] Institut de Tècniques Energètiques, Universitat Politècnica de Catalunya, 08028 Barcelona, Spain

[¥] ICREA, Pg. Lluís Companys 23, 08010 Barcelona, Spain

KEYWORDS. Nanoparticle, iron oxide, magnetite, core-shell nanostructure, electrocatalysts, oxygen evolution reaction, OER.

ABSTRACT

The design and engineering of earth-abundant catalysts that are both cost-effective and highly active for water splitting is a crucial challenge in a number of energy conversion and storage technologies. In this direction, herein we report the synthesis of $\text{Fe}_3\text{O}_4@\text{NiFe}_x\text{O}_y$ core-shell nano-heterostructures and the characterization of their electrocatalytic performance toward the oxygen evolution reaction (OER). Such nanoparticles (NPs) were produced by a two-step synthesis procedure involving the colloidal synthesis of Fe_3O_4 nanocubes with a defective shell and the posterior diffusion of nickel cations within this defective shell. $\text{Fe}_3\text{O}_4@\text{NiFe}_x\text{O}_y$ NPs were subsequently spin-coated over ITO-covered glass and their electrocatalytic activity toward water oxidation in carbonate electrolyte was characterized. $\text{Fe}_3\text{O}_4@\text{NiFe}_x\text{O}_y$ catalysts reached current densities above 1 mA/cm^2 with a 410 mV overpotential and Tafel slopes of 48 mV/dec, which is among the best electrocatalytic performances reported in carbonate electrolyte.

1. INTRODUCTION

The electrocatalytic OER has a key and limiting role in several energy conversion and storage technologies such as metal-air batteries, fuel cells, and electrolyzers.¹⁻³ A main challenge of water oxidation is its slow kinetics associated to a multistep proton-coupled electron transfer process that involves four protons and four electrons ($4\text{OH}^- \rightarrow 2\text{H}_2\text{O} + \text{O}_2 + 4\text{e}^-$, in basic media). OER generally requires voltages significantly above the thermodynamic potential for water splitting, which has an efficiency cost. To reduce this potential, OER catalysts based on expensive and scarce noble metals, such as IrO_2 and RuO_2 ,⁴⁻⁶ are currently used, which have an economic cost that limits the penetration of related technologies in huge markets such as transportation and grid integration of renewable energies. Consequently, an enormous interest

exists in developing stable OER catalysts that are able to lower the kinetic barriers associated with the OER and at the same time are based on earth-abundant metals.

Over the years, a plethora of compounds have been explored as OER catalysts.⁷⁻¹⁹ A good catalyst must have: i) small energy steps between the involved chemical and charge transfer steps, to minimize overall overpotential; ii) a proper strength of the bond between metal cations and oxygen/hydroxide species;^{5,7-8} iii) high surface areas with proper porosity to maximize the density of accessible reaction sites per electrode unit area; iv) large density of proper reaction sites, which may call for defective structures with low energy of formation of proper defects and even amorphous materials;⁹⁻¹⁰ v) high electrical conductivities to maximize current densities, especially in thick porous layers providing large number of sites per electrode area unit; vi) proper catalyst-electrode energy band alignment preventing Schottky barriers in the common case of using semiconductor catalysts; and vii) high stability at operation conditions.

A number of transition metal compounds have exhibited particularly attractive activities and durabilities for water oxidation in alkaline electrolytes. Among them Ni-Fe oxides, hydroxides, or oxyhydroxides at reaction conditions are the most promising earth-abundant OER catalysts under alkaline conditions.^{9,20-33} Within these materials, Ni is generally considered the active oxygen evolution center.^{8,31} On the other hand, Fe incorporation provides improved electrical conductivities,^{20,34} partial charge transfer modifying Ni site energy,^{20,33} stabilization of proper crystal phases and/or proper Ni oxidation states, and also an increased strain, defect density, and overall lower crystallinity.²¹ Some authors have also proposed iron cations within the Ni-Fe oxide structure as the active sites with near optimal adsorption energies for the intermediates formed during the OER.¹¹ In this regard the iron chemical state is also modified by the Ni environment and even Fe⁴⁺ species, which may be the active species when in corners, edges or

defect sites, were identified under OER conditions in Ni-Fe catalysts using Mössbauer spectroscopy.²²

The pH has a particularly strong influence in Ni-Fe oxide/oxyhydroxide catalysts, which was attributed to a deprotonation of Ni-based catalysts to form active oxygen species that may act as the OER precursor.²³ OER metal oxide catalysts are operated at high pH values to maximize activity. However, the use of pH values closer to neutral has advantages such as an improved stability of the cell components and improved safety during processing and use.³⁵⁻³⁸ As an example, Cao and coworkers reported a Fe-based film as highly active electrocatalysts in neutral aqueous solution.³⁶ Besides, Zaharieva et al. demonstrated an excellent performance of electrodeposited Mn oxide catalysts for electrochemical water oxidation at neutral pH solution.³⁷ CO₂-saturated carbonate solutions are increasingly used as relatively low pH electrolyte with the additional potential of multi-functionality as water splitting can be combined with CO₂ reduction to produce carbon-based liquid fuels. Another potential advantage is that carbonate solutions are also more environmental friendly than for instance the phosphate buffer which may cause critical eutrophication of water body.³⁹⁻⁴⁰ Considerable effort has been devoted to the development of transition metal oxides as OER catalysts in carbonate electrolyte.⁴¹⁻⁴³ As an example, Sun et al. reported a Fe-based electrocatalyst in carbonate electrolyte having a 560 mV overpotential at 10 mA/cm² and 34 mV/dec of Tafel slope.¹⁹ Joya and co-workers demonstrated that Ni-based electrocatalysts in a bicarbonate electrolyte reached a slope of -63 mV/pH, close to the theoretical value of -59 mV/pH for a PCET mechanism involving one electron and one proton.⁴⁴

In terms of processing, most electrocatalysts are currently coated as powders onto conductive substrates with the aid of polymeric binders such as Nafion.⁴⁵ The use of a binder can decrease liquid-solid interface and reduce electrical conductivity of the electrode, while at the same time it

can have associated stability problems due to peel off. Over flat substrates, electrodeposition and vacuum-based thin film techniques generally yield compact crystalline layers, with low specific surfaces and thus activities. Instead the use of mesostructured supports, such as stainless steel meshes or nickel foams provides much higher areas and activities.^{24,46} Alternatively, the printing or deposition of colloidal NPs with tuned compositions not only potentially provides highly porous layers, but also an unmatched composition control at the nanometer scale using high-throughput and high yield chemical routes at ambient pressure and low temperature.⁴⁷⁻⁵¹ The huge potential of such solution-based strategies to tune material properties at the nanoscale resides in the ability to chemically manipulate material growth from the very initial combination of atoms into a cluster, and to do so in parallel for huge amounts of NPs, all self-evolving at the same rate and in the same conditions. Thus, very large amounts of material in the form of colloidal NPs with precisely tuned properties can be produced in a simple, fast, and cost-effective manner. Colloidal synthesis routes are also extremely versatile, allowing production of elemental or multinary nanoparticles with a wide range of compositions and also multi-material nano-heterostructures with organized phase distribution by the parallel or sequential growth of one material at the surface of the other or by replacing part of the ions of a preformed nanostructure.⁵²⁻⁵⁵

Herein, we report the colloidal synthesis of a novel Fe-Ni oxide OER catalyst based on core-shell NPs containing a Fe_3O_4 core and a NiFe_xO_y shell. Such $\text{Fe}_3\text{O}_4@\text{NiFe}_x\text{O}_y$ core-shell NPs were produced by a simple and scalable protocol involving the diffusion of nickel cations within the defective shell of Fe_3O_4 NPs. This simple strategy yielded a catalyst ink that was easily applicable to any support using low cost solution-processing technologies and without the use of polymeric binders. We further demonstrate the suitability of the synthesized materials and used

processes to produce OER catalysts in a carbonate electrolyte that are beyond the state-of-the-art in terms of activity and stability.

2. EXPERIMENTAL

Chemicals: Cobalt(II) perchlorate hexahydrate ($\text{Co}(\text{ClO}_4)_2 \cdot 6\text{H}_2\text{O}$), nickel(II) perchlorate hexahydrate ($\text{Ni}(\text{ClO}_4)_2 \cdot 6\text{H}_2\text{O}$), sodium oleate (Na-OA, $\geq 82\%$), octadecene (ODE, 90%) xylenes ($\geq 98.5\%$), oleylamine (OLA, $>70\%$), oleic acid (OA, 90%) were purchased from Sigma-Aldrich. Toluene, hexane, chloroform, acetone, and ethanol were of analytical grade and obtained from various sources. Milli-Q water was supplied by the PURELAB flex from ELGA. All chemicals were used as received without further purification, except OLA, which was purified by distillation.

Synthesis Fe_3O_4 nanocubes: Fe_3O_4 nanocubes were used as a template for the synthesis of $\text{Fe}_3\text{O}_4@ \text{NiFe}_x\text{O}_y$ core-shell NPs. Several routes can be found in the literature to produce such nanostructures. We followed and detail here a procedure developed from merging two previously reported protocols.⁵⁶⁻⁵⁷ First, iron oleate (Fe-OA) was obtained by dissolving 1.3 g (8 mmol) of FeCl_3 and 7.3 g (24 mmol) of sodium oleate (Na-OA) in a mixture of 12 mL H_2O , 16 mL ethanol, and 28 mL hexane. The resulting mixture was stirred overnight at room temperature and purified in a separatory funnel by washing 5-6 times with preheated (80°C) MQ-water (18.2 M Ω , filtered with filter pore size 0.22 μM , Millipore). The resulting organic layer was dried under reduced pressure in a rotary evaporator until all remaining H_2O was removed. Once purified, 0.4 g of Fe-OA (4.44 mmols), 0.1 g of Na-OA (3.28 mmols), 0.1 mL of OA (0.32 mmols), and 10 mL of ODE were mixed in a 25 mL three-neck flask and degassed under magnetic stirring for 1.5 h at 70°C (0.2-0.3 mbar). The reaction mixture was then heated to 330°C ($5.5^\circ\text{C}/\text{min}$) under an Argon blanket and kept at that temperature for 30 min. The solution was then cooled down to

room temperature and NPs were collected by adding 20 mL of acetone and centrifuging at 9000 rpm for 10 min. The black/brown precipitate was re-dispersed in 5 mL of chloroform under sonication and washed at least 2 times more. Finally the NPs were dispersed and stored in 5 mL of chloroform. Within this synthesis protocol, variation of the OA concentration, heating ramp and reflux temperature would allow for size tuning.

Synthesis of $\text{Fe}_3\text{O}_4@\text{NiFe}_x\text{O}_y$ NPs: In a 25 mL three-neck flask, 10 mg of Fe_3O_4 NPs, weighted after precipitation and drying, were dissolved in 5 mL of xylene along with 0.41 mL of OLA (1.26 mmols) and 0.08 mL (0.26 mmols) of OA and heated to 90°C. Then, 0.5 mL of $\text{Ni}(\text{ClO})_2 \cdot 6\text{H}_2\text{O}$ aqueous solution (0.2 M) was injected into the reaction solution under vigorous stirring and kept at 90 °C in air for 5 h. Finally, the solution was cooled down to room temperature and NPs were collected by adding 15 mL of ethanol. The precipitate was re-dispersed in 5 mL of toluene and precipitated again with ethanol. Finally NPs were re-suspended in 5 mL of toluene for further characterization.

Structural, chemical and magnetic characterization: Transmission electron microscopy (TEM) analyses were carried out using a ZEISS LIBRA 120, operating at 120 kV. High-resolution TEM (HRTEM) and Scanning TEM (STEM) studies were conducted using a field emission gun FEI™ Tecnai F20 microscope at 200 kV with a point-to-point resolution of 0.19 nm. High angle annular dark-field (HAADF) STEM was combined with electron energy loss spectroscopy (EELS) in the Tecnai F20, by using a GATAN QUANTUM filter. Samples were prepared by drop casting a solution of NPs on a 200 mesh copper grid. Scanning electron microscopy (SEM) analyses were performed using a ZEISS Auriga microscope with an energy dispersive X-ray spectroscopy (EDS) detector operating at 20 kV, that allowed for analysis of the NP composition. For SEM characterization, the materials were dispersed in

chloroform and drop casted onto silicon substrates. Powder X-ray diffraction (XRD) patterns were collected directly from the as-synthesized NPs dropped on Si(501) substrate on a Bruker AXS D8 Advance X-ray diffractometer with Ni-filtered (2 μm thickness) Cu K radiation ($\lambda = 1.5406 \text{ \AA}$) operating at 40 kV and 40 mA. A LynxEye linear position-sensitive detector was used in reflection geometry. X-ray photoelectron spectroscopy (XPS) was done on a SPECS system equipped with an Al anode XR50 source operating at 150 mW and a Phoibos 150 MCD-9 detector. The pressure in the analysis chamber was always below 10^{-7} Pa. The area analyzed was about $2 \text{ mm} \times 2 \text{ mm}$. The pass energy of the hemispherical analyzer was set at 25 eV and the energy step was set at 0.1 eV. Data processing was performed with the CasaXPS program (Casa Software Ltd., UK). Binding energy (BE) values were centered using the C 1s peak at 284.8 eV. The atomic fractions (%) were calculated using peak areas. Magnetic hysteresis loops of the powder material were recorded at room temperature using an Oxford Instruments 1.2 H/CF/HT vibrating sample magnetometer (VSM) with a maximum applied field of 1 Tesla. Magnetizations were corrected for the organic content of the materials (20-30 %) as measured by thermogravimetry.

Electrolytes and Catalyst Preparation: The carbonate buffer solution was prepared by mixing equal volume of 0.2 M Na_2CO_3 and 0.2 M NaHCO_3 aqueous solutions.¹⁹ The pH was monitored by using a pH meter. To prepare the catalysts films, Fe_3O_4 and $\text{Fe}_3\text{O}_4@\text{NiFe}_x\text{O}_y$ NPs were dispersed in octane with a concentration of about 10 mg/mL. ITO glass substrates were coated with the NPs by spin-coating. Briefly, 200 μL of the suspension was gradually dropped at 200 rpm. After the substrate was spun for 1 minute, the speed was increased up to 900 rpm and kept at this speed for 1 additional minute. To make different NPs layers, the iron-based films were dried on a hot-plate ($\sim 110 \text{ }^\circ\text{C}$) to completely evaporate the solvent and then the spin-

coating process was repeated. The obtained films were denoted ITO-Fe₃O₄ for Fe₃O₄ NPs and ITO-Fe₃O₄-Ni# for Fe₃O₄@NiFe_xO_y NPs, where # is the number of layers deposited by the spin-coating process (# = 1-4). Then these films were annealed for 30 min at 300°C in 5% H₂/Ar atmosphere.

Electrochemical characterization: Electrochemical measurements were carried out on a computer-controlled workstation bipotentiostat (Versa STAT 3, Princeton Applied Research). The custom-made three-electrode system that was used included 25 mL of carbonate electrolyte with a pH of 9.75, a silver-silver chloride reference electrode (Ag/AgCl with saturated KCl encapsulated, 012167 RE-1B, ALS Co. Ltd-BAS Inc.), a platinum foil for the counter electrode, and a 1.5 cm² ITO glass with or without catalysts for the working electrode. A scan rate of 50 mV/s was used for all the current density measurements. All potentials are reported versus the reversible hydrogen electrode (RHE) using the Nernst equation as follows:

$$E_{\text{RHE}} = E_{\text{Ag/AgCl}} + 0.059 \times \text{pH} + E^{\circ}_{\text{Ag/AgCl}} \text{ (V)} \quad (1)$$

where pH is the electrolyte pH and $E^{\circ}_{\text{Ag/AgCl}} = 0.197$ V versus the normal hydrogen electrode (NHE) at 25°C for the Ag/AgCl/ saturated KCl solution (CH Instruments, Inc.). The OER overpotential (η) was calculated using the equation below:

$$\eta = E_{\text{Ag/Ag}} - E^{\circ}(\text{O}_2/\text{H}_2\text{O}) \text{ (V)} \quad (2)$$

where $E^{\circ}(\text{O}_2/\text{H}_2\text{O})$ is the thermodynamic potential for water oxidation (the OER) relative to Ag/AgCl at pH = 9.75, which was calculated to be 0.65 V using,

$$E^{\circ}(\text{O}_2/\text{H}_2\text{O}) = 1.23 - 0.059 \times \text{pH} - E^{\circ}_{\text{Ag/AgCl}} \text{ (V)} \quad (3)$$

All the potentials reported here were iR-corrected. Current densities were calculated using geometric surface areas.

O₂ evolution evaluation: We used gas chromatography to analyze the reaction products and calculate the Faradaic efficiency for O₂ production. For this measurement, the electrochemical reaction was carried out within a gas-tight electrochemical cell containing a silver-silver chloride reference electrode (Ag/AgCl with saturated KCl encapsulated), a glass fritted isolated platinum counter-electrode and a 1.5 cm² ITO-Fe₃O₄-Ni anodized catalysts as the working electrode. Before measurement, the electrochemical cell was purged by bubbling Ar for 2h. The experiment was carried out at 1.3 V vs. RHE in 80 ml carbonate buffer solution. The produced oxygen was extracted using a 18 ml/min Ar flow introduced using a mass flow controller. The gaseous outlet flow from the cell were analyzed on-line every 10 min using a two channel gas micro-chromatograph (490 Micro GC) equipped with an M5A 20 m and a PPQ 10 m columns and TCD detectors. The steam water was condensed before the gas chromatography analyses using a trap kept at 175 K. The Faradaic efficiency was calculated by measuring the amount of oxygen in the effluent gas, taking into account the Ar gas flow and comparing these values with the charge transferred calculated from the current density measured with the potentiostat. Figure S1 shows a photograph of the experimental set-up used for this measurement.

Figure 1 shows a scheme of the synthetic protocol used to prepare the Fe-Ni oxide NPs and the process used to produce the NP-based electrocatalyst.

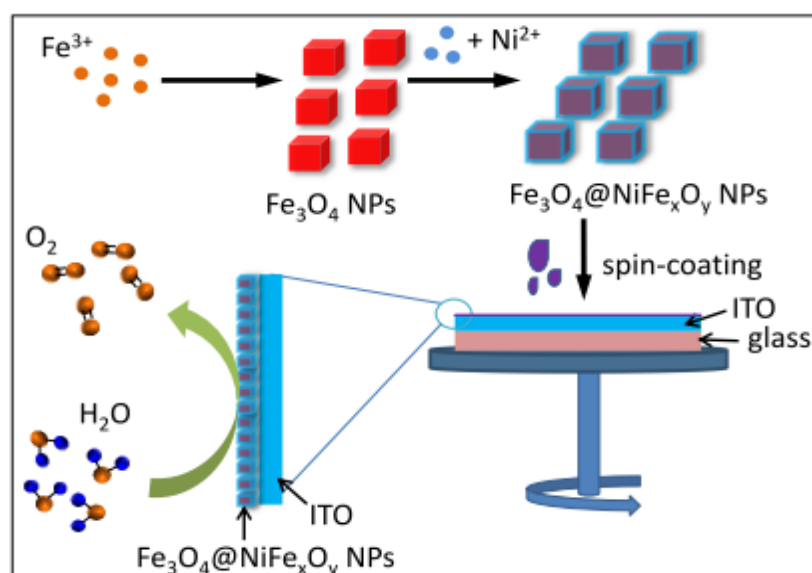


Figure 1. Scheme of the synthesis of core-shell $\text{Fe}_3\text{O}_4@\text{NiFe}_x\text{O}_y$ NPs as a result of the growth of a shell on top of Fe_3O_4 seeds. Thin films were fabricated by spin coating a solution of NPs on top of an ITO substrate and their electrocatalytic performance in water oxidation was tested.

3. RESULTS AND DISCUSSION

Figure 2 shows representative TEM images, size distribution histograms, and XRD patterns of the initial iron oxide NPs and the final iron-nickel oxide NPs produced following the above detailed procedure. The NP's morphology did not change with the introduction of nickel ions and the average size just very slightly increased from 17 ± 2 nm to 18 ± 2 nm (Figure 2c). XRD patterns (Figure 2d) revealed the initial iron oxide NPs and the final iron-nickel oxide NPs to have a cubic inverse spinel structure, as it corresponds to magnetite Fe_3O_4 and the maghemite γ - Fe_2O_3 defective structure. Following previous reports, we indexed it as magnetite (JCPDS 01-086-1350).⁵⁶⁻⁵⁷ The peak broadening due to the small crystal domain size and the very similar unit cell parameters of Fe_3O_4 and iron-nickel oxides with an inverse spinel structure, such as $\text{Ni}_{0.6}\text{Fe}_{2.4}\text{O}_4$ (JCPDS 01-087-2338), prevented an explicit identification of any effect of Ni on the

NP's crystal phase from the XRD pattern. Using Scherrer's equation, we calculated the size of Fe_3O_4 and iron-nickel oxide NPs to be 17 nm and 20 nm respectively, in good agreement with TEM results.

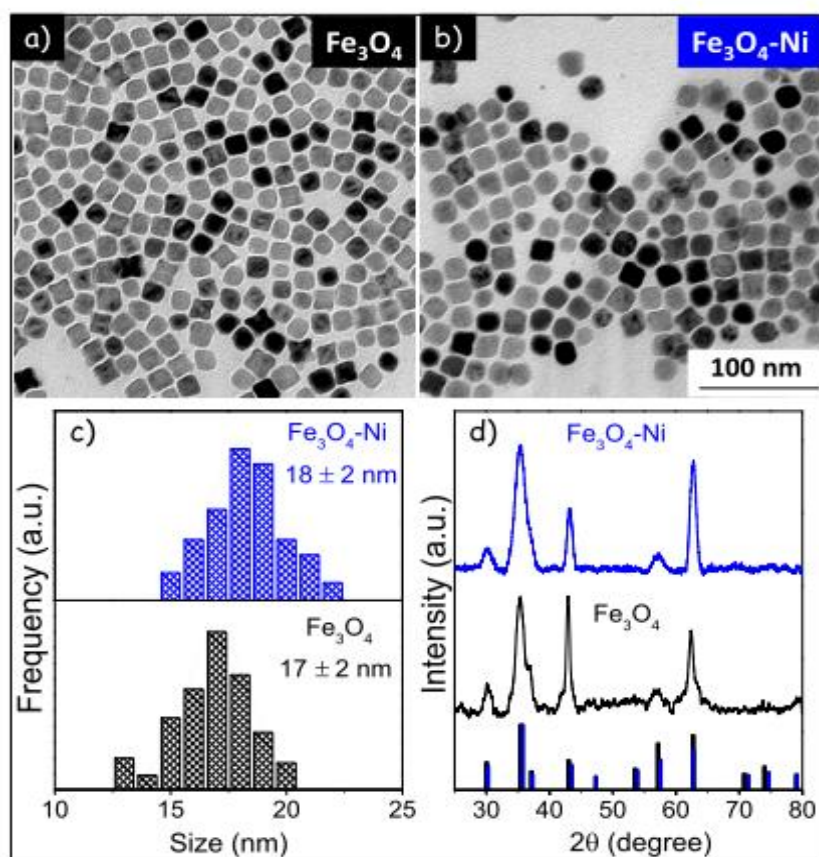


Figure 2. Representative TEM micrograph of Fe_3O_4 NPs (a) and Fe_3O_4 -Ni NPs (b). Their corresponding size distribution histograms (c) and XRD patterns (d), including reference patterns for Fe_3O_4 (black bars, JCPDS 00-001-1111) and $\text{Ni}_{0.6}\text{Fe}_{2.4}\text{O}_4$ (blue bars, JCPDS 01-087-2338).

ICP analysis revealed the overall $[\text{Ni}]/[\text{Fe}]$ ratio of the NP ensemble to be $[\text{Ni}]/[\text{Fe}] = 0.1$. SEM-EDX analyses at different points of the sample confirmed this elemental ratio and demonstrated excellent compositional homogeneity at the micrometer scale. To determine the elemental distribution within each NP, low magnification annular dark field (ADF) STEM and

chemical maps were further acquired (Figure 3a). Elemental compositional maps, obtained by EELS using O K, Fe L_{2,3} and Ni L_{2,3} edges, revealed the presence of Fe and O throughout all the cubic-shaped NPs, but with a 3 % increase in oxygen content and 6 % reduction in Fe atomic percent at the outer parts of the NP with respect to the centre. On the other hand, Ni was only detected at the outer parts of the NPs (Figure 3a), reaching almost 5% of the total composition there.

Figure S2 and Figure 3b show representative HRTEM micrograph of Fe₃O₄ and Fe₃O₄@NiFe_xO_y NPs, respectively, and details of their crystal structure. The power spectrum of the HRTEM of Fe₃O₄@NiFe_xO_y (figure 3b) could be fitted with that of magnetite (space group FD3-MZ) with $a = b = c = 8.4082 \text{ \AA}$. Both the core and the shell showed the same cubic Space Group: FD3-MZ. The dark contrasts that can be observed in the micrographs might correspond to Moiré fringes caused by two lattices with a small mismatch. Geometrical Phase Analysis (GPA) analyses also showed a decrease in the $d_{(040)}$ -spacing on the outer parts of the NP (Figure 3b). From these results, we calculated differences of cell spacing between the core and the shell of around 4%, which cannot be explained by just taking into account the Ni diffusion. Notice that the difference in lattice parameter between Fe₃O₄ and NiFe₂O₄ structures should be about 1%, and that the amount of Ni in the shell of the NPs here produced was even lower: [Ni]/[Fe]~0.12. Besides, similar contrasts were also observed on the original iron oxide NPs (Figure 2a). Checking for the relative composition of the oxygen in Figure 3a it is clearly observed that the shell is more oxidized than the core. Thus we hypothesize that original NPs already have a core-shell structure with a magnetite core and a more oxidized, defective maghemite shell. This hypothesis explains the difference in lattice constant and the contrasts observed in the low magnification TEM image on Fe₃O₄ and Fe₃O₄@NiFe_xO_y NPs.

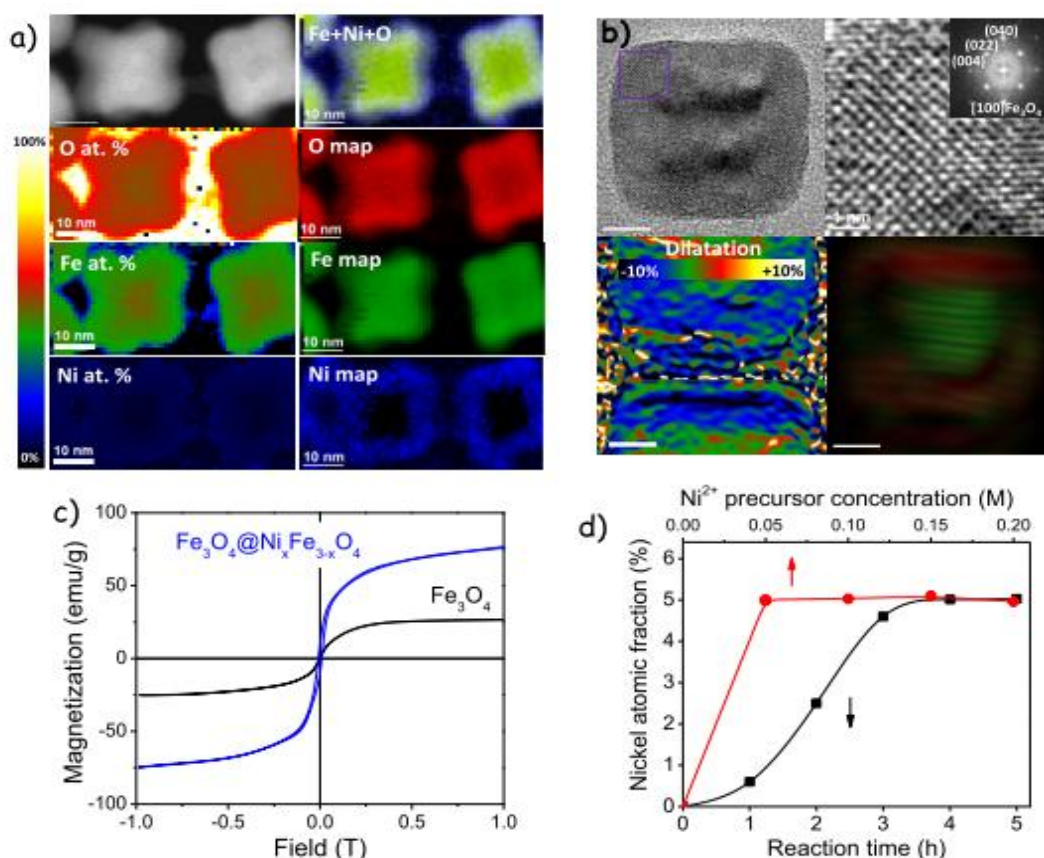


Figure 3. a) Low magnification ADF STEM image, relative atomic composition, and elemental maps of Ni, Fe and O; b) HRTEM micrographs of $\text{Fe}_3\text{O}_4@ \text{NiFe}_x\text{O}_y$, detail of the squared region and their corresponding indexed power spectrum (inset), HRTEM shows Moiré contrasts, dilatation map applying GPA to the (040) planes of $\text{Fe}_3\text{O}_4@ \text{NiFe}_x\text{O}_y$ core-shell NPs and structural map obtained with the (040) plane revealing differences in d-spacing between core and shell; c) Magnetization hysteresis loops of Fe_3O_4 and $\text{Fe}_3\text{O}_4@ \text{NiFe}_x\text{O}_y$ NPs; d) EDX data showing the molar fraction of Ni as a function of the molarity of the precursor solution of Ni^{2+} added during the synthesis (red line, 0.5 mL injected, reaction time = 5h) and as a function of the reaction time increasing (black line, 0.5 mL injected of a 0.2 M Ni^{2+} precursor solution).

To support this hypothesis, we measured the magnetic properties of the produced NPs, magnetization being a property particularly sensitive to crystallinity. As observed in Figure 3c, Fe_3O_4 NPs were characterized by relatively low magnetization values compared with bulk magnetite, which clearly points toward the presence of a defective surface structure. Surprisingly, the addition of Ni significantly increased magnetization, in opposition to what is expected taking into account the lower saturation magnetization of nickel ferrite when compared to that of magnetite. We believe that such an increase of the saturation might be associated to the partial reconstruction of the magnetically frustrated layer on the surface of the Fe_3O_4 seeds due directly to the Ni incorporation or to the additional annealing of the NPs at temperatures close to 100 °C during the Ni diffusion.

From these results, we further hypothesize that the defective shell helps Ni incorporation to the lattice and that this Ni incorporation is limited to the defective shell structure. We observe that the Ni diffusion is self-limited in terms of localization (Figure 3a) and concentration. In this last direction, the amount of Ni in the final core-shell NPs gradually increased with the reaction time up to 4 hours and remained stable after this mark (Figure 3d). The concentration of Ni in the core-shell NPs was kept almost the same even when increasing amounts of nickel precursor were introduced (Figure 3d). These experimental evidences and the low nickel ratio obtained even at relatively high nickel precursor concentrations and after long reaction times point toward a self-limited diffusion of Ni within the Fe_3O_4 structure.

The use of a perchlorate precursor was critical to incorporate nickel within the iron oxide and to produce NPs with a core-shell compositional distribution. When following the exact same procedure but using a chloride (NiCl_2) instead of a perchlorate precursor, Ni was not detected within the NPs. Differences may be ascribed to the lower coordination ability of perchlorate

rather than chloride ions, which make perchlorate precursors slightly more reactive and thus inclined to the cation incorporation within the Fe_3O_4 structure than chloride precursors.⁵² The reaction of the nickel perchlorate precursor in the absence of Fe_3O_4 seeds resulted in the formation of $\text{Ni}(\text{OH})_2$ nanosheets (Figure S3).

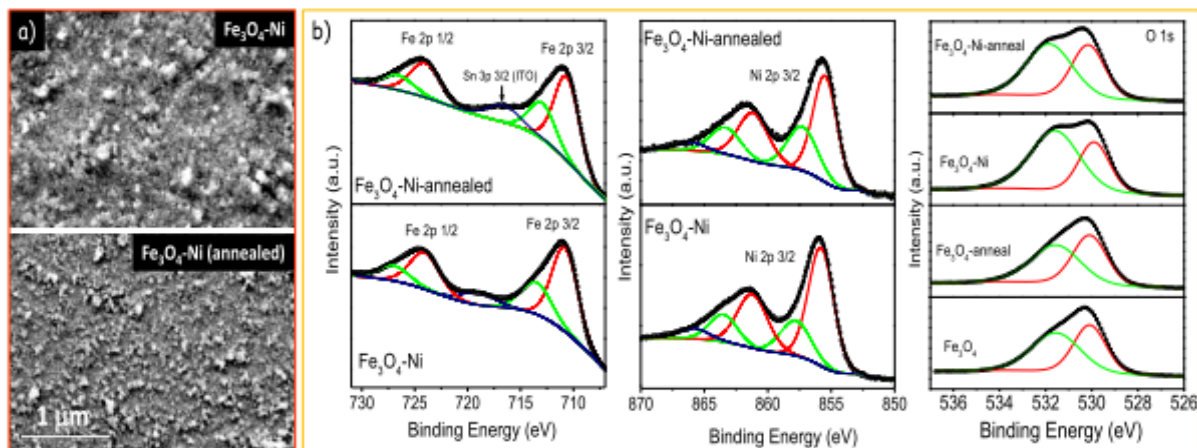


Figure 4. a) SEM micrographs of $\text{Fe}_3\text{O}_4@\text{NiFe}_x\text{O}_y$ catalyst film before and after annealing. B) Fe 2p, Ni 2p and O 1s regions of the XPS spectra of the catalyst layers before and after annealing.

To study Fe_3O_4 and $\text{Fe}_3\text{O}_4@\text{NiFe}_x\text{O}_y$ core-shell NPs toward OER, NPs were spin coated onto ITO-coated glass substrates (Figure 1). The layer thickness could be controlled by the number of spin coating steps or the concentration of the deposited NP solution. SEM micrographs of the ITO- Fe_3O_4 and ITO- Fe_3O_4 -Ni films revealed the catalyst to have a relatively rough surface (Figure 4a). After deposition, the catalysts were annealed under 5 % H_2/Ar atmosphere at 300 °C for 30 min. This annealing process did not significantly change the composition or distribution of the chemical states of the films according to XPS analysis (Figure 4b); the surface atomic $[\text{Ni}]/[\text{Fe}]$ ratio changed slightly from 0.62 to 0.55 after annealing and a slight negative shift, ~ 0.3 eV, of the Ni $2\text{P}_{3/2}$ binding energy was obtained with the annealing process in a hydrogen atmosphere. XPS further demonstrated the presence of at least two types of oxygen at the NP

surface. The component at lower binding energies (529.9-530.1 eV) corresponds to lattice oxygen in metal oxide and the component at higher binding energies (531.6-531.8 eV) to hydroxide groups at the surface. Significantly higher contributions of the hydroxide groups at the surface of the Ni-containing sample were observed.

The OER catalytic activity of the as-prepared catalyst films were evaluated by cyclic voltammetry (CV) using a carbonate buffer solution as electrolyte (pH = 9.75). To optimize the catalyst thickness, the ITO-Fe₃O₄-Ni performance was initially analyzed as a function of the number of layers deposited. Catalyst films that were too thin provided a reduced number of sites for the water oxidation reaction, resulting in relatively low current densities. On the other hand, catalyst films that were rather thick had associated lower performances due to an increase of the electrical resistivity. We found the optimum thickness to be around 60 nm, which corresponded to two spin coating processes (Figure 5a, 5b).

Setting a constant potential above the water oxidation onset, we observed that the current density increases over time (Figure S4). This beneficial anodization process has been previously used to electrochemically activate the catalyst. For example, Nocera and co-workers reported that the anodization process lead to changes of the oxidation state and the structure of electrodeposited Ni-based catalyst films, resulting in markedly improved catalytic activity.⁵⁸ Sun et al. also demonstrated that after anodization, electrodeposited FeOOH catalysts exhibited lower overpotential and Tafel slope and higher current density compared with non-anodized films.¹⁹ However, I. Roger and M. D. Symes demonstrated the incorporation of small amounts of impurities, such as Ni, during anodization processes could result in strong increase of current densities.⁵⁹ Our catalytic films were not produced by electrodeposition but by the spin coating of previously formed nanocrystals, which have a relatively high chemical and structural stability.

Furthermore, we found similar relative anodization effects in catalysts with different surface compositions, but final current densities for the different anodized catalysts were quite different, discarding a main electrocatalytic effect of an incorporated impurity. Minor crystallographic and/or chemical modification of the NCs may take place during anodization (although no evidences in this direction could be obtained) and these could have an effect on the electrocatalytic performance. However, we hypothesize the main anodization effect on our materials could be associated to the removal by oxidation of residual organic species and possibly carbon from the NCs surface freeing surface sites for electrochemical reaction. Actually, SEM analysis shows the electrodes after anodization to present more clearly defined NCs, denoting a lower contamination (Figure S5).

Figure 5c shows CV characterization of ITO-Fe₃O₄ and ITO-Fe₃O₄-Ni, before and after anodization. The CV profile of ITO is also plotted as a reference although it exhibited almost no catalytic activity. Generally, the as-anodized catalyst films showed superior OER activities compared to non-anodized films. In particular, ITO-Fe₃O₄-Ni-ano displayed a much lower overpotential ($\eta = 410$ mV at $1 \text{ mA} \cdot \text{cm}^{-2}$) than ITO-Fe₃O₄-Ni ($\eta = 520$ mV), ITO-Fe₃O₄ ($\eta = 750$ mV) and ITO-Fe₃O₄-ano ($\eta = 640$ mV). The corresponding Tafel slopes are shown in Figure 5d. ITO-Fe₃O₄-Ni-ano also showed the lowest Tafel slopes, down to 48 mV/dec, as compared to ITO-Fe₃O₄-Ni (65 mV/dec), ITO-Fe₃O₄ (140 mV/dec), and ITO-Fe₃O₄-ano (171 mV/dec). The catalyst stability at a current density of $1 \text{ mA} \cdot \text{cm}^{-2}$ in carbonate electrolyte was also evaluated. As shown in Figure 5e, the anodized catalysts displayed no decrease of activity with time, but a slight increase of current density was obtained. Overall, such ITO-Fe₃O₄-Ni-ano catalyst films were superior to most transition metal-based OER catalysts at near neutral pH conditions previously reported (Figure 5f and Table 1).

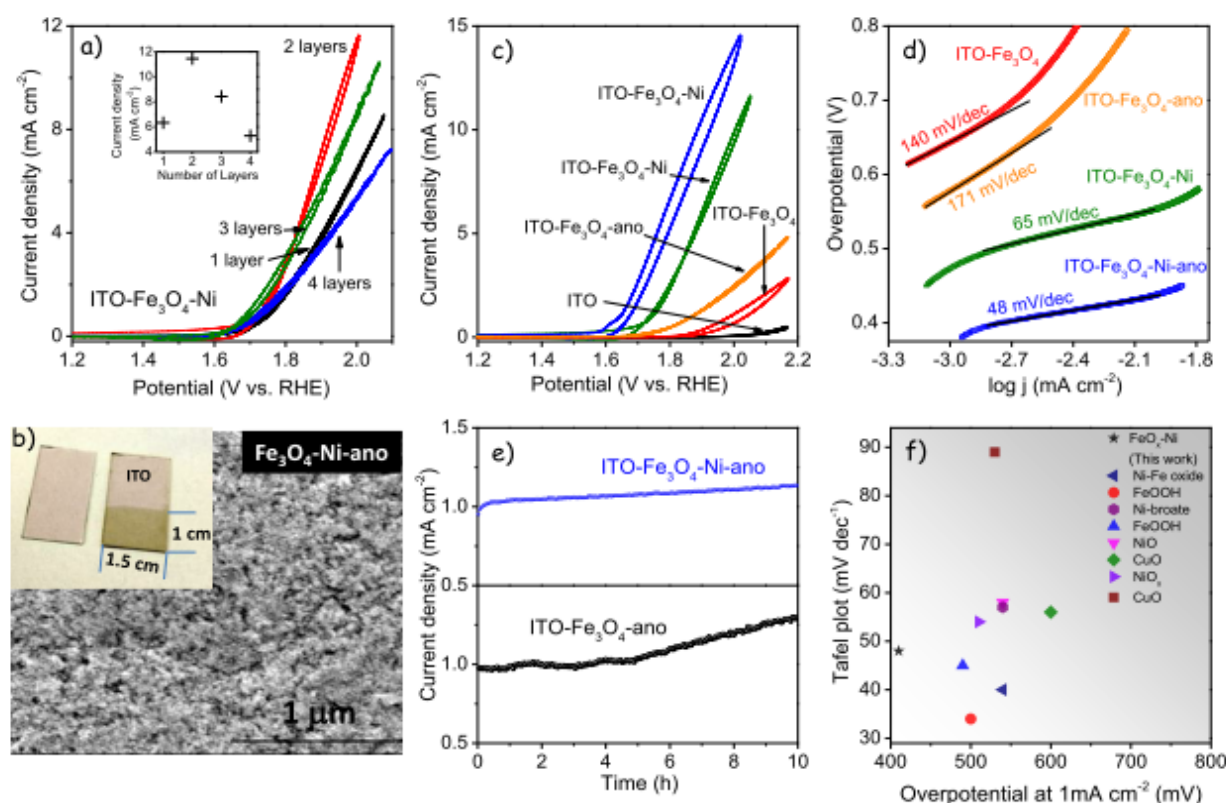


Figure 5. a) CV of ITO-Fe₃O₄-Ni catalysts with different film thicknesses; b) Photograph (inset) of ITO glass (left) and ITO-Fe₃O₄-Ni catalyst film after anodization (right) and SEM image of the ITO-Fe₃O₄-Ni catalysts after the anodization process; c) CV of ITO and the different catalysts; d) Corresponding Tafel plot of the different catalyst; e) Stability measurements of ITO-Fe₃O₄-ano and ITO-Fe₃O₄-Ni-ano catalyst films; f) Comparison of overpotential at 1 mA/cm² and Tafel slopes between transition metal-based OER catalysts reported at neutral or near neutral pH condition.^{19,21,59-64} Conditions: 0.2 M pH 9.75 carbonate buffer electrolyte, RE is Ag/AgCl, CE is Pt foil, scan rate 50 mV/s, electrode area 1.5 cm².

We used the ITO-Fe₃O₄-Ni anodized catalysts operated at 1.3V vs. RHE to measure the Faradaic efficiency for O₂ production. At this potential, the working electrode provided a current of 4.5 ±

0.1 mA (Figure S8), which corresponds to around $2.8 \pm 0.6 \times 10^{16}$ e/s and would translate to the production of $7.0 \pm 0.2 \times 10^{15}$ O₂/s. The gaseous reaction products were extracted using a 18 ± 1 ml/min Ar flow, which in the stationary state and considering a 100% O₂ production yield would translate into an oxygen concentration of a 0.095 ± 0.06 %. After calibrating our gas chromatograph to measure oxygen concentrations in this range, we measured an oxygen concentration on the effluent gas of 0.096 ± 0.008 % (Figure S8). Thus, a Faradaic efficiency of 101 ± 8 % was calculated.

The same strategies were applied to incorporate cobalt and manganese ions into Fe₃O₄ NPs using cobalt and manganese perchlorates as cation precursors, and catalysts were fabricated with the obtained NPs. In Figure 6, the electrocatalytic properties of the obtained compounds are plotted. The ITO-Fe₃O₄-Co catalyst film exhibited higher OER activity than ITO-Fe₃O₄ catalyst, with an overpotential $\eta=620$ mV at $1 \text{ mA}\cdot\text{cm}^{-2}$, and a corresponding Tafel slope of 158 mV/dec. However, the ITO-Fe₃O₄-Mn catalyst film showed a lower OER activity compared with all other catalysts tested, indicating the incorporation of Mn to reduce the Fe₃O₄ performance toward water oxidation.

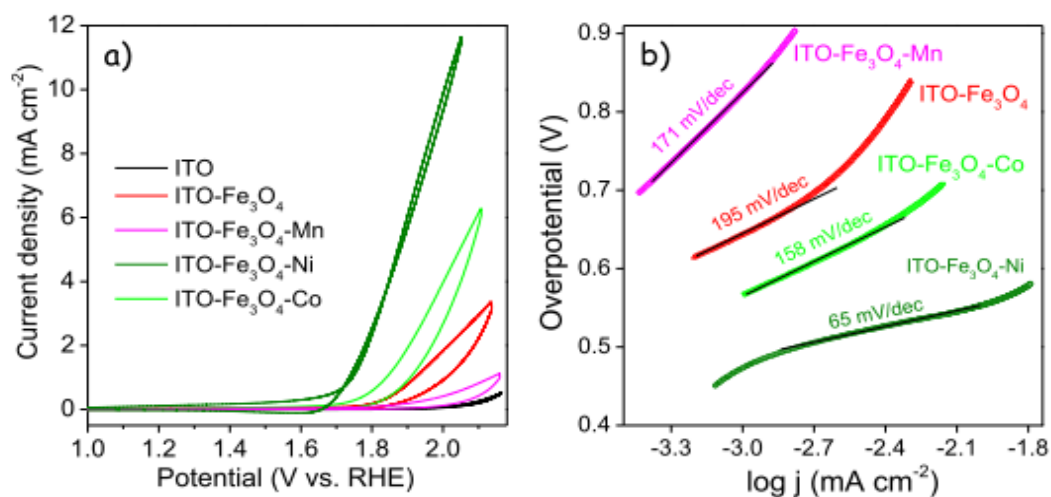


Figure 6. a) CV of ITO and different catalysts; b) Corresponding Tafel plot of the different catalyst. Conditions: 0.2 M pH 9.75 carbonate buffer electrolyte, RE is Ag/AgCl, CE is Pt foil, scan rate 50 mV/s, electrode area 1.5 cm².

Table 1. Comparisons of different earth-abundant transition metal water oxidation catalysts at pH 9-9.75.

Catalyst	Overpotential at 1mA cm ⁻² (mV)	Tafel Slope (mV dec ⁻¹)	pH	Reference
FeO _x -Ni	410	48	9.75	This work
FeOOH	500	34	9.75	19
Ni-Fe Oxide	540	40	9.2	21
Nickel-broate	540	57	9.2	59
FeOOH	490	45	9.2	60
NiO	540	58	9.2	61
CuO	600	56	9.2	62
NiO _x	510	54	9.2	63
CuO	530	89	9.0	64
IrO _x ·nH ₂ O	200 (1.5 mA cm ⁻²)	52	9.0	65

4. CONCLUSION

In summary, Fe₃O₄@NiFe_xO_y core-shell NPs were synthesized at low temperature and in air atmosphere by a two-step method involving Ni cation diffusion within the outer defective shell of Fe₃O₄ template NPs. Such core-shell NPs were deposited onto ITO glass by a spin-coating process to form thin catalyst films, which exhibited high electrocatalytic activity for OER in carbonate electrolyte. In particular, the as-anodized core-shell catalyst film showed low overpotential of 410 mV at 1 mA/cm² and Tafel slope of 48 mV/dec. This core-shell NP

synthetic protocol can be expanded as a general strategy to grow metal oxide heterostructures for OER or for other applications. Furthermore, the magnetic properties of the NPs could be improved during the shell growth process, providing potentially useful materials for environmental remediation, purification, and biomedical applications, among others.

ASSOCIATED CONTENT

Supporting Information. Additional experimental details and structural, chemical and functional characterization results. This material is available free of charge via the Internet at <http://pubs.acs.org>.

AUTHOR INFORMATION

Corresponding Author

* acabot@irec.cat.

Notes

The authors declare no competing financial interests..

ACKNOWLEDGMENT

This work was supported by the European Regional Development Funds and the Spanish MINECO project BOOSTER, TNT-FUELS, e-TNT, Severo Ochoa Excellence Program and PEC-CO2. ZL thanks the China Scholarship Council for scholarship support. PG acknowledges the People Programme (Marie Curie Actions) of the FP7/2007-2013 European Union Program (TECNIOspring grant agreement no. 600388) and the Agency for Business Competitiveness of the Government of Catalonia, ACCIÓ. MI thanks AGAUR for Beatriu de Pinós postdoctoral

grant (2013 BP-A00344). JL is Serra Hünter Fellow and is grateful to ICREA Academia program. SMS acknowledges funding from "Programa Internacional de Becas "la Caixa"-Severo Ochoa" Authors also acknowledge the funding from Generalitat de Catalunya 2014 SGR 1638.

REFERENCES

1. Jiao, Y.; Zheng, Y.; Jaroniec, M.; Qiao, S. Z., Design of Electrocatalysts for Oxygen- and Hydrogen-involving Energy Conversion Reactions. *Chem. Soc. Rev.* **2015**, *44*, 2060-2086.
2. Chen, D.; Chen, C.; Baiyee, Z. M.; Shao, Z.; Ciucci, F., Nonstoichiometric Oxides as Low-Cost and Highly-Efficient Oxygen Reduction/Evolution Catalysts for Low-Temperature Electrochemical Devices. *Chem. Rev.* **2015**, *115*, 9869-9921.
3. Neburchilov, V.; Wang, H.; Martin, J. J.; Qu, W., A Review on Air Cathodes for Zinc-air Fuel Cells. *J. Power Sources* **2010**, *195*, 1271-1291.
4. Trasatti, S., Electrocatalysis by Oxides-Attempt at A Unifying Approach. *J. Electroanal. Chem. Interfacial Electrochem.* **1980**, *111*, 125-131.
5. Reier, T.; Oezaslan, M.; Strasser, P., Electrocatalytic Oxygen Evolution Reaction (OER) on Ru, Ir, and Pt Catalysts: A Comparative Study of Nanoparticles and Bulk Materials. *ACS Catal.* **2012**, *2*, 1765-1772.
6. McCrory, C. C. L.; Jung, S.; Peters, J. C.; Jaramillo, T. F., Benchmarking Heterogeneous Electrocatalysts for the Oxygen Evolution Reaction. *J. Am. Chem. Soc.* **2013**, *135*, 16977-16987.
7. Burke, M. S.; Enman, L. J.; Batchellor, A. S.; Zou, S.; Boettcher, S. W., Oxygen Evolution Reaction Electrocatalysis on Transition Metal Oxides and (Oxy)hydroxides: Activity Trends and Design Principles. *Chem. Mater.* **2015**, *27*, 7549-7558.

8. Trotochaud, L.; Ranney, J. K.; Williams, K. N.; Boettcher, S. W., Solution-Cast Metal Oxide Thin Film Electrocatalysts for Oxygen Evolution. *J. Am. Chem. Soc.* **2012**, *134*, 17253-17261.
9. Smith, R. D. L.; Prévot, M. S.; Fagan, R. D.; Zhang, Z.; Sedach, P. A.; Siu, M. K. J.; Trudel, S.; Berlinguette, C. P., Photochemical Route for Accessing Amorphous Metal Oxide Materials for Water Oxidation Catalysis. *Science* **2013**, *340*, 60-63.
10. Bockris, J. O.; Otagawa, T., Mechanism of Oxygen Evolution on Perovskites. *J. Phys. Chem.* **1983**, *87*, 2960-2971.
11. Friebel, D.; Louie, M. W.; Bajdich, M.; Sanwald, K. E.; Cai, Y.; Wise, A. M.; Cheng, M.-J.; Sokaras, D.; Weng, T.-C.; Alonso-Mori, R.; Davis, R. C.; Bargar, J. R.; Nørskov, J. K.; Nilsson, A.; Bell, A. T., Identification of Highly Active Fe Sites in (Ni,Fe)OOH for Electrocatalytic Water Splitting. *J. Am. Chem. Soc.* **2015**, *137*, 1305-1313.
12. Gong, M.; Zhou, W.; Tsai, M.-C.; Zhou, J.; Guan, M.; Lin, M.-C.; Zhang, B.; Hu, Y.; Wang, D.-Y.; Yang, J.; Pennycook, S. J.; Hwang, B.-J.; Dai, H., Nanoscale nickel oxide/nickel heterostructures for active hydrogen evolution electrocatalysis. *Nat. Commun.* **2014**, *5*, 4695.
13. Cheng, Y.; Jiang, S. P., Advances in electrocatalysts for oxygen evolution reaction of water electrolysis-from metal oxides to carbon nanotubes. *Pro.Nat. Sci. Mater. Int.* **2015**, *25*, 545-553.
14. Galán-Mascarós, J. R., Water Oxidation at Electrodes Modified with Earth-Abundant Transition-Metal Catalysts. *ChemElectroChem* **2015**, *2*, 37-50.
15. Smith, R. D. L.; Prévot, M. S.; Fagan, R. D.; Trudel, S.; Berlinguette, C. P., Water Oxidation Catalysis: Electrocatalytic Response to Metal Stoichiometry in Amorphous Metal Oxide Films Containing Iron, Cobalt, and Nickel. *J. Am. Chem. Soc.* **2013**, *135*, 11580-11586.

16. Menezes, P. W.; Indra, A.; Levy, O.; Kailasam, K.; Gutkin, V.; Pfrommer, J.; Driess, M., Using nickel manganese oxide catalysts for efficient water oxidation. *Chem. Commun.* **2015**, *51*, 5005-5008.
17. Roger, I.; Symes, M. D., First Row Transition Metal Catalysts for Solar-driven Water Oxidation Produced by Electrodeposition. *J. Mater. Chem. A* **2016**, *4*, 6724-6741.
18. Fabbri, E.; Haberer, A.; Waltar, K.; Kötz, R.; Schmidt, T., Developments and Perspectives of Oxide-based Catalysts for The Oxygen Evolution Reaction. *Catalysis Science & Technology* **2014**, *4*, 3800-3821.
19. Li, F.; Bai, L.; Li, H.; Wang, Y.; Yu, F.; Sun, L., An Iron-based Thin Film as A Highly Efficient Catalyst for Electrochemical Water Oxidation in A Carbonate Electrolyte. *Chem. Commun.* **2016**, *52*, 5753-5756.
20. Trotochaud, L.; Young, S. L.; Ranney, J. K.; Boettcher, S. W., Nickel–Iron Oxyhydroxide Oxygen-Evolution Electrocatalysts: The Role of Intentional and Incidental Iron Incorporation. *J. Am. Chem. Soc.* **2014**, *136*, 6744-6753.
21. Louie, M. W.; Bell, A. T., An Investigation of Thin-Film Ni–Fe Oxide Catalysts for the Electrochemical Evolution of Oxygen. *J. Am. Chem. Soc.* **2013**, *135*, 12329-12337.
22. Chen, J. Y. C.; Dang, L.; Liang, H.; Bi, W.; Gerken, J. B.; Jin, S.; Alp, E. E.; Stahl, S. S., Operando Analysis of NiFe and Fe Oxyhydroxide Electrocatalysts for Water Oxidation: Detection of Fe⁴⁺ by Mössbauer Spectroscopy. *J. Am. Chem. Soc.* **2015**, *137*, 15090-15093.
23. Trzeźniewski, B. J.; Diaz-Morales, O.; Vermaas, D. A.; Longo, A.; Bras, W.; Koper, M. T. M.; Smith, W. A., In Situ Observation of Active Oxygen Species in Fe-Containing Ni-Based Oxygen Evolution Catalysts: The Effect of pH on Electrochemical Activity. *J. Am. Chem. Soc.* **2015**, *137*, 15112-15121.

24. Lu, X.; Zhao, C., Electrodeposition of hierarchically structured three-dimensional nickel–iron electrodes for efficient oxygen evolution at high current densities. *Nat. Commun.* **2015**, *6*, 6616.
25. Hoang, T. T. H.; Gewirth, A. A., High Activity Oxygen Evolution Reaction Catalysts from Additive-Controlled Electrodeposited Ni and NiFe Films. *ACS Catal.* **2016**, *6*, 1159-1164.
26. Chen, H.; Huang, X.; Zhou, L.-J.; Li, G.-D.; Fan, M.; Zou, X., Electrospinning Synthesis of Bimetallic Nickel–Iron Oxide/Carbon Composite Nanofibers for Efficient Water Oxidation Electrocatalysis. *ChemCatChem* **2016**, *8*, 992-1000.
27. Görlin, M.; Chernev, P.; Ferreira de Araújo, J.; Reier, T.; Dresch, S.; Paul, B.; Krähnert, R.; Dau, H.; Strasser, P., Oxygen Evolution Reaction Dynamics, Faradaic Charge Efficiency, and the Active Metal Redox States of Ni–Fe Oxide Water Splitting Electrocatalysts. *J. Am. Chem. Soc.* **2016**, *138*, 5603-5614.
28. Qi, J.; Zhang, W.; Xiang, R.; Liu, K.; Wang, H.-Y.; Chen, M.; Han, Y.; Cao, R., Porous Nickel–Iron Oxide as a Highly Efficient Electrocatalyst for Oxygen Evolution Reaction. *Adv. Sci.* **2015**, *2*, 1500199.
29. Ali-Löytty, H.; Louie, M. W.; Singh, M. R.; Li, L.; Sanchez Casalongue, H. G.; Ogasawara, H.; Crumlin, E. J.; Liu, Z.; Bell, A. T.; Nilsson, A.; Friebel, D., Ambient-Pressure XPS Study of a Ni–Fe Electrocatalyst for the Oxygen Evolution Reaction. *J. Phys. Chem. C* **2016**, *120*, 2247-2253.
30. Long, X.; Li, J.; Xiao, S.; Yan, K.; Wang, Z.; Chen, H.; Yang, S., A Strongly Coupled Graphene and FeNi Double Hydroxide Hybrid as an Excellent Electrocatalyst for the Oxygen Evolution Reaction. *Angew. Chem. Int. Ed.* **2014**, *53*, 7584-7588.

31. Zhang, W.; Qi, J.; Liu, K.; Cao, R., A Nickel-Based Integrated Electrode from an Autologous Growth Strategy for Highly Efficient Water Oxidation. *Adv. Energy Mater.* **2016**, *6*, 1502489.
32. Song, F.; Hu, X., Exfoliation of layered double hydroxides for enhanced oxygen evolution catalysis. *Nature Communications* **2014**, *5*, 4477.
33. Gong, M.; Li, Y.; Wang, H.; Liang, Y.; Wu, J. Z.; Zhou, J.; Wang, J.; Regier, T.; Wei, F.; Dai, H., An Advanced Ni–Fe Layered Double Hydroxide Electrocatalyst for Water Oxidation. *J. Am. Chem. Soc.* **2013**, *135*, 8452-8455.
34. Corrigan, D. A., The Catalysis of The Oxygen Evolution Reaction by Iron Impurities in Thin Film Nickel Oxide Electrodes. *J. Electrochem. Soc.* **1987**, *134*, 377-384.
35. Wu, Y.; Chen, M.; Han, Y.; Luo, H.; Su, X.; Zhang, M.-T.; Lin, X.; Sun, J.; Wang, L.; Deng, L.; Zhang, W.; Cao, R., Fast and Simple Preparation of Iron-Based Thin Films as Highly Efficient Water-Oxidation Catalysts in Neutral Aqueous Solution. *Angew. Chem. Int. Ed.* **2015**, *54*, 4870-4875.
36. Chen, M.; Wu, Y.; Han, Y.; Lin, X.; Sun, J.; Zhang, W.; Cao, R., An Iron-based Film for Highly Efficient Electrocatalytic Oxygen Evolution from Neutral Aqueous Solution. *ACS Appl. Mat. Interfaces* **2015**, *7*, 21852-21859.
37. Zaharieva, I.; Chernev, P.; Risch, M.; Klingan, K.; Kohlhoff, M.; Fischer, A.; Dau, H., Electrosynthesis, Functional, and Structural Characterization of A Water-oxidizing Manganese Oxide. *Energy Environ. Sci.* **2012**, *5*, 7081-7089.
38. Kanan, M. W.; Nocera, D. G., In Situ Formation of an Oxygen-Evolving Catalyst in Neutral Water Containing Phosphate and Co^{2+} . *Science* **2008**, *321*, 1072-1075.

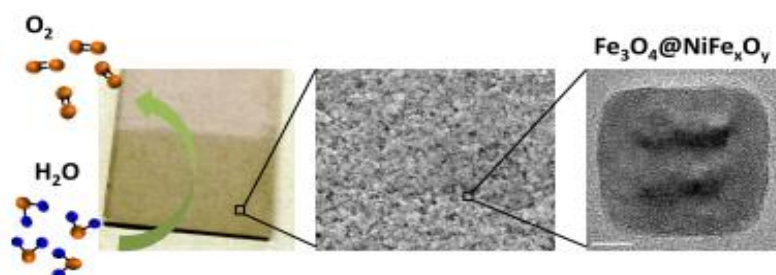
39. Paytan, A.; McLaughlin, K., The Oceanic Phosphorus Cycle. *Chem. Rev.* **2007**, *107*, 563-576.
40. Diaz, J.; Ingall, E.; Benitez-Nelson, C.; Paterson, D.; de Jonge, M. D.; McNulty, I.; Brandes, J. A., Marine Polyphosphate: A Key Player in Geologic Phosphorus Sequestration. *Science* **2008**, *320*, 652-655.
41. Kim, J. H.; Magesh, G.; Kang, H. J.; Banu, M.; Kim, J. H.; Lee, J.; Lee, J. S., Carbonate-coordinated Cobalt Co-catalyzed BiVO₄/WO₃ Composite Photoanode Tailored for CO₂ Reduction to Fuels. *Nano Energy* **2015**, *15*, 153-163.
42. Surendranath, Y.; Dincă, M.; Nocera, D. G., Electrolyte-Dependent Electrosynthesis and Activity of Cobalt-Based Water Oxidation Catalysts. *J. Am. Chem. Soc.* **2009**, *131*, 2615-2620.
43. Chen, Z.; Kang, P.; Zhang, M.-T.; Stoner, B. R.; Meyer, T. J., Cu(ii)/Cu(0) Electrocatalyzed CO₂ and H₂O Splitting. *Energy Environ. Sci.* **2013**, *6*, 813-817.
44. Joya, K. S.; Takanabe, K.; de Groot, H. J. M., Surface Generation of a Cobalt-Derived Water Oxidation Electrocatalyst Developed in a Neutral HCO₃⁻/CO₂ System. *Adv. Energy Mater.* **2014**, *4*, 1400252.
45. Herranz, T.; Ibáñez, M.; Gómez de la Fuente, J. L.; Pérez-Alonso, F. J.; Peña, M. A.; Cabot, A.; Rojas, S., In Situ Study of Ethanol Electrooxidation on Monodispersed Pt₃Sn Nanoparticles. *ChemElectroChem* **2014**, *1*, 885-895.
46. Perez-Alonso, F.; Adan, C.; Rojas, S.; Pena, M.; Fierro, J., Ni/Fe Electrodes Prepared by Electrodeposition Method over Different Substrates for Oxygen Evolution Reaction in Alkaline Medium. *Int. J. Hydrogen Energy* **2014**, *39*, 5204-5212.
47. Ibáñez, M.; Cabot, A., All Change for Nanocrystals. *Science* **2013**, *340*, 935-936.

48. Nafria, R.; Genç, A.; Ibáñez, M.; Arbiol, J.; Ramírez de la Piscina, P.; Homs, N.; Cabot, A., Co–Cu Nanoparticles: Synthesis by Galvanic Replacement and Phase Rearrangement during Catalytic Activation. *Langmuir* **2016**, *32*, 2267-2276.
49. Luo, Z.; Ibáñez, M.; Antolín, A. M.; Genç, A.; Shavel, A.; Contreras, S.; Medina, F.; Arbiol, J.; Cabot, A., Size and Aspect Ratio Control of Pd₂Sn Nanorods and Their Water Denitration Properties. *Langmuir* **2015**, *31*, 3952-3957.
50. Zamani, R. R.; Ibáñez, M.; Luysberg, M.; García-Castelló, N.; Houben, L.; Prades, J. D.; Grillo, V.; Dunin-Borkowski, R. E.; Morante, J. R.; Cabot, A.; Arbiol, J., Polarity-Driven Polytypic Branching in Cu-Based Quaternary Chalcogenide Nanostructures. *ACS Nano* **2014**, *8*, 2290-2301.
51. Ibáñez, M.; Luo, Z.; Genç, A.; Piveteau, L.; Ortega, S.; Cadavid, D.; Dobrozhan, O.; Liu, Y.; Nachttegaal, M.; Zebarjadi, M.; Arbiol, J.; Kovalenko, M. V.; Cabot, A., High-performance thermoelectric nanocomposites from nanocrystal building blocks. *Nat. Commun.* **2016**, *7*, 10766.
52. Luo, Z.; Irtem, E.; Ibáñez, M.; Nafria, R.; Marti, S.; Genç, A.; de la Mata, M.; Liu, Y.; Cadavid, D.; Llorca, J.; Arbiol, J.; Andreu, T.; Morante, J. R.; Cabot, A., Mn₃O₄@CoMn₂O₄-Co_xO_y Nanoparticles: Partial Cation Exchange Synthesis and Electrocatalytic Properties toward the Oxygen Reduction and Evolution Reactions. *ACS Appl. Mat. Interfaces* **2016**.
53. Yu, X.; Liu, J.; Genç, A.; Ibáñez, M.; Luo, Z.; Shavel, A.; Arbiol, J.; Zhang, G.; Zhang, Y.; Cabot, A., Cu₂ZnSnS₄-Ag₂S Nanoscale p–n Heterostructures as Sensitizers for Photoelectrochemical Water Splitting. *Langmuir* **2015**, *31*, 10555-10561.
54. Yu, X.; Shavel, A.; An, X.; Luo, Z.; Ibáñez, M.; Cabot, A., Cu₂ZnSnS₄-Pt and Cu₂ZnSnS₄-Au Heterostructured Nanoparticles for Photocatalytic Water Splitting and Pollutant Degradation. *J. Am. Chem. Soc.* **2014**, *136*, 9236-9239.

55. Yu, X.; An, X.; Genç, A.; Ibáñez, M.; Arbiol, J.; Zhang, Y.; Cabot, A., Cu₂ZnSnS₄-PtM (M = Co, Ni) Nanoheterostructures for Photocatalytic Hydrogen Evolution. *J. Phys. Chem. C* **2015**, *119*, 21882-21888.
56. Shavel, A.; Rodríguez-González, B.; Spasova, M.; Farle, M.; Liz-Marzán, L. M., Synthesis and Characterization of Iron/Iron Oxide Core/Shell Nanocubes. *Adv. Funct. Mater.* **2007**, *17*, 3870-3876.
57. Sharma, V. K.; Alipour, A.; Soran-Erdem, Z.; Aykut, Z. G.; Demir, H. V., Highly Monodisperse Low-magnetization Magnetite Nanocubes as Simultaneous T1-T2 MRI Contrast Agents. *Nanoscale* **2015**, *7*, 10519-10526.
58. Bediako, D. K.; Lassalle-Kaiser, B.; Surendranath, Y.; Yano, J.; Yachandra, V. K.; Nocera, D. G., Structure-Activity Correlations in a Nickel-Borate Oxygen Evolution Catalyst. *J. Am. Chem. Soc.* **2012**, *134*, 6801-6809.
59. Roger, I.; Symes, M. D., Efficient Electrocatalytic Water Oxidation at Neutral and High pH by Adventitious Nickel at Nanomolar Concentrations. *J. Am. Chem. Soc.* **2015**, *137*, 13980-13988.
60. Chowdhury, D. R.; Spiccia, L.; Amritphale, S. S.; Paul, A.; Singh, A., A Robust Iron Oxyhydroxide Water Oxidation Catalyst Operating under Near Neutral and Alkaline Conditions. *J. Mater. Chem. A* **2016**, *4*, 3655-3660.
61. Dincă, M.; Surendranath, Y.; Nocera, D. G., Nickel-borate Oxygen-evolving Catalyst That Functions under Benign Conditions. *PNAS* **2010**, *107*, 10337-10341.
62. Liu, X.; Jia, H.; Sun, Z.; Chen, H.; Xu, P.; Du, P., Nanostructured Copper Oxide Electrodeposited from Copper(II) Complexes as An Active Catalyst for Electrocatalytic Oxygen Evolution Reaction. *Electrochem. Commun.* **2014**, *46*, 1-4.

63. Singh, A.; Chang, S. L. Y.; Hocking, R. K.; Bach, U.; Spiccia, L., Highly Active Nickel Oxide Water Oxidation Catalysts Deposited from Molecular Complexes. *Energy Environ. Sci.* **2013**, *6*, 579-586.
64. Yu, F.; Li, F.; Zhang, B.; Li, H.; Sun, L., Efficient Electrocatalytic Water Oxidation by a Copper Oxide Thin Film in Borate Buffer. *ACS Catal.* **2015**, *5*, 627-630.
65. Zhao, Y.; Vargas-Barbosa, N. M.; Hernandez-Pagan, E. A.; Mallouk, T. E., Anodic Deposition of Colloidal Iridium Oxide Thin Films from Hexahydroxyiridate(IV) Solutions. *Small* **2011**, *7*, 2087-2093.

TOC



SUPPORTING INFORMATION

$\text{Fe}_3\text{O}_4@ \text{NiFe}_x\text{O}_y$ nanoparticles with enhanced electrocatalytic properties for oxygen evolution in carbonate electrolyte

Zhishan Luo,[†] Sara Martí,[¶] Raquel Nafria[†] Gihan Joshua,[†] Maria de la Mata,[¶] Pablo Guardia,^{†,1} Cristina Flox,[†] Carlos Martínez-Boubeta,[⊥] Konstantinos Simeonidis,[§] Jordi Llorca,[□] Joan Ramon Morante,[†] Jordi Arbiol,^{¶,¥} Maria Ibáñez,[†] Andreu Cabot^{†,,*}*

[†] Catalonia Institute for Energy Research - IREC, Sant Adrià de Besòs, Barcelona, 08930, Spain

[¶]Catalan Institute of Nanoscience and Nanotechnology (ICN2), CSIC and The Barcelona Institute of Science and Technology (BIST), Campus UAB, Bellaterra, 08193 Barcelona, Spain

^lCentro de Tecnologia Química de Catalunya and Universitat Rovira i Virgili, Carrer de Marcel·li Domingo s/n, 43007 Tarragona, Spain

[⊥]Freelancer in Santiago de Compostela, Spain

[§]Department of Physics, Aristotle University Thessaloniki, 54124 Thessaloniki, Greece

[□]Institut de Tècniques Energètiques, Universitat Politècnica de Catalunya, 08028 Barcelona, Spain

[¥]ICREA, Pg. Lluís Companys 23, 08010 Barcelona, Spain

* acabot@irec.cat

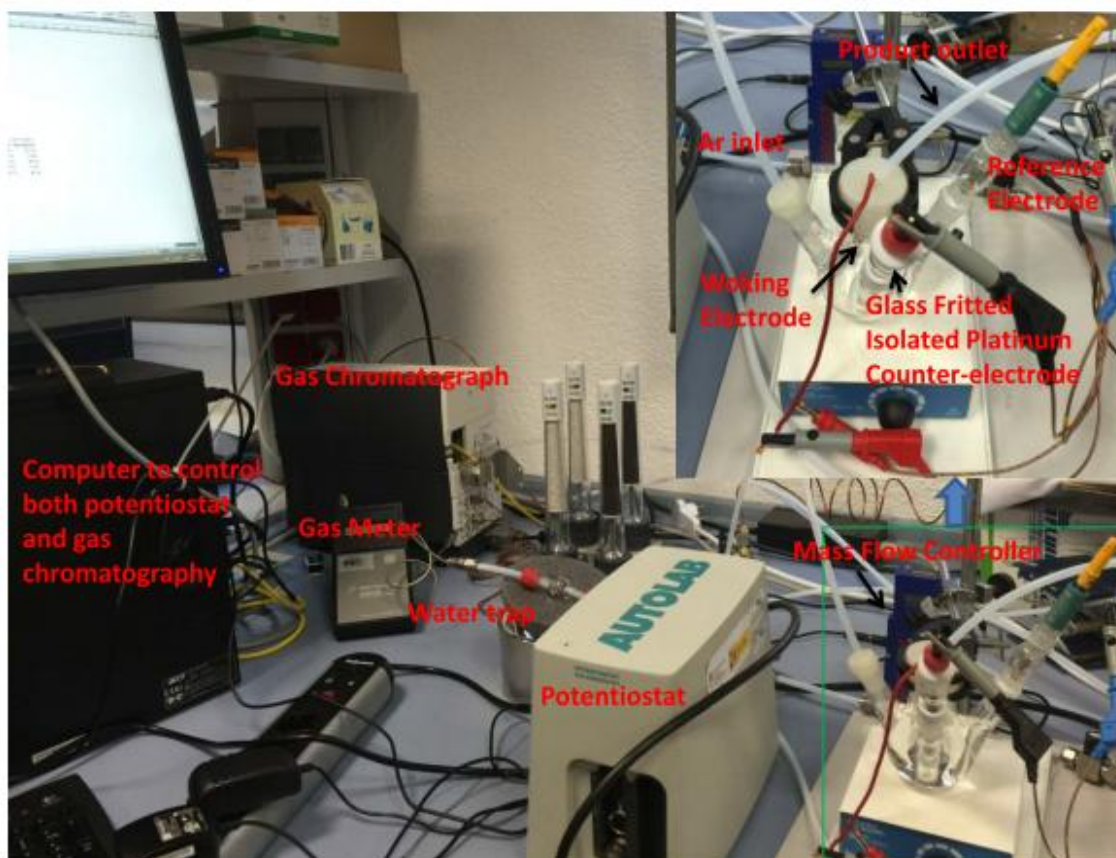


Figure S1. Experimental set-up used to measure the Faradaic efficiency of O_2 production.

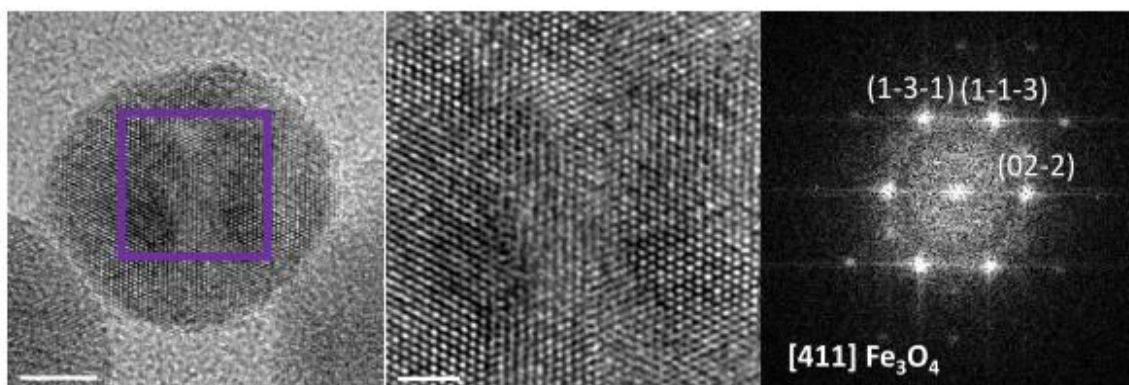


Figure S2. HRTEM micrograph of a Fe_3O_4 NP and its corresponding power spectrum.

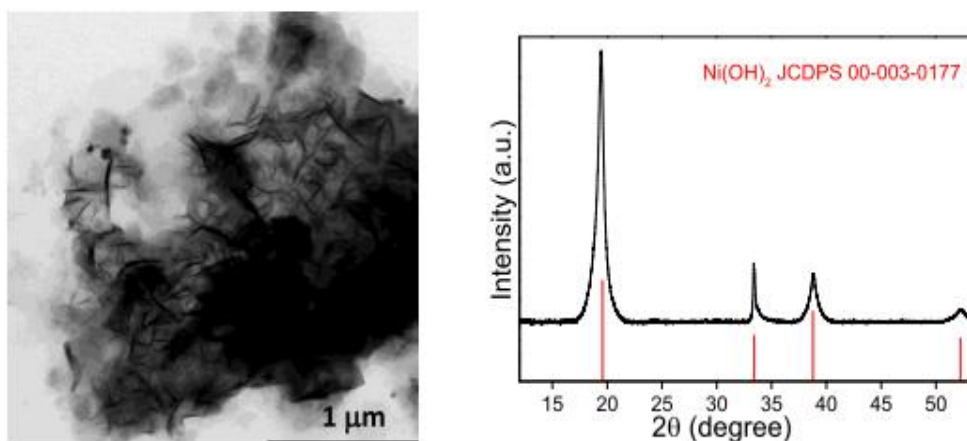


Figure S3. TEM micrograph and XRD pattern of the Ni(OH)₂ nanosheets obtained when reacting the nickel perchlorate precursor without the presence of Fe₃O₄ seeds.

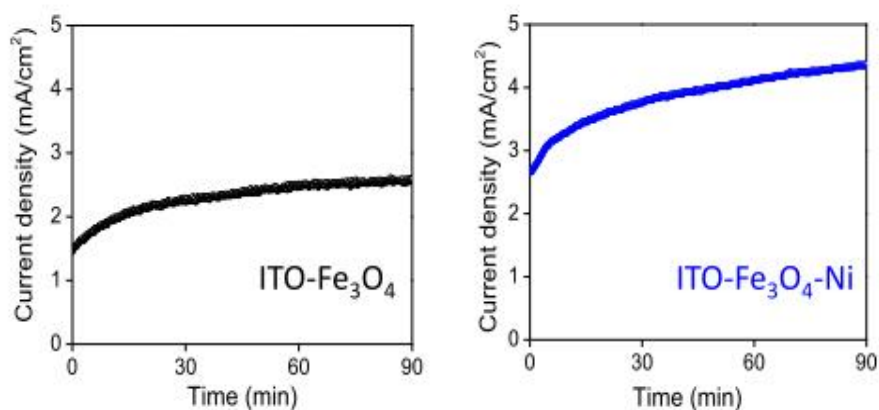


Figure S4. Chronoamperometric curves during anodization of ITO-Fe₃O₄ and ITO-Fe₃O₄-Ni catalysts.

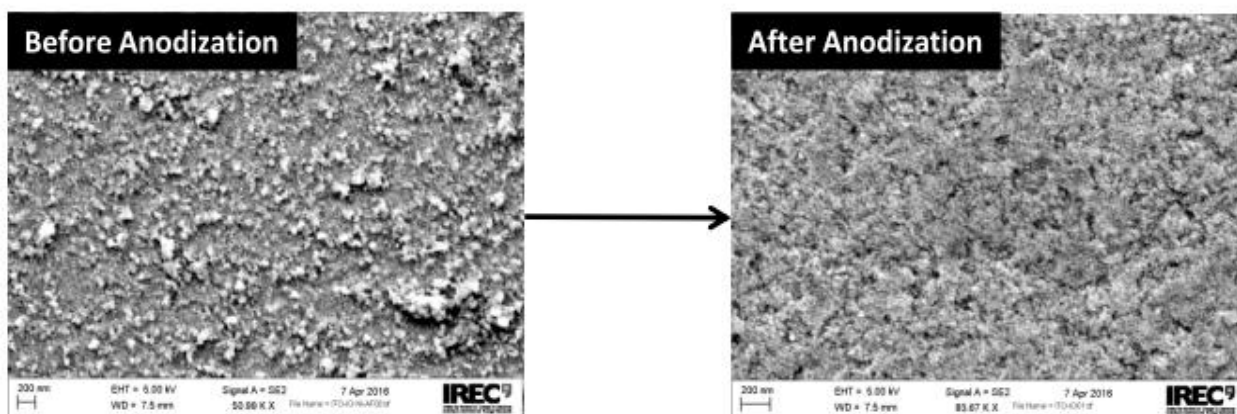


Figure S5. SEM images of the ITO-Fe₃O₄-Ni electrode before and after anodization

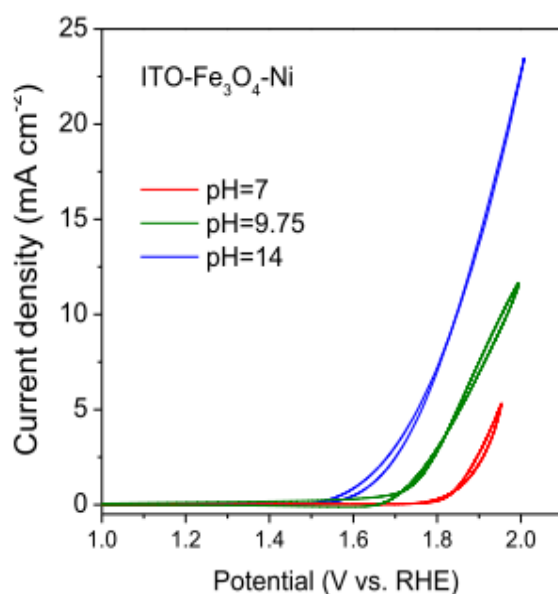


Figure S6. CV of ITO-Fe₃O₄-Ni at different pH

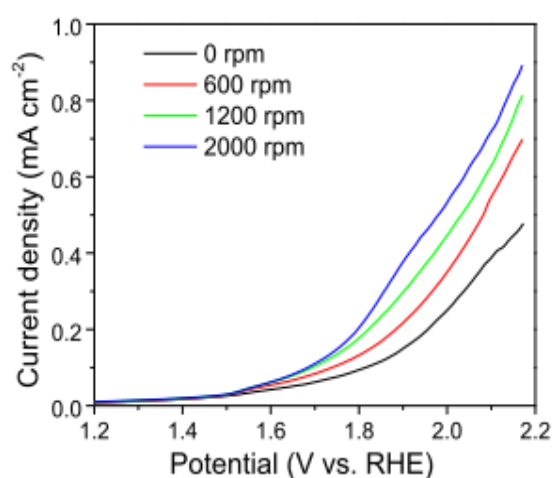


Figure S7. Linear sweep voltammograms of ITO-Fe₃O₄-Ni at different rotation rates.

CV data of most materials showed a hysteresis. While a small capacitance effect may be present, we hypothesize the irreversible effect to be attributed to the oxygen bubbles easily adhere to the electrode surface. When the bubble grows up to a critical value, it will move along the electrode surface and coalesce with other bubbles. Bubble coalescence easily gives rise to a layer of gas membrane in the vicinity of the electrode, which can increase ohmic resistance or/and decrease the active site available for EOR, producing an

“irreversible” effect. Depending on the quantity and size of oxygen bubbles and the capacity of coalescence, this effect could be increased. For this reason, several catalysts show different “irreversible” effect. Additionally, oxide structure before and during the EOR can suffer changes in oxidation state (i.e. between hydroxide and oxyhydroxide forms) and oxide forms associated with chemical “irreversibility” in electrode composition and roughness. This effect is largely reported in the literature.^{S1}

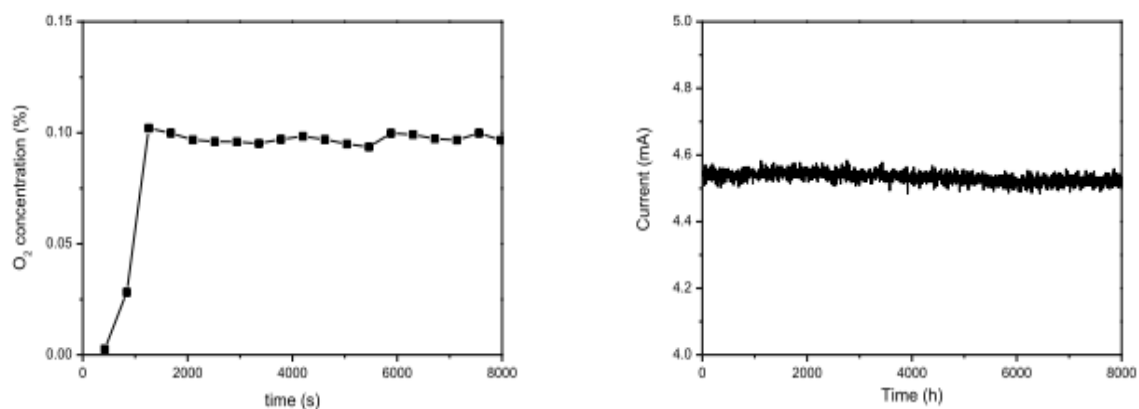


Figure S8. O₂ concentration measured at the gas chromatograph (left) and current measured at the ITO-Fe₃O₄-Ni working electrode (right)

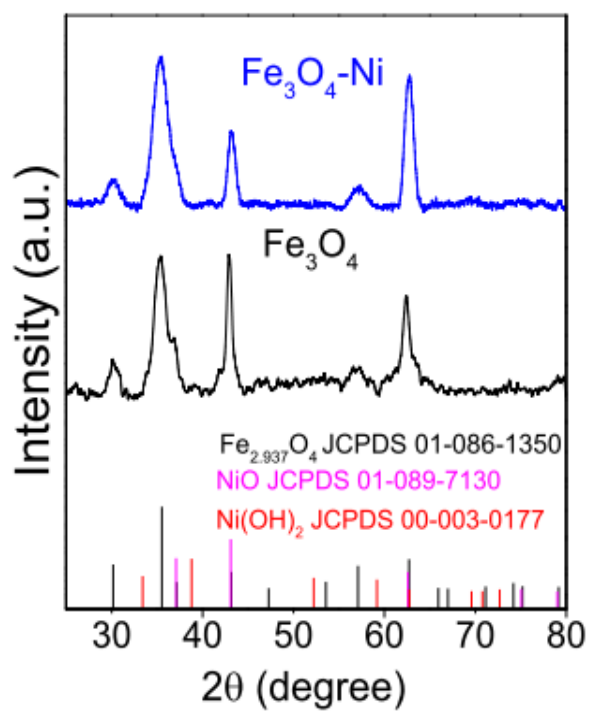


Figure S9. XRD patterns of Fe₃O₄ NPs and Fe₃O₄-Ni NPs including reference patterns for Fe₃O₄, NiO and Ni(OH)₂

Reference

- S1. Hoang, T. T. H.; Cohen, Y.; Gewirth, A. A., In Situ Electrochemical Stress Measurements Examining the Oxygen Evolution Reaction in Basic Electrolytes. *Anal. Chem.* **2014**, *86* (22), 11290-11297.

Chapter 5

Conclusions

The main objective of this thesis focuses on compositional design and engineering colloidal NPs and their application in energy conversion. This principally included the synthesis and characterization of colloidal NPs, and in-depth exploration of their catalytic properties. Special focus is the synthesis and characterization of copper-based chalcogenides, bimetallic and multicomponent metal oxide NPs. The results were shown in the series of articles which have been published or are under review in high impact peer-review journals.

These works can be extracted to conclusions as following:

(1) Copper-based chalcogenides NPs: Detailed synthetic routes to produce CZTS and CZTS-based HNPs i.e. CZTS-Au, CZTS-Pt and CZTS-Ag₂S. The composition, size and shape control of CZTS NCs have been achieved by tuning the precursor concentration, surfactants, gas bubbling and heating ramp. This synthetic strategy method can be easy to scale up to grams at the same time keeping above 90% yield per batch by a simple vacuum free heating-up method. We used CZTS NCs as electrocatalysts with controlled crystal phases for the ORR measurements. First-principles calculations and experiments both indicated the kesterite CZTS NCs exhibit improving electrocatalytic activities toward ORR. In addition, monodisperse CZTS-Au and CZTS-Pt HNPs were obtained based on CZTS as seeds by seed-mediated growth method. Various characterizations confirm the structure of noble-semiconductors HNPs. Such HNPs were investigated on photocatalytic degradation of dye and hydrogen evolution reaction in water, exhibited high catalytic activity. The research of CZTS-based HNPs is extended to a detailed synthesis of CZTS-Ag₂S HNPs involving cation exchange reaction. The structure and composition of CZTS-Ag₂S could be tuned by control the ratio of Ag precursors and CZTS seeds. When employing CZTS-Ag₂S as sensitizers apply photoelectrochemical cell for water splitting, showed improved photocurrent response under visible-light illumination.

(2) Bimetallic NPs: The synthesized Pd₂Sn NPs were successfully used solution-based strategy. A mechanism of morphology structure was discussed in detail based on different ratio of OLA, chlorine and TOP precursors. When evaluating catalytic properties of geometry of Pd₂Sn NPs, reduction of nitrophenol, water denitration and EOR were measured resulting in Pd₂Sn NRs had outperformance catalytic activity over Pd₂Sn spherical NPs, while Pd₂Sn alloy NPs exhibited better catalytic performance compared to Pd NPs. The formation of novel Au-Pd₂Sn heterostructured NRs was described in detail as well. Au-Pd₂Sn heterostructured NRs were synthesized via a seed-mediated growth method, which Au domains were selected to grow on the Pd₂Sn seeds. The result establishes a new strategy for the development of multifunctional nanomaterials.

(3) Multicomponent metal oxide NPs: Mn₃O₄@CoMn₂O₄ core-shell and Mn₃O₄@CoMn₂O₄-CoO HNPs were prepared via partial cation exchange reaction via Mn₃O₄ seeds NPs and different cobalt precursors, which playing a crucial role whether additional nucleation of a CoO phase depending on the coordination ability of cobalt precursors. The lower coordination ability of cobalt perchlorate had a higher reactivity to grow CoO phase on Mn₃O₄@CoMn₂O₄

to form $\text{Mn}_3\text{O}_4@\text{CoMn}_2\text{O}_4\text{-CoO}$ HNPs. In particular, such HNPs showed a superior catalytic activity and stability over the core shell catalysts and state-of-the-art electrocatalysts for ORR and OER in alkaline solution. Based on this colloidal synthetic route, $\text{Fe}_3\text{O}_4@\text{Ni}_x\text{Fe}_{3-x}\text{O}_4$ core shell NPs was obtained involving nickel perchlorate precursors to Fe_3O_4 seeds solution. The fabrication of this core shell NPs and ITO glass to form thin film as water oxidation catalyst exhibited an improved catalytic activity. This colloidal synthetic route offers an easy scale-up, low temperature and ambient pressure protocol to design earth-abundant, cost-effective and high activity water oxidation catalysts.

References

1. Kazdagli, M. B. K. a. H., The Development of Energy Markets in Europe. In *The Development of Energy Markets in Europe*, 2011.
2. Xia, Y.; Xiong, Y.; Lim, B.; Skrabalak, S. E. *Angew. Chem. Int. Ed.* **2009**, *48*, (1), 60-103.
3. Tao, A. R.; Habas, S.; Yang, P. *Small* **2008**, *4*, (3), 310-325.
4. Sau, T. K.; Rogach, A. L. *Adv. Mater.* **2010**, *22*, (16), 1781-804.
5. Herves, P.; Perez-Lorenzo, M.; Liz-Marzan, L. M.; Dzubielia, J.; Lu, Y.; Ballauff, M. *Chem. Soc. Rev.* **2012**, *41*, (17), 5577-87.
6. Huang, B.; Cao, M.-h.; Nie, F.-d.; Huang, H.; Hu, C.-w. *Def. Technol.* **2013**, *9*, (2), 59-79.
7. Papp, S.; Kőrösi, L.; Patakfalvi, R.; Dékány, I., Some Colloidal Routes to Synthesize Metal Nanoparticle-Based Catalysts. In *Catalysis for Alternative Energy Generation*, Guzzi, L.; Erdőhelyi, A., Eds. Springer New York: New York, NY, 2012; pp 413-457.
8. Alivisatos, A. P. *Science* **1996**, *271*, (5251), 933-937.
9. Kovalenko, M. V.; Manna, L.; Cabot, A.; Hens, Z.; Talapin, D. V.; Kagan, C. R.; Klimov, V. I.; Rogach, A. L.; Reiss, P.; Milliron, D. J.; Guyot-Sionnest, P.; Konstantatos, G.; Parak, W. J.; Hyeon, T.; Korgel, B. A.; Murray, C. B.; Heiss, W. *ACS Nano* **2015**, *9*, (2), 1012-1057.
10. Jun, Y. W.; Choi, J. S.; Cheon, J. *Angew. Chem. Int. Ed.* **2006**, *45*, (21), 3414-39.
11. Helms, B. A.; Williams, T. E.; Buonsanti, R.; Milliron, D. J. *Adv. Mater.* **2015**, *27*, (38), 5820-5829.
12. Williamson, C. B.; Nevers, D. R.; Hanrath, T.; Robinson, R. D. *J. Am. Chem. Soc.* **2015**, *137*, (50), 15843-15851.
13. Ibáñez, M.; Cabot, A. *Science* **2013**, *340*, (6135), 935-936.
14. Anderson, B. D.; Tracy, J. B. *Nanoscale* **2014**, *6*, (21), 12195-216.
15. Murphy, C. J.; Buriak, J. M. *Chem. Mater.* **2015**, *27*, (14), 4911-4913.
16. Buck, M. R.; Schaak, R. E. *Angew. Chem. Int. Ed.* **2013**, *52*, (24), 6154-78.
17. Mer, V. K. L. *Industrial & Engineering Chemistry* **1952**, *44*, (6), 1270-1277.
18. Polte, J. *CrystEngComm* **2015**, *17*, (36), 6809-6830.

19. Vreeland, E. C.; Watt, J.; Schober, G. B.; Hance, B. G.; Austin, M. J.; Price, A. D.; Fellows, B. D.; Monson, T. C.; Hudak, N. S.; Maldonado-Camargo, L.; Bohorquez, A. C.; Rinaldi, C.; Huber, D. L. *Chem. Mater.* **2015**, *27*, (17), 6059-6066.
20. Thanh, N. T. K.; Maclean, N.; Mahiddine, S. *Chem. Rev.* **2014**, *114*, (15), 7610-7630.
21. Sugimoto, T. *Adv. Colloid Interface Sci.* **1987**, *28*, 65-108.
22. Vivekchand, S. R. C.; Govindaraj, A.; Rao, C. N. R., Nanotubes and Nanowires: Recent Developments. In *Nanomaterials Chemistry*, Wiley-VCH Verlag GmbH & Co. KGaA: 2007; pp 45-118.
23. Talapin, D. V.; Rogach, A. L.; Haase, M.; Weller, H. *J. Phys. Chem. B* **2001**, *105*, (49), 12278-12285.
24. Rao, C. N. R.; Ramakrishna Matte, H. S. S.; Voggu, R.; Govindaraj, A. *Dalton Trans.* **2012**, *41*, (17), 5089-5120.
25. Kwon, S. G.; Hyeon, T. *Acc. Chem. Res.* **2008**, *41*, (12), 1696-1709.
26. Murray, C. B.; Sun, S.; Gaschler, W.; Doyle, H.; Betley, T. A.; Kagan, C. R. *IBM J. Res. Dev.* **2001**, *45*, (1), 47-56.
27. Amiens, C.; Ciuculescu-Pradines, D.; Philippot, K. *Coord. Chem. Rev.* **2016**, *308*, Part 2, 409-432.
28. Hu, X.; Li, G.; Yu, J. C. *Langmuir* **2010**, *26*, (5), 3031-3039.
29. Kawahara, Y.; Petrykin, V.; Ichihara, T.; Kijima, N.; Kakihana, M. *Chem. Mater.* **2006**, *18*, (26), 6303-6307.
30. Nazari, M.; Ghasemi, N.; Maddah, H.; Motlagh, M. M. *J. Nanostructure Chem.* **2014**, *4*, (2), 1-5.
31. Li, J.; Wu, Q.; Wu, J., Synthesis of Nanoparticles via Solvothermal and Hydrothermal Methods. In *Handbook of Nanoparticles*, Aliofkhaezrai, M., Ed. Springer International Publishing: Cham, 2016; pp 295-328.
32. Devaraju, M. K.; Honma, I. *Adv. Energy Mater.* **2012**, *2*, (3), 284-297.
33. Wang, X.; Zhuang, J.; Peng, Q.; Li, Y. *Inorg. Chem.* **2006**, *45*, (17), 6661-6665.
34. Wang, X.; Li, Y. *Chem. Commun.* **2007**, (28), 2901-2910.
35. Wang, X.; Zhuang, J.; Peng, Q.; Li, Y. *Nature* **2005**, *437*, (7055), 121-124.
36. Kwon, S. G.; Hyeon, T. *Small* **2011**, *7*, (19), 2685-702.
37. Sun, S.; Murray, C. B.; Weller, D.; Folks, L.; Moser, A. *Science* **2000**, *287*, (5460), 1989-1992.

38. Nguyen, T.-D. *Nanoscale* **2013**, 5, (20), 9455-9482.
39. Zhang, W.; Zhang, H.; Feng, Y.; Zhong, X. *ACS Nano* **2012**, 6, (12), 11066-11073.
40. Park, J.; An, K.; Hwang, Y.; Park, J.-G.; Noh, H.-J.; Kim, J.-Y.; Park, J.-H.; Hwang, N.-M.; Hyeon, T. *Nat. Mater.* **2004**, 3, (12), 891-895.
41. Noruzi, M.; Zare, D.; Davoodi, D. *Spectrochim. Acta, Part A* **2012**, 94, 84-88.
42. Świądrych, A.; Lorenc-Kukuła, K.; Skiryicz, A.; Szopa, J. *Plant Physiol. Biochem.* **2004**, 42, (7-8), 593-600.
43. Nagajyothi, P. C.; Minh An, T. N.; Sreekanth, T. V. M.; Lee, J.-i.; Joo Lee, D.; Lee, K. D. *Mater. Lett.* **2013**, 108, 160-163.
44. Niederberger, M. *Acc. Chem. Res.* **2007**, 40, (9), 793-800.
45. Kahoul, A.; Nkeng, P.; Hammouche, A.; Naamoune, F.; Poillerat, G. *J. Solid State Chem.* **2001**, 161, (2), 379-384.
46. Hosgor, Z.; Kayaman-Apohan, N.; Karatas, S.; Gungor, A.; Menciloglu, Y. *Adv. Polym. Tech.* **2012**, 31, (4), 390-400.
47. Wang, H.-Q.; Nann, T. *ACS Nano* **2009**, 3, (11), 3804-3808.
48. Baghbanzadeh, M.; Carbone, L.; Cozzoli, P. D.; Kappe, C. O. *Angew. Chem. Int. Ed.* **2011**, 50, (48), 11312-11359.
49. Zhu, Y.-J.; Chen, F. *Chem. Rev.* **2014**, 114, (12), 6462-6555.
50. He, Y.; Lu, H.-T.; Sai, L.-M.; Su, Y.-Y.; Hu, M.; Fan, C.-H.; Huang, W.; Wang, L.-H. *Adv. Mater.* **2008**, 20, (18), 3416-3421.
51. Liu, X.; Ma, R.; Bando, Y.; Sasaki, T. *Angew. Chem. Int. Ed.* **2010**, 49, (44), 8253-8256.
52. Tian, N.; Zhou, Z.-Y.; Yu, N.-F.; Wang, L.-Y.; Sun, S.-G. *J. Am. Chem. Soc.* **2010**, 132, (22), 7580-7581.
53. Zhang, Y.; Feng, H.; Wu, X.; Wang, L.; Zhang, A.; Xia, T.; Dong, H.; Li, X.; Zhang, L. *Int. J. Hydrogen Energy* **2009**, 34, (11), 4889-4899.
54. Lee, W.; Scholz, R.; Nielsch, K.; Gösele, U. *Angew. Chem. Int. Ed.* **2005**, 117, (37), 6204-6208.
55. Tian, N.; Zhou, Z.-Y.; Sun, S.-G.; Ding, Y.; Wang, Z. L. *Science* **2007**, 316, (5825), 732-735.

56. Fan, F.-J.; Wu, L.; Yu, S.-H. *Energy Environ. Sci.* **2014**, *7*, (1), 190-208.
57. Wang, C.; Chen, S.; Yang, J.-H.; Lang, L.; Xiang, H.-J.; Gong, X.-G.; Walsh, A.; Wei, S.-H. *Chem. Mater.* **2014**, *26*, (11), 3411-3417.
58. Regulacio, M. D.; Han, M.-Y. *Acc. Chem. Res.* **2016**, *49*, (3), 511-519.
59. van der Stam, W.; Berends, A. C.; de Mello Donega, C. *ChemPhysChem* **2016**, *17*, (5), 559-581.
60. Singh, S.; Ryan, K. M. *J. Phys. Chem. Lett.* **2015**, *6*, (16), 3141-3148.
61. Jackson, P.; Hariskos, D.; Lotter, E.; Paetel, S.; Wuerz, R.; Menner, R.; Wischmann, W.; Powalla, M. *Prog. Photovoltaics Res. Appl.* **2011**, *19*, (7), 894-897.
62. Li, W.; Ibáñez, M.; Cadavid, D.; Zamani, R. R.; Rubio-Garcia, J.; Gorse, S.; Morante, J. R.; Arbiol, J.; Cabot, A. *J. Nanopart. Res.* **2014**, *16*, (3), 1-6.
63. Li, W.; Ibanez, M.; Zamani, R. R.; Garcia-Castello, N.; Gorse, S.; Cadavid, D.; Prades, J. D.; Arbiol, J.; Cabot, A. *CrystEngComm* **2013**, *15*, (44), 8966-8971.
64. Shavel, A.; Arbiol, J.; Cabot, A. *J. Am. Chem. Soc.* **2010**, *132*, (13), 4514-4515.
65. Carrete, A.; Shavel, A.; Fontane, X.; Montserrat, J.; Fan, J.; Ibanez, M.; Saucedo, E.; Perez-Rodriguez, A.; Cabot, A. *J. Am. Chem. Soc.* **2013**, *135*, (43), 15982-5.
66. Ibanez, M.; Zamani, R.; LaLonde, A.; Cadavid, D.; Li, W.; Shavel, A.; Arbiol, J.; Morante, J. R.; Gorse, S.; Snyder, G. J.; Cabot, A. *J. Am. Chem. Soc.* **2012**, *134*, (9), 4060-3.
67. Ibáñez, M.; Cadavid, D.; Zamani, R.; García-Castelló, N.; Izquierdo-Roca, V.; Li, W.; Fairbrother, A.; Prades, J. D.; Shavel, A.; Arbiol, J.; Pérez-Rodríguez, A.; Morante, J. R.; Cabot, A. *Chem. Mater.* **2012**, *24*, (3), 562-570.
68. Ibáñez, M.; Zamani, R.; Li, W.; Cadavid, D.; Gorse, S.; Katcho, N. A.; Shavel, A.; López, A. M.; Morante, J. R.; Arbiol, J.; Cabot, A. *Chem. Mater.* **2012**, *24*, (23), 4615-4622.
69. Ibáñez, M.; Zamani, R.; Li, W.; Shavel, A.; Arbiol, J.; Morante, J. R.; Cabot, A. *Cryst. Growth Des.* **2012**, *12*, (3), 1085-1090.
70. Yu, X.; An, X.; Shavel, A.; Ibáñez, M.; Cabot, A. *J. Mater. Chem. A* **2014**, *2*, (31), 12317.
71. Ibáñez, M.; Cadavid, D.; Anselmi-Tamburini, U.; Zamani, R.; Gorse, S.; Li, W.; López, A. M.; Morante, J. R.; Arbiol, J.; Cabot, A. *J. Mater. Chem. A* **2013**, *1*, (4), 1421-1426.

72. Zhou, H.; Hsu, W.-C.; Duan, H.-S.; Bob, B.; Yang, W.; Song, T.-B.; Hsu, C.-J.; Yang, Y. *Energy Environ. Sci.* **2013**, 6, (10), 2822.
73. Singh, A.; Geaney, H.; Laffir, F.; Ryan, K. M. *J. Am. Chem. Soc.* **2012**, 134, (6), 2910-2913.
74. Tan, J. M. R.; Lee, Y. H.; Pedireddy, S.; Baikie, T.; Ling, X. Y.; Wong, L. H. *J. Am. Chem. Soc.* **2014**, 136, (18), 6684-6692.
75. Coughlan, C.; Ryan, K. M. *CrystEngComm* **2015**, 17, (36), 6914-6922.
76. Shavel, A.; Cadavid, D.; Ibanez, M.; Carrete, A.; Cabot, A. *J. Am. Chem. Soc.* **2012**, 134, (3), 1438-41.
77. Casciato, M. J.; Levitin, G.; Hess, D. W.; Grover, M. A. *ChemSusChem* **2012**, 5, (7), 1186-1189.
78. Buck, M. R.; Bondi, J. F.; Schaak, R. E. *Nat. Chem.* **2012**, 4, (1), 37-44.
79. Jiang, R.; Li, B.; Fang, C.; Wang, J. *Adv. Mater.* **2014**, 26, (31), 5274-5309.
80. Carbone, L.; Cozzoli, P. D. *Nano Today* **2010**, 5, (5), 449-493.
81. Vaneski, A.; Susha, A. S.; Rodríguez-Fernández, J.; Berr, M.; Jäckel, F.; Feldmann, J.; Rogach, A. L. *Adv. Funct. Mater.* **2011**, 21, (9), 1547-1556.
82. Jie Zeng; Wang, X.; Hou, J. G., Colloidal Hybrid Nanocrystals: Synthesis, Properties, and Perspectives. In *Nanocrystal*, Masuda, Y., Ed. InTech: 2011; p 504.
83. Zhang, J.; Ji, M.; Liu, J.; Xu, M., Metal/Semiconductor Hybrid Nanocrystals and Synergistic Photocatalysis Applications. In *Nanocrystal*, InTech: 2016.
84. Chen, Y.; Zeng, D.; Cortie, M. B.; Dowd, A.; Guo, H.; Wang, J.; Peng, D.-L. *Small* **2015**, 11, (12), 1460-1469.
85. Dutta, A.; Dutta, S. K.; Mehetor, S. K.; Mondal, I.; Pal, U.; Pradhan, N. *Chem. Mater.* **2016**, 28, (6), 1872-1878.
86. Hernández-Pagán, E. A.; Leach, A. D. P.; Rhodes, J. M.; Sarkar, S.; Macdonald, J. E. *Chem. Mater.* **2015**, 27, (23), 7969-7976.
87. Meyns, M.; Willing, S.; Lehmann, H.; Klinke, C. *ACS Nano* **2015**, 9, (6), 6077-6087.
88. Dilsaver, P. S.; Reichert, M. D.; Hallmark, B. L.; Thompson, M. J.; Vela, J. J. *Phys. Chem. C* **2014**, 118, (36), 21226-21234.
89. Gu, H.; Yang, Z.; Gao, J.; Chang, C. K.; Xu, B. *J. Am. Chem. Soc.* **2005**, 127, (1), 34-35.

90. Ha, E.; Lee, L. Y. S.; Wang, J.; Li, F.; Wong, K.-Y.; Tsang, S. C. E. *Adv. Mater.* **2014**, *26*, (21), 3496-3500.
91. Patra, B. K.; Shit, A.; Guria, A. K.; Sarkar, S.; Prusty, G.; Pradhan, N. *Chem. Mater.* **2015**, *27*, (3), 650-657.
92. Yu, X.; Shavel, A.; An, X.; Luo, Z.; Ibáñez, M.; Cabot, A. *J. Am. Chem. Soc.* **2014**, *136*, (26), 9236-9239.
93. Yu, X.; An, X.; Genç, A.; Ibáñez, M.; Arbiol, J.; Zhang, Y.; Cabot, A. *J. Phys. Chem. C* **2015**, *119*, (38), 21882-21888.
94. Yu, X.; Liu, J.; Genç, A.; Ibáñez, M.; Luo, Z.; Shavel, A.; Arbiol, J.; Zhang, G.; Zhang, Y.; Cabot, A. *Langmuir* **2015**, *31*, (38), 10555-10561.
95. Nasrabadi, H. T.; Abbasi, E.; Davaran, S.; Kouhi, M.; Akbarzadeh, A. *Artificial Cells, Nanomedicine, and Biotechnology* **2016**, *44*, (1), 376-380.
96. Sankar, M.; Dimitratos, N.; Miedziak, P. J.; Wells, P. P.; Kiely, C. J.; Hutchings, G. J. *Chem. Soc. Rev.* **2012**, *41*, (24), 8099-8139.
97. Wei, Z.; Sun, J.; Li, Y.; Datye, A. K.; Wang, Y. *Chem. Soc. Rev.* **2012**, *41*, (24), 7994-8008.
98. Singh, A. K.; Xu, Q. *ChemCatChem* **2013**, *5*, (3), 652-676.
99. Peng, X.; Pan, Q.; Rempel, G. L. *Chem. Soc. Rev.* **2008**, *37*, (8), 1619-1628.
100. Toshima, N.; Yonezawa, T. *New J. Chem.* **1998**, *22*, (11), 1179-1201.
101. Gu, J.; Zhang, Y.-W.; Tao, F. *Chem. Soc. Rev.* **2012**, *41*, (24), 8050-8065.
102. Nafria, R.; Genç, A.; Ibáñez, M.; Arbiol, J.; Ramírez de la Piscina, P.; Homs, N.; Cabot, A. *Langmuir* **2016**, *32*, (9), 2267-2276.
103. Hong, J. W.; Kim, D.; Lee, Y. W.; Kim, M.; Kang, S. W.; Han, S. W. *Angew. Chem. Int. Ed.* **2011**, *50*, (38), 8876-8880.
104. Habas, S. E.; Lee, H.; Radmilovic, V.; Somorjai, G. A.; Yang, P. *Nat. Mater.* **2007**, *6*, (9), 692-697.
105. Yin, A.-X.; Min, X.-Q.; Zhu, W.; Wu, H.-S.; Zhang, Y.-W.; Yan, C.-H. *Chem. Commun.* **2012**, *48*, (4), 543-545.
106. Zhang, J.; Yang, H.; Fang, J.; Zou, S. *Nano Lett.* **2010**, *10*, (2), 638-644.
107. Jin, M.; Zhang, H.; Wang, J.; Zhong, X.; Lu, N.; Li, Z.; Xie, Z.; Kim, M. J.; Xia, Y. *ACS Nano* **2012**, *6*, (3), 2566-2573.

108. Luo, Z.; Ibáñez, M.; Antolín, A. M.; Genç, A.; Shavel, A.; Contreras, S.; Medina, F.; Arbiol, J.; Cabot, A. *Langmuir* **2015**, *31*, (13), 3952-3957.
109. Nagao, A.; Higashimine, K.; Cuya Huaman, J. L.; Iwamoto, T.; Matsumoto, T.; Inoue, Y.; Maenosono, S.; Miyamura, H.; Jeyadevan, B. *Nanoscale* **2015**, *7*, (21), 9927-9934.
110. Wu, J.; Gross, A.; Yang, H. *Nano Lett.* **2011**, *11*, (2), 798-802.
111. He, D. S.; He, D.; Wang, J.; Lin, Y.; Yin, P.; Hong, X.; Wu, Y.; Li, Y. *J. Am. Chem. Soc.* **2016**, *138*, (5), 1494-1497.
112. Shi, L.; Wang, A.; Zhang, T.; Zhang, B.; Su, D.; Li, H.; Song, Y. *J. Phys. Chem. C* **2013**, *117*, (24), 12526-12536.
113. Fu, H.; Yang, X.; Jiang, X.; Yu, A. *Langmuir* **2013**, *29*, (23), 7134-7142.
114. Wang, L.; Yamauchi, Y. *J. Am. Chem. Soc.* **2013**, *135*, (45), 16762-16765.
115. Liu, X.; Wang, W.; Li, H.; Li, L.; Zhou, G.; Yu, R.; Wang, D.; Li, Y. *Sci. Rep.* **2013**, *3*, 1404.
116. De Clercq, A.; Margeat, O.; Sitja, G.; Henry, C. R.; Giorgio, S. *J. Catal.* **2016**, *336*, 33-40.
117. Kobayashi, H.; Lim, B.; Wang, J.; Camargo, P. H. C.; Yu, T.; Kim, M. J.; Xia, Y. *Chem. Phys. Lett.* **2010**, *494*, (4-6), 249-254.
118. Zhang, H.; Li, W.; Jin, M.; Zeng, J.; Yu, T.; Yang, D.; Xia, Y. *Nano Lett.* **2011**, *11*, (2), 898-903.
119. Ye, F.; Liu, H.; Hu, W.; Zhong, J.; Chen, Y.; Cao, H.; Yang, J. *Dalton Trans.* **2012**, *41*, (10), 2898-2903.
120. Zhang, H.; Jin, M.; Wang, J.; Li, W.; Camargo, P. H. C.; Kim, M. J.; Yang, D.; Xie, Z.; Xia, Y. *J. Am. Chem. Soc.* **2011**, *133*, (15), 6078-6089.
121. Yin, Z.; Zhou, W.; Gao, Y.; Ma, D.; Kiely, C. J.; Bao, X. *Chem. Eur. J.* **2012**, *18*, (16), 4887-4893.
122. Zalineeva, A.; Serov, A.; Padilla, M.; Martinez, U.; Artyushkova, K.; Baranton, S.; Coutanceau, C.; Atanassov, P. B. *J. Am. Chem. Soc.* **2014**, *136*, (10), 3937-3945.
123. Hosseini, H.; Mahyari, M.; Bagheri, A.; Shaabani, A. *J. Power Sources* **2014**, *247*, 70-77.
124. Liu, X.; Li, X.; Wang, D.; Yu, R.; Cui, Y.; Peng, Q.; Li, Y. *Chem. Commun.* **2012**, *48*, (11), 1683-1685.
125. Freakley, S. J.; He, Q.; Harrhy, J. H.; Lu, L.; Crole, D. A.; Morgan, D. J.; Ntainjua, E. N.; Edwards, J. K.; Carley, A. F.; Borisevich, A. Y.; Kiely, C. J.; Hutchings, G. J. *Science* **2016**, *351*, (6276), 965-968.

126. Du, W.; Mackenzie, K. E.; Milano, D. F.; Deskins, N. A.; Su, D.; Teng, X. *ACS Catal.* **2012**, *2*, (2), 287-297.
127. Teitelboim, A.; Oron, D. *ACS Nano* **2016**, *10*, (1), 446-452.
128. Tang, H.; Wei, J.; Liu, F.; Qiao, B.; Pan, X.; Li, L.; Liu, J.; Wang, J.; Zhang, T. *J. Am. Chem. Soc.* **2016**, *138*, (1), 56-59.
129. Read, C. G.; Gordon, T. R.; Hodges, J. M.; Schaak, R. E. *J. Am. Chem. Soc.* **2015**, *137*, (39), 12514-12517.
130. Qu, J.; Ye, F.; Chen, D.; Feng, Y.; Yao, Q.; Liu, H.; Xie, J.; Yang, J. *Adv. Colloid Interface Sci.* **2016**, *230*, 29-53.
131. Day, R. W.; Mankin, M. N.; Lieber, C. M. *Nano Lett.* **2016**, *16*, (4), 2830-2836.
132. Huang, Q.; Li, W.; Lin, Q.; Pi, D.; Hu, C.; Shao, C.; Zhang, H. *Chin. J. Catal.* **2016**, *37*, (5), 681-691.
133. Zhang, Z.-c.; Xu, B.; Wang, X. *Chem. Soc. Rev.* **2014**, *43*, (22), 7870-7886.
134. Benelmekki, M., *Designing Hybrid Nanoparticles*. Morgan & Claypool Publishers: 2015.
135. Buck, M. R.; Schaak, R. E. *Angew. Chem. Int. Ed.* **2013**, *52*, (24), 6154-6178.
136. Costi, R.; Saunders, A. E.; Banin, U. *Angew. Chem. Int. Ed.* **2010**, *49*, (29), 4878-4897.
137. Yue, Z.; Cai, B.; Wang, L.; Wang, X.; Gu, M. *Sci. Adv.* **2016**, *2*, (3).
138. Liu, R.; Priestley, R. D. *J. Mater. Chem. A* **2016**, *4*, (18), 6680-6692.
139. Zhong, C. J.; Maye, M. M. *Adv. Mater.* **2001**, *13*, (19), 1507-1511.
140. Li, Z.; Li, M.; Bian, Z.; Kathiraser, Y.; Kawi, S. *Appl. Catal., B* **2016**, *188*, 324-341.
141. Yang, H. *Angew. Chem. Int. Ed.* **2011**, *50*, (12), 2674-2676.
142. Li, Q.; Yuan, Y.; Chen, Z.; Jin, X.; Wei, T.-h.; Li, Y.; Qin, Y.; Sun, W. *ACS Appl. Mat. Interfaces* **2014**, *6*, (15), 12798-12807.
143. Sanchez, C.; Belleville, P.; Popall, M.; Nicole, L. *Chem. Soc. Rev.* **2011**, *40*, (2), 696-753.
144. Lohse, S. E.; Murphy, C. J. *J. Am. Chem. Soc.* **2012**, *134*, (38), 15607-15620.
145. Wu, K.; Sun, L.-D.; Yan, C.-H. *Adv. Energy Mater.* **2016**, n/a-n/a.
146. Gawande, M. B.; Goswami, A.; Asefa, T.; Guo, H.; Biradar, A. V.; Peng, D.-L.; Zboril, R.; Varma, R. S. *Chem. Soc. Rev.* **2015**, *44*, (21), 7540-7590.

147. Long, N. V.; Yang, Y.; Minh Thi, C.; Minh, N. V.; Cao, Y.; Nogami, M. *Nano Energy* **2013**, 2, (5), 636-676.
148. Schaak, R. E. *J. Solid State Chem.* **2008**, 181, (7), 1507-1508.
149. Vasquez, Y.; Henkes, A. E.; Chris Bauer, J.; Schaak, R. E. *J. Solid State Chem.* **2008**, 181, (7), 1509-1523.
150. Banin, U.; Ben-Shahar, Y.; Vinokurov, K. *Chem. Mater.* **2014**, 26, (1), 97-110.
151. Sytnyk, M.; Kirchsclager, R.; Bodnarchuk, M. I.; Primetzhofer, D.; Kriegner, D.; Enser, H.; Stangl, J.; Bauer, P.; Voith, M.; Hassel, A. W.; Krumeich, F.; Ludwig, F.; Meingast, A.; Kothleitner, G.; Kovalenko, M. V.; Heiss, W. *Nano Lett.* **2013**, 13, (2), 586-93.
152. Wark, S. E.; Hsia, C.-H.; Son, D. H. *J. Am. Chem. Soc.* **2008**, 130, (29), 9550-9555.
153. Casavola, M.; van Huis, M. A.; Bals, S.; Lambert, K.; Hens, Z.; Vanmaekelbergh, D. *Chem. Mater.* **2012**, 24, (2), 294-302.
154. Zhao, H.; Chaker, M.; Wu, N.; Ma, D. *J. Mater. Chem.* **2011**, 21, (24), 8898-8904.
155. Kovalenko, M. V.; Schaller, R. D.; Jarzab, D.; Loi, M. A.; Talapin, D. V. *J. Am. Chem. Soc.* **2012**, 134, (5), 2457-2460.
156. Justo, Y.; Goris, B.; Kamal, J. S.; Geiregat, P.; Bals, S.; Hens, Z. *J. Am. Chem. Soc.* **2012**, 134, (12), 5484-5487.
157. Zhou, H. S.; Sasahara, H.; Honma, I.; Komiyama, H.; Haus, J. W. *Chem. Mater.* **1994**, 6, (9), 1534-1541.
158. Mews, A.; Eychmueller, A.; Giersig, M.; Schooss, D.; Weller, H. *J. Phys. Chem.* **1994**, 98, (3), 934-941.
159. Zhang, D.; Wong, A. B.; Yu, Y.; Brittman, S.; Sun, J.; Fu, A.; Beberwyck, B.; Alivisatos, A. P.; Yang, P. *J. Am. Chem. Soc.* **2014**, 136, (50), 17430-17433.
160. Park, J.; Kim, S.-W. *J. Mater. Chem.* **2011**, 21, (11), 3745-3750.
161. Wang, X.; Liu, X.; Zhu, D.; Swihart, M. T. *Nanoscale* **2014**, 6, (15), 8852-8857.
162. Ha, D.-H.; Caldwell, A. H.; Ward, M. J.; Honrao, S.; Mathew, K.; Hovden, R.; Koker, M. K. A.; Muller, D. A.; Hennig, R. G.; Robinson, R. D. *Nano Lett.* **2014**, 14, (12), 7090-7099.
163. Lee, S.; Baek, S.; Park, J. P.; Park, J. H.; Hwang, D. Y.; Kwak, S. K.; Kim, S.-W. *Chem. Mater.* **2016**, 28, (10), 3337-3344.

164. Jeong, S.; Han, J. H.; Jang, J.-t.; Seo, J.-w.; Kim, J.-G.; Cheon, J. *J. Am. Chem. Soc.* **2011**, 133, (37), 14500-14503.
165. Dong, C.; Korinek, A.; Blasiak, B.; Tomanek, B.; van Veggel, F. C. J. M. *Chem. Mater.* **2012**, 24, (7), 1297-1305.
166. Lambert, K.; Geyter, B. D.; Moreels, I.; Hens, Z. *Chem. Mater.* **2009**, 21, (5), 778-780.
167. Tu, R.; Xie, Y.; Bertoni, G.; Lak, A.; Gaspari, R.; Rapallo, A.; Cavalli, A.; Trizio, L. D.; Manna, L. *J. Am. Chem. Soc.* **2016**.
168. McDaniel, H.; Fuke, N.; Pietryga, J. M.; Klimov, V. I. *J. Phys. Chem. Lett.* **2013**, 4, (3), 355-361.
169. Bouet, C.; Laufer, D.; Mahler, B.; Nadal, B.; Heuclin, H.; Pedetti, S.; Patriarche, G.; Dubertret, B. *Chem. Mater.* **2014**, 26, (9), 3002-3008.
170. Jain, P. K.; Beberwyck, B. J.; Fong, L.-K.; Polking, M. J.; Alivisatos, A. P. *Angew. Chem. Int. Ed.* **2012**, 51, (10), 2387-2390.
171. Jain, P. K.; Amirav, L.; Aloni, S.; Alivisatos, A. P. *J. Am. Chem. Soc.* **2010**, 132, (29), 9997-9999.
172. Li, H.; Brescia, R.; Krahne, R.; Bertoni, G.; Alcocer, M. J. P.; D'Andrea, C.; Scotognella, F.; Tassone, F.; Zanella, M.; De Giorgi, M.; Manna, L. *ACS Nano* **2012**, 6, (2), 1637-1647.
173. Lambright, S.; Butaeva, E.; Razgoniaeva, N.; Hopkins, T.; Smith, B.; Perera, D.; Corbin, J.; Khon, E.; Thomas, R.; Moroz, P.; Mereshchenko, A.; Tarnovsky, A.; Zamkov, M. *ACS Nano* **2014**, 8, (1), 352-361.
174. Jeong, U.; Kim, J.-U.; Xia, Y.; Li, Z.-Y. *Nano Lett.* **2005**, 5, (5), 937-942.
175. Camargo, P. H. C.; Lee, Y. H.; Jeong, U.; Zou, Z.; Xia, Y. *Langmuir* **2007**, 23, (6), 2985-2992.
176. Zhang, J.; Tang, Y.; Lee, K.; Ouyang, M. *Science* **2010**, 327, (5973), 1634-1638.
177. Zhuang, Z.; Sheng, W.; Yan, Y. *Adv. Mater.* **2014**, 26, (23), 3950-3955.
178. Guo, S.; Zhang, S.; Su, D.; Sun, S. *J. Am. Chem. Soc.* **2013**, 135, (37), 13879-13884.
179. Nong, H. N.; Gan, L.; Willinger, E.; Teschner, D.; Strasser, P. *Chem. Sci.* **2014**, 5, (8), 2955-2963.
180. Hu, H.; Guan, B.; Xia, B.; Lou, X. W. *J. Am. Chem. Soc.* **2015**, 137, (16), 5590-5.

Curriculum Vitae

Personal Data

Name: Luo Zhishan

M/F: Male

Date of Birth: 03/01/1986

Nationality: People's Republic of China

Address: Jardins de les Dones de Negre, 1, 2^a pl., 08930 Sant Adrià de Besòs,

Barcelona, Spain

Phone: +34 675613590

E-mail: sm3536036@gmail.com



Academic Background

Education

- Bachelor of Science (2005-2009)
 - Major: Light Chemical Engineering
 - Tianjin Polytechnic University
- Master of Science (2009-2012)
 - Major: Applied Chemistry
 - East China University of Science and Technology.
- PhD of Science
 - Major: Nanoscience
 - University of Barcelona

Research Interests

- Specialized in the preparation of functionalized inorganic nanocrystals, multi-step synthesis, purification and characterization of various types of inorganic compounds and good at anhydrous, anaerobic operation.

- Skilled in X-ray powder diffraction (XRD), transition electronic microscopy (TEM) and scanning electron microscope (SEM) for structural characterization of nanomaterials; Fluorescence, IR, UV, CV spectroscopy for solution sample characterization.

Research Interests

Synthesis of heterostructured nanoparticles: Solution phase synthesis, structural and spectroscopic characterization. General aspects of nucleation and growth of nanometer sized heterostructured nanoparticles to control size, morphology and composition.

Energy-related applications of nanomaterials: Application of heterostructured nanoparticles in photovoltaic and thermoelectric devices, photo- and electrocatalyst. In particular, focus on the development of new nanocatalyst based on colloidal nanocrystals for photo- and electrocatalytic application, such as water splitting (oxygen/hydrogen evolution reaction), CO₂ reduction, oxygen reduction reaction etc.

Research Experience

Sep. 2009~ Mar. 2012 Graduate Research

Supervisor: Prof. Xinhua Zhong

Projects include: Synthesis of high quality semiconductor nanocrystals in aqueous phase and their application Synthesis of water-soluble AgInS₂ and ZnS-AgInS₂ composite nanocrystals using the ligand of glutathione (GSH) as capping agent in aqueous phase. The nanocomposites show promising photocatalytic activity in degrading Rhodamine B (RhB).

Sep. 2012~ present PhD research

Supervisor: Prof. Andreu Cabot and Dr. Maria Ibáñez

Project: Rational design of nanocatalysts for sustainable energy production.

Designation of multicomponent nanocatalysts for heterogeneous photo- and electrocatalyst. In the 4 years, I focus on the development of new nanocatalyst based on colloidal nanocrystals. In this regard I have been working on different systems: Pd₂Sn and Au-Pd₂Sn, CZTS and CZTS-Ag₂S, transition metal oxide heterostructured nanoparticles, such as Mn₃O₄@CoMn₂O₄-Co_xO_y, Fe₃O₄-Ni_xFe_{3-x}O₄, Fe@FeO_x-Mn₃O₄ etc.

Publications List

1. **Luo, Z.;** Zhang, H.; Huang, J.; Zhong, X. H. One-Step Synthesis of Water-Soluble AgInS₂ and ZnS-AgInS₂ Composite Nanocrystals and Their Photocatalytic Activities. *J. Colloid Interface Sci.* 2012, 377, 27–33

2. **Luo, Z.**; Ibáñez, M.; Antolín, A. M.; Genç, A., Shavel, A.; Contreras, S.; Medina, F.; Arbiol, J.; Cabot, A. Size and Aspect Ratio Control of Pd₂Sn Nanorods and Their Water Denitration Properties. *Langmuir* 2015, 31, 3952-3957.
3. **Luo, Z.**; Irtem, E.; Ibáñez, M.; Nafria, R.; Marti, S.; Genç, A.; Mata, M.; Liu, Y.; Cadavid, D.; Llorca, J.; Arbiol, J.; Andreu, T.; Morante, J. R.; Andreu, C. Mn₃O₄@CoMn₂O₄-Co_xO_y Nanoparticles: Partial Cation Exchange Synthesis and Electrocatalytic Properties Toward the Oxygen Reduction and Evolution Reactions. *ACS Appl. Mater. Interface*. 2016, 8, 17435-17444.
4. **Luo, Z.**; Marti, S.; Joshua, G.; Mata, M.; Nafria, R.; Guardia, P.; Boubeta, C.; Simeonidis, K.; Llorca, J.; Arbiol, J.; Ibáñez, M.; Cabot, A. Fe₃O₄@NiFe_xO_y Nanoparticles with Enhanced Electrocatalytic Properties for Oxygen Evolution in Carbonate Electrolyte. *ACS Appl. Mater. Interfaces*. 2016. Accepted.
5. **Luo, Z.**; Lu, J.; Flox, C.; Nafria, R.; Genç, A.; Arbiol, J.; Llorca, J.; Ibáñez, M.; Morante, J. R.; Cabot, A. Pd₂Sn [010] Nanorods as a Highly Active and Stable Ethanol Oxidation Catalyst. *Journal of Materials Chemistry A*. Major corrections required (under second round review).
6. Nafria, R.;(†) **Luo, Z.**;(†) Ibáñez, M.; Marti, S.; Mata, M.; Llorca, J.; Arbiol, J.; Kovalenko, M. V.; Grabulosa, A.; Muller, G.; Cabot, A. Pd₂Sn and Au-Pd₂Sn Nanorods in Catalytic Hydrogenation and Sonogashira Coupling Reactions. (submitted) (Equal authors).
7. Ibáñez, M.; **Luo, Z.**; Genç, A.; Piveteau, L.; Ortega, S.; Cadavid, D.; Dobrozhan, O.; Liu, Y.; Nachtegaal, M.; Zebarjadi, M.; Arbiol, J.; Kovalenko, M. V.; Cabot, A. High-Performance Thermoelectric Nanocomposites from Nanocrystal Building Blocks. *Nat. Commun.* 2016, 7, 10766. DOI: 10.1038/ncomms10766.
8. Yu, X.; Shavel, A.; An, X.; **Luo, Z.**; Ibáñez, M.; Cabot, A. Cu₂ZnSnS₄-Pt and Cu₂ZnSnS₄-Au Heterostructured Nanoparticles for Photocatalytic Water Splitting and Pollutant Degradation. *J. Am. Chem. Soc.* 2014, 136, 9236-9239.
9. Ibáñez, M.; Korkosz, R. J.; **Luo, Z.**; Riba, P.; Cadavid, D.; Ortega, S.; Cabot, A.; Kanatzidis, M. G. Electron Doping in Bottom-Up Engineered Thermoelectric Nanomaterials through HCl-Mediated Ligand Displacement. *J. Am. Chem. Soc.* 2015, 137, 4046-4049.
10. Shavel, A.; Ibáñez, M.; **Luo, Z.**; De Roo, J.; Carrete, A.; Dimitrievska, M.; Genç, A.; Meyns, M.; Pérez-Rodríguez, A.; Kovalenko, M. V.; Arbiol, J.; Cabot, A. Scalable Heating-Up Synthesis of Monodisperse Cu₂ZnSnS₄ Nanocrystals. *Chem. Mater.* 2016, 28(3), 720-726.
11. Yu, X.; Wang, D.; Liu, J.; **Luo, Z.**; Du, R.; Liu, L-M.; Zhang, G.; Zhang, Y.; Cabot, A. Cu₂ZnSnS₄ Nanocrystals as Highly Active and Stable Electrocatalysts for the Oxygen Reduction Reaction. (submitted)

12. Yu, X.; Liu, J.; Genç, A.; Ibáñez, M.; **Luo, Z.**; Shavel, A.; Arbiol, J.; Zhang, G.; Zhang, Y.; Cabot, A. Cu₂ZnSnS₄-Ag₂S Nanoscale p-n Heterostructures as Sensitizers for Photoelectrochemical Water Splitting. *Langmuir* 2015, 31 (38), 10555-10561.

13. Zheng, Z.; Gu, Z.; Huo, R.; **Luo, Z.** Fabrication of Self-cleaning Poly(vinylidene fluoride) Membrane with Micro/nanoscaled Two-tier Roughness. *J. Appl. Polym. Sci.* 2011, 1268-1274.

Under list is preparation for submission

1. Fe@FeO_x-Mn₃O₄ Heterostructured Nanoparticles: Size and Composition Control, and Their Electrocatalytic Properties

2. A General Strategy for Hollow Metal Oxide Heterostructured Nanoparticles

3. Intermetallic NiSn Nanocrystals as a Non-precious Metal Electrocatalyst for Ethanol Oxidation

4. The Effect of the Co₃O₄ Core on the Oxygen Evolution Reaction of Co₃O₄@Mn₃O₄ Core-shell Nanoparticles

Conference and seminars

1. **Luo, Z.**; Zhong, X.; Cabot, A. AuPt/carbon Alloy Nanoparticles Electrocatalysts for Formic Acid Oxidation. EMRS Spring meeting, 2013. Strasbourg, France

2. Ibáñez, M.; **Luo, Z.**; Genç, A.; Piveteau, L.; Ortega, S.; Cadavid, D.; Dobrozhan, O.; Liu, Y.; Nachtegaal, M.; Zebarjadi, M.; Arbiol, J.; Kovalenko, M. V.; Cabot, A. High-Performance Thermoelectric Nanocomposites from Nanocrystal Building Blocks. The 35th International Conference & The 1st Asia Conference on Thermoelectrics ICT/ACT, 2016. Wuhan, China